Measurements of the mass and width of the W-boson, and test of lepton universality in W-boson decays with the ATLAS detector

Dissertation
zur
Erlangung des Doktorgrades (Dr. rer. nat.)
der
Mathematisch-Naturwissenschaftlichen Fakultät
der
Rheinischen Friedrich-Wilhelms-Universität Bonn

von
Philipp Thomas König
aus
Andernach

Bonn, April 2022

Angefertigt mit Genehmigung der Mathematisch-Naturwissenschaftlichen Fakultät der Rheinischen Friedrich-Wilhelms-Universität Bonn

1. Gutachter:	Prof. Dr. Klaus Desch
2. Gutachter:	Prof. Dr. Ian C. Brock
Tag der Promotion:	09.02.2023
Erscheinungsjahr:	2023

Abstract

The Standard Model of particle physics serves as the predominant theory of the microscopic world for many decades. Many discoveries have been predicted by this model and it still provides a good fit for a wide variety of measurements. The W-boson is the charged massive mediator of the weak force, one out of three elementary forces which can be described by a quantum field theory. The discovery of the Higgs boson in 2012 was the final piece in the puzzle of the Standard Model to explain the masses of massive bosons via the Higgs mechanism. Since its discovery in 1983, many properties of the W-boson have been studied quite intensively. Measurements of the W-boson mass and width are crucial to test the overall consistency of the Standard Model and constrain other parameters. A newly published measurement by the CDF collaboration doubts that the Standard Model can fully explain the W-boson mass as it is in clear tension with the predicted value and all other experimental measurements.

The presented thesis revisits and extends the W-boson mass measurement published by the ATLAS collaboration in 2017 based on data provided by the Large Hadron Collider in 2011 with a centre-of-mass energy of $\sqrt{s} = 7\,\text{TeV}$ and an integrated luminosity of $\mathcal{L}_{\text{int}} = 4.59\,\text{fb}^{-1}$. The main improvements are an enhanced fit methodology, an advanced background determination, and the treatment and incorporation of systematic uncertainties. This thesis presents a new measurement of the W-boson mass of $m_W = (80\,354.7 \pm 15.7)\,\text{MeV}$, where the total uncertainty is reduced by more than 10 % compared to the 2017 analysis. The discrepancy with the measurement by the CDF collaboration remains an open issue for further studies. Beyond that, the first measurement of the W-boson width, Γ_W, by the ATLAS collaboration is added. The result of $\Gamma_W = (2\,154 \pm 48)\,\text{MeV}$ is the most precise single measurement so far and is still in agreement with the Standard Model prediction. Lastly, the lepton universality in the W-boson decay, $R_{\tau\ell}$, is measured to $R_{\tau\ell} = 0.96 \pm 0.11$ by comparing the branching ratios of tau lepton decays to those to electrons or muons.

Contents

CHAPTER 1

The fascination with particle physics

ἓν ἕκαστον μὲν τοῦ γένους ἑκάστου διὰ σμικρότητα οὐδὲν ὁρώμενον ὑφ᾽ ἡμῶν, συναθροισθέντων δὲ πολλῶν τοὺς ὄγκους αὐτῶν ὁρᾶσθαι: καὶ δὴ καὶ τὸ τῶν ἀναλογιῶν περί τε τὰ πλήθη καὶ τὰς κινήσεις καὶ τὰς ἄλλας δυνάμεις πανταχῇ τὸν θεόν, ὅπηπερ ἡ τῆς ἀνάγκης ἑκοῦσα πεισθεῖσά τε φύσις ὑπεῖκεν, ταύτῃ πάντῃ δι᾽ ἀκριβείας ἀποτελεσθεισῶν ὑπ᾽ αὐτοῦ συνηρμόσθαι ταῦτα ἀνὰ λόγον.

When taken singly each in its several kinds, is seen by us, but when many are collected together their masses are seen. And, moreover, as regards the numerical proportions which govern their masses and motions and their other qualities, we must conceive that God realized these everywhere with exactness, in so far as the nature of necessity submitted voluntarily or under persuasion, and thus ordered all in harmonious proportion.

Plato, Timaeus, section 56c [1].

Science, as we know it today, started in the times of the ancient Greeks. Nowadays, pupils around the globe still learn Pythagoras' theorem. Many renowned personalities famous for their great research were known as philosophers as well. The list of universal geniuses whose legacy is still known seems to be endless: Pythagoras of Samos, Democritus, Platon, Pliny the Elder, Leonardo da Vinci, Isaac Newton, Gottfried Wilhelm Leibniz, Alexander von Humboldt, and many more. They all aimed to describe Nature in all its fundamental components and mechanisms. A model has to meet two requirements: On the one hand, it must be able to prepare the foundations of understanding all the phenomena that have been observed so far. On the other hand, it should forecast new observations following the predictions of the model. Each theory is just a picture trying to describe the world we live in. Some theories are more accurate than others but none is so far perfect. Over time, humanity evolved a more and more complete picture of our world and everything surrounding us. It is a natural desire driving researchers and their curiosity to push the limit of the known a bit further.

In the 19^{th} century, science and philosophy split up because both groups of themes became more and more complex. The profundity of topics intensified and could not be overseen by a single person anymore. In the second half of the 20^{th} century, the concept of modern particle physics evolved from quantum and relativistic descriptions of individual phenomena into one common based quantum-field theory of the entire known microscopic world: the Standard Model of particle physics. Even more than 50 years later, this theory is still the keystone and state of the art theory. It characterises all elementary particles and their interactions. The Standard Model was able to describe observations

that have been made before its inception but to predict in addition the existence of new particles and phenomena. The interplay between theoretical predictions and experimental observations encouraged the progress in particle physics.

The construction of particle accelerators was the main accomplishment on the experimental side to reveal the building blocks of matter. Amongst many other institutes in the world, the European organisation for nuclear research, CERN, operated successfully many accelerators. The UA1 and UA2 collaborations discovered the W-boson and the Z-boson in 1983 in proton-antiproton collisions ibidem. Parts of this machine still serve as a pre-accelerator for the Large Hadron Collider. It marks the best performance of an accelerator in terms of length and collision energy down to the present day. Since 2008, a high number of protons have been smashed in bunches at four different collision points around which the same number of particle detectors record the outcome. The ATLAS detector is the largest of the four experiments and recorded the data used in this thesis in 2011.

Since its discovery in the 1980s, the properties mass, width, and lepton universality of the W-boson have been measured several times. A new set of measurements will be added in this thesis. The Large Hadron Collider provides good conditions for this purpose as it can be considered as a "W factory": It produces on average 1 000 W-bosons per second given a centre-of-mass energy of $\sqrt{s} = 7\,\text{TeV}$ and the designed instantaneous peak luminosity. The resulting kinematic distributions of the W-boson decay products recorded by the detector allow to achieve an unprecedented precision. Improving the accuracy of the measurements increases the sensitivity to tiny deviations between the prediction of the theory and reality. Hence, this thesis will contribute to testing the overall consistency of the Standard Model.

This thesis is structured as follows: Chapter 2 describes the theoretical foundations. The Standard Model is introduced including all needed quantum field theories and the Higgs-Brout-Englert mechanism giving mass to elementary particles. Furthermore, the deficiencies of the Standard Model are covered. A dedicated focus will be put on the Standard Model predictions of the W-boson and its measured properties. In Chapter 3, the experimental setup consisting of the Large Hadron Collider and the ATLAS detector is presented in detail. The presented analysis of the W-boson properties stands in the tradition of many predecessor measurements outlined in Chapter 4. In particular, this thesis is based on the W-boson mass measurement by the ATLAS collaboration published in 2017. Furthermore, the connection of the fitted kinematic observables to the W-boson mass is drawn presenting step by step influences of theoretical and experimental considerations. The analysis design including the signature of signal and background processes and the event selection is given in Chapter 5. The intermediate steps are compared to the results of the reference measurement. An emphasis is put on the estimation of the multijet background. Chapter 6 depicts the statistical essentials of the two used fit methods, the χ^2 fit and the profile likelihood fit. It characterises differences in the basic concepts and the way uncertainties are treated. The calibration of physical objects accompanied by systematic uncertainties and the physics modelling are outlined in Chapter 7. Finally, the fit setup and the results of the three individual measurements of W-boson properties are presented in Chapter 8. The thesis closes with a summary and an outlook in Chapter 9.

CHAPTER 2

The theoretical foundations

In this chapter, the theoretical foundation necessary to understand the measurements performed will be laid out. The Standard Model (SM) [2–4] of particle physics is introduced as the theory still represents the state of research. The SM Lagrangian is described and a mass giving mechanism to the elementary particles is explained. A focus will be on the properties of the W-boson being the headliner of this thesis. The information of this chapter is mainly taken from [5–7].

2.1 The particle content of the Standard Model

The SM of particle physics is a successful quantum field theory describing fermionic matter and bosonic messenger particles. Being developed in the 1960s, it was able to predict the observation of new particles and is still in agreement with almost all of the measurements taken in the context of the SM properties. Its particle content can be summarised in one picture displayed in Fig. 2.1.

The *fermions* with spin $\frac{1}{2}$ are the matter particles with twelve different appearances grouped in three different families or generations. The first generation explains our everyday matter. Protons and neutrons, the nucleons in the atomic core, are made of up (u) and down quarks (d). The total charge is the sum of the individual charges of the quarks, e.g. $q_{\text{Proton}} = +\frac{2}{3} + \frac{2}{3} - \frac{1}{3} = +1$ for the proton[1]. The quarks obey all fundamental forces of the SM but are the only particles taking part in the strong interaction and carry a colour charge. In addition to the quarks, each family encloses a charged and a chargeless lepton. The electrons (e^-), the charged leptons of the first generation, spin around the atomic core with the same number as protons being in the core. Hence, the atom is electrically neutral. The chargeless electron neutrino ν_e is only weakly interacting. The second and third generations of the fermions are heavier copies of the first generation.

The masses in Fig. 2.1 are given in natural units with the convention

$$\hbar = c = 1. \tag{2.1}$$

Using Eq. (2.1), the quantities' energy, momentum, mass, inverse time, and inverse length can be

[1] Bound states of three quarks are called *baryons*.

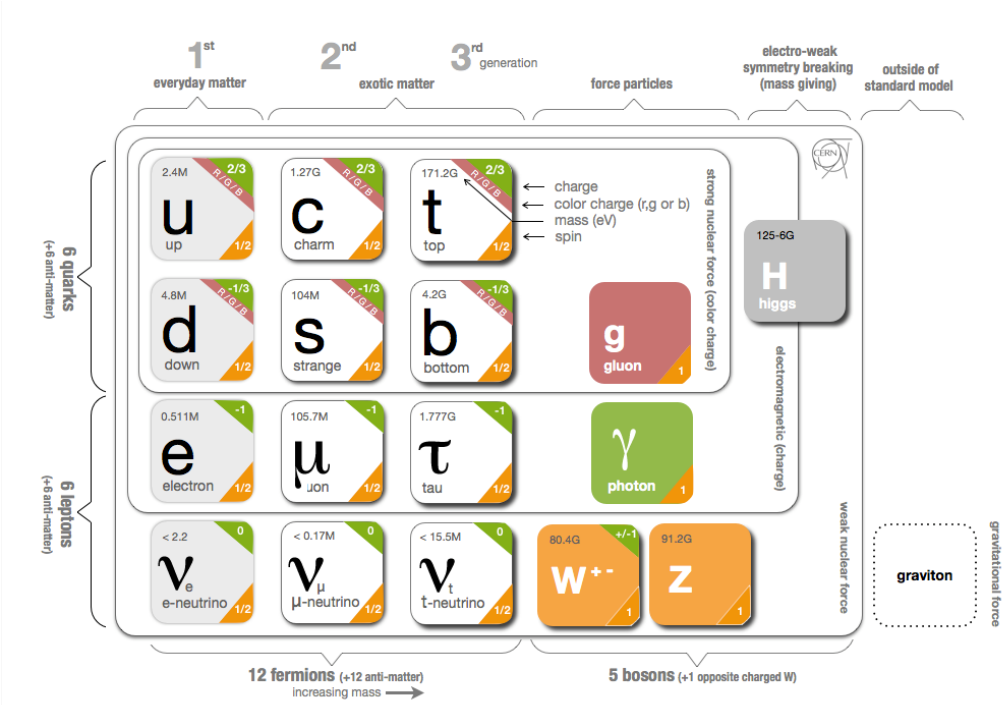

Figure 2.1: Overview of the SM and its particle content. Shown are the 12 fermions grouped in three families and the 5 bosons which are the force particles. The Higgs-boson gives masses to the particles of the SM (taken from [8]).

measured in units of eV (electronvolt)

$$[E] = [p] = [m] = \left[\frac{1}{t}\right] = \left[\frac{1}{l}\right] = \text{eV}.$$

Not only units of quantities are simplified, but in addition, important equations like the relativistic energy-momentum-mass relation take the easy form

$$E^2 = \mathbf{p}^2 + m^2. \tag{2.2}$$

By using operator substitution in Eq. (2.2) and the D'Alembertian operator $\Box^2\phi = -\frac{\partial^2\phi}{\partial t^2} + \nabla^2\phi$ one gets the Klein-Gordon equation[2]

$$\left(\Box^2 - m^2\right)\phi = 0. \tag{2.3}$$

Equation (2.3) has two solutions: positive energy solutions representing the particles and negative energy solutions which can be interpreted as antiparticles. Each particle of the fermionic sector

[2] Equation (2.3) could be called the relativistic Schrödinger equation, with the non-relativistic time-dependent Schrödinger equation being $i\frac{\partial\phi}{\partial t} = -\frac{1}{2m}\frac{\partial^2\phi}{\partial x^2} + \hat{V}\phi$

of Fig. 2.1 receives an antiparticle representation having the same mass, but all additive quantum numbers have opposite signs.

The *bosons* having spin 1 are the interactions particles acting as mediators for the three fundamental forces of the SM. Gravity is not described within the context of the SM and is negligible at the discussed scales compared to the other forces. The gluon g is the carrier of the strong force, the photon γ the mediator of the electromagnetic force, and the W- and Z-boson transfer the weak force. The Higgs-boson was discovered in 2012 by the ATLAS [9] and the CMS collaboration [10] at CERN. It is responsible to give mass not only to the massive bosons of the weak interaction but to the fermions of the SM as well. More of the underlying mechanism is explained in Section 2.3.2 [5, 6].

2.2 Composing the Standard Model Lagrangian

Symmetry principles are a key concept in theoretical physics. The connection between symmetries on the one hand and interactions and conservation laws on the other hand is discussed in the context of the Lagrange formalism. The Lagrange formalism extends the equation of motion (e.o.m.) of classical mechanics, Lagrange's equation, from discrete coordinates to a continuous system with continuously varying coordinates $\phi(\mathbf{x}, t)$. The following representations of a Lagrangian are important in the next chapters:

$$\mathscr{L}_{\text{scalar}} = \frac{1}{2}\left(\partial_\mu \phi\right)\left(\partial^\mu \phi\right) - \frac{1}{2}m^2\phi^2 \tag{2.4}$$

$$\mathscr{L}_{\text{spin-half}} = i\overline{\psi}\gamma^\mu \partial_\mu \psi - m\overline{\psi}\psi \tag{2.5}$$

$$\mathscr{L}_{\text{vector}} = -\frac{1}{4}F^{\mu\nu}F_{\mu\nu} - j^\mu A_\mu. \tag{2.6}$$

The Lagrangian of Eq. (2.4) with the scalar field ϕ describing spin-0 scalar particles satisfies the Klein-Gordon Eq. (2.3). Equation (2.5) satisfies the Dirac equation[3], where ψ is a spinor field and the four components of ψ and $\overline{\psi}$ are independent field variables. The Maxwell equation

$$\partial_\mu F^{\mu\nu} = j^\nu$$

follows from Eq. (2.6) where $F^{\mu\nu} = \partial^\mu A^\nu - \partial^\nu A^\mu$ is the field strength tensor, $A_\mu = (\phi, \mathbf{A})$ is the electromagnetic field, and $j^\nu = (\rho, \mathbf{J})$ the source of the field. In the Lagrange density, different terms represent different physical realisations:

- *Kinetic energy terms* can be identified by partial derivatives like $\frac{1}{2}\left(\partial_\mu \phi\right)\left(\partial^\mu \phi\right)$ for a scalar field, $i\overline{\psi}\gamma^\mu\partial_\mu\psi$ for a spin-$\frac{1}{2}$ field, and $\frac{1}{4}F^{\mu\nu}F_{\mu\nu}$ for a vector field.
- *Mass terms* are represented by a constant factor, which is proportional to the mass, multiplied with the square of a field, e.g. $m^2\phi^2$ (scalar field) or $m\overline{\psi}\psi$ (spin-$\frac{1}{2}$ field).
- *Interaction terms* are given by at least three fields (can be three times the same field) multiplied with a constant factor representing the vertex factor at the interaction point. An example for the

[3] The Dirac equation is $\left(i\gamma^\mu\partial_\mu - m\right)\psi = 0$.

interaction of the spin-$\frac{1}{2}$ field with the electromagnetic field A_μ is $e\overline{\psi}\gamma^\mu Q\psi A_\mu$, where $eQ\gamma^\mu$ is the vertex coupling.

In classical mechanics, the Noether theorem predicts a conservation law for every symmetry principle, e.g. the conservation of momentum follows from the invariance under translations. In the Lagrange formalism, the invariance of the Lagrangian under internal symmetry transformations is referred to as *global gauge invariance*.

2.2.1 The electroweak interaction

The electromagnetic interaction plays an important role in particle physics as it has only one gauge boson, the photon. Its quantum field theory is referred to as Quantum Electrodynamics (QED). It is used as an example to introduce the principle of gauge invariance. The weak interaction has the same physical description as the electromagnetic force resulting in the electroweak (EW) unification.

Quantum Electrodynamics

Only the mass term of $\mathscr{L}_{\text{spin-half}}$ in Eq. (2.5) is invariant under the local $U(1)_{\text{em}}$ gauge invariance

$$\psi(x) \rightarrow e^{iQ\alpha(x)}\psi(x), \tag{2.7}$$

where $\alpha(x)$ is an arbitrary function depending on space and time and Q is the generator of $U(1)_{\text{em}}$. To keep the kinetic energy term invariant as well, a modified derivative D_μ, called "covariant derivative", of the form

$$D_\mu \equiv \partial_\mu - ieQA_\mu,$$

with the gauge field A_μ transforming like $A_\mu \rightarrow A_\mu - \frac{1}{e}\partial_\mu\alpha(x)$, is introduced. For now, e is just a proportional factor, but its physical interpretation will become clear later. The gauge field A_μ cancels out unwanted terms appearing by applying the local $U(1)$ gauge invariance given in Eq. (2.7) in the kinetic term of $\mathscr{L}_{\text{spin-half}}$. To achieve the invariance of the Lagrangian as a whole, ∂_μ is replaced by the covariant derivative D_μ as defined in Section 2.2.1

$$\begin{aligned}\mathscr{L}_{\text{QED}} &= i\overline{\psi}\gamma^\mu D_\mu\psi - m\overline{\psi}\psi \\ &= \overline{\psi}\left(i\gamma^\mu\partial_\mu - m\right)\psi + e\overline{\psi}\gamma^\mu Q\psi A_\mu.\end{aligned} \tag{2.8}$$

The gauge field A_μ couples directly to the Dirac particle proportional to the electric charge of the particle, where e is the elementary charge and Q the eigenvalue, e.g. $Q = -1$ for the electron. To obtain a physical photon field, a kinetic energy term invariant under the local transformation of A_μ has to be added to Eq. (2.8) which is the gauge-invariant field strength tensor $F_{\mu\nu} = \partial_\mu A_\nu - \partial_\nu A_\mu$. This leads to the final Lagrangian of QED

$$\mathscr{L}_{\text{QED}} = \underbrace{\overline{\psi}\left(i\gamma^\mu\partial_\mu - m\right)\psi}_{\substack{\text{Kinetic energy and mass}\\ \text{of fermionic field}}} + \underbrace{e\overline{\psi}\gamma^\mu Q\psi A_\mu}_{\text{Interaction}} - \underbrace{\frac{1}{4}F_{\mu\nu}F^{\mu\nu}}_{\substack{\text{Kinetic energy of}\\ \text{photon field } A_\mu}}. \tag{2.9}$$

Equation (2.9) consists of several terms:

- the interaction between the fermionic field and the photon field, i.e. interaction between lepton, antilepton and photon, with coupling strength $ie\gamma^{\mu}$. An exemplary Feynman diagram[4] of this interaction is shown in Fig. 2.2(a).
- the kinetic energy and the mass of a fermionic field, which can be any of the charged leptons.
- the kinetic energy of the photon field.

Adding a mass term $\frac{1}{2}m^2 A_{\mu}A^{\mu}$ of the photon field A_{μ} to Eq. (2.9) is not invariant under the transformation Eq. (2.7) and hence breaks the gauge invariance. Therefore, the photon remains massless and the photon field A_{μ} has an infinite range.

The dominant contribution to a cross-section or a decay rate is given by the leading-order (LO) Feynman diagram. As shown in the tree-like graphs of the interaction between the photon and fermions in Fig. 2.2(a), the LO diagram has a minimal number of interaction vertices. Diagrams having exactly one more interaction are called next-to-leading-order (NLO) as shown in Figs. 2.2(b) and 2.2(c). Due to the additional interaction factor, the contribution to the overall matrix element is reduced by the additional vertex factor.

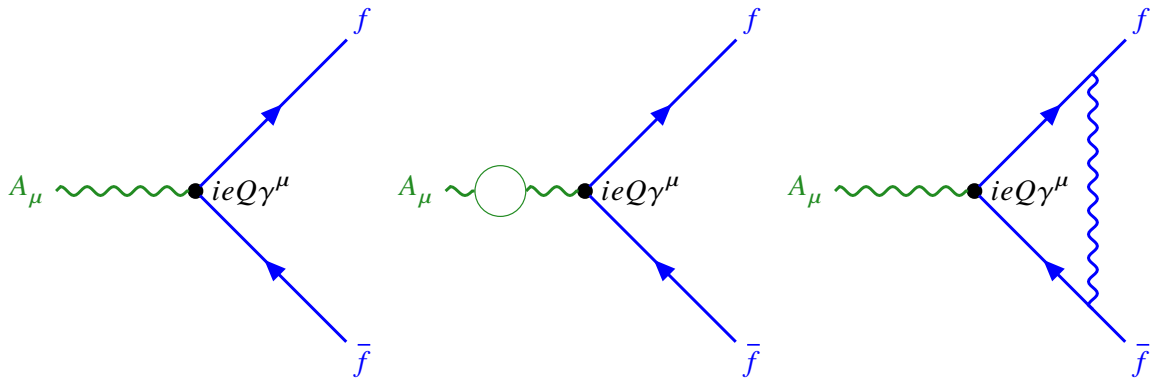

(a) LO process. (b) NLO propagator. (c) NLO vertex.

Figure 2.2: Exemplary interactions of the fermionic and the photon field in QED. The lepton f and antilepton $\bar{f}$ are shown in blue, whereas the photon field A_{μ} is displayed in green. $ieQ\gamma^{\mu}$ is the proportional factor at the interaction vertex. Figure (a) shows the LO representation, whereas figures (b) and (c) illustrate the NLO versions.

With this recipe, is it possible to construct higher-order diagrams. As it is a perturbation theory, each order is connected to a higher order of $\alpha\,(x)$ which is the constant of the expansion. The contribution to the overall matrix element becomes less significant with increasing order as $\alpha\,(x) < 1$ [5–7].

[4] Feynman diagrams are a graphical representation of the processes described in quantum field theories. As time runs from left to right, the left-hand side shows the initial state, whereas the right-hand side represents the final state. With a Feynman diagram it is possible to write down the matrix element of the described transition using the corresponding Feynman rules.

The electroweak unification

The weak interaction is another fundamental force of the SM realised in fusion processes in the core of the sun or radioactive decays. Measured long lifetimes in the decays of known particles like π^- and μ^- lead to the prediction of the existence of a new interaction of weak strength [5, 7]. From the Wu [11] and the Goldhaber experiment [12] it was known since the late 1950s that the weak interaction violates parity maximally[5]. The gauge bosons of the weak force only interact with left-handed particles or right-handed antiparticles. To split the particles of the SM into their chiral or handed projections, the chiral projection operators are used

$$P_R = \frac{1}{2}\left(1 + \gamma^5\right) \quad \text{and} \quad P_L = \frac{1}{2}\left(1 - \gamma^5\right),$$

where γ^5 is the fifth gamma matrix[6]. In the SM, all particles have a left-handed and a right-handed version except for the neutrino. The neutrino does not couple to any other force than the weak interaction and hence only appears in a left-handed particle or a right-handed antiparticle version. Left-handed particles are grouped into doubles, whereas right-handed particles are singlets

$$\begin{pmatrix} u \\ d \end{pmatrix}_L, \begin{pmatrix} \nu \\ e \end{pmatrix}_L = \chi_L \qquad \text{and} \qquad u_R,\ d_R,\ e_R = \psi_R. \tag{2.10}$$

Glasberg, Weinberg, and Salam developed a theory where the weak and the electromagnetic interaction can be described by one common quantum field theory known as the EW unification. The weak interaction only couples to left-handed particles and the generating $SU(2)_L$ algebra receives the subscript L. To incorporate QED, a symmetry group coupling to both chiralities of the particles is added as the electromagnetic interaction does not depend on the chirality of a particle. The generator of this algebra, the hypercharge operator Y, is obeying the Gell-Mann-Nishijima relation

$$Q = T_3 + \frac{Y}{2},$$

where Q is the charge operator of $U(1)_{\text{em}}$ which is replaced by the new $U(1)_Y$ gauge symmetry. T_3 is the third component of the weak isospin with $T_3 = \pm\frac{1}{2}$ for doublets and $T_3 = 0$ for singlets. Similar to QED and as explained in Section 2.2.1, the full Lagrangian of the EW unification has to be invariant under $SU(2)_L \times U(1)_Y$ gauge transformations. Therefore, a covariant derivative D_μ is being introduced to keep the Lagrangian invariant coming with four additional gauge fields

$$D_\mu = \partial_\mu + ig\boldsymbol{T} \cdot \boldsymbol{W}_\mu + ig'\frac{Y}{2}B_\mu.$$

The $\boldsymbol{T}$ are the generators of the $SU(2)$ algebra being in relation with the Pauli matrices $\left(\boldsymbol{T} = \frac{\sigma}{2}\right)$. g is the coupling constant and W^1_μ, W^2_μ and W^3_μ the three gauge fields corresponding to three gauge bosons of the $SU(2)_L$. For $U(1)_Y$, only one gauge field B_μ with the coupling constant g' is needed to keep the invariance of the Lagrangian. The unification of $SU(2)$ and $U(1)$ leads to the EW Lagrangian for

[5] Invariance under the parity operation is equivalent to point reflection at the origin, e.g. $\boldsymbol{x} \to -\boldsymbol{x}$. In quantum mechanics, this operation is performed by the parity operator $\hat{P}$ defined by $\hat{P}\psi(\boldsymbol{x}, t) = \psi(-\boldsymbol{x}, t)$.

[6] The fifth gamma matrix can be described with the following equation in the Dirac representation: $\gamma^5 = \begin{pmatrix} \mathbf{0}_2 & \mathbf{1}_2 \\ \mathbf{1}_2 & \mathbf{0}_2 \end{pmatrix}$.

a lepton-neutrino pair using the naming conventions defined in Eq. (2.10)

$$\begin{aligned}\mathscr{L}_{\mathrm{EW}} = &\underbrace{\bar{\chi_L}\gamma^\mu\left[i\partial_\mu - g\frac{\boldsymbol{\sigma}}{2}\boldsymbol{W_\mu} - g'\left(-\frac{1}{2}\right)B_\mu\right]\chi_L}_{\substack{\text{Kinetic energy of the left-handed leptonic fields}\\ \text{and interactions with gauge fields}}} + \underbrace{\bar{e_R}\gamma^\mu\left[i\partial_\mu - g'\,(-1)\,B_\mu\right]e_R}_{\substack{\text{Kinetic energy of the right-handed leptonic fields}\\ \text{and interactions with gauge fields}}} \\ &+ \underbrace{\frac{1}{4}\boldsymbol{W_{\mu\nu}}\boldsymbol{W^{\mu\nu}} - \frac{1}{4}B_{\mu\nu}B^{\mu\nu}}_{\text{Kinetic energy of the gauge fields of } SU(2)_L \text{ and } U(1)_Y},\end{aligned} \tag{2.11}$$

with

$$B_{\mu\nu} = \partial_\mu B_\nu - \partial_\nu B_\mu \quad \text{and} \quad \boldsymbol{W_{\mu\nu}} = \partial_\mu \boldsymbol{W_\nu} - \partial_\nu \boldsymbol{W_\mu} - g\boldsymbol{W_\mu}\times\boldsymbol{W_\nu},$$

where the last term in the definition of $\boldsymbol{W_{\mu\nu}}$ arises from the non-abelian character of $SU(2)_L$. The hypercharge values $Y_L = -1$ and $Y_R = -2$ have been used in Eq. (2.11) only showing the Lagrangian of one lepton-neutrino pair. A summation over all three generations is needed to get the full EW Lagrangian $\mathscr{L}_{\mathrm{EW}}$ of the leptonic sector. The first two summands of Eq. (2.11) represents the interactions between leptons and bosons, whereas the third summand shows the kinetic energy terms of the gauge field itself.

The four introduced gauge fields W^1_μ, W^2_μ, W^3_μ, and B_μ are not the physical gauge bosons but are a mixture of those. The physical $W^\pm$-bosons are a linear combination of the fields W^1_μ and W^2_μ

$$W^\pm = \frac{1}{\sqrt{2}}\left(W^1_\mu \mp iW^2_\mu\right). \tag{2.12}$$

The photon and the Z-boson, both being electrically neutral, are a linear combination of the B_μ of the $U(1)_Y$ and the W^3_μ of the $SU(2)_L$

$$\begin{aligned}A_\mu &= +B_\mu\cos\theta_W + W^3_\mu\sin\theta_W \\ Z_\mu &= -B_\mu\sin\theta_W + W^3_\mu\cos\theta_W\end{aligned} \tag{2.13}$$

being a great example of the EW unification, where θ_W is the weak mixing angle known as the Weinberg angle. As the electromagnetic interaction does not distinguish between left- and right-handed particles, it fixes the couplings g and g' resulting in the equation

$$e = g_W\sin\theta_W = g'\cos\theta_W,$$

within the context of the EW unification. With the help of Eqs. (2.12) and (2.13), one can identify the terms of interactions between leptons and the physical gauge fields in Eq. (2.11). Some of these interactions are shown in Fig. 2.3. The W-boson decays to a lepton having the same charge as the mother particle and the corresponding lepton neutrino, whereas the Z^0 decays to a lepton antilepton pair. In the W-boson decay, the vertex factor $-i\frac{g}{\sqrt{2}}\gamma^\mu\frac{1}{2}\left(1-\gamma^5\right)$ does not depend on the mass of the lepton in the first order. Hence, the branching ratio in all three lepton flavours should be equal. This is referred to as lepton universality.

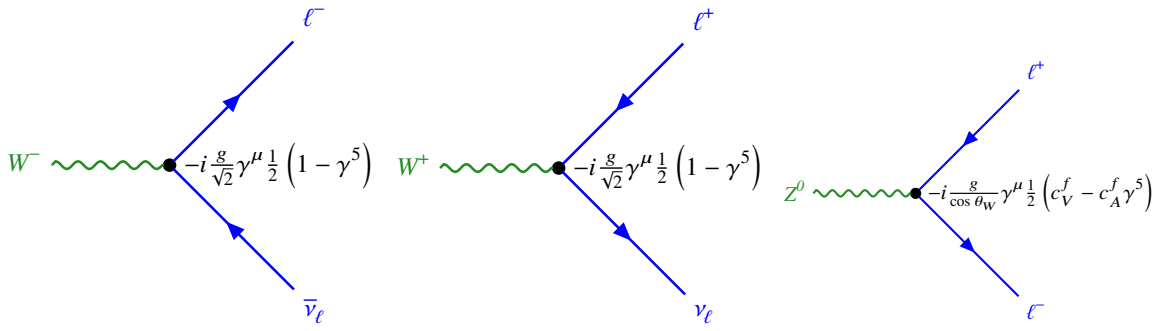

(a) W^- decay. (b) W^+ decay. (c) Z^0 decay.

Figure 2.3: Exemplary interaction of the leptonic and the gauge fields in the context of EW unification. The leptons ℓ^-, ℓ^+, ν_ℓ, and $\overline{\nu}_\ell$ are shown in blue, whereas the gauge bosons W^-, W^+, and Z^0 are displayed in green. The proportional factors at the interaction vertices are given for each decay. The vector and axial-vector couplings are given with $c_V^f = T_f^3 - 2\sin^2\theta_W Q_f$ and $c_A^f = T_f^3$, respectively, where T_f^3 is the third component of the weak isospin and Q_f the charge of the fermion f.

For the up-type quarks, the weak and mass eigenstates[7] are the same. In the sector of the down-type quarks, the weak eigenstates are connected to the mass eigenstates by the Cabibbo-Kobayashi-Maskawa matrix (CKM matrix) V [14, 15]

$$\begin{pmatrix} d' \\ s' \\ b' \end{pmatrix} = \begin{pmatrix} V_{ud} & V_{us} & V_{ub} \\ V_{cd} & V_{cs} & V_{cb} \\ V_{td} & V_{ts} & V_{tb} \end{pmatrix} \begin{pmatrix} d \\ s \\ b \end{pmatrix}. \tag{2.14}$$

The CKM matrix is unitary in the SM, which implies that $V^\dagger V = 1$ [5, 6].

2.2.2 The strong interaction

Before the actual discovery of the quarks, several strongly interacting particles, called hadrons, were discovered in the late 1960s. Especially the discovery of the Δ^{++} was challenging as it seemed to have a symmetric wave function. However, with the hadrons being fermions having half-integer spin, such symmetric wave functions are forbidden by the Pauli exclusion principle. To remedy this problem, a new quantum number called "colour" was introduced. The colour charge is the charge of the strong interaction. Besides electrical charges, the quarks carry colour charges like *red*, *green*, and *blue*. The colour charge is exchanged by eight coloured gluons. As they carry the colour charge themselves, they can interact with each other [5].

The quark-gluon colour theory or Quantum Chromodynamics (QCD) is theoretically described by a renormalisable non-abelian $SU(3)_C$ gauge theory. Following again the guiding principle of local

[7] The weak eigenstates are defined as a part of the weak isospin doublet which can transform into each other by interacting with the W-boson. The mass eigenstates give mass to the particles by interaction with the Higgs-boson and correspond to the freely propagating particles [13].

gauge invariance, the Lagrangian of QCD is received

$$\mathscr{L}_{\text{QCD}} = \overline{q}\left(i\gamma^{\mu}\partial_{\mu} - m\right)q - g_S\left(\overline{q}\gamma^{\mu}T_a q\right)G^a_{\mu} - \frac{1}{4}G^a_{\mu\nu}G^{\mu\nu}_a. \tag{2.15}$$

Here, q are quark fields with six different representations of the quark flavours up, down, strange, charm, bottom, and top. g_S is the coupling constant of QCD and G^a_{μ} with $a = 1, \ldots, 8$ are eight gauge fields, the gluon fields. To keep the local gauge invariance of Eq. (2.15), it has to transform like

$$G^a_{\mu} \rightarrow G^a_{\mu} - \frac{1}{g}\partial_{mu}\alpha^a - f_{abc}\alpha_b G^c_{\mu}, \tag{2.16}$$

where f_{abc} are the structure constants of the group. The QCD $SU(3)_C$ is non-abelian as not all generators T_a commute with each other. The T_a with $a = 1, \ldots, 8$ are a set of linearly independent

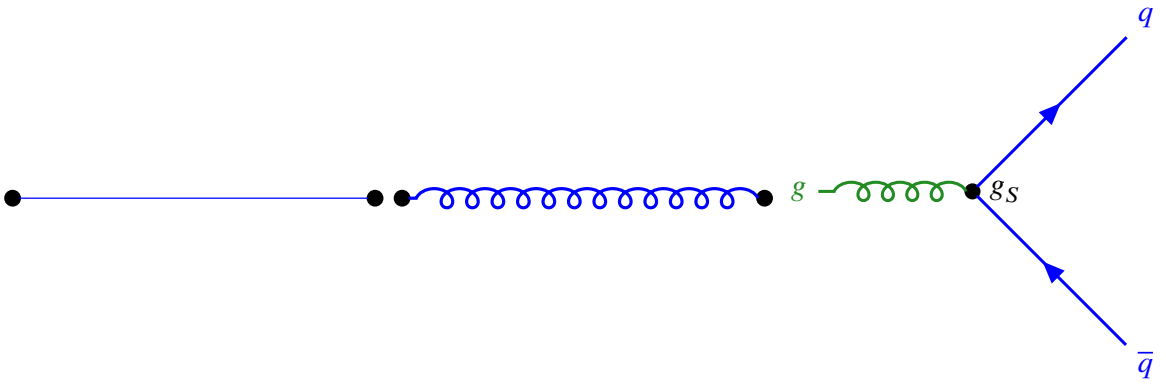

(a) Free propagation of quarks.

(b) Free propagation of gluons.

(c) Gluon-quark interaction.

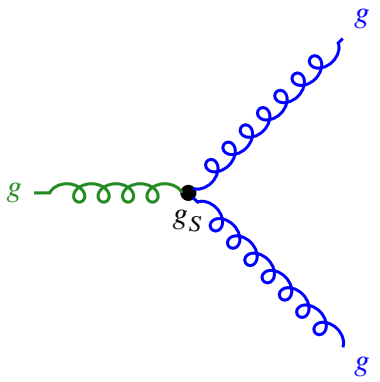

(d) Gluon self-interaction of three gauge bosons.

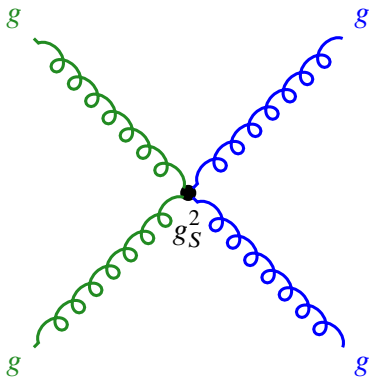

(e) Gluon self-interaction of four gauge bosons.

Figure 2.4: Exemplary propagations and interactions in the context of the strong interaction. Figures (a) and (b) show the free propagation of quarks and gluons. Figure (c) shows the quark-gluon interaction with the corresponding coupling strength at the vertex. The gluon self-interactions of three and four gauge bosons are shown in (d) and (e), respectively. This feature of the strong interaction arises from the non-abelian characteristic.

traceless 3×3 matrices and are connected to the Gell-Mann matrices λ_a via the relation $T_a = \frac{\lambda_a}{2}$.

The kinetic energy term of Eq. (2.15) contains self-interaction terms of gauge bosons. Using a symbolic form of the QCD Lagrangian

$$\mathscr{L}_{\mathrm{QCD}} = \text{“}\overline{q}q\text{”} + \text{“}G^2\text{”} + g_S\text{“}\overline{q}qG\text{”} + g_S\text{“}G^3\text{”} + g_S^2\text{“}G^4\text{”}, \tag{2.17}$$

permits a graphical representation shown in Fig. 2.4. The first three terms of Eq. (2.17) have analogues in QED and correspond to the graphs of Figs. 2.4(a), 2.4(b) and 2.4(c). They describe the free propagation of the gauge boson and the Dirac particle as well as the interaction between the two fields. Unique to the QCD theory are the terms describing the three and four gluon vertices. Due to the gluon self-interactions and their contribution to the coupling constant g_S of QCD, the coupling constant increases with decreasing energy. Hence, free quarks have never been observed directly. This phenomenon is referred to as *colour confinement*. Quarks always appear in bound states having an overall zero colour charge.

2.3 The origin of massive particles

The local gauge principle introduced in Section 2.2.1 is an elegant way to obtain Lagrangians and derive possible interactions within the SM. However, mass terms break the local gauge invariance of the SM, e.g. for the photon (cf. Section 2.2.1). This restriction limits not only the $U(1)_{\mathrm{em}}$ local gauge symmetry of the QED, but holds in addition to the $SU(2)_L$ and $SU(3)_C$ of the weak interaction and the QCD. This is not a problem for QED and QCD as the mediator particles, the photon and the gluons, are massless. In contrast, the force carriers of the weak force, the W- and Z-bosons, were observed with large masses.

To solve this problem, a mechanism called the “Brout-Englert-Higgs mechanism” has been proposed in the 1960s [16–19]. The key concepts of this mechanism will be introduced in the following.

2.3.1 An introdcution to spontaneous symmetry breaking

The idea of spontaneous symmetry breaking (SSB) is crucial to understand the concept of the mass giving mechanism suggested by Higgs, Brout and Englert. It starts with the introduction of a complex scalar field with a potential

$$\phi = \frac{1}{\sqrt{2}}\left(\phi_1 + i\phi_2\right), \quad V\left(\phi\right) = \frac{1}{2}\mu^2\left(\phi^*\phi\right) + \frac{1}{4}\lambda^4\left(\phi^*\phi\right)^2, \tag{2.18}$$

such that the corresponding Lagrangian is then given by

$$\mathscr{L}_{\mathrm{SSB}} = \frac{1}{2}\left(\partial_\mu\phi\right)^*\left(\partial^\mu\phi\right) - \frac{1}{2}\mu^2\left(\phi^*\phi\right) - \frac{1}{4}\lambda^4\left(\phi^*\phi\right)^2. \tag{2.19}$$

The term $\frac{1}{2}\left(\partial_\mu\phi\right)^*\left(\partial^\mu\phi\right)$ relates to the kinetic energy of the scalar particle, $\frac{1}{2}\mu^2\left(\phi^*\phi\right)$ can be associated with the mass of the particle and $\frac{1}{4}\lambda^4$ with self-interactions of the scalar field. The coefficient λ must be positive ($\lambda > 0$) allowing the field ϕ to have a finite minimum. Depending on the choice of the sign of μ^2, two different scenarios of the minima of the complex scalar field ϕ are

possible. The shape of the potential of the two different scenarios depending on the choice of μ^2 is illustrated in Fig. 2.5.

- $\mu^2 > 0$: the resulting potential has a minimum at $\phi = (0, 0)$ if both fields ϕ_1 and ϕ_2 are zero as shown in Fig. 2.5(a). The Lagrangian represents a scalar particle with mass μ and a four-point self-interaction. The Lagrangian of Eq. (2.19) is invariant under the transformation $\phi \rightarrow \phi^{'} = e^{i\alpha}\phi$ and hence has a global $U(1)$ symmetry.

- $\mu^2 < 0$: the potential has not only one minimum at $\phi = (0, 0)$ anymore, but many minima at

$$v^2 = \sqrt{\frac{-\mu^2}{\lambda}},$$

where v is the non-zero vacuum expectation value (VEV). Graphically, it can be interpreted as a circle of minima indicated by the dashed line in Fig. 2.5(b) showing the shape of the potential. The choice of one among the infinite set of minima breaks the global $U(1)$ symmetry of the Lagrangian and is referred to as *spontaneous symmetry breaking*.

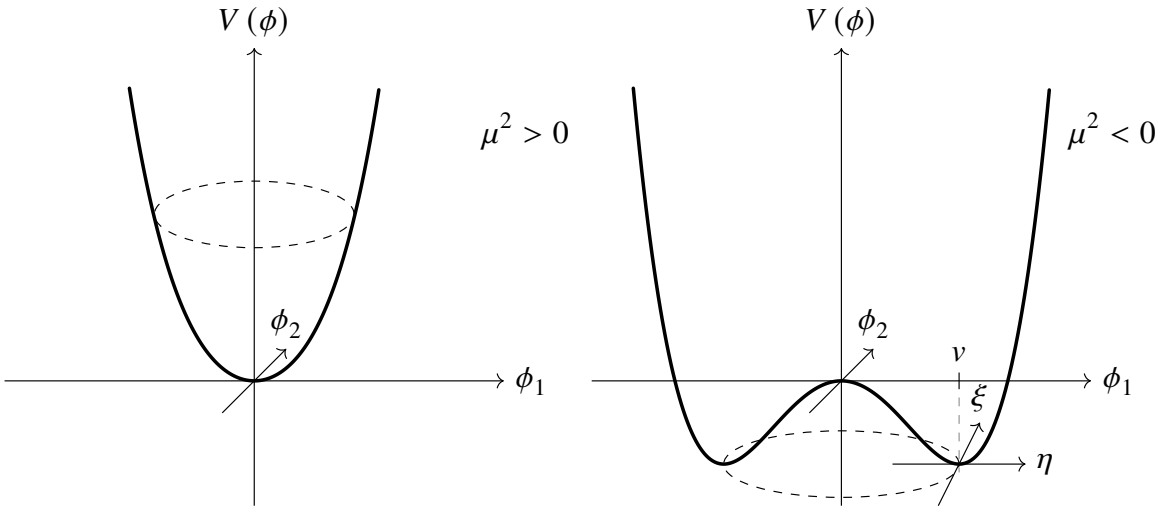

(a) $\mu^2 > 0$. (b) $\mu^2 < 0$.

Figure 2.5: Shape of the introduced quartic potential in the context of a complex scalar field. Figure (a) shows the symmetric case of $\mu^2 > 0$, whereas (b) shows the shape after the potential was spontaneously broken with the choice $\mu^2 < 0$.

The vacuum state can be chosen to be $\phi = (v, 0)$ without loss of generality. The expansion of the complex scalar field ϕ about the vacuum state by defining $\phi_1 = \eta(x) + v$ and $\phi_2 = \xi(x)$ transforms the potential defined in Eq. (2.18) to

$$\phi = \frac{1}{\sqrt{2}}(\eta + v + i\xi). \tag{2.20}$$

A graphical interpretation of η and ξ is shown in Fig. 2.5(b). The potential introduced in Eq. (2.18) becomes

$$V(\eta, \xi) = -\frac{1}{4}\lambda v^4 + \lambda v^2 \eta^2 + \lambda v \eta^3 + \frac{1}{4}\lambda \eta^4 + \frac{1}{4}\lambda \xi^4 + \lambda v \eta \xi^2 + \frac{1}{2}\lambda \eta^2 \xi^2 \tag{2.21}$$

and describes a massive scalar field η with mass $m_\eta = \sqrt{2\lambda v^2}$ and a massless scalar field ξ. All terms with three or four powers of the field are interaction terms. The first term of Eq. (2.21) $-\frac{1}{4}\lambda v^4$ is just a constant without physical consequences. The excitations of the massless scalar field ξ are in the direction where the potential is not changing and correspond to the circle of minima (cf. Fig. 2.5(b)). The massless scalar modes are called Goldstone bosons named after Goldstone's theorem [20]. The excitations of the massive scalar field η are in the direction out of the minima up the quadratic slope of the potential [5, 6].

2.3.2 The Brout-Englert-Higgs mechanism

The massive scalar field introduced in Section 2.3.1 is known as the SM Higgs-boson. However, a necessary local $SU(2)_L \times U(1)_Y$ gauge symmetry has to be embedded into the theory to be connected to the EW interaction of the SM. The Goldstone bosons introduced in Section 2.3.1 are not a physical state and have not been observed. The Goldstone scalar field ξ disappears by choosing an appropriate gauge transformation. This degree of freedom (d.o.f.) will turn into a longitudinal polarisation giving mass to a physical particle. Three degrees of freedom are needed to give masses to the W^+-, W^--, and Z-bosons and the fourth d.o.f. transforms into a massive scalar particle being the self-excitation of the field itself. To account for the different charges of the massive gauge bosons, a charged and a neutral component of the scalar field are required. Hence, the minimal choice of the complex scalar field is placed in a weak isospin doublet

$$\phi = \begin{pmatrix} \phi^+ \\ \phi^0 \end{pmatrix} = \frac{1}{\sqrt{2}} \begin{pmatrix} \phi_1 + i\phi_2 \\ \phi_3 + i\phi_4 \end{pmatrix}. \tag{2.22}$$

The mechanism of spontaneous symmetry breaking works exactly as described in Section 2.3.1. In the degenerate state, the minimum corresponding to a non-zero VEV has to be chosen in a way that the photon remains massless which can be achieved with the choice

$$\phi = \frac{1}{\sqrt{2}} \begin{pmatrix} 0 \\ v \end{pmatrix}.$$

The expansion of the complex scalar field doublet ϕ around the minimum like in Eq. (2.20) creates again a massless scalar field ξ (the Goldstone bosons). To remedy this unphysical remnant, an appropriate gauge transformation has to be made to eliminate the Goldstone field ξ. This unitary gauge "gauges away" the Goldstone fields and the Higgs doublet becomes

$$\phi(x) = \frac{1}{\sqrt{2}} \begin{pmatrix} 0 \\ v + h(x) \end{pmatrix}.$$

After applying the covariant derivative D_μ and the unitary gauge to the Lagrangian, the mass and interaction terms have to be identified. The Lagrangian of the EW sector is

$$\begin{aligned}\mathscr{L}_{\text{EW, SBS}} = & \underbrace{\frac{1}{2}\left(\partial_\mu h\right)\left(\partial^\mu h\right) - \lambda v^2 h^2 - \lambda v h^3 - \frac{1}{4}\lambda h^4}_{\text{Kinetic energy, mass and self-interactions of the Higgs field}} \\ & + \underbrace{\frac{1}{4}v^2 g_W^2 W_\mu^- W^{+\mu}\left(1 + \frac{2}{v}h + \frac{1}{v^2}h^2\right)}_{\text{Mass and interactions of the } W\text{-bosons with the Higgs field}} \\ & + \underbrace{\frac{1}{8}v^2\left(g_W^2 + g'^2\right)Z_\mu Z^\mu\left(1 + \frac{2}{v}h + \frac{1}{v^2}h^2\right)}_{\text{Mass and interactions of the } Z\text{-boson with the Higgs field}} + \underbrace{0 \cdot A_\mu A^\mu}_{\text{Mass of the photon}} \\ & + \underbrace{\frac{1}{4}\boldsymbol{W}_{\mu\nu}\boldsymbol{W}^{\mu\nu} - \frac{1}{4}B_{\mu\nu}B^{\mu\nu}}_{\text{Kinetic energy of the gauge fields of } SU(2)_L \text{ and } U(1)_Y} .\end{aligned} \tag{2.23}$$

Equation (2.23) allows identifying mass terms for the Higgs particle and the gauge bosons of the EW sector which are

$$m_H = \sqrt{2\lambda}v, \quad m_W = \frac{1}{2}g_W v, \quad m_Z = \frac{1}{2}v\sqrt{g_W^2 + g'^2} = \frac{m_W}{\cos\theta_W}, \quad m_A = 0. \tag{2.24}$$

By construction, the mechanism produces a massive self-excitation of the introduced field being the Higgs particle and three massive gauge bosons, W^+, W^-, and Z^0, whereas the photon remains massless. The masses of the W- and Z-bosons, m_W and m_Z, are connected via the Weinberg angle θ_W and the inequality originates from the mixing of the W_μ^3 and B_μ fields. Figures 2.6(a) and 2.6(b) show a graphical representation of the trilinear and quartic Higgs self-coupling as it can be read of Eq. (2.23). Furthermore, Figs. 2.6(c) and 2.6(d) show the couplings hW^+W^- and hZ^0Z^0, whereas the Lagrangian of Eq. (2.23) contains terms of the form hhW^+W^- and hhZ^0Z^0 in addition. The Brout-Englert-Higgs mechanism cannot only explain the masses of the massive EW gauge bosons but to the fermions in addition. The mechanism is ad hoc applied to the fermionic sector. Terms of the form $\overline{L}\phi R$ are invariant under $SU(2)_L$ and $U(1)_Y$ transformations. Exemplary, the Brout-Englert-Higgs mechanism is applied to the electron where g_e is the Yukawa coupling of the electron with the Higgs field. Using the unitary gauge, the corresponding Lagrangian can be written as

$$\mathscr{L}_e = \underbrace{-\frac{g_e}{\sqrt{2}}v\left(\overline{e}_L e_R + \overline{e}_R e_L\right)}_{\text{Mass term of the electron}} \quad \underbrace{-\frac{g_e}{\sqrt{2}}h\left(\overline{e}_L e_R + \overline{e}_R e_L\right)}_{\text{Interaction of the electron with the Higgs field}} . \tag{2.25}$$

The value of the Yukawa coupling g_e is neither predicted by the Higgs mechanism nor by the SM. It is defined as $g_e = \sqrt{2}\frac{m_e}{v}$ to be consistent with the measured electron mass m_e which is a free parameter of the SM. A graphical illustration of the coupling he^-e^+ is shown in Fig. 2.6(e). The mechanism works similarly for quarks. The combination of left- and right-handed fields as in Eq. (2.25) can only

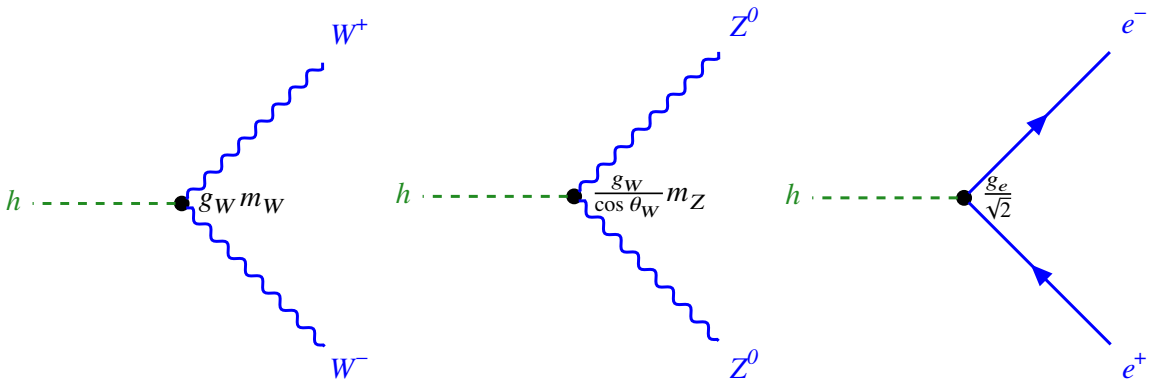

(a) Higgs decay to W-bosons.

(b) Higgs decay to Z-bosons.

(c) Higgs decay to an electron-positron-pair.

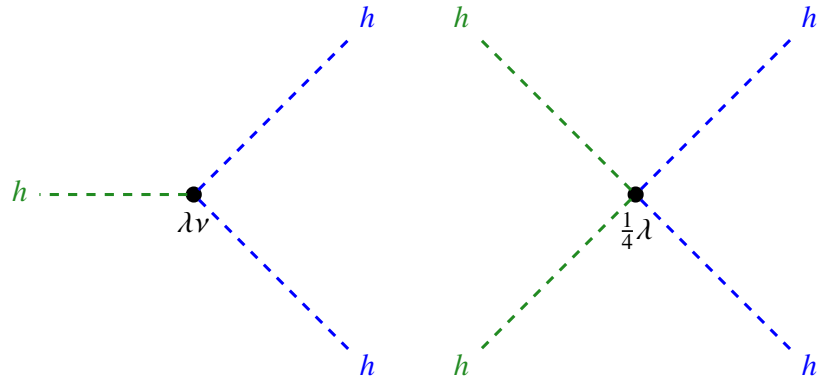

(d) Trilinear self-interaction of the Higgs-boson.

(e) Quartic self-interaction of the Higgs-boson.

Figure 2.6: Higgs interactions with the corresponding couplings at the interaction vertices. Figures (a) to (c) show the decay of the Higgs to the EW bosons, and (d) and (e) the self-interactions.

generate mass terms for the lower component of a $SU(2)_L$ doublet. To explain the mass of the up-type quarks, the conjugate doublet ϕ_c of the fields defined in Eq. (2.22) has to be introduced

$$\phi = \begin{pmatrix} -\phi^{0*} \\ \phi^- \end{pmatrix} = \frac{1}{\sqrt{2}} \begin{pmatrix} -\phi_3 + i\phi_4 \\ \phi_1 - i\phi_2. \end{pmatrix}.$$

This allows to construct a gauge-invariant mass term for up-type quarks the same way as shown for electrons

$$\mathscr{L}_u = \underbrace{-\frac{g_u}{\sqrt{2}} v \left(\overline{u}_L u_R + \overline{u}_R u_L\right)}_{\text{Mass term of the up quark}} \quad \underbrace{-\frac{g_u}{\sqrt{2}} h \left(\overline{u}_L u_R + \overline{u}_R u_L\right)}_{\text{Interaction of the up quark with the Higgs field}} .$$

Similar as for the electron, the coupling g_u is chosen to be consistent with the measured up quark mass.

No right-handed representation of the neutrino has been observed so far. Thus, the Brout-Engler-

Higgs mechanism cannot generate a mass term for the neutrinos as a mixture of both chirality states is needed. But neutrino oscillations have been observed by the Super-Kamiokande experiment [21] for atmospheric neutrinos and the Sudbury Neutrino Observatory [22] for solar neutrinos which require a mass for the chargeless leptons. However, the mass giving mechanism and a measurement of the absolute mass scale of the neutrinos is an active field of current research [5–7].

2.4 Relevant properties of the W-boson

The W-boson is the most important particle of this analysis and its properties will be presented in the following. It was discovered in 1983 by the UA1 [23] and UA2 [24] collaboration with a mass of around 80 GeV. The W-boson is so heavy that it can decay to both, quarks and leptons, as can be seen in Fig. 2.7. The branching fractions can be determined from the corresponding terms of the EW Lagrangian. The hadronic decays occur in 67.41 % of the cases. The W-boson decays into a quark

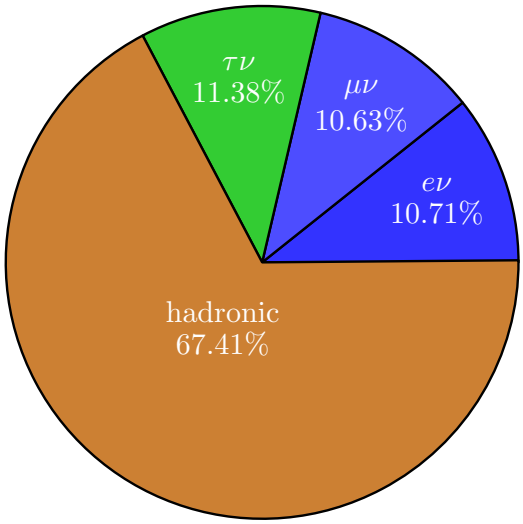

Figure 2.7: Pie chart visualising the different decay modes of the W-boson (values taken from [25]).

and antiquark of the opposite type. The hadronic decays are proportional to the corresponding CKM matrix elements times the colour factor $N_C = 3$. In 32.72 % the W-boson decays into a charged lepton and the corresponding neutrino. Depending on the charge of the W-boson the charged lepton is either a lepton for the W^- or an antilepton for the W^+.

2.4.1 The mass of the W-boson

The mass of the W-boson is one of the fundamental parameters measured in this thesis. The observed mass is like for the Z-boson generated by a symmetry-breaking mechanism introduced in Section 2.3.2. The theoretical value of the W-boson mass according to the coupling to the Higgs field is $m_W = \frac{1}{2} g_W v$ (cf. Eq. (2.24)). The most accurate measured SM parameters are the fine-structure constant $\alpha_{\text{em}} = \frac{e^2}{4\pi}$, the Fermi constant $G_{\text{F}} = \frac{1}{\sqrt{2}v^2}$ and the Weinberg angle $\sin^2 \theta_{\text{W}} = \left(\frac{e}{g_W}\right)^2$. The mass equation of the

W-boson can be rewritten in terms of these SM parameters or by replacing $\sin\theta_W$

$$\begin{aligned} m_W &= \frac{g_W v}{2} = \frac{e}{2 \cdot \sin\theta_{\mathrm{W}}} \left(\frac{1}{\sqrt{2} G_{\mathrm{F}}}\right)^{\frac{1}{2}} = \left(\frac{\pi \alpha_{\mathrm{em}}}{\sqrt{2} G_{\mathrm{F}}}\right)^{\frac{1}{2}} \frac{1}{\sin\theta_{\mathrm{W}}} \\ m_W^2 \sin^2\theta_{\mathrm{W}} &= m_W^2 \left(1 - \cos^2\theta_{\mathrm{W}}\right) = m_W^2 \left(1 - \frac{m_W^2}{m_Z^2}\right) = \frac{\pi \alpha_{\mathrm{em}}}{\sqrt{2} G_{\mathrm{F}}}. \end{aligned} \tag{2.26}$$

An approach of how the W-boson mass can be estimated at tree level is introduced in Section 4.3.1. Radiative corrections to m_W can be absorbed in a redefinition of g_W by $g_W \to \hat{g}_W$ with

$$\hat{g}_W^2 = g_W^2 \left[1 + \Delta r\right],$$

such that Eq. (2.26) can be written with a radiative correction Δr

$$\begin{aligned} m_W &= \left(\frac{\pi \alpha_{\mathrm{em}}}{\sqrt{2} G_{\mathrm{F}}}\right)^{\frac{1}{2}} \frac{\sqrt{1 + \Delta r}}{\sin\theta_{\mathrm{W}}} \\ m_W^2 \left(1 - \frac{m_W^2}{m_Z^2}\right) &= \frac{\pi \alpha_{\mathrm{em}}}{\sqrt{2} G_{\mathrm{F}}} \left(1 + \Delta r\right). \end{aligned} \tag{2.27}$$

The quantity Δr summarises the effect of all higher-order corrections to m_W. The LO corrections of Δr can be written as

$$\Delta r^{(\alpha)} = \Delta\alpha - \frac{\cos^2\theta_{\mathrm{W}}}{\sin^2\theta_{\mathrm{W}}} \Delta\rho + \Delta r_{\mathrm{rem}}\left(m_H\right),$$

where $\Delta\alpha \propto \log m_f$ are fermionic corrections from the shift in the fine-structure constant α_{em} due to light fermions. The parameter $\Delta\rho$ depends quadratically on the top quark mass m_t and Δr_{rem} combines any dependences on the Higgs mass m_H. The LO contribution of Δr assuming a Higgs mass of $m_H = 100\,\mathrm{GeV}$ is calculated to be

$$\Delta r^{(\alpha)} = 283.41 \times 10^{-4}. \tag{2.28}$$

The used values of the other parameters can be found in [26]. In the context of the SM, the radiative correction Δr is sensitive to the top quark and the Higgs-boson mass, whereas additional contributions are obtained by new particles and interactions in beyond Standard Model (BSM) extensions. A precise measurement of the W-boson mass cannot only test the theoretical prediction of fundamental SM parameters and the overall consistency of the SM but is in addition sensitive to BSM effects [26, 27].

A global EW fit including the theoretical predictions of the SM parameters used in Eq. (2.27) is performed in [28]. The parameter m_W is fitted without any experimental measurement. The fit indirectly determines the value of the W-boson mass to

$$\begin{aligned} m_W = \;& 80\,358.4 \pm 4.6(m_t) \pm 3.0(\delta_{\mathrm{theo}} m_t) \pm 2.6(m_Z) \pm 1.8(\Delta\alpha_{\mathrm{had}}) \\ & \pm 2.0(\alpha_{\mathrm{em}}) \pm 0.1(m_H) \pm 4.0(\delta_{\mathrm{theo}} m_W)\,\mathrm{MeV} \\ = \;& 80\,358.4 \pm 7.8(\mathrm{tot})\,\mathrm{MeV}. \end{aligned} \tag{2.29}$$

The largest uncertainties are due to the experimental (m_t) and theoretical ($\delta_{\text{theo}} m_t$) uncertainties of the mass of the top quark, the theoretical uncertainty of the W-boson mass $\delta_{\text{theo}} m_W$ and the uncertainty on the Z-boson mass m_Z. Other sources of uncertainties are related to the fine-structure constant α_{em}, the hadronic contribution to the fine-structure constant evaluated at the Z-boson mass scale $\Delta\alpha_{\text{had}}$, and the Higgs mass m_H. A two-dimensional scan of the confidence level (CL) of m_W versus m_t is shown in Fig. 2.8. It checks the overall consistency of the SM by indirect measurements of m_W and m_t with and without the Higgs mass m_H. The indirect determination of these parameters agrees with the direct measurements illustrated with the green bands and ellipses.

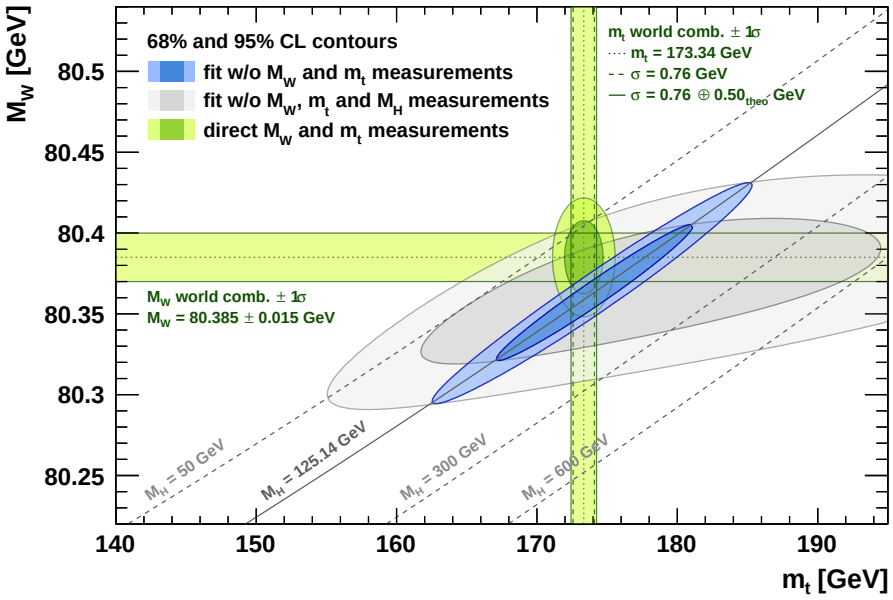

Figure 2.8: Two-dimensional scans with contours at 68 % and 95 % CL of m_W versus m_t. Shown are indirect measurements of the two parameters including m_H (blue) and excluding m_H (grey) as well as a direct measurement of m_W and m_t (green bands and ellipses) (taken from [28]).

2.4.2 The width of the W-boson

The W-boson is a spin-1 particle. It can be described by a plane wave and a polarisation four-vector ϵ^μ_λ

$$W^\mu = \epsilon^\mu_\lambda e^{-ip\cdot x}.$$

Travelling in the z-direction, the W-boson has three orthogonal polarisation states λ with the three polarisation modes ϵ defined as

$$\epsilon^\mu_- = \frac{1}{\sqrt{2}}(0,1,-i,0)\,, \quad \epsilon^\mu_L = \frac{1}{m_W}(p_z,0,0,E)\,, \quad \epsilon^\mu_+ = -\frac{1}{\sqrt{2}}(0,1,i,0)\,. \tag{2.30}$$

The first and the last state of Eq. (2.30) represent the two transverse polarisation modes $\epsilon_\pm$ corresponding to circularly polarised spin-1 states, whereas the state ϵ^μ_L describes the longitudinal polarised state.

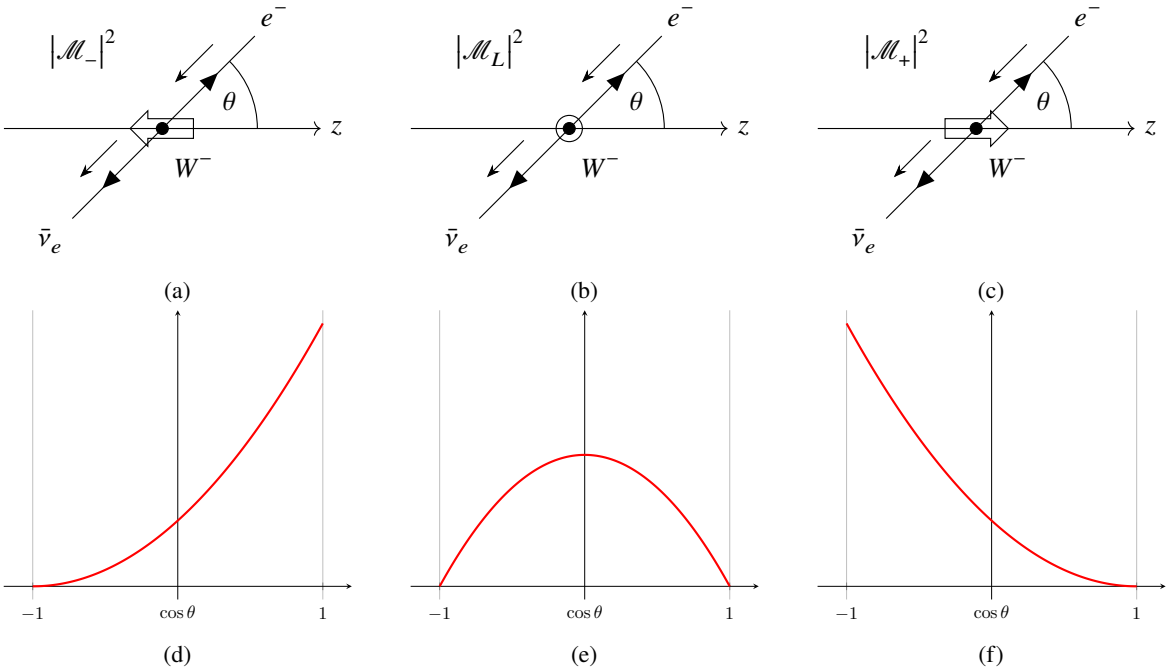

Figure 2.9: Graphical representation of the $W^- \to e^- \overline{\nu}_e$ decay for different polarisation states of the W-boson with the corresponding angular distributions. Whereas (a)-(c) illustrate the decay in the W-boson rest-frame for the three different polarisation states of the W-boson, (d)-(f) show the angular distributions (based on [6]).

The matrix elements for the three possible W-boson polarisation states are

$$\begin{aligned} |\mathcal{M}_-|^2 &= g_W^2 m_W^2 \frac{1}{4} (1+\cos\theta)^2 , \\ |\mathcal{M}_L|^2 &= g_W^2 m_W^2 \frac{1}{2} \sin^2\theta, \\ |\mathcal{M}_+|^2 &= g_W^2 m_W^2 \frac{1}{4} (1-\cos\theta)^2 . \end{aligned} \tag{2.31}$$

The different polarisation states of a decay to electrons are shown in Fig. 2.9 together with the angular distributions. The spin-averaged matrix element squared is then the average of the three matrix elements of Eq. (2.31).

$$\begin{aligned} \left\langle |\mathcal{M}_{fi}|^2 \right\rangle &= \frac{1}{3} \left(|\mathcal{M}_-|^2 + |\mathcal{M}_L|^2 + |\mathcal{M}_+|^2 \right) \\ &= \frac{1}{3} g_W^2 m_W^2 . \end{aligned} \tag{2.32}$$

Inserting the matrix element squared of Eq. (2.32) into the decay formula of a two-body decay, the decay rate of the process $W^- \to e^- \overline{\nu}_e$ can be calculated to be

$$\Gamma\left(W^- \to e^- \overline{\nu}_e\right) = \frac{p^*}{32\pi^2 m_W^2} \int \left\langle |\mathcal{M}_{fi}|^2 \right\rangle \mathrm{d}\Omega^* \quad = \frac{g_W^2 m_W}{48\pi},$$

where p^* is the momentum of the electron or antineutrino in the centre-of-mass frame which is $p^* = \frac{m_W}{2}$ when neglecting the masses of the decay products. The W-boson can decay to all quark flavours except for the top quark as it is heavier than the W-boson. Given the colours and the unitarity of the CKM matrix, the LO prediction of the W-boson decay rate to quarks is

$$\Gamma\left(W^- \to qq'\right) = 6\Gamma\left(W^- \to e^-\overline{\nu}_e\right).$$

In addition to this LO process, QCD corrections arise from NLO Feynman diagrams enhancing the hadronic decay rate of the W-boson by a factor of $\kappa_{\mathrm{QCD}} = \left[1 + \frac{\alpha_{\mathrm{S}}\left(m_W\right)}{\pi}\right]$. The total decay rate of the W-boson to quarks and the three leptonic final states is given by

$$\Gamma_W = \left(3 + 6\kappa_{\mathrm{QCD}}\right)\Gamma\left(W^- \to e^-\overline{\nu}_e\right) \approx 9.2 \times \frac{g_W^2 m_W}{48\pi} = 2\,071\,\mathrm{MeV}.$$

As the mass of the W-boson is large, so is the total decay width, whereas the lifetime of the W-boson is small with $\tau_W \approx 10^{-25}$ s [6].

2.4.3 Lepton universality in the W-boson decay

The coupling in the decay of the weak charged current to a leptonic final state is $-i\frac{g}{\sqrt{2}}\gamma^\mu \frac{1}{2}\left(1 - \gamma^5\right)$ as can be seen in Fig. 2.3. The coupling does not depend on the masses of the leptons at LO which means that the W-boson couples to all leptons with the same strength. This is what is understood under the term *lepton universality*. Assuming the lepton universality of the weak charged current and neglecting the small differences of the lepton masses compared to the W-boson mass, the decay rate of the three leptonic decay modes are the same at LO

$$\Gamma\left(W \to e\nu_e\right) = \Gamma\left(W \to \mu\nu_\mu\right) = \Gamma\left(W \to \tau\nu_\tau\right).$$

The EW interaction preserves this unversality but the Higgs-Brout-Englert mechanism already breaks it. The Higgs field couples differently to the three charged leptons, hence they gain different masses. In this thesis, the ratio of the branching ratios is considered as this should be one in case the lepton universality of the W-boson is preserved. Therefore, the leptonic decays of the W-boson are considered, which are displayed in Fig. 2.10. As the tau lepton is not stable, the leptonic decays are used having again a light lepton in the final state. The question is if there is an additional mechanism breaking lepton universality. As new physics is expected to couple predominantly to heavier particles, the investigated quantities are

$$R_{\tau\mu} = \frac{\Gamma\left(W \to \tau\nu_\tau \to \mu\nu_\mu\nu_\tau\nu_\tau\right)}{\Gamma\left(W \to \mu\nu_\mu\right)}, \qquad R_{\tau e} = \frac{\Gamma\left(W \to \tau\nu_\tau \to e\nu_e\nu_\tau\nu_\tau\right)}{\Gamma\left(W \to e\nu_e\right)}, \tag{2.33}$$

where $R_{\tau\mu}$ and $R_{\tau e}$ are referred to as $R_{\tau\ell}$ independent from the leptonic decay channel. If $R_{\tau\ell}$ deviates from unity, this would be a clear indication of new physics. Possible Feynman diagrams implementing new physics are shown in Fig. 2.11. In addition, other new physics scenarios could

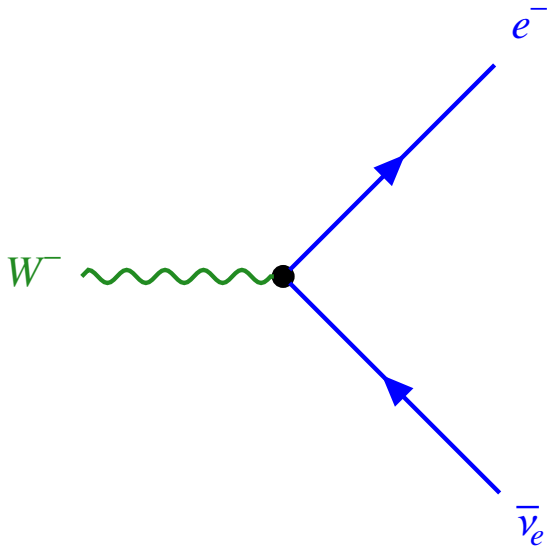

(a) W-boson decay to the electron final state.

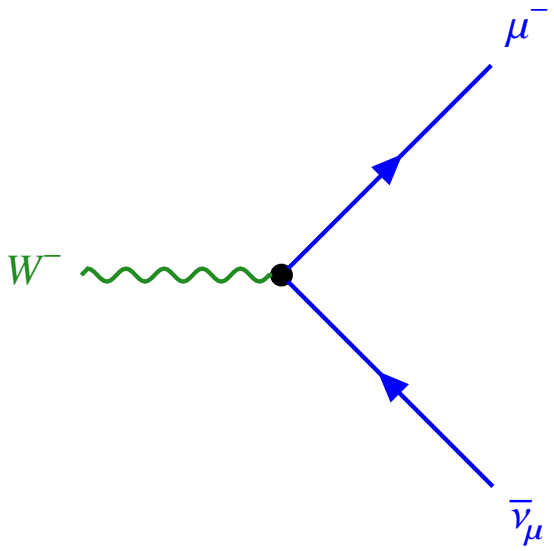

(b) W-boson decay to the muon final state.

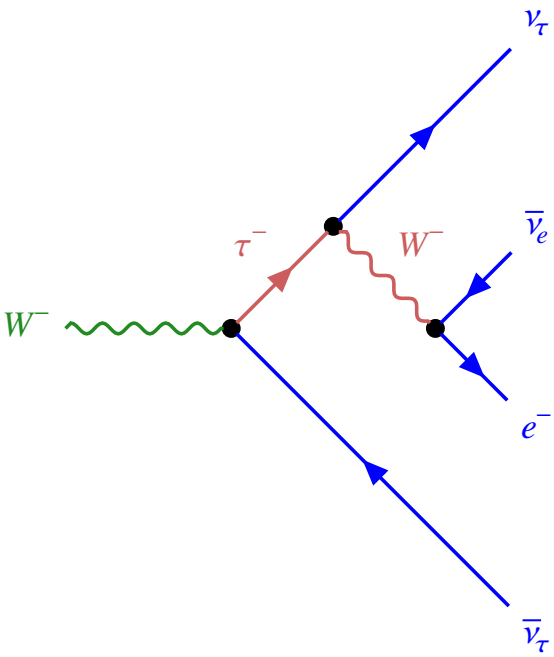

(c) W-boson decay to the electron final state via an intermediate tau lepton.

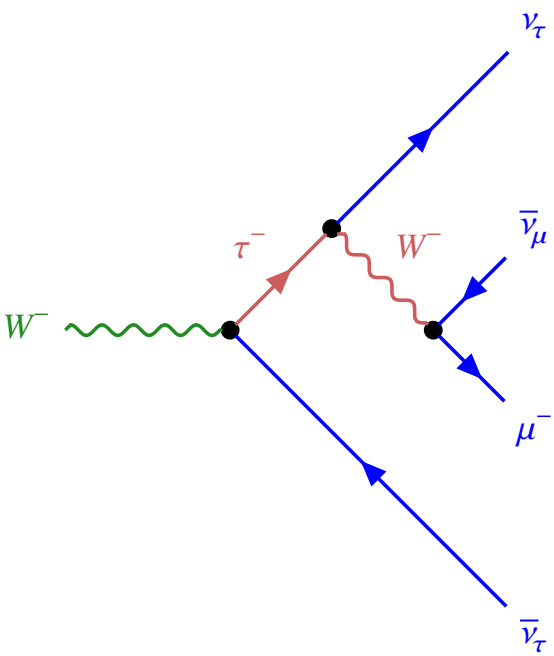

(d) W-boson decay to the muon final state via an intermediate tau lepton.

Figure 2.10: Feynman diagrams of the four possible leptonic decays of the W-boson containing a light lepton in the final state. Whereas (a) and (b) show the prompt decay of a W-boson (green) to a light lepton and the corresponding neutrino (both in blue), (c) and (d) show the decay via an intermediate tau lepton (red). Shown are only diagrams for negatively charged particles, whereas the decay chains for positively charged particles look similar.

explain the difference seen from the lepton universality. One is a new vector boson W' coupling with varying strength to the different lepton and quark flavours, the other physics scenarios are leptoquarks coupling to quarks and leptons at one interaction vertex. However, both scenarios are kinematicly different because the W' and the leptoquarks have different masses than the SM W-boson and will thus not be covered in this thesis. A second W-boson is appearing in the tau lepton decay to a light

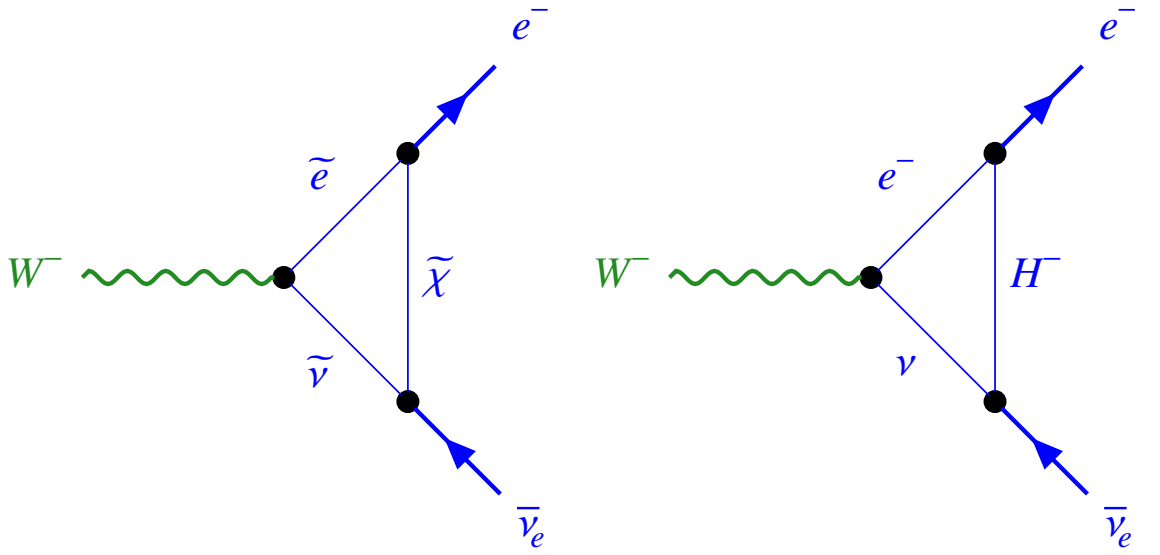

(a) W-boson decay via an intermediate loop containing supersymmetric particles.

(b) W-boson decay via an intermediate loop containing a charged Higgs-boson.

Figure 2.11: Feynman diagrams of the W-boson decay to an electron final state via loops including BSM particles. (a) includes a loop of supersymmetric particles and (b) includes a loop containing a charged Higgs-boson.

lepton. These branching ratios have been measured and the uncertainty on this decay rate will be taken as a systematic uncertainty. In addition, the second W-boson is produced virtually in the rest frame of the tau lepton, and any BSM physics scenario would couple stronger to the first vertex where the W-boson decays to a tau lepton than to the second vertex including the virtual W-boson.

2.5 Measuring properties of vector bosons at hadron colliders

The data analysed in this thesis were taken by a hadron collider using protons which will be introduced in Section 3.1. The colliding protons can produce vector bosons like the W- or the Z-boson. To study the properties of the W-boson, it is crucial to understand the production of vector bosons by looking inside the proton. The information in this section is mainly taken from [29].

2.5.1 The structure of the proton

The proton as introduced in Section 2.1 consists of three valence quarks (uud) determining quantum numbers like the charge. The valence quarks are bound by exchanging gluons. Due to the non-abelian structure of the underlying symmetry group $SU(3)_C$ of QCD, the gluons can self-interact and produce pairs of sea quarks. The valence and sea quarks are constituents of the proton and are referred to as

the partons. The structure of a proton is more complex than the structure of an electron or a positron explaining why the phenomenology of hadron collisions is more complicated than for e^-e^+-collisions.

The partons carry a different fraction of the total proton's momentum. Deep inelastic scattering (DIS) experiments entailed a precise knowledge about the momentum distribution functions of each parton within the proton which are commonly known as the parton distribution functions (PDFs). They describe the probability of a parton having a momentum fraction x[8] of the proton at some energy scale Q. The PDFs $f_i\left(x,\, Q^2\right)$ of a given global analysis for the most important partons are illustrated in Fig. 2.12. The functionality of f_i over x at a fixed Q^2 cannot be determined analytically but is calculated with the help of a global fit using different experimental data as an input. The choice of the parametrisation of the fit and the input data lead to different PDF tunes with a certain set of eigenvectors describing the uncertainty.

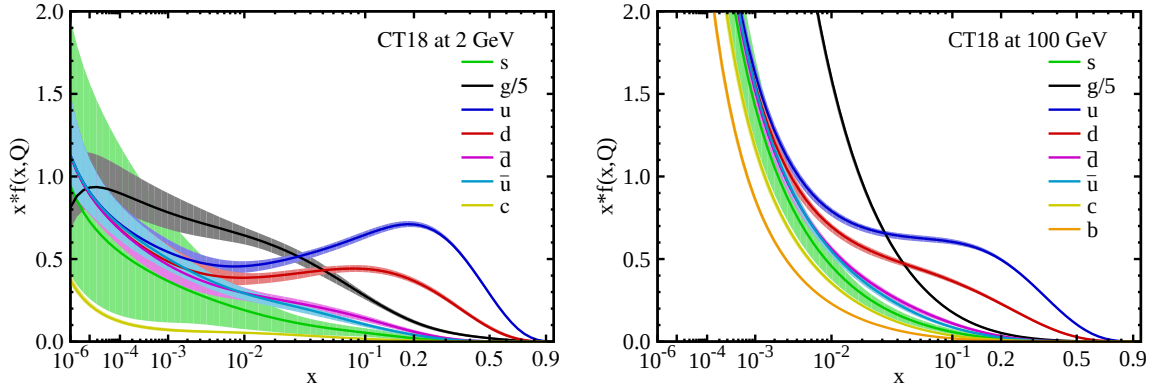

(a) $Q = 2\,\text{GeV}$. (b) $Q = 100\,\text{GeV}$.

Figure 2.12: The PDFs of the CT18 global analysis at (a) $Q = 2\,\text{GeV}$ and (b) $Q = 100\,\text{GeV}$ for u, $\overline{u}$, d, $\overline{d}$, $s = \overline{s}$ and g. The gluon PDF is scaled down by a factor of 5 (taken from [30]).

2.5.2 The production of vector bosons

The scattering process at hadron colliders can be categorised into two categories: "Soft" collisions describe the interaction of two partons with low momentum transfer and are difficult to predict as non-perturbative QCD effects dominate this energy regime. "Hard" scattering processes include parton interactions with high momentum transfer and are needed to produce vector bosons. The collision of two partons A and B with the corresponding momenta p_1 and p_2 resulting in the creation of a vector boson V

$$A(p_1) + B(p_2) \rightarrow V + X, \tag{2.34}$$

can be calculated using perturbation theory, where X represents the remaining final state objects. The hadronic cross-section $\sigma\left(A + B \rightarrow V + X\right)$ of Eq. (2.34) can be achieved by weighting the subprocess

[8] x is known as the Bjorken scaling variable.

cross-sections $\hat{\sigma}_{ab\to V}$ with the corresponding PDFs $f_i(x_i, Q^2)$ using the factorisation theorem

$$\sigma_V = \int \mathrm{d}x_a \, \mathrm{d}x_b \, f_a(x_a, \mu_F^2) f_b(x_b, \mu F^2) \hat{\sigma}_{ab\to V}, \tag{2.35}$$

where a and b are all possible combinations of partons that can produce the asked vector boson V. μ_F is the *factorisation scale* separating the "hard" and the "soft" regime of QCD. The partonic cross-section of Eq. (2.35) can be expanded in terms of the running coupling constant of QCD α_S

$$\hat{\sigma}_{ab\to V} = \left[\hat{\sigma}_0 + \alpha_\mathrm{S}\left(\mu_R^2\right) \cdot \hat{\sigma}_1 + \dots\right]_{ab\to V}, \tag{2.36}$$

where μ_R is the *renormalisation scale* of the QCD running coupling. More information on how to calculate the partonic cross-section for the different types of vector bosons or the bosons transverse momentum can be read up in [29].

2.6 The physics of the tau lepton decay

The tau lepton is the heaviest of the charged leptons with a mass of $m_\tau = 1.78\,\mathrm{GeV}$. In contrast to the two lighter charged leptons, it decays within the usual dimension of a particle detector. Hence, the physics of the tau lepton decays is presented. The heaviest lepton was found in the 1970s at SLAC in e^-e^+ annihilation [31]. The tau lepton has a mean lifetime of $\tau_\tau = 290.3 \times 10^{-15}\,\mathrm{s}$ and a mean decay length of $c\tau_\tau = 87\,\mu\mathrm{m}$ [25]. It decays not only to lighter leptons but due to its high mass it is the only lepton decaying into hadrons. A pie chart of the different decay modes is shown in Fig. 2.13.

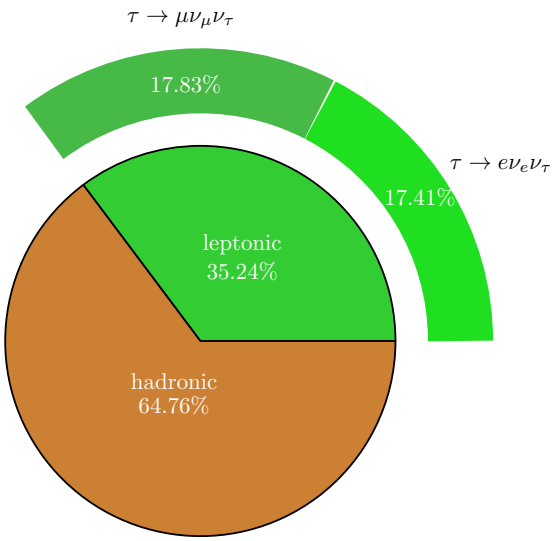

Figure 2.13: Pie chart visualising the different decay modes of the tau lepton. The chart is split up into hadronic decays (orange) and leptonic decays (green) in different flavours (values taken from [25]).

The hadronic decay occurs in about 64.76 % of the cases. The hadronic decay modes usually contain one or three charged pions coming along with an arbitrary number of neutral pions. Depending on

the number of charged particles, these decay modes are referred to as "1-prong" or "3-prong". The hadronic decays of the tau lepton are not used in this thesis and will not further be discussed. In the other 35.24 % of the cases, the tau lepton decays almost equally to a muon (17.83 %) or an electron (17.41 %) together with the corresponding neutrinos to preserve the lepton family number.

2.7 Beyond the Standard Model

The SM is a successful theory and can describe physics phenomena since many decades into the TeV range. However, it is only a work in progress as it has several shortcomings based on observations or theoretical concepts which it cannot explain. The main ones will be presented in the following.

The **hierarchy problem** [32–35] is the sensitivity of the Higgs potential (cf. Eq. (2.23)) to a new physics scenario. The Higgs mass m_H^2 receives large quantum corrections of every particle coupling to the Higgs-boson. The Higgs field couples to a fermion f with mass m_f leading to a correction of the squared Higgs mass of

$$\Delta m_H^2 = -\frac{\left|\lambda_f\right|^2}{8\pi^2}\Lambda_{\mathrm{UV}}^2 + \ldots, \tag{2.37}$$

where Λ_{UV}^2 is an ultraviolet momentum cutoff to regulate the loop integral. It is the energy scale where BSM physics scenarios enter. This happens at the latest at the reduced Planck scale $M_{\mathrm{P}} = \left(8\pi G_{\mathrm{Newton}}\right)^{-12} = 2.4 \times 10^{18}\,\mathrm{GeV}$ where quantum gravity effects play a significant role and cannot be neglected anymore. In this case, the quantum corrections of Eq. (2.37) would be 30 orders of magnitude larger than the observed Higgs mass by ATLAS [9] and CMS [10] which is known as the hierarchy problem. An exemplary interaction of a fermion to the Higgs field is shown in Fig. 2.14(a).

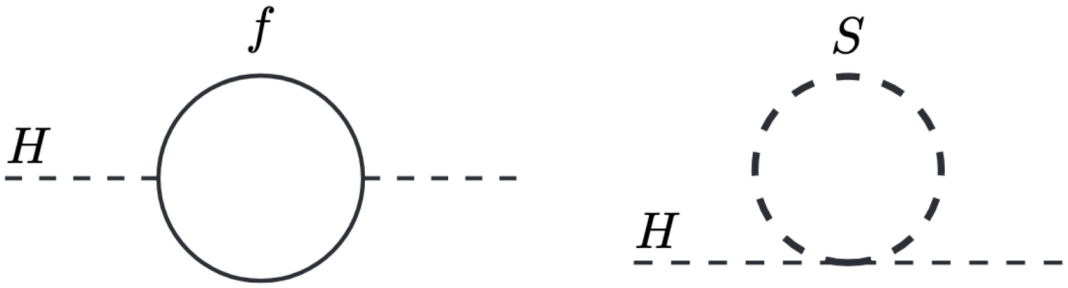

(a) (b)

Figure 2.14: One-loop contributions of (a) a fermion and (b) a scalar particle to the mass of the Higgs-boson (taken from [36]).

If a heavy complex scalar particle S with mass m_S exists, it will couple with a strength of λ_S and the Lagrangian term $-\lambda_S \left|H\right|^2 \left|S\right|^2$. A loop contribution like in Fig. 2.14(b) leads to a correction to the squared Higgs mass of

$$\Delta m_H^2 = \frac{\lambda_S}{16\pi^2}\left[\Lambda_{\mathrm{UV}}^2 - 2m_S^2 \ln\left(\Lambda_{\mathrm{UV}}/m_S\right) + \ldots\right].$$

If every fermion has two complex scalar particles as partners with $\lambda_S = |\lambda_f|^2$, the contributions of the order of Λ_{UV}^2 to the squared Higgs mass would cancel out each other [36].

Dark Matter has never been observed directly so far but indirect measurements lead to the existence of this new type of matter. It is assumed to interact gravitationally but not electromagnetically and hence remains dark for our eyes. The observed velocity distributions of galaxies do not match the prediction explained by the centripetal acceleration compensated by the gravitational force of visible matter. The difference becomes larger for outer radii meaning there is a significant amount of non-luminous matter in galaxies. Recent observations measured the universe to consist of 68.3 % dark energy, 26.5 % dark matter, and 4.9 % ordinary matter as shown in Fig. 2.15 [6].

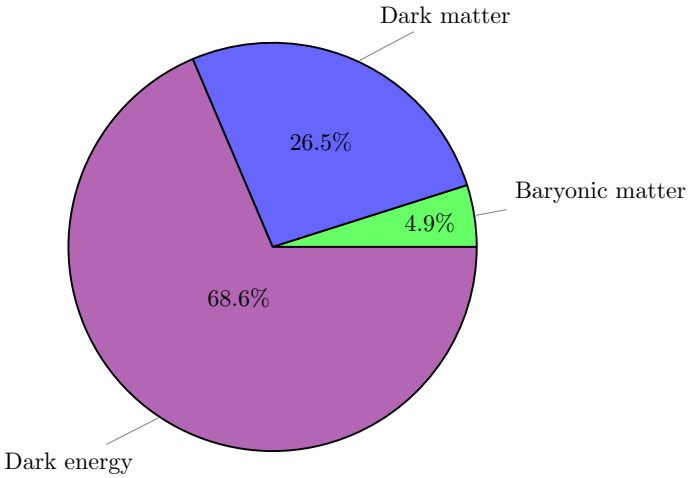

Figure 2.15: The distribution of dark energy, dark matter and baryonic matter in the universe (values taken from [37]).

Other shortcomings of the SM are the origin of the neutrino masses which were observed due to neutrino oscillation, the observed matter-antimatter asymmetry in the universe which cannot be covered by the known CP[9] violating processes, and a theory providing a grand unification of the three forces described in the context of the SM like the EW theory is unifying the electromagnetic and the weak force.

Numerous BSM theories explain one or more shortcomings mentioned above. Two prominent ones are used in this thesis and will be shortly presented in the following. Supersymmetry (SUSY) [38–43] introduces a new symmetry between bosons and fermions. It can explain the hierarchy problem as it provides two scalar partner particles for every fermion and presents promising candidates to explain Dark Matter because the lightest SUSY particle is stable in many theories, but interacts only weakly and gravitationally. The minimal supersymmetric extension is referred to as the Minimal Supersymmetric Standard Model (MSSM) [44–46] which is doubling the particle of the SM [36].

Even though no experiment has made a direct observation of supersymmetric processes, they might influence other properties of the SM. The W-boson mass is sensitive to loop corrections Δr introduced in Eq. (2.27). Any deviation of the measured m_W from the theoretical prediction implies a contribution of not yet discovered particles. Therefore, it is crucial to achieve a high precision in

[9] CP violation is the breaking of the combined charge (C) and parity (P) symmetry.

both, the experimental measurement and the theoretical prediction. Supersymmetric particles can give contributions to the radiative corrections of the W-boson mass. The dominant contributions at the one-loop level originate from the supersymmetric partners of the top and the bottom quark [47, 48]. The mass scale of the MSSM can vary at the order of several hundreds of GeV which can impact the W-boson mass at the order of a few hundreds of MeV as shown in Fig. 2.16. The ultimate goal of the m_W measurement, for future experiments as well, is to achieve such precision to constrain the parameter space of BSM scenarios further [48].

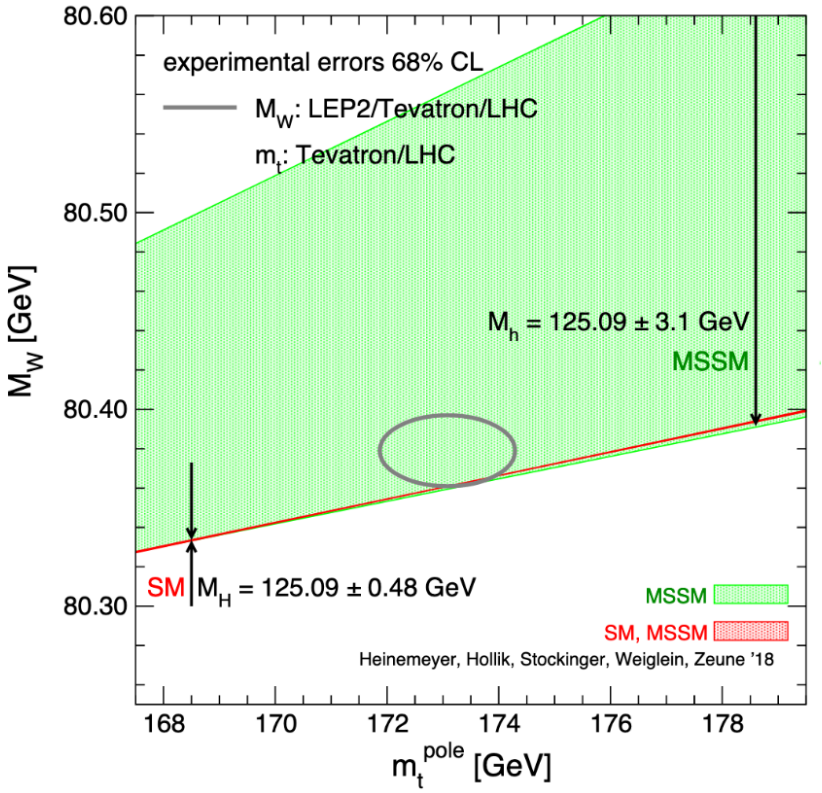

Figure 2.16: Dependence of the W-boson mass on the top quark pole mass. The green area represents a parameter scan of the MSSM with a Higgs mass of (125.09 ± 3.1) GeV. The red line shows the overlap between SM and MSSM with a Higgs mass of (125.09 ± 0.48) GeV. The grey circle indicates the experimentally measured W-boson and top quark mass with the extent of the circle representing the experimental errors with 68 % CL (taken from [49]).

The two Higgs-doublet model (2HDM) [50] is well motivated by the introduction of SUSY. The 2HDM could explain the asymmetry between matter and antimatter in the universe due to additional sources of CP violation. In addition to the presented Higg potential (cf. Eq. (2.22)), a second complex scalar $SU(2)_L$ doublet is introduced such that there are eight fields. Three of these d.o.f.s give mass the massive gauge bosons and the remaining five fields are physical scalar Higgs fields. There is a neutral light Higgs-boson h^0 being the SM Higgs-boson, a neutral heavy scalar H^0, two charged Higgs-bosons H^+ and H^-, and a neutral pseudoscalar boson A^0 [51].

CHAPTER 3

The experimental setup

The W-boson is one of the heaviest particles of the SM. One way to measure the properties of this particle, is to produce it in pp -collisions with a sufficient centre-of-mass energy and measure its decay products. The Large Hadron Collider provides large amounts of such pp -collisions that can be detected in the ATLAS detector. Both will be presented in this chapter together with the routines to reconstruct events and objects as well as how to simulate particle collisions.

3.1 The Large Hadron Collider

The Large Hadron Collider (LHC) [52] is a circular particle accelerator and up to date the most powerful collider ever built. It is situated at CERN (Conseil europeen pour la recherche nucleaire), the European organisation for nuclear research, close to Geneva, Switzerland. The LHC is located in a 27 km long tunnel approximately 100 m under the Swiss-French border, where the particles are circulating in two separated rings clockwise and counterclockwise, respectively. It can technically collide up to 2 808[1] hadron bunches (either protons or lead ions) separated by 25 ns. The protons can reach an energy of up to 7 TeV per beam. The centre-of-mass energy $E_{\text{cm}} = \sqrt{s}$, a key parameter of a particle accelerator, is defined as

$$s = (\mathbf{p_1} + \mathbf{p_2})^2,$$

where $\mathbf{p_i}$ is the four-momentum of the incoming particle $i = 1, 2$. The designed centre-of-mass energy at the LHC is $E_{\text{cm}} = 14$ TeV. In the 2011 data taking used for this measurement, the approximately 1 400 proton bunches had a separation of 50 ns and the centre-of-mass energy was $E_{\text{cm}} = 7$ TeV [53].

The pre-accelerated protons have an energy of 450 GeV when they are injected into the LHC after completing a complex consisting of different stages as shown in Fig. 3.1). Starting from a hydrogen bottle, the protons are accelerated by the LINear ACcelerator 2 (LINAC 2) [55], the Proton Synchrotron Booster (PBS) [56], the Proton Synchrotron (PS) [57], and the Super Proton Synchrotron (SPS) [58]. The LINAC 2 was part of the accelerator chain in 2011 and was replaced by the LINear ACcelerator 4 (LINAC 4) during the long shutdown starting in 2019. The bunches are subsequently filled into the next accelerator after reaching the designed energy of each stage, and create a bunch structure that is filled into the LHC and accelerated to the desired energy.

[1] So far the maximum number of bunches reached is 2 556 in 2017 and 2018 [53].

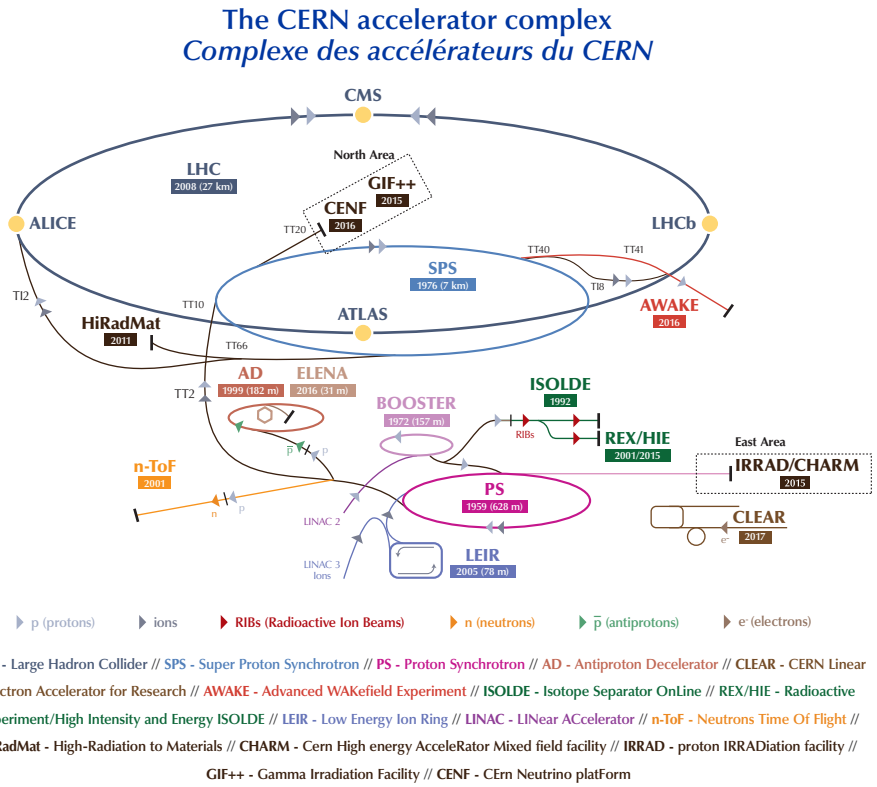

Figure 3.1: Overview of the LHC and the pre-accelerator complex (taken from [54]).

The charged particles gain energy through passing the electric field of 16 radio frequency (RF) cavities, eight cavities per beam, with an oscillating voltage of $f_{\mathrm{RF}} = 400\,\mathrm{MHz}$ and an accelerating field of $5\,\mathrm{MV\,m^{-1}}$. To keep the protons on the circular track, the Lorentz force opposes the centrifugal force of the protons

$$q\left(\vec{V} \times \vec{B}\right) = \frac{mV^2}{r}. \tag{3.1}$$

1 232 superconducting dipole magnets with a length of 15 m and a weight of 35 t, each, provide a bending field of up to 8.33 T. The dipole magnets made out of niobium-titanium are operated at a temperature of 1.9 K to become superconducting. The maximum current is 11 080 A. The required magnetic field can be calculated by simplifying Eq. (3.1) with $B = \frac{E_{\mathrm{beam}}}{qR}$. As protons are electrically charged, they would diverge if not being focused. 858 quadrupole magnets keep the protons in a tight beam raising the interaction probability when two bunches collide. Other magnetic multipoles, e.g. sextupole, octupole, and decapole magnets, are used for smaller corrections of the beam.

The two rings storing the proton bunches rotating in opposite directions meet at four dedicated spots, referred to as interaction points (IPs), allowing the proton bunches to collide. Four particle detectors are built around these IPs to detect the outcome of those collisions, namely ATLAS, CMS, ALICE, and LHCb. The data analysed in this thesis was recorded by the biggest experiment, the ATLAS detector (A Toroidal LHC Apparatus) [59]. It will be described in detail in Section 3.2.

The CMS experiment (Compact Muon Solenoid) [60] is the second multi-purpose detector. It has a similar physics program as ATLAS but uses different detector technologies and a different magnet design. The LHCb detector (LHC beauty) [61] is dedicated to the "b quark" to study differences in the matter-antimatter asymmetry. In contrast to the two multi-purpose detectors, it detects particles mainly in the forward region. The ALICE experiment (A Large Ion Collider Experiment) [62] focuses on the measurement of heavy-ion collisions to find out more about the physics of the strong interaction by studying quark-gluon plasmas.

The concept of luminosity Besides the centre-of-mass energy $\sqrt{s}$, luminosity is another important measure used at particle accelerators. It defines the number of collisions via the relation

$$\dot{N} = \sigma \mathcal{L},$$
$$N = \sigma \int \mathcal{L}\, \mathrm{d}t = \sigma \mathcal{L}_{\mathrm{int}},$$

where $\dot{N}$ is the event rate, N the total number of events, σ is the cross-section of a given process, $\mathcal{L}$ the instantaneous luminosity, and $\mathcal{L}_{\mathrm{int}} = \int \mathcal{L}\, \mathrm{d}t$ the integrated luminosity over time. At particle accelerators, two three-dimensional Gaussian beams are colliding head-on. The instantaneous luminosity can be calculated by the overlap of the core of the Gaussian distributions for two colliding bunches $n_b = 2$ via the formula

$$\mathcal{L} = \frac{f N_1 N_2}{A} = \frac{f N_1 N_2}{4\pi \sigma_x \sigma_y}. \tag{3.2}$$

Here, f is the frequency of collisions, N_i the number of particles in bunch i, and A is the transverse beam area at the crossing point. The overlapping area A of the two beams at the IP is determined by the overlap $\sigma_{x,y}$ of the Gaussian beams in x and y direction, respectively. Equation (3.2) only considers two dimensions of the three-dimensional Gaussian beams as it integrates over the z-component. The amplitude function β describes the "squeezing" of the beam and is defined as

$$\beta = \frac{\sigma_x \sigma_y}{\epsilon},$$

where ϵ is the transverse emittance. The transverse emittance is the area of the ellipse of the phase space divided by π and can be understood as the smallest opening the beam can be squeezed through. At low emittance, the particles are packed in a small volume and the luminosity is higher than for high emittance values. The emittance is constant along the trajectory of the beam.

Of particular interest is the amplitude function at the IP β^*. It is referred to as the distance between the point where the beam width is twice as large as at the IP and the IP itself. To raise the instantaneous luminosity, the beam has to be squeezed at the IP and β^* needs to be as low as possible. The designed instantaneous peak luminosity of the LHC is $\mathcal{L} = 10^{34}\,\mathrm{cm}^{-2}\,\mathrm{s}^{-1}$ corresponding to an amplitude function of $\beta^* = 0.55\,\mathrm{m}$ [63–65].

[2] The LHC already reached 2018 twice the instant peak luminosity and an amplitude function of $\beta^* = 0.25\,\mathrm{m}$.

3.2 The ATLAS Detector

The ATLAS detector is a multi-purpose detector with an onion-like structure. Its purpose is to detect the particles which are produced in the proton-proton collisions of the LHC by measuring their energy, momentum, charge, and identifying the particle type. Several layers are stacked from the inside around the IP to the outside, each subdetector having a different purpose which will be explained in the following. A schematic view of the ATLAS detector with all the different subdetectors is shown in Fig. 3.2.

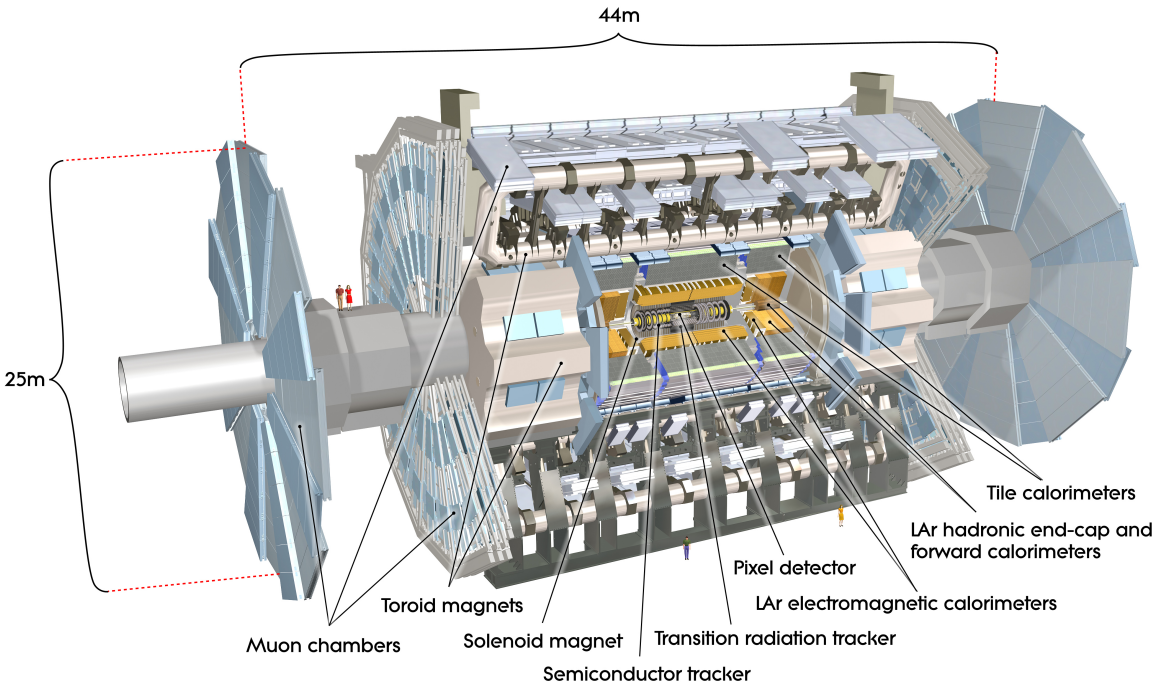

Figure 3.2: Schematic overview of the ATLAS detector. Shown are all relevant subdetectors and the magnet system (taken from [66]).

ATLAS is the biggest of the four collider experiments located at the LHC with dimensions of 44 m length, 25 m height, and 25 m width. The central region of the detector is called the "barrel" with the layers being orientated parallel to the beam pipe. The forward and backward parts of the detector are called the "endcaps", where the "A side" points to the airport of Geneva and the "C side" is in the direction of the Jura Mountains.

Coordinate System ATLAS uses a right-handed coordinate system with the IP determining the centre of the detector. The z-axis is defined along the beam pipe. The x-axis points from the IP to the centre of the LHC ring and the y-axis from the IP upwards. In the transverse plane, cylindrical coordinates (r, ϕ) are used with ϕ being the azimuthal angle around the beam pipe. Instead of the polar angle θ, ATLAS uses the quantity pseudorapidity η as a third component of the coordinate

system. It is defined as

$$\eta = -\log \tan \frac{\theta}{2}.$$

Using the pseudorapidity instead of the polar angle is motivated by the fact that the difference in pseudorapidity $\Delta\eta$ between two particles is invariant under Lorentz boosts parallel to the beam axis. Most particles scatter close to the beam axis so the distribution of the polar angle θ peaks around 0° which is close to the beam axis. In contrast, a distribution of the pseudorapidity η is almost flat as the particle flow is constant over η due to its logarithmic definition. By using these coordinates, a distance ΔR invariant under boosts along the z-axis between two particles can be defined as

$$\Delta R = \sqrt{(\Delta\eta)^2 + (\Delta\phi)^2}. \tag{3.3}$$

The definition of Eq. (3.3) is used in ATLAS to calculate any distance between two physical objects.

The usage of cylindrical coordinates has another advantage: as the initial momentum in the z-direction is not known due to the unknown momenta of the colliding partons, transverse quantities like the transverse momentum p_{T} are used as the total momentum of the colliding particles in the transverse plane is known to be zero.

3.2.1 Inner Detector

The Inner Detector (ID) [67] is the innermost part of the ATLAS detector and the first subdetector traversed by any particle. It encloses directly the beam pipe. Charged particles are passing through the several layers of the ID by leaving "hits", e.g. through ionisation. A dedicated software takes these hits to reconstruct the tracks of the charged particles. As the ID is immersed in a magnetic field, the trajectories of charged particles are bent due to the Lorentz force. By measuring the radius of the curvature it is possible to determine the momentum of the charged particle assuming it carries one elementary charge. From the direction of the curvature, the charge of the particle can be assessed. The ID consists of three different subsystems as shown in Fig. 3.3 and will be explained in the following. They cover a range up to $|\eta| < 2.5$ and are responsible for the measurement of the vertices to provide a good determination of the impact parameters which can be used to identify decays of short-lived particles like heavy-flavour quarks and tau leptons.

Pixel Detector The Pixel Detector (Pixel) is the innermost subdetector of the ID working with the semiconductor technology. It records the first traces of charged particles in the detector which is crucial for efficient track reconstruction and the reconstruction of primary and secondary vertices. The requirements on the material are challenging: on the one hand, the material budget should be as low as possible to avoid multiple scattering; on the other hand, it has to resist the high radiation. The Pixel covers a total area of 1.7 m^2. 80 million silicon pixels, each one having a size of $50 \times 400\,\mu\mathrm{m}^2$, compose a total of 1 744 modules. The high number of readout channels requires advanced electronic techniques connected to an elaborate readout structure.

Silicon Tracker The Silicon Tracker (SCT) is a silicon microstrip detector and encloses the Pixel. 4 088 two-sided modules are combined to more than 6 million readout channels. Each module consists of 768 strips with a pitch of 80 µm and a position resolution of 17 µm in the transverse direction. The back-side detector pair is rotated by 20 mrad to provide position information in the direction of the

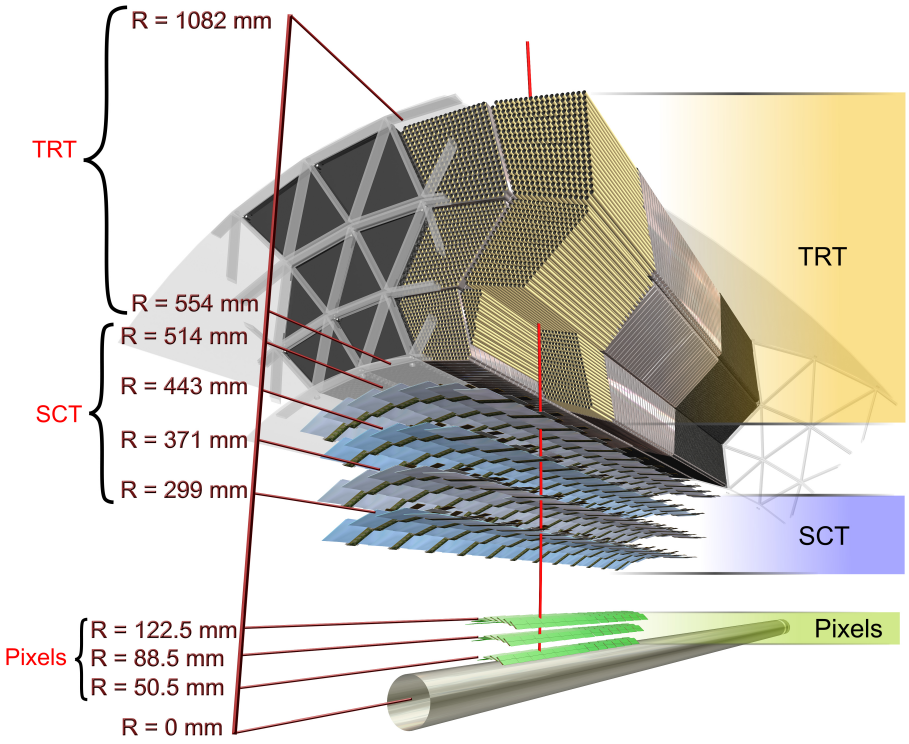

Figure 3.3: Profile of the ID with the three subdetectors and the corresponding length scales (taken from [68]).

readout strips with a resolution of 580 µm. It has a total area of 60 m^2 composed out of 4 barrel layers and 18 planar endcap discs. The SCT provides at least four hits for every charged traversing particle.

Transition Radiation Tracker The Transition Radiation Tracker (TRT) is the outermost part of the ID. In contrast to the other two subdetectors, it is not based on the semiconductor technology but a gaseous detector. It consists of 350 000 straw tubes with a diameter of 4 mm filled with a gas mixture of 70 % Xe, 27 % CO_2, and 3 % O_2[3]. When traversing the ID, each track crosses at least seven layers of semiconductor chips. The TRT gives on average 36 hits per track which constitutes an important part of efficient tracking. The track extension from the silicon subdetectors is achieved with less material and lower costs. However, the precision in the ϕ and the z coordinates is good compared to the semiconductor subdetectors.

Particles with a high relativistic factor of $\beta\gamma \gtrsim 1\,000$ send out transition radiation when passing the boundary of two different homogeneous materials, hence the name of the subdetector. As the

[3] Gas leakages were discovered in the TRT over the last years. The expensive xenon was therefore replaced in some layers by the cheaper gas argon.

relation $\beta\gamma = \frac{p}{m}$ holds, lighter particles have a high relativistic factor meaning the momentum needs to be lower to produce transition radiation than for more massive particles. The transition radiation causes a higher signal in a straw which is picked up by the high-threshold of a hit. The amount of high-threshold hits per track is used to distinguish electrons from hadrons, e.g. pions. A second quantity used for particle identification is the specific energy loss per path length $\frac{\mathrm{d}E}{\mathrm{d}x}$ which is provided by Pixel and SCT. According to the Bethe-Bloch formula, it allows separating kaons from pions from protons which is crucial to study B physics. It uses a time-over-threshold based approach as a pattern of connected low-threshold hits are calibrated following the detector geometry.

3.2.2 Calorimeters

The calorimeters enclose the ID, are responsible to stop electrically charged and neutral particles, and measure their energy. Furthermore, it is possible to trigger on the calorimeters. In addition, they play a crucial role in the calculation process of the quantity $E_{\mathrm{T}}^{\mathrm{miss}}$ which is described in Section 3.3.4. A sketch of the calorimeters and their components is displayed in Fig. 3.4. Due to the different interaction

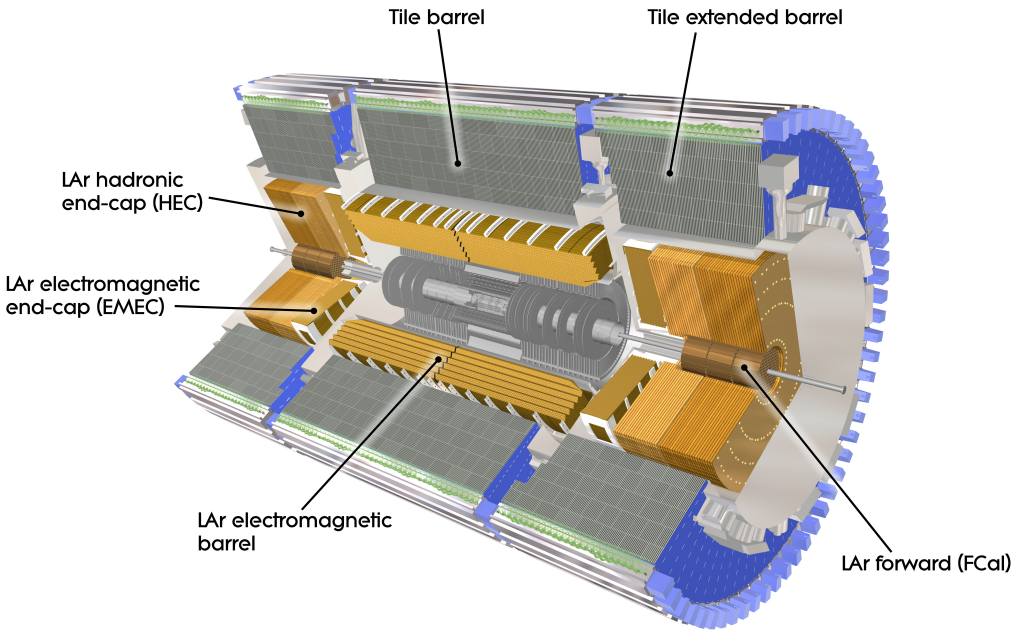

Figure 3.4: Sketch of the calorimeter system with the three subdetectors (taken from [69]).

processes of the different particle species, the calorimeters have specific types of sub-calorimeters again enclosing each other.

Electromagnetic Calorimeter The Electromagnetic Calorimeter (ECAL) [70] is a Liquid-Argon Calorimeter (LAr). It stops electromagnetically interacting particles, e.g. photons and electrons. They are forced to produce a cascade of photons, electrons, and positrons creating a narrow and short electromagnetic shower. A typical quantity to describe those electromagnetic showers is the radiation

length X_0 after which the incoming particle on average has decreased to $\frac{1}{e}$ of its initial energy. The ECAL is an accordion-shaped sampling calorimeter with fine granularity, especially in the first layer, using electrodes and lead absorbers in liquid argon. It has a fine granularity in η and ϕ. Like the ID, it consists of a barrel and an endcap part. The barrel part of this subdetector is 6.4 m long and covers a region of up to $|\eta| < 1.475$. The endcap consists of two wheels, one spanning between $1.375 < |\eta| < 2.5$ and the other one between $2.5 < |\eta| < 3.2$. As argon boils already at a temperature of approximately 87 K, the liquid argon is operated at cryogenic temperatures. The energy resolution of the ECAL is usually parametrised as

$$\frac{\sigma_E}{E} = \frac{a}{\sqrt{E}} \oplus \frac{b}{E} \oplus c, \tag{3.4}$$

where a is the stochastic term, b is the noise term, and c is the constant term. The energy E is given in the units of GeV. The typical values for the electron energy resolution of this subdetector are $a \simeq 10\,\%$, $b \simeq 170\,\text{MeV}$, and $c = 0.7\,\%$.

Hadronic Calorimeter The Hadronic Calorimeter (HCAL) [71] stops strongly interacting particles. Two different technical approaches have been chosen for the different pseudorapidity regions. In the barrel region of $|\eta| < 1.7$, a Tile Calorimeter () is employed with an alternating structure of iron plates and scintillating tiles. The tiles are read out by wave-length-shifter fibres on both sides, carrying the signal to photomultipliers. The tiles allow for a good sampling frequency and a compact design. The thickness of the barrel part in terms of the mean free path length λ is up to $7.4\,\lambda$. Each of the 5 000 calorimeter cells has a granularity of $\Delta\eta \times \Delta\phi = 0.1 \times 0.1$. The energy resolution of the Tile can be again described by Eq. (3.4). The specific values depend on the particle type but are at the order of 40–50 % for the stochastic term a and approximately 3 % for the constant term c. The overall resolution of the Tile is worse than for the ECAL [72].

The Hadronic End-Cap Calorimeter (HEC) consists of two independent wheels and uses liquid argon as well. The wheels of the HEC are built of 25 mm and 50 mm thick copper plates, respectively, stacked parallel to the beam direction and absorbing the particle's energy. The 8.5 mm gap between the plates is filled with liquid argon and three electrodes, where the main one transmissions the signal to amplifiers and the other two serve as power suppliers. The readout electrode provides a granularity of $\Delta\eta \times \Delta\phi = 0.1 \times 0.1$ in the region of $|\eta| < 2.5$ and of $\Delta\eta \times \Delta\phi = 0.2 \times 0.2$ in the region of $2.5 < |\eta| < 3.2$.

Forward Calorimeter The Forward Calorimeter (FCAL) covers the forward region and is supposed to stop particles flying close to the beam pipe. It encloses the pseudorapidity region of $3.1 < |\eta| < 4.9$ and has to cope with a high level of radiation and huge particle flux. The FCAL uses again liquid argon as a sensitive medium. It consists of three sections where the first one is made out of copper and the other two are made out of tungsten, both materials act as passive absorbers. Each section consists of a metal matrix with longitudinal channels parallel to the beam axis. A channel has a concentric rod enclosed by a tube where the small gap is filled with the liquid argon. These small gaps allow a compact construction of the FCAL with a thickness of integrated $9.5\,\lambda$.

3.2.3 Muon Spectrometer

The Muon Spectrometer (MS) [73] is the last and outermost of the big subdetector systems of the ATLAS detector. A sketch is displayed in Fig. 3.5. Muons leave only a little Bremsstrahlung in the ECAL due to the higher mass compared to the electrons. Hence, they pass the calorimeter system. A dedicated subdetector system is designed to allow for a precise momentum measurement and particle identification of muons. A toroidal magnet system bends the muon tracks due to the provided mostly

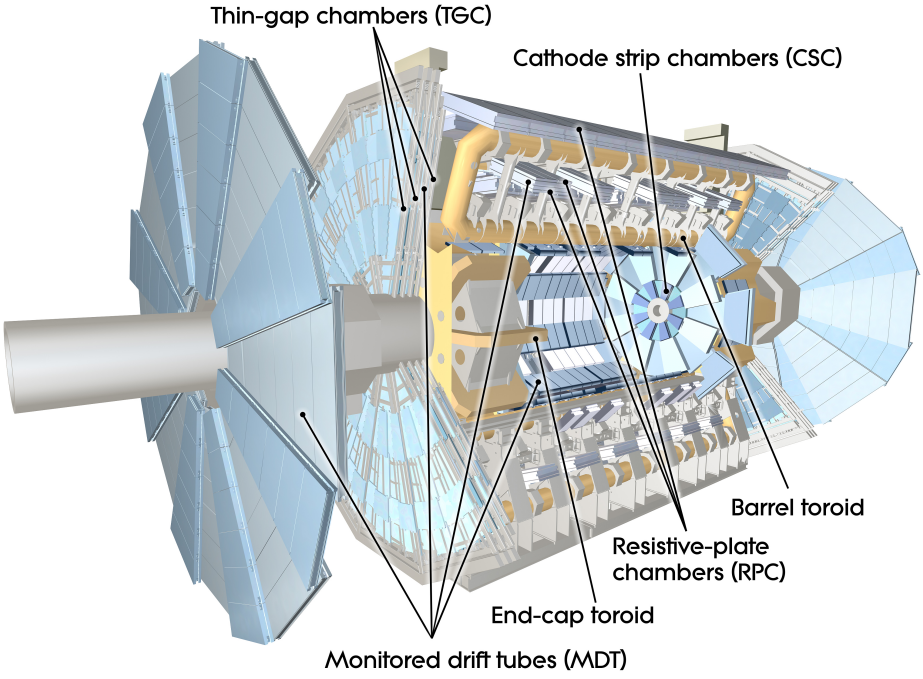

Figure 3.5: Overview of the MS and its four subsystems (taken from [74]).

orthogonal field. The coordinates of the muon tracks are measured precisely by the Muon Drift Tubes (MDTs) over a wide pseudorapidity range. The MDTs are arranged in three layers of cylindrical form around the beam pipe in the barrel ($|\eta| < 1.0$). In both endcaps, four wheels are installed at distances of 7.4 m, 10.8 m, 14 m, and 21.5 m from the IP, respectively. The MDTs are 354 240 aluminium tubes combined in 1 171 chambers. Each tube has a diameter of 30 mm and a length between 0.85 and 6.5 m. They are filled with a gas mixture of 91 % Ar, 5 % CH_4, and 4 % N_2. The resolution is 80 µm per tube. Cathode Strip Chambers (CSCs) are used closer to the beam pipe at higher pseudorapidity values of $2.0 < |\eta| < 2.7$. They have a fine granularity to cope with the high particle rates and provide a better time resolution. The CSCs are multiwire proportional chambers readout by cathode strips with a resolution of 60 µm. A gas mixture of 30 % Ar, 50 % CO_2, and 20 % CF_4 is used as it is less sensitive to variations of the gas parameters in comparison to the gas mixture of the MDTs. The conceptional design of the gas system is mostly the same in both precision chambers.

The MS has a separate trigger function in a pseudorapidity range of up to $|\eta| < 2.4$. A better timing resolution than the bunch spacing of the LHC of 25 ns is needed and a second coordinate orthogonal to the one taken by the precision chambers should be measured. Two different detector technologies are used in different regions of the detector. The Resistive Plate Chambers (RPCs) are

gaseous detectors installed in the barrel part. They use two rectangular detector layers where the "η-strips" are oriented parallel to the MDTs wires and the "ϕ-strips" are orthogonal to the MDTs wires and serve the required measurement of the second coordinate in the non-bending direction of the muon track. The two detector layers are readout by four strip panels optimised for a good transmission to allow for an excellent time resolution. In the endcap of the MS, Thin Gap Chambers (TGCs) are employed. They are multiwire proportional chambers but with the difference that the anode wire pitch is larger than the distance between cathode and anode. The readout strips arranged orthogonal to the MDTs wires provide the measurement of the second coordinate and are responsible for the triggering together with the anode wires.

3.2.4 Magnet System

The ATLAS detector uses two different magnet systems [75] to bend charged particles and allow for precise momentum measurement. The superconducting magnet system has an overall dimension of 26 m in length and 20 m in diameter. The Central Solenoid [76] encloses the ID and provides a magnetic field for the innermost subdetectors. It is 5.3 m long, 2.4 m in diameter, 4.5 cm thick, and weighs 5 t. A single layer coil with a length of 9 km is wound in a supporting cylinder. The superconducting wires traversed by a current of 7.73 kA create a magnetic field of 2 T. The whole Solenoid is supported by the cryostat of the LAr.

The toroidal magnets are part of the muon system and provide a toroidal field configuration for the MS. As this magnet technology is unique, it entered into the name of the ATLAS detector. The toroidal magnets are split into three different subsystems, namely the air-core Barrel Toroid [77] and two air-cored End-Cap Toroids [78], to simplify the design and assembly, and to make it easier to access the inner parts of the detector. Each toroid provides a magnetic field of about 4 T created by eight coils made of aluminium stabilised NbTi superconductors using a current of 20.5 kA. Pumps are forcing helium to flow through the toroidal magnets and cool the wires down to a temperature of 4.5 K.

3.2.5 Trigger System

The LHC provides a collision of two proton bunches every 50 ns in Run-1 and every 25 ns at the design instantaneous luminosity of $\mathcal{L} = 10^{34}\,\mathrm{cm}^{-2}\,\mathrm{s}^{-1}$ [53]. This means a bunch crossing rate of up to 40 MHz but ATLAS can only record approximately 200 events per second equivalent to $\approx 300\,\mathrm{MB/s}$ due to the limited offline storage resources. A three staged trigger system is responsible to level down the event rate to the desired value. It looks for interesting physics event signatures like muons, electrons, photons, tau leptons, and jets but global signatures as missing transverse energy.

The first level (L1) is a purely hardware-based trigger using information from the calorimeters and the muon system. The second level (L2) and the third level, often referred to as Event Filter (EF), are software-based triggers using information from all subsystems. The combination of L2 and EF is referred to as a High-Level Trigger (HLT). The whole trigger system fires only if one out of hundreds of different trigger conditions is fulfilled.

The signal from different subdetectors is propagated to front-end pipelines waiting for a decision of the L1 trigger stage. As this stage has to be fast to cope with the huge rate of bunch crossing, a latency of fewer than 2.5 µs is achieved by using fast custom electronics. In this step, the rate should be reduced to 75 kHz and Regions of Interest (RoIs) are identified which are the detector part where interesting event signatures have been found. These RoIs are propagated and further used by the HLT.

If an event is accepted by the L1 trigger, it is propagated to detector-specific Readout Buffers (ROBs) depending on the decision of the L2 stage. The L2 trigger reduces the rate further to 3 kHz with an average processing time of 40 ms per event. The L2 stage uses fast custom algorithms to select events based on partial event reconstruction within the RoIs found by L1. All event fragments of ROBs accepted by the L2 trigger are put together by an event builder. Full event information prepared for the EF allows offline algorithms to decide within about 4 s. Events passing the last stage of the trigger system are finally recorded, stored, and made available for offline processing and data analyses. The whole HLT is a processor farm and consists of about 1 100 nodes each having eight cores. Based on the trigger configuration, the physics streams have dedicated names where "Egamma", "Muons", "JetTauEtmiss", and "MinBias" are the four main ones [79, 80].

3.2.6 Data taking procedure

The presented analysis uses data recorded between March and October 2011 at $\sqrt{s} = 7\,\text{TeV}$. The integrated luminosity $\mathcal{L}_{\text{int}}$ delivered during this period by the LHC sums up to $5.46\,\text{fb}^{-1}$ and has an uncertainty of 1.8 % as described in [63]. After LHC has declared "stable beams", it takes several minutes for all subsystems of ATLAS to go into a state where data can be recorded. e.g. the Pixel has to turn on the high voltage. Hence, not all but $5.08\,\text{fb}^{-1}$ data delivered by the LHC were recorded by ATLAS. This corresponds to a data taking efficiency of 93.04 %. If subsystems have a malfunction, the recorded data are not labelled "Good for Physics" which is required to be further analysed. A total of $4.57\,\text{fb}^{-1}$ is used in this analysis corresponding to a detector efficiency of 89.96 %. All data which fulfil the requirement "Good for Physics" are saved in the Good Run List (GRL). A graphical summary of the different labelled integrated luminosity values over time is given in Fig. 3.6(a).

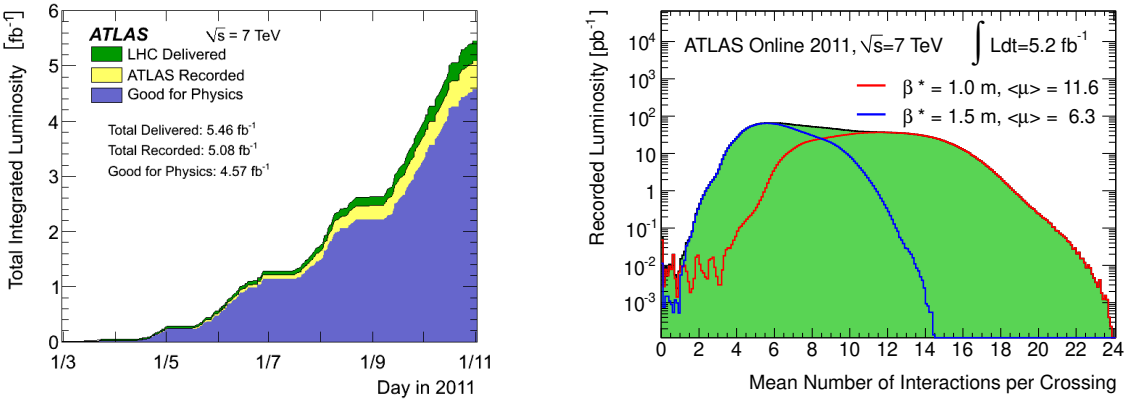

(a) Integrated luminosity.

(b) Pileup.

Figure 3.6: Performance plots of the 2011 data taking period. (a) shows the integrated luminosity over the course of time and (b) the distribution of the mean number of interactions per crossing (taken from [81]).

The maximum instantaneous luminosity $\mathcal{L}$ in 2011 was $3.65 \times 10^{33}\,\text{cm}^{-2}\,\text{s}^{-1}$ [81]. Often, there are several interactions per bunch crossing, for the 2011 data taking period it has been up to 24. Whereas one of these interactions might result in an interesting physics signature in the detector, the others are referred to as "pile-up" and have to be taken into account in the reconstruction of data and simulated events. The recorded luminosity over the mean number of interactions per bunch crossing $\langle\mu\rangle$ is

shown in Fig. 3.6(b). The two overlaid pile-up distributions are due to the changed β^* (cf. Section 3.1) which was reduced after a technical stop in September 2011 from 1.5 m to 1.0 m. This decreased $\langle\mu\rangle$ from 6.3 to 11.6. The events at low pile-up μ ~0 are from pilot bunches used in early LHC fills and have a more than 100 times smaller luminosity than the main bunches.

3.3 The event and object reconstruction

The different specialised subsystems of the ATLAS detector work nicely together to reconstruct different types of particles which are stable in the dimensions of the detector. A profile of the detector parts with various particles leaving traces is shown in Fig. 3.7. The reconstruction and identification processes of all particle flavours relevant for this thesis are presented in the following.

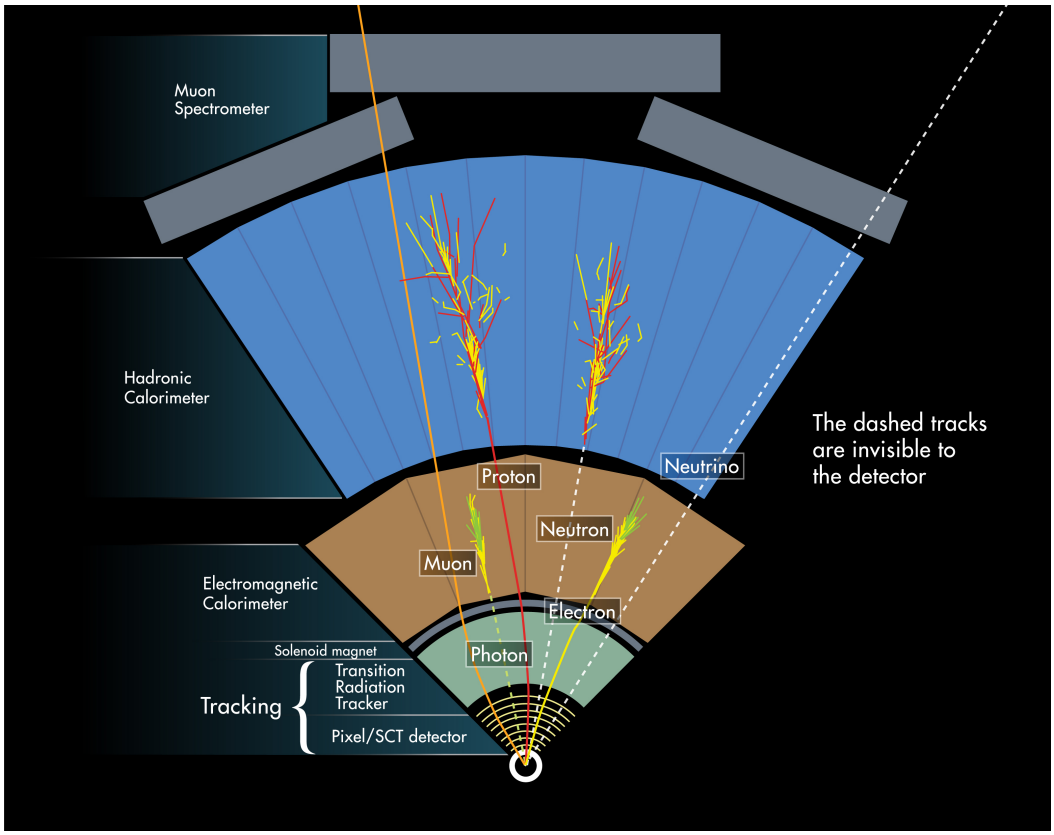

Figure 3.7: Illustration of different particle types interacting with the detector material. Each of the shown particles (photon, electron, muon, neutron, proton, neutrino) leaves a unique signature in the different subdetectors which is the foundation of the object reconstruction (taken from [82]).

3.3.1 Electrons

Electrons traversing the detector in the central region ($|\eta| < 2.5$) are reconstructed in a three-step process. Clusters in the ECAL are seeded if a certain group of cells has a transverse energy $E_T > 2.5$ GeV. Tracks of the ID with $p_T > 0.5$ GeV are extrapolated from the last hit to the middle

layer of the ECAL. A track is successfully matched to a corresponding cluster if the coordinates η and ϕ are within a range of $|\Delta\eta| < 0.05$ and $|\Delta\phi| < 0.1$, respectively. A reconstructed electron candidate is required to have one track with an associated cell cluster. If a track is matched with more than one cluster, the cluster with the lowest ΔR compared to the hits in the Pixel and the SCT is chosen. A cell cluster without a matched track is identified as an unconverted photon candidate. After this step, the calorimeter clusters are enlarged to determine the energy of the electron candidate.

Electrons in the forward region ($2.5 < |\eta| < 4.9$) lack a track as the tracking detector does not cover this region in pseudorapidity and a distinction between electrons and photons is not possible. Only information of the ECAL endcaps and the FCAL can be used and electron candidates are required to have $E_{\mathrm{T}} > 5\,\mathrm{GeV}$. An iterative topological cluster algorithm is used to determine the cluster size of the cells. These forward electrons are not used in the presented analysis and hence the reconstruction will not be further discussed but can be read in [83].

Three different working points for the electron identification of central electrons, namely loose, medium, and tight are defined based on sequential cuts on track, calorimeter, and combined variables. The tighter the working point is the better is the background rejection arising from misidentified hadrons, non-isolated electrons from semi-leptonic heavy flavour decays, and photon conversions but the tighter is the selection on the isolated electrons. The identification efficiency, defined as the data-to-simulation efficiency or referred to as scale factors (SFs), in % over the transverse energy E_{T} for the three different working points is shown for the 2011 dataset in Fig. 3.8(a). The identification efficiency is higher the looser the working point. It is clearly visible that the efficiency rises with transverse energy [83, 84].

The online reconstruction of electrons uses the electron trigger of Run-1 [85]. A reduced granularity of the ECAL is used to find electromagnetic showers for the L1 stage and calculate the transverse energy of the cluster with a precision of 1 GeV. The identified RoIs found by L1 are taken as a seed for the HLT reconstruction. Information like shower shape variables, track quality, and electron identification information from the TRT are used to discriminate against the background. The threshold on E_{T} was raised from 20 GeV to 22 GeV to cope with the increasing luminosity.

Electron candidates used in this analysis are required to have a transverse momentum of $p_{\mathrm{T}}^{\ell} > 15\,\mathrm{GeV}$ and to pass the tight working point. The pseudorapidity is required to be $|\eta| < 2.4$ and the range $1.2 < |\eta| < 1.82$ is excluded as the passive material in front of the calorimeters in this region is large such as the energy response is not correctly described. To reject background events, isolation requirements on the scalar sum of the p_{T} of the tracks within a cone of $\Delta R < 0.4$, $p_{\mathrm{T}}^{e,\mathrm{cone}}$, and on the transverse calorimeter energy deposited in a cone of $\Delta R < 0.2$, $E_{\mathrm{T}}^{\mathrm{cone}}$, are set to be small, whereas the contribution of the electron candidate itself to the isolation requirements is excluded [86].

3.3.2 Muons

In the process of muon reconstruction and identification, information of the MS, the ID, and to less extent of the calorimeters is used. Based on the used information of the different sub-systems, four main muon types can be defined:

- For **Stand-Alone muons (SA muons)**, the muon trajectory is only reconstructed in the MS if the track traverses at least two chambers. The parameters of the IP are calculated by extrapolating the muon track back to the beamline. The SA muons are used to extend the acceptance region in pseudorapidity to $2.5 < |\eta| < 2.7$ to account for the lack of track reconstruction.

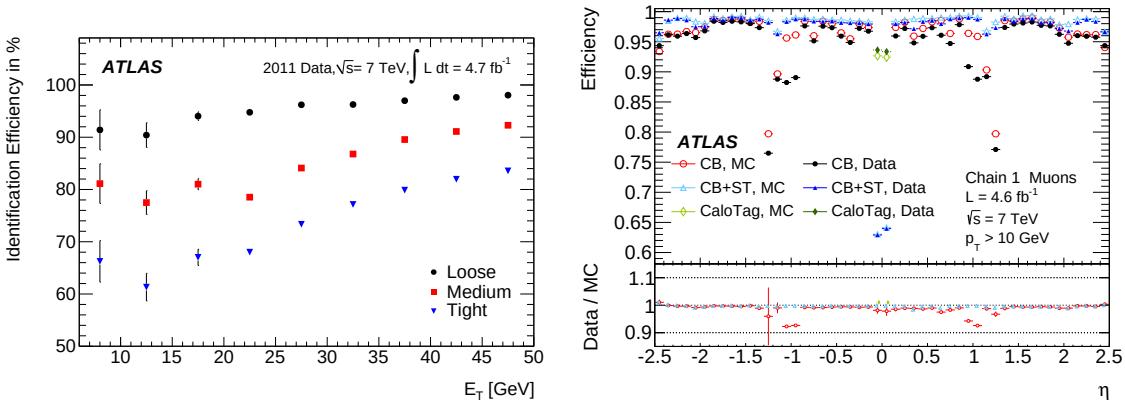

(a) Electron performance.

(b) Muon performance.

Figure 3.8: Performance of the light lepton identification for the 2011 data taking period. a) shows the identification efficiency over the quantity E_{T} for the three different working points, and b) the muon efficiency versus η for the different muon types comparing simulation to data (taken from [83, 87]).

- **Combined muons (CB muons)** use a separate track reconstruction in the ID and the MS which are afterwards combined to a combined track by matching the information of the two subdetectors.

- **Segment-tagged muons (ST muons)** are reconstructed tracks in the ID that can be matched with a segment in the MDTs or the CSCs if it is extrapolated. This kind of muons can increase the sensitivity in regions of low acceptance in the MS or if the muon track has low p_{T} and therefore only crosses one layer of the MS chambers.

- **Calorimeter-tagged muons (CaloTag muons)** use the information of the calorimeter as an ID track is associated with an energy deposit of a minimum ionising particle. The purity of this muon type is the lowest but not instrumented regions of the MS are covered as well.

The CB muons have the highest purity of all muon types. The SA muons and CB muons are suffering from low acceptance in two regions of the MS: the central region around $\eta \approx 0$ is only partially equipped with muon chambers to leave space for services of the ID and the calorimeters. The region $1.1 < \eta < 1.3$ between the barrel and the positive η endcap was not equipped with all layers in some regions in ϕ. The reconstruction of all muon types using ID and MS information is performed by a reconstruction software package called “Chain 1”. A statistical combination of the track parameters of SA muons and ID muon tracks is performed. The reconstruction efficiency of the different muon types over the pseudorapidity η is shown in Fig. 3.8(b).

The presented efficiencies are calculated using a “tag and probe” method in the decay of $Z \rightarrow \mu\mu$. The combination of CB muons and ST muons has the highest efficiency, usually around 99 %. However, one sees a drop in the central region due to a crack in the MS and around the region $|\eta| \approx 1.2$. A layer of MDTs was not installed there for the detector setup in 2012 leading to an inefficiency introduced by the ID selection [87].

Similar to the electrons, a single muon trigger is used for the online reconstruction of this measurement. The L1 stage of the muon trigger of Run-1[88] collects information on the transverse

momentum and the position of the detector region. The position information defines the RoIs for the HLT stage which adds precision data from the MDTs. The L2 stage uses SA muons based on tracks in the RoIs found by the L1 stage in the MS to further reduce the amount of data. There are three different triggers on the EF level: the standalone trigger uses only information of the MS, the combined trigger pursuing the "outside-in" strategy where the MS track is combined with an ID track, and the "inside-out" trigger which starts from the ID track and extrapolates then to the muon detectors. This three triggers were run in parallel for the 2011 data taking period to minimise the probabilty of losing an event in the online selection. The trigger threshold of all stages is 18 GeV.

In this analysis, muon candidates are required to have $p_{\mathrm{T}}^{\ell} > 20\,\mathrm{GeV}$ and $|\eta| < 2.4$, and to be CB muons. Only the information of the ID is used to define the kinematic properties of the muon to simplify the calibration procedure. The ID tracks of the muon candidate must fulfil certain quality requirements on the number of hits in every subdetector. To suppress background from cosmic rays, a cut on the longitudinal impact parameter is applied to be $|z_0| < 10\,\mathrm{mm}$. An isolation requirement on the scalar sum of the p_{T} of the tracks within a cone of $\Delta R < 0.2$, $p_{\mathrm{T}}^{\mu,\mathrm{cone}}$, is set to be less than 10 % of the muon candidate, such that $\frac{p_{\mathrm{T}}^{\mu,\mathrm{cone}}}{p_{\mathrm{T}}^{\mu}} < 0.1$ [86].

3.3.3 Hadronically decaying tau leptons

As outlined in Section 2.6, tau leptons can decay both, hadronically and leptonically. The latter one cannot be easily differentiated from prompt the light leptons, electrons and muons. Only hadronically decaying tau leptons can be identified and reconstructed as such. Hence, the terms *light leptons* and *leptons* used in the context of reconstructed objects refer always to the two lightest charged leptons, the electron and the muon.

Each jet above 10 GeV is considered a tau candidate. In principle, strongly interacting particles like gluons and quarks leaving a signature are understood under the term "jets". Due to the confinement, single quarks and gluons hadronise when traversing the detector and leave a spray-like structure in the detector. This makes the reconstruction challenging for jet finding algorithms. The calorimeter cells are clustered in an iterative approach. A common cluster algorithm used within the ATLAS collaboration is the anti-k_T algorithm with $R = 0.4$ [89].

The technique referred to as Boosted Decision Trees (BDTs) is used to discriminate tau leptons from quark- or gluon-initiated jets. The discrimination is based on a set of shower shape and tracking observables. A second BDT is trained using calorimeter and transition radiation information of the TRT to differentiate tau leptons from electrons. Similar to the electron reconstruction, three working points with different signal efficiency and background rejection are implemented for tau leptons. More information can be found in [90] as the reconstruction algorithm of hadronically decaying tau leptons has been the same for the 2011 and 2012 datasets. In this analysis, only leptonically decaying tau leptons are considered.

3.3.4 Missing transverse momentum

The missing transverse momentum is a common concept at hadron colliders. As the initial longitudinal momentum is not known due to the structure of the proton, momentum conservation is only considered in the transverse plane as the protons do not have any initial momentum in this plane. The missing transverse momentum $\vec{p}_{\mathrm{T}}^{\,\mathrm{miss}}$ and its magnitude $E_{\mathrm{T}}^{\mathrm{miss}}$ are important quantities as they describe particles

leaving the detector unnoticed. This is the case not only for all analyses including neutrinos but all searches for BSM scenarios like SUSY and extra dimensions looking for new stable particles not interacting with the detector material.

The quantity $E_{\mathrm{T}}^{\mathrm{miss}}$ is reconstructed by including contributions from the calorimeters and the MS. The individual components of the transverse plane are calculated like

$$\begin{aligned} E_{x(y)}^{\mathrm{miss}} &= E_{x(y)}^{\mathrm{miss,calo}} + E_{x(y)}^{\mathrm{miss},\mu} \\ E_{x(y)}^{\mathrm{miss}} &= E_{x(y)}^{\mathrm{miss},e} + E_{x(y)}^{\mathrm{miss},\gamma} + E_{x(y)}^{\mathrm{miss},\tau} + E_{x(y)}^{\mathrm{miss,jets}} + E_{x(y)}^{\mathrm{miss,softjets}} + E_{x(y)}^{\mathrm{miss,CellOut}} + E_{x(y)}^{\mathrm{miss},\mu}. \end{aligned} \tag{3.5}$$

All reconstructed objects originating from a high p_{T} source are used, namely electrons, photons, hadronically decaying tau leptons, jets, and muons. Calorimeter cells not associated with one of these objects are taken into account under the term $E_{x(y)}^{\mathrm{miss,CellOut}}$ playing a crucial role in the resolution of $E_{\mathrm{T}}^{\mathrm{miss}}$. Each term of Eq. (3.5) is calculated by the negative sum of all energy cells associated with the given object. The muon term is calculated from the negative sum of all momenta matched with CB muons. All individual components of $E_{x(y)}^{\mathrm{miss}}$ are calibrated separately. The final values of $E_{\mathrm{T}}^{\mathrm{miss}}$ and its azimuthal angle ϕ^{miss} are defined as

$$\begin{aligned} E_{\mathrm{T}}^{\mathrm{miss}} &= \sqrt{\left(E_x^{\mathrm{miss}}\right)^2 + \left(E_y^{\mathrm{miss}}\right)^2} \\ \phi^{\mathrm{miss}} &= \arctan\left(E_y^{\mathrm{miss}}, E_x^{\mathrm{miss}}\right). \end{aligned}$$

More information about the reconstruction and calibration procedure of the missing transverse momentum can be found in [91].

3.3.5 Hadronic recoil

The momentum of the vector boson cannot be measured directly in ATLAS as one of the decay products, the neutrino, escapes the detector unnoticed. The hadronic recoil in the transverse plane $\vec{u}_{\mathrm{T}}$ gives a good estimate for the momentum of the vector boson and is defined as

$$\vec{u}_{\mathrm{T}} = \sum_i \vec{E}_{\mathrm{T},i}.$$

It is the vector sum of the transverse energy of all clusters except for the ones associated with a decayed light lepton, where $\vec{E}_{\mathrm{T},i}$ is the contribution of cluster i. The vector $\vec{E}_{\mathrm{T}}$ of the transverse energy is determined by its magnitude $E_{\mathrm{T}} = E/\cosh\eta$, where E is the energy and η the pseudorapidity of the given cluster, and the azimuthal angle ϕ comes from the coordinate of the cluster in the transverse plane. The negative recoil $-\vec{u}_{\mathrm{T}}$ should provide a good estimate of the transverse momentum of the W- and Z-boson in the corresponding decays.

The calorimeters measure the energy deposits of a particle in a range of $|\eta| < 4.9$ and a topological clustering algorithm [92] is based on cells with a sufficient signal-to-noise ratio of at least four times than what is expected from electronics and pile-up. The energy deposits are considered to be initiated only by the electromagnetic interaction in the first step. Later, the calorimeter responses are corrected for hadrons and electromagnetic particles, losses caused by dead material, and energy not considered by the clustering algorithm. The reconstruction of particle jets is not included to avoid threshold

effects.

Calorimeter clusters located in a region of $\Delta R < 0.2$ around a lepton candidate are not taken into account in the reconstruction process of the recoil. This should guarantee that the energy deposit of the lepton itself and possible coexisting photons is not biasing the recoil reconstruction. The energy deposit of soft particles might be removed using this procedure. Therefore, the total transverse energy in a cone with the same size $\Delta R = 0.2$ at the same pseudorapidity as the lepton but with randomly chosen sign and at different azimuth ϕ is rotated to the position of the lepton and added to the reconstruction of the recoil vector $\vec{u}_{\mathrm{T}}$.

3.4 The simulation of particle collisions

The simulation of the investigated processes is crucial for any physics analysis. A reliable prediction provides the prediction for the expected signal and background processes and is needed to optimise the event selection to increase the signal over background ratio. The simulation of particle collisions is based on the Monte Carlo (MC) technique using the concept of *factorisation* introduced in Section 2.5.2. The separation between the "hard" and the "soft" regime is illustrated in Fig. 3.9. The hard scattering part shown in red can be calculated up to higher orders using perturbation theory. The blue lines symbolise initial and final state radiations. The underlying event (purple) and the hadronisation (green) with the subsequent showering into jets can only be accessed on a phenomenological level [93].

According to Eqs. (2.35) and (2.36), the renormalisation and factorisation scale is set equal to the considered energy scale $\mu_F = \mu_R = Q$. In the case of a resonance production of the W-boson, the hard scale is identified with the mass m_W of the simulated particle $Q = m_W$ [29, 94]. The order of α_S in the expansion of the partonic cross-section (cf. Eq. (2.36)) determines the order of the MC simulation, e.g. LO or NLO.

3.4.1 The prediction of Standard Model processes

Simulated MC samples are prepared for the signal processes $W \to \ell\nu$ ($\ell = \mu, e$) and $W \to \tau\nu$ as well as the background contributions $Z \to \ell\ell$ ($\ell = \mu, e$), $Z \to \tau\tau$, diboson (WW, WZ, ZZ), and $t\bar{t}$ +singletop. All events of the generated samples are put through the whole ATLAS simulation and reconstruction chain based on a software [95] using `Geant4` [96]. The multijet background with non-prompt leptons in the final state is determined using a data-driven technique and described in Section 5.3.

The vector boson samples are produced assuming certain values for important SM parameters: the masses of the W- and Z-samples were set to $m_W = 80\,399.0\,\mathrm{MeV}$ and $m_Z = 91\,187.5\,\mathrm{MeV}$ and the widths to $\Gamma_W = 2\,085.0\,\mathrm{MeV}$ and $\Gamma_Z = 2\,495.2\,\mathrm{MeV}$. Distributions with varying W-boson mass and width are produced based on these nominal values as described in Section 4.4. The used generators for the different types of SM processes are listed in the following. A detailed overview of the MC samples, the used generator, the cross-section, the number of generated events and the corresponding integrated luminosity is given in Table 3.1.

W-samples The hard-scattering part of this process is simulated by the `Powheg` MC generator [97–99] using the CT10 PDF set [100] for the matrix element calculations. The step of parton showering, hadronisation and the underlying event is simulated by `Pythia8` [101, 102] based on the CTEQ6L1

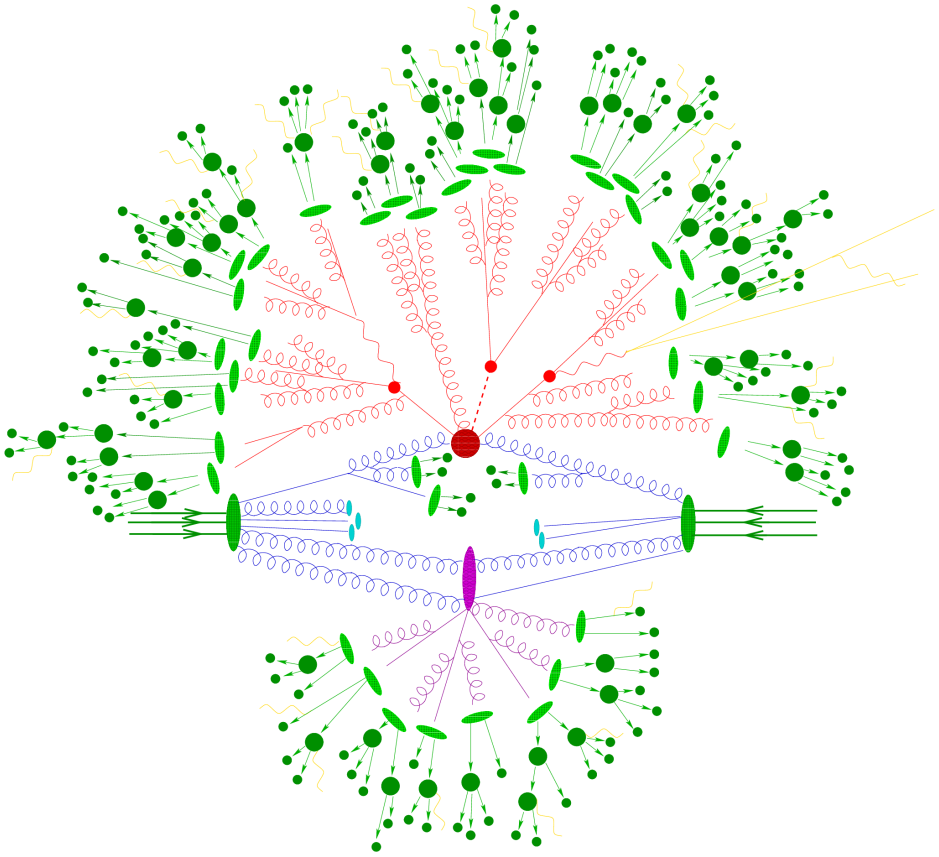

Figure 3.9: Graphical illustration of the simulation of a proton–proton collision. The different colours represent different simulation aspects: the red parts stand for the hard scattering, the blue pieces denote the radiation processes, the purple parts represent the underlying event, and the green pieces highlight the hadronisation (taken from [93]).

PDF set [103] with the parameters set according to the AZNLO tune [104]. For the tau lepton decays, `Pythia8` takes care of polarisation effects. The final-state radiation effects due to QED are simulated with `Photos` [105].

Z-samples The simulation step of the hard-scattering process and the part including parton showering, hadronisation and the underlying event is the same as for the W-samples. The effect of virtual photon production γ^* and the interference of Z and γ^* is included.

Other backgrounds The top background consist of $t\bar{t}$-pair-production, which is dominant, and single pair production processes including s- and t-channel production as well as Wt-events. These are simulated by the `MC@NLO` MC generator [106–108] and interfaced with `Herwig` [109] and `Jimmy` [110]. The gauge boson pair production (WW, WZ, ZZ) is simulated by `Herwig` at NLO. For the mentioned samples, the CT10 PDF set is used. Heavy-flavour multijet samples $b\bar{b} + X$ and $c\bar{c} + X$ are simulated by `Pythia8` at LO to validate the data-driven multijet background technique.

Several corrections have to be applied to the MC samples to remedy differences between simulation

Process	Generator	Dataset ID	$\sigma \times BR$[pb]	$\mathcal{L}_{\text{int}}$[fb^{-1}]
		W-samples		
$W^+ \to \mu^+\nu_\mu$	Powheg+Pythia8	147401	6 344.9	15.042
$W^- \to \mu^-\overline{\nu}_\mu$	Powheg+Pythia8	147404	4 376.5	14.891
$W^+ \to e^+\nu_e$	Powheg+Pythia8	147400	6 344.9	14.778
$W^- \to \mu^-\overline{\nu}_\mu$	Powheg+Pythia8	147403	4 376.5	15.062
$W^+ \to \tau^+(\to e^+, \mu^+)\nu_\tau$	Powheg+Pythia8	147412	930.04	16.000
$W^- \to \tau^-(\to e^-, \mu^-)\overline{\nu}_\tau$	Powheg+Pythia8	147415	603.63	16.550
		Z-samples		
$Z \to \mu^+\mu^-$	Powheg+Pythia8	147407	990.3	29.784
$Z \to e^+e^-$	Powheg+Pythia8	147406	990.3	29.808
$Z \to \tau^+\tau^-(\to e, \mu)$	Powheg+Pythia8	147418	260.42	22.543
		Other backgrounds		
WW	Herwig	105985	17.47	140.742
ZZ	Herwig	105986	1.28	193.562
WZ	Herwig	105987	5.38	184.397
$t\bar{t}$	MC@NLO+Herwig+Jimmy	105200	96.26	119.110
single-top, t-channel $e\nu$	MC@NLO+Herwig+Jimmy	108340	6.83	25.737
single-top, t-channel $\mu\nu$	MC@NLO+Herwig+Jimmy	108341	6.82	25.731
single-top, t-channel $\tau\nu$	MC@NLO+Herwig+Jimmy	108342	6.81	25.670
single-top, s-channel $e\nu$	MC@NLO+Herwig+Jimmy	108343	0.46	546.170
single-top, s-channel $\mu\nu$	MC@NLO+Herwig+Jimmy	108344	0.46	546.370
single-top, s-channel $\tau\nu$	MC@NLO+Herwig+Jimmy	108345	0.46	546.608
single-top, Wt	MC@NLO+Herwig+Jimmy	108346	14.37	54.954

Table 3.1: MC samples used in the analysis, with the respective cross-sections, initial number of events and corresponding integrated luminosity of each sample.

and data. Differences related to efficiencies and energy scales are provided by the collaboration in the form of SFs and their uncertainties are discussed in Chapter 7. A certain pile-up $\langle\mu\rangle$ distribution is assumed in the MC samples before the data is taken. This best guess has to be corrected to fit the actually measured distribution (cf. Fig. 3.6(b)).

CHAPTER 4

The premise

The investigated properties of the W-boson cannot be measured directly in the detector. The ATLAS detector solely provides information about the momentum, the energy, the particle type, and the path the particle took in the detector. Furthermore, the W-boson decays before it can be measured in the ATLAS detector. The kinematic distributions of interest are obtained from decay particles or compound quantities. To measure the mass m_W and the width Γ_W of the W-boson, the impact of changes to these properties upon the shape of kinematic distributions is studied. In contrast, the lepton universality measurement compares the event yields of the different decay processes by using the differently shaped kinematic distribution. The kinematic spectrum of processes involving an intermediate tau lepton is softer since the additionally produced neutrinos carrying some part of the total momentum and energy away.

The presented measurements of the quantities m_W, Γ_W, and the lepton universality of the W-boson are not the first ones of their kind but line up in the history of several predecessor measurements. To understand the challenges of these analyses, former measurements of relevant properties of the W-boson are presented. First, important observables are introduced followed by the strategy of the cited publications. The theoretical expected values of the W-boson properties and a motivation why precise measurements are important is outlined in Section 2.4.

4.1 Observables for the measurement of W-boson properties

Several kinematic observables of leptonic W- and Z-boson decays are used in all the presented analyses. They are not only part of the event selection to distinguish signal from background processes, but in addition important for the determination of the measured quantity in a fit procedure.

- The transverse momentum $\boldsymbol{p}_{\mathbf{T}}^{\boldsymbol{\ell}}$ of the charged lepton in W and Z decays. The four-vector is completed by the pseudorapidity $\boldsymbol{\eta}_{\boldsymbol{\ell}}$, the azimuthal angle $\boldsymbol{\phi}_{\boldsymbol{\ell}}$ and the mass of the lepton $\boldsymbol{m}_{\boldsymbol{\ell}}$.

- The invariant mass $\boldsymbol{m}_{\boldsymbol{\ell\ell}}$, the rapidity $\boldsymbol{y}_{\boldsymbol{\ell\ell}}$, and the transverse momentum $\boldsymbol{p}_{\mathbf{T}}^{\boldsymbol{\ell\ell}}$ are calculated by combining the two four-vectors of the leptons in the decay of Z-bosons.

- The recoil in the transverse plane $\vec{\boldsymbol{u}}_{\mathbf{T}}$ as described in Section 3.3.5. In Z-boson decays, the quantities $\boldsymbol{u}_{\parallel}^{\boldsymbol{Z}}$ and $\boldsymbol{u}_{\perp}^{\boldsymbol{Z}}$ are defined as the projections of the recoil parallel and perpendicular on

the transverse momentum of the Z-boson, respectively. Whereas $u_{\parallel}^{Z}$ is compatible with $-p_{\mathrm{T}}^{\ell\ell}$ and is a good check of the detector linearity and resolution of the recoil. The mean of the perpendicular projection of the recoil $\langle u_{\perp}^{Z} \rangle = 0$ should vanish and the width of this distribution is a good measure for the recoil resolution. In W decays, $\boldsymbol{u}_{\parallel}^{\boldsymbol{\ell}}$ and $\boldsymbol{u}_{\perp}^{\boldsymbol{\ell}}$ are the projections of the recoil parallel and perpendicular onto the transverse momentum of the charged lepton ℓ.

- The vector of the missing transverse momentum $\vec{\boldsymbol{p}}_{\mathbf{T}}^{\mathbf{miss}}$ and its magnitude $\boldsymbol{E}_{\mathbf{T}}^{\mathbf{miss}}$ should describe the decayed neutrino and its properties. The missing transverse momentum vector is defined as

$$\vec{p}_{\mathrm{T}}^{\,\mathrm{miss}} = -\left(\vec{p}_{\mathrm{T}}^{\,l} + \vec{u}_{\mathrm{T}}\right)$$

- The transverse mass $\boldsymbol{m}_{\mathbf{T}}^{\boldsymbol{W}}$ of the W-boson is defined as

$$m_{\mathrm{T}}^{W} = \sqrt{2 p_{\mathrm{T}}^{\ell} p_{\mathrm{T}}^{\mathrm{miss}} \left(1 - \Delta\phi\left(p_{\mathrm{T}}^{\ell}, p_{\mathrm{T}}^{\mathrm{miss}}\right)\right)} \tag{4.1}$$

4.2 The origin of the Jacobian peak

The transverse momentum of the decayed lepton, p_{T}^{ℓ}, and the transverse mass of the W-boson, m_{T}^{W}, are sensitive observables to m_W at hadron colliders and hence considered in the fit to identify the signal contribution. The connection of the analysed distributions to the W-boson mass is presented in the following, starting from the production of W-bosons. One possibility to produce a W^+ at the LHC is via the fusion of an up-quark and an antidown-quark. The positively charged W-boson decays then further to a positively charged lepton and the corresponding neutrino. Assuming no natural decay width of the W, the partial cross-section of this process at LO is

$$\hat{\sigma}_{u\bar{d}\to\ell^{+}\nu} = \frac{1}{2}\frac{|V_{ud}|^2}{3\pi}\left(\frac{G_{\mathrm{F}} m_W^2}{\sqrt{2}}\right)^2 \delta\left(m^2 - m_W^2\right), \tag{4.2}$$

where $|V_{ud}|^2$ is the transition element of the quark flavours u and d of the CKM matrix (cf. Eq. (2.14)), and m the invariant mass of the W-boson decay system. The unpolarised differential cross-section as a function of p_{T}^{ℓ} at LO can then be described as

$$\frac{\mathrm{d}\hat{\sigma}_{u\bar{d}\to\ell^{+}\nu}}{\mathrm{d}p_{\mathrm{T}}^{\ell}} \propto \frac{\left(1 - \frac{2p_{\mathrm{T}}^{\ell}}{m_W^2}\right)}{\sqrt{1 - \frac{4p_{\mathrm{T}}^{\ell}}{m_W^2}}}. \tag{4.3}$$

Equation (4.3) defines the "Jacobian peak". If the W-boson decays at rest, the p_{T}^{ℓ} distribution of the lepton has a Jacobian edge at the value $m/2$ and the m_{T}^{W} distribution has an endpoint at the value of m [111] with m being the invariant mass of the system of the decay products of the W-boson as shown in Fig. 4.1. Assuming a natural decay width of the W-boson with a value of 2 100 MeV, the δ function

of Eq. (4.2) transforms like

$$\delta\left(m^2 - m_W^2\right) \rightarrow \frac{m^2}{\left(m^2 - m_W^2\right)^2 + \left(m^2\Gamma_W/m_W\right)^2}. \tag{4.4}$$

Introducing the natural width of the W-boson smears the hard Jacobian edge for both distributions. By increasing the order of the considered decay chain, the possibility of gluon emissions from the producing quarks are taken into account which is referred to as initial state radiation (ISR). The ISR of QCD contributes to the LO cross-section of Eq. (4.2). The gluon emissions alter the W-boson transverse momentum which does not decay at rest anymore. The transverse momentum distribution of the lepton changes as the Jacobian peak reduces by a factor of approximately 2 and the tail distribution is smeared further to higher kinematic regions. The ISR correction influences the m_{T}^{W} distribution marginally. In addition, photons can radiate off the charged lepton which is known under the term final state radiation (FSR). The QED-initiated process has to be corrected for with a small impact on the kinematic distributions of p_{T}^{ℓ} and m_{T}^{W}. The whole evolution of the physics corrections and their impact on the fitted observables is visualised step-by-step in Fig. 4.1. The transverse momentum distribution of the lepton suffers most from the theoretical considerations and the Jacobian edge is smeared in particular by introducing corrections on the ISR of QCD. The W-boson transverse mass changes only slightly by the applied physics corrections and promises a better sensitivity from a theoretical perspective.

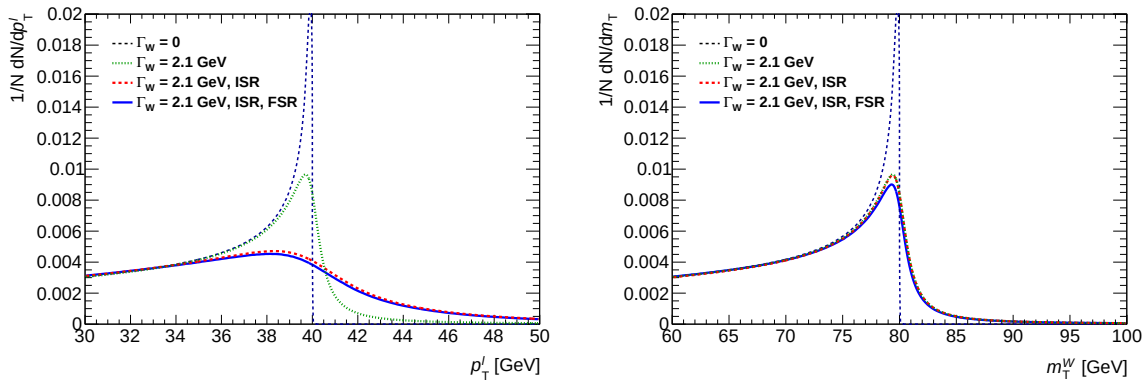

(a) p_{T}^{ℓ} (b) m_{T}^{W}

Figure 4.1: Evolution of the distribution of the kinematic observables p_{T}^{ℓ} and m_{T}^{W} taking different theoretical aspects into account. Shown is the normalised event rate for the unpolarised cross-section at LO, introducing a natural width of the W-boson of 2 100 MeV, adding corrections of the ISR QCD, and finally implementing, in addition, the FSR corrections of QED (taken from [112]).

The physical objects are reconstructed using an imperfect detector which further smears the analysed kinematic observables. Figure 4.2 shows the change of the distributions considering different experimental issues. The distribution on detector level corresponds to the final distribution of Fig. 4.1 taking all physics corrections into account. The resolution of the leptonic properties is around 2 % and the resolution of $E_{\mathrm{T}}^{\mathrm{miss}}$ is approximately 5–15 %. The resolution impacts the p_{T}^{ℓ} distribution only

slightly, whereas the $E_{\mathrm{T}}^{\mathrm{miss}}$ resolution deteriorates the m_{T}^{W} distribution as it enters into the definition of W-boson transverse mass (cf. Eq. (4.1)). The Jacobian edge at m_W is smeared by the detector resolution and disappears. Furthermore, an event selection outlined in Section 5.2 is applied with non-trivial dependence on the kinematic observables. The efficiency and acceptance of the single W-boson processes is around 15 % lowering the event rate of the considered kinematic distributions in particular in the low m_{T} region. The whole evolution of the fitted observables from the generator level to introducing resolution effects to applying the event selection is visualised in Fig. 4.2. Whereas the m_{T}^{W} distribution is the best after the physics corrections, it suffers from detector effects, e.g. the $E_{\mathrm{T}}^{\mathrm{miss}}$ resolution. In contrast, the p_{T}^{ℓ} distribution does not change its shape because of the detector effects but is lowered due to the applied cuts. From an experimental point of view, the transverse momentum of the lepton is the more auspicious observable.

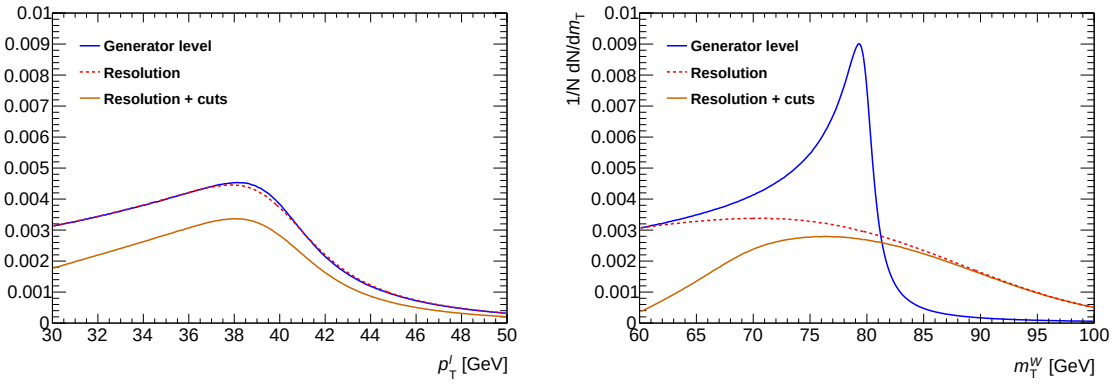

(a) p_{T}^{ℓ} (b) m_{T}^{W}

Figure 4.2: Evolution of the distribution of the kinematic observables p_{T}^{ℓ} and m_{T}^{W} taking detector effects into account. Shown is the normalised event rate at the generator level, including the resolution, and cuts on different event observables (taken from [112]).

4.3 Former measurements

Several measurements of the mass, the width, and the lepton universality of the W-boson have been carried out since its discovery in the 1980s. It is still an active field of research underlined by many recently published results which are presented in the following.

4.3.1 Measurement of m_{W}

Before the W-boson was discovered, good constraints on the expected mass window of the W-boson were set by calculating m_W at LO with the help of Eq. (2.26). The W-boson mass is determined by previous measurements of α_{em}, G_{F}, and $\sin^2\theta_{\mathrm{W}}$. The fine-structure constant α_{em} was determined in fine-structure and Lambshift measurements in deuterium and in the hyperfine interval in hydrogen to a value of $\alpha_{\mathrm{em}}^{-1} = 137.03604(11)$ [113]. The Fermi constant was deduced from the muon lifetime and known to be $G_{\mathrm{F}} = (1.16632 \pm 0.00002) \times 10^{-5}\,\mathrm{GeV}^{-2}$ [27, 114]. The Weinberg angle

$\sin^2\theta_\mathrm{W}$ was measured in different neutrino deep-inelastic scattering experiments and combined to $\sin^2\theta_\mathrm{W} = 0.206 \pm 0.010$ [115]. This information is sufficient to calculate the expected value of m_W at LO before the actual discovery

$$m_W = (82\,141 \pm 1\,994)\ \mathrm{MeV}.$$

Using this information it was possible to setup an experimental environment to produce the W-boson. The UA1 [23] and UA2 [24] collaborations discovered the W-boson in the process of analysing data of the Super Proton-Antiproton Synchrotron (Sp$\bar{\mathrm{p}}$S) colliding protons and antiprotons. The two analyses searched for leptonic decays of the W-boson and found highly energetic electrons opposite to large missing transverse energy. The latter one was identified with neutrinos. The UA1 and UA2 collaborations detected six and four electrons respectively, which form together with the missing transverse energy the signature of a two-body decay. The mass of the mother particle of this two-body decay was measured to

$$m_W^{\mathrm{UA1}} = (81\,000\,^{+5\,000}_{-5\,000})\ \mathrm{MeV},$$
$$m_W^{\mathrm{UA2}} = (80\,000\,^{+10\,000}_{-6\,000})\ \mathrm{MeV}.$$

The mass of the W-boson was fitted in kinematic distributions of the electron and the neutrino. These were the first direct measurements of the W-boson mass that have been performed already in the context of the observation of the particle itself.

Figure 4.3(a) summarises the result of later measurements. All four major experiments at the Large Electron-Positron Collider (LEP), located in the same tunnel as the LHC today, measured the mass of the W-boson in the process $e^+e^- \to W^+W^-$. The detectors Delphi [116], Opal [117], L3 [118], and Aleph [119] measured m_W individually by analysing the different decay channels of the two W-bosons. Mainly the full hadronic $W^+W^- \to q\bar{q}q\bar{q}$ and the semi-leptonic channel $W^+W^- \to q\bar{q}\ell\nu$ were used because the fully leptonic channel $W^+W^- \to \ell\nu\ell\nu$ is statistically limited. This was only used by the Opal experiment. In the fully hadronic state, the events were reconstructed from hadronic jets in the final state using different jet clustering algorithms. Combinatorial algorithms exarcerbated the assignment of pairs of jets to the originating W-boson. In the semi-leptonic decays, all three lepton flavour channels were considered. A pair of hadronic jets is accompanied by an isolated jet and missing momentum due to momentum conservation as the neutrino is not detected. An unbinned maximum likelihood fit was performed to extract the mass of the W-boson in kinematic observables of the decay products. The four individual LEP measurements were statistically combined [120] taking the correlation between systematic uncertainties into account finding a combined value of

$$m_W^{\mathrm{LEP}} = (80\,376\ \pm 33)\ \mathrm{MeV}.$$

The W-boson mass was measured at the Tevatron collider, located at Fermilab in the US, studying the outcome of proton-antiproton collisions. The two major experiments D0 [122] and CDF [123] determined the W-boson mass by applying a χ^2 fit (D0) or a binned maximum-likelihood fit (CDF) to the distribution of different transverse kinematic observables. While the D0 collaboration explored only the electron decay channel of the W-boson, the CDF collaboration used in addition the muonic decay channel. Again, a statistical combination of the two measurements was performed in [124] leading to a value of

$$m_W^{\mathrm{Tevatron}} = (80\,387\ \pm 16)\ \mathrm{MeV}.$$

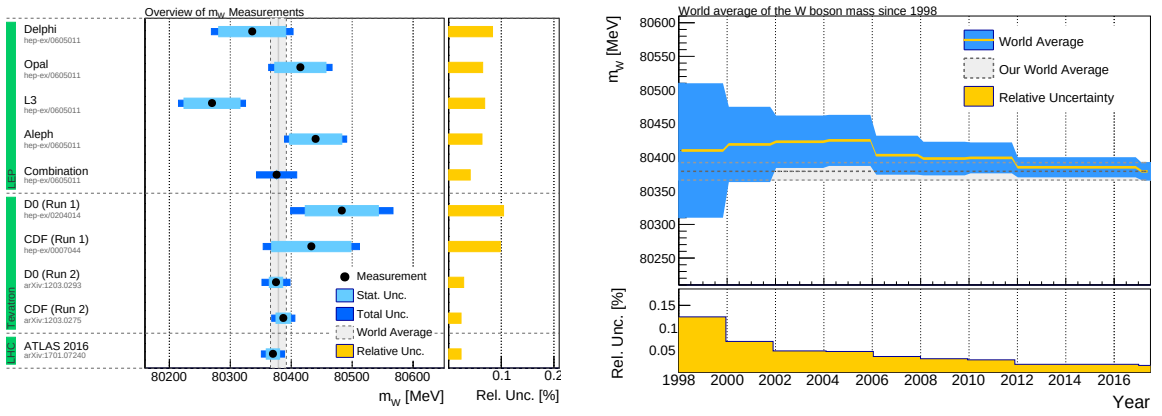

(a) Different m_W measurements.

(b) Precision of the m_W measurement over the course of time.

Figure 4.3: Evolution of the m_W measurement. Shown are (a) the central values and uncertainties of the individual measurements and (b) the absolute and relative uncertainty with the world average since the late 1990s (modified from [121] by fixing the sources of the LEP measurements).

This thesis is based on the m_W measurement by the ATLAS collaboration published in the year 2017 [86] which has a result of

$$m_W^{\text{ATLAS}} = (80\,369.5 \pm 18.5)\,\text{MeV}.$$

At that time, it was the most precise single measurement of the W-boson mass. The details of this analysis are subject of Section 4.4. The cited result will serve as a base of this thesis and a benchmark to classify the achieved precision. It can be seen nicely in Fig. 4.3(b) how the world average and the uncertainty of m_W evolved over time. The relative uncertainty of the W-boson mass measurement decreased significantly over the years by the individual performed measurements. The above-mentioned measurements were combined by the particle data group [25] to the current world average value of

$$m_W^{\text{world average}} = (80\,379 \pm 12)\,\text{MeV}. \tag{4.5}$$

The current world average value of Eq. (4.5) has a difference of 21 MeV compared to the value extracted from a global EW fit (cf. Eq. (2.29)) and turns out to be $1.5\,\sigma$ higher.

Since ATLAS published its measurement in 2017, there have been two additional measurements of m_W where one was published by the LHCb collaboration [125]

$$m_W^{\text{LHCb}} = (80\,354 \pm 32)\,\text{MeV}.$$

They analysed the 2016 dataset provided by the LHC with a centre-of-mass-energy of $\sqrt{s} = 13\,\text{TeV}$ and an integrated luminosity of $\mathcal{L}_{\text{int}} = 1.7\,\text{fb}^{-1}$. A simultaneous fit to the distribution of q/p_{T} in the muonic decay channel of the W-boson and to the ϕ^* distribution[1] in the $Z \to \mu\mu$ decay channel. The cited result is the average of the three used PDF sets. The central value of the LHCb result is closer to the value from the global EW fit than the measured masses by ATLAS, the LEP, and the Tevatron

[1] For the definition of the observable of ϕ^*, it is referred to in the cited publication.

experiments.

The most recent result, which exceeds the precision of all previous single measurements and combinations of the W-boson mass, was published by the CDF result [126] with a value of

$$m_W^{\text{CDF II}} = (80\,433.5 \pm 9.4)\,\text{MeV}.$$

Similar to the previous CDF measurement [123], data from the Tevatron collider taken between 2002 and 2011 with a centre-of-mass energy of $\sqrt{s} = 1.96\,\text{TeV}$ and an integrated luminosity of $\mathcal{L}_{\text{int}} = 8.8\,\text{fb}^{-1}$ are used which corresponds to four times the data size of the predecessor measurement. A binned-likelihood fit is performed in the observables p_{T}^{ℓ}, m_{T}^{W}, and $E_{\text{T}}^{\text{miss}}$ in the leptonic decays to electrons and muons and combined using correlation information between the individual categories. This result is in tension with the global EW fit (cf. Eq. (2.29)) at the order of $7\,\sigma$ as can be seen in Fig. 4.4. Similar to Fig. 2.16, the shown illustration indicates how the introduction of SUSY can vary the W-boson mass scale and which scenario the CDF measurement prefers.

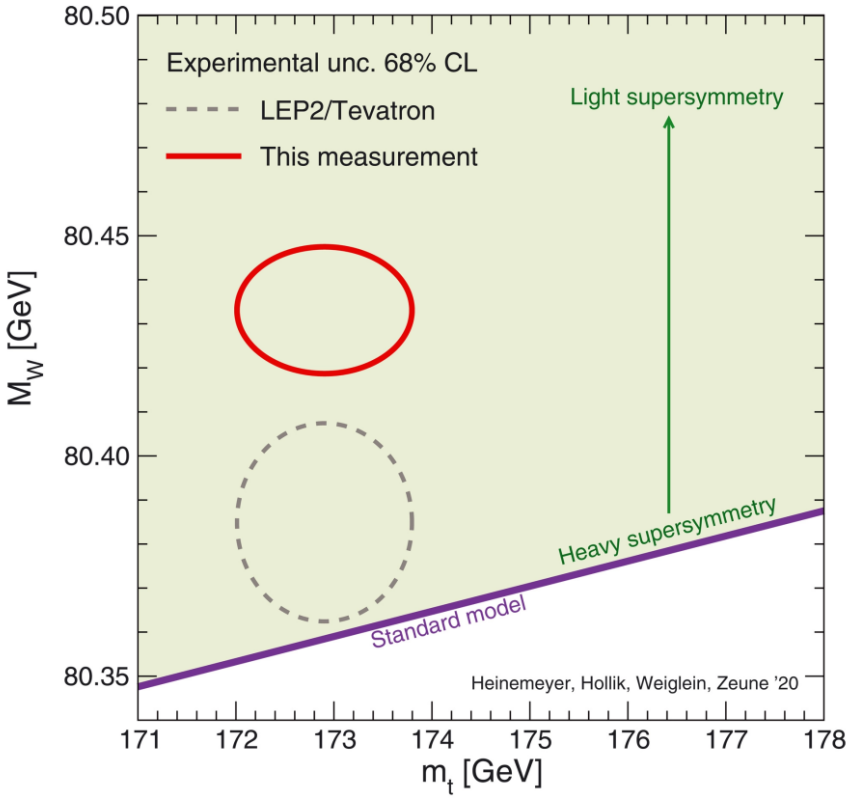

Figure 4.4: Dependence of the W-boson mass on the top quark pole mass including the 2022 CDF W-boson mass measurement. The green area represents a parameter scan of the MSSM for illustrative purposes where the arrow indicates the variation of the W-boson mass if lowering the mass scale of the supersymmetric particles. The purple line shows the overlap between SM and MSSM with a Higgs mass of (125.10 ± 0.14) GeV. The grey dashed circle indicates the combined W-boson mass value from LEP and Tevatron with a top quark mass of (172.89 ± 0.59) GeV with the extent of the circle representing the experimental errors with 68 % CL. The red circle represents again a combination of the W-boson and the top quark mass with the reported m_W value of the CDF collaboration (taken from [126]).

4.3.2 Measurement of Γ_W

Compared to the great number of m_W measurements, there are only a handful of measurements of the width of the W-boson. The four LEP experiments measured Γ_W in the same publications [116–119] as the measurement of the W-boson mass. Again, they were statistically combined in [120] to a result of

$$\Gamma_W^{\text{LEP}} = (2\,195 \pm 83)\,\text{MeV}.$$

Similar to the determination of m_W, MC samples with known values of Γ_W were compared to the data and fitted in kinematic distributions. The correlation between mass and width was found to be less than 5 % and hence considered negligible.

The two major experiments at the Tevatron measured the width of the W-boson at a centre-of-mass energy of $\sqrt{s} = 1.96\,\text{TeV}$. The D0 collaboration [127] performed a direct measurement of Γ_W in the decay $W \to e\nu$ using an integrated luminosity of $\mathcal{L}_{\text{int}} = 1\,\text{fb}^{-1}$. A fit was applied to the m_{T} data distribution to a set of templates with different Γ_W values. The CDF collaboration [128] conducted a binned likelihood fit to simulated m_{T} spectra with Γ_W as a free parameter in the decay of the W-boson to light leptons using an integrated luminosity of $\mathcal{L}_{\text{int}} = 350\,\text{pb}^{-1}$. The fitted results of the two detectors were

$$\Gamma_W^{\text{D0}} = (2\,028 \pm 72)\,\text{MeV},$$
$$\Gamma_W^{\text{CDF}} = (2\,032 \pm 73)\,\text{MeV}.$$

The central values and uncertainties of the individual measurements of the four LEP experiments and the two Tevatron experiments as well as the evolution of the uncertainty on the measurement of Γ_W over time are shown in Fig. 4.5. The measurements of the LEP and the Tevatron experiments were

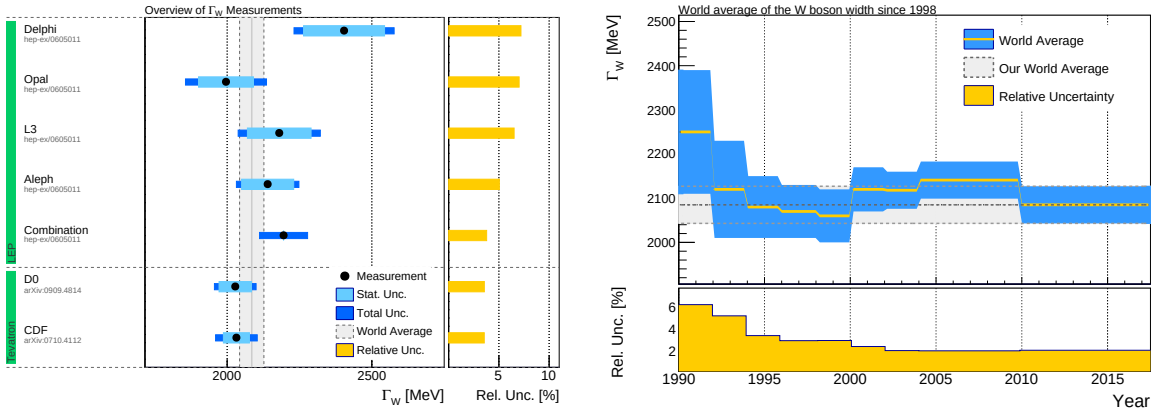

(a) Different Γ_W measurements.

(b) Precision of the Γ_W measurement over the course of time.

Figure 4.5: Evolution of the Γ_W measurement. Shown are (a) the central values and uncertainties of the individual measurements and (b) the absolute and relative uncertainty with the world average since the 1990s (modified from [121] by fixing the sources of the LEP measurements).

again combined by the particle data group [25] leading to the current world average value of

$$\Gamma_W^{\text{world average}} = (2\,085 \pm 42)\,\text{MeV}.$$

There is a small tension in the central value of Γ_W between the LEP and the Tevatron experiments. While the D0 and the CDF experiments agree well within their uncertainties, the combined LEP value differs by more than 150 MeV mainly caused by the measurement of the Delphi experiment. So far, there is no result of any collaboration using data from the LHC.

4.3.3 Measurement of the lepton universality

The leptonic branching ratios in the W-boson decay have been derived from W-boson pair production cross-section measurements by all four LEP experiments and were statistically combined in [120]. The combined data set corresponds to an integrated luminosity of $\mathcal{L}_{\text{int}} = 3\,\text{fb}^{-1}$ with centre-of-mass-energies ranging from $\sqrt{s} = 130\,\text{GeV}$ to $\sqrt{s} = 209\,\text{GeV}$. The results are graphically displayed in Fig. 4.6. The W-boson couples predominantly to the tau lepton as the ratio between the branching

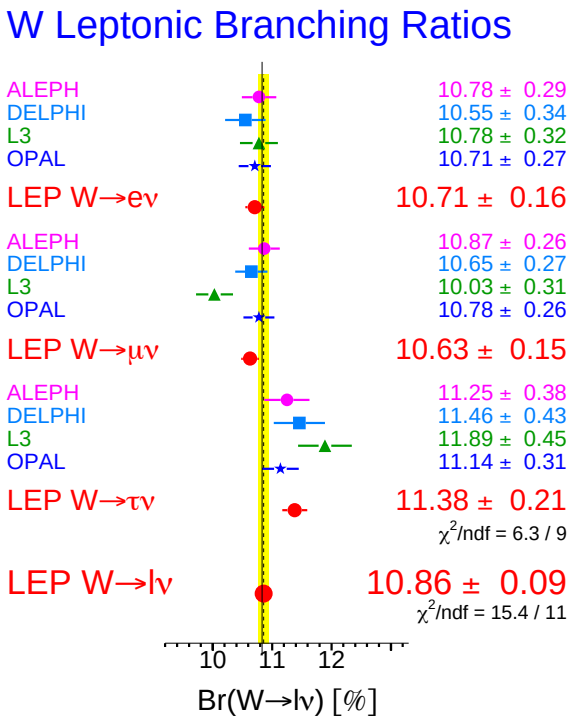

Figure 4.6: Leptonic branching ratios in the W decay. Shown are the results for the three lepton flavours for the individual experiments as well as their combination and the combination of all lepton families (taken from [120]).

fraction to the tau lepton and the average fraction to electrons and muons was determined to be

$$\frac{2\mathcal{B}\left(W \to \tau\nu_\tau\right)}{\mathcal{B}\left(W \to e\nu_e\right) + \mathcal{B}\left(W \to \mu\nu_\mu\right)} = 1.066 \pm 0.025 \tag{4.6}$$

This result is only at the level of $2.6\,\sigma$ in agreement with the assumed lepton universality of the SM.

The LHCb collaboration measured the branching fraction ratio $\mathcal{R}\left(D^*\right) = \frac{\mathcal{B}\left(\overline{B}^0 \to D^{*+}\tau^-\overline{\nu}_\tau\right)}{\mathcal{B}\left(\overline{B}^0 \to D^{*+}\mu^-\overline{\nu}_\mu\right)}$ using a data set with an integrated luminosity of $\mathcal{L}_{\text{int}} = 3\,\text{fb}^{-1}$ taken during the 2011 and 2012 runs [129]. The tau lepton was identified in the leptonic decay mode to muons $\tau^- \to \mu^-\overline{\nu}_\mu\nu_\tau$ such that the final state is the same as for the direct decay to muons. A multidimensional fit to kinematic distributions of the decay products of the $\overline{B}^0$ candidate was performed. This measurement was the first test ever of this quantity at a hadron collider and has a final value of

$$\mathcal{R}\left(D^*\right) = 0.336 \pm 0.027(\text{stat}) \pm 0.030(\text{syst}).$$

The result is 2.1 σ larger than what is expected from assuming lepton universality in the SM.

The latest measurement was taken by the ATLAS collaboration [130] analysing the full Run-2 dataset with a centre-of-mass-energy of $\sqrt{s} = 13\,\text{TeV}$ and an integrated luminosity of $\mathcal{L}_{\text{int}} = 139\,\text{fb}^{-1}$. The ratio of the decay rate of the W-boson to tau leptons and muons was measured in di-leptonic $t\bar{t}$ decays to

$$R_{\tau\mu} = 0.992 \pm 0.013.$$

The definition of $R_{\tau\mu}$ follows Eq. (2.33). A two-dimensional profile likelihood fit (PLH fit) was performed in the transverse impact parameter $|d_0^\mu|$ and the transverse momentum of the muon p_{T}^μ. The result is in good agreement with the SM prediction of unity and doubles the precision with respect to the LEP measurement.

4.4 Outline and strategy of the 2017 analysis

As already stressed several times, the measurement presented in this thesis is based on the m_W measurement published by the ATLAS collaboration in 2017[2] [86]. The information in this section is mainly taken from ibidem and the supporting document [131]. The reference publication analysed data provided by LHC in 2011 with a centre-of-mass-energy of $\sqrt{s} = 7\,\text{TeV}$ and an integrated luminosity of $\mathcal{L}_{\text{int}} = 4.59\,\text{fb}^{-1}$. The mass of the W-boson was determined from fits on the transverse momentum of the decayed charged lepton p_{T}^ℓ and the transverse mass of the W-boson m_{T}^W. Their connection to the W-boson mass is outlined in Section 4.2. Fits on the $E_{\text{T}}^{\text{miss}}$ distribution were used as a cross-check for the fit procedure but are not part of the reanalysis.

The 2017 analysis took advantage of the mentioned correlation between m_W and the kinematic distributions of the W-boson decay products. Therefore, different mass hypotheses of the W-boson, referred to as mass templates, were obtained by utilising the natural width of the W-boson resonance. To minimise the computing time, a reweighting of the invariant mass of the W-boson from a reference mass value (cf. Section 3.4.1) to any desired mass point has been performed using the Breit-Wigner parametrisation with a running width (cf. Eq. (4.4))

$$\frac{\mathrm{d}\sigma}{\mathrm{d}m} \propto \frac{m^2}{\left(m^2 - m_V^2\right)^2 + m^4\Gamma_V^2/m_V^2}, \tag{4.7}$$

[2] This analysis will be referred to as the *2017 analysis*, *legacy*, or *reference publication* during this thesis.

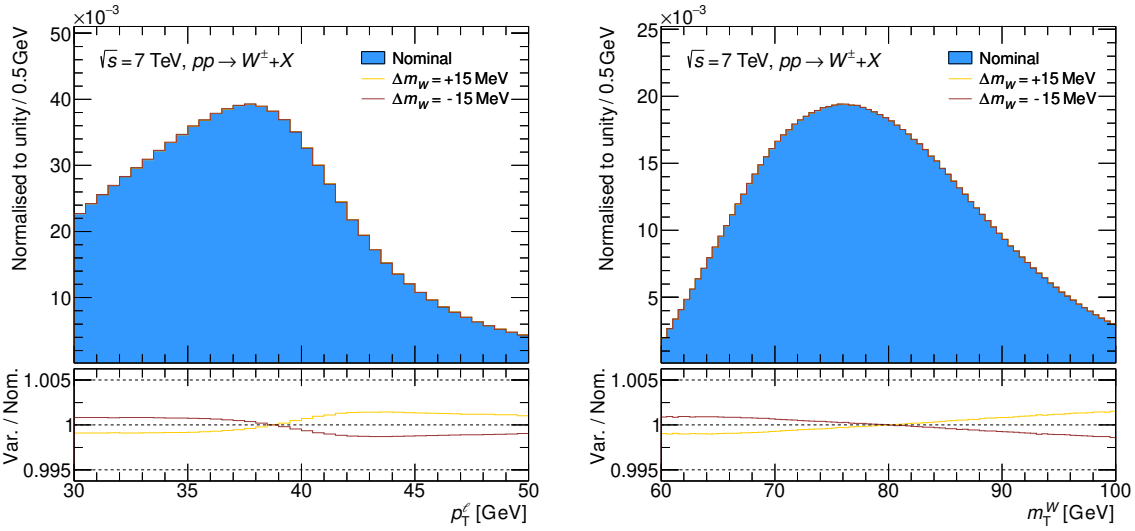

(a) p_{T}^{ℓ} (b) m_{T}^{W}

Figure 4.7: Normalised mass templates for the nominal hypothesis and two mass variations. Shown is the sum of all fit categories of both processes initiated by a W-boson, $W \to \ell\nu$ and $W \to \tau\nu$, for the kinematic distributions p_{T}^{ℓ} (a) and m_{T}^{W} (b). The lower panel illustrates the ratio of the mass variations compared to the nominal mass template.

where m is the invariant mass of the charged lepton and neutrino system, and m_V and Γ_V ($V = W, Z$) are the masses and the widths of the vector bosons respectively. This method was introduced in [132]. The obtained kinematic distributions for the different mass points were compared to the actual measurement. The width of the W-boson was scaled using the SM relation $\Gamma_W \propto m_W^3$ and kept fixed. The impact of the uncertainty of the W-boson width on m_W was assumed to be negligible. The normalised variation of two mass templates concerning the nominal hypothesis is shown in Fig. 4.7. The mass variations of $\Delta m_W = \pm 15\,\mathrm{MeV}$ correspond to the uncertainty of the world average without the 2017 analysis result [133]. It can be seen nicely how a different W-boson mass changes the shape of the considered kinematic distributions. Increasing m_W leads to less expected events in the low kinematic region and more expected events in the high kinematic region, whereas it is vice versa for decreasing the W-boson mass.

The distribution of p_{T}^{ℓ} is influenced by the lepton energy and the recoil calibration. Furthermore, the distribution is widened by the p_{T}^{W} distribution and sensitive to the helicity states of the W-boson which is affected by the PDFs [134]. The m_{T}^{W} distribution has higher uncertainties due to the recoil but is less sensitive to physics-modelling effects compared to p_{T}^{ℓ}.

The used calibration procedure follows methods published earlier by ATLAS [83, 84, 87] and is based on W and Z samples at $\sqrt{s} = 7\,\mathrm{TeV}$ and $\sqrt{s} = 8\,\mathrm{TeV}$. The detector response is corrected with $Z \to \ell\ell$ events because for this process no particles are expected to leave the detector unnoticed. The lepton momentum is calibrated by taking advantage of the precisely measured Z-boson mass [135], and corrections on the recoil response are calculated using the expected momentum balance with $p_{\mathrm{T}}^{\ell\ell}$. A

tag-and-probe based on events containing W- and Z-bosons [83, 87] helps to derive identification and reconstruction efficiency corrections. The mentioned corrections are crucial for a good description of the p_{T}^{ℓ} distribution. Z-boson events were used to cross-check the physics modelling and the corrections of the detector response by measuring m_Z with the help of the template fit method and comparing it to the combined LEP result. The mentioned calibration and correction procedures are part of Chapter 7 and implicate the introduction of systematic uncertainties.

Decay channel	$W \to e\nu$	$W \to \mu\nu$
Kinematic distribution	p_{T}^{ℓ}, m_{T}^{W}	
Charge category	$q = +1$, $q = -1$	
$\lvert\eta_\ell\rvert$ category	[0.0, 0.6], [0.6, 1.2], [1.8, 2.4]	[0.0, 0.8], [0.8, 1.4], [1.4, 2.0], [2.0, 2.4]

Table 4.1: Different fit categories used for the combination of the m_W measurement. Each distribution is split up into 14 single measurement categories (taken from [86]).

The final value of m_W was a combination of individual fits carried out in the electron and the muon decay channel, and in charge and $|\eta_\ell|$ categories as given in Table 4.1. The boundaries of the $|\eta_\ell|$ bins are set according to the detector's geometry and to account for determination limits of systematic uncertainties. A consistent result between the two decay channels implies a good experimental calibration, whereas the compatibility of the charge and $|\eta_\ell|$ categories proves the chosen physics model.

The 2017 analysis was blinded by introducing an offset to the reference mass value of the template production drawn from a random uniform distribution in the range of ±100 MeV. The offset was kept consistent between the different fit categories by using the same random seed. This allows checking the consistency of the experimental calibrations and the production model of the W-boson. To receive the final result, the central values were corrected for the blinding value of m_W which was revealed to be −17.8 MeV.

The fit ranges for both kinematic distributions were varied in the scope between 30 and 50 GeV for p_{T}^{ℓ}, and between 60 and 100 GeV for m_{T}^{W}. The optimal fit range was determined by identifying the smallest total uncertainty to be $32 < p_{\mathrm{T}}^{\ell} < 45$ GeV and $66 < m_{\mathrm{T}}^{W} < 99$ GeV. A detailed insight into the used χ^2 fit is given in Section 6.1.

4.5 Motivation of the reanalysis of the m_{W} measurement

The first inspiration of the reanalysis effort is to reduce the total uncertainty of the W-boson mass measurement. Concerning this aspect, the main improvement affects the fit method. The 2017 analysis used a χ^2 fit approach where all systematic uncertainties were considered uncorrelated and added in quadrature in each fit category. The advanced technique of a PLH fit allows correlating systematic uncertainties among each other and between the different fit categories. This manifests itself in the ability of the data to constrain the systematic uncertainties, to exploit their correlations, and to reduce the total uncertainty. In addition, the reported final value of the PLH fit is the result of a global optimisation including all uncertainties and not only of the fit with statistical errors. The improvement of the used statistical methods is further discussed in Chapter 6.

The validation procedure includes the repetition of the whole event selection chain and the

determination of the multi-jet background using a data-driven technique. These topics are treated in Chapter 5. In this context, a new method to perform the shape extrapolation (cf. Section 5.3.2) and to estimate the shape uncertainty of the multi-jet background is introduced (cf. Section 7.5.1).

As the original publication only covered the measurement of the W-boson mass, this measurement will in addition incorporate the first W-boson width measurement by ATLAS and the first test of lepton universality by ATLAS using the 2011 dataset. To measure the W-boson width, the reanalysis uses the reweighting approach to produce different width templates again starting from a reference width value (cf. Section 3.4.1). This allows for a simultaneous modification of m_W and Γ_W. The shape variation of two width points representing the total uncertainty of the current world average compared to the nominal distribution is shown in Fig. 4.8. The non-normalised variations and their behaviour concerning the nominal hypotheses for both, m_W and Γ_W, are shown in Appendix B. Another improvement is a global fit of m_W and Γ_W either with both properties as free parameters or including the respective other property with an external constraint into the fit. This means that the world average of the width with its uncertainty [25] is fed into the mass fit, and the other way around. For the mass constraint, the world average without the ATLAS measurement is taken from the year 2016 [133].

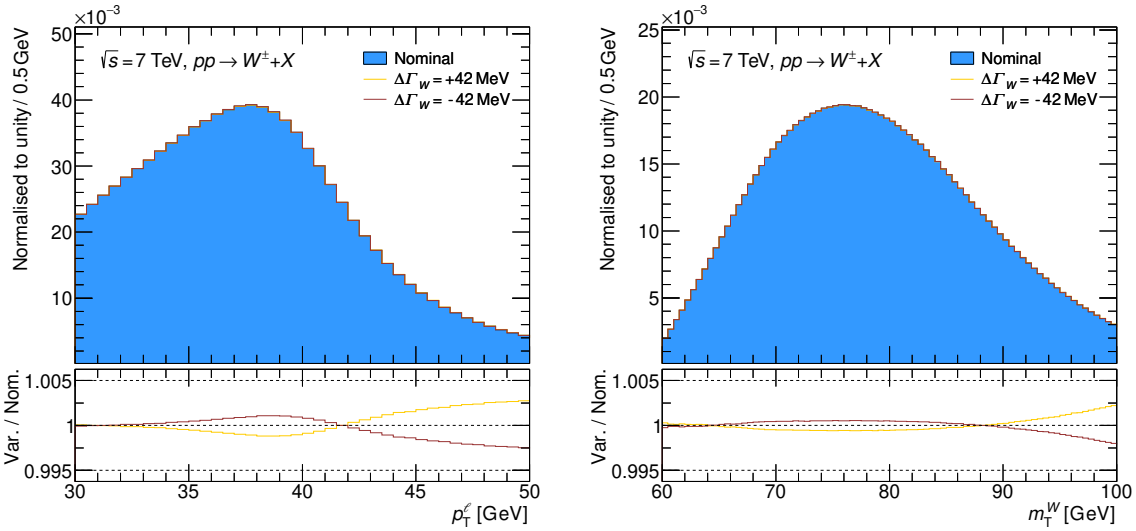

(a) p_{T}^{ℓ} (b) m_{T}^{W}

Figure 4.8: Normalised width templates for the nominal hypothesis and two width variations. Shown is the sum of all fit categories of both processes initiated by a W-boson, $W \to \ell\nu$ and $W \to \tau\nu$, for the kinematic distributions p_{T}^{ℓ} (a) and m_{T}^{W} (b). The lower panel illustrates the ratio of the width variations compared to the nominal width template.

The measurement of the lepton universality determines the ratio of the W-boson decay to tau leptons and light leptons. Therefore, the shapes of the two processes are compared in kinematic distributions. The spectrum of $W \to \tau\nu$ is softer due to the two additional neutrinos compared to the $W \to \ell\nu$ decay. The normalisations of the two samples are compared to check if the W-boson couples predominantly to heavier charged leptons. A precision of the order of approximately 2 % is desired as reached for the lepton universality measurement performed by the LEP experiments as given in Eq. (4.6).

CHAPTER 5

The analysis design

This chapter describes the effort to reproduce the basic results of the 2017 analysis. The signal and background processes are characterised in Section 5.1 followed by the event selection in Section 5.2 trying to separate the two categories as much as possible. A detailed validation of the reanalysis selection criteria and distributions is part of the discussion as well as an explanation of the repeated multijet background fit in Section 5.3.

5.1 Signal and background processes

The signal processes $W \to \ell\nu$ ($\ell = \mu,\ e$) and $W \to \tau\nu$ are illustrated in Fig. 2.10. They both have a light lepton and at least one neutrino in the final state. Background contributions are other SM processes with a similar final state but misidentified or missed objects which lead to a similar signature in the detector.

The process $Z \to \ell\ell$ ($\ell = \mu,\ e$) mimics the signal signature if one of the light leptons is not detected. If one of the tau leptons of $Z \to \tau\tau$ decays leptonically and the other one hadronically, the detector measures a lepton accompanied by other objects and missing transverse momentum. The production of two vector bosons, referred to as diboson (WW, WZ, ZZ), can fake the signal process if one of the bosons decays leptonically and the other one hadronically. Finally, the processes of $t\bar{t}$ pairs and single top quarks can decay to a W-boson decaying further to the signal final state. An illustration of these background processes with a light lepton ($\ell = \mu,\ e$) in the final state are depicted in Fig. 5.1.

The contributions of the background processes after the event selection discussed in Section 5.2 are small compared to the signal because the cross-section to produce a single W-boson is in the same order as for the background processes. Unlike in searches for BSM physics scenarios where the production cross-section is usually orders of magnitudes lower, the background can be well separated from the signal with an appropriate event selection. The distribution of the total simulated prediction is split up into the different processes in Table 5.1. In all channels, the process $W \to \ell\nu$ has a high purity of more than 90 %, whereas the decay $W \to \tau\nu$ represents only about 1 % of the total prediction. The major background is the process $Z \to \ell\ell$ with a percentage of 2.90–6.24 % depending on the leptonic decay channel. The other three background processes are negligible. They contribute about 0.1 % for $Z \to \tau\tau$ and top, and even less for the diboson background.

The signal plus background prediction is normalised to the dataset (cf. Section 3.2.6) used for the final χ^2 fit of the 2017 analysis. The measurement of m_W is only sensitive to the shape and does not

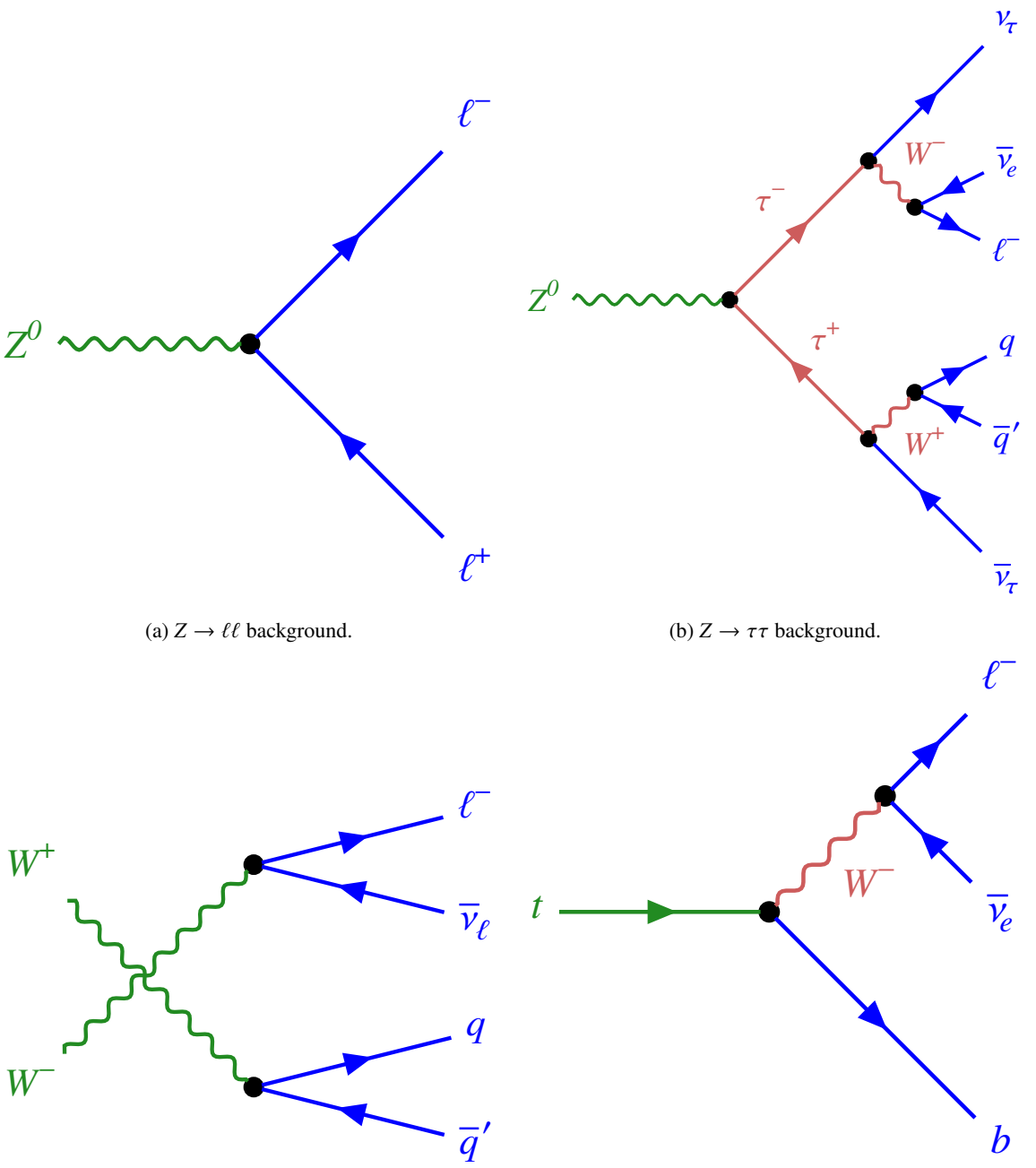

(a) $Z \to \ell\ell$ background.

(b) $Z \to \tau\tau$ background.

(c) Diboson background.

(d) Single top background.

Figure 5.1: Feynman diagrams of the four exemplary background processes. Shown are the decays of (a) $Z \to \ell\ell$, (b) $Z \to \tau\tau$, (c) dibosons, and (d) a single top quark including a light lepton accompanied by other objects in the final state.

Decay channel	$W \to \ell\nu$ [%]	$W \to \tau\nu$ [%]	$Z \to \ell\ell$ [%]	$Z \to \tau\tau$ [%]	diboson [%]	top [%]
$W^+ \to e^+\nu_e$	95.86	0.97	2.90	0.10	0.06	0.10
$W^- \to e^-\overline{\nu}_e$	94.70	1.03	3.93	0.14	0.08	0.13
$W^+ \to \mu^+\nu_\mu$	93.99	0.99	4.78	0.10	0.05	0.09
$W^- \to \mu^-\overline{\nu}_\mu$	92.40	1.03	6.24	0.13	0.07	0.11

Table 5.1: The fraction of the total simulated prediction of each simulated sample for the different charged lepton decay channels. The numbers are given in % and the calculations do not include the contribution from the multijet background which are calculated in Section 5.3.1.

depend on the normalisation. Hence, no cross-section uncertainty for $W \to \ell\nu$ is assigned. A relative uncertainty of 0.04 % is considered to account for the uncertainty of the tau lepton decay into the lighter charged leptons [25]. For the backgrounds including a Z-boson, relative cross-section uncertainties concerning the measured W cross-section are assigned separately for the two charges which are 1.8 % for W^+/Z and 2.3 % for W^-/Z [136]. The process $t\bar{t}$ is normalised to its measured cross-section with an uncertainty of 3.9 % [137], the single top background is normalised according to [138–140] with an uncertainty of 7 %. The diboson samples are normalised to the corresponding NLO cross-section [141] and an uncertainty of 10 %, which describes the difference to the next-to-next-to-leading-order (NNLO) prediction [142].

5.2 Event selection

The interesting signal processes for the mass and the width measurement of the W-boson are the decays into light leptons and the corresponding neutrinos which include the decays via intermediate tau leptons. Hence, different mass and width templates are produced for the processes $W \to \mu\nu$, $W \to e\nu$, and $W \to \tau\nu$. Furthermore, all leptonic decays of the W-boson are important for the lepton universality measurement as the ratio of the branching ratio of tau lepton decays to the branching ratio of light lepton decays is the parameter of interest (POI). The event selection aims to enrich the signal over the background processes resulting in a similar signature in the ATLAS detector. The unique signature of the signal processes is a high momentum light lepton and a neutrino. Only the light lepton is leaving a unique signature in the detector, whereas the presence of a neutrino is connected to the quantities $E_{\mathrm{T}}^{\mathrm{miss}}$ and u_{T}. The reanalysis aims to reproduce the important steps of the 2017 analysis publication where the event selection is the first crucial stage.

5.2.1 Pre-selection

The pre-selection is common for both decay channels. It checks if the detector was in a good condition during data taking and a light lepton candidate fires a trigger with a certain momentum threshold.

- **GRL** The detector was in good conditions and the examined event is part of the GRL (cf. Section 3.2.6). The GRL used for this particular analysis is `data11_7TeV.periodAllYear_ DetStatus-v36-pro10_CoolRunQuery-00-04-08_WZjets_allchannels.xml`. For the presented measurements, not all subsystems had to be in a proper state which explains the higher luminosity of $\mathcal{L}_{\mathrm{int}} = 4.59\,\mathrm{fb}^{-1}$ compared to the $\mathcal{L}_{\mathrm{int}} = 4.57\,\mathrm{fb}^{-1}$ declared as "good for physics" where all subsystems had to be in good conditions (cf. Section 3.2.6).

- **Good PV** The reconstructed primary vertex (PV) of the event is associated with at least three tracks.
- **Trigger** A leptonic trigger requires a muon candidate with a transverse momentum of $p_{\mathrm{T}}^{\mu} > 18\,\mathrm{GeV}$ and an electron candidate with a transverse momentum of $p_{\mathrm{T}}^{e} > 20\,\mathrm{GeV}$ or $p_{\mathrm{T}}^{e} > 22\,\mathrm{GeV}$ on the detector level. The requirement for the electron single lepton trigger was raised from 20 to 22 GeV during the data taking period to cope with the increased luminosity.

5.2.2 Muon selection

The muon candidates are identified and selected as described in Section 3.3.2. The selection process of the muons splits up into different cut stages corresponding to these requirements:

- **Muon base selection** An event must contain at least one combined muon candidate within $|\eta| < 2.4$ and $p_{\mathrm{T}}^{\mu} > 15\,\mathrm{GeV}$ fulfilling certain requirements on the track kinematics in the ID. The muon candidate is required to have a longitudinal impact parameter of $|z_0| < 10\,\mathrm{mm}$ to reduce the background from cosmic muons. It needs to be isolated in a region of $\Delta R < 0.2$ meaning the sum of all tracks within this cone excluding the contribution of the muon itself is less than 10 % of the muon transverse momentum: $\sum p_{\mathrm{T}}^{\mathrm{cone20}} / p_{\mathrm{T}}^{\mu} < 0.1$.
- $\boldsymbol{p_{\mathrm{T}}^{\mu} > 20\,\mathrm{GeV}}$ The considered muon candidate has a transverse momentum of more than 20 GeV.
- **Veto second muon** The event is rejected if there is an additional muon passing the former cut stages.
- **Trigger matching** The selected muon matches the triggered muon object.

5.2.3 Electron selection

Electrons leave a unique signature in the ATLAS detector. The reconstruction procedure is described in Section 3.3.1. The selection of electrons and muons share the requirement of the trigger matching. Due to the different interactions with the detector, the electron selection process is slightly different as for muons and the cut stages are described by the following criteria:

- $\boldsymbol{p_{\mathrm{T}}^{e} > 30\,\mathrm{GeV}}$ The electron candidate is reconstructed from an energy deposit in the electromagnetic calorimeter associated with at least one well-reconstructed track in the ID. It should be within a range of $|\eta| < 2.4$, whereas the pseudorapidity region between $1.2 < |\eta| < 1.82$ is excluded. The candidate is required to have $p_{\mathrm{T}}^{e} > 15\,\mathrm{GeV}$ but this cut stage is directly connected with the higher transverse momentum requirement for the leptons of $p_{\mathrm{T}}^{e} > 30\,\mathrm{GeV}$.
- **Veto tight++** The event is discarded if it contains more than one electron candidate passing the tight identification requirement (cf. Section 3.3.1).
- **One tight++** The event contains exactly one electron candidate passing the tight identification requirement.
- $\boldsymbol{E_{\mathrm{T}}^{\mathrm{cone20}}}$ This cut stage acts on the calorimeter deposit leading to isolated electrons. The energy deposit within a cone of $\Delta R < 0.2$ around the electron candidate is required to be small while the contribution of the electron candidate itself is removed.

- $\boldsymbol{p_{\mathrm{T}}^{\mathrm{cone40}}}$ The scalar sum of the p_{T} of tracks in a cone of $\Delta R < 0.4$ around the electron is required to be small. Again, the contribution of the electron itself is neglected.

5.2.4 Jet and event cleaning

After the lepton selection, events have to pass the following requirements related to jets and the LAr:

- **Jet cleaning** Jets formed from calorimeter information are not originating from hard scattering processes. As they interfere with the reconstruction of the missing transverse energy, the complete event is discarded.
- **LAr simple veto** Six Front-End Boards of the LAr lost signal during some time of the 2011 data taking period. If a calorimeter jet falls into the vicinity of the LAr hole ($-0.1 < \eta < 1.5$ and $-0.9 < \phi < -0.5$), events of the affected data runs are discarded.
- **LAr noise bursts** If the energy deposition is large and correlated across the LAr, this phenomenon is considered as a "noise burst" and the whole event is discarded.

This part of the selection is performed before applying the isolation requirements in the electron channel or the requirement on LAr noise bursts is applied before the pre-selection.

5.2.5 W-boson candidate selection

Beyond the pre-selection and the lepton specific selections, an event must pass four signal cuts to further reduce the number of other background sources:

- Exactly one well-reconstructed electron or muon is required to have $\boldsymbol{p_{\mathrm{T}}^{\ell} > 30\,\mathrm{GeV}}$ and to match the trigger object. In the muon channel, the trigger periods L3 and L4 have been discarded due to a timing problem in the RPCs of the MS, which affects the muon trigger efficiency[1]. This problem is not covered by the GRL as analyses not using muons can still use this data. To mimic the loss of $\mathcal{L}_{\mathrm{int}} = 532\,\mathrm{pb}^{-1}$ of data in simulated samples, a reweighting tool is used to ensure the fraction of discarded events is the same for data and MC samples. Those two periods are excluded together with the requirement on the well-reconstructed muon.
- The reconstructed recoil transverse momentum is required to fulfil $\boldsymbol{u_{\mathrm{T}} < 30\,\mathrm{GeV}}$. The reconstruction is explained in Section 3.3.5.
- The transverse mass of the W-boson must match the condition $\boldsymbol{m_{\mathrm{T}}^{W} > 60\,\mathrm{GeV}}$.
- The event needs to have a missing transverse momentum of $\boldsymbol{E_{\mathrm{T}}^{\mathrm{miss}} > 30\,\mathrm{GeV}}$.

These event selection cuts are chosen to reduce the amount of multijet background and to minimise the effect of model uncertainties occurring in the W-boson decay at high transverse momenta.

Z-boson events are used to calibrate the response of the detector to light leptons and to correct the recoil. Therefore, a dedicated event selection has been chosen, whereas the single lepton trigger requirement remains the same. In addition, an event has to fulfil the following requirements to be declared as originating from a Z-boson:

[1] The timing problem occured between the runs 189 205 and 189 610 (September 2011) which correspond to the trigger periods L3 and L4. The trigger performance, e.g. SFs, is calculated per trigger period.

- Two well-reconstructed light leptons of the same flavour and opposite charge are required to have $p_{\mathrm{T}}^{\ell} > 25\,\mathrm{GeV}$. Both leptons need to fulfil the same isolation requirements as for the W-boson selection.
- The invariant mass of the dilepton system needs to be in a window around the Z-mass, namely $80\,\mathrm{GeV} < m_{\ell\ell} < 100\,\mathrm{GeV}$.

5.2.6 Validation of the reanalysis selection criteria

The reanalysis of the 2017 analysis publication [86] includes the full reanalysis of all data and MC samples. The labels of the different cut stages are explained in Sections 5.2.1, 5.2.2 and 5.2.3. The **No cut** label refers to the initial number of events of the corresponding sample. The simulated samples contain a pre-selection common to W- and Z-boson analyses with ATLAS requiring at least one identified lepton per event.

To ensure the technical migration of the 2017 analysis has been implemented correctly, the absolute event yields of the data and the MC samples are compared to the numbers of the 2017 analysis at each cut stage. The numbers of the MC samples are normalised to the corresponding cross-section of each sample and an integrated luminosity of $\mathcal{L}_{\mathrm{int}} = 4\,591.01\,\mathrm{pb}^{-1}$ of the data sample. The validation of the selection criteria is conducted separately for the muon and the electron channel due to the different lepton selection procedures.

Muon channel Table 5.3 summarises the cutflow validation of the muon channel. It compares the event yields of the internal support document [131] to the reprocessed yields. Each of the individual comparisons of the data and seven groups of the MC samples shows not only the event yields but the agreement between the reanalysis and the 2017 analysis given in per cent as well.

Initially, the event yields for the top pair production and diboson samples differed by a few per cent between the reanalysis and the 2017 analysis. This difference could be traced down to wrong cross-section values used in the 2017 analysis. The wrong and the correct cross-section values of the three subsamples describing diboson processes and the top pair production are shown in Table 5.2. The cross-sections and the integrated luminosities of the MC samples listed in Table 3.1 are corrected for this fallacy as well as the cutflow numbers of the 2017 analysis presented in Table 5.3.

Process	Generator	Dataset ID	2017 analysis $\sigma \times \mathrm{BR}[\mathrm{pb}]$	Correct $\sigma \times \mathrm{BR}[\mathrm{pb}]$
WW	`Herwig`	105985	20.86	17.47
WZ	`Herwig`	105986	1.54	1.28
ZZ	`Herwig`	105987	6.97	5.38
$t\bar{t}$	`MC@NLO`	105200	101.51	96.26

Table 5.2: Processes for which the wrong cross-section in the 2017 analysis has been used. Shown are the used generator, the dataset ID, and the wrong and the correct $\sigma \times \mathrm{BR}[\mathrm{pb}]$.

The cutflow of the reprocessed data matches perfectly the numbers of the 2017 analysis. The deviations of the simulated samples are less than 1 ‰. A small difference is expected due to the choice of random seeds and rounding errors as the MC samples are corrected by various calibration procedures. Hence, the reprocessing of the samples of the muon channel is considered to be successful and closed.

	Data			$W^+ \to \mu^+\nu_\mu$			$W^- \to \mu^-\bar{\nu}_\mu$			$W \to \tau\nu$		
Cut	2017 analysis	Reanalysis	Agreement [%]	2017 analysis	Reanalysis	Agreement [%]	2017 analysis	Reanalysis	Agreement [%]	2017 analysis	Reanalysis	Agreement [%]
No cut	154 532 753	154 532 753	100.00	29 129 499	29 129 499	100.00	20 092 555	20 092 555	100.00	7 041 098	7 041 098	100.00
GRL	140 976 111	140 976 111	100.00	29 129 499	29 129 499	100.00	20 092 555	20 092 555	100.00	7 041 098	7 041 098	100.00
Good PV	139 003 866	139 003 866	100.00	28 956 395	28 956 386	100.00	19 991 586	19 991 572	100.00	7 003 914	7 003 846	100.00
Trigger	116 109 480	116 109 480	100.00	14 838 771	14 837 129	99.99	9 035 835	9 034 913	99.99	1 319 622	1 318 512	99.92
Muon base selection	43 803 081	43 803 081	100.00	12 776 948	12 775 350	99.99	7 934 334	7 933 339	99.99	930 906	930 123	99.92
$p_{\mathrm{T}}^{\mu} > 20$ GeV	42 951 700	42 951 700	100.00	12 713 212	12 711 615	99.99	7 903 333	7 902 343	99.99	912 106	911 341	99.92
Veto second muon	41 153 751	41 153 751	100.00	12 713 068	12 711 471	99.99	7 903 195	7 902 205	99.99	912 084	911 319	99.92
Trigger matching	41 044 423	41 044 423	100.00	12 710 370	12 708 772	99.99	7 901 520	7 900 531	99.99	911 863	911 098	99.92
Jet cleaning	40 996 618	40 996 618	100.00	12 705 864	12 704 266	99.99	7 898 825	7 897 836	99.99	911 546	910 781	99.92
LAr simple veto	40 915 645	40 915 645	100.00	12 694 963	12 693 363	99.99	7 891 061	7 890 071	99.99	910 452	909 688	99.92
LAr noise bursts	40 801 743	40 801 743	100.00	12 694 963	12 693 363	99.99	7 891 061	7 890 071	99.99	910 452	909 688	99.92
$p_{\mathrm{T}}^{\mu} > 30$ GeV and remove periods L3+L4	16 077 674	16 077 674	100.00	7 670 767	7 669 244	99.98	5 181 689	5 181 049	99.99	242 669	242 470	99.92
$u_{\mathrm{T}} < 30$ GeV	10 811 788	10 811 788	100.00	5 814 759	5 813 597	99.98	3 894 645	3 894 166	99.99	142 062	141 944	99.92
$m_{\mathrm{T}}^{W} > 60$ GeV	8 851 402	8 851 402	100.00	4 885 304	4 884 327	99.98	3 322 739	3 322 331	99.99	90 351	90 276	99.92
$E_{\mathrm{T}}^{\mathrm{miss}} > 30$ GeV	7 844 778	7 844 778	100.00	4 342 572	4 341 705	99.98	2 950 049	2 949 683	99.99	78 674	78 609	99.92

	$Z \to \mu\mu$			top			diboson			$Z \to \tau\tau$		
Cut	2017 analysis	Reanalysis	Agreement [%]	2017 analysis	Reanalysis	Agreement [%]	2017 analysis	Reanalysis	Agreement [%]	2017 analysis	Reanalysis	Agreement [%]
No cut	4 546 477	4 546 477	100.00	632 302	632 302	100.00	110 722	110 722	100.00	1 195 589	1 195 589	100.00
GRL	4 546 477	4 546 477	100.00	632 302	632 302	100.00	110 722	110 722	100.00	1 195 589	1 195 589	100.00
Good PV	4 519 068	4 519 065	100.00	632 027	632 026	100.00	110 505	110 505	100.00	1 191 224	1 191 220	100.00
Trigger	3 304 329	3 304 386	100.00	168 595	168 511	99.95	37 262	37 235	99.93	249 997	249 983	99.99
Muon base selection	3 109 210	3 109 268	100.00	132 693	132 622	99.95	32 140	32 117	99.93	183 105	183 095	99.99
$p_{\mathrm{T}}^{\mu} > 20$ GeV	3 102 010	3 102 069	100.00	132 256	132 185	99.95	32 024	32 001	99.93	179 908	179 898	99.99
Veto second muon	1 423 848	1 423 925	100.01	126 006	125 939	99.95	28 652	28 630	99.92	175 628	175 619	99.99
Trigger matching	1 369 356	1 369 429	100.01	124 299	124 233	99.95	28 516	28 494	99.92	175 123	175 114	99.99
Jet cleaning	1 365 933	1 366 006	100.01	124 148	124 082	99.95	28 482	28 460	99.92	174 768	174 759	99.99
LAr simple veto	1 364 188	1 364 262	100.01	122 172	122 107	99.95	28 311	28 289	99.92	174 181	174 172	99.99
LAr noise bursts	1 364 188	1 364 262	100.01	122 172	122 107	99.95	28 311	28 289	99.92	174 181	174 172	99.99
$p_{\mathrm{T}}^{\mu} > 30$ GeV and remove periods L3+L4	839 816	839 860	100.01	86 257	86 211	99.95	19 235	19 220	99.92	54 751	54 748	99.99
$u_{\mathrm{T}} < 30$ GeV	577 069	577 100	100.01	10 041	10 036	99.95	6 331	6 326	99.92	22 405	22 404	100.00
$m_{\mathrm{T}}^{W} > 60$ GeV	476 111	476 137	100.01	8 639	8 635	99.95	5 478	5 474	99.93	10 715	10 715	100.00
$E_{\mathrm{T}}^{\mathrm{miss}} > 30$ GeV	420 111	420 133	100.01	7 771	7 767	99.95	4 916	4 912	99.92	8 721	8 721	100.00

Table 5.3: The cutflow comparison for the muon channel. Shown are the event yields of the data and seven simulated samples for the 2017 analysis and the reanalysis after each cut stage. The numbers of the MC samples are normalised to their cross-section and an integrated luminosity of $\mathcal{L}_{\mathrm{int}} = 4\,591.01\,\mathrm{pb}^{-1}$. The agreement is the number of the reanalysis divided by the number of the 2017 analysis.

Electron channel Similar to the muon channel, Table 5.4 summarises the cutflow comparison of the electron channel. The issue found in the muon channel concerning the wrongly used cross-sections of the diboson samples and the top pair production affects the electron channel as well. The stated numbers of the 2017 analysis are normalised using the correct cross-section values.

The cutflows of the simulated samples agree with the 2017 analysis within 2 ‰ which is reasonable and can be justified again by choices of random seeds and rounding errors. The reanalysis numbers of the data cutflow are higher than those of the 2017 analysis. Whereas the initial number of events is about 0.75 % higher for the reanalysis, it is about 1.5 % after the event selection. The attention directs to the change of the agreement rate after the trigger rate. This behaviour and the differences in the number of events can be fully explained by several issues found in the 2017 analysis.

The difference at the **No cut** level can be explained by five missing data files due to a typo in a file listing the individual data files of the 2017 analysis. The data files affected by this bug contain 1 377 210 events explaining the difference at the start of the cutflow. The final data production was missing another data file containing 721 276 events due to an unclear reason. Only the number of events after the trigger cut was updated, whereas the first five cuts reflect a previous production containing the mentioned data file. A third issue is found concerning the electron energy calibration. The energy is smeared using a random procedure. The initial seed for the random generator was set to a fixed value. Hence, the random generator was dependent on the job splitting. This bug is fixed by setting the initial seed of the random generator to an event-based property.

A detailed comparison of the data and signal MC samples has been carried out and is shown in Table 5.5. This table describes the behaviour of the data and the $W^+ \to e^+\nu_e$ sample, whereas the numbers of the process $W^- \to e^-\overline{\nu}_e$ are shown in the appendix in Appendix C, Table C.1 for the sake of completeness.

Six different production sets are produced to study the effect of the different issues. The naming scheme is as follows:

- Production **A** is performed on the IN2P3 computing centre located in Lyon, where all the samples used for the 2017 analysis have been processed. It excludes the missed data files and replicates the electron energy calibration seed bug by recreating the same job splitting as for the 2017 analysis. The mass of the W-boson was blinded with a shift of $\Delta m_W^{\text{shift}} = -17.9\,\text{MeV}$ resulting in a mass of $m_W = 80\,381.1\,\text{MeV}$.
- Production **B** is processed with all data files missing in production A.
- Production **C** uses the raw MC mass of the W-boson of $m_W = 80\,399\,\text{MeV}$ and is the same as production B but including an unblinded mass.
- Production **D** is a change of the site. These samples were produced on the BAF2 cluster located in Bonn.
- Production **E** fixes the energy calibration seed bug. The initial seed is no longer connected with the job splitting but an event-based property.

The values of the 2017 analysis in Table 5.5 are always given as a point of reference. The only difference for data is between production A and all other productions. Hence, it is enough to compare productions A and B as shown in Table 5.5. Production A agrees with the 2017 analysis except for the first five cut stages. These numbers can be reproduced by including the excluded file containing

	Data			$W^+ \to e^+\nu_e$			$W^- \to e^-\bar{\nu}_e$			$W \to \tau\nu$		
Cut	2017 analysis	Reanalysis	Agreement [%]	2017 analysis	Reanalysis	Agreement [%]	2017 analysis	Reanalysis	Agreement [%]	2017 analysis	Reanalysis	Agreement [%]
No cut	185 039 772	186 416 982	100.74	29 129 499	29 129 531	100.00	20 092 555	20 092 577	100.00	7 041 098	7 041 106	100.00
LAr noise bursts	184 421 049	185 796 322	100.75	29 129 499	29 129 531	100.00	20 092 555	20 092 577	100.00	7 041 098	7 041 106	100.00
Good PV	184 249 665	185 623 226	100.75	28 998 609	28 998 640	100.00	20 014 265	20 014 287	100.00	7 003 917	7 003 921	100.00
GRL	167 449 232	168 773 690	100.79	28 998 609	28 998 640	100.00	20 014 265	20 014 287	100.00	7 003 917	7 003 921	100.00
Trigger	153 832 216	154 988 628	100.75	13 838 494	13 838 509	100.00	8 929 879	8 929 889	100.00	848 239	848 240	100.00
$p_{\mathrm{T}}^{e} > 30\,\mathrm{GeV}$	22 902 461	23 238 336	101.47	7 589 574	7 589 835	100.00	5 292 189	5 292 160	100.00	238 701	238 685	99.99
Veto tight++	16 902 915	17 151 290	101.47	6 077 780	6 077 893	100.00	4 295 834	4 295 796	100.00	193 059	193 055	100.00
One tight++	16 233 973	16 472 398	101.47	6 077 664	6 077 776	100.00	4 295 749	4 295 712	100.00	193 044	193 039	100.00
Trigger matching	16 164 844	16 402 322	101.47	6 077 518	6 077 629	100.00	4 295 640	4 295 602	100.00	193 038	193 034	100.00
Jet cleaning	16 147 902	16 385 161	101.47	6 075 311	6 075 429	100.00	4 294 135	4 294 097	100.00	192 957	192 953	100.00
LAr simple veto	16 105 063	16 341 782	101.47	6 069 418	6 069 560	100.00	4 289 625	4 289 584	100.00	192 533	192 529	100.00
$E_{\mathrm{T}}^{\mathrm{cone20}}$	14 198 159	14 407 314	101.47	5 998 321	5 998 507	100.00	4 237 721	4 237 674	100.00	190 571	190 566	100.00
$p_{\mathrm{T}}^{\mathrm{cone40}}$	12 830 863	13 020 186	101.48	5 866 093	5 866 359	100.00	4 145 913	4 145 871	100.00	186 783	186 780	100.00
$u_{\mathrm{T}} < 30\,\mathrm{GeV}$	8 390 077	8 514 155	101.48	4 405 066	4 405 182	100.00	3 090 832	3 090 798	100.00	106 568	106 565	100.00
$m_{\mathrm{T}}^{W} > 60\,\mathrm{GeV}$	6 681 997	6 780 789	101.48	3 699 439	3 699 526	100.00	2 637 380	2 637 405	100.00	67 357	67 350	99.99
$E_{\mathrm{T}}^{\mathrm{miss}} > 30\,\mathrm{GeV}$	5 885 241	5 972 274	101.48	3 278 533	3 278 781	100.01	2 335 603	2 335 608	100.00	58 453	58 453	100.00

	$Z \to ee$			top			diboson			$Z \to \tau\tau$		
Cut	2017 analysis	Reanalysis	Agreement [%]	2017 analysis	Reanalysis	Agreement [%]	2017 analysis	Reanalysis	Agreement [%]	2017 analysis	Reanalysis	Agreement [%]
No cut	4 546 477	4 546 482	100.00	632 302	632 302	100.00	110 722	110 722	100.00	1 195 589	1 195 590	100.00
LAr noise bursts	4 546 477	4 546 482	100.00	632 302	632 302	100.00	110 722	110 722	100.00	1 195 589	1 195 590	100.00
Good PV	4 525 771	4 525 776	100.00	632 027	632 028	100.00	110 505	110 506	100.00	1 191 224	1 191 225	100.00
GRL	4 525 771	4 525 776	100.00	632 027	632 028	100.00	110 505	110 506	100.00	1 191 224	1 191 225	100.00
Trigger	3 163 313	3 163 317	100.00	159 168	159 169	100.00	36 640	36 614	99.93	173 267	173 267	100.00
$p_{\mathrm{T}}^{e} > 30\,\mathrm{GeV}$	2 101 526	2 101 528	100.00	107 606	107 598	99.99	23 750	23 734	99.93	56 279	56 280	100.00
Veto tight++	1 562 570	1 562 571	100.00	91 044	91 039	99.99	19 037	19 024	99.93	45 550	45 550	100.00
One tight++	929 921	929 923	100.00	88 143	88 138	99.99	17 632	17 620	99.93	44 636	44 636	100.00
Trigger matching	924 780	924 781	100.00	88 117	88 112	99.99	17 621	17 609	99.93	44 629	44 629	100.00
Jet cleaning	924 096	924 097	100.00	88 007	88 002	99.99	17 599	17 587	99.93	44 559	44 559	100.00
LAr simple veto	914 458	914 459	100.00	86 644	86 639	99.99	17 483	17 471	99.93	44 365	44 365	100.00
$E_{\mathrm{T}}^{\mathrm{cone20}}$	901 816	901 817	100.00	83 747	83 742	99.99	17 115	17 102	99.92	43 890	43 890	100.00
$p_{\mathrm{T}}^{\mathrm{cone40}}$	880 120	880 121	100.00	77 842	77 839	100.00	16 382	16 370	99.93	42 965	42 965	100.00
$u_{\mathrm{T}} < 30\,\mathrm{GeV}$	332 214	332 214	100.00	8 619	8 615	99.95	5 294	5 289	99.91	17 372	17 372	100.00
$m_{\mathrm{T}}^{W} > 60\,\mathrm{GeV}$	229 545	229 545	100.00	7 516	7 509	99.91	4 606	4 605	99.98	8 438	8 438	100.00
$E_{\mathrm{T}}^{\mathrm{miss}} > 30\,\mathrm{GeV}$	196 292	196 293	100.00	6 787	6 779	99.88	4 145	4 142	99.93	6 855	6 855	100.00

Table 5.4: The cutflow comparison for the electron channel. Shown are the event yields of the data and seven simulated samples for the 2017 analysis and the reanalysis after each cut stage. The numbers of the MC samples are normalised to their cross-section and an integrated luminosity of $\mathcal{L}_{\mathrm{int}} = 4\,591.01\,\mathrm{pb}^{-1}$. The agreement is the number of the reanalysis divided by the number of the 2017 analysis.

	Data			$W^+ \to e^+\nu_e$				
Cut \ Production	A	B	2017 analysis	B	C	D	E	2017 analysis
No cut	184318496	186416982	185039772	29129531	29129531	29129531	29129531	29129499
LAr noise bursts	183703035	185796322	184421049	29129531	29129531	29129531	29129531	29129499
Good PV	183532092	185623226	184249665	28998640	28998639	28998639	28998642	28998609
GRL	166746550	168773690	167449232	28998640	28998639	28998639	28998642	28998609
Trigger	153213320	154988628	153832216	13838509	13841999	13841999	13841162	13838494
$p_{\mathrm{T}}^{e} > 30\,\mathrm{GeV}$	22902461	23238336	22902461	7589835	7593539	7593539	7592879	7589574
Veto tight++	16902915	17151290	16902915	6077893	6080809	6080809	6080172	6077780
One tight++	16233973	16472398	16233973	6077776	6080692	6080692	6080056	6077664
Trigger matching	16164844	16402322	16164844	6077629	6080545	6080545	6079910	6077518
Jet cleaning	16147902	16385161	16147902	6075429	6078343	6078343	6077706	6075311
LAr simple veto	16105063	16341782	16105063	6069560	6072473	6072473	6071838	6069418
$E_{\mathrm{T}}^{\mathrm{cone20}}$	14198159	14407314	14198159	5998507	6001358	6001358	6000690	5998321
$p_{\mathrm{T}}^{\mathrm{cone40}}$	12830863	13020186	12830863	5866359	5869114	5869114	5868461	5866093
$p_{\mathrm{T}}^{W} < 30\,\mathrm{GeV}$	8390077	8514155	8390077	4405182	4407235	4407235	4406849	4405066
$m_{\mathrm{T}}^{W} > 60\,\mathrm{GeV}$	6681997	6780789	6681997	3699526	3701845	3701845	3701403	3699439
$E_{\mathrm{T}}^{\mathrm{miss}} > 30\,\mathrm{GeV}$	5885241	5972274	5885241	3278781	3280980	3280980	3280752	3278533

Table 5.5: Cutflow comparison for the data and the $W^+ \to e^+\nu_e$ sample of the electron channel. Compared are the number of events for the interesting production sets and the 2017 analysis for the given cut stages. The numbers of the MC samples are normalised to their cross-section and an integrated luminosity of $\mathcal{L}_{\mathrm{int}} = 4\,591.01\,\mathrm{pb}^{-1}$.

721 276 events. As expected, the inclusion of the data files missing in the 2017 analysis in production B increases the event numbers. The initial number of data events increases by 1.14 % including the missing data files resulting in 1.48 % more events after the selection.

For the MC signal samples, there is no difference between the cutflows of production A and B. The event numbers of the process $W^+ \to e^+\nu_e$ normalised to cross-section and luminosity are shown in Table 5.5. The numbers of production C only change slightly compared to production B due to a shift of the W-boson mass. The change of production site for production D does not affect the cutflow as expected. The electron energy calibration seed bug is fixed in production E but the numbers change only slightly. The difference to the 2017 analysis is of the order of 10^{-4} which proves this issue has a minor influence on the event selection numbers. The disagreement between the reanalysis and the 2017 analysis was encountered and fully explained. Hence, the validation of the reanalysis selection criteria can be considered successful and closed. New MC samples with a different mass template spacing are produced for the reanalysis. This does not change the cutflow numbers and reflects the event yields of production E.

5.2.7 Validation of distributions

The template fit method used in this analysis is sensitive to the shape of the fitted distributions. Hence, it is important to not only compare the event yields but, in addition, the shape of the distributions with the 2017 analysis.

The χ^2 fit of the 2017 analysis was performed on the p_{T}^{ℓ} and m_{T}^{W} distributions of both channels. Those distributions are compared in Fig. 5.2 for the data sample and the two signal samples for positively charged muons. The data sample of the reanalysis matches perfectly to the 2017 analysis for the two investigated distributions. The distribution of $W^+ \to \mu^+\nu_\mu$ is a bit higher in the low kinematic region and a bit lower in the high kinematic region. The reference distribution of the 2017 analysis used the measured mass value of $m_W = 80\,369.5\,\mathrm{MeV}$ for the MC samples. For the reanalysis, the

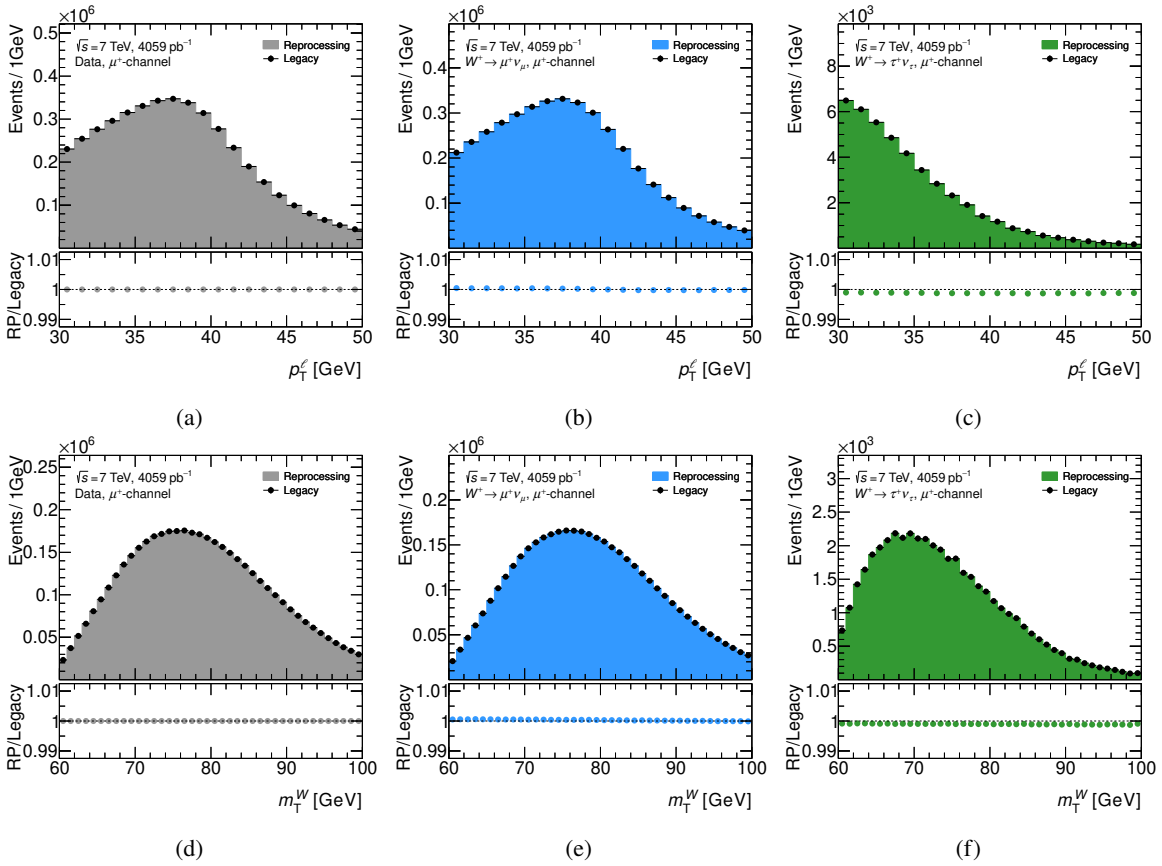

Figure 5.2: Comparison between distributions published in the 2017 analysis (black dots) and the reprocessed samples (coloured filled areas) for positively charged muons and the observables p_{T}^{ℓ} (first row) and m_{T}^{W} (second row). Shown are the distributions of the data sample (grey) and the two signal samples $W^{+} \to \mu^{+}\nu_{\mu}$ (blue) and $W^{+} \to \tau^{+}\nu_{\tau}$ (green).

template which is closest to the measured mass value is shown. As only discrete mass templates are produced, the presented template is smaller than the previously measured $m_W = 80\,369.5\,\mathrm{MeV}$ of the 2017 analysis which explains the observed difference in the kinematic distributions. The small deviation of the $W^{+} \to \tau^{+}\nu_{\tau}$ sample to the 2017 analysis can be understood by taking the same line of argumentation as for the $W^{+} \to \mu^{+}\nu_{\mu}$ distribution. The difference is more a normalisation effect of the order of 1 ‰ rather than a change of the shape.

The comparison of the electron channel shown in Fig. 5.3 is carried out between the 2017 analysis and production A of the reanalysis because this production mimics the setup of the publication as close as possible. Again, the data samples show perfect agreement between the reanalysis and the 2017 analysis. The signal samples fluctuate around the 2017 analysis distribution with larger deviations for the $W^{+} \to \tau^{+}\nu_{\tau}$ sample than for the $W^{+} \to e^{+}\nu_{e}$ sample. This fluctuation is caused by a different choice of the random seed for the electron energy calibration. The job splitting influences the seed choice as described in Section 5.2.6. Unfortunately, it is not possible to get the same job splitting as for the 2017 analysis but it is simulated as best as possible using the same number of sub-jobs. Understanding this difference in the electron channel, the validation of the distribution is successful

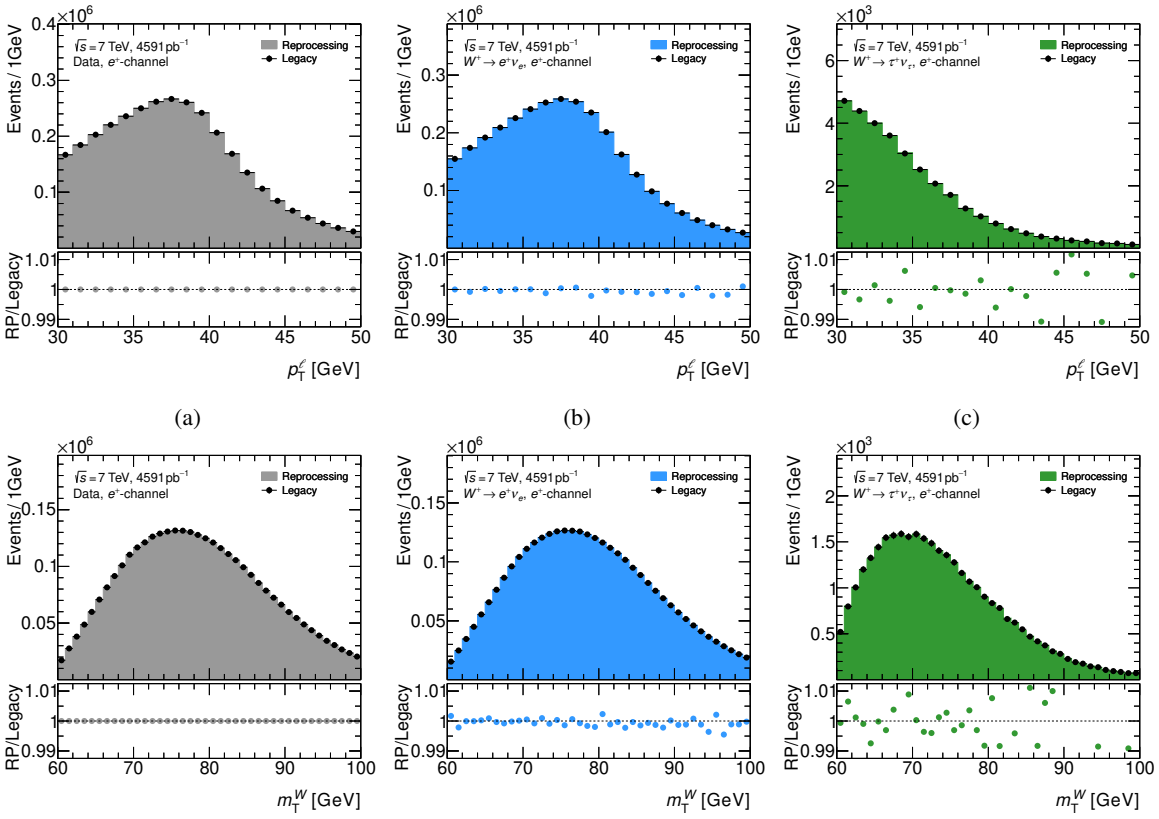

Figure 5.3: Comparison between distributions published in the 2017 analysis (black dots) and the reprocessed samples (coloured filled areas) for positively charged electrons and the observables p_{T}^{ℓ} (first row) and m_{T}^{W} (second row). Shown are the distributions of the data sample (grey) and the two signal samples $W^{+} \rightarrow e^{+}\nu_{e}$ (blue) and $W^{+} \rightarrow \tau^{+}\nu_{\tau}$ (green).

for both channels and the two fitted distributions p_{T}^{ℓ} and m_{T}^{W}. The comparison of more kinematic distributions for the data and all MC samples can be found in Appendix C.1.2.

5.3 Multijet background fit

All EW and top processes of this measurement can be derived using the technique of MC, regardless of whether the process is considered as signal or background. The derived samples are explained in Section 3.4.1. Multijet events originating from strong interaction processes are another source of background. If the multijet event contains a bottom or a charm quark, they can decay semi-leptonically and produce a light lepton with an associated neutrino which allows the event to pass the event selection. In addition, a jet can be misidentified as a light lepton and can be selected as a W-boson event if accompanied by missing transverse momentum. This source of background can be well suppressed by the isolation criteria on the leptons. However, the multijet events cannot be neglected and need to be estimated reliably as the multijet production has a huge cross-section. Due to the complex modelling

of the hadronisation process of QCD and the need for high MC statistics, the multijet background cannot be simulated and a data-driven technique is used to calculate this background. Therefore, the fraction and the shape of the multijet events in the signal region (SR) are determined.

5.3.1 Determination of the multijet contamination fraction

The fraction of multijet background events corresponds to the cross-section of the EW and top processes and determines the number of events in the SR. This is calculated by extrapolating the fraction of control regions (CRs) enriching multijet events to the SR. The presented procedure is performed separately for both lepton channels and the different measurement categories which are explained in Section 4.4.

Muon channel In addition to the mentioned possibilities of how multijet events can mimic the signal final state, the decay of kaons and pions within the tracking region is another possibility to mimic a W-boson event containing a muon. However, semi-leptonic heavy-flavour decays are the main source of multijet background in the muon channel. The muons originating from that decay are often accompanied by other particles. Therefore, the isolation requirements of the leptons are good criteria to get jet-enriched CRs by inverting or relaxing the isolation cuts.

In the muon channel, the isolation criteria on the sum of all tracks being in a cone of the size $\Delta R \leq 0.2$ around the muon candidate over the momentum of the muon candidate itself, $p_{\mathrm{T}}^{\mathrm{cone20}}/p_{\mathrm{T}}$, are reversed. Ten different isolation regions of width 0.03 in the range 0.10–0.40 are used as CRs. The closer the isolation slice to the SR, the closer is the multijet distribution to the actual one in the SR. This can be understood by studying Fig. 5.4. In the CR with a tighter isolation requirement on $p_{\mathrm{T}}^{\mathrm{cone20}}/p_{\mathrm{T}}$, the data is better described by the prediction compared to the region with a looser isolation cut in particular in the low kinematic region where more multijet background events are expected.

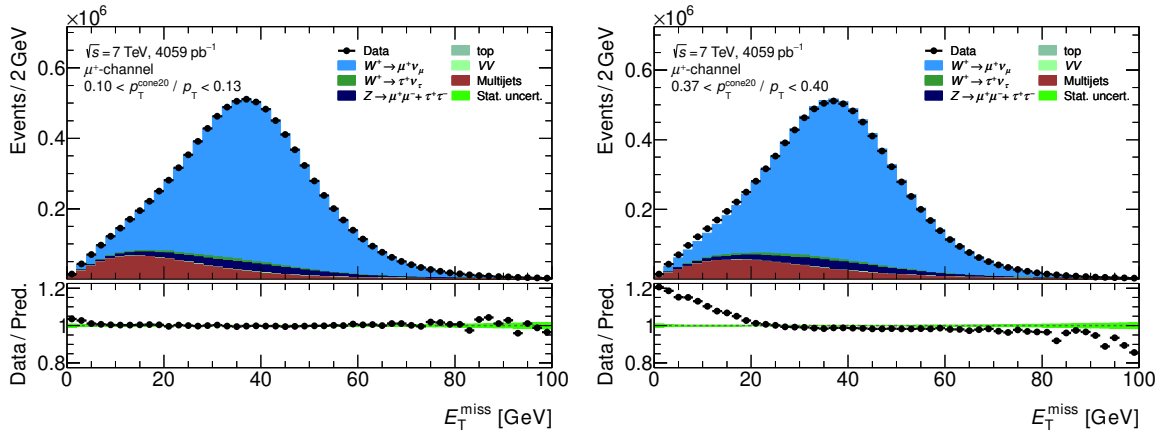

(a) (b)

Figure 5.4: The $E_{\mathrm{T}}^{\mathrm{miss}}$ distribution in the μ^{+}-channel for data and simulation where the shape of the multijet background is extracted from different isolation regions but the fraction is the same. Compared are the first CR $0.10 < p_{\mathrm{T}}^{\mathrm{cone20}}/p_{\mathrm{T}} < 0.13$ (a) and the last CR $0.37 < p_{\mathrm{T}}^{\mathrm{cone20}}/p_{\mathrm{T}} < 0.40$ (b). The cuts $E_{\mathrm{T}}^{\mathrm{miss}} > 30\,\mathrm{GeV}$, $m_{\mathrm{T}}^{W} > 60\,\mathrm{GeV}$ and $p_{\mathrm{T}}^{W} < 30\,\mathrm{GeV}$ are removed to increase the impact of the multijet background.

In each of the CRs, the correct normalisation of the multijet background is unknown and has to be determined by a fraction fit to different discriminating observables:

- The missing transverse momentum $E_{\mathrm{T}}^{\mathrm{miss}}$ is preferably at lower values for multijet events.
- The transverse mass of the W-boson m_{T}^{W} peaks at lower kinematic regions for multijet events.
- The ratio $p_{\mathrm{T}}^{\ell}/m_{\mathrm{T}}^{W}$ reveals the angular correlation between the muon and the missing transverse momentum vector corresponding to the neutrino. In the case of a prompt muon decay from a W-boson, the distribution peaks at 0.5, whereas for multijet events the tail of this distribution is more populated.

To further enrich the multijet background in the fitted observables, two fit regions are designed by removing some of the signal cuts. For the fitting region 1 (FR1), the cuts $E_{\mathrm{T}}^{\mathrm{miss}} > 30\,\mathrm{GeV}$ and $m_{\mathrm{T}}^{W} > 60\,\mathrm{GeV}$ are removed, whereas for fitting region 2 (FR2) the cut on $p_{\mathrm{T}}^{W} < 30\,\mathrm{GeV}$ is discarded in addition. The FR2 is used as a cross-check for the results of the FR1.

A fraction fit method determines the normalisation of the multijet background in the SR. This fit method is based on a binned maximum-likelihood fit taking into account the data events and all events from EW and top background sources. The method is explained based on the $E_{\mathrm{T}}^{\mathrm{miss}}$ distribution in FR1 and follows the presented steps.

1. Samples for both, data and MC, are produced in the SR and the FR1 using isolated muons. The number of events in the $E_{\mathrm{T}}^{\mathrm{miss}}$ distribution is $N_{\mathrm{data}}^{\mathrm{FR1\text{-}iso}}$ for the data sample and $N_{\mathrm{mc}}^{\mathrm{FR1\text{-}iso}}$ for the MC samples in the FR1 and correspondingly $N_{\mathrm{data}}^{\mathrm{SR\text{-}iso}}$ and $N_{\mathrm{mc}}^{\mathrm{SR\text{-}iso}}$ in the SR.

2. Samples in the SR and the FR1 are produced using anti-isolated muons with the actual cut depending on the CR. The number of events in the simulated samples is subtracted from data to get the number of pure multijet events, namely $N_{\mathrm{MJ}}^{\mathrm{FR1\text{-}anti\text{-}iso}} = N_{\mathrm{data}}^{\mathrm{FR1\text{-}anti\text{-}iso}} \left(1 - f_{\mathrm{mc}}^{\mathrm{FR1\text{-}anti\text{-}iso}}\right)$, where $f_{\mathrm{mc}}^{\mathrm{FR1\text{-}anti\text{-}iso}}$ is the fraction of the EW and top contamination in this region. Accordingly, the number of pure multijet events in the SR is determined to be $N_{\mathrm{MJ}}^{\mathrm{SR\text{-}anti\text{-}iso}} = N_{\mathrm{data}}^{\mathrm{SR\text{-}anti\text{-}iso}} \left(1 - f_{\mathrm{mc}}^{\mathrm{SR\text{-}anti\text{-}iso}}\right)$.

3. A binned likelihood fit is done in the $E_{\mathrm{T}}^{\mathrm{miss}}$ distribution. Therefore, the distributions of the pure multijet events in the anti-isolated FR1 and the MC samples in the isolated FR1 are combined like
$$T \cdot N_{\mathrm{MJ}}^{\mathrm{FR1\text{-}anti\text{-}iso}} + \alpha \cdot N_{\mathrm{mc}}^{\mathrm{FR1\text{-}iso}} = N_{\mathrm{data}}^{\mathrm{FR1\text{-}iso}}, \tag{5.1}$$
where T and α are normalisation parameters left free in the fit. The normalisation parameter for the MC samples is expected to be $\alpha \approx 1$ as the MC samples should be properly normalised by their cross-section. The global transfer factor T determines the scale of the multijet events from the anti-isolated region to the isolated region. The results of this binned likelihood fit for all used observables are illustrated in Fig. 5.5. Compared are the fits of the two fit regions in the μ^{+}-channel performed inclusively in pseudorapidity. For the sake of completeness, the figures of the μ^{-}-channel are shown in Appendix C, Fig. C.24.

The described procedure is repeated for all the used observables $E_{\mathrm{T}}^{\mathrm{miss}}$, m_{T}^{W} and $p_{\mathrm{T}}^{\ell}/m_{\mathrm{T}}^{W}$ in both fit regions. The data describes well the shape of the fit results of Eq. (5.1) in the three fitted distributions (cf. Fig. 5.5).

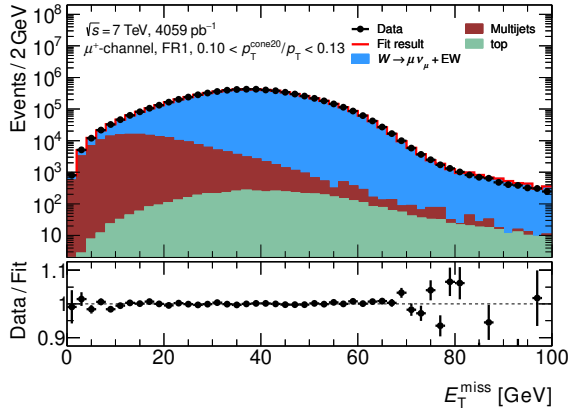

(a)

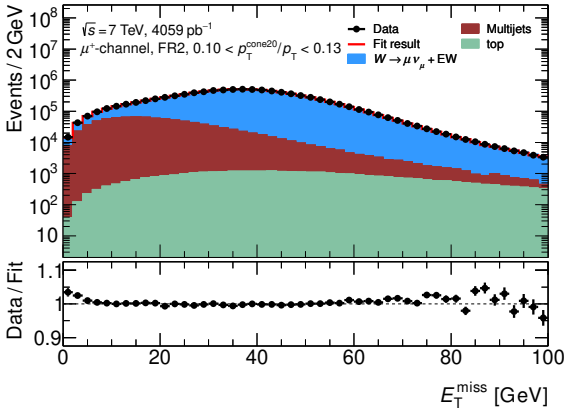

(b)

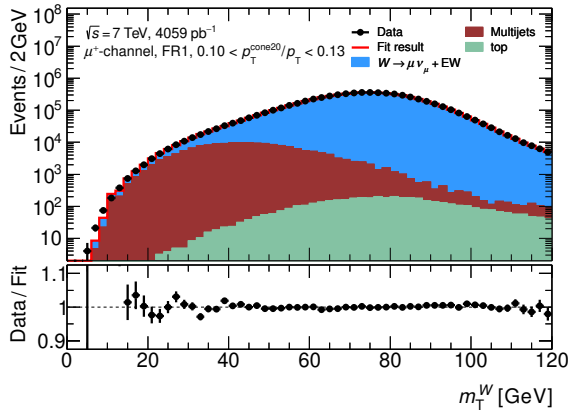

(c)

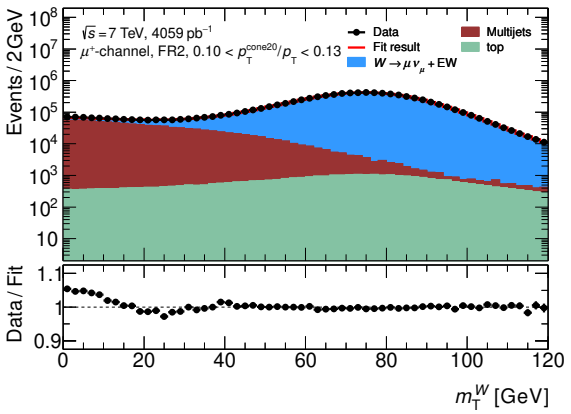

(d)

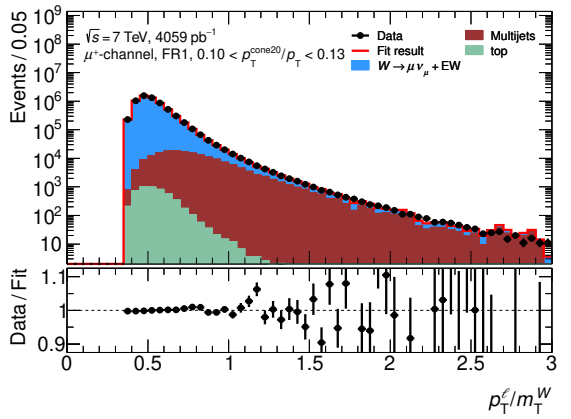

(e) FR1 without $E_{\mathrm{T}}^{\mathrm{miss}}$ and m_{T}^{W} cuts.

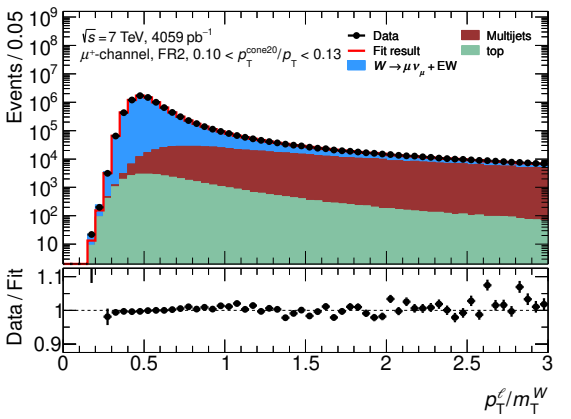

(f) FR2 without $E_{\mathrm{T}}^{\mathrm{miss}}$, m_{T}^{W}, and p_{T}^{W} cuts.

Figure 5.5: Example of multijet template fits of the observables $E_{\mathrm{T}}^{\mathrm{miss}}$, m_{T}^{W}, and $p_{\mathrm{T}}^{\ell}/m_{\mathrm{T}}^{W}$ in FR1 (left) and FR2 (right) for the μ^{+}-channel. The multijet distribution is extracted from the first CR ($0.10 < p_{\mathrm{T}}^{\mathrm{cone20}}/p_{\mathrm{T}} < 0.13$). The ratio shows the agreement between data and the template fits.

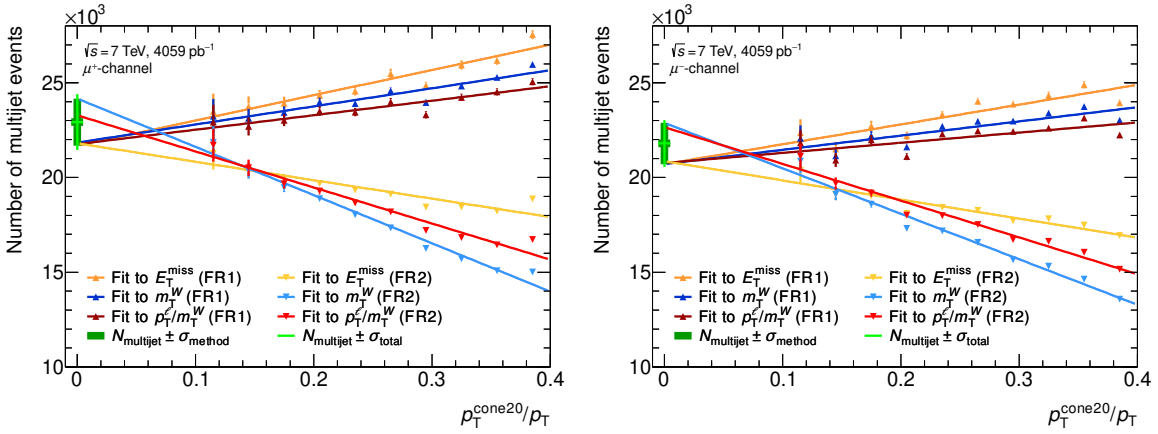

(a) μ^+-channel (b) μ^--channel

Figure 5.6: Illustration of the multijet background scanning in the muon channel. Shown is the derived number of multijet events over the isolation observable $p_{\mathrm{T}}^{\mathrm{cone20}}/p_{\mathrm{T}}$ for (a) the fit of positively charged and (b) negatively charged muons. The two fit regions FR1 and FR2, and the three fitted distributions contribute to the final estimate. The uncertainty on the number of multijet events is marked with the green lines at the isolation region.

In Fig. 5.6, the estimate of the number of pure multijet background events $T \cdot N_{\mathrm{MJ}}^{\text{SR-anti-iso}}$ is plotted over the isolation requirement. Each possible combination of the observable and fit region is linearly extrapolated to the isolated SR. The different lines are in good agreement at $p_{\mathrm{T}}^{\mathrm{cone20}}/p_{\mathrm{T}} = 0$ which justifies this method. The value of the multijet background number in the isolated SR is determined to be

$$N_{\mathrm{MJ}}^{\text{SR-iso}} = \frac{N_{\mathrm{MJ}}^{\text{max, SR-anti-iso}} + N_{\mathrm{MJ}}^{\text{min, SR-anti-iso}}}{2},$$

where $N_{\mathrm{MJ}}^{\text{max, SR-anti-iso}}$ is the highest yield of the multijet background at the isolation region and correspondingly $N_{\mathrm{MJ}}^{\text{min, SR-anti-iso}}$ the lowest yield. This central value corresponds to the centre of the green cross in Fig. 5.6. There are two sources of uncertainties in this process of the determination of the multijet background. The first is the uncertainty of the method itself which is determined to be

$$\sigma_{\text{method}} = \frac{N_{\mathrm{MJ}}^{\text{max, SR-anti-iso}} - N_{\mathrm{MJ}}^{\text{min, SR-anti-iso}}}{2},$$

which corresponds to the length of the dark green cross in the y-direction at the isolation region. Graphically, the size of this uncertainty describes well the difference between the extreme function values at the isolation region. The second source of uncertainty is due to the uncertainty on the cross-section of all EW and top processes used in MC simulations. Therefore, the cross-section for each background sample is varied by 2.5 % up and down and the whole procedure of the determination of the number of multijet background events in the isolated SR is repeated. The value of 2.5 % refers to the W cross-section measurement at $\sqrt{s} = 7$ TeV [136]. The difference between the numbers based on the cross-section varied EW and top samples to the central value of the unvaried EW and top samples is taken as the uncertainty σ_{EW}. Both sources of uncertainty are added in quadrature to receive the total uncertainty σ_{tot} corresponding to the length of the light green cross as illustrated in Fig. 5.6. The uncertainty found by varying the fit range in the binned likelihood fit of the fitted

observables is negligible.

The fraction of the multijet background in the SR is estimated to be the ratio of the multijet events divided by the number of all data events

$$f_{\mathrm{MJ}} = N_{\mathrm{MJ}}^{\text{SR-iso}} / N_{\mathrm{data}}^{\text{SR-iso}}.$$

The fractions of the multijet background for different categories are shown in Table 5.6. The stated uncertainties are the total uncertainties σ_{tot}. The reanalysis fit is performed twice using the two different luminosity values $\mathcal{L}_{\mathrm{int}} = 4\,591.01\,\mathrm{pb}^{-1}$ and $\mathcal{L}_{\mathrm{int}} = 4\,737\,\mathrm{pb}^{-1}$. While the lower value is the correct one, it is found in the revision of the 2017 analysis that the higher luminosity value might have been used to determine the fraction of multijet background events. Judging from the given numbers this cannot be completely verified or falsified as the fractions are too close in the muon channel due to the low contamination of this source of background. However, the central values and the total uncertainties of the repeated multijet background fraction fit using the correct luminosity agrees well with the results of the 2017 analysis. For this measurement, the numbers of the reanalysis serve as the baseline. The choice of the multijet background fractions and the impact on the m_W measurement is investigated in Section 6.1.3.

	2017 analysis [%]	Reanalysis $\mathcal{L}_{\mathrm{int}} = 4\,591.01\,\mathrm{pb}^{-1}$ [%]	Reanalysis $\mathcal{L}_{\mathrm{int}} = 4\,737\,\mathrm{pb}^{-1}$ [%]
W^+	0.51 ± 0.04	0.50 ± 0.03	0.47 ± 0.03
W^+, $\lvert\eta\rvert < 0.8$	0.66 ± 0.07	0.63 ± 0.05	0.61 ± 0.05
W^+, $0.8 < \lvert\eta\rvert < 1.4$	0.50 ± 0.04	0.49 ± 0.03	0.47 ± 0.03
W^+, $1.4 < \lvert\eta\rvert < 2.0$	0.44 ± 0.03	0.43 ± 0.03	0.41 ± 0.03
W^+, $2.0 < \lvert\eta\rvert < 2.4$	0.40 ± 0.03	0.42 ± 0.04	0.40 ± 0.04
W^-	0.68 ± 0.05	0.67 ± 0.04	0.65 ± 0.04
W^-, $\lvert\eta\rvert < 0.8$	0.79 ± 0.07	0.78 ± 0.05	0.76 ± 0.05
W^-, $0.8 < \lvert\eta\rvert < 1.4$	0.67 ± 0.05	0.67 ± 0.04	0.64 ± 0.04
W^-, $1.4 < \lvert\eta\rvert < 2.0$	0.62 ± 0.04	0.60 ± 0.03	0.58 ± 0.04
W^-, $2.0 < \lvert\eta\rvert < 2.4$	0.61 ± 0.04	0.60 ± 0.04	0.58 ± 0.04

Table 5.6: Multijet background fractions f_{MJ} in the muon channel. Shown are the results and uncertainties for both charges of the W-boson and the different regions in pseudorapidity as well as the η inclusive result. Compared are the results of the 2017 analysis and the reanalysis given in per cent using two different values for the luminosity.

Electron channel Additionally to the mentioned common sources of multijet background events, photon conversions and mis-identified hadrons can mimic the final state in the electron channel. The detected electrons originating from multijet events are often accompanied by a jet. The electron isolation criteria include the track based observable $p_{\mathrm{T}}^{\text{cone40}}$ and the calorimeter based observable $E_{\mathrm{T}}^{\text{cone20}}$. Anti-isolated CRs are constructed by slicing $p_{\mathrm{T}}^{\text{cone40}}$ in different CRs in the range of 4–10 GeV where each region has a width of 1 GeV. For each of these six CRs, the cut on $E_{\mathrm{T}}^{\text{cone20}}$ is removed. Similar to the muon channel, the isolation slice closer to the SR describes the multijet distribution of the SR better (cf. Figs. C.25 and C.26 in Appendix C).

The correct normalisation is found using the fraction fit on the discriminating observables $E_{\mathrm{T}}^{\mathrm{miss}}$, m_{T}^{W}, $p_{\mathrm{T}}^{\ell}/m_{\mathrm{T}}^{W}$ as the region populated by the multijet background is different from the signal events. Similar to the muon channel, the fit procedure is performed in the two fit regions FR1 and FR2. The plots illustrating the fit results for both charges of the electron channel can be found in Appendix C, Figs. C.27 and C.28.

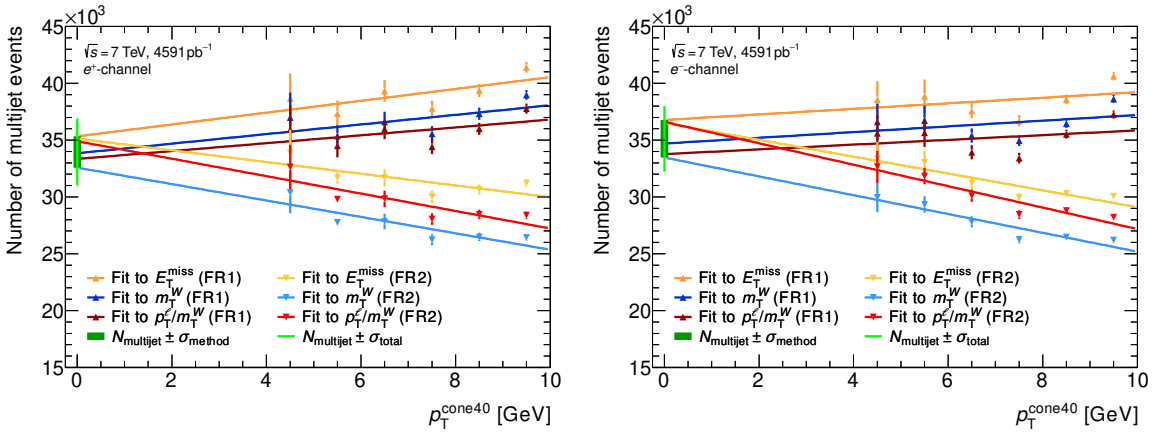

(a) e^{+}-channel (b) e^{-}-channel

Figure 5.7: Illustration of the multijet background scanning in the electron channel. Shown is the derived number of multijet events over the isolation observable $p_{\mathrm{T}}^{\mathrm{cone40}}$ for (a) the fit of positively charged and (b) negatively charged electrons. The two fit regions FR1 and FR2, and the three fitted distributions contribute to the final estimate. The uncertainty on the number of multijet events is marked with the green lines at the isolation region.

In Fig. 5.7, the calculated number of multijet background events $T \cdot N_{\mathrm{MJ}}^{\text{SR-anti-iso}}$ is plotted over the different isolation slices. The final value of the number of multijet background events in the isolated SR $N_{\mathrm{MJ}}^{\text{SR-iso}}$ and the total uncertainty of this method σ_{tot} is derived using the same procedure as in the muon channel. The derived number of multijet events in the isolation region is higher in the electron channel compared to the muon channel due to the higher contamination of the multijet background.

Table 5.7 shows the multijet background fractions f_{MJ} for the different measurement categories in the isolated SR. The fraction fit is again performed twice using two different luminosity values. The numbers using the high luminosity value are based on samples repeating the issues concerning the missing data files and the electron energy calibration. However, the impact of fixing these problems on the resulting fractions is negligible. The fits using the low and correct luminosity value of $\mathcal{L}_{\mathrm{int}} = 4\,591.01\,\mathrm{pb}^{-1}$ are performed on samples correcting for all the found issues in the electron channel. The numbers of the setup with the high luminosity agree better with the reference values of the 2017 analysis than those with the low luminosity. It is assumed that the wrong luminosity value of $\mathcal{L}_{\mathrm{int}} = 4\,737\,\mathrm{pb}^{-1}$ has been used for the fraction fit of the 2017 analysis. If using the correct luminosity, the fractions and the uncertainties of the multijet background increase compared to the values of the 2017 analysis. In general, the fractions of the multijet background contamination are higher in the electron channel than in the muon channel (cf. Table 5.6). The presented measurement corrects for the fallacy of the wrongly used luminosity value. Again, the impact on the central values of the W-boson mass measurement by changing the fractions of the multijet background is explored in Section 6.1.3.

	2017 analysis [%]	Reanalysis $\mathcal{L}_{\text{int}} = 4\,591.01\,\text{pb}^{-1}$ [%]	Reanalysis production A $\mathcal{L}_{\text{int}} = 4\,737\,\text{pb}^{-1}$ [%]
W^+	0.83 ± 0.09	1.00 ± 0.09	0.89 ± 0.10
W^+, $\lvert\eta\rvert < 0.6$	0.47 ± 0.08	0.65 ± 0.10	0.55 ± 0.10
W^+, $0.6 < \lvert\eta\rvert < 1.2$	0.67 ± 0.09	0.87 ± 0.13	0.78 ± 0.12
W^+, $1.8 < \lvert\eta\rvert < 2.4$	1.36 ± 0.19	1.50 ± 0.16	1.40 ± 0.18
W^-	1.21 ± 0.10	1.40 ± 0.12	1.30 ± 0.11
W^-, $\lvert\eta\rvert < 0.6$	0.74 ± 0.09	0.92 ± 0.10	0.82 ± 0.10
W^-, $0.6 < \lvert\eta\rvert < 1.2$	0.90 ± 0.09	1.10 ± 0.12	1.00 ± 0.12
W^-, $1.8 < \lvert\eta\rvert < 2.4$	2.33 ± 0.18	2.60 ± 0.26	2.50 ± 0.19

Table 5.7: Multijet background fractions f_{MJ} in the electron channel. Shown are the results and uncertainties for both charges of the W-boson and the different regions in pseudorapidity as well as the η inclusive result. Compared are the results of the 2017 analysis and the reanalysis given in per cent with two different luminosities.

5.3.2 Extrapolation of the multijet background shapes

The W-boson mass extraction relies on precise modelling of the multijet background yields but is even more sensitive to the shapes of the fitted distributions. Background shapes available in the non-isolated CR often do not represent the real shapes in the isolated SR within the desired accuracy. Even if a CR is defined to be close to SR, the shape mis-modelling can introduce a sizable bias to the extracted m_W value.

In order to quantify how the m_{T}^W and p_{T}^ℓ background distributions evolve depending on the isolation criteria, two disjoint regions are defined using cuts on the lepton isolation: one is close to the SR (control region 1 (CR1)) and one is further away (control region 2 (CR2)). The ratio of these distributions is parametrised with a *transfer function*. This function is then used to transform the multijet background shape from CR1 into the one corresponding to the SR. The slices of CR1 and CR2 are chosen to guarantee a simple transition CR2→CR1→SR. For every considered distribution, the content of every bin of the multijet template of the two CRs is divided. The transfer function of the form

$$R(x) = 1 + \frac{\sum_{n=0}^{2} a_n (x - x_0)^n}{(x - x_1)^m}, \tag{5.2}$$

is then fitted to the ratio distributions of CR2/CR1. The parameters a_0, a_1, and a_2 are left free in the fit, whereas the other parameters are fixed to be $x_0 = 30\,\text{GeV}$, $x_1 = 25\,\text{GeV}$, and $m = 2$ for p_{T}^ℓ, and $x_0 = 60\,\text{GeV}$, $x_1 = 50\,\text{GeV}$, and $m = 1.9$ for m_{T}^W. The denominator's role is to prevent the function to deviate significantly at higher values where statistical uncertainties are large. The background shape extrapolation procedure is the same for both lepton channels except for the definitions of the two CRs. The following isolation requirements are used in the muon channel:

- CR1: $0.1 < p_{\text{T}}^{\text{cone20}}/p_{\text{T}}^\ell < 0.25$,
- CR2: $0.25 < p_{\text{T}}^{\text{cone20}}/p_{\text{T}}^\ell < 0.4$,

whereas the electron channel uses the following isolation slices of the same width:

- CR1: $4\,\text{GeV} < p_{\text{T}}^{\text{cone40}} < 7\,\text{GeV}$,

- CR2: $7\,\text{GeV} < p_{\text{T}}^{\text{cone40}} < 10\,\text{GeV}$.

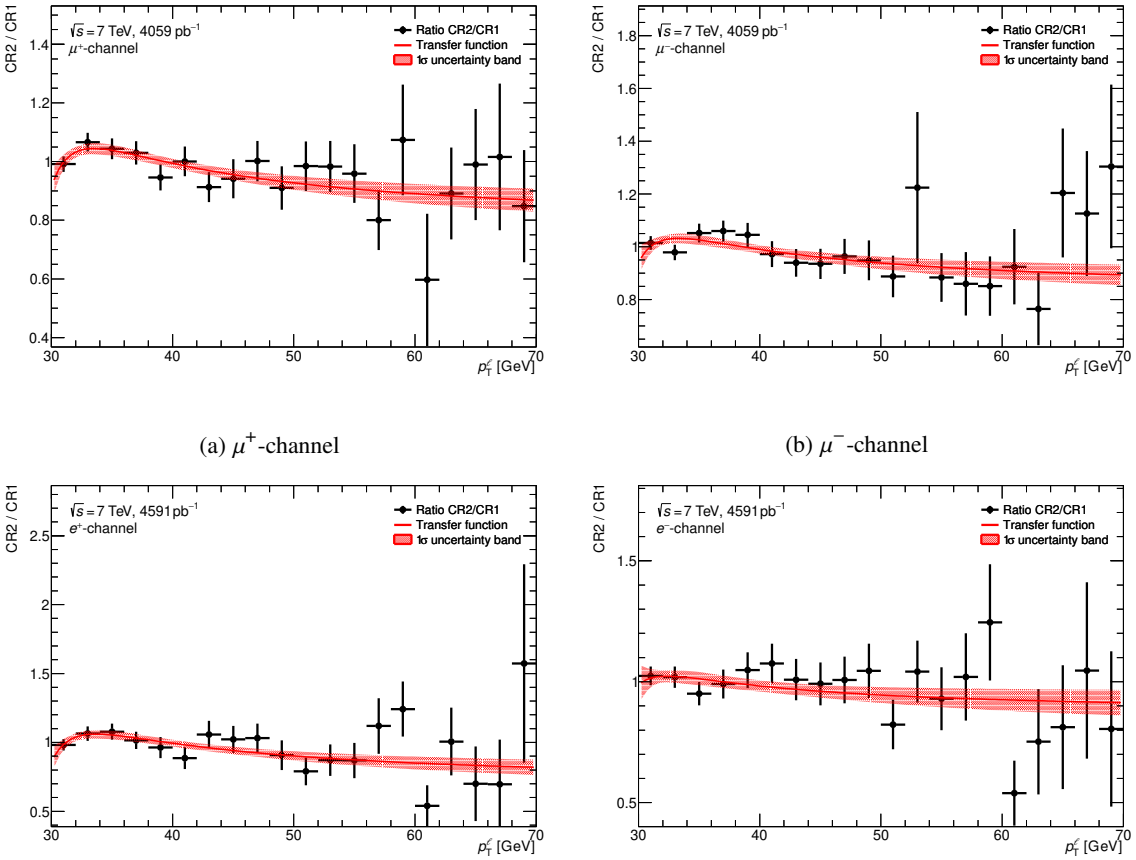

Figure 5.8: Ratio of the multijet background distributions of the two control regions CR2/CR1 for the p_{T}^{ℓ} distribution. The black points represent the ratio of the histograms of the two CRs, the red line refers to the fitted transfer function and the red band corresponds to the 1 σ confidence interval. The shape extrapolation is shown for W^+ (a,c) and W^- (b,d) for the muon (a,b) and the electron channel (c,d).

The fit results of the transfer function of Eq. (5.2) are illustrated in Fig. 5.8 for the transverse momentum of the light lepton. The fitted transfer function has a maximum in the low kinematic region and looks similar in the two channels. The uncertainty in the high kinematic tail becomes larger due to higher uncertainties in the ratio histogram of the two CRs. The corresponding ratio histograms and fitted transfer function of the m_{T}^{W} distribution are shown in Appendix C, Fig. C.29.

The multijet background shape of CR1 is multiplied by the fit result of $R(x)$ as introduced in Eq. (5.2) and normalised by scaling it with the ratio of the integrals of the multijet background distributions of the two CRs. This method is not only done separately for the two lepton channels but for the other measurement categories, charge and pseudorapidity, as well.

The presented procedure of extrapolating the multijet background shape follows closely the one of the legacy analysis but fixes the exponent of the denominator to the given values. This simplifies

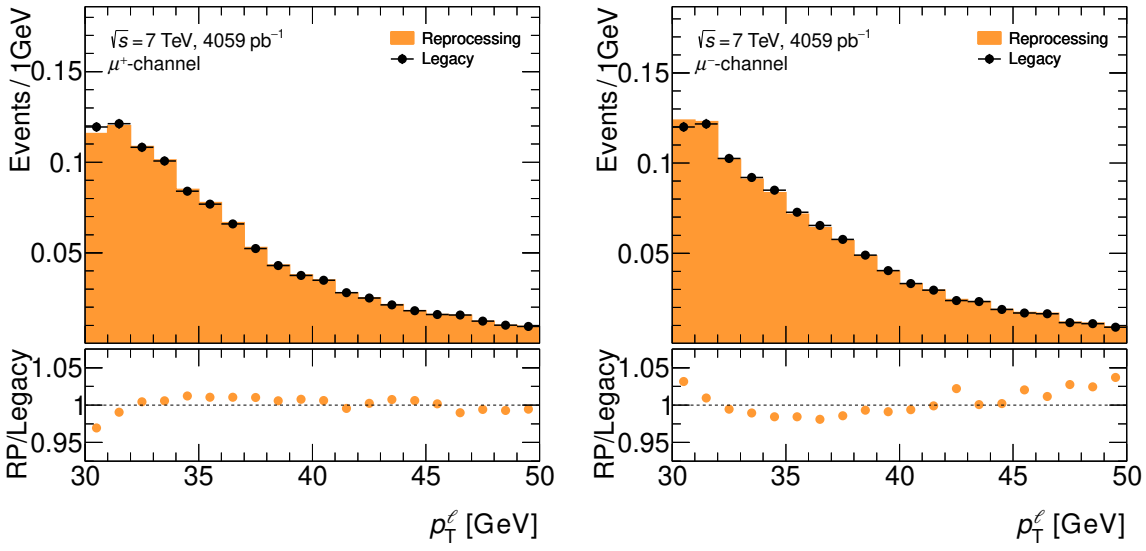

(a) μ^+-channel

(b) μ^--channel

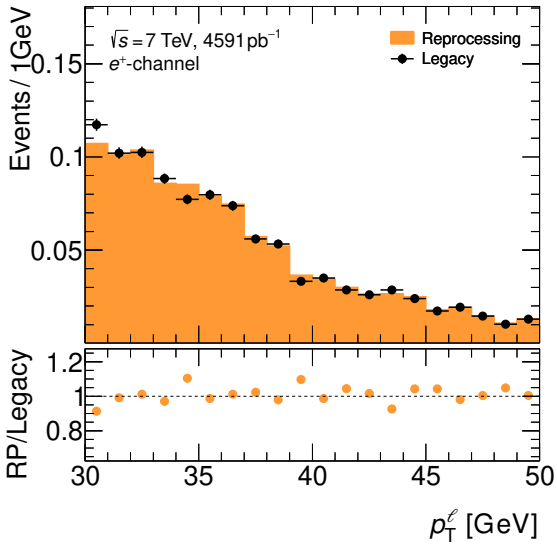

(c) e^+-channel

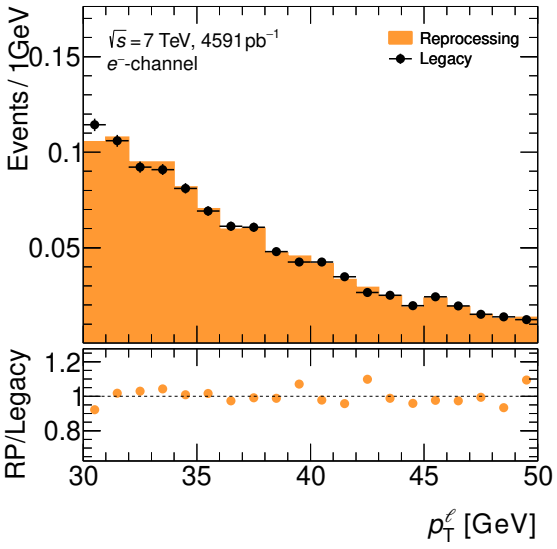

(d) e^--channel

Figure 5.9: Comparison of the multijet background shape between the 2017 analysis and the reanalysis in the observable p_{T}^{ℓ}. The agreement is shown for W^+ (a,c) and W^- (b,d) for the muon (a,b) and the electron channel (c,d).

the method and prepares for a new way to determine the uncertainty of the multijet background shape extrapolation which is explained in Section 7.5.1. The comparison of the shape between the reprocessed samples and the 2017 analysis is shown in Fig. 5.9. The difference in the muon channel is small, whereas statistical fluctuations of the order of 20 % appear in the electron channel. However, the agreement between the reanalysis and the 2017 analysis is sufficient for the observable p_{T}^{ℓ} in both channels. The agreement for the other observables m_{T}^{W}, $E_{\mathrm{T}}^{\mathrm{miss}}$, and p_{T}^{W} is illustrated in Appendix C, Figs. C.30, C.31 and C.32. The task of extrapolating the shapes of the multijet background is considered to be closed.

CHAPTER 6

The statistical methods

The recipe to measure the W-boson mass and further properties is to compare the MC prediction with the actual data. Different mass hypotheses are taken to find the template describing the data distribution best. The question of quantifying the agreement between hypothesis and data follows statistical methods and is referred to as fit. The 2017 analysis used the method of a χ^2 fit, the presented thesis goes a step further and incorporates the sophisticated technique of a PLH fit. The details covering the aspects of the treatment of uncertainties and the strategy of handling mass and width templates are introduced in the following for both fit procedures. An emphasis is put on the comparison with the 2017 analysis results.

6.1 The χ^2 fit

The χ^2 fit method has already been used by the Tevatron experiments D0 and CDF to determine m_W (cf. Section 4.3.1). The general idea is simple and allows to investigate the impact of one systematic uncertainty at a time. The basic concept follows the approach taken in the 2017 analysis and is repeated for this analysis. A good closure at the sub-MeV-level between the central values and the statistical uncertainties implies a successfully recovered event selection including all applied calibrations.

6.1.1 Basic concept

The template fit procedure compares the simulation prediction of different mass hypotheses with the actual data. The change of the W-boson mass is solely reflected in the processes $W \to \ell\nu$ and $W \to \tau\nu$. The nominal mass hypothesis of $m_W = 80\,399$ MeV is normalised to the NNLO cross-section prediction for both W samples. The other mass templates are obtained by reweighting the nominal mass template using the Breit-Wigner parametrisation as introduced in Eq. (4.7). The cross-section dependence on m_W is taken into account during the reweighting procedure. The strategy to construct templates for different Γ_W hypotheses follows the same idea, but the cross-section dependence is more pronounced when altering Γ_W.

The simulation templates used in the fit are the sum of the W processes templates and the remaining backgrounds. The EW background samples are normalised to their respective cross-section, whereas the multi-jet background normalisation was determined in Section 5.3. The 2017 analysis uses only shape information. Therefore, the fitted distribution of every simulation template is normalised within

the corresponding fit range to the data yield in each fit category. The normalisation of each sample to its predicted cross-section ensures the relative fraction between the processes is retained. A χ^2 value is calculated for every template summing over all bins of the fitted distribution

$$\chi^2 = \sum_{i=1}^{n_{\text{bins}}} \frac{\left(f_{i,\text{simulation}} - f_{i,\text{data}}\right)^2}{\sigma^2_{i,\text{simulation}} + \sigma^2_{i,\text{data}}}, \tag{6.1}$$

where $f_{i,\text{simulation}}$ and $f_{i,\text{data}}$ are the bin content of bin i for the simulation template and the data, respectively, and $\sigma_{i,\text{simulation}}$ and $\sigma_{i,\text{data}}$ are the corresponding bin uncertainties. Figure 6.1(a) shows a well-working fit of MC templates to data. The upper panel illustrates the distribution of data, the closest template describing the distribution of the data best and the two templates with the most extreme mass hypotheses. The ratio of data to the closest template shows how well the data are matched. Figure 6.1(b) demonstrates the different χ^2 values for the discrete mass points produced. The mass

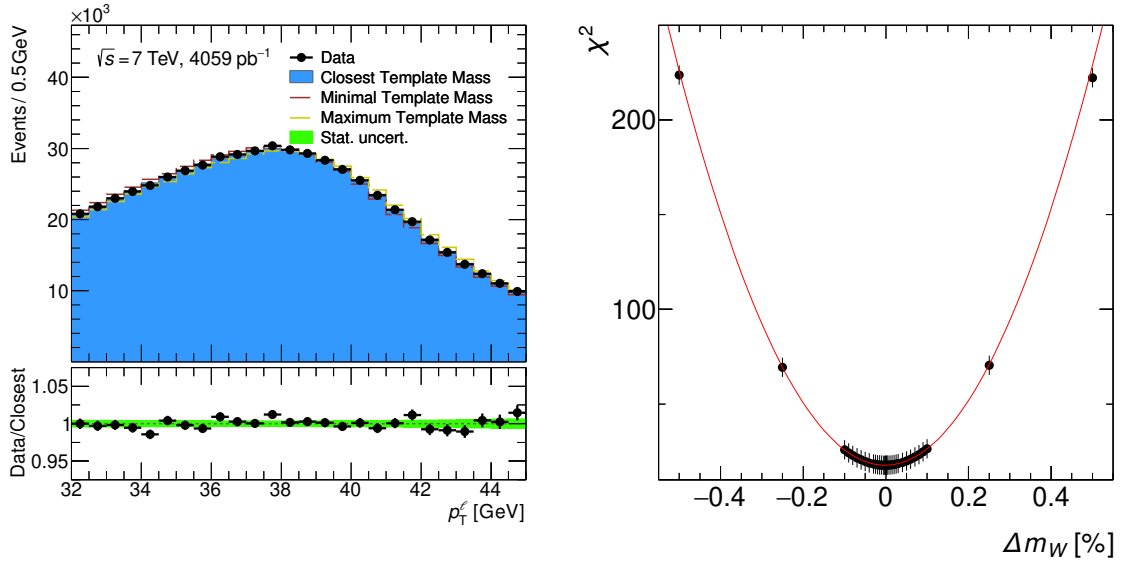

(a) (b)

Figure 6.1: Illustration of the χ^2 fit. The left plot shows the shape of data compared to the templates with the minimal and the maximal mass, and the template describing the data profile best for p_{T}^{ℓ} as well as the ratio of data to the closest template. The right plot gives the χ^2 values for the different mass points and the fitted parabolic function.

templates are generated for concrete points and not as a continuous spectrum due to computational limitations. For the 2017 analysis, 35 of these mass templates have been generated and used for the fit. Their mass values are determined by the relative deviation with respect to the nominal mass point and the template set contains the following points

$$\begin{aligned}\Delta m_W = [&-0.5, -0.25, -0.1, -0.09, -0.08, -0.07, -0.06, -0.05, -0.04, -0.03, -0.025, -0.02,\\ &-0.015, -0.01, -0.005, -0.003, -0.001, 0, 0.001, 0.003, 0.005, 0.01, 0.015, 0.02,\\ &0.025, 0.03, 0.04, 0.05, 0.06, 0.07, 0.08, 0.09, 0.1, 0.25, 0.5]\,\%\end{aligned} \tag{6.2}$$

The mass points were chosen denser around the nominal MC mass and fewer templates were produced for more extreme mass scenarios. However, the χ^2 values of the different templates describe a parabola that can be parametrised by

$$\chi^2 \approx \chi^2_{\text{min}} + \frac{\left(m_W^{\text{template}} - m_W^{\text{best}}\right)^2}{\sigma^2_{m_W}}, \tag{6.3}$$

where m_W^{template} is the mass value for the disjunct template points, m_W^{best} the best fit mass hypothesis, and $\sigma^2_{m_W}$ the corresponding uncertainty. The total statistical uncertainty $\sigma^2_{m_W}$, as defined in the 2017 analysis [86], includes the contribution from both, data and simulation samples, and corresponds to the point where the parabola value is $\chi^2_{\text{min}} + 1$. A fit of the parabola introduced in Eq. (6.3) is displayed in Fig. 6.1. The fitted function describes nicely the χ^2 values of the different mass hypotheses.

6.1.2 Treatment of uncertainties

The basic concept of the χ^2 fit describes the procedure of how the MC templates are fitted to data to determine the central values in each fit category. The assigned uncertainty is the total statistical uncertainty consisting of the data and the simulation statistical uncertainty. The same fit approach is used to evaluate the impact of each systematic uncertainty on the final uncertainty estimation.

The individual contributions of the total statistical uncertainty from data and simulation were evaluated with the bootstrap method for the 2017 analysis. Good agreement between adding the individual components in quadrature and the total statistical uncertainty of the χ^2 parabola was found. This proves that the χ^2 fit correctly accounts for both types of uncertainties and the found statistical uncertainty will be used for the final total uncertainty.

The impact of each systematic uncertainty is derived for each source of uncertainty separately. A pseudo data set is created by changing the parameter belonging to the corresponding systematic uncertainty with respect to the nominal sample. If necessary the modification is applied for signal and background processes. The pseudo data are the sum of the considered samples normalised to their corresponding cross-section. The nominal MC templates are then fitted to these pseudo data sets. A χ^2 value is calculated as in Eq. (6.1) for each template but to pseudo data instead of data and a parabola as in Eq. (6.3) is adjusted to the χ^2 curve. This approach is purely based on MC samples and independent of the statistical fluctuation of data. A good description of the data by the MC samples is therefore necessary. Three different types of uncertainties can be classified:

- **Paired**: Paired systematics have both, an up and a down type variation. If a systematic uncertainty consists of different components, the individual results have to be combined to get the final uncertainty. Therefore, the differences of the fit results between up and down variation are added in quadrature and symmetrised afterwards

$$\Delta = \frac{1}{2}\sqrt{\sum_{i=1}^{N}\left(x_{\text{up},i} - x_{\text{down},i}\right)^2}.$$

- **Shifts**: A shift systematic has only one variation which is varied with respect to the nominal configuration. The hadronic recoil correction is an example of such a shift systematic where

three variations change the baseline setting to receive the final uncertainty. The fit results of the shifts are evaluated with respect to the nominal result and added in quadrature if several components are present

$$\Delta = \sqrt{\sum_{i=1}^{N} \left(x_{\text{shift},i} - x_{\text{nominal},i}\right)^2}.$$

- **Toy MCs**: A proper bin-to-bin correlation between several parameters is obscure to create for some systematic uncertainties, e.g. statistical-based errors like the lepton SFs. N toy MC simulations are produced by smearing the underlying systematic variation within its uncertainties with a Gaussian random distribution. A pseudo data set is constructed for each toy and fit repeated N times using a different toy. The fit results of all toys build a distribution of which the standard deviation serves as the total uncertainty

$$\Delta = \sqrt{\frac{1}{N-1} \sum_{i=1}^{N} \left(x_{\text{shift},i} - \bar{x}_{\text{shift}}\right)^2}.$$

All sources of uncertainties are considered to be uncorrelated to each other. Hence, a set of systematic uncertainties can be combined by adding the individual uncertainties in quadrature. For the 2017 analysis, some systematic uncertainties were evaluated based on a preliminary MC prediction not using the latest set of physics corrections. In the process of determining the impact of an uncertainty source on m_W, the templates and the pseudo data sets are produced based on these preliminary MC samples.

6.1.3 Nominal fit results

The χ^2 fit of the 2017 analysis is repeated for this measurement based only on statistical uncertainties. This allows proving the correctness of the revised samples by comparing the central values and the size of the uncertainty to each other. The results can be found in Fig. 6.2.

Compared are the χ^2 fit results of the individual channels and the combination for the two leptonic channels separately. The individual fits of the two channels consist of separate measurements split up for the charge and $|\eta|$ categories and the observables p_{T}^{ℓ} and m_{T}^{W}. The fits on the distribution on p_{T}^{ℓ} and m_{T}^{W} use the same data and can hence not be combined easily by just taking the uncertainty weighted average. Instead, the correlation between the two observables was determined in the 2017 analysis and is described in [131]. The study included 1 000 different pseudo data sets which were obtained by weighting each MC event with a random number taken from a Poissonian distribution with a mean of 1. The correlation coefficient r on the m_W values using the m_{T}^{W} distribution against the m_W values based on p_{T}^{ℓ} fits was determined to be $r \sim 50\,\%$. The combined value m_W^{combined} is calculated with the relation

$$m_W^{\text{combined}} = w m_W^A + (1-w)\, m_W^B, \tag{6.4}$$

where m_W^A and m_W^B are the mass values determined in fits to the observables p_{T}^{ℓ} and m_{T}^{W}, respectively, and w is the weight between the individual measurements. The uncertainty on the combined value

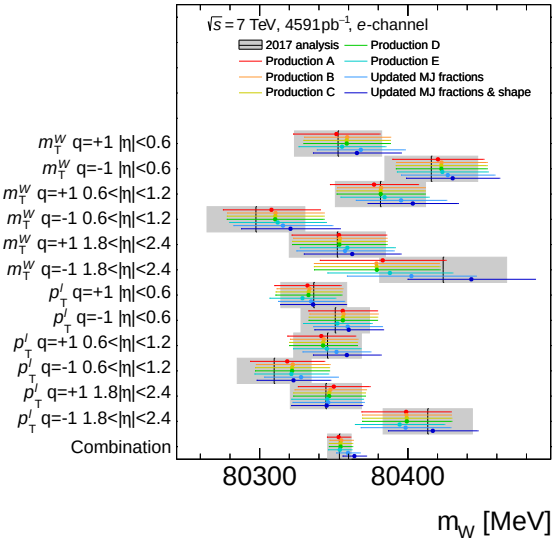

(a) Individual fits e-channel.

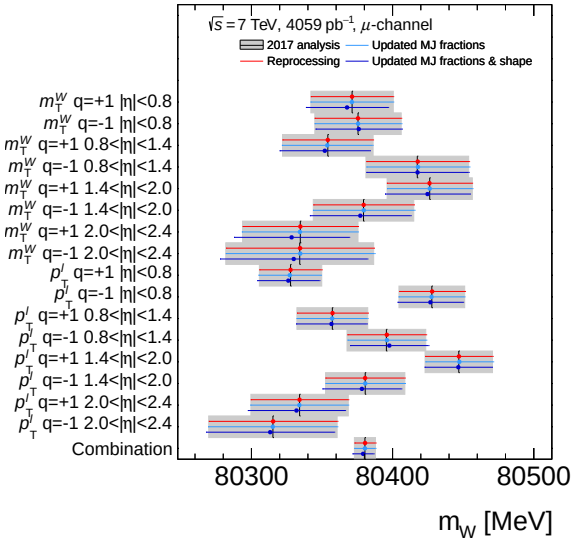

(b) Individual fits μ-channel.

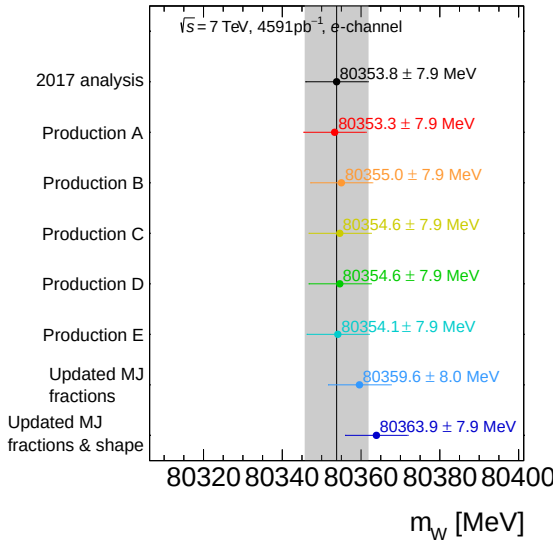

(c) Combination e-channel.

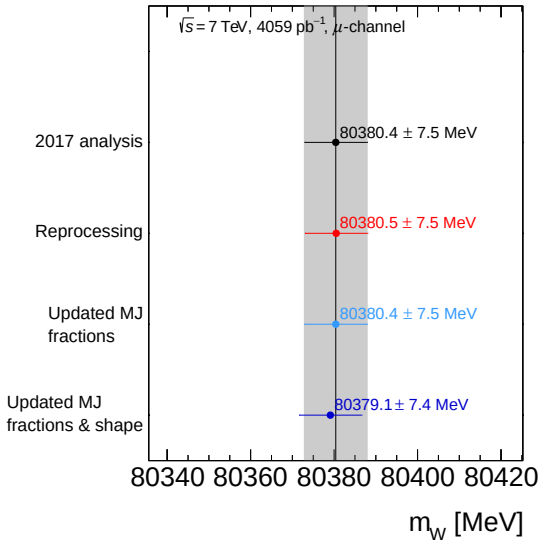

(d) Combination μ-channel.

Figure 6.2: Results of the χ^2 fit taking solely statistical uncertainties into account. Shown is the comparison to the 2017 analysis and the evolution of the central value by introducing different cross-check productions and updating the multijet background determination. The numbers are given for individual fits for (a) the electron channel and (b) the muon channel, and the combinations explicitly quote the central values and uncertainties for (c) the electron channel and (d) the muon channel.

m_W^{combined} defined in Eq. (6.4) is derived as

$$\sigma^2_{\text{combined}} = w^2\sigma_A^2 + 2rw\,(1-w)\,\sigma_A\sigma_B + (1-w)^2\,\sigma_B^2, \tag{6.5}$$

where r is the correlation on the two observables calculated with the pseudo data method. The quantities σ_A and σ_B are the uncertainties of the χ^2 fit mass results of the observables p_{T}^{ℓ} and m_{T}^{W}, respectively. The weight w can be chosen in a way to minimise the total uncertainty of the combined W-boson mass value defined in Eq. (6.5) with the equation

$$w = \frac{\sigma_B^2 - r\sigma_A\sigma_B}{\sigma_A^2 + 2r\sigma_A\sigma_B + \sigma_B^2}.$$

The combination is performed with the help of the BLUE method [143].

In the electron channel, the individual fit results of the reprocessing represented by production A (the mentioned production names are explained in Section 5.2.6) are in good agreement for low absolute values of the pseudorapidity as can be seen in Fig. 6.2. The central value of the fit for the measurement category $q = -1$, $1.8 < |\eta| < 2.4$ (cf. Table 4.1) differs most from the 2017 analysis result. The combination of the individual measurement categories of production A has a central value of 80 353.3 MeV. Hence, it is 0.5 MeV lower than the 2017 analysis result. Fixing the issue with the missing data in production B shifts the central values of the single fits to slightly higher values with respect to production A. Hence, the combined value is 80 355.0 MeV and a bit higher than for the previous production. The unblinding of the used MC W-boson mass in production C influences both, the single fits and the combination, only little with respect to production B. Changing the site between production C and D has almost no impact on the result and the combined value stays at 80 354.6 MeV. The fix of the electron energy calibration seed bug in production E shifts the central values of the individual fits for the observable m_{T}^{W} mostly to slightly higher values and for the observable p_{T}^{ℓ} to lower values in most cases. This leads to a combination of 80 354.1 MeV which is half a MeV lower than the combined value of production D. Updating the fractions of the multijet background in the SR moves the central values of most single fits up as well as the combination with a value of 80 359.6 MeV which is more than 5 MeV higher than for production E. This can be explained by the higher background fractions f_{MJ} calculated for the reanalysis as a wrong luminosity value has been used in the 2017 analysis (cf. Table 5.7). Finally, improving in addition the shape description of the multijet background shifts the combined value upwards to 80 363.9 MeV. The fraction of the multijet background in the SR is around 1 % depending on the measurement category which means it is a dominant source of background contamination. Hence, a change in the shape of the multijet background has a significant impact on the fit result of m_W. By fixing all issues found in the electron channel and updating the multijet background accordingly the combined central value of the χ^2 fit shifts about 10 MeV up.

In the muon channel, the picture is more consistent. The fit results of the reprocessing agree well with the 2017 analysis result for the individual fits and the combination which only differs by 0.1 MeV. Updating the fractions of the multijet background has almost no impact on the fit results and the combined central value changes only by 0.1 MeV with respect to the reprocessing. This is expected as no big difference in the restored fraction numbers with respect to the 2017 analysis has been found. The new evaluation of the multijet background shape means the biggest change for the fit results in

the muon channel. Most single fit results are slightly lower compared to the previous benchmarks. Hence, the combination moves downwards to a value of 80 379.1 MeV. The development of the multijet background has a limited influence on the fit results for the muon channel as in the electron channel because the multijet background contamination is smaller. Overall, the consistency in the muon channel is good. The combined central values of the electron and the muon channel move closer together and differ by 15.2 MeV instead of 26.6 MeV for the 2017 analysis. The revision of the χ^2 fit with the reprocessed samples is considered successful.

6.2 The profile likelihood fit

The advanced technique of a PLH fit is more complex than the χ^2 fit and allows for an in situ reductions of systematic uncertainties. In contrast to the χ^2 fit, all sources of systematic uncertainties are fitted simultaneously and can be correlated easily between the different measurement categories. The PLH fit is implemented in the `TRExFitter` framework constructing the model in the `HistFactory` [144] format which is based on `RooFit` [145] and `RooStats` [146].

6.2.1 Basic concept

The likelihood function $\mathscr{L}$ describes the measurement as a probability density function (p.d.f.) and includes all necessary observables. The measurement is characterised by a set of measured observables which are represented in a histogram $\boldsymbol{n} = (n_1, \ldots, n_N)$ with N bins where n_j represents the number of data events found in the given bin. The usage of histograms instead of an event-based evaluation is less computationally intensive and does not require an analytically known p.d.f. of the prediction and every systematic uncertainty. The MC prediction consists of signal and background processes which are represented by their yields s_j and b_j for a given bin j, respectively. The determined quantity of the PLH fit is the POI which can be one of the three measured properties m_W, Γ_W and $R_{\tau\ell}$. In the case of the lepton universality measurement, the POI is the ratio of normalisation factors acting on two different signal samples. The normalisation factor or signal strength μ will serve as the guideline to introduce the principles of a PLH fit. The measurement of m_W and Γ_W is based on the technique of morphing and interpolation which is separately explained in Section 6.2.2.

The χ^2 fit determines the central values by fits using only statistical uncertainties. The systematic uncertainties are evaluated separately in fits to pseudo data sets. The PLH fit goes one step further and incorporates the systematic uncertainties into the profile likelihood approach as a set of M unknown parameters $\boldsymbol{\theta} = (\theta_1, \cdots, \theta_M)$, referred to as nuisance parameters (NPs). The global likelihood function is composed of two main terms factorising the measured quantities and the unknown parameters in the extended likelihood function

$$\mathscr{L}(\mu, \boldsymbol{\theta}) = \prod_{j \in \text{bins}} \mathscr{P}\left(n_j | \mu s_j + b_j\right) \times \prod_{i \in \text{systematics}} \mathscr{G}\left(\theta_i^0 | \theta_i, \Delta\theta_i\right), \tag{6.6}$$

where θ_i^0 is the mean value and $\Delta\theta_i$ the spread of the i^{th} NP θ_i. Often in physics, the measured quantity and its function $\mathscr{P}$ can be expressed by a Poissonian distribution described by the background yields

s_j and b_j and the signal strength μ

$$\mathscr{P}\left(n_j|\mu s_j + b_j\right) = \prod_{j=1}^{N} \frac{\left(\mu s_j + b_j\right)^{n_j}}{n_j!} e^{-(\mu s_j + b_j)}. \tag{6.7}$$

In the presented measurement, the fit includes only SRs but the part of the likelihood function $\mathscr{P}$ representing the measured quantities can be extended by one or several CRs. The function given in Eq. (6.7) is then multiplied by a product of Poissonian distributions with the means being the bin contents of the histograms in the CRs [147]. Not only one histogram but several split up in different measurement categories are part of this analysis. Each of these channels further factorises the likelihood term of Eq. (6.7). The NPs can follow in principle any distribution but are incorporated best using a Gaussian distribution

$$\mathscr{G}\left(\theta_i^0|\theta_i, \Delta\theta_i\right) = \prod_{i=1}^{M} \frac{1}{\sqrt{2\pi\Delta_{\theta_i}^2}} e^{-\frac{\left(\theta_i - \theta_i^0\right)^2}{2\Delta_{\theta_i}^2}},$$

which penalises a deviation of the NP from the corresponding mean value θ_j^0.

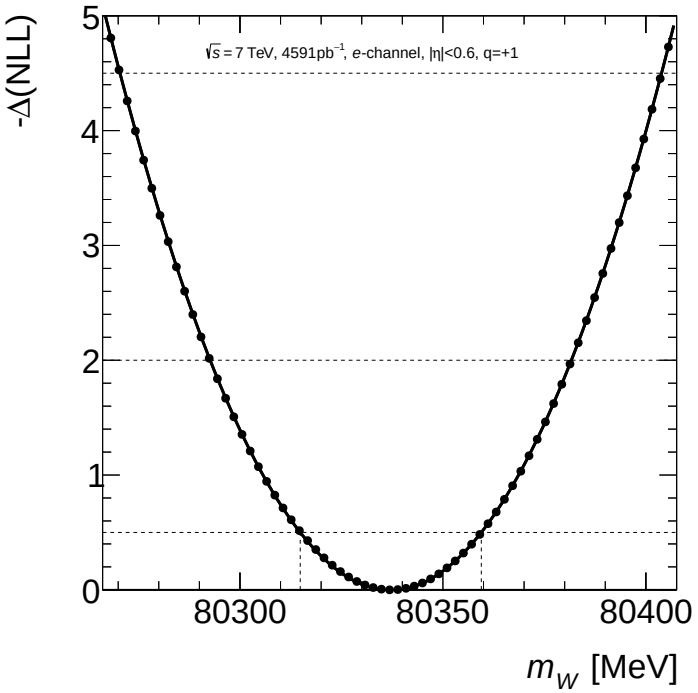

Figure 6.3: Illustration of the likelihood curve of the PLH fit. Shown is the negative logarithmic likelihood value $-\Delta$ (NLL) in a defined mass window for a PLH fit only considering statistical uncertainties in the electron channel for a given measurement category ($q = +1$, $|\eta| < 0.6$). The dots represent a likelihood scan, the curve is a fitted parabolic function and the dashed lines illustrate the determination of the standard deviation.

The maximum likelihood estimates $\hat{\mu}$ and $\hat{\boldsymbol{\theta}}$ determine the values of these parameters for which the likelihood function $\mathscr{L}(\mu, \boldsymbol{\theta})$ (cf. Eq. (6.6)) of the measurement is maximum. The conditional likelihood estimate $\hat{\hat{\boldsymbol{\theta}}}(\mu)$ is the value of $\boldsymbol{\theta}$ maximising the likelihood function for a given μ. This is referred to as the profiled value of $\boldsymbol{\theta}$ [148]. The profile likelihood ratio can then be defined as

$$\lambda(\mu) = \frac{\mathscr{L}\left(\mu, \hat{\hat{\boldsymbol{\theta}}}\right)}{\mathscr{L}\left(\hat{\mu}, \hat{\boldsymbol{\theta}}\right)}. \tag{6.8}$$

Instead of the likelihood ratio itself, the negative logarithm $-\log\lambda(\mu)$ of Eq. (6.8) is used because it turns the product in the likelihood definition into a sum and the maximisation into a minimisation problem which is both numerically easier to calculate.

The profiling of the likelihood is characterised by building the ratio of the likelihood functions as in Eq. (6.8) or taking the difference if the negative logarithm definition is used which makes it possible to directly determine the uncertainty on the POI. A fit of $-\log\lambda(\mu)$, referred to as $-\Delta$ (NLL), finds by construction the minimum at the value $\mu = \hat{\mu}$ where the corresponding function has a minimum value of 0. The standard deviation is defined as the intersection of the fit curve with a straight line at $-\Delta$ (NLL) $= \frac{1}{2}$. If the found estimate of μ is the true value, the log-likelihood curve corresponds to a $\chi^2_{\text{NDF=1}}$ curve with one degree of freedom [149]. This is illustrated in Fig. 6.3.

6.2.2 Morphing and interpolation

The technique of histogram interpolation and extrapolation is well established in the context of a PLH fit as the NPs are handled like this. For each NP, a nominal reference $\theta_i = 0$ and an up- ($\theta_i = 1$) and a down-variation ($\theta_i = -1$) are given. The interpolation of each NP can influence the signal and background yields $s_j(\theta_i)$ and $b_j(\theta_i)$, respectively. The measurement of m_W and Γ_W does not optimise the likelihood function by finding the best signal strength as a POI but rather evaluates the likelihood value for different mass or width values. It can be formalised by removing the signal normalisation factor μ and adding a dependence of the signal strength on this normalisation parameter which is correlated with the mass

$$\mu s_j(\theta_i) \rightarrow s_j(\mu, \theta_i)$$

For this transformation, a certain number of templates with different mass or width values is fed into the PLH fit. To prove the consistency with the χ^2 fit, the same mass splitting as given in Eq. (6.2) is used for the first cross-check. The fit interpolates between the distinct template hypotheses to be able to measure any value of m_W or Γ_W. The technique of vertical morphing is used and explained with the example of the m_W measurement. To interpolate between the given mass templates, any template $T\left(m_W\right)$ of any mass value m_W can be achieved by weighting each template, T_k, with a weight factor w_k

$$T\left(m_W\right) = \sum_{k=1}^{N} w_k\left(m_W\right) T_k,$$

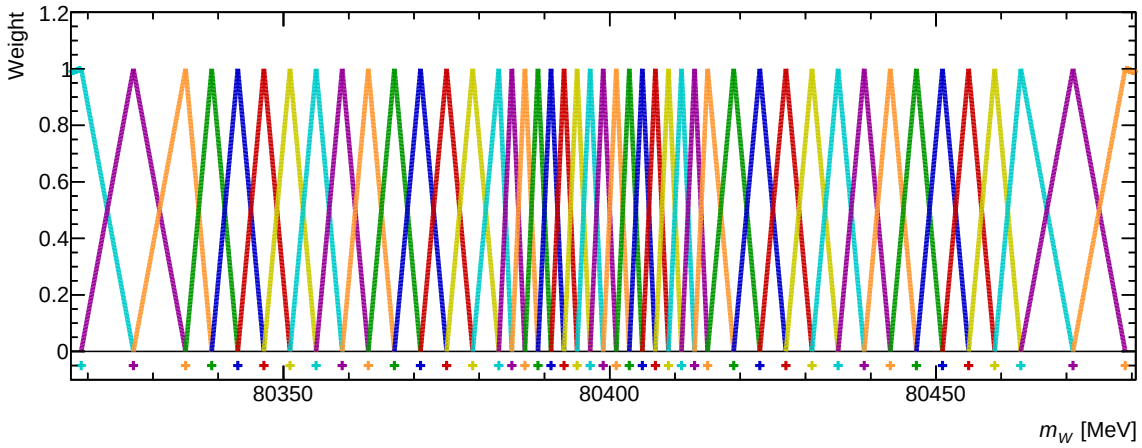

Figure 6.4: Graphical illustration of the linear morphing for the W-boson mass. The different mass templates are indicated with a coloured cross below the x-axis. Shown is the weight for each template where the interpolation function belonging to a given template is inked with the same colour as the template itself.

where N is the total number of templates that have been produced. The individual weights of the templates are defined with a piece-wise linear interpolation

$$w_k\left(m_W\right) = \begin{cases} 1 - \frac{m_W^k - m_W}{m_W^k - m_W^{k-1}}, & \text{for } m_W^{k-1} \leq m_W \leq m_W^k \\ 1 - \frac{m_W - m_W^k}{m_W^{k+1} - m_W^k}, & \text{for } m_W^k \leq m_W \leq m_W^{k+1} \\ 0, & \text{else.} \end{cases} \tag{6.9}$$

For any mass value m_W, only two templates contribute to the interpolated distribution. To receive a template with $\Delta m_W = 0.035\,\%$, the two templates with $\Delta m_W = 0.03\,\%$ and $\Delta m_W = 0.04\,\%$ are each weighted by a factor of 0.5 (cf. Eq. (6.2)). The morphing of Γ_W works the same as the presented procedure for the measurement of m_W. The linear interpolation method is illustrated in Fig. 6.4. It demonstrates the weight of each template to receive any template mass with the help of linear functions.

As the templates exist in the form of binned histograms, the template $T\left(m_W\right)$ is technically achieved by weighting each bin with the weight factor derived in Eq. (6.9). A linear dependence of the bin content on the templates is desired. The bin content of given bins for the different mass templates is shown in Fig. 6.5 for a given measurement category (μ^+-channel, $|\eta| < 0.8$). Only some slices of the observable p_{T}^{ℓ} are shown for illustration. The red line illustrates a linear fit to the bin entries versus the different mass templates given as a difference Δm_W to the reference mass point. Most of the slices show a good linear behaviour with slight deviations for the outlier mass templates. An exception is the slice $38\,\mathrm{GeV} < p_{\mathrm{T}}^{\ell} < 39\,\mathrm{GeV}$ which shows a non-linear behaviour. This is the kinematic region where the different mass templates change the ratio of the bin entries compared to the nominal template (cf. Fig. 4.7). To remedy this deficit, the distance of the template points has to be small. Instead of the template spacing given in Eq. (6.2) used for the 2017 analysis and the PLH fit taking only statistical uncertainties into account, a finer template spacing is applied for the final result with systematic

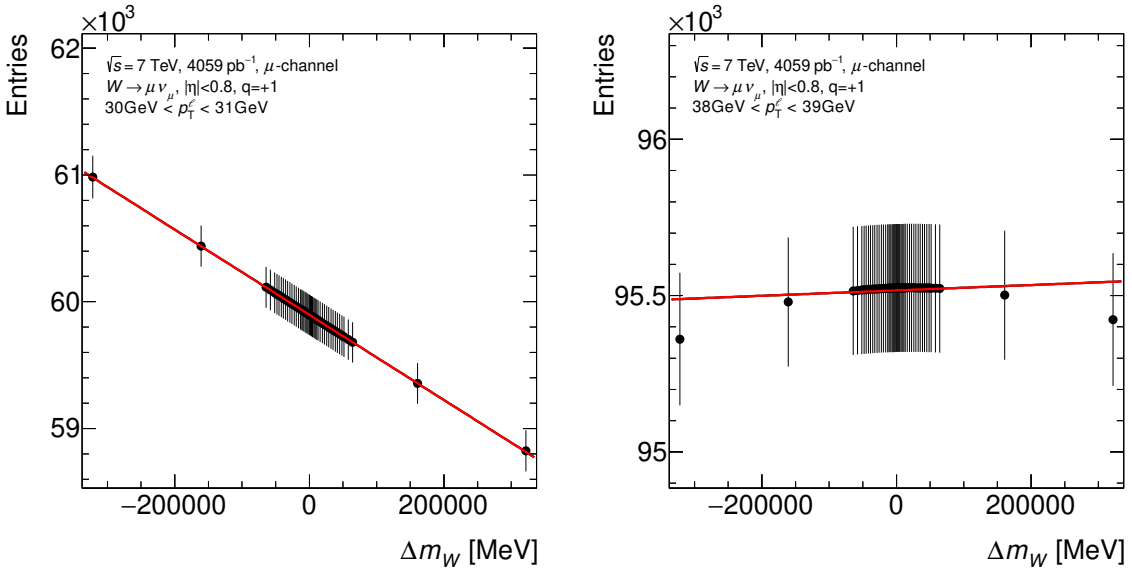

(a) 30 GeV $< p_{\mathrm{T}}^{\ell} <$ 31 GeV

(b) 38 GeV $< p_{\mathrm{T}}^{\ell} <$ 39 GeV

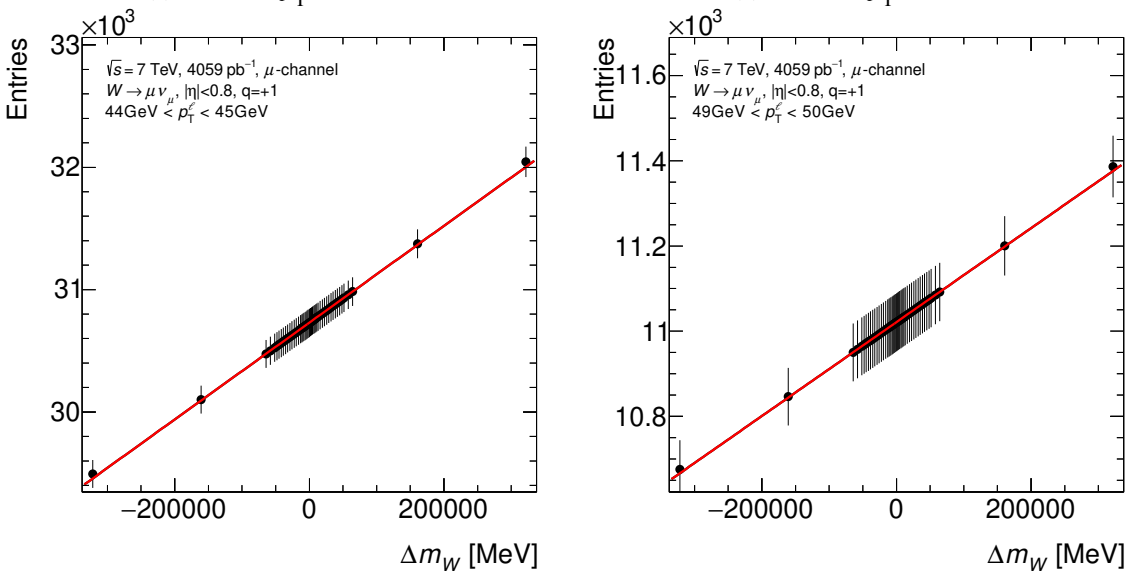

(c) 44 GeV $< p_{\mathrm{T}}^{\ell} <$ 45 GeV

(d) 49 GeV $< p_{\mathrm{T}}^{\ell} <$ 50 GeV

Figure 6.5: Dependence of the bin entries versus the difference of the mass templates to the reference point in the muon channel. Shown is the dependence for four different bins in the observable p_{T}^{ℓ} for the muon channel and the measurement category $|\eta| < 0.8$, $q = +1$. The red curve represents a linear fit to the plotted points.

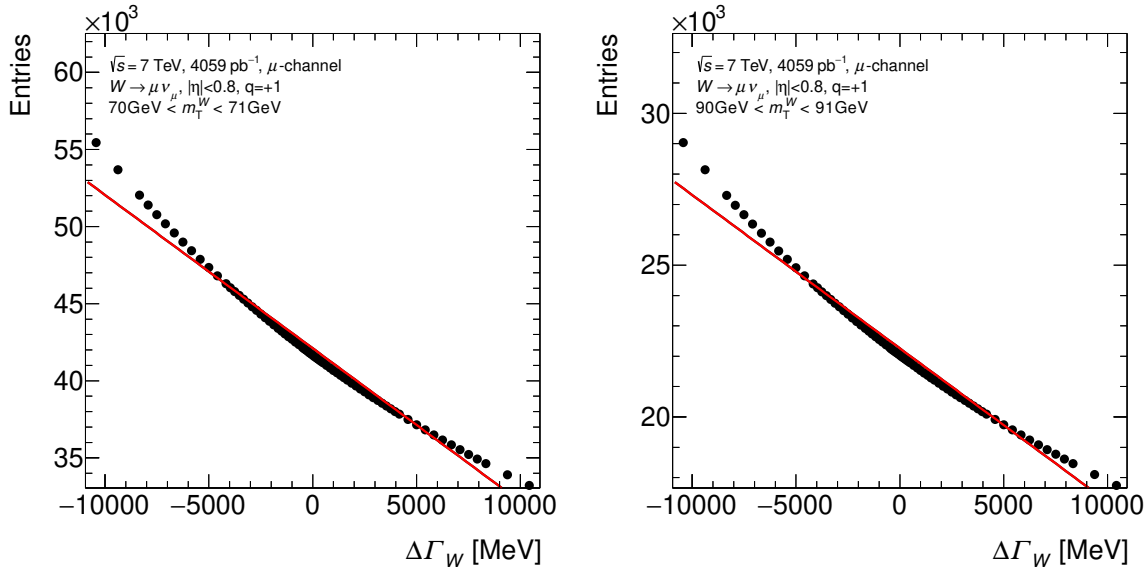

(a) 70 GeV $< m_{\mathrm{T}}^{W} <$ 71 GeV (b) 90 GeV $< m_{\mathrm{T}}^{W} <$ 91 GeV

Figure 6.6: Dependence of the bin entries versus the difference of the width templates to the reference point in the muon channel. Shown is the dependence for two different bins in the observable m_{T}^{W} for the muon channel and the measurement category $|\eta| < 0.8$, $q = +1$. The red curve represents a linear fit to the plotted points.

uncertainties.

Figure 6.6 shows the dependence of the bin entries for different width templates for selected slices of the observable m_{T}^{W}. The functional dependence on the difference in width to the reference point is for none of the shown bins linear. All bins of the observable m_{T}^{W} show a similar dependence of the bin entries on the width hypothesis as the presented examples. Hence, it is important to produce a fine enough template spacing to justify the piece-wise linear interpolation. A better approach to the template interpolation of histograms is the technique of horizontal morphing [150, 151] but this is not yet implemented in `TRExFitter`. Within the scope of this thesis, a quadratic interpolation of a single POI with the help of one-dimensional quadratic basis functions and a method to interpolate and fit two morphing POIs at the same time is developed and technically implemented. These techniques are not used for the final result but explained in Appendix D.

6.2.3 Treatment of uncertainties

The systematic uncertainties model the imperfect knowledge of our prediction, both experimentally and theoretically. These external measurements are injected as the unknown parameters $\boldsymbol{\theta}$ or NPs in the fit. By convention, the mean value θ_i^0 and the spread $\Delta\theta_i$ are set initially to $\theta_i^0 = 0$ and $\Delta\theta_i = 1$. If a feature of the data distribution is well described by the shape of a NP with a value θ_i different from the pre-fit mean value θ_i^0, this could hint at inconsistencies in the prediction. The particular NP is "pulled" which manifests in a difference between the pre-fit and post-fit mean value θ_i^0. If the size of a NP is overestimated, either the shape or the normalisation or both, the NP is "constrained". The constraint value is the ratio of the pre-fit and post-fit width $\Delta\theta_i$.

The uncertainties of the MC samples are often referred to as *gammas* or γs. Uncertainties with a statistical origin like those from simulated samples are best described by a Poissonian distribution. The Poissonian p.d.f. together with a uniform prior results in a gamma posterior explaining the name of the MC gammas [148]. If the MC simulation is sparsely populated in some regions, it is not a good description of the distribution but still an estimate with some statistical uncertainty. Barlow and Beeston suggested to give each bin of each sample a separate NP for the MC gammas [152]. This would lead to several hundred NPs for the MC statistical uncertainty in this analysis but `HistFactory` can condense this situation by assigning one NP per bin representing the uncertainty on the total MC estimate. The contribution of any bin b to the statistical model is the factor

$$\text{Pois}\left(n_b|\nu_b\left(\boldsymbol{\alpha}\right)+\gamma_b\nu_b^{\text{MC}}\left(\boldsymbol{\alpha}\right)\right)\text{Pois}\left(m_b|\gamma_b\tau_b\right), \tag{6.10}$$

where n_b is the number of observed events in bin b, $\nu_b\left(\boldsymbol{\alpha}\right)$ the number of expected events where the MC statistical uncertainties can be neglected (either because the estimate is data-driven or the statistics of the simulated sample sufficiently large), and $\nu_b^{\text{MC}}\left(\boldsymbol{\alpha}\right)$ the number of events where the gammas are considered. The latter two depend on the parameters $\left(\boldsymbol{\alpha}\right)$. The factor γ_b measures the difference between the true rate and the MC estimate $\nu_b^{\text{MC}}\left(\boldsymbol{\alpha}\right)$. Considering the MC simulation as an auxiliary measurement, the constraint term $\text{Pois}\left(m_b|\gamma_b\tau_b\right)$ is introduced. The MC sample size in bin b, m_b, fluctuates around the mean of the Poisson $\gamma_b\tau_b$ if generating a new MC sample where τ_b is the nominal rate. If assuming a flat prior on γ_b, the posterior distribution is a gamma distribution [148].

The presented measurement has three different types of systematic uncertainties as introduced in Section 6.1.2. However, the systematic uncertainties have to be provided as envelopes with an up and down type variation to the PLH fit. The paired systematics fulfil this requirement by definition and do not need any further preparation. The shift systematics consist of only one variation. These one-sided variations are symmetrised for the input as otherwise, they would introduce instabilities in the PLH fit. The fit would suffer from the highly non-gaussian shapes of the one-sided shift systematics and the post-fit uncertainty on the one-sided nuisance parameter is problematic to define if its post-fit central value is close to zero. The kind of shift systematics used in this analysis compares two different setups justifying the symmetrisation procedure. The toy MC systematics are even more problematic to feed into the PLH fit than the shifts systematics as they need to be converted back to the original uncertainty variation. Including several toy shapes as for the χ^2 fit is not possible in this case. The transformation is done with the help of methods based on linear algebra discussed in Section 7.6.

6.2.4 Nominal fit results

The first step to change to an advanced fit method is to perform the PLH fit with statistical uncertainties only and compare it to the results of the 2017 analysis and the revised χ^2 fit. To mimic the normalisation scheme of the χ^2 fit as much as possible, the fit is set up in the following way: all templates are normalised to the integral of the nominal template which means they all have the same visible cross-section. In each measurement category, the signal processes $W \to \ell\nu$ and $W \to \tau\nu$ are scaled such that the sum of their expected number of events matches the number of events of the data subtracted by the backgrounds. The derived normalisation factors are different for each fit category and kept constant in the fit. Hence, only information about the shapes of the distributions are considered. This mimics the normalisation scheme of the χ^2 fit with the difference that there signal and background are both scaled to match the data integral. The scaling of the background samples means a change of

the cross-section value which is avoided for the PLH fit. This normalisation model is solely used for the comparing the fit results using only statistical uncertainties between the two different fit methods. The comparison of the individual fits and the combination is shown in Fig. 6.7 for the two considered observables p_{T}^{ℓ} and m_{T}^{W}.

One important aspect is the handling of the MC gammas in the PLH fit. The different mass templates are injected as separate samples assigning the corresponding mass value. In contrast to Eq. (6.10), the MC gammas of all template samples have to be separated from the total MC uncertainty due to technical reasons increasing the number of NPs associated with the MC statistical uncertainty by a factor of three. If not doing so, the total MC statistical uncertainty would be overestimated and get constrained in the fit. Furthermore, as the individual template masses are obtained by reweighting from the nominal mass hypothesis, the MC gammas of the individual template samples are correlated with the nominal template sample to account for correct statistical treatment.

Overall, the individual fits of the reprocessing agree well for the muon channel but differ in the electron channel for both observables. Updating the multijet background leads to noticeable shifts due to the higher contamination compared to the 2017 analysis and the dominant contribution compared to other background processes. The fit results of the two productions, one just updating the multijet fractions and the other updating the multijet shapes as well, conform between the two different fit methods. An exception is the eta slice $2.0 < |\eta| < 2.4$ in the muon channel, where the PLH fit tends to smaller values than the χ^2 fit in both observables. The agreement between the two fit methods for the two considered productions is visible in the electron channel, even though the central values differ more from the 2017 analysis results.

In the combination of the individual fits, the reprocessing is in good agreement for p_{T}^{ℓ} with the 2017 analysis result while showing a small shift of 1.1 MeV for m_{T}^{W}. The electron channel causes the different fit result in m_{T}^{W} which is due to the non-reproducable setup used for the 2017 analysis. Updating the multijet fractions leads to higher central values of approximately 0.7 MeV for p_{T}^{ℓ} and 4.3 MeV for m_{T}^{W} compared to the 2017 analysis result. Updating the multijet shapes as well, the combined fit results increase even further: the value of p_{T}^{ℓ} grows by around 1.6 MeV and the one of m_{T}^{W} by roughly 6.3 MeV, again compared to the central value of the 2017 analysis. By renewing the multijet background, the difference in the central values between p_{T}^{ℓ} and m_{T}^{W} increases by 2 MeV to approximately 13 MeV. The higher fractions of the multijet background in the SR and the general sensitivity of the mass measurement to shape changes of the multijet background in the electron channel initiate this increase of the central values. The combined values for the two productions updating the multijet background in two steps are in good agreement between the χ^2 fit and the PLH fit with differences of less than 0.2 MeV. In addition, the statistical uncertainty is close between the two fit methods. Hence, the implementation of the PLH fit can be considered successful and closes with the results of the χ^2 fit.

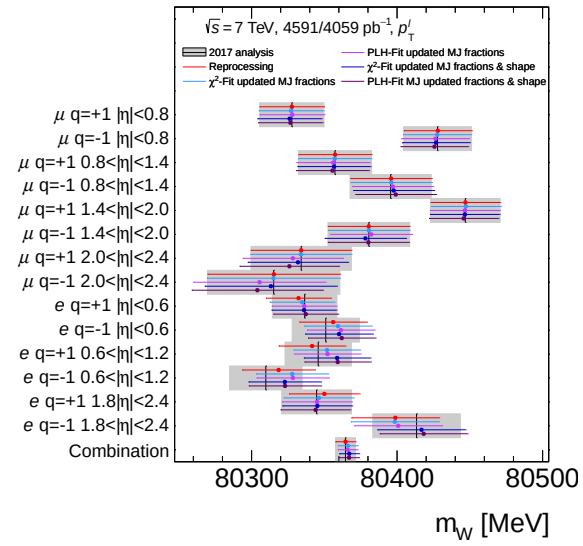

(a) Individual fits p_{T}^{ℓ}.

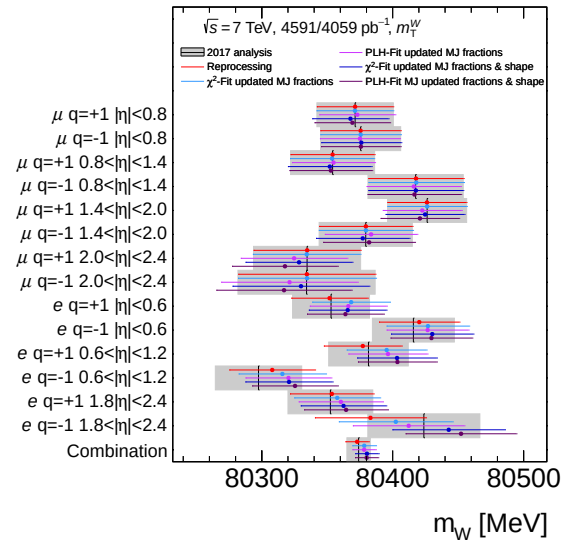

(b) Individual fits m_{T}^{W}.

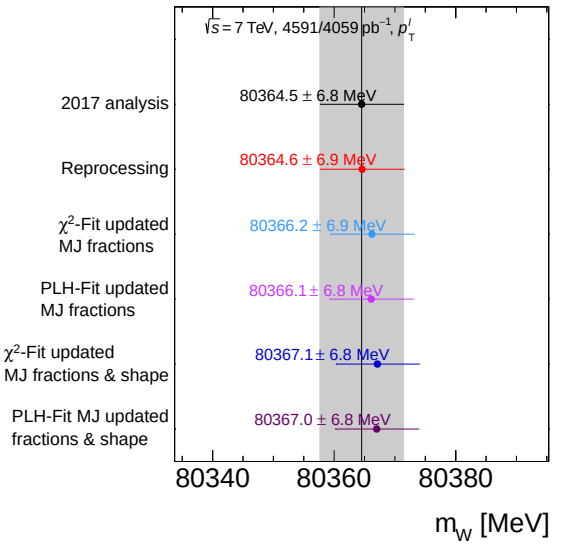

(c) Combination p_{T}^{ℓ}.

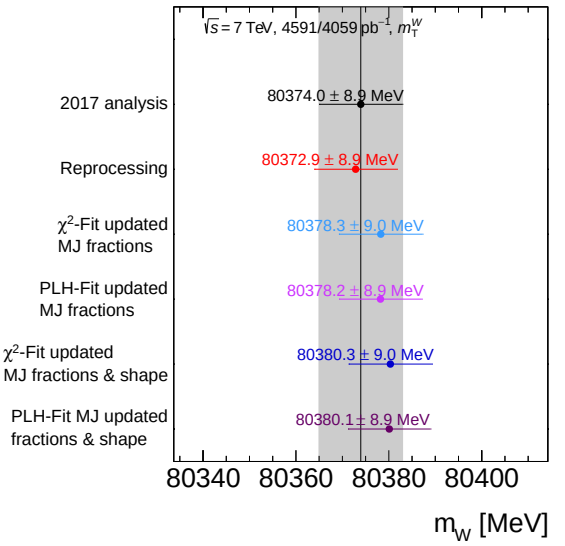

(d) Combination m_{T}^{W}.

Figure 6.7: Comparison of the fit results between the χ^2 fit and the PLH fit for different productions taking solely statistical uncertainties into account. Shown is the comparison to the 2017 analysis and the evolution of the central value by updating the multijet fractions and the multijet fractions and shapes. The numbers are given for individual fits for the observables (a) p_{T}^{ℓ} and (b) m_{T}^{W}, and the combinations explicitly quote the central values and uncertainties for (c) p_{T}^{ℓ} and (d) m_{T}^{W}.

CHAPTER 7

The systematic uncertainties

Every measurement includes uncertainties, whereas the goal of every research work is to understand and reduce the uncertainties as much as possible. The total uncertainty consists of statistical and systematic components. Statistical uncertainties originate from the limited number of performed measurements. They can be reduced by repeating an experiment over and over again. Another source of uncertainty of statistical nature arises from the limited size of the simulated samples. Infinite computing resources would allow to approximate this uncertainty to zero but ensuring surpassing the data statistics by a factor of two is considered sufficient for this analysis. The uncertainties of statistical origin are characterised by the uncertainty of a Poissonian counting experiment. Systematic uncertainties parametrise the limited knowledge of experimental conditions or theoretical predictions. In contrast to statistical uncertainties, the systematic effects need to be studied thoroughly to be estimated properly and reduce their impact on the final uncertainty as much as possible.

The motivation of the experimental calibrations is to improve the agreement between simulation and data. One example is the decay of a Z-boson into two leptons which is used for the experimental calibration procedures as the final state can be identified easily. Plots comparing the corrected simulation and data are shown through this chapter to illustrate the correct implementation of the calibrations. The samples for all these systematics are reprocessed and the impact on the measurement of m_W evaluated with the help of the χ^2 fit using toy pseudodata smeared by the considered systematic. In contrast to Asimov data, toy data do not represent the sum of all simulated samples but include fluctuations of the NPs. The fit results are combined following the treatment of systematic uncertainties of the χ^2 fit as outlined in Section 6.1.2. The impact of each individual systematic uncertainty on m_W is compared to the numbers of the 2017 analysis. Important findings of this cross-check are discussed below. The comparison for each uncertainty category between the 2017 analysis and the revision is shown in the form of tables after the explanation of the corresponding uncertainty category. All sources of uncertainties are assumed to be fully correlated between the electron and the muon decay channels, the two charges of the W-boson and all $|\eta_\ell|$ categories if not stated otherwise. The numbers and information of the different systematic uncertainties are taken from the reference publication [86].

7.1 The production and decay of vector bosons

The most important process studied in this measurement is the production and decay of a single W-boson. In addition, the $Z \to \ell\ell$ process is the largest background in the context of measuring mass,

width and lepton universality of the W-boson. Hence, a good theoretical description and an accurate physics modelling of the single vector boson production is crucial as well as a good understanding of the decay and the properties of the decay products. As mentioned in Section 3.4.1, the MC samples of the production of a single W- or Z-boson are simulated using `Powheg+Pythia8`.

The W- and Z-boson samples are reweighted to include effects of higher-order QCD and EW corrections, and fit results to simulated kinematic distributions which improve the agreement between simulation and data. The fully differential Drell-Yan cross-section [153] is factorised into four terms

$$\begin{aligned}\frac{\mathrm{d}\sigma}{\mathrm{d}p_1\,\mathrm{d}p_2} = &\left[\frac{\mathrm{d}\sigma\,(m)}{\mathrm{d}m}\right]\left[\frac{\mathrm{d}\sigma\,(y)}{\mathrm{d}y}\right]\left[\frac{\mathrm{d}\sigma\left(p_\mathrm{T},y\right)}{\mathrm{d}p_\mathrm{T}\,\mathrm{d}y}\left(\frac{\mathrm{d}\sigma\,(y)}{\mathrm{d}y}\right)^{-1}\right] \\ &\left[\left(1+\cos^2\theta\right)+\sum_{i=0}^{7}A_i\left(p_\mathrm{T},y\right)P_i\left(\cos\theta,\phi\right)\right],\end{aligned} \tag{7.1}$$

where p_1 and p_2 represent the four momenta of the decayed lepton and antilepton; m is the invariant mass, p_T the transverse momentum and y the rapidity of the dilepton system; θ is the azimuth and ϕ the polar angle of the lepton[1] in any restframe of the dilepton system; the eight A_i numerical coefficients are connected to the spherical harmonics P_i of order one, two and zero [86]. The four terms of Eq. (7.1) are subject to different correction procedures described in the following.

7.1.1 Electroweak corrections and uncertainties

The first part of Eq. (7.1), the differential cross-section as a function of the invariant mass of the dilepton system, is modelled with the Breit-Wigner parametrisation given in Eq. (4.7). The main source of EW theory corrections applied to the vector boson samples originates from QED FSR. The influence of the QED ISR is covered by the parton showering of `Pythia8`. The corresponding uncertainty of the FSR modelling is found to be negligible. Other sources of EW corrections are not included in the used MC samples but their effect is taken as systematic uncertainties. They incorporate the interference between ISR and FSR QED corrections, and pure weak corrections caused by virtual-loop and box diagrams. The final-state emission of lepton pairs radiated off in the process $\gamma^* \to \ell\ell$ is considered as a higher-order correction but strengthens the energy loss of the W-boson decay products [86]. The last type of uncertainty in the EW category is the uncertainty on the Z-boson mass scaled to the W-boson mass because the lepton momentum calibration is performed on the invariant mass distribution of dilepton Z events [86].

The mentioned uncertainties were evaluated at the particle level[2] and inclusively in all measurement categories for the 2017 analysis [86]. For the reanalysis, all of them have been resurrected at detector level for all measurement categories. The total uncertainty for both lepton channels and the two fitted kinematic observables m_T^W and p_T^ℓ is shown in Table 7.1. The effect on m_T^W is found to be approximately 1 MeV higher in the reanalysis consistent for all measurement categories and similar between the two channels. The impact on p_T^ℓ is larger compared to m_T^W and a difference at the MeV-level between 2017 analysis and reanalysis is stated. Despite this small discrepancy, this uncertainty category is considered successfully closed.

[1] Here, a lepton means either the negatively charged lepton in the case of W^-- or Z-decays, or the neutrino for W^+-decays.
[2] The particle level refers to the generator level without running the reconstruction algorithms of the detector.

Uncertainty category [MeV]			EWK unc.	
Channel			Legacy	Reanalysis
m_{T}^{W}	W^-	$\lvert\eta\rvert < 0.6$	3.4	4.4
		$0.6 < \lvert\eta\rvert < 1.2$	3.4	4.5
		$1.8 < \lvert\eta\rvert < 2.4$	3.4	4.5
	W^+	$\lvert\eta\rvert < 0.6$	3.4	4.7
		$0.6 < \lvert\eta\rvert < 1.2$	3.4	4.7
		$1.8 < \lvert\eta\rvert < 2.4$	3.4	4.5
p_{T}^{ℓ}	W^-	$\lvert\eta\rvert < 0.6$	5.3	6.4
		$0.6 < \lvert\eta\rvert < 1.2$	5.3	6.6
		$1.8 < \lvert\eta\rvert < 2.4$	5.3	6.3
	W^+	$\lvert\eta\rvert < 0.6$	5.3	6.9
		$0.6 < \lvert\eta\rvert < 1.2$	5.3	7.0
		$1.8 < \lvert\eta\rvert < 2.4$	5.3	6.5

(a) Electron channel.

Uncertainty category [MeV]			EWK unc.	
Channel			Legacy	Reanalysis
m_{T}^{W}	W^-	$\lvert\eta\rvert < 0.8$	3.4	4.5
		$0.8 < \lvert\eta\rvert < 1.4$	3.4	4.6
		$1.4 < \lvert\eta\rvert < 2.0$	3.4	4.7
		$2.0 < \lvert\eta\rvert < 2.4$	3.4	5.1
	W^+	$\lvert\eta\rvert < 0.8$	3.4	4.8
		$0.8 < \lvert\eta\rvert < 1.4$	3.4	4.7
		$1.4 < \lvert\eta\rvert < 2.0$	3.4	5.0
		$2.0 < \lvert\eta\rvert < 2.4$	3.4	5.2
p_{T}^{ℓ}	W^-	$\lvert\eta\rvert < 0.8$	6.0	6.2
		$0.8 < \lvert\eta\rvert < 1.4$	6.0	6.5
		$1.4 < \lvert\eta\rvert < 2.0$	6.0	6.8
		$2.0 < \lvert\eta\rvert < 2.4$	6.0	8.3
	W^+	$\lvert\eta\rvert < 0.8$	6.0	6.6
		$0.8 < \lvert\eta\rvert < 1.4$	6.0	6.8
		$1.4 < \lvert\eta\rvert < 2.0$	6.0	7.3
		$2.0 < \lvert\eta\rvert < 2.4$	6.0	8.5

(b) Muon channel.

Table 7.1: Comparison of the size of the total uncertainty for the EW category between the 2017 analysis [86] and the reanalysis. The uncertainties are given in MeV for the two observables m_{T}^{W} and p_{T}^{ℓ} in all measurement categories for both leptonic decay channels. The χ^2 fits to evaluate the size of the uncertainty are performed on the combination of signal and background samples.

7.1.2 Rapidity distribution and angular coefficients

The differential cross-sections depending on the vector boson rapidity y, the second part of Eq. (7.1), and the A_i coefficients are modelled with perturbative QCD fixed-order predictions.

Higher-order corrections caused by ISR introduce an azimuthal asymmetry in the angular distribution of the decayed lepton as the vector bosons are not produced with zero transverse momentum which is the case at leading order. Helicity effects cause this asymmetry and are described by eight harmonic polynomials P_i and the same number of dimensionless angular coefficients A_i which represent the ratio of the helicity cross-sections compared to the unpolarised cross-section [154]. The harmonic polynomials are a function of the polar angle and azimuth of the decayed lepton measured in the boson rest frame, whereas the angular coefficients are a function of p_{T}, m, and y of the boson. The differential cross-section depending on the boson rapidity and the angular coefficients are predicted with fixed-order perturbative QCD calculations at order $O\left(\alpha_S^2\right)$ of the strong coupling constant with the CT10nnlo PDF set [155]. An optimised version of `DYNNLO` is used for the NNLO calculation of the predictions [156, 157].

The values of the angular coefficients differ between the `Powheg+Pythia8` samples and the NNLO predictions. This difference is treated with a reweighting procedure formalised in Eq. (7.2). Larger differences in the p_{T}^{W} spectrum are observed for the coefficients A_0, A_1 and A_2. The coefficients A_5, A_6 and A_7 differ from zero only for order $O\left(\alpha_S^2\right)$ and higher. They are small in the studied p_{T}^{W} region and hence found to be negligible. The coefficients A_3 and A_4 are sensitive to the coupling between Z-boson and fermions and are predicted with the help of the weak mixing angle [135].

7.1.3 Transverse momentum distribution

The modelling of the boson transverse momentum distribution at a given rapidity, the third term of Eq. (7.1), is performed with the parton shower generator of `Pythia8`. In the low transverse momentum region $p_{\mathrm{T}}^{W} < 30\,\mathrm{GeV}$, large logarithmic terms of the form $\log\left(m_W/p_{\mathrm{T}}^{W}\right)$ need to be summarised and non-perturbative effects to be taken into account [158–162].

The QCD parameters used in `Pythia8` utilise a measurement of the Z-boson transverse momentum distribution with the ATLAS detector at $\sqrt{s} = 7\,\mathrm{TeV}$ [104]. The three parameters considered in the fit are the intrinsic transverse momentum of the incoming partons, the value of $\alpha_S\left(m_Z\right)$, and the value of the infrared cut-off taken for the QCD ISR. The fit results establish the AZ tune of the `Pythia8` parameters. This tune is used to predict the p_{T}^{W} distribution as other MC generators predict a harder p_{T}^{W} spectrum for a given p_{T}^{Z} distribution which show discrepancies for some detector-level distributions [86]. The results of the parameter optimisation in `Pythia8` for the AZ and the 4C [163] tune are compared to the p_{T}^{Z} distribution and the corresponding ATLAS measurement of the boson transverse momentum [104, 164] in Fig. 7.1. Compared are the normalised differential cross-section

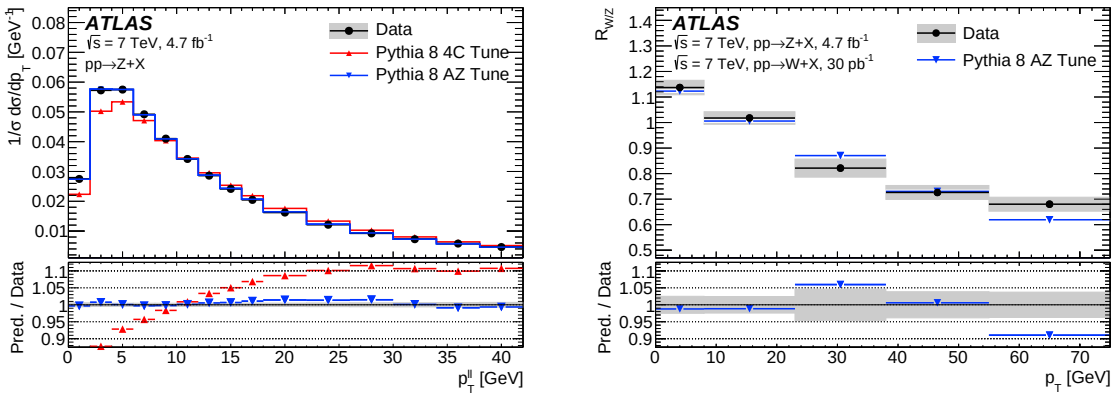

(a) (b)

Figure 7.1: Cross-section as a dependence of kinematic observables. Whereas (a) shows the normalised differential cross-section over $p_{\mathrm{T}}^{\ell\ell}$ of Z-boson events [104], (b) shows the cross-section ratio $R_{W/Z}\left(p_{\mathrm{T}}\right)$ over the boson p_{T} [104, 164]. The measured cross-sections (data) are compared to `Pythia8` prediction with the AZ Tune and the 4C Tune only for (a). The grey band indicated the total experimental uncertainty (taken from [86]).

and the cross-section ratio which is defined as

$$R_{W/Z}\left(p_{\mathrm{T}}\right) = \left(\frac{1}{\sigma_W}\cdot\frac{\mathrm{d}\sigma_W\left(p_{\mathrm{T}}\right)}{\mathrm{d}p_{\mathrm{T}}}\right)\left(\frac{1}{\sigma_Z}\cdot\frac{\mathrm{d}\sigma_Z\left(p_{\mathrm{T}}\right)}{\mathrm{d}p_{\mathrm{T}}}\right)^{-1}.$$

The theoretical prediction match the experimental measurement for the low kinematic region $p_{\mathrm{T}}^{W} < 30\,\mathrm{GeV}$ which is relevant for this analysis due to the corresponding requirement in the W-boson event selection (cf. Section 5.2.5).

7.1.4 Reweighting procedure

The vector boson MC samples using the described decay model are reweighted on an event-by-event basis. The kinematic distributions of the vector bosons and their decay products can be predicted using subsequently a reweighting of the three-dimensional boson production phase space (m, p_{T}, and y) and afterwards a reweighting of the two-dimensional boson decay phase space (θ, ϕ) due to the factorisation of the cross-section.

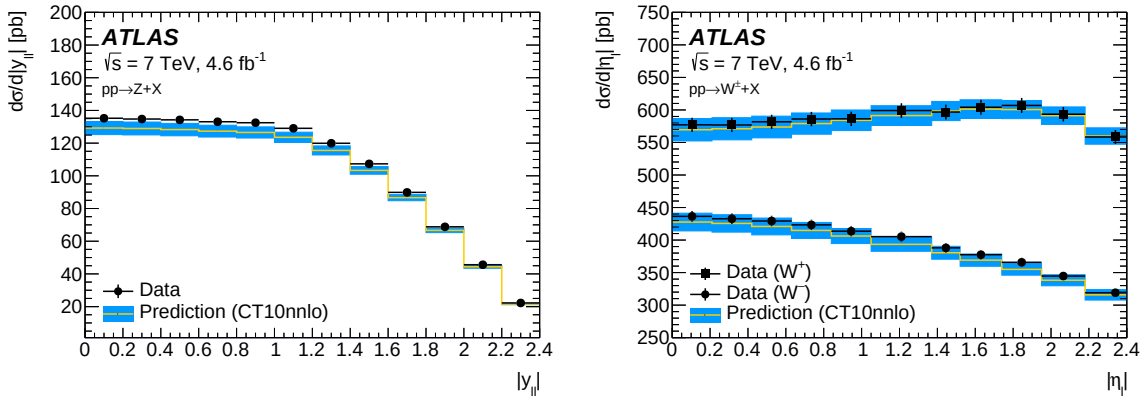

(a) (b)

Figure 7.2: Comparison of differential vector boson cross-section between simulation and data. (a) shows the Z-boson cross-section versus the boson rapidity and (b) the W^+ and W^- cross-section over the lepton pseudorapidity [136]. The `Powheg+Pythia8` simulation using the CT10nnlo set is compared to the measured cross-section. The error bars represent the total experimental uncertainty, whereas the bands show the PDF uncertainties of the used set (taken from [86]).

The reweighting procedure itself is split up into several steps. At first, the inclusive rapidity distribution y of the boson is reweighted to the QCD prediction at NNLO. In a second stage, the `Pythia8` AZ tune is used for the reweighting of the vector boson transverse momentum at a given rapidity. Lastly, the angular decay distributions for a given rapidity and transverse momentum are reweighted corresponding to

$$w\left(\cos\theta, \phi, p_{\mathrm{T}}, y\right) = \frac{1 + \cos^2\theta + \Sigma_i A_i'\left(p_{\mathrm{T}}, y\right) P_i\left(\cos\theta, \phi\right)}{1 + \cos^2\theta + \Sigma_i A_i\left(p_{\mathrm{T}}, y\right) P_i\left(\cos\theta, \phi\right)}, \tag{7.2}$$

where the A_i' coefficients are evaluated at order $O\left(\alpha_S^2\right)$ and the A_i coefficients belonging to the MC samples produced with `Powheg+Pythia8`. This method includes the corrections described in Sections 7.1.1 and 7.1.2 and the impact of the uncertainties in the QCD modelling explained in Section 7.1.5.

The reweighting procedure is probed with different PDF sets. The CT10nnlo, CT14 [165], and MMHT2014 [166] sets are compared to the corresponding ATLAS measurement [136, 167]. The CT10nnlo PDF set comparison with the W- and Z-boson cross-section measurement is shown in Fig. 7.2. A χ^2 compatibility test was performed in the context of the 2017 analysis to quantify the agreement of the predictions with data for different PDF sets. The CT10nnlo set provides the best

description of the actual data and is hence considered as the baseline PDF set for this analysis. The other two sets provide an acceptable description and outperform other theoretical predictions [86].

7.1.5 Uncertainties in the QCD modelling

The production and decay of vector bosons are affected by different kinds of systematic uncertainties originating from the perturbative and non-perturbative modelling of QCD [168–171]. To estimate the size of uncertainty, the parameters corresponding to the second, third and fourth terms of Eq. (7.1) are changed and with the help of the described reweighting procedure in Section 7.1.4 propagated to the varied MC samples.

Uncertainties in the fixed-order predictions

The uncertainty of the chosen PDF set CT10nnlo is derived using the Hessian method [172]. The resulting 25 eigenvectors each consist of a pair of variations which are given at 90 % CL. Each eigenvector pair is scaled to a CL of 68 % as all uncertainties are defined at the 1 σ envelope. The PDF variations influence the boson rapidity and the angular coefficients which are assessed with `DYNNLO`, and the effect on the p_{T}^{W} distribution is checked with `Pythia8`.

Uncertainty category [MeV]			PDFs	
Channel			Legacy	Reanalysis
m_{T}^{W}	W^-	$\lvert\eta\rvert < 0.6$	31.3	31.0
		$0.6 < \lvert\eta\rvert < 1.2$	23.9	23.6
		$1.8 < \lvert\eta\rvert < 2.4$	28.1	27.4
	W^+	$\lvert\eta\rvert < 0.6$	28.5	27.9
		$0.6 < \lvert\eta\rvert < 1.2$	23.5	23.1
		$1.8 < \lvert\eta\rvert < 2.4$	27.3	27.3
p_{T}^{ℓ}	W^-	$\lvert\eta\rvert < 0.6$	26.6	26.3
		$0.6 < \lvert\eta\rvert < 1.2$	20.9	20.3
		$1.8 < \lvert\eta\rvert < 2.4$	22.7	22.3
	W^+	$\lvert\eta\rvert < 0.6$	24.5	24.0
		$0.6 < \lvert\eta\rvert < 1.2$	20.5	20.2
		$1.8 < \lvert\eta\rvert < 2.4$	24.1	23.7

(a) Electron channel.

Uncertainty category [MeV]			PDFs	
Channel			Legacy	Reanalysis
m_{T}^{W}	W^-	$\lvert\eta\rvert < 0.8$	30.6	30.5
		$0.8 < \lvert\eta\rvert < 1.4$	22.2	21.7
		$1.4 < \lvert\eta\rvert < 2.0$	23.1	22.8
		$2.0 < \lvert\eta\rvert < 2.4$	34.1	33.5
	W^+	$\lvert\eta\rvert < 0.8$	28.4	28.2
		$0.8 < \lvert\eta\rvert < 1.4$	23.3	22.4
		$1.4 < \lvert\eta\rvert < 2.0$	27.2	26.6
		$2.0 < \lvert\eta\rvert < 2.4$	32.8	32.8
p_{T}^{ℓ}	W^-	$\lvert\eta\rvert < 0.8$	26.4	26.3
		$0.8 < \lvert\eta\rvert < 1.4$	19.8	19.2
		$1.4 < \lvert\eta\rvert < 2.0$	20.6	20.1
		$2.0 < \lvert\eta\rvert < 2.4$	32.7	31.6
	W^+	$\lvert\eta\rvert < 0.8$	24.7	24.4
		$0.8 < \lvert\eta\rvert < 1.4$	20.6	20.3
		$1.4 < \lvert\eta\rvert < 2.0$	25.2	24.3
		$2.0 < \lvert\eta\rvert < 2.4$	31.8	31.2

(b) Muon channel.

Table 7.2: Comparison of the size of the total uncertainty for the PDF category between the 2017 analysis [86] and the reanalysis. The uncertainties are given in MeV for the two observables m_{T}^{W} and p_{T}^{ℓ} in all measurement categories for both leptonic decay channels. The χ^2 fits to evaluate the size of the uncertainty are performed on the combination of signal and background samples.

The PDF uncertainties are the dominant source of physics-modelling uncertainties in this measurement. The combination of the 25 eigenvectors of the 2017 analysis and the reanalysis is summarised in Table 7.2. The comparison between the two analyses shows a consistent picture with a closure at the

MeV level. The size of this uncertainty is of similar magnitude between the two observables m_{T}^{W} and p_{T}^{ℓ} and between the two lepton channels. The uncertainties in the PDFs are strongly anti-correlated between the opposite charges of the W-boson. The reason is that the total sea PDF of light quarks is well constrained by deep inelastic scattering experiments but the individual sea decomposition of the u-, d- and s-quark is less precisely known [173]. Changing the contribution of $\overline{u}$ in the production of W^- directly influences the contribution of $\overline{d}$ for the W^+ production as the total amount is constant [134].

The other PDF sets MMHT2014 and CT14 are considered as alternative choices and the envelope in m_W fits is taken as an additional PDF uncertainty which was determined to be 3.8 MeV for the 2017 analysis. The effect of missing higher-order corrections at NNLO and the uncertainty of the LHC beam energy were studied for the 2017 analysis but found to be negligible. To summarise, this uncertainty category can be considered successfully closed between the 2017 analysis and the reanalysis.

Uncertainties in the parton shower predictions and angular coefficients

The dominant and only considered source of systematic uncertainty for the parton shower predictions relates to the decorrelation of the transverse-momentum distribution between W- and Z-bosons if the production is induced by a heavy quark. A large correlation is expected for the production by light quarks which is not the case anymore for the charm and bottom quarks. The reason is the variable-flavour-number scheme PDF evolution for the flavour matching scales μ_c and μ_b [174]. Therefore, the scale μ_F is varied in the QCD ISR simultaneously for the light quarks in the processes $q\overline{q} \to W, Z$ ($q = u, d, s$), but independently for each of the processes $c\overline{c} \to Z$, $b\overline{b} \to Z$ and $c\overline{q} \to W$ ($\overline{q} = \overline{d}, \overline{s}$). The consequence of the scale variation in the process $c\overline{q} \to W$ is scaled down by a factor of two to account for the presence of only one charm quark in the initial state. In the 2017 analysis, a data-driven check verified this source of systematic using $u_{\parallel}^{\ell}$ as a control distribution. The fit found a good agreement using the scale variation of the mentioned process, identified the envelope of $c\overline{q} \to W$ as the process which impacts the m_W fits most and is therefore the only systematic uncertainty considered for this source of uncertainty.

The dominant uncertainty originating from the modelling of the angular coefficients is due to the experimental uncertainty of the Z-boson measurement which is used to validate the predictions at NNLO [167]. A pseudodata set containing 1 000 toys is produced by fluctuating the angular coefficients within the experimental uncertainties. The difference between the fluctuated and the nominal value of an A_i coefficient is propagated to the same angular coefficient in the production of the W-boson. The standard deviation of the m_W distribution originating from the χ^2 fit results to kinematic distributions of the complete pseudodata set is taken as the uncertainty to describe this effect.

The two main uncertainties in the parton shower predictions and angular coefficients are summarised in the QCD uncertainty category shown in Table 7.3. The uncertainty of this category is quite constant across the two observables, the two channels and all measurement categories. There is a good agreement of the size of uncertainty between the 2017 analysis and the reanalysis at the MeV level. This ensures that the dominant sources of uncertainties have been considered while neglecting smaller contributions of other effects and closes the comparison for this uncertainty category successfully.

Uncertainty category [MeV]			QCD unc.	
Channel			Legacy	Reanalysis
m_{T}^{W}	W^-	$\lvert\eta\rvert < 0.6$	9.5	10.0
		$0.6 < \lvert\eta\rvert < 1.2$	9.7	9.7
		$1.8 < \lvert\eta\rvert < 2.4$	9.9	10.1
	W^+	$\lvert\eta\rvert < 0.6$	9.9	9.7
		$0.6 < \lvert\eta\rvert < 1.2$	9.6	10.1
		$1.8 < \lvert\eta\rvert < 2.4$	8.4	8.9
p_{T}^{ℓ}	W^-	$\lvert\eta\rvert < 0.6$	8.1	8.9
		$0.6 < \lvert\eta\rvert < 1.2$	8.0	8.8
		$1.8 < \lvert\eta\rvert < 2.4$	8.3	9.1
	W^+	$\lvert\eta\rvert < 0.6$	9.0	9.1
		$0.6 < \lvert\eta\rvert < 1.2$	8.9	9.7
		$1.8 < \lvert\eta\rvert < 2.4$	6.7	8.8

(a) Electron channel.

Uncertainty category [MeV]			QCD unc.	
Channel			Legacy	Reanalysis
m_{T}^{W}	W^-	$\lvert\eta\rvert < 0.8$	9.5	9.8
		$0.8 < \lvert\eta\rvert < 1.4$	9.7	9.3
		$1.4 < \lvert\eta\rvert < 2.0$	9.7	9.3
		$2.0 < \lvert\eta\rvert < 2.4$	9.9	9.4
	W^+	$\lvert\eta\rvert < 0.8$	9.9	9.5
		$0.8 < \lvert\eta\rvert < 1.4$	9.6	9.6
		$1.4 < \lvert\eta\rvert < 2.0$	9.3	9.5
		$2.0 < \lvert\eta\rvert < 2.4$	8.4	8.9
p_{T}^{ℓ}	W^-	$\lvert\eta\rvert < 0.8$	8.1	8.6
		$0.8 < \lvert\eta\rvert < 1.4$	8.0	8.1
		$1.4 < \lvert\eta\rvert < 2.0$	8.0	8.2
		$2.0 < \lvert\eta\rvert < 2.4$	8.3	8.8
	W^+	$\lvert\eta\rvert < 0.8$	9.0	8.7
		$0.8 < \lvert\eta\rvert < 1.4$	8.9	9.0
		$1.4 < \lvert\eta\rvert < 2.0$	8.2	8.6
		$2.0 < \lvert\eta\rvert < 2.4$	6.7	8.0

(b) Muon channel.

Table 7.3: Comparison of the size of the total uncertainty for the QCD category between the 2017 analysis [86] and the reanalysis. The uncertainties are given in MeV for the two observables m_{T}^{W} and p_{T}^{ℓ} in all measurement categories for both leptonic decay channels. The χ^2 fits to evaluate the size of the uncertainty are performed on the combination of signal and background samples.

7.2 Calibration of light leptons

A good calibration of the simulated data is crucial for the presented measurements as the fitted kinematic distributions are shape sensitive to the properties of the W-boson. In addition, the fitted distributions are distorted by the energy and momentum resolutions of the leptons as well as the lepton-selection efficiencies. The process of simulation includes resolution effects but the presented calibration procedure aims to correct the resolution to match with the data. All corrections are applied to the simulation samples except for the muon sagitta bias correction and the electron energy response correction which are both applied to data. All corrections aim to improve the agreement between MC prediction and data and are, together with the corresponding systematic uncertainties, discussed in the following sections.

7.2.1 Calibration of muons

The reconstruction of muons is described in detail in Section 3.3.2. The kinematic properties of the muons are taken only from the information of the ID to reduce the complexity of the calibration.

Muon momentum calibration

The muon momentum can be biased due to two reasons: a radial bias is caused by detector movements along the particle trajectory, while a sagitta bias is due to curl-distortions or linear twists of the detector around the z-axis [175]. The muon momentum scale and resolution corrections are applied

on simulation, whereas the muon sagitta bias correction is applied on data to correct for misalignment following the equations

$$p_{\mathrm{T}}^{\mathrm{MC,corr}} = p_{\mathrm{T}}^{\mathrm{MC}} \times [1 + \alpha\,(\eta, \phi)] \times \left[1 + \beta_{\mathrm{curv}}\,(\eta) \cdot G\,(0, 1) \cdot p_{\mathrm{T}}^{\mathrm{MC}}\right]$$

$$p_{\mathrm{T}}^{\mathrm{data,corr}} = \frac{p_{\mathrm{T}}^{\mathrm{data}}}{1 + q \cdot \delta\,(\eta, \phi) \cdot p_{\mathrm{T}}^{\mathrm{data}}},$$

where $p_{\mathrm{T}}^{\mathrm{MC}}$ and $p_{\mathrm{T}}^{\mathrm{data}}$ are the uncorrected values of MC and data, respectively, and $G\,(0, 1)$ a Gaussian distributed random variable with mean zero and width one. The free parameters α, β_{curv} and δ determine the momentum scale, intrinsic resolution and sagitta bias corrections, respectively [86].

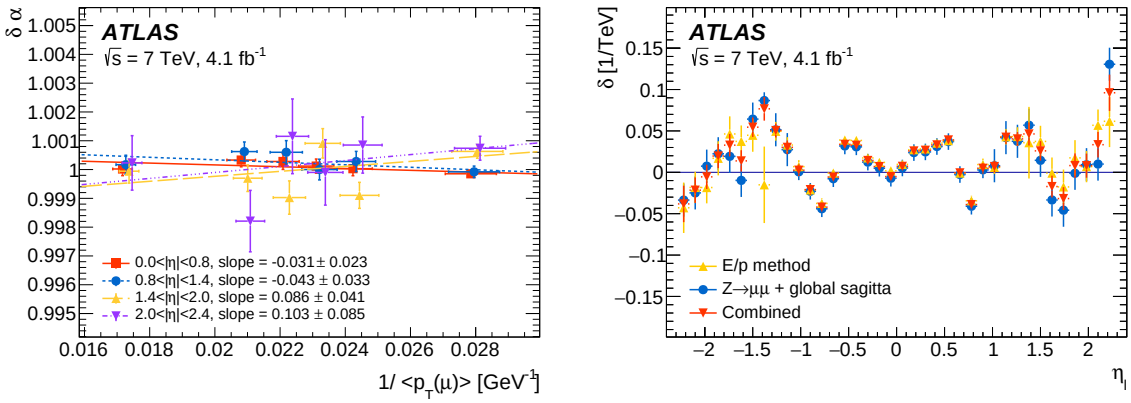

(a) Residual scale

(b) Sagitta bias

Figure 7.3: Performance plots of the muon momentum calibration. (a) shows the residual muon momentum scale corrections over the inverse transverse momentum of the muon for different pseudorapidity regions. A linear function is fitted to the points where the errors bars indicate the statistical uncertainty. (b) illustrates the sagitta bias δ as a function of η_ℓ averaged over ϕ_ℓ. Shown are the E/p and the $Z \to \mu\mu$ methods and the combination of both assuming the two measurements are uncorrelated. The error bars of the points give the statistical uncertainty (taken from [86]).

The former two are calculated using the dimuon invariant mass distribution of $Z \to \mu\mu$ decays employing the method described in [87]. Samples including the momentum scale and resolution corrections are compared to data in a χ^2 minimisation of the invariant mass distribution to determine the best values for α and β_{curv} separately in different detector regions. The parameters α and β_{curv} are sensitive to several sources of uncertainties: the choice of the fit range, a bias caused by the fit methodology, the background contributions, the theoretical modelling of the Z-boson production, the non-linear behaviour of contributions, and the material distribution in the ID [86]. The uncertainties related to the momentum scale α and the momentum resolution β_{curv} are summarised in a single envelope. The resolution uncertainties were evaluated in bins of pseudorapidity η instead of the absolute pseudorapidity bins $|\eta|$ which define the measurement categories. As the statistical uncertainty is evaluated with the inverse of the square-root of the number of events $1/\sqrt{N}$, the resolution systematics have to be corrected with a factor of $1/\sqrt{2}$ and are considered uncorrelated across the muon pseudorapidity. In addition, these two aspects hold for the statistical uncertainty of the $Z \to \mu\mu$ sample on which the calibration is performed.

The uncertainty caused by the extrapolation of the $Z \to \mu\mu$ momentum range to the one of $W \to \mu\nu$ is parametrised as

$$\delta\alpha = p_0 + \frac{p_1}{\langle p_{\mathrm{T}}^{\ell}(W)\rangle},$$

where $\langle p_{\mathrm{T}}^{\ell}(W)\rangle$ is the average muon p_{T} from W-bosons decays, and p_0 and p_1 are free parameters. The parameters are expected to have the values $p_0 = 1$ and $p_1 = 0$ if the correction is momentum-independent. The fits of $\delta\alpha$ over $1/\langle p_{\mathrm{T}}^{\ell}(W)\rangle$ in the different $|\eta|$ categories are illustrated in Fig. 7.3(a). A momentum non-linearity characterised by the maximum of the fitted value of p_1 and its uncertainty determines the extrapolation systematic uncertainty. This uncertainty is taken uncorrelated over the pseudorapidity range due to the statistical nature of this uncertainty [86].

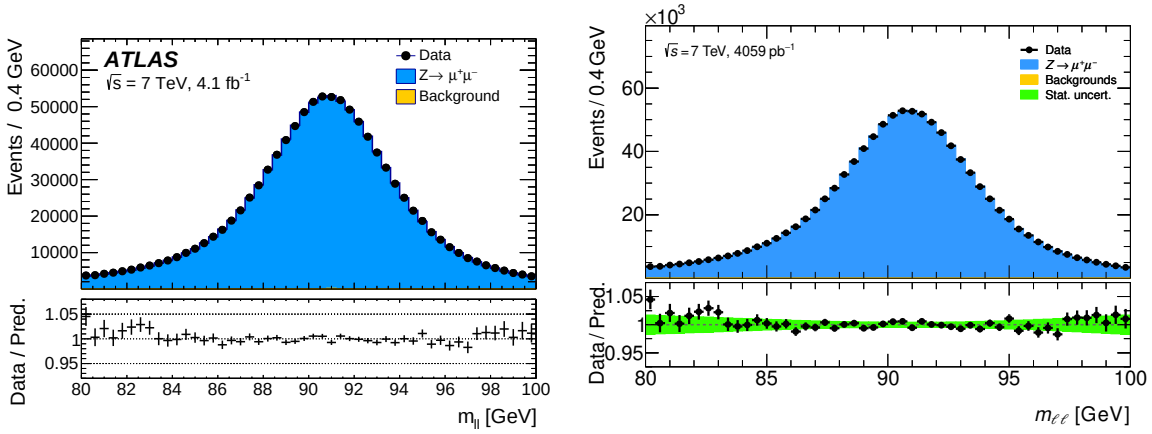

(a) (b)

Figure 7.4: Comparison of the data to simulation agreement of the invariant dimuon mass in $Z \to \mu\mu$ events between (a) the 2017 analysis (taken from [86]) and (b) the reanalysis. All corrections concerning the momentum calibration and the selection efficiency are applied to the simulation, whereas the sagitta bias correction is applied to data. The lower panel shows the ratio of data to simulation where the error bars indicate the statistical uncertainty and the green band represents the uncertainty caused by the limited simulation sample size.

The derivation of the muon sagitta bias δ is based on two different methods: the first uses $Z \to \mu\mu$ events to determine the peak position of the dimuon invariant mass spectrum of data and simulation. This method can determine the charge dependence of the momentum scale for p_{T} values of approximately 42 GeV for different categories in charge and pseudorapidity which corresponds to the average transverse momentum of muons in Z-boson decays. The second method rests upon tightly identified electrons in the $W \to e\nu$ decay [83] and uses the ratio of the electron energy E measured in the ECAL to the electron momentum p measured in the ID. This permits a charge-dependent determination of the correction factors for p_{T} values of approximately 38 GeV which corresponds to the average transverse momentum of muons in W-boson decays. The sagitta bias correction factors combine the two presented methods in different η and ϕ bins which is shown in Fig. 7.3(b). The two methods agree within their statistical uncertainties. The total combined uncertainty of this correction is mainly caused by the finite statistics of the used samples [86]. The envelope describing the final uncertainty is determined as a fully integrated effect over the pseudorapidity of the lepton. Due to the four different $|\eta|$ measurement categories, this effect has to be multiplied by a factor of two and is

uncorrelated across the muon pseudorapidity.

The outcome of the calibration procedure of the muons is shown in Fig. 7.4 which compares the invariant mass spectrum of data to simulated $Z \rightarrow \mu\mu$ events. The plot is given for the 2017 analysis and the reanalysis, respectively, to check if all muon calibrations have been implemented successfully. The data-to-prediction ratio panel indicates a similar trend over the whole invariant mass spectrum with a good description at the Z mass peak and some slight deviations at the tails. Hence, it can be assumed that all muon related corrections are applied correctly in the reanalysis measurement.

Muon selection efficiency

In the selection of W- and Z-boson events, the muons must pass a set of requirements on the reconstruction, trigger and isolation. Differences in the efficiency of these three conditions between data and simulation can affect the shape of the fitted kinematic observables. Hence, they introduce a shift in the measured properties. All systematic uncertainties related to the selection efficiency are treated as uncorrelated between the pseudorapidity categories.

The trigger and reconstruction efficiencies are expected to be constant over p_{T}^{ℓ} for muons with a transverse momentum of $p_{\mathrm{T}}^{\ell} > 15\,\mathrm{GeV}$, whereas the isolation efficiency varies versus p_{T}^{ℓ}. In addition, the muon selection inefficiency is impacted by the efficiency corrections. This affects the estimate of the $Z \rightarrow \mu\mu$ background and contributes to the $W \rightarrow \mu\nu$ selection if a muon is not passing the reconstruction and selection requirements. A systematic uncertainty is applied for these "missed" muons.

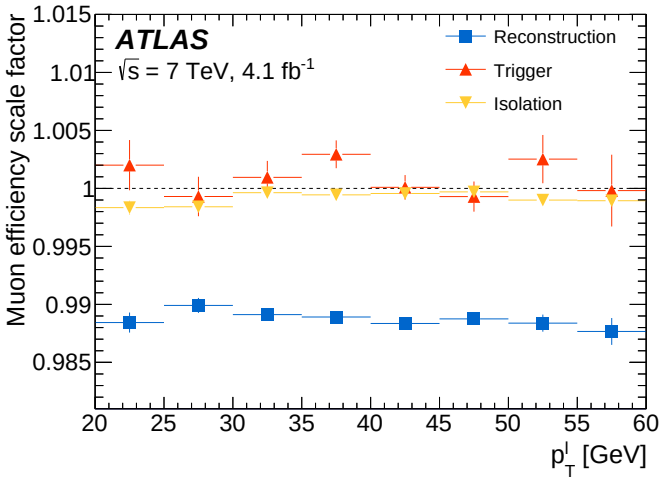

Figure 7.5: SFs for the different muon selection efficiencies as a function of the muon transverse momentum. Given are the reconstruction, trigger and isolation efficiencies received using the tag-and-probe method in $Z \rightarrow \mu\mu$ events. The error bars indicate statistical uncertainties (taken from [86]).

The correction factors of the muon efficiencies are determined between data and simulation using the tag-and-probe method in $Z \rightarrow \mu\mu$ events [87]. The SFs are calculated in different regions split in η and ϕ to account for the detector geometry. The results of the SF efficiencies are shown in Fig. 7.5 where the trigger and isolation SFs deviate on average less than 0.3 % and the reconstruction SF about 1.1 % from unity. The SF uncertainties consist of the dominant statistical uncertainty of the used

$Z \to \mu\mu$ sample and the systematic uncertainties due to the multijet background contribution and the momentum-scale uncertainty. The ID tracking efficiency is above 99.5 % for muon candidates and the corresponding uncertainty is neglected as it is below the per mille level [86]. The plausibility of the efficiency corrections is checked by comparing corrected simulated kinematic distributions to data as shown in Fig. 7.4. Further distributions of the pseudorapidity are given in Appendix E.1.

Comparison of muon systematic uncertainties

The mentioned systematic uncertainties affecting the muon momentum calibration and the muon selection efficiencies are added in quadrature for each measurement category and presented in Table 7.4.

Uncertainty category [MeV]			Muon Unc.	
Channel			Legacy	Reanalysis
m_{T}^{W}	W^-	$\lvert\eta\rvert < 0.8$	11.6	12.1
		$0.8 < \lvert\eta\rvert < 1.4$	18.5	19.7
		$1.4 < \lvert\eta\rvert < 2.0$	33.9	34.4
		$2.0 < \lvert\eta\rvert < 2.4$	123.7	124.4
	W^+	$\lvert\eta\rvert < 0.8$	12.4	11.3
		$0.8 < \lvert\eta\rvert < 1.4$	19.3	18.8
		$1.4 < \lvert\eta\rvert < 2.0$	35.1	34.2
		$2.0 < \lvert\eta\rvert < 2.4$	112.4	111.9
p_{T}^{ℓ}	W^-	$\lvert\eta\rvert < 0.8$	11.6	12.6
		$0.8 < \lvert\eta\rvert < 1.4$	18.3	18.8
		$1.4 < \lvert\eta\rvert < 2.0$	35.1	34.0
		$2.0 < \lvert\eta\rvert < 2.4$	116.1	115.3
	W^+	$\lvert\eta\rvert < 0.8$	12.2	12.6
		$0.8 < \lvert\eta\rvert < 1.4$	19.1	19.6
		$1.4 < \lvert\eta\rvert < 2.0$	33.1	32.0
		$2.0 < \lvert\eta\rvert < 2.4$	110.1	110.3

Table 7.4: Comparison of the size of the total uncertainty for the muon calibration between the 2017 analysis [86] and the reanalysis. The uncertainties are given in MeV for the two observables m_{T}^{W} and p_{T}^{ℓ} in all measurement categories for the muon decay channel. The χ^2 fits to evaluate the size of the uncertainty are performed on the combination of signal and background samples.

The uncertainties are comparable between the two observables m_{T}^{W} and p_{T}^{ℓ} and the two charges of the W-boson. However, the uncertainties increase by a factor of approximately ten when going from the low pseudorapidity region $|\eta| < 0.8$ to the one closest to the beampipe ($2.0 < |\eta| < 2.4$). Most of the systematic uncertainties of this category have a statistical origin and the region $2.0 < |\eta| < 2.4$ has the lowest statistics. Another reason for this trend is the poor resolution as only the muon kinematic properties measured by the ID are used to simplify the calibration procedure. Complications as alignment and energy loss related to the MS are avoided but this detector part provides a good resolution in the endcaps. The reference analysis and the revision consistently differ by less than 1.2 MeV, and the recreation of the muon related systematic uncertainties can be closed with success.

7.2.2 Calibration of electrons

Electrons are reconstructed by geometrically matching an energy deposit found in the ECAL to a track of the ID as outlined in Section 3.3.1.

Electron energy response

The electron energy calibration is based on the electron and photon energy calibration of ATLAS for Run-1 using $Z \to ee$ events [84]. In the initial step, detector effects are corrected for, whereas energy-scale and calorimeter energy resolution corrections are derived with the dilepton invariant mass distribution [86]. The term energy response unifies the energy scale and resolution.

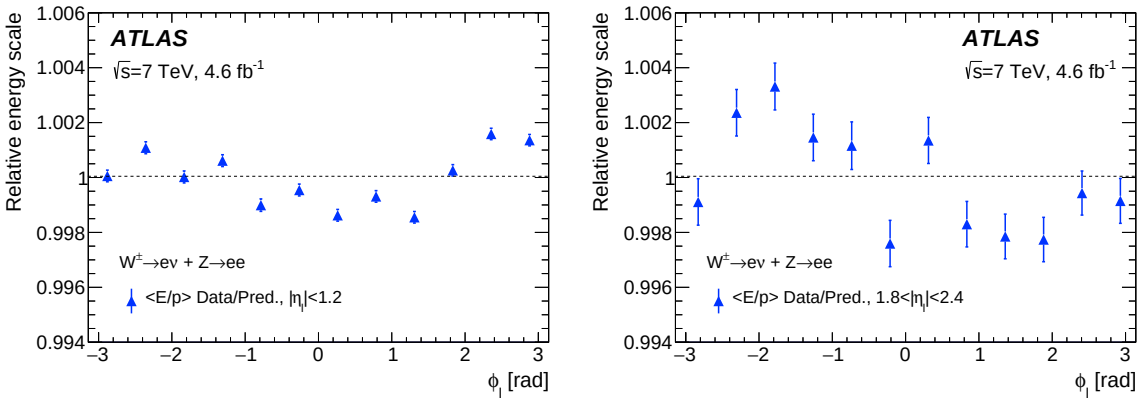

Figure 7.6: Relative data to simulation ratio of the energy-momentum ratio as a function of the azimuth for electrons. The variations are shown for W- and Z-boson events for (a) $|\eta_\ell| < 1.2$ and (b) $1.8 < |\eta_\ell| < 2.4$. Corrections of the electron energy, the momentum scale, resolution, and sagitta bias are applied. The mean of the $\langle E/p \rangle$ distribution is normalised to unity. The error bars indicate the statistical uncertainties (taken from [86]).

The corresponding uncertainties of the energy response originate from the limited statistics of the simulated $Z \to ee$ sample, the physics modelling of the resonance, and the calibration procedure. Additional sources of uncertainties arise from the extrapolation of the electron and photon energy calibration from the Z-boson calibration to a broad energy spectrum. Furthermore, uncertainties arise from the non-linearity of the energy response from Z to W-boson decays. The parametrisation of the inter-calibration of calorimeter layers and in the passive material, the calorimeter read-out calibrations, and the imperfect electronics pedestal subtraction affect the data, whereas the modelling of interactions between electrons and the detector material in `GEANT4` belongs to the simulation [86]. The corresponding uncertainties are then applied to the simulated samples.

The azimuthal dependence of the electron-energy response due to mechanical deformations in the ECAL is detected in particular in the endcaps as shown in Fig. 7.6. This deviation is corrected with the mean of the energy to momentum ratio $\langle E/p \rangle$. The belonging uncertainty is neglectable. The non-Gaussian tails in the energy response are mis-modelled when looking at the E/p distribution due to the imperfect shower reconstruction in the calorimeters. Electrons in mis-modelled regions are removed and a dedicated systematic uncertainty is assigned [86].

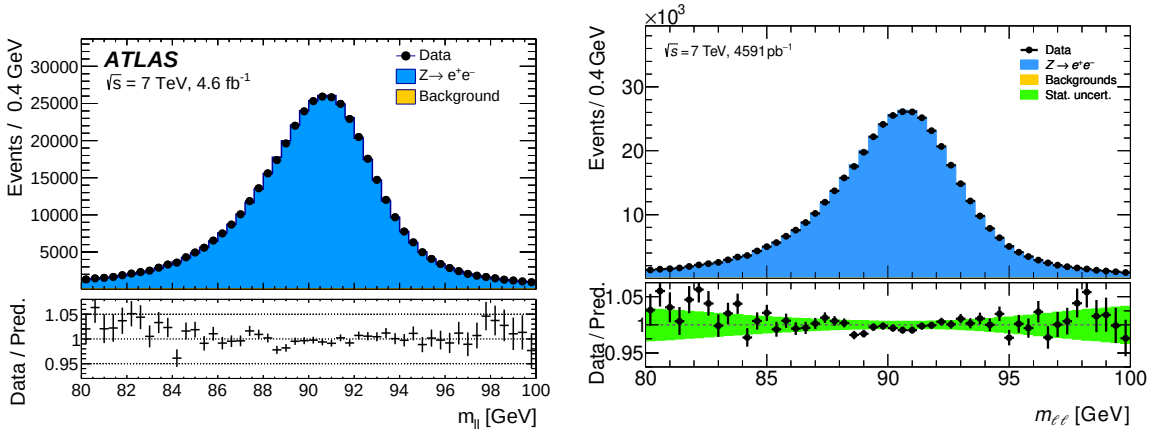

(a) (b)

Figure 7.7: Comparison of the data to simulation agreement of the invariant dielectron mass in $Z \to ee$ events between (a) the 2017 analysis (taken from [86]) and (b) the reanalysis. The corrections concerning the energy resolution and the selection efficiency are applied to the simulation, whereas the energy scale corrections are applied to the data. The lower panel shows the ratio of data to simulation where the error bars indicate the statistical uncertainty and the green band represents the uncertainty caused by the limited simulation sample size.

The uncertainties related to the mis-modelled energy tails, the response of the detector, the pedestal subtraction, the inter-calibration of the first and the second calorimeter layers, the energy resolution of the calorimeter (cf. Eq. (3.4)), and the statistical uncertainty on the Z-based absolute scale determination are considered uncorrelated across the electron pseudorapidity. The latter two are statistically dominated and similar to the muon systematic uncertainties evaluated in bins of pseudorapidity implying half the number of events compared to a binning in absolute values of pseudorapidity. Hence, the corresponding systematics have to be corrected with a factor of $1/\sqrt{2}$ to account for the used measurement categories binned in absolute values of the pseudorapidity.

The complete calibration procedure is applied to the corresponding samples and a comparison of the dielectron invariant mass in $Z \to ee$ events between data and simulation is shown in Fig. 7.7. The relation of the agreement between the reference publication and the reanalysis is presented as well. The data-to-prediction ratio in the lower panel indicates a tendency between the two with good agreement around the Z mass peak and small discrepancies in some tail bins. A perfect agreement between the two analyses would not have been expected due to the found issues in the electron channel including an issue in the electron energy calibration (cf. Section 5.2.6). Overall, the energy corrections are accurately implemented in the reanalysis.

Electron selection efficiency

Similar to muons, efficiency corrections due to the electron selection are derived with $W \to e\nu$, $Z \to ee$ and $J/\psi \to ee$ samples for the reconstruction, identification, trigger and isolation [83]. The corresponding uncertainties are at the sub per cent level between 0.1–0.3 % depending on the SF type and the detector part [86].

The LAr simple veto is part of the lepton selection first mentioned in Section 5.2.2 and is due to

a failure of several Front-End Boards. Electrons were not reconstructed in the affected parts of the detector but the trigger acceptance lost could not be simulated perfectly and a dedicated efficiency correction factor is determined to correct for the mis-modelling. The systematic uncertainty related to the charge mis-measurement of electrons plays a minor role in the selection efficiency uncertainties and is therefore neglected for the reanalysis [86].

The correct implementation of the selection efficiency calibrations is illustrated with a good data-to-simulation agreement as outlined in Fig. 7.7. Further plots of the pseudorapidity distributions can be found in Appendix E.1.

Comparison of electron systematic uncertainties

The presented electron systematic uncertainties are added in quadrature and summarised in Table 7.5. Similar to the muon related uncertainties, there is good comparability between the kinematic observables m_{T}^{W} and p_{T}^{ℓ} and the charges in the electron channel. There is a slight increase in the size of the total uncertainty when going from low to high absolute values of the lepton pseudorapidity. The consistency between the 2017 analysis and the reanalysis is acceptable with small differences for the measurement categories $|\eta| < 0.6$ and $0.6 < |\eta| < 1.2$ but discrepancies of up to 2.7 MeV for $1.8 < |\eta| < 2.4$. However, the systematic uncertainties related to the electron calibration are well reproduced.

Uncertainty category [MeV]			Elec Unc.	
Channel			Legacy	Reanalysis
m_{T}^{W}	W^-	$\lvert\eta\rvert < 0.6$	16.4	17.4
		$0.6 < \lvert\eta\rvert < 1.2$	18.7	19.5
		$1.8 < \lvert\eta\rvert < 2.4$	33.2	30.8
	W^+	$\lvert\eta\rvert < 0.6$	19.5	18.9
		$0.6 < \lvert\eta\rvert < 1.2$	21.4	21.5
		$1.8 < \lvert\eta\rvert < 2.4$	26.6	29.3
p_{T}^{ℓ}	W^-	$\lvert\eta\rvert < 0.6$	19.8	19.8
		$0.6 < \lvert\eta\rvert < 1.2$	19.7	21.3
		$1.8 < \lvert\eta\rvert < 2.4$	30.7	33.1
	W^+	$\lvert\eta\rvert < 0.6$	20.1	21.8
		$0.6 < \lvert\eta\rvert < 1.2$	21.4	22.2
		$1.8 < \lvert\eta\rvert < 2.4$	30.8	33.5

Table 7.5: Comparison of the size of the total uncertainty for the electron calibration between the 2017 analysis [86] and the reanalysis. The uncertainties are given in MeV for the two observables m_{T}^{W} and p_{T}^{ℓ} in all measurement categories for the electron decay channel. The χ^2 fits to evaluate the size of the uncertainty are performed on the combination of signal and background samples.

7.3 Calibration of the recoil

The reconstruction of the recoil u_{T} is outlined in Section 3.3.5. The recoil itself is not fitted directly to determine the properties of the W-boson but affects the distribution of the transverse mass of the W-boson directly and the transverse lepton momentum in addition through the event selection.

7.3.1 Event activity corrections

The mis-modelling of the event activity is corrected in the simulated samples separately for W- and Z-boson events. The average pile-up $\langle\mu\rangle$ deteriorates the resolution of the recoil. Uncertainties in the cross-section and in the inelastic collisions cause differences between data and simulation in the pile-up distribution which are corrected [86].

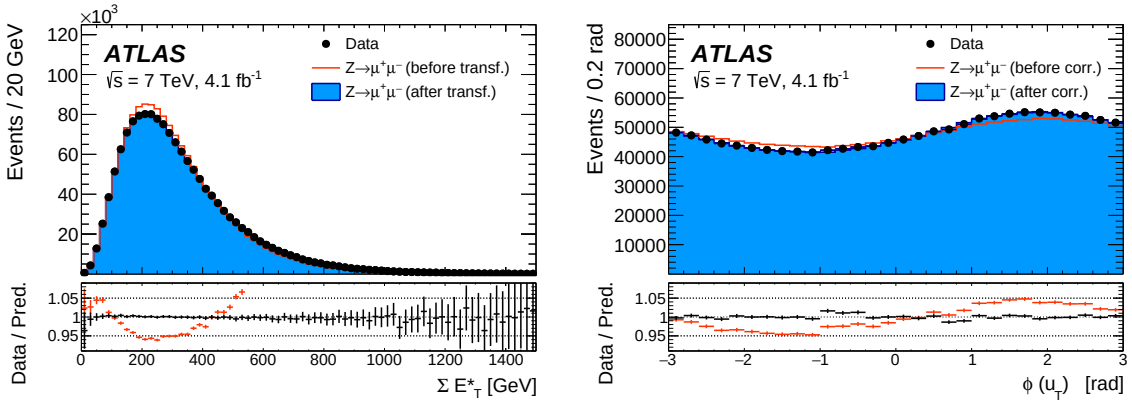

(a) $\Sigma E_{\mathrm{T}}^{*}$ (b) $\phi\left(u_{\mathrm{T}}\right)$

Figure 7.8: Distributions visualising the effect of the recoil calibration in $Z \rightarrow \mu\mu$ events. Shown are (a) the $\Sigma E_{\mathrm{T}}^{*}$ distribution before and after the Smirnov transformation and (b) the azimuth $\phi\left(u_{\mathrm{T}}\right)$ distribution before and after the $u_{x,y}$ correction. The error bars on the data-to-prediction ratio in the lower panel indicate the statistical uncertainties (taken from [86]).

The remaining differences are due to the mis-modelling of other processes involved in the primary interaction. The distribution of the transverse energy corrected by the magnitude of the recoil, the $\Sigma E_{\mathrm{T}}^{*}$ distribution

$$\Sigma E_{\mathrm{T}}^{*} = E_{\mathrm{T}} - |\vec{u}_{\mathrm{T}}|,$$

is sensitive to such mis-modelling and the residual effects are corrected by a Smirnov transformation [176] to match the distribution between data and simulation. The differences in the $\Sigma E_{\mathrm{T}}^{*}$ distribution depend on $p_{\mathrm{T}}^{\ell\ell}$ of the Z-boson which is why the correction factors are computed for different boson transverse momentum bins. The results of applying the Smirnov transformation are shown in Fig. 7.8(a) where the correction significantly improves the agreement between data and simulation. The transverse momentum of the W-boson can only be deduced from the recoil momentum which suffers from a worse resolution compared to the one of $p_{\mathrm{T}}^{\ell\ell}$. Hence, it is assumed that the p_{T} dependent differences in the $\Sigma E_{\mathrm{T}}^{*}$ distribution in W-boson events follow the corresponding differences in Z-boson events. Subsequently, the correction derived on the $p_{\mathrm{T}}^{\ell\ell}$ of Z-boson events is directly applied to the transverse momentum p_{T}^{W} of the W-boson [86].

7.3.2 Residual response corrections

The transverse momentum distribution of vector bosons is biased in the ϕ direction caused by a difference between the IP and the centre of the detector, a non-zero crossing angle of the colliding proton beams and imperfections in the calorimeter response. Therefore, the components of the

transverse momentum, u_x and u_y, are corrected for the difference between data and simulation using Z-boson events [86]. The corrected simulation describes much better the data as it is shown for the ϕ distribution of the recoil in Fig. 7.8(b).

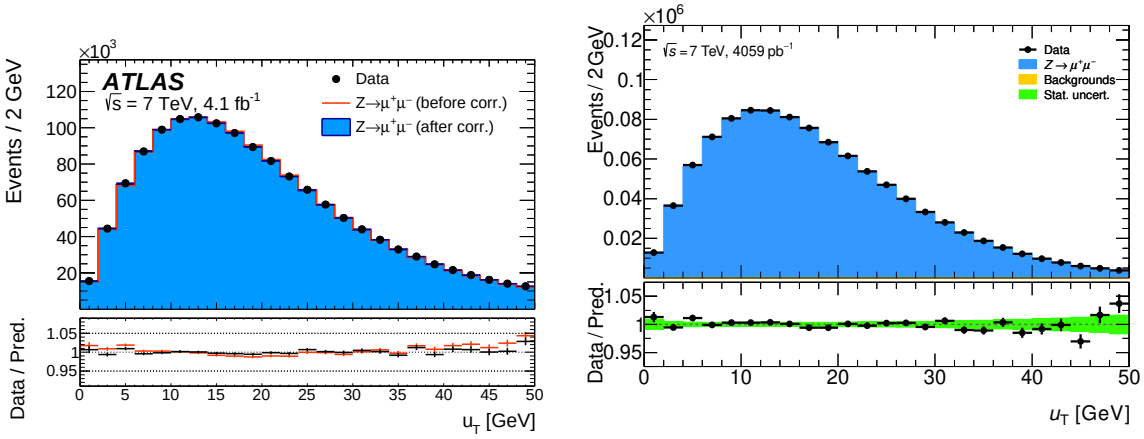

(a) (b)

Figure 7.9: Comparison of the data to simulation agreement of the u_T distribution in $Z \to \mu\mu$ events between (a) the 2017 analysis before and after applying all corrections (taken from [86]) and (b) the reanalysis including all recoil corrections. The lower panel shows the ratio of data to simulation where the error bars indicate the statistical uncertainty and the green band represents the uncertainty caused by the limited simulation sample size.

The recoil energy scale and resolution are corrected in bins of ΣE_T^* and $p_T^{\ell\ell}$ based on Z-boson events at the reconstruction level. The energy scale correction removes the difference in $u_{\parallel}^Z + p_T^{\ell\ell}$ between data and simulation, whereas the resolution correction removes any deviations based on the $u_{\perp}^Z$ distribution. The derived correction functions are applied to $u_{\perp}$ and $u_{\parallel}$ of the vector bosons while taking into account the transverse momentum of the W- and Z-boson at the particle level. The recoil calibration leads to a decent agreement between data and simulation as shown for the u_T distribution in $Z \to \mu\mu$ events in Fig. 7.9. A comparison to the uncalibrated u_T distribution is shown only for the 2017 analysis in Fig. 7.8(a). Again, the resurrection of the recoil calibrations leads to a good agreement between the reference publication and the reanalysis, in particular, visible in the data-to-prediction ratio panel. Other recoil distributions for $Z \to \mu\mu$ and $Z \to ee$ are given in Appendix E.2. The calculated corrections were cross-checked with the alternative MC generator `Powheg+Herwig` leading to similar results in the 2017 analysis [86].

7.3.3 Systematic uncertainties on the recoil

Every step of the recoil calibration is potentially a source of uncertainty. Starting with the correction of the pile-up, the SF is varied within its uncertainty and the recoil calibration procedure is repeated. This uncertainty plays a minor role in the recoil uncertainty category as found out in the 2017 analysis and is therefore neglected for the reanalysis. The uncertainty on the Smirnov transformation is evaluated by comparing the ΣE_T^* correction on the transverse momentum of the W-boson to a p_T-inclusive correction [86]. The systematic uncertainty covers the maximal difference in the p_T dependence between W- and Z-boson events. Fractions of this uncertainty are taken as a residual difference and are

determined separately for the two charges to be 0.62 for W^+ and 0.5 for W^-. The produced systematic envelopes are multiplied with the corresponding factor [177].

The corrections on the recoil energy scale and resolution are applied by extrapolation from Z- to W-boson events. The correction functions are varied by 6 % to determine the systematic uncertainty related to the $Z \rightarrow W$ extrapolation which corresponds to the size of the residual resolution correction explaining observed differences in the $u_\perp$ distribution between W- and Z-boson events. An additional uncertainty in this correction procedure is the statistical uncertainty of the correction factors. Finally, the binned correction is compared to a smooth interpolation between the bins and assigned as an additional systematic uncertainty [86].

Uncertainty category [MeV]			Recoil	
Channel			Legacy	Reanalysis
m_{T}^{W}	W^-	$\lvert\eta\rvert < 0.6$	11.8	12.1
		$0.6 < \lvert\eta\rvert < 1.2$	11.2	12.8
		$1.8 < \lvert\eta\rvert < 2.4$	12.8	11.8
	W^+	$\lvert\eta\rvert < 0.6$	13.1	16.7
		$0.6 < \lvert\eta\rvert < 1.2$	15.1	19.1
		$1.8 < \lvert\eta\rvert < 2.4$	16.4	18.9
p_{T}^{ℓ}	W^-	$\lvert\eta\rvert < 0.6$	2.6	2.1
		$0.6 < \lvert\eta\rvert < 1.2$	2.7	2.9
		$1.8 < \lvert\eta\rvert < 2.4$	2.7	3.3
	W^+	$\lvert\eta\rvert < 0.6$	2.6	1.8
		$0.6 < \lvert\eta\rvert < 1.2$	2.7	2.1
		$1.8 < \lvert\eta\rvert < 2.4$	2.7	2.6

(a) Electron channel.

Uncertainty category [MeV]			Recoil	
Channel			Legacy	Reanalysis
m_{T}^{W}	W^-	$\lvert\eta\rvert < 0.8$	13.1	13.5
		$0.8 < \lvert\eta\rvert < 1.4$	12.2	12.7
		$1.4 < \lvert\eta\rvert < 2.0$	10.5	12.0
		$2.0 < \lvert\eta\rvert < 2.4$	11.6	14.1
	W^+	$\lvert\eta\rvert < 0.8$	15.2	19.5
		$0.8 < \lvert\eta\rvert < 1.4$	13.0	17.1
		$1.4 < \lvert\eta\rvert < 2.0$	14.3	17.7
		$2.0 < \lvert\eta\rvert < 2.4$	14.4	17.0
p_{T}^{ℓ}	W^-	$\lvert\eta\rvert < 0.8$	2.6	2.0
		$0.8 < \lvert\eta\rvert < 1.4$	2.5	4.1
		$1.4 < \lvert\eta\rvert < 2.0$	2.6	3.9
		$2.0 < \lvert\eta\rvert < 2.4$	2.6	2.3
	W^+	$\lvert\eta\rvert < 0.8$	2.6	2.1
		$0.8 < \lvert\eta\rvert < 1.4$	2.5	2.7
		$1.4 < \lvert\eta\rvert < 2.0$	2.5	2.1
		$2.0 < \lvert\eta\rvert < 2.4$	2.5	3.0

(b) Muon channel.

Table 7.6: Comparison of the size of the total uncertainty for the recoil category between the 2017 analysis [86] and the reanalysis. The uncertainties are given in MeV for the two observables m_{T}^{W} and p_{T}^{ℓ} in all measurement categories for both leptonic decay channels. The χ^2 fits to evaluate the size of the uncertainty are performed on the combination of signal and background samples.

The systematic uncertainties related to the calibration procedure of the recoil are again added in quadrature and shown in Table 7.6. Overall, the observable m_{T}^{W} is directly affected by the recoil and the total uncertainties are higher than for p_{T}^{ℓ} where the uncertainties only enter through the event selection. There is a good consistency in the size of uncertainty between the 2017 analysis and the reanalysis for m_{T}^{W} with bigger differences for W^+ of more than 4 MeV which is caused by the $\Sigma E_{\mathrm{T}}^{*}$ correction. In addition, the $\Sigma E_{\mathrm{T}}^{*}$ correction is responsible for the constantly higher uncertainty in m_{T}^{W} for the positively charged leptons compared to negatively charged leptons. The difference for p_{T}^{ℓ} is often less than 1 MeV with some bigger differences in the muon channel of up to 1.6 MeV. This can be explained by an issue found concerning the initial seed of the recoil calibration which was not properly set in the reference publication but fixed for the reanalysis. However, this uncertainty category is considered closed.

7.4 Cross check tests with Z-boson events

Dilepton events originating from Z-boson decays are used not only to determine calibrations but to check their correctness in kinematic distributions. A Z-boson candidate event selection is set up similar to the one for W-bosons as mentioned in Section 5.2.5. In addition to the aforementioned cuts, a requirement on the transverse momentum of the dilepton system is demanded to $p_{\mathrm{T}}^{\ell\ell} < 30\,\mathrm{GeV}$.

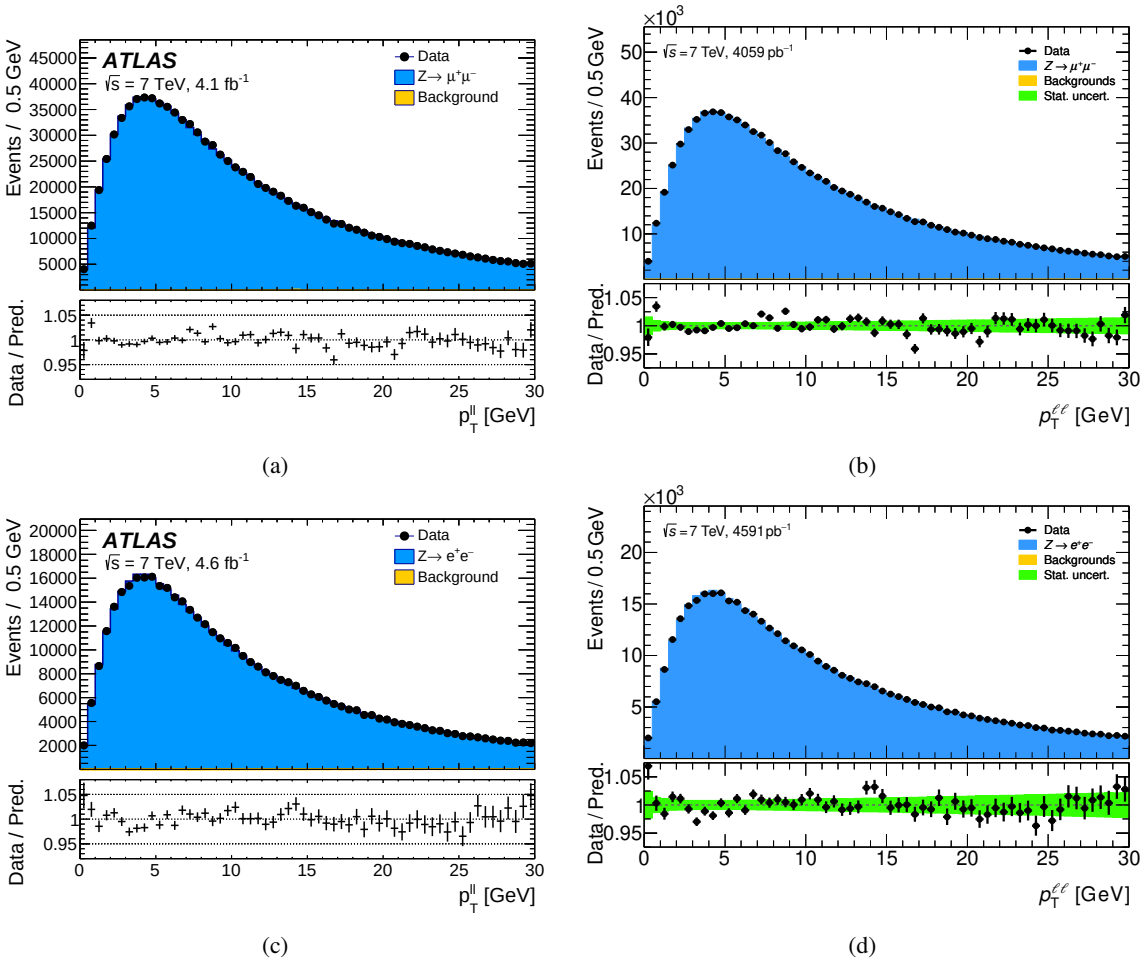

Figure 7.10: Comparison of the data to simulation agreement of the $p_{\mathrm{T}}^{\ell\ell}$ distributions from Z-boson events between the 2017 analysis (a,c) (taken from [86]) and the reanalysis (b,d). Shown are $Z \to \mu\mu$ events (a,b) and $Z \to ee$ events (c,d). The physics-modelling corrections and detector calibrations are applied to the simulation. The lower panel illustrates the data-to-prediction ratio with the error bars indicating the statistical uncertainties and the green band represents the uncertainty caused by the limited simulation sample size.

The fundamental difference between a W- and Z-boson decay is, besides the mass of the mother particle, the neutrino in the final state of the W-boson. The presence of a neutrino allows it to define kinematic quantities like $E_{\mathrm{T}}^{\mathrm{miss}}$ and the transverse mass of the boson m_{T}. To overcome this difference in Z-boson decays, one of the leptons is considered as the neutrino to define the mentioned properties. This method is repeated per Z-boson event by removing the positively and the negatively charged

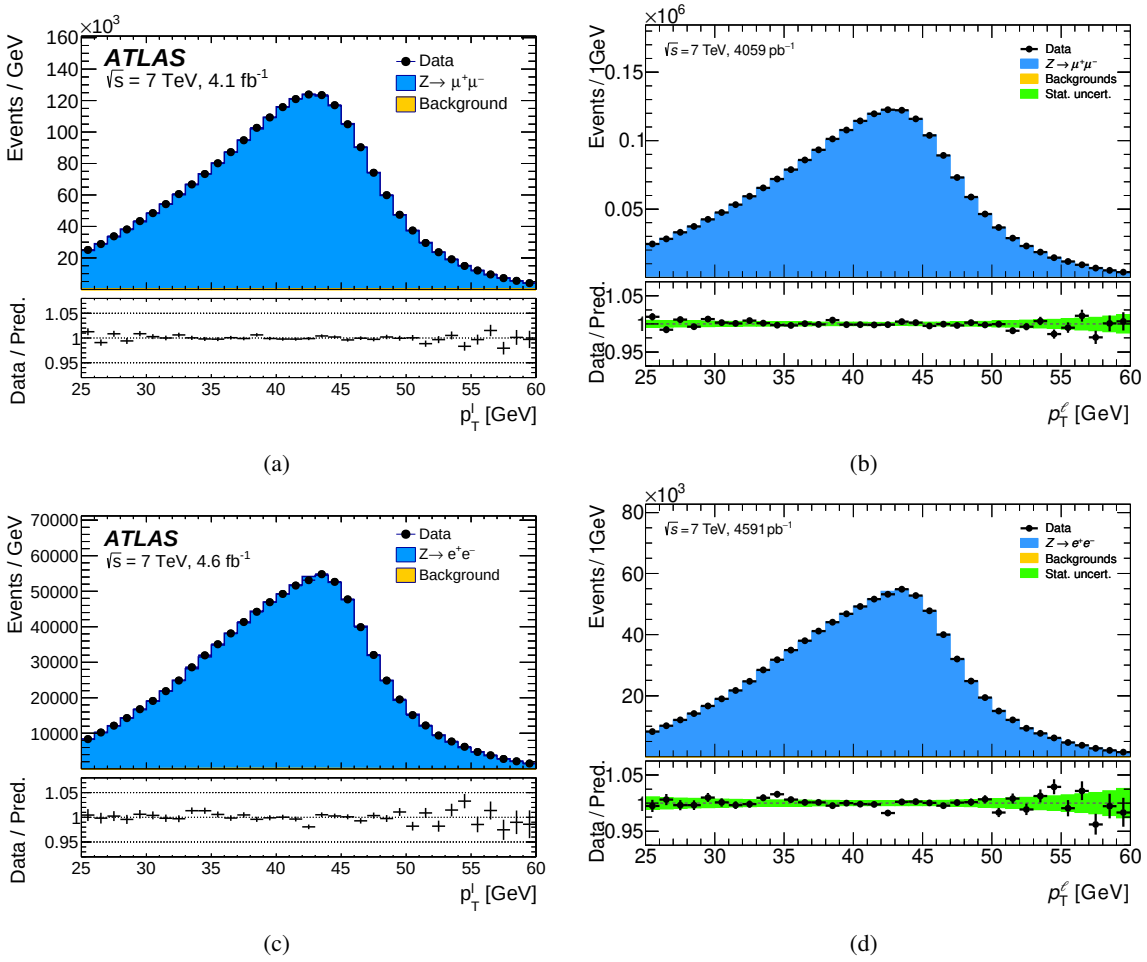

Figure 7.11: Comparison of the data to simulation agreement of the p_{T}^{ℓ} distributions illustrating the transverse momentum of both decayed leptons from Z-boson events between the 2017 analysis (a,c) (taken from [86]) and the reanalysis (b,d). Shown are $Z \to \mu\mu$ events (a,b) and $Z \to ee$ events (c,d). The physics-modelling corrections and detector calibrations are applied to the simulation. The lower panel illustrates the data-to-prediction ratio with the error bars indicating the statistical uncertainties and the green band represents the uncertainty caused by the limited simulation sample size.

lepton one by one [86].

The background contributions from EW contributions and top-quark processes are evaluated using the MC samples discussed in Section 3.4.1. The backgrounds are normalised to the corresponding cross-section. They contribute around 0.1 % to both decay channels. The multijet background was found to be negligible in the 2017 publication [86]. The contribution was checked with $b\bar{b}$ and $c\bar{c}$ MC samples in the muon channel and a data-driven estimate in the electron channel similarly to the multijet background estimation for the W-boson candidate selection (cf. Section 5.3).

The $p_{\mathrm{T}}^{\ell\ell}$ distribution shown in Fig. 7.10 proves the correctness of the applied calibration in Z-boson events. It is insensitive to m_Z as the observable reflects the transverse momentum of the boson. The Z-boson decays at rest at LO and the distribution is smeared by ISR, FSR and the detector resolution (cf.

the considerations to the origin of the Jacobian peak in Section 4.2). In contrast, the p_{T}^{ℓ} distributions illustrated in Fig. 7.11 are sensitive to the Z-boson mass similar to the observable p_{T}^{ℓ} of the decayed charged lepton in the W-boson decay (cf. Section 4.2). The agreement between data and simulation is at the per cent level for the transverse momentum distributions of the dilepton system and the single lepton. Furthermore, Figs. 7.10 and 7.11 compare the agreement between the 2017 analysis and the reanalysis. The lower panel shows a similar trend of the data-to-prediction ratio with a slightly better agreement for $Z \to \mu\mu$ events compared to $Z \to ee$ events. Further cross-check distributions of Z-boson events can be found in Appendix E.3. The reference publication performed a template χ^2 fit of the Z-boson mass in different measurement categories in the kinematic observables $m_{\ell\ell}$, p_{T}^{ℓ} and m_{T}. This proves the consistency of the applied calibrations and corrections [86] but is not repeated for this measurement.

7.5 Uncertainties of background processes

The physics of the signal and background processes is discussed in Section 5.1. The used cross-section values and the corresponding uncertainties are elucidated there. The multijet background is estimated with a data-driven technique and the uncertainties of the fraction fit are outlined in Section 5.3. The shape extrapolation which is different to the reference analysis is followed by a new uncertainty estimation of the multijet background shape extrapolation for this thesis. Both types of uncertainties belonging to the multijet background, the fraction and the shape in the SR, are determined individually for the two lepton channels, the different charges and the pseudorapidity regions. Hence, these uncertainties are considered uncorrelated across all measurement categories.

7.5.1 Uncertainty of the multijet background shape extrapolation

In the 2017 analysis, the uncertainty was evaluated using the toy MC method. Therefore, the bin contents of the histograms of the CR1 and the CR2 were changed within their statistical uncertainties. The fit of the transfer function (cf. Eq. (5.2)) was repeated on the ratio histogram of CR2 divided by CR1. The result was injected as the shape of the multijet background and the W-boson mass fit repeated. This procedure was rerun 500 times and the spread of the resulting m_W distribution was taken as the uncertainty of the shape extrapolation method.

For the reanalysis, the uncertainty is based on the eigenvector decomposition of the covariance matrix of the transfer function fit result. The three free parameters in the fit eventuate in three eigenvectors. Each of them corresponds to a different systematic uncertainty. The first systematic uncertainty is based on the first eigenvector and so forth. The systematic of eigenvector i is a variation of all three free parameters of the transfer function following

$$a_{n,i}^{\text{up, down}} = a_n \pm \sqrt{\lambda_i} v_{n,i},$$

where n is the index of the free parameter and $v_{n,i}$ represents the eigenvector value of parameter n for eigenvector i. The eigenvector value is subtracted to build the down variation or added in case of the up variation. The multiplication of the eigenvector value with the square root of the corresponding eigenvalue λ_i is necessary to correctly normalise. The three envelopes for positively charged muons and the distribution p_{T}^{ℓ} are shown in Fig. 7.12.

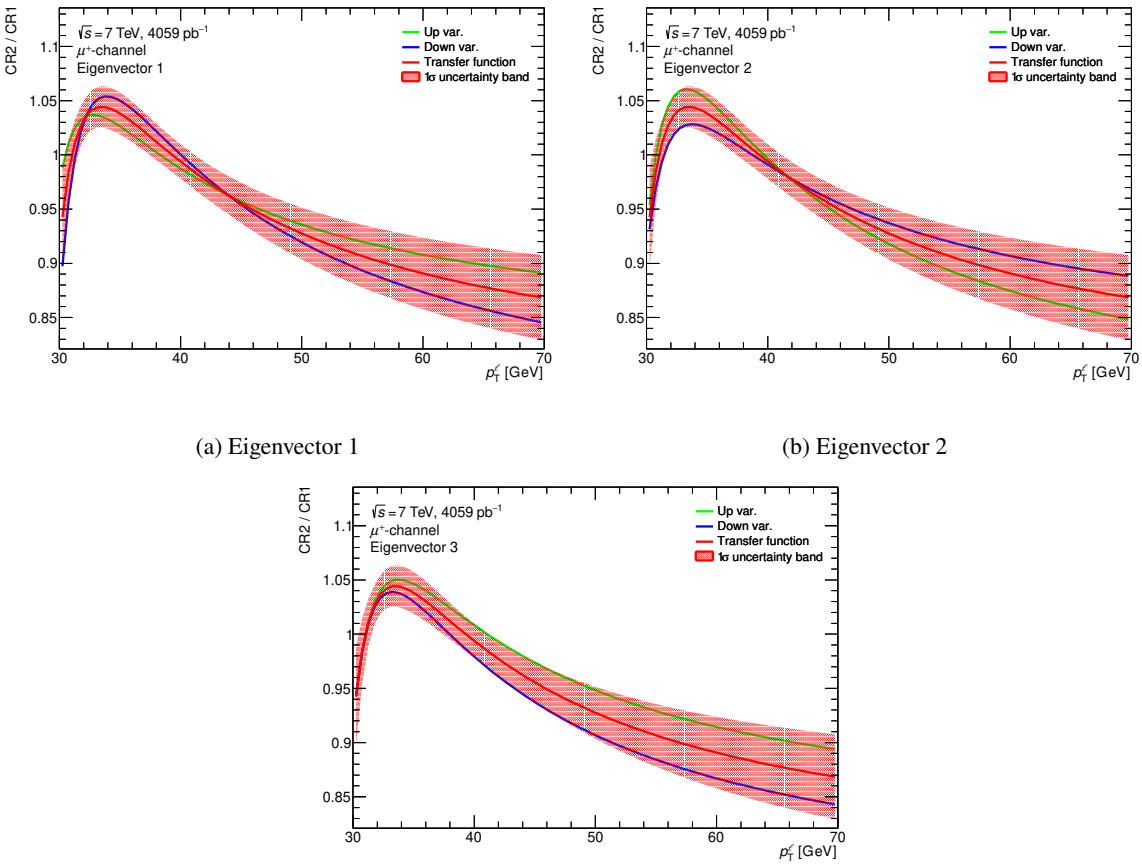

(a) Eigenvector 1

(b) Eigenvector 2

(c) Eigenvector 3

Figure 7.12: Illustration of three exemplary eigenvector envelopes describing the uncertainty of the multijet background shape extrapolation. Shown is the ratio of the bin contents of CR1 divided by CR2 versus p_{T}^{ℓ} of positively charged muons. The green and blue lines represent the up and down variations of the extrapolation method, respectively, the red line represents the transfer function, and the red band represents the 1 σ uncertainty band of the transfer function.

The new method to evaluate the uncertainty on the shape extrapolation has the advantage that the resulting envelopes can be used in both fit methods, the χ^2 fit and the PLH fit. The 500 toys would have been converted into envelopes to be suited for the PLH fit. Hence, the toy MC method is not repeated. Instead, the new envelopes are used to provide the impact on the mass measurement and to compare the size of the systematic uncertainty with the 2017 analysis.

7.5.2 Comparison of background systematic uncertainties

The impact on the W-boson mass fits by the uncertainties related to the simulated samples and the multijet background fit method are evaluated and added in quadrature. They are compared to the ones of the 2017 analysis in Table 7.7. Compared to the other uncertainty categories, this is the one with the largest differences between the reference analysis and the reanalysis visible across both lepton channels,

Uncertainty category [MeV]			Bkg unc.	
Channel			Legacy	Reanalysis
m_{T}^{W}	W^-	$\lvert\eta\rvert < 0.6$	15.5	8.4
		$0.6 < \lvert\eta\rvert < 1.2$	12.8	10.6
		$1.8 < \lvert\eta\rvert < 2.4$	35.1	23.1
	W^+	$\lvert\eta\rvert < 0.6$	15.3	8.5
		$0.6 < \lvert\eta\rvert < 1.2$	13.2	9.8
		$1.8 < \lvert\eta\rvert < 2.4$	32.8	21.3
p_{T}^{ℓ}	W^-	$\lvert\eta\rvert < 0.6$	7.2	5.4
		$0.6 < \lvert\eta\rvert < 1.2$	7.3	7.0
		$1.8 < \lvert\eta\rvert < 2.4$	11.5	8.9
	W^+	$\lvert\eta\rvert < 0.6$	6.4	5.1
		$0.6 < \lvert\eta\rvert < 1.2$	6.7	5.3
		$1.8 < \lvert\eta\rvert < 2.4$	11.9	7.0

(a) Electron channel.

Uncertainty category [MeV]			Bkg unc.	
Channel			Legacy	Reanalysis
m_{T}^{W}	W^-	$\lvert\eta\rvert < 0.8$	8.5	8.2
		$0.8 < \lvert\eta\rvert < 1.4$	7.7	6.1
		$1.4 < \lvert\eta\rvert < 2.0$	8.1	7.0
		$2.0 < \lvert\eta\rvert < 2.4$	10.2	18.2
	W^+	$\lvert\eta\rvert < 0.8$	8.1	8.2
		$0.8 < \lvert\eta\rvert < 1.4$	6.8	4.5
		$1.4 < \lvert\eta\rvert < 2.0$	7.2	5.9
		$2.0 < \lvert\eta\rvert < 2.4$	9.0	12.0
p_{T}^{ℓ}	W^-	$\lvert\eta\rvert < 0.8$	5.8	4.9
		$0.8 < \lvert\eta\rvert < 1.4$	5.6	3.2
		$1.4 < \lvert\eta\rvert < 2.0$	5.6	5.4
		$2.0 < \lvert\eta\rvert < 2.4$	7.6	15.9
	W^+	$\lvert\eta\rvert < 0.8$	5.1	4.3
		$0.8 < \lvert\eta\rvert < 1.4$	4.7	2.6
		$1.4 < \lvert\eta\rvert < 2.0$	4.9	4.5
		$2.0 < \lvert\eta\rvert < 2.4$	6.4	9.7

(b) Muon channel.

Table 7.7: Comparison of the size of the total uncertainty for the background category between the 2017 analysis [86] and the reanalysis. The uncertainties are given in MeV for the two observables m_{T}^{W} and p_{T}^{ℓ} in all measurement categories for both leptonic decay channels. The χ^2 fits to evaluate the size of the uncertainty are performed on the combination of signal and background samples.

both observables and all other measurement categories. The uncertainties on the cross-section for the simulated samples did not change, whereas the uncertainty on the fractions of the multijet background differs little between the 2017 analysis and the reanalysis. The main discrepancy is due to the new estimate of the multijet background shape extrapolation uncertainties which are more accurate and smaller than for the old method. This explains the smaller uncertainties for the reanalysis which can be found in all measurement categories except for the last pseudorapidity bin $2.0 < |\eta| < 2.4$ in the muon channel. This higher uncertainty is mainly caused by the cross-section uncertainty on the $Z \to \mu\mu$ processes which is evaluated separately for the pseudorapidity regions in contrast to the inclusive determination of the 2017 analysis. The fraction of $Z \to \mu\mu$ background processes on the total yield increases with higer values of η_ℓ because the muon reconstruction efficiency drops at high pseudorapidity values (cf. Fig. 3.8(b)) and it is therefore more likely that one of the two muons in the Z-boson decay is missed in the detector. The size of the total uncertainties approximates between the two lepton channels as the electron channel is suffering more from multijet background contamination and hence profiting more from the better uncertainty estimate. Despite the explained variations, the total uncertainty size for the reanalysis is in the same order as for the 2017 analysis and the uncertainty category is considered successfully closed.

7.6 Principal component analysis

Some systematic uncertainties are only available in the format of toy systematics (cf. Section 6.1.2). The creation of the toy pseudodata sets for the studied systematics is outlined in Sections 7.1 to 7.3.

An underlying distribution describing the systematic effect was used to generate a number of toys fluctuating in the given variation. The toy systematics are then fitted in the χ^2 fit and the size of the uncertainty is determined by the width of all fit results. This approach is not suitable for the PLH fit as only one- or two-sided envelope systematics can be handled. Unfortunately, the distributions characterising the systematic effect are not available anymore. Hence, methods of linear algebra have to be used to express the concerned systematic uncertainties by uncorrelated variables. With the help of an orthogonal matrix, a rotation of the original pattern space into a new set of uncorrelated coordinate vectors is accomplished. The theory of this section is based on [178, 179].

By means of a Principal Component Analysis (PCA) [180, 181], all toys are linearly transformed to the original variables. The entirety of the correlated toy space is described by n individual toys having p components $x_1, \ldots, x_p$ each. The $n \times p$ matrix $\mathbf{X}$ characterises the toy matrix where the j^{th} column represents the bin contents of toy j with the vector $\mathbf{x}_j$. The PCA seeks for a linear combination of the columns of the matrix $\mathbf{X}$ to transform it into a new set of uncorrelated coordinate vectors

$$\mathbf{z} = \mathbf{A}'\mathbf{x}, \tag{7.3}$$

where the j^{th} element of $\mathbf{z}$, z_j, serves as the j^{th} principal component. The orthogonal matrix $\mathbf{A}$[3] plays a key role in this concept as the j^{th} column, α_j, is the j^{th} eigenvector of the covariance matrix $\mathbf{\Sigma}$ of $\mathbf{X}$. In this measurement, the covariance matrix is unknown and replaced by the sample covariance matrix $\mathbf{S}$. The j^{th} principal component can be expressed as

$$z_j = \alpha_j'\mathbf{x},$$

and connects via the relation

$$\text{var}\left(z_j\right) = \lambda_j$$

the j^{th} eigenvector $\alpha_\mathbf{j}$ of unit length with the j^{th} largest eigenvalue λ_j, where var $\left(z_j\right)$ is the variance of z_j. The methods of deriving the results can be read up in the cited literature.

The scikit-learn package is used to perform the PCA [182]. In order to prove the concept and find the correct normalisation of the eigenvectors, a toy example has been implemented and is described in detail in Appendix E.4.1. The number of components is always set to be higher than the number of bins of the analysed histogram to allow the PCA to close. The relative deviation of the systematic toys with respect to the nominal distribution serves as an input for the PCA. If the sum of the eigenvalues starting with the highest eigenvalue and adding subsequently decreasing eigenvalues is greater than 99 % of the sum of all eigenvalues, the termination criterion is reached and only those eigenvectors are considered.

A figure of merit is defined in a way to prove the integrity of the PCA. Therefore, the root-mean-square (RMS) of the correlated toys and the uncorrelated PCA eigenvectors is compared

$$x_{\text{RMS}}^{\text{correlated}} = \sqrt{\frac{1}{N}\sum_i^N \left(\frac{x_i - x_{\text{nom}}}{x_{\text{nom}}}\right)}, \qquad x_{\text{RMS}}^{\text{uncorrelated}} = \sqrt{\sum_i^N \left(\frac{x_i - x_{\text{nom}}}{x_{\text{nom}}}\right)}. \tag{7.4}$$

In the case of toy systematics, the correlated definition of the RMS of Eq. (7.4) is taken by summing

[3] In Eq. (7.3), $\mathbf{A}'$ denotes the transpose of $\mathbf{A}$

over all toys while the uncorrelated definition of the RMS is used for all eigenvectors of the PCA included by the termination criterion.

Systematic uncertainty	p_{T}^{ℓ}	m_{T}^{W}
A_i	2	1
Electron ID SF	12	8
Electron Isolation SF	12	8
Electron Reconstruction SF	12	7
Electron Trigger SF	12	8
Muon Isolation SF	[35, 34, 34, 34]	[35, 34, 34, 33]
Muon Reconstruction SF	[36, 36, 36, 36]	[36, 36, 35, 36]
Muon Trigger SF	[37, 37, 36, 36]	[36, 36, 36, 36]
Recoil Z statistics	17	57

Table 7.8: Number of considered eigenvectors for toy systematic uncertainties given for the observable p_{T}^{ℓ} and m_{T}^{W}. The eigenvectors of the muon SF toys are calculated separately for the four η_{ℓ} bins of the muon channel.

The number for found eigenvectors of every systematic uncertainty transformed by the PCA is shown in Table 7.8. The eigenvectors of the A_i and the recoil Z statistics uncertainties are evaluated inclusively for both channels, $W \to e\nu$ and $W \to \mu\nu$, both charges and all η_{ℓ} bins allowing to correlate the eigenvectors in the fit. The electron SF toys are correlated across the three η_{ℓ} bins by concatenating the histograms of the different η_{ℓ} categories. This type of uncertainty was determined in 5 GeV wide bins for the p_{T}^{ℓ} distribution. As the considered range for p_{T}^{ℓ} is between 30–50 GeV, four of these 5 GeV wide bins imply in total twelve bins for all η_{ℓ} categories. This is exactly the number of eigenvectors that was found for the electron SF toys illustrating again the reasonableness of the PCA. The muon SF toys are evaluated separately for the four η_{ℓ} categories of the muon channel, but inclusively in both charges explaining the occurrence of four different numbers of eigenvectors for both observables.

Some exemplary figures of merit demonstrating the closure of the PCA are shown in Fig. 7.13. The plots show a good description of the toys by the eigenvectors of the PCA. The ratio of the RMS of the two deviates by just a few per cent. Additionally, the eigenvectors of the PCA show a much smoother behaviour than the toys having some spikes in the distribution of the RMS over the observable p_{T}^{ℓ}. The 5 GeV structure which is visible for the electron isolation SF systematic can be explained by the trigger architecture making it necessary to evaluate the SF in these 5 GeV bins. All figures of merit for all PCAs carried out can be found in Appendix E.4.2. For the mentioned systematic uncertainties, the methods presented in Sections 7.1 to 7.3 explain the production of toy pseudodata sets, whereas the demonstrated PCA transforms them into envelopes which can be used in a PLH fit.

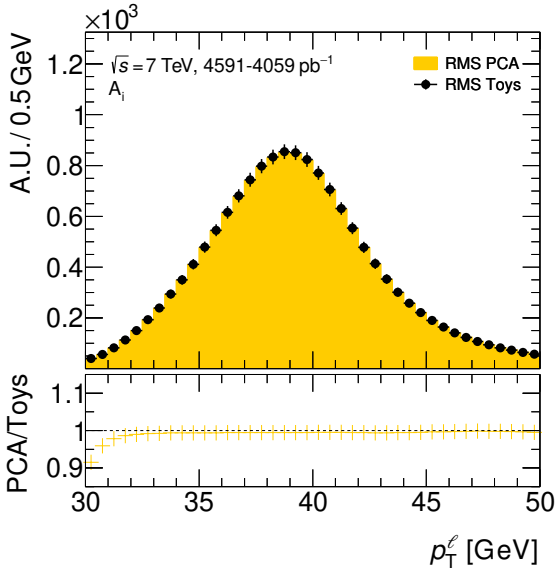

(a) A_i systematic

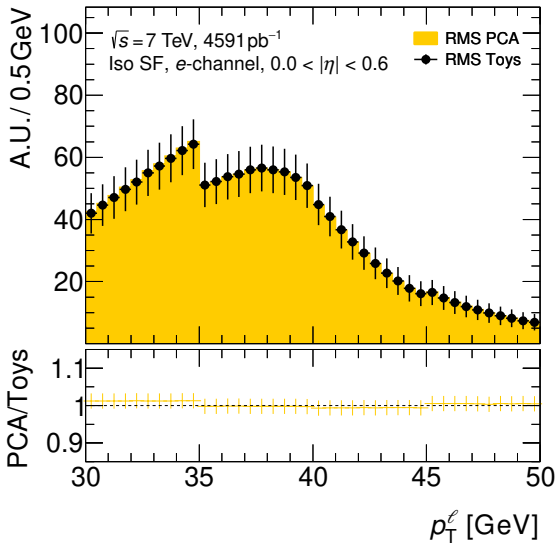

(b) Electron SF systematic

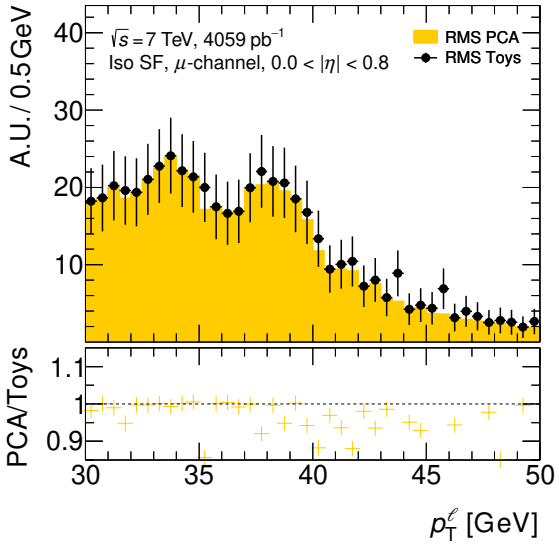

(c) Muon SF systematic

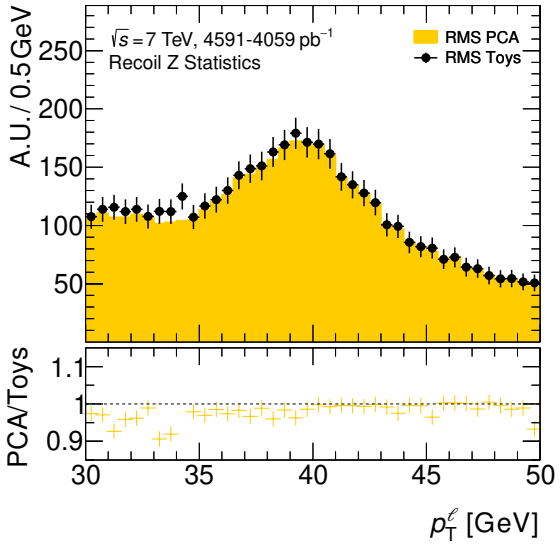

(d) Recoil Z statistics systematic

Figure 7.13: Figure of merits demonstrating the closure of the four major PCA categories. Shown is the RMS for toys (black points) compared to the RMS of the PCA eigenvectors (orange) for (a) the A_i systematic, (b) the electron isolation SF, (c) the muon isolation SF, and (d) the Recoil Z statistics systematic.

CHAPTER 8

The fit results

The topics presented above are the groundwork for the final fit results: they rely on the data and the simulated samples passing the event selection, and the data-driven multijet background estimate; they use the statistical methods to determine the W-boson properties by comparing data to signal and background processes and quantifying their compatibility; and they include the corrections and systematic uncertainties of the physics-modelling, the lepton calibrations, the recoil calibrations, and the background processes.

Different aspects of the fit setup are optimised to simplify the structure of the likelihood function (cf. Eq. (6.6)). Finally, the measured W-boson properties mass, width, and lepton universality are discussed one at a time. The studies on the W-boson width and the lepton universality presented in Sections 8.3 and 8.4 are first checked with blinded simulated samples where the width is shifted by an unknown value in the range between −100 and 100 MeV and the $W \to \tau\nu$ MC sample scaled with a random number drawn from a Gaussian distribution with mean 0 and width 0.1 for the lepton universality studies. After achieving consistent results for the fits using the blinded quantity as a free parameter compared to the other fits including this quantity as an external constraint, the presented numbers are unblinded.

8.1 The optimisation of the fit setup

The setup of the χ^2 fit remains unchanged compared to the 2017 analysis measuring the mass in 14 different measurement categories (cf. Table 4.1) accounting for the charges of the final state lepton, the categories in the lepton pseudorapidity, and the lepton flavour of the final state lepton, e.g. electron or muon, for both considered kinematic observables p_{T}^{ℓ} and m_{T}^{W}. The individual results are then combined using the method of BLUE. The PLH fit including systematic uncertainties uses the same measurement categories but combines them all in one global fit which is referred to as the "multi-fit".

A few aspects concerning some systematic uncertainties are treated differently in the PLH fit than in the χ^2 fit. The PDF uncertainties related to the process $W \to \tau\nu$ were not handled correctly in the 2017 analysis. They need to be evaluated at the particle level but the information about the tau leptons is not available at the generator level. Hence, the relative uncertainties were assumed to be the same between $W \to \ell\nu$ and $W \to \tau\nu$ which is not right. To correct this mistake, the PDF uncertainty of the process $W \to \tau\nu$ is doubled to be more conservative. The impact on the final result is expected to be negligible for the mass and the width measurement but can significantly impact the sensitivity of the

lepton universality measurement. Other options determining the characteristics of the PLH fit are presented in the following.

8.1.1 Normalisation

The normalisation is an important aspect of the mass and the width measurements due to their cross-section dependence which is more pronounced for the width. Two different normalisation models are defined to account for various needs:

- **Model-independent**: The normalisation of the different templates is left free in the fit. A global normalisation factor is applied to all signal samples which can vary simultaneously across all measurement categories to not overrate one template over another and to take the cross-section dependence out. The 1.8 % luminosity uncertainty (cf. Section 3.2.6) is applied as an overall normalisation envelope to the simulated background samples to allow for a change in the normalisation. The model focuses on the shapes of the distributions for the signal processes. It does not utilise the full information available but limits the sensitivity of the measurement to the systematic uncertainties.
- **Model-dependent**: The normalisation of the different templates is left free in the fit and the cross-section dependence is considered. No normalisation factor is introduced but the uncertainty on the luminosity is taken as an overall normalisation uncertainty on all simulated samples. The dependence of the expected number of events on the measured quantities constrains the fitted NPs and POIs. This normalisation scheme is model-dependent and explores the full potential providing the best sensitivity for the mass and width measurement.

The presented PLH fit results of the W-boson mass and width use the model-independent scheme, whereas sensitivity of the model-dependent scheme is outlined in Appendix F.1.4.

For the lepton universality measurement, a set of three normalisation factors is introduced. The sum of all histograms with a normalisation factor is required to match the data

$$\begin{aligned} H_{\text{data}} &\stackrel{!}{=} \mu_\tau \cdot H_{W\to\tau\nu} + \mu_\ell \cdot H_{W\to\ell\nu} + \mu_{\text{bkg}} \cdot H_{\text{bkg}} \\ &= \mu_{\text{all}} \left(R_{\tau\ell} \cdot H_{W\to\tau\nu} + H_{W\to\ell\nu} + R_{\text{bkg}\ell} \cdot H_{\text{bkg}} \right), \end{aligned}$$

where H_x is the histogram of data, $W \to \tau\nu$, $W \to \ell\nu$, or the background samples, respectively. Instead of applying separate normalisation factors μ_τ, μ_ℓ, and μ_{bkg} to each sample, a single factor $\mu_{\text{all}} = \mu_\ell$ is used as an overall normalisation applied to all samples and the normalisation factors $R_{\tau\ell} = \mu_\tau/\mu_\ell$ and $R_{\text{bkg}\ell} = \mu_{\text{bkg}}/\mu_\ell$ are introduced to the tau and the background samples, respectively. The factor $R_{\tau\ell}$ acts as a POI and is 100 % correlated to the ratio of the branching ratios of the tauonic W-boson decay to the (light) leptonic W-boson decay (cf. Eq. (2.33)).

8.1.2 Template spacing

A new production ensures a minimum number of templates is incorporated into the likelihood fit still providing a sufficient accuracy of the interpolation outlined in Section 6.2.2. A test checks how accurate the morphing algorithm works with a different number of templates. Therefore, a given

template is taken as pseudodata but left out for the interpolation. Ideally, the PLH fit finds back the value of the template inserted as data. The results of this study are shown in Table 8.1 using the model-dependent normalisation scheme. Out of 49 mass templates already the following 13 provided a sufficient accuracy

$$\Delta m_W = [-400, -200, -80, -60, -40, -20, 0, 20, 40, 60, 80, 200, 400]\ \text{MeV},$$

where the spacing is given in MeV compared to the nominal mass template. The number of templates used for the PLH fit is less than the 34 different mass hypotheses considered for the χ^2 fit results (cf. Eq. (6.2)). The bin entries depending on the width value of the templates show a non-linear behaviour (cf. Fig. 6.6). Hence, 75 templates are produced to allow for a precise linear interpolation between any two template points. 25 templates provide a good precision for the pseudodata study

$$\begin{aligned}\Delta\Gamma_W = [&-500, -450, -400, -360, -320, -280, -240, -200, -160, -120, -80,\\ &-40, 0, 40, 80, 120, 160, 200, 240, 280, 320, 360, 400, 450, 500]\ \text{MeV},\end{aligned}$$

where the chosen width template spacing is given as a difference to the nominal hypothesis in MeV. The linear interpolation works well for the mass and width fits and finds back the inserted value even for extreme scenarios within 0.2 MeV. The accuracy for the mass fits in p_{T}^{ℓ} shows no deviations from

	m_W		
	80 407.0 MeV	80 431.0 MeV	80 471.0 MeV
p_{T}^{ℓ}	$(80\,407.0\,^{+5.9}_{-5.9})$ MeV	$(80\,431.0\,^{+5.9}_{-5.9})$ MeV	$(80\,471.0\,^{+5.9}_{-5.9})$ MeV
m_{T}^{W}	$(80\,407.1\,^{+8.0}_{-7.9})$ MeV	$(80\,431.1\,^{+8.0}_{-8.0})$ MeV	$(80\,471.1\,^{+8.0}_{-8.0})$ MeV
	Γ_W		
	2 117.0 MeV	2 255.0 MeV	2 425.0 MeV
p_{T}^{ℓ}	$(2\,117.1\,^{+0.7}_{-0.7})$ MeV	$(2\,255.1\,^{+0.8}_{-0.8})$ MeV	$(2\,425.2\,^{+0.9}_{-0.9})$ MeV
p_{T}^{ℓ}	$(2\,117.1\,^{+0.7}_{-0.7})$ MeV	$(2\,255.1\,^{+0.8}_{-0.8})$ MeV	$(2\,425.2\,^{+0.9}_{-0.9})$ MeV

Table 8.1: Study of the linear interpolation for the two morphing POIs m_W and Γ_W. Shown are the results of the PLH fit for three different injected mass and width values, respectively, into pseudodata. The PLH fit is performed in the kinematic observable p_{T}^{ℓ} in the fitting range 30–50 GeV, and in the kinematic observable m_{T}^{W} in the fitting range 60–100 GeV. The model-dependent normalisation scheme is used. Only the statistical uncertainties of the data and simulation are taken into account.

the expected result, whereas the difference in m_{T}^{W} fits is at the level of 0.1 MeV accompanied by a higher uncertainty. Increasing the number of templates to nine or 13 does not improve the accuracy of the m_{T}^{W} fits. For the width fits, the precision and uncertainty are similar between the kinematic observables with an accuracy level of 0.1 MeV for the template values 2 117 MeV and 2 255 MeV, and 0.2 MeV for the width hypothesis 2 425 MeV. Using fewer templates for Γ_W fits shows significant deviations of several MeV to the inserted template values.

8.1.3 Smoothing and symmetrisation

The systematic uncertainties related to leptonic and recoil calibrations are statistically dominated. They show large bin-to-bin variations in the fitted kinematic observables which are not caused by physical conditions but rather by statistical fluctuations. The bin-to-bin fluctuations can introduce some instabilities in the PLH fit. Hence, a smoothing procedure of the variations is performed to

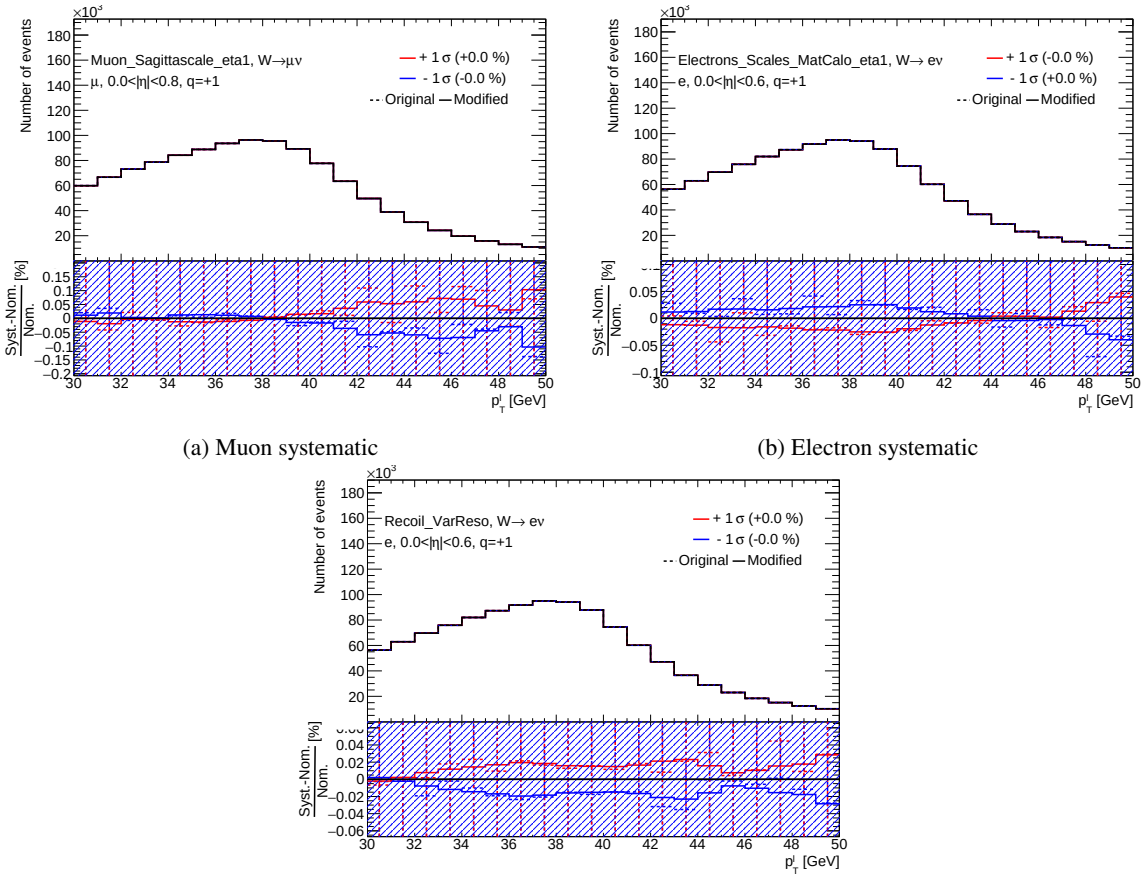

(a) Muon systematic

(b) Electron systematic

(c) Recoil systematic

Figure 8.1: Distributions of different systematic uncertainties comparing the original (dashed lines) and the modified (solid lines) envelopes. Shown are the up (red) and down (blue) variations for (a) the muon sagitta, (b) the electron scale material calorimeter, and (c) the recoil energy resolution systematic uncertainties for a given measurement category of the leptonic decay channels. The lower panel illustrates the relative uncertainty compared to the nominal distribution given in per cent where the hatched area represents the statistical uncertainty of the nominal distribution.

remove the fluctuations of the up and down variations of the corresponding uncertainties. The applied smoothing procedure is a weighted average over three neighbouring bins

$$b\,(i) = \frac{b\,(i-1) + e \cdot b\,(i) + b\,(i+1)}{e+2}, \tag{8.1}$$

where e is the scale factor of the middle bin. For this measurement, the value $e = 2$ is chosen. Equation (8.1) is applied to each relative uncertainty envelope and afterwards scaled again to the same integral. This prevents that the variations change their normalisation. The first bin and last bin of the smoothed distribution remain unchanged by this smoothing procedure as they only have one neighbouring bin.

The smoothing procedure is applied to the systematic uncertainties of the muon momentum calibration, the electron energy response, and the recoil corrections but not to the lepton selection efficiencies and the recoil Z statistics as those are treated by the PCA (cf. Section 7.6). Furthermore, those systematic uncertainties are expected to be symmetric in terms of the source and to have a symmetric effect on the variation. Some of the considered envelopes show an artificial asymmetry caused by statistical fluctuations. Hence, the relative uncertainty of the up and the down envelope are symmetrised.

The p_{T}^{ℓ} distributions of one exemplary systematic uncertainty related to the muon, the electron, and the recoil calibration visualising the smoothing and symmetrisation procedure are visualised in Fig. 8.1. The envelopes of the other smoothed and symmetrised uncertainties are shown in Appendix F. The impact of the smoothing and symmetrisation method can be well understood in the lower panel where the relative deviation compared to the nominal distribution is shown for the uncertainty before (dashed lines) and after (solid lines) applying the procedure. The smoothing removes the statistical fluctuations visible in the ratio panel without flattening the envelopes as a whole.

Kinematic observable	m_W		Γ_W		$R_{\tau\ell}$	
	raw	smoothed & symmetrised	raw	smoothed & symmetrised	raw	smoothed & symmetrised
p_{T}^{ℓ}	$^{+7.6}_{-7.2}$ MeV	$^{+7.8}_{-7.8}$ MeV	$^{+21.8}_{-21.4}$ MeV	$^{+22.7}_{-22.6}$ MeV	$^{+4.5}_{-4.5}$ ‰	$^{+4.6}_{-4.6}$ ‰
m_{T}^{W}	$^{+11.6}_{-11.0}$ MeV	$^{+12.4}_{-12.4}$ MeV	$^{+32.1}_{-31.5}$ MeV	$^{+33.5}_{-33.3}$ MeV	$^{+6.4}_{-6.5}$ ‰	$^{+6.7}_{-6.7}$ ‰

Table 8.2: Impact of the smoothing and symmetrisation procedure on the different measurements of W-boson properties for the two kinematic observables p_{T}^{ℓ} and m_{T}^{W}. For each of the three POIs m_W, Γ_W, and $R_{\tau\ell}$, the direct comparison of the total uncertainty using the raw or smoothed and symmetrised envelopes of the systematic uncertainties is stated. The PLH fit on Asimov data is performed in the fitting ranges 30–50 GeV and 60–100 GeV for p_{T}^{ℓ} and m_{T}^{W}, respectively, using the model-independent normalisation scheme for the morphing POIs. Only the statistical uncertainties of the data and systematic uncertainties taking part in the smoothing and symmetrisation procedure are considered.

The impact on the total uncertainty is checked by performing the three measurements considering only those systematic uncertainties where the smoothing and symmetrisation are applied and the statistical uncertainty of the data. The total uncertainties including raw or smoothed and symmetrised variations are compared in Table 8.2. An Asimov dataset[1] acts as a placeholder for the real data to focus only on the total uncertainty. The total uncertainty using the smoothed and symmetrised envelopes is higher than taking the raw uncertainty but in all cases more symmetric. Hence, the choice of smoothing and symmetrizing certain NPs is rather motivated by overhauling statistical fluctuations and unexpected asymmetries than lowering the total uncertainty.

[1] The Asimov dataset is a pseudodata set that assumes the nominal signal and background distributions.

8.1.4 Pruning

Propagating all systematic uncertainties as NPs to the PLH fit complicates the extended likelihood function of Eq. (6.6). Those systematic uncertainties having a negligible impact on the shape or the normalisation can be pruned away as they might arise from statistical fluctuations. The shape and the normalisation of a systematic uncertainty are treated independently.

The optimal threshold value for the pruning combines trimming most of the NPs without reducing the total uncertainty too much. The optimal pruning values for the shape are determined to be 0.2 ‰ for p_{T}^{ℓ} and 0.1 ‰ for m_{T}^{W}, whereas a normalisation pruning threshold of 0.5 ‰ is chosen for the measurements of m_W and Γ_W, and 0.25 ‰ for the lepton universality measurement for both kinematic observables. The full study for both kinematic observables and the three measurements can be found in Appendix F.1.3.

8.1.5 Fitting ranges

The fitting ranges of the χ^2 fit were optimised in the 2017 analysis to get the smallest total uncertainty which were determined to be 32–45 GeV and 66–99 GeV for the p_{T}^{ℓ} and the m_{T}^{W} distributions, respectively. However, the situation is different for the PLH fit and five different fitting ranges are studied. A fit on all considered POIs is performed on Asimov data to spot the best fitting range with the expected best sensitivity. The total uncertainties of the three measurements are shown in Table 8.3. In both fitted observables, all three measurements show the smallest uncertainty for the full kinematic range which means 30–50 GeV for the p_{T}^{ℓ} distribution and 60–100 GeV for the m_{T}^{W} distribution. The fits on m_W and $R_{\tau\ell}$ provide the best sensitivity for the observable p_{T}^{ℓ}, whereas the tranveser mass of the W-boson supplies the highest precision for Γ_W fits.

p_{T}^{ℓ}				m_{T}^{W}			
Range	m_W	Γ_W	$R_{\tau\ell}$	Range	m_W	Γ_W	$R_{\tau\ell}$
30–45 GeV	16.0 MeV	73.0 MeV	11.7 %	60–90 GeV	23.7 MeV	91.0 MeV	15.8 %
32–45 GeV	16.3 MeV	73.4 MeV	16.9 %	66–99 GeV	23.4 MeV	52.7 MeV	19.7 %
35–50 GeV	16.2 MeV	70.7 MeV	35.6 %	70–100 GeV	25.1 MeV	52.9 MeV	26.0 %
35–45 GeV	16.5 MeV	73.9 MeV	36.3 %	70–90 GeV	26.3 MeV	132.3 MeV	26.4 %
30–50 GeV	15.7 MeV	70.4 MeV	11.2 %	60–100 GeV	23.0 MeV	47.8 MeV	15.2 %

Table 8.3: Expected total uncertainty for different fitting ranges on the different measurements of W-boson properties. The sensitivity is evaluated with fits on Asimov data in both kinematic observables p_{T}^{ℓ} and m_{T}^{W} for the indicated ranges and all three POIs. The model-independent normalisation scheme is used for the morphing fits. All kinds of uncertainties are considered in this study.

The mass measurement shows no preferred kinematic region in the distributions of p_{T}^{ℓ} and m_{T}^{W}. The fitting regions 30–45 GeV and 35–50 GeV show a similar uncertainty in p_{T}^{ℓ} fits, whereas in m_{T}^{W} fits the region 60–90 GeV outperforms the range 70–100 GeV. Extending the kinematic range establishes the most promising possibility to decrease the total uncertainty for W-boson mass fits. The estimated sensitivity could reach 15.7 MeV which is more than 10 % better than the quoted uncertainty of the 2017 analysis. The width measurement prefers the high kinematic region as a change of Γ_W reflects the most at the endpoints of the kinematic distributions. For p_{T}^{ℓ} fits, the kinematic region 35–50 GeV has

a 2.3 MeV lower uncertainty than the region 30–45 GeV. This difference is more pronounced for m_{T}^{W} fits where the fit region 70–100 GeV has a total uncertainty that is approximately 38 GeV lower than for the region 60–90 GeV. Still, the full kinematic range of 60–100 GeV provides the best sensitivity with an uncertainty of 47.8 MeV which is close to the uncertainty of 42 MeV of the world average [25]. The presented results use the model-independent normalisation scheme for the measurements of m_W and Γ_W but those of the model-dependent normalisation outlined in Appendix F.1.4 permit the same conclusions.

For the lepton universality measurement, the sensitivity increases in the low kinematic regions of both observables as the total uncertainty in the fitting ranges 30–45 GeV (p_{T}^{ℓ}) and 60–90 GeV (m_{T}^{W}) is significantly lower than in the ranges 35–50 GeV (p_{T}^{ℓ}) and 70–100 GeV (m_{T}^{W}). Due to the additional neutrinos in the final state of the decay $W \to \tau\nu$ (cf. Fig. 2.10), the kinematic spectrum is softer than for the prompt lepton decay of the W-boson and the distribution of the intermediate tau lepton decay more populated in the low kinematic region. The expected sensitivity is approximately 11 % which is above the aimed per cent level sensitivity achieved by the LEP experiments (cf. Section 4.3.3).

8.2 Measurement of the W-boson mass

The result with the total uncertainty is revised with the χ^2 fit using the reprocessed samples and systematic uncertainties. In the next step, the mass is fitted with the PLH fit. First, the fit is performed in a similar setup to the 2017 analysis to draw comparisons between the two fitting methods for the full result. Afterwards, the setup of the PLH fit is changed to explore the full potential of this measurement.

8.2.1 Updated χ^2 fit combinations

The central values of the χ^2 fit of the reanalysis as given in Section 6.1.3 and the impact of the re-evaluated systematic uncertainties on m_W as presented in Chapter 7 are combined using the BLUE method [143] as carried out for the 2017 analysis. The results are shown in Table 8.4.

Validation step	m_W (e- and μ-channel)	δm_W	m_W (e-channel)	m_W (μ-channel)
Published	80369.5	18.5	80349.8	80381.9
Production A	80369.2	18.6	80350.0	80382.1
Production B	80369.4	18.5	80351.3	80382.1
Production C	80369.2	18.6	80350.9	80382.1
Production D	80369.2	18.6	80350.9	80382.1
Production E	80368.4	18.5	80349.3	80382.1
New multijet background fractions	80370.2	18.5	80354.6	80381.9
New multijet background fractions and shapes	80371.3	18.5	80357.9	80381.2
Reprocessing all systematic uncertainties	80371.9	18.8	80356.6	80382.7

Table 8.4: Evolution of the fully combined central value of m_W, its total uncertainty δm_W, and the central values respectively obtained from combining the electron and muon channels separately.

The evolution of the central value and the total uncertainty from the published result of the reference analysis to the result of the reanalysis is presented in several steps:

- First, the published results of the 2017 analysis are stated.
- The results from the reprocessed samples using the central values of the statistics only fit from the different cross-check productions of the electron channel are presented afterwards. The central values in the muon channel from production A to E reflect the paper setup of the reanalysis which changes the central value by 0.2 MeV.

  From production A to E, the central values of the electron channel change and impacts the combined central value. The result of production A drops by 0.3 MeV compared to the published analysis. Including the missing data in production B changes the combined central value slightly by 0.2 MeV and goes back to the 80 369.2 MeV for the productions C and D which unblind the mass of the W-boson and change the production site. Fixing the electron energy calibration seed bug in production E drops the central value by ∼1 MeV compared to production D. The impact of the systematic uncertainties on m_W is taken from the 2017 analysis. The total uncertainty stays around 18.5 MeV.
- In the next two combinations, the multijet background is updated: first, the fractions in the different measurement categories are modified, and second the new extrapolated shapes. The systematic uncertainties remain unchanged compared to the published analysis. The central values of the combination of both leptonic channels increase by about 2 MeV for updating only the multijet background fractions and by another ∼1 MeV for updating the whole multijet background. This increment is driven by the electron channel which is more affected by the multijet background than the muon channel as discussed in Section 6.1.3.
- The central values of the statistics only fit remain unchanged compared to the previous combinations but the impact of the systematic uncertainties on m_W is revised with the reprocessed samples of the systematic uncertainties. This changes the central value of the combination by 0.6 MeV compared to the previous combination. The total uncertainty increases by 0.3 MeV, whereas it only varied by maximally 0.1 MeV for introducing the different cross-check productions and the new multijet background estimate. The increase is mainly caused by the uncertainties on the electron selection efficiencies which were underestimated in the 2017 analysis. Furthermore, the uncertainty on the Z-boson mass scaled to the W-boson mass was double-counted in the 2017 analysis as it was considered on particle level in the category of the EW corrections and on detector level in the category of the electron energy response. The latter one is removed in this step with a negligible impact on the final result.

The result of fixing all issues in the event selection, updating the multijet background, reprocessing and combining all systematic uncertainties is as in the 2017 analysis is $m_W = (80\,371.9 \pm 18.8)$ MeV. However, the multijet background was found to be considered fully correlated across the leptonic decay channels for the 2017 analysis. This is not optimal as the evaluation is performed separately in the two channels. Correcting this fallacy, the fit result is $m_W = (80\,371.7 \pm 18.5)$ MeV. So far, the uncertainty on the choice of the PDF set, with a value of 3.8 MeV (cf. Section 7.1.5), is added in quadrature to the combined uncertainty. In the last step, this uncertainty is evaluated inclusively in all single measurement categories and accounted for the error weighted combined value. This represents

a statistical improvement compared to the 2017 analysis. Hence, the final χ^2 fit result of the reanalysis is

$$m_W = (80\,374.0 \pm 18.3)\,\text{MeV}. \tag{8.2}$$

Different measurement categories are combined in Table 8.5. In the first step, the calculation of the W-boson mass in the m_{T}^W distribution for the electron and the muon decay channels is performed separately for the positive, the negative, and both charge categories. The central values are compatible with each other within their uncertainties. The same combination for fits in the p_{T}^ℓ distribution shows a similar compatibility. The uncertainty of the determination in the m_{T}^W distribution is higher than for fits in the p_{T}^ℓ distribution caused by the recoil calibrations. For the determination in the p_{T}^ℓ distribution, the effect of the PDF and p_{T}^W uncertainties could be reduced by the choice of the optimal fitting range [86]. In the next step, the electron and muon decay channels are combined for the mass determination from p_{T}^ℓ or m_{T}^W distributions. Again, the results are compatible. When combining the results of the fits in p_{T}^ℓ and m_{T}^W, the difference between the electron and the muon decay channels is 23.5 MeV. The stated

Combined categories	Central value [MeV]	Total uncertainty [MeV]
m_{T}^W, W^+, e-μ	80 372.4	32.0
m_{T}^W, W^-, e-μ	80 393.4	29.9
m_{T}^W, $W^\pm$, e-μ	80 385.1	25.1
p_{T}^ℓ, W^+, e-μ	80 353.2	23.5
p_{T}^ℓ, W^-, e-μ	80 387.9	24.2
p_{T}^ℓ, $W^\pm$, e-μ	80 373.6	18.6
p_{T}^ℓ, $W^\pm$, e	80 354.0	23.5
m_{T}^W, $W^\pm$, e	80 385.8	30.0
m_{T}^W-p_{T}^ℓ, $W^\pm$, e	80 359.5	23.1
p_{T}^ℓ, $W^\pm$, μ	80 384.4	21.0
m_{T}^W, $W^\pm$, μ	80 381.3	27.7
m_{T}^W-p_{T}^ℓ, $W^\pm$, μ	80 383.0	20.6
m_{T}^W-p_{T}^ℓ, W^+, e-μ	80 353.2	23.3
m_{T}^W-p_{T}^ℓ, W^-, e-μ	80 389.6	23.8
m_{T}^W-p_{T}^ℓ, $W^\pm$, e-μ	80 374.0	18.3

Table 8.5: Results of the m_W measurements for various combinations of individual categories. Given are the central values and the total uncertainties in MeV.

values agree within their uncertainties which validates the consistent implementation of electron and muon calibrations. The exclusive combinations of the positive and the negative charge categories give a difference of 36.4 MeV which is comparable to the difference of 30.9 MeV stated for the 2017 analysis [86].

8.2.2 Results of the PLH fit

The updated χ^2 fit result of Eq. (8.2) combines the result of the fits in the kinematic observables p_{T}^{ℓ} and m_{T}^{W} with the BLUE method. The PLH fit avoids this step as all uncertainties are correlated in this statistical method which complicates the combination. Already the fit in the p_{T}^{ℓ} distribution exceeds the sensitivity of the χ^2 fit combination. The m_W determination in the m_{T}^{W} distribution serves as a cross-check as the study on the fitting ranges (cf. Table 8.3) promises a smaller uncertainty if using the transverse momentum of the lepton. As the differences for the model-dependent normalisation scheme are expected to be small from the study on the fitting ranges (cf. Section 8.1.5), this normalisation model is not considered further for the W-boson mass. The p_{T}^{ℓ} fit results of the individual measurement categories and the combination of both fitting methods are shown in Fig. 8.2. Whereas the χ^2 fit determined the optimal fitting range with the lowest total uncertainty to 32–45 GeV, the complete orifice of the kinematic range to 30–50 GeV offers the highest sensitivity for the PLH fit. The latter one includes the uncertainty on the W-boson width from the combination of the predecessor measurements. Adding the width as an external constraint to the fit increases the total uncertainty of the combination by 0.1 MeV which justifies retrospectively the neglection in the 2017 analysis. It can be nicely seen that incorporating the systematic uncertainties into the optimisation of the PLH fit shifts the central values with respect to the χ^2 fit. The central values of some single fits agree within a few MeV between the PLH fit and the χ^2 fit, e.g. μ, $|\eta| < 0.8$, $q = -1$, whereas others differ by more than 40 MeV, e.g. e, $|\eta| < 0.6$, $q = +1$. In summary, it can be said that the central values between the two fitting methods agree within their uncertainties. Combining the 14 single measurement categories produces a fit result of

$$m_W = (80\,354.7 \pm 15.7)\,\mathrm{MeV}. \tag{8.3}$$

With an accuracy of 2×10^{-4}, this measurement is sensitive to the LO corrections on the radiative corrections (cf. Eq. (2.28)) which are two orders of magnitude higher. Within the stated uncertainties, it is in agreement with the indirectly determined value of the W-boson mass in a global EW fit (cf. Eq. (2.29)). Compared to the χ^2 fit in the p_{T}^{ℓ} distribution, the central value decreases by approximately 19 MeV and the uncertainty by more than 10 %. In every single measurement category, the total uncertainty decreases if changing the fit method from the χ^2 fit to the PLH fit. On the one hand, this is caused by incorporating the systematic uncertainties as NPs into the global optimisation of the minimal likelihood value which allows exploring correlations between the different uncertainties. On the other hand, the extension of the fitting range reduces the statistical uncertainties but allows the PLH fit to constrain the NP even more.

Similar to other experimental measurements, the result stated in Eq. (8.3) is in tension with the recently published measurement by the CDF collaboration [126]. Before an interpretation in terms of the consistency of the experimental results with the Standard Model prediction is pursued, the discrepancy of the central values needs to be understood. A good theoretical description and accurate physics modelling of the production and decay of vector bosons (cf. Section 7.1) is crucial for a

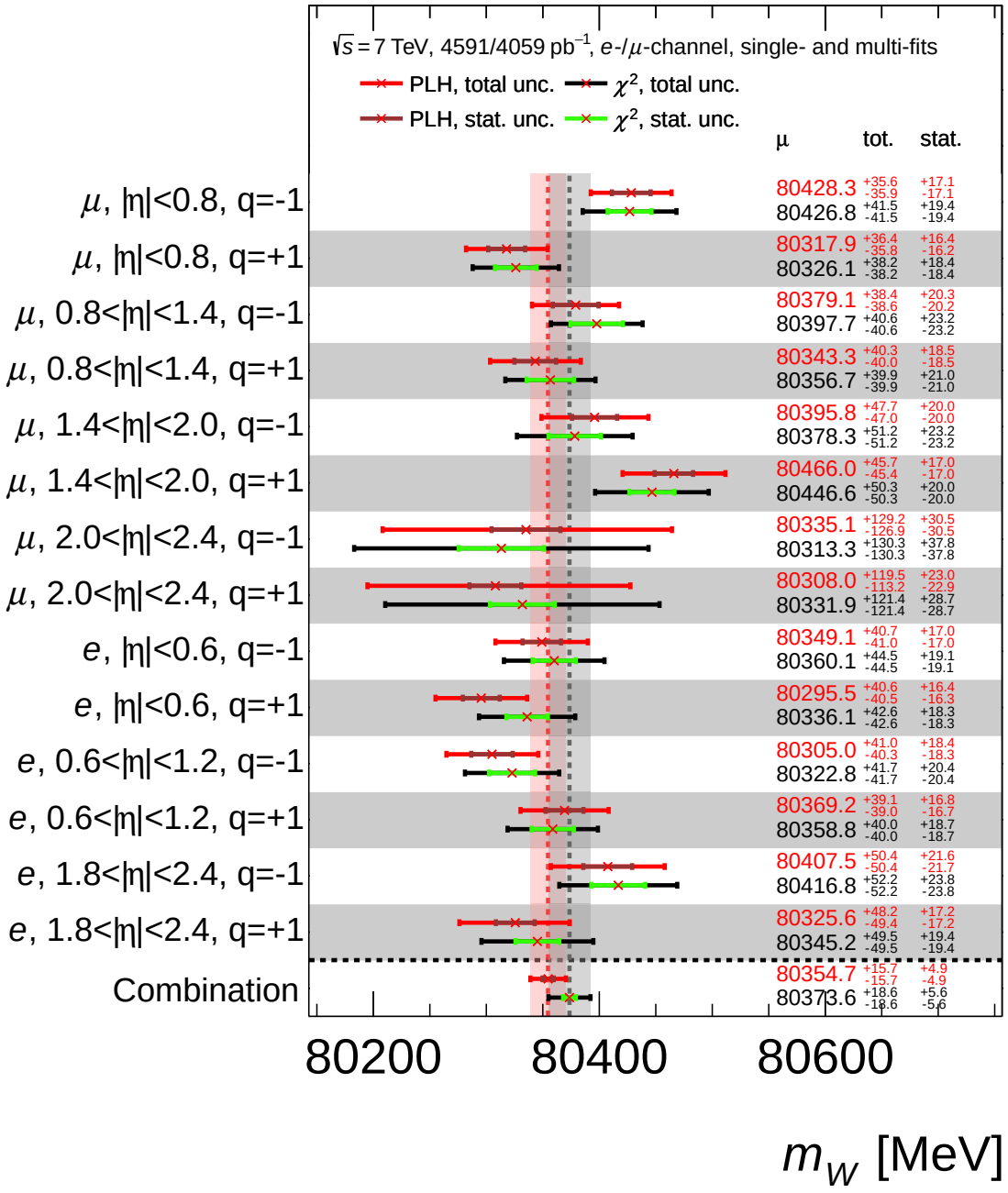

Figure 8.2: Comparison of the results of the PLH fit and the χ^2 fit for the W-boson mass measurement performed in the p_{T}^{ℓ} distribution for the individual measurement categories and their combined fit. Indicated are the central values, the total uncertainties, and the statistical uncertainties. The red and the black line mark the central values of the combination.

correct treatment of higher-order QCD effects. A common standard of the QCD modelling needs to be defined. It is important to describe the hard process in the simulation step with the used PDF set which is not done for the CDF measurement [183]. Spin-effects of the W-boson decay products are covered by a reweighting procedure of the angular coefficients. The scientific discourse between the LHC experiments and the CDF collaboration will be essential to understand this discrepancy.

The mass value of the fit in the p_{T}^{ℓ} distribution given in Eq. (8.3) agrees with the combined fit in the m_{T}^{W} distribution which is determined to (80 373.0 ± 22.9) MeV. Unfortunately, a fully correlated simultaneous fit between the two kinematic observables would be statistically inconsistent as they both use the same data. Hence, it is not straightforward to determine the correlation between fits using different kinematic observables but still the ultimate goal. A possible determination of a combined result needs to use the statistical correlation between the two kinematic distributions and the correlation of all incorporated NPs. A combined value would be mainly influenced by the result of the fit performed in the observable p_{T}^{ℓ} as its uncertainty is lower than for fits carried out in the m_{T}^{W} distribution. A full comparison of all measurement categories and the combination between fits in the p_{T}^{ℓ} and m_{T}^{W} distributions is shown in Appendix F.2, Fig. F.11. All other tables and illustrations for the PLH fit carried out in the m_{T}^{W} distribution can as well be found in Appendix F.2.

Source of uncertainty	Impact on m_W [MeV]		Ratio
	PLH fit	χ^2 fit	$\frac{\chi^2 \text{ fit}}{\text{PLH fit}}$
Electron calibrations	7.6	6.5	0.84
Muon calibrations	6.7	6.3	0.95
PDFs	6.1	8.6	1.41
EW corrections	6.1	6.7	1.09
Parton shower predictions and angular coefficients	5.3	8.7	1.64
External measurement constraint	2.4	not included	-
Cross-section and multijet background uncertainties	2.1	2.8	1.35
Recoil calibrations	1.8	2.4	1.29
Simulation sample size	1.7	3.7	2.12
Luminosity	1.4	not included	-
Total systematic uncertainty	14.9	17.5	1.17
Data sample size	4.9	5.7	1.15
Total	15.7	18.3	1.17

Table 8.6: Comparison of the impact of the different uncertainty categories on the total uncertainty of the W-boson mass measurement performed in the p_{T}^{ℓ} distribution between the χ^2 fit and the PLH fit. Shown are the 1 σ standard deviations which are in the PLH fit calculated by leaving out a group of systematic uncertainties and determining the impact via quadratic error propagation compared to the original fit. In addition, the ratio of the impacts between the two fitting methods is given.

The impact of different sources of uncertainty on the m_W measurement for the PLH fit and the χ^2 fit, as well as their ratio, is shown in Table 8.6. To determine the impact of a group of systematic uncertainties in the PLH fit, the group is left out for the combined fit which reduced the total uncertainty. The impact is then determined by quadratic error propagation by comparing the reduced uncertainty to the total uncertainty of the full fit including all systematic uncertainties. Due to the correlations

of the NPs among each other, the quadratic sum of the impacts does not necessarily result in the total uncertainty which states an important difference to the quoted numbers of the χ^2 fit. Added in quadrature, they result in the total uncertainty. The increase in the impact of the lepton calibrations on the W-boson mass measurement from the χ^2 fit to the PLH fit can be explained by the correlations to other systematic uncertainties in the fit. Beyond, all sources of uncertainty improve due to the profiling with a particularly large decrease for the parton shower predictions and angular coefficients, and the PDF uncertainties. The impact of the latter source of uncertainty could be significantly reduced by introducing the PLH fit which is important as the uncertainty on the PDFs is still the category with the third-highest impact on the W-boson mass measurement using this improved fit technique. No separate uncertainty for the choice of the PDF set is assigned as the normalisation of the systematic uncertainties, in contrast to the χ^2 fit, is considered which should describe the uncertainty made by the selection of a certain PDF variation. To prove this assumption, a fit with different PDF sets has to assure the central values are close enough due to the profiling that the differences are covered by the uncertainty of the PDF modelling.

Furthermore, a more exclusive determination which individual NPs impact the W-boson mass fit are ranked in Fig. 8.3 for the combined fit. This ranking is determined by comparing the central value of the nominal fit to fits where the individual NPs are fixed to their post-fit pulls varied by the constraints in both directions. Only the ten most important NPs are given in Fig. 8.3. The highest and the ten

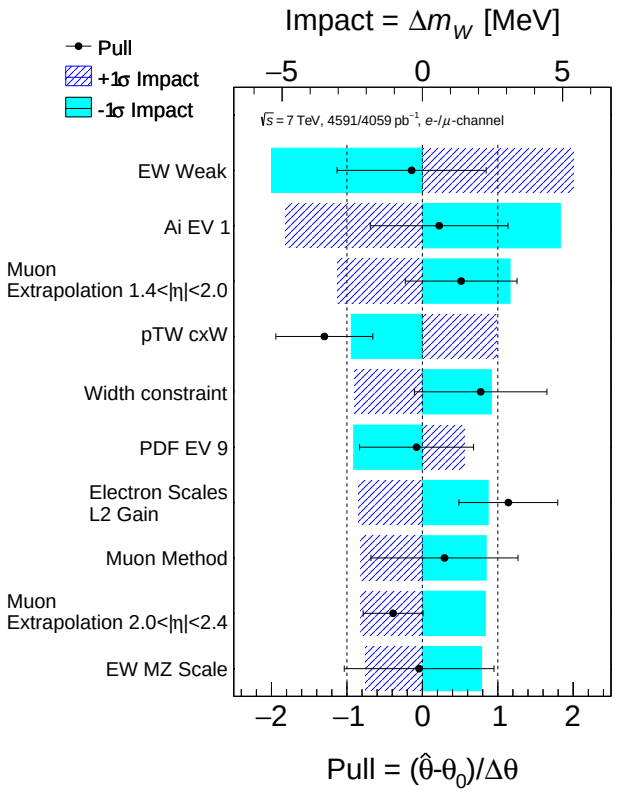

Figure 8.3: The ten NPs with the highest impact on the W-boson mass measurement performed in the p_{T}^{ℓ} distribution. Indicated are the $+1\,\sigma$ and $-1\,\sigma$ impacts, as well as the pull with its uncertainty.

highest ranked NPs both belong the uncertainty category of the EW corrections which has the fourth highest impact in Table 8.6 and only includes one other systematic uncertainty which is not among the ten highest ranked NPs given in Fig. 8.3. The second and fourth highest ranked NPs are the parton shower predictions and angular coefficients. Three muon calibration uncertainties are listed in Fig. 8.3 but solely one of the electron calibration uncertainties though this category has a higher impact on the W-boson mass measurement. This can be explained as the electron calibrations incorporate a greater number of different effects leading to more NPs where their impact does not concentrate on single uncertainties. The ranking is completed by one PDF eigenvector and the external constraint from the width measurement at position five and six, respectively.

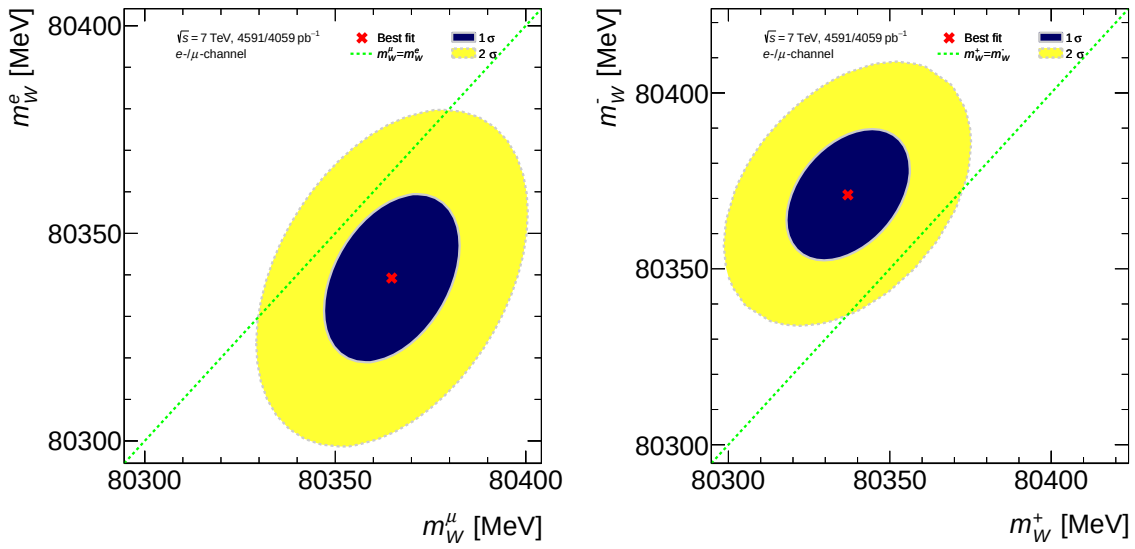

(a) (b)

Figure 8.4: Consistency plots for different sub-fits of the W-boson mass measurement performed in the p_{T}^{ℓ} distribution. Shown are the central value and the $1\,\sigma$ and $2\,\sigma$ uncertainty contours for two POIs acting (a) on the different leptonic decay channels and (b) on the different charges of the final state lepton.

In addition to the fit results of the combination, the consistency of different combinations of individual measurement categories targeting the lepton flavour of the decay channel or the positive and negative charge categories is crucial to check. Therefore, different POIs affecting the corresponding measurement categories are fitted simultaneously taking the correlation of all systematic uncertainties into account. This allows to not only receive a combination of central values but to determine the uncertainty contour in the respective plane in addition. The corresponding fit results are shown in Fig. 8.4. The shown $1\,\sigma$ and $2\,\sigma$ contours belong to the combination of W-boson mass values whose Δ (NLL) differs by 0.5 and 2.0, respectively, from the likelihood value of the minimum. In contrast to a one-dimensional problem, the given contours correspond to CLs of 39.4 % and 63.2 %, respectively, as those quantiles mark one and two standard deviations of a two-dimensional Gaussian distribution. The central values between the leptonic decay channels show a difference of 25.6 MeV which is smaller compared to the difference of 30.4 MeV in the χ^2 fit results of the reanalysis (cf. Table 8.5). This difference agrees at about $1\,\sigma$ with the hypothesis of an equal mass value for the decays into

electrons and muons. The combined fit to the different charges of the final state leptons returns a difference of 34.0 MeV which agrees at the $2\,\sigma$ level with the hypothesis of equal mass values for W^+ and W^- as illustrated in Fig. 8.4. The χ^2 fit indicates a comparable difference of 34.7 MeV between the two charges.

Figures 8.5 and 8.6 compare the post-fit distributions of p_{T}^{ℓ} between the fitted value of the χ^2 fit (cf. Eq. (8.2)) and the PLH fit (cf. Eq. (8.3)) for the electron and the muon channel, respectively. As for the 2017 publication, the m_W value of the χ^2 fit is determined in the range 32–45 GeV but shown over the full kinematic range. In every measurement category, the simulation samples are normalised to data for the post-fit χ^2 fit distributions. In the ratio panel of the illustrated plots, a better data to prediction ratio is clearly visible for the PLH fit compared to the χ^2 fit. The difference relates to the pulls of the systematic uncertainties which are part of the global optimisation in the PLH fit. Further post-fit distributions of the observables p_{T}^{W}, $u_{\parallel}^{\ell}$, and $u_{\perp}^{\ell}$ are given in Appendix F.2, Figs. F.9 and F.10.

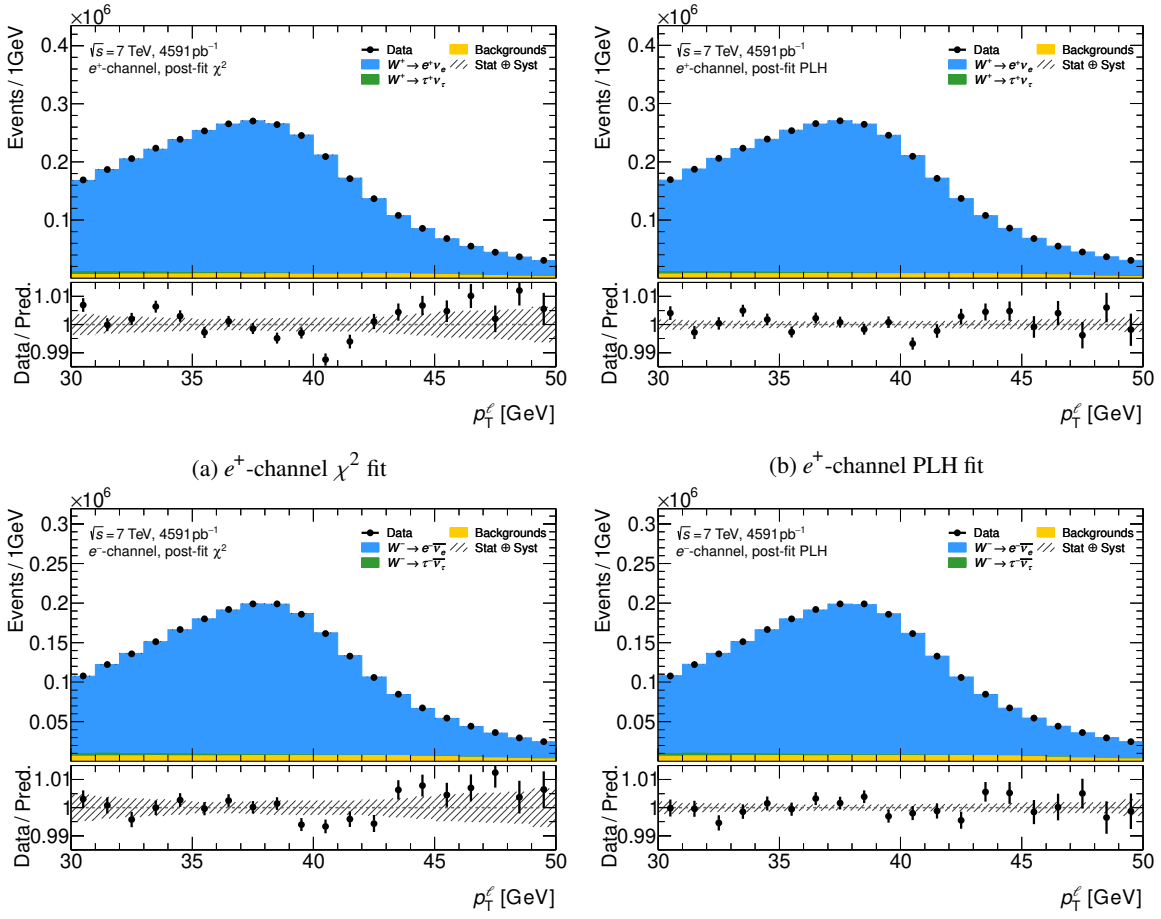

(a) e^+-channel χ^2 fit

(b) e^+-channel PLH fit

(c) e^--channel χ^2 fit

(d) e^--channel PLH fit

Figure 8.5: Comparison of the post-fit p_{T}^{ℓ} distributions in the electron channel between χ^2 fit (a,c) and PLH fit (b,d) for the W-boson mass measurement. The distributions are inclusive in pseudorapidity but given explicitly for positively (a,b) and negatively charged electrons (c,d). The lower panel shows the ratio of data to simulation where the error bars indicate the statistical uncertainty and the shaded band represents the total uncertainty.

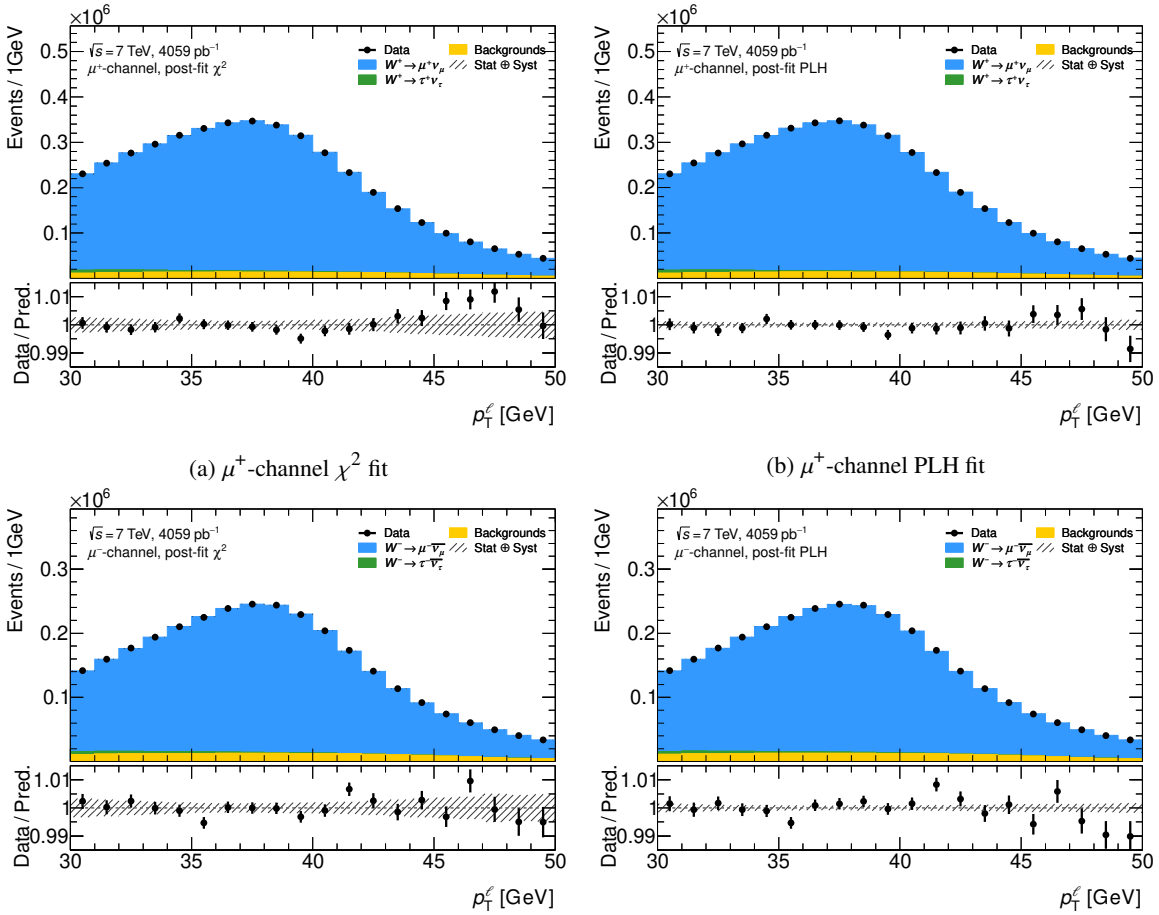

(a) μ^+-channel χ^2 fit

(b) μ^+-channel PLH fit

(c) μ^--channel χ^2 fit

(d) μ^+-channel PLH fit

Figure 8.6: Comparison of the post-fit p_{T}^{ℓ} distributions in the muon channel between χ^2 fit (a,c) and PLH fit (b,d) for the W-boson mass measurement. The distributions are inclusive in pseudorapidity but given explicitly for positively (a,b) and negatively charged muons (c,d). The lower panel shows the ratio of data to simulation where the error bars indicate the statistical uncertainty and the shaded band represents the total uncertainty.

By reference to these distributions, one can study the impact of the individual NPs post-fit pulls on the data to simulation agreement. As an improvement of this measurement, the recoil distributions could be included as CRs into the fit to further constrain systematic uncertainties related to the recoil or p_{T}^{W}.

8.3 Measurement of the W-boson width

In contrast to the mass fits, the W-boson width measurement is solely performed with a PLH fit. Hence, no comparison can be drawn to a reference χ^2 fit. The different measurement categories as well as the combined result between fits in the p_{T}^{ℓ} and the m_{T}^{W} distribution are compared in Fig. 8.7. In general, the fits performed in the p_{T}^{ℓ} distribution prefer a higher central value than those carried out in the m_{T}^{W} distribution for all single measurement categories except for three. The single fit categories show a smaller total uncertainty for p_{T}^{ℓ} than for m_{T}^{W} fits, whereas the combination of fits

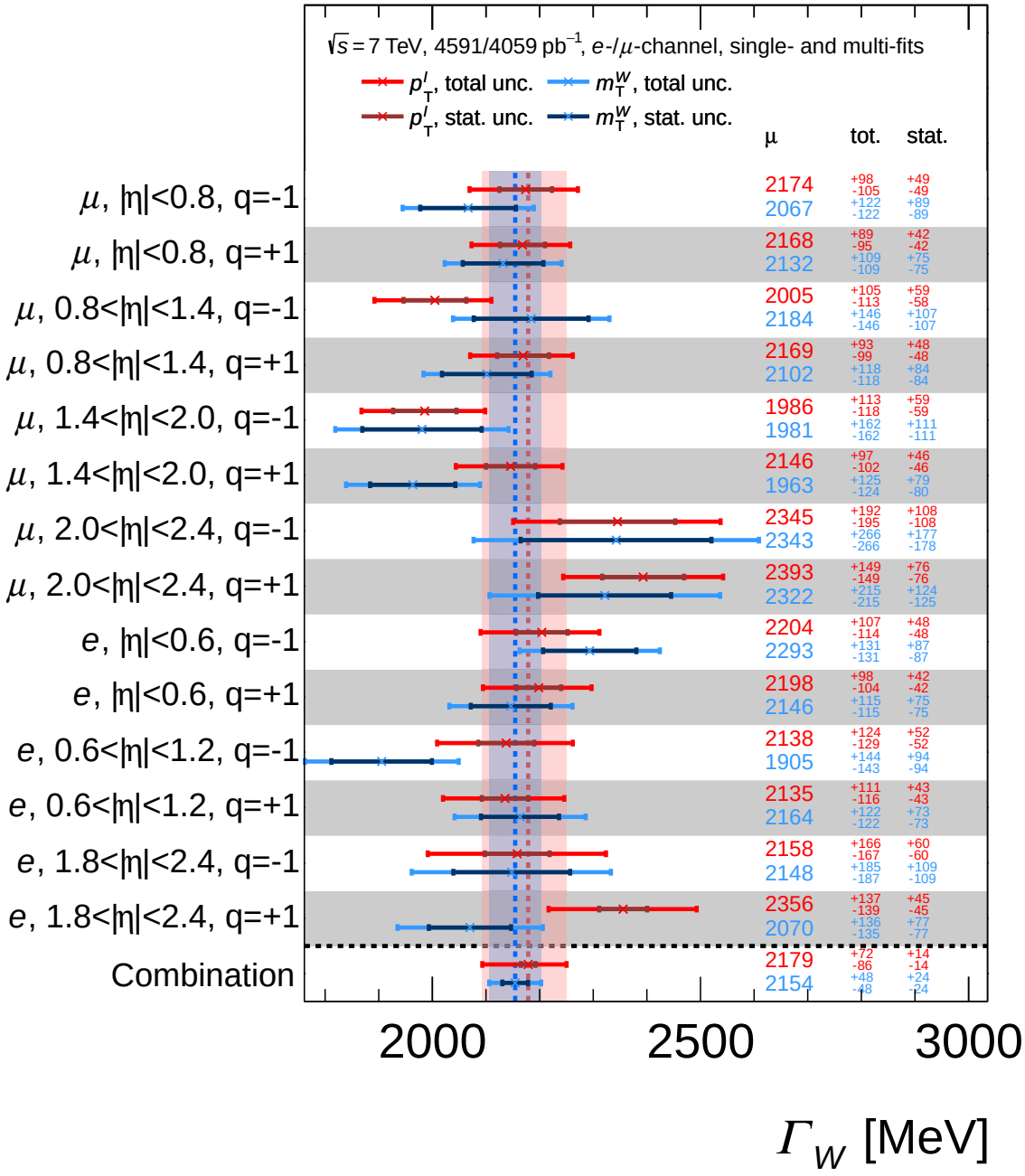

Figure 8.7: Results of the PLH fit for the measurement of the W-boson width for the individual measurement categories and their combined fit using the kinematic observables p_{T}^{ℓ} (red) and m_{T}^{W} (blue). Indicated are the central values, the total uncertainties, and the statistical uncertainties.

in the m_{T}^{W} distribution profits a lot from connecting the single fits and exceeds the combination of fits in the p_{T}^{ℓ} distribution with still worse statistical uncertainties. Comparing the central values of individual measurement categories of fits carried out in p_{T}^{ℓ} or m_{T}^{W} distributions, most of them agree within their uncertainties. Only three sub-fits show a difference of approximately 200 MeV of PLH fits performed in the two considered kinematic distributions. The combination of the p_{T}^{ℓ} fits shows an asymmetric total uncertainty which is due to systematic uncertainties as the statistical uncertainty is completely symmetric. This behaviour of asymmetric uncertainties becomes visible in all single measurements of both leptonic decay channels except for the fits performed in regions with large values of pseudorapidity. The result stated for this thesis is the combination of all individual m_{T}^{W} fits as it reaches the highest sensitivity with a W-boson width value of

$$\Gamma_W = (2\,154 \pm 48)\,\mathrm{MeV}. \tag{8.4}$$

This is the most accurate measurement of the W-boson width down to the present day which achieves a precision of about 2 %. The W-boson width is fitted as a NP in the same global EW fit as the indirect determination of the mass [28] where the result of $(2\,091 \pm 1)$ MeV is still in good agreement with the result of Eq. (8.4) within the uncertainties. The result of Eq. (8.4) achieved in fits in the m_{T}^{W} distributions is comparable to the best fit in the p_{T}^{ℓ} distributions which is $\Gamma_W = (2\,179 \pm 79)$ MeV. Similar to the W-boson mass measurement, a statistical combination of the results of p_{T}^{ℓ} and m_{T}^{W} fits is desired but not completed within the scope of this thesis. A combination will be dominated by the results of the fits carried out in m_{T}^{W} distributions due to the lower total uncertainty. As suggested in Section 8.1.5, extending the fit range in the m_{T}^{W} distribution to higher kinematic ranges could reduce the total uncertainty even further. A fit performed on Asimov data in the range 60–120 GeV leads

Source of uncertainty	Impact on Γ_W [MeV]
Recoil calibrations	17.1
Electron calibrations	15.9
Parton shower predictions and angular coefficients	13.8
External measurement constraint	12.0
Muon calibrations	10.5
Cross-section and multijet background uncertainties	10.4
Luminosity	8.9
PDFs	7.1
Simulation sample size	6.0
EW corrections	2.0
Total systematic uncertainty	42.0
Data sample size	24.0
Total	48.3

Table 8.7: Impact of the different uncertainty categories on the total uncertainty of the W-boson width measurement performed in the m_{T}^{W} distribution. Shown are the 1 σ standard deviations which are calculated by leaving out a group of systematic uncertainties and determining the impact via quadratic error propagation compared to the original fit.

to a total uncertainty of approximately 30 MeV. Detailed studies of the multijet background and the systematic uncertainties beyond the range of 100 GeV need to be done to explore the full potential of the W-boson width measurement.

Table 8.7 gives an overview how the total uncertainty splits up into different categories. The impact of the different sources of uncertainties is derived the same way as for the mass measurement. The highest impact on the W-boson width measurement is due to the recoil calibrations with an impact of more than 17 MeV. It is expected that they have a higher impact for fits performed in the m_{T}^{W} distribution than for those done in the p_{T}^{ℓ} distribution due to the definition of the kinematic observable. The electron calibrations play a more dominant role with an impact of around 16 MeV compared to the muon calibrations having an impact of approximately 10 MeV. The uncertainties on the PDFs contribute less to the total uncertainty than for the mass measurement. The external constraint of the mass using all measurements taken so far except the 2017 analysis has a significant impact of approximately 12 MeV. The parton shower predictions and angular coefficients are the third most contributing uncertainty category which consists just of the p_{T}^{W} uncertainty and one eigenvector of the A_i uncertainty in contrast to two eigenvectors which are used for p_{T}^{ℓ} fits.

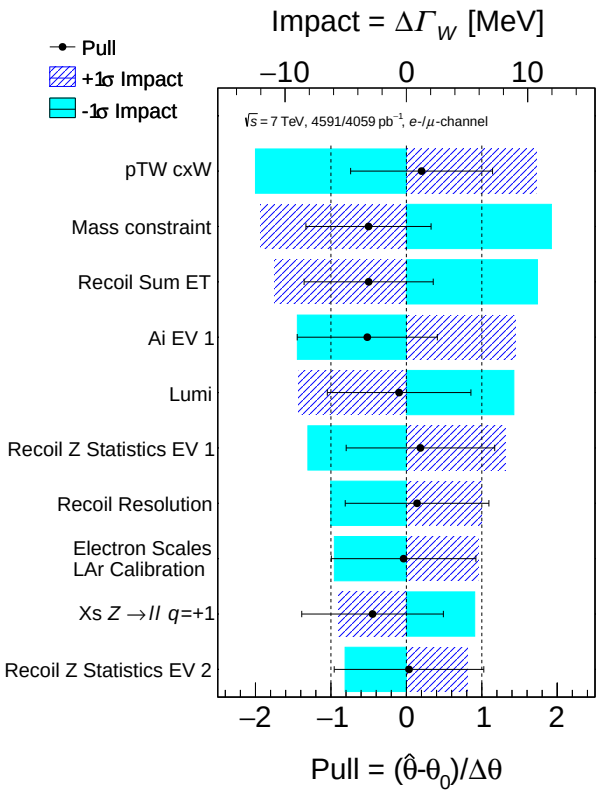

Figure 8.8: The ten NPs with the highest impact on the W-boson width measurement performed in the m_{T}^{W} distribution. Indicated are the $+1\,\sigma$ and $-1\,\sigma$ impacts, as well as the pull with its uncertainty.

Hence, it is not surprising that these two individual uncertainties are placed as first and fourth among the ten highest-ranked single NPs as it is shown in Fig. 8.8. The external mass constraint is listed in the second place and the fit pulls the mass constraint downwards which is in agreement with the W-boson

mass fits itself where a value below the world average without the 2017 ATLAS measurement of 80 399 MeV is preferred. Individual NPs of the electron and recoil calibration categories represent the other rankings as well as the uncertainty on the luminosity and the cross-section uncertainty on the $Z \to \ell\ell$ background for the positively charged leptons. The latter two affect only the normalisation of one or all simulated background processes.

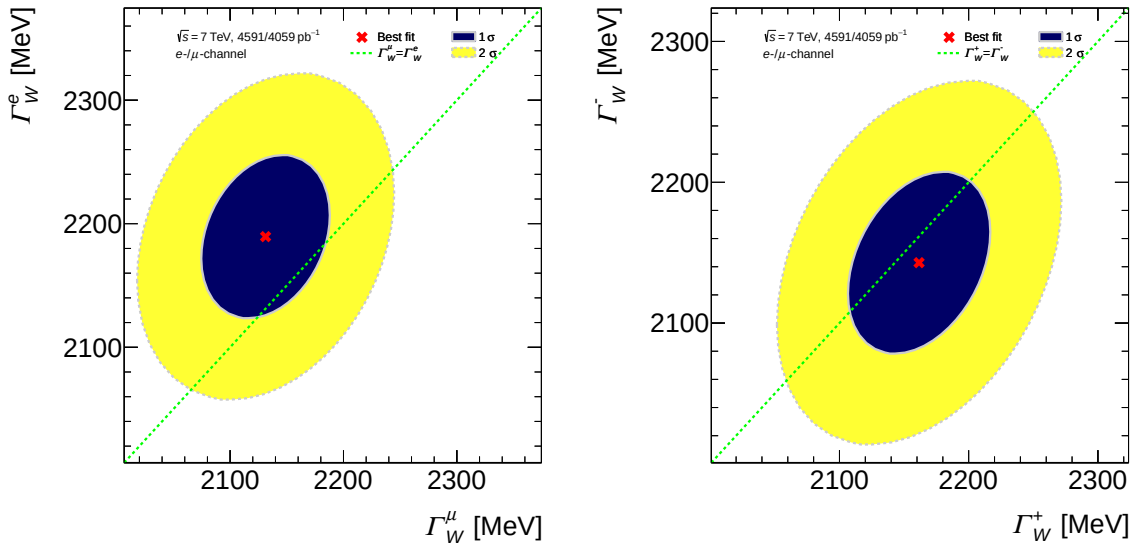

(a) (b)

Figure 8.9: Consistency plots for different sub-fits of the W-boson width measurement performed in the m_{T}^{W} distribution. Shown are the central value and the $1\,\sigma$ and $2\,\sigma$ uncertainty contours for two POIs acting (a) on the different leptonic decay channels and (b) on the different charges of the final state lepton.

It is crucial to check if combining several individual measurement categories still return a consistent result of the W-boson width between the fits performed on the two different leptonic decay channels and the two charges of the final state lepton. The best fit values can be found in Fig. 8.9. The difference of fits performed on the different flavours of the final state leptons is 58 MeV which agrees at the $1\,\sigma$ level with the hypothesis of equal widths for decays into electrons and muons. Fits combining the different measurement categories according to a given charge of the final state lepton indicate a difference of 19 MeV which is close to the hypothesis of equal widths for W^{+} and W^{-} decays.

The post-fit agreement of the fitted simulation samples to data is shown in Fig. 8.10 separately for the electron and the muon decay channels and the positively and negatively charged leptons but inclusively in pseudorapidity. In the lower panels, the good agreement between data and the post-fit prediction within the total uncertainties is visible. The post-fit illustrations of recoil distributions p_{T}^{W}, $u_{\parallel}^{\ell}$, and $u_{\perp}^{\ell}$ as well as all W-boson width results for fits performed in the p_{T}^{ℓ} distributions can be found in Appendix F.3.

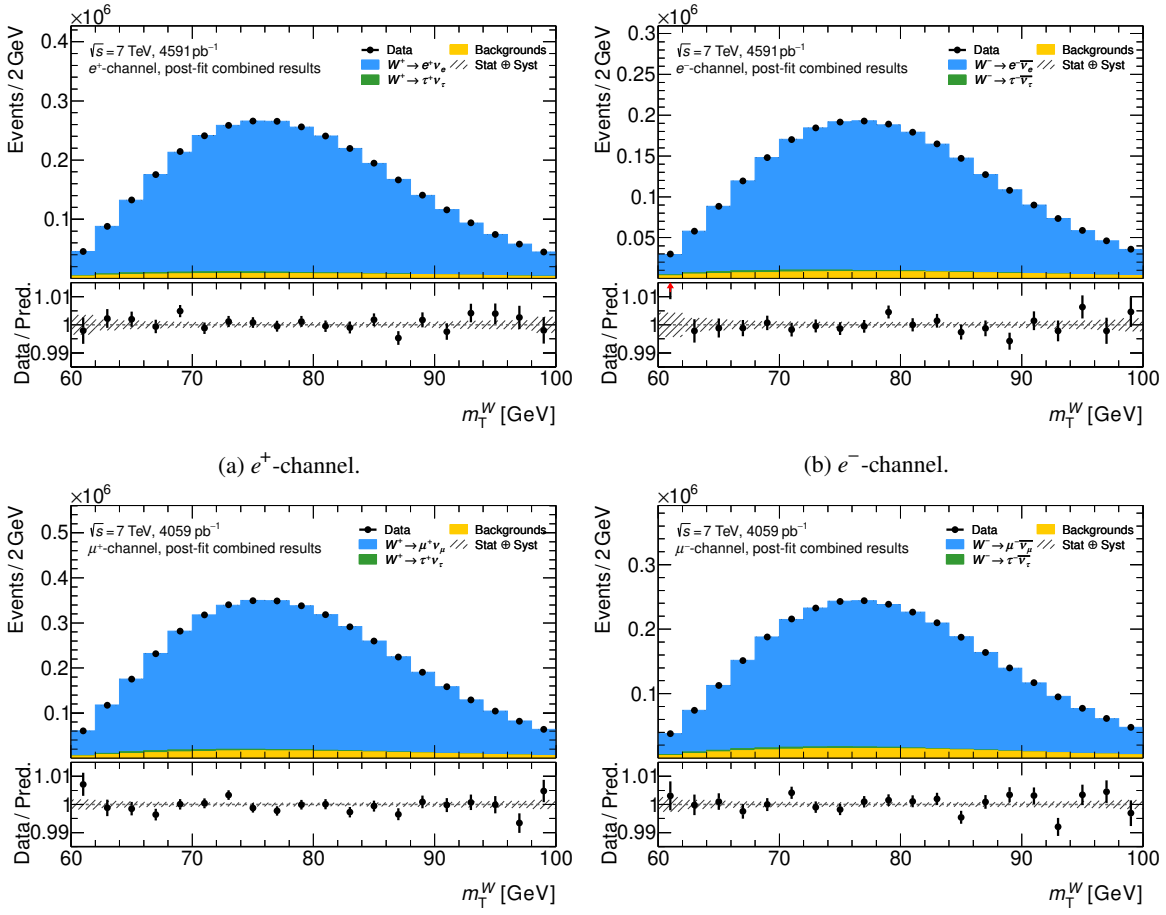

(a) e^+-channel.

(b) e^--channel.

(c) μ^+-channel.

(d) μ^--channel.

Figure 8.10: Post-fit distributions of m_{T}^{W} for the W-boson width measurement. The distributions are inclusive in pseudorapidity but given explicitly for positively (a) and negatively charged electrons (b), and positively (c) and negatively charged muons (d). The lower panel shows the ratio of data to simulation where the error bars indicate the statistical uncertainty and the shaded band represents the total uncertainty.

8.4 Measurement of the lepton universality

The results of fits performed in the p_{T}^{ℓ} and the m_{T}^{W} distributions are compared in Fig. 8.11. As expected from fits to Asimov data (cf. Table 8.3), fits carried out in the p_{T}^{ℓ} distribution are more sensitive than those done in m_{T}^{W}. The stated value of this thesis for the lepton universality measurement origins from the p_{T}^{ℓ} fits and is

$$R_{\tau\ell} = 0.96 \pm 0.11. \tag{8.5}$$

The sensitivity is one order of magnitude worse than the combination of the lepton universality measurements of the LEP experiments (cf. Eq. (4.6)). The result of Eq. (8.5) is in agreement with the best fit value achieved in m_{T}^{W} fits which is $R_{\tau\ell} = 1.16 \pm 0.15$. Furthermore, the individual measurements of fits performed in the p_{T}^{ℓ} and the m_{T}^{W} distributions are compared in Fig. 8.11. The fit

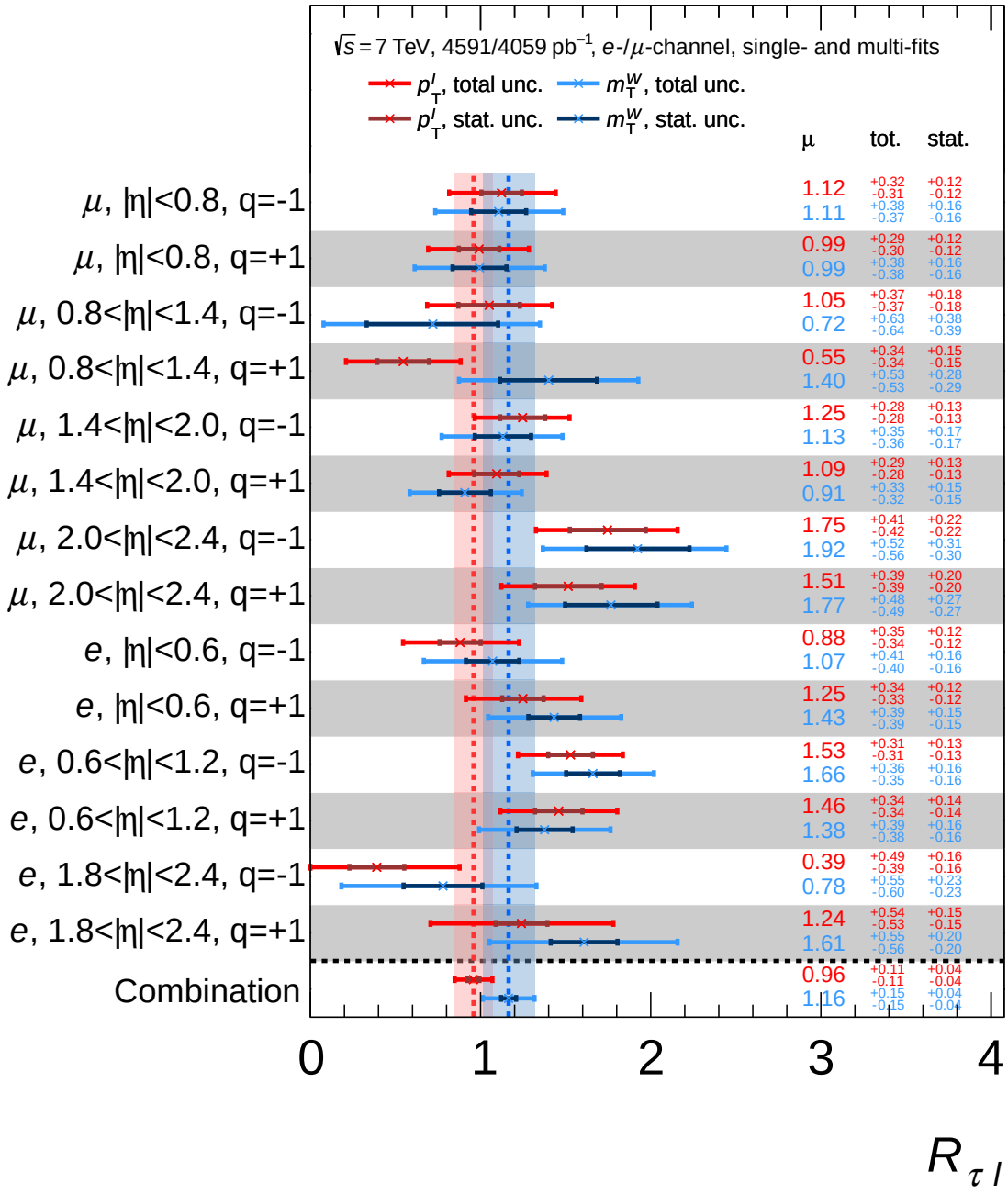

Figure 8.11: Results of the PLH fit for the measurement of the lepton universality for the individual measurement categories and their combined fit using the kinematic observables p_{T}^{ℓ} (red) and m_{T}^{W} (blue). Indicated are the central values, the total uncertainties, and the statistical uncertainties.

results of both kinematic observables agree with each other.

The total uncertainty can be split up into the contribution of different categories of sources of uncertainties as in Table 8.8. The PDFs are dominating this measurement with an impact of 5.0 %. The usage of a more modern PDF set could decrease the total uncertainty of this measurement. Another possibility to improve the sensitivity is to produce a higher statistics of simulated MC samples as their impact of 4.2 % is the third higest on $R_{\tau\ell}$. The contribution of the parton shower predicitons and angular coefficients is the second largest, whereas the EW corrections, the external measurement constraints, and the recoil calibrations contribute only little to the total uncertainty.

Source of uncertainty	Impact on $R_{\tau\ell}$ [%]
PDFs	5.0
Parton shower predictions and angular coefficients	4.5
Simulation sample size	4.2
Muon calibrations	3.8
Electron calibrations	3.6
Cross-section and multijet background uncertainties	3.3
EW corrections	2.8
External measurement constraints	2.1
Recoil calibrations	2.0
Total systematic uncertainty	10.9
Data sample size	3.5
Total	11.1

Table 8.8: Impact of the different uncertainty categories on the total uncertainty of the lepton universality measurement performed in the p_{T}^{ℓ} distribution. Shown are the 1 σ standard deviations which are calculated by leaving out a group of systematic uncertainties and determining the impact via quadratic error propagation compared to the original fit.

The impact of individual NPs to the lepton universality measurement is further split up in Fig. 8.12. The first A_i eigenvector is the uncertainty with the highest impact followed by two PDF eigenvectors. The ranking plot is completed by two uncertainties belonging to the EW corrections, the mass constraint, two muon extrapolation uncertainties applied to different pseudorapidity slices, and a shape uncertainty on the multijet background. The latter one shows an asymmetric impact behaviour.

The consistency between the leptonic decay channels and the two charges of the final state lepton is illustrated in Fig. 8.13. Due to technical reasons, the contours representing the 2 σ uncertainty ellipses could not be produced but are extrapolated. The central values of the different combinations of the leptonic decay channels differ by 0.20 which agrees at about 2 σ with the hypothesis of equal ratios of branching ratios. The combinations of different charges of the final state leptons differ by 0.08 which represents a good consistency.

Figure 8.14 shows the post-fit agreement of data to simulation. A good data to prediciton ratio is visible for the electon and the muon decay channel as well as for positively and negatively charged leptons. The post-fit plots of the recoil distributions p_{T}^{W}, $u_{\parallel}^{\ell}$, and $u_{\perp}^{\ell}$ as well as more information about the lepton universality fits performed in the m_{T}^{W} distribution can be found in Appendix F.4.

The sensitivity of the lepton universality measurement can be further increased by using lifetime information of the tau lepton decay. The tau lepton decays on average after travelling a distance of

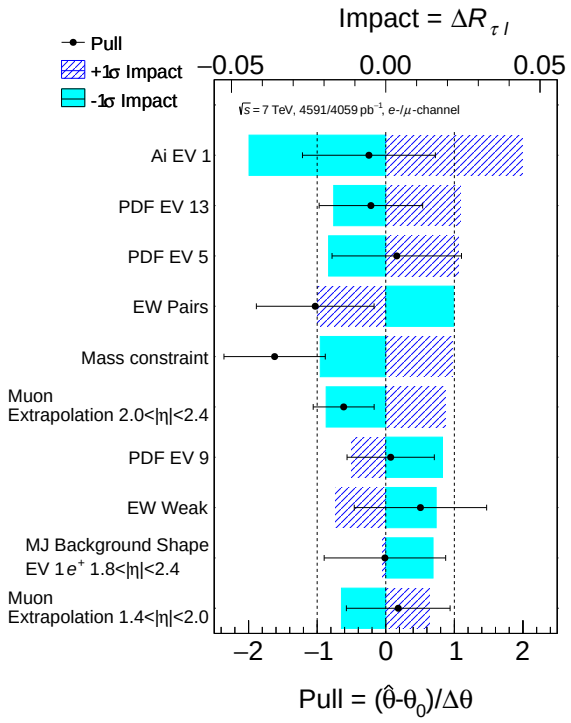

Figure 8.12: The ten NPs with the highest impact on the lepton universality measurement performed in the p_{T}^{ℓ} distribution. Indicated are the $+1\,\sigma$ and $-1\,\sigma$ impacts, as well as the pull with its uncertainty.

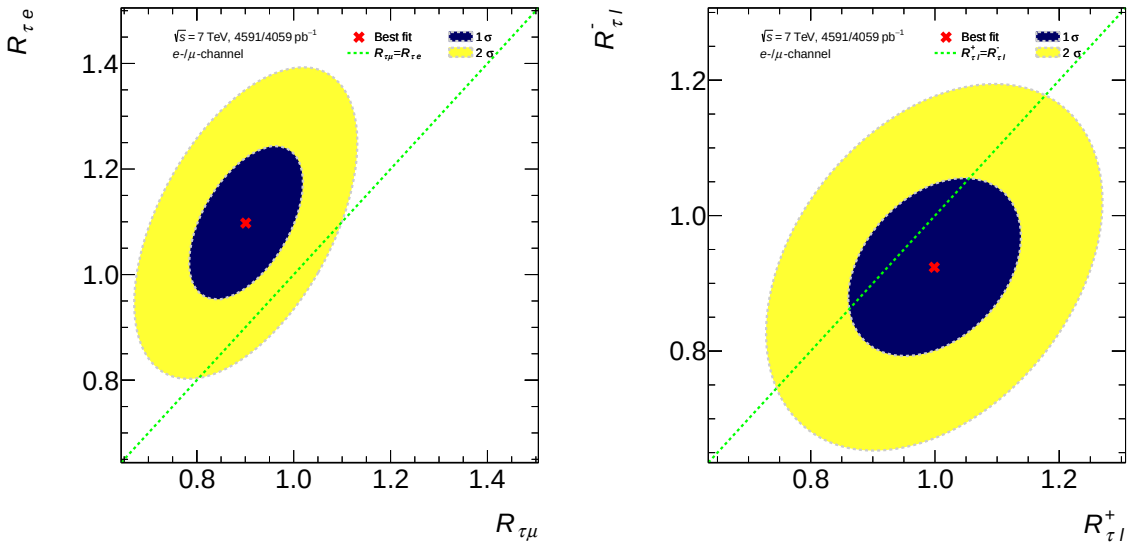

(a) (b)

Figure 8.13: Consistency plots for different sub-fits of the lepton universality measurement performed in the p_{T}^{ℓ} distribution. Shown are the central value and the $1\,\sigma$ and $2\,\sigma$ uncertainty contours for two POIs acting (a) on the different leptonic decay channels and (b) on the different charges of the final state lepton.

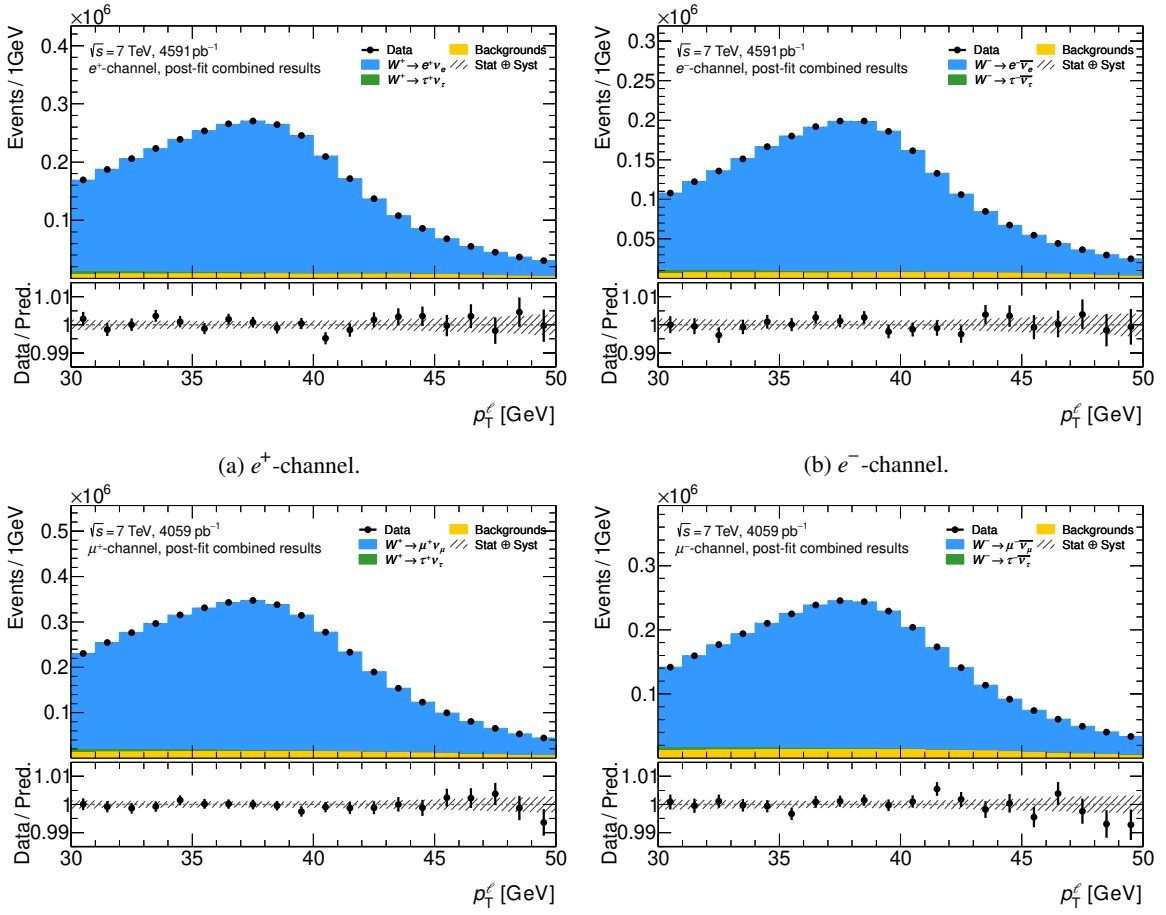

(a) e^+-channel.

(b) e^--channel.

(c) μ^+-channel.

(d) μ^--channel.

Figure 8.14: Post-fit distributions of p_{T}^{ℓ} for the lepton universality measurement. The distributions are inclusive in pseudorapidity but given explicitly for positively (a) and negatively charged electrons (b), and positively (c) and negatively charged muons (d). The lower panel shows the ratio of data to simulation where the error bars indicate the statistical uncertainty and the shaded band represents the total uncertainty.

87 µm in the detector in contrast to the prompt light lepton decay. The ID measures the distance of secondary vertices to the primary vertex in the transverse and longitudinal projection. The inclusion of the transverse impact parameter d_0 or the longitudinal impact parameter z_0 into the PLH fit would decrease the total uncertainty. The different shapes of the $W \to \tau\nu$ and the $W \to \mu\nu$ processes are shown in Fig. 8.15(b). However, the simulation of the impact parameters agrees not well with the data as illustrated in Fig. 8.15(c) due to known issues in the simulation, e.g. underestimation of the impact parameter resolution, a d_0 bias introduced by the Pixel clustering, and a charge asymmetric bias added in the `Geant4` simulation step. The sensitivity of incorporating the transverse impact parameter into the PLH fit was studied in a thesis [184]. The total statistical uncertainty can be reduced from 3.6 % when just fitting in p_{T}^{ℓ} by implementing a two-dimensional fit of p_{T}^{ℓ} and the transverse impact parameter d_0 to 2.1 %. An attempt to calibrate the MC samples to get a sufficient data-to-simulation agreement was performed in a thesis [185]. The longitudinal impact parameter z_0 is easier to calibrate

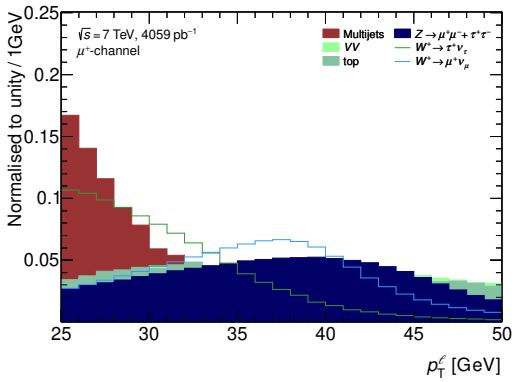

(a) Normalised p_{T}^{ℓ} distribution.

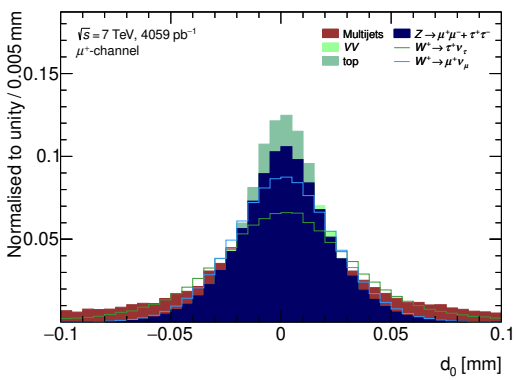

(b) Normalised d_0 distribution.

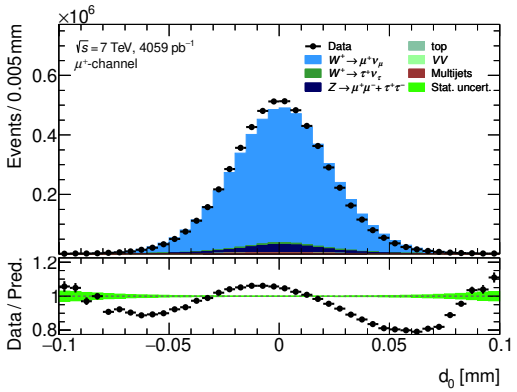

(c) d_0 data-simulation agreement.

Figure 8.15: Several illustrations indicate possible improvements in the context of the lepton universality measurement. (a) and (b) show the normalised p_{T}^{ℓ} and d_0 distributions, respectively, where the background, the $W \to \tau\nu$, and the $W \to \mu\nu$ processes are separately normalised to a unity integral. (c) shows the data to MC simulation agreement for d_0 with the black dots in the lower panel indicating the ratio where the green band illustrates the statistical uncertainty of the simulation and the error bars the statistical uncertainty of the data.

but the question of assigning an appropriate systematic uncertainty could not be answered definitely.

In addition, the relaxation of kinematic cuts increases the statistics of the $W \to \tau\nu$ process and hence increases the sensitivity. The distributions of $W \to \tau\nu$ processes are preferably found at low kinematic regions as shown in Fig. 8.15(a) due to the additional neutrinos in the final state (cf. Fig. 2.10). The requirement $p_{\mathrm{T}}^{\ell} > 30\,\mathrm{GeV}$ removes about 48 % of the $W \to \tau\nu$ process but only approximately 16 % of the $W \to \ell\nu$ process compared to a cut at $p_{\mathrm{T}}^{\ell} > 25\,\mathrm{GeV}$. Due to the correlations of the two observables, the kinematic cut on m_{T}^{W} should be relaxed to 50 GeV instead of 60 GeV. Further relaxing of the kinematic cuts is not possible due to the trigger threshold of 22 GeV in the electron channel and a common W-boson event selection for both decay channels. The multijet background estimate procedure (cf. Section 5.3) is repeated for the relaxed kinematic cuts as outlined in Appendix F and the corresponding multijet background shapes are used for the illustrations in Fig. 8.15. By relaxing the kinematic cuts, the statistical sensitivity can be reduced by a factor of approximately 2.3 [184] which manifests the potential of this measurement.

CHAPTER 9

Summary and Conclusions

The Standard Model of particle physics provides an excellent showcase for a quantum field theory describing elementary particles and their interactions. The W-boson is the charged mediator of the weak force, one of the three forces incorporated by the Standard Model. Its mass requires the existence of the electroweak symmetry breaking. In the Standard Model, this is facilitated via the Higgs mechanism. The interaction between the aforementioned field and the W-boson generates the W-boson mass, m_W, which can be expressed by the following Standard Model parameters: the fine-structure constant α_{em}, the Fermi constant G_{F}, and the sine of the Weinberg angle $\sin\theta_{\text{W}}$. Hence, it was possible to estimate the W-boson mass already before its discovery in 1983 at the Sp$\bar{\text{p}}$S collider. Higher-order corrections on m_W depend on the top mass, m_t, and the Higgs mass, m_H, and are at the order of 10^{-2}. The description of the W-boson as a spin-1 particle and a plane wave allows to predict the W-boson width, Γ_W, at next-to-leading order. Measuring the W-boson mass and width is crucial to test the overall consistency of the Standard Model by comparing it to indirect measurements. It helps to constrain other Standard Model parameters and effects of physics beyond the Standard Model. Furthermore, the weak charged current does not differentiate in terms of the coupling strength to the different leptonic final states at leading-order which is known as lepton universality.

This thesis presented measurements of the W-boson properties mass, width, and lepton universality using the leptonic decay modes of the W-boson. It uses data provided by the Large Hadron Collider in 2011 with a centre-of-mass energy $\sqrt{s} = 7\,\text{TeV}$ recorded by the ATLAS detector with an integrated luminosity of $\mathcal{L}_{\text{int}} = 4.59\,\text{fb}^{-1}$. The reference analysis was published in 2017 [86] and was the most precise measurement of the W-boson at the time it was published. Based on the extensive studies of systematic uncertainties in the 2017 publication, the presented analysis shares the same event selection. The data-driven estimate of the multijet background was improved. In addition, the treatment of several systematic uncertainties has been advanced by utilizing a principal component analysis.

The 2017 analysis evaluated the central value of m_W with a χ^2 fit in different fitting categories for the lepton flavour, the charge of the lepton, and different slices of η_ℓ to account for the detector geometry. The fit was performed in the kinematic observables p_{T}^{ℓ} and m_{T}^{W} which reflect the Jacobian edge and are therefore sensitive to the mass. Templates using different mass and width hypotheses were produced based on the Breit-Wigner parametrisation with a running width and then compared to data. The impact of the systematic uncertainties was calculated independently, taken uncorrelated among each other, and did not affect the central value. Both, the determination of the central value and the size of the considered uncertainties were repeated with success and close to the published results

at the MeV level. However, the statistical treatment of the analysis can be optimised by introducing a profile likelihood fit. It allows the data to profile the systematic uncertainties and explore their correlations. The fitted central value is the result of an optimisation taking statistical and systematic errors into account. Therefore, this fitting technique is expected to lower the total uncertainty and to change the central value of the parameter of interest compared to a fit including only statistical uncertainties.

Using the improvements in systematic uncertainties and background determination, the W-boson mass, m_W, measurement was repeated with the χ^2 fit method leading to a result of m_W =(80 374.0 ± 18.3) MeV which has a higher central value of 4.5 MeV and a smaller total uncertainty of 0.2 MeV compared to the 2017 analysis. Improving the fitting technique further using a profile likelihood fit led to a result of

$$m_W = (80\,354.7 \pm 15.7)\,\text{MeV}.$$

This result is in agreement with the indirect determination of the W-boson mass in a global electroweak fit. The central value decreases by 19.3 MeV compared to the χ^2 fit result of the reanalysis which is due to incorporating the systematic uncertainties as nuisance parameters into the global fit optimisation. The total uncertainty decreases from 18.3 MeV of the χ^2 fit to 15.7 MeV achieved by the profile likelihood fit which marks an accuracy of around 2×10^{-4}. Therefore, the analysis is sensitive to higher-order corrections. The profile likelihood fit shows good consistency between fits performed in the two kinematic observables p_{T}^{ℓ} and m_{T}^{W}, between the charges of the decayed leptons, and the flavours of the decayed leptons. The presented W-boson mass measurement surpasses the one of the 2017 publication but gives a larger total uncertainty than the recently published result by the CDF collaboration [126]. The present measurement is in tension with the recent result from CDF. To

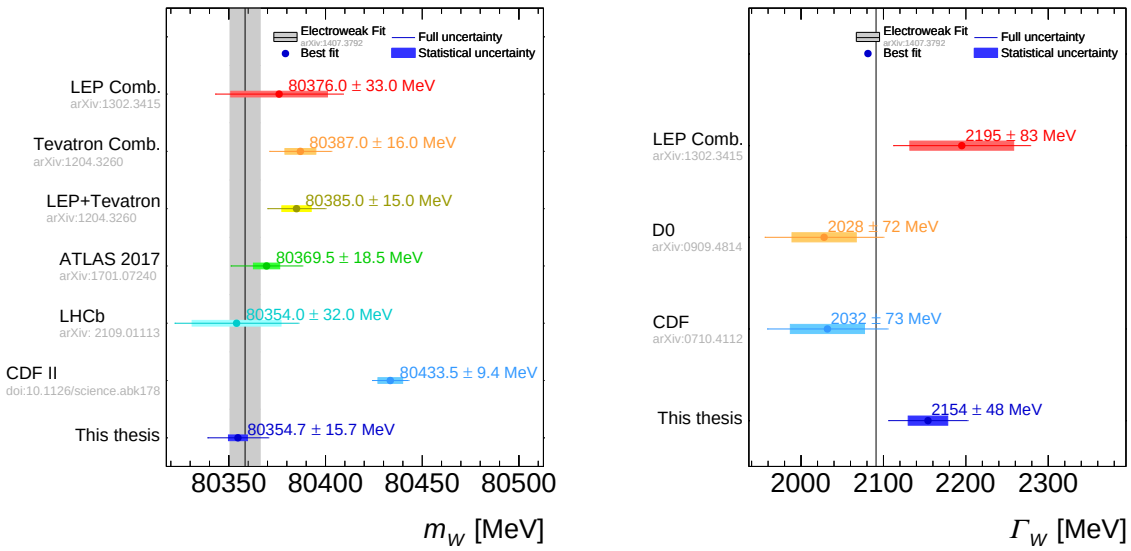

(a) m_W measurements.

(b) Γ_W measurements.

Figure 9.1: Overview and comparison of different mass and width measurements to the global electroweak fit. Shown are the best fit values, the full uncertainties, and the statistical uncertainties for different individual measurements and combinations indicating the reference.

further study the tension between the CDF result and this measurement, a focus should be set on a consistent integration of the hard process with the used parton distribution functions in the simulation process, and a correct treatment and reweighting procedure of the angular coefficients representing the ratio of the helicity weighted cross-sections compared to the unpolarised cross-sections. Once these differences are understood, a final interpretation of the results in terms of their consistency with the Standard Model prediction can be attempted. It can be expected that further precision measurements of the W-boson mass will be a highlight for the physics program of the Large Hadron Collider and future experiments to shed light on the current tension between the individual best fit values.

The measurement of the W-boson width, Γ_W, is the first determination with the ATLAS detector and at the Large Hadron Collider with a result of

$$\Gamma_W = (2\,154 \pm 48)\,\text{MeV}.$$

Again, all fits performed in separate categories are consistent with each other. The stated uncertainty is comparable with the uncertainty of the current world average. The result of Γ_W marks the most precise single measurement of this quantity down to the present day. The central value is still in agreement with the W-boson width value preferred by the global electroweak fit within the stated uncertainties. The best fit values and their uncertainties of different individual measurements and combinations are compared to the global electroweak fit for the W-boson mass and the width in Fig. 9.1. Whereas all measurements of the W-boson width are consistent with each other, the newly published result by the CDF collaboration shows a clear tension with the electroweak fit and all other experimental results as well as with the best fit presented in this thesis.

Last but not least, a measurement of the lepton universality, $R_{\tau\ell}$, was presented by comparing the branching ratios of W-boson decays to electrons or muons to those decaying to tau leptons. The fitted value of

$$R_{\tau\ell} = 0.96 \pm 0.11$$

is in agreement with the Standard Model value of 1 but its uncertainty cannot compete with the most sensitive existing experimental measurements. Relaxing kinematic requirements in the event selection and using lifetime information of the decayed lepton could significantly improve this measurement.

The future at the Large Hadron Collider A prospect study [186] has been carried out by ATLAS to evaluate the potential of the m_W measurement for the high luminosity [187] and the high energy [188] Large Hadron Collider. The high luminosity is the planned extension of the Large Hadron Collider with a five times higher instantaneous luminosity compared to the design value of the Large Hadron Collider starting its physics programm in the late 2020s. The idea of the high energy Large Hadron Collider covers an additional upgrade of the centre-of-mass energy to $\sqrt{s} = 27\,\text{TeV}$. A dataset of $\int \mathcal{L}\,\mathrm{d}t = 200\,\text{pb}^{-1}$ collected in one week of low pile-up runs ($\mathcal{L} \sim 5 \times 10^{32}\,\text{cm}^{-2}\,\text{s}^{-1}$, $\langle\mu\rangle \sim 2$) at both energy scales would result in a statistical precision of below 10 MeV on m_W.

APPENDIX A

Additional information on the theoretical foundations

A.1 Composing the Standard Model Lagrangian

This section explains in detail the way from Lagrange's equation to the Euler-Lagrange equation. The equation of motion of classical mechanics, Lagrange's equation, is

$$\frac{\mathrm{d}}{\mathrm{d}t}\left(\frac{\partial L}{\partial \dot{q}_i}\right) - \frac{\partial L}{\partial q_i} = 0, \tag{A.1}$$

where $q_i(t)$ are discrete coordinates depending on the time variable t. The Lagrange formalism is extended from discrete coordinates to a continuous system with continuously varying coordinates $\phi(\mathbf{x}, t)$

$$L\left(q_i, \dot{q}_i, t\right) \rightarrow \mathscr{L}\left(\phi, \frac{\partial \phi}{\partial x_\mu}, x_\mu\right). \tag{A.2}$$

Equation (A.1) becomes the Euler-Lagrange equation (Equation (A.3)) by using the transformation Equation (A.2)

$$\frac{\partial}{\partial x_\mu}\left(\frac{\partial\, \mathscr{L}}{\partial\left(\partial\phi/\partial x_\mu\right)}\right) - \frac{\partial \mathscr{L}}{\partial \phi} = 0, \tag{A.3}$$

where $\mathscr{L}$ is named the Lagrangian density.

A.1.1 The strong interaction

This section contains additional information on the transformation of the gauge fields in the context of QCD. Due to the additional term in Equation (2.16) including the structure constants f_{abc}, the field strength tensor $G^a_{\mu\nu}$ has a more complicated form than its counterpart in QED

$$G^a_{\mu\nu} = \partial_\mu G^a_\nu - \partial_\nu G^a_\mu - g_S f_{abc} G^b_\mu G^c_\nu.$$

A.2 Relevant properties of the W-boson

Similar to Fig. 2.8, Fig. A.1 shows a two-dimensional scan of the CL of m_W versus $\sin^2\left(\theta^l_{\text{eff}}\right)$.

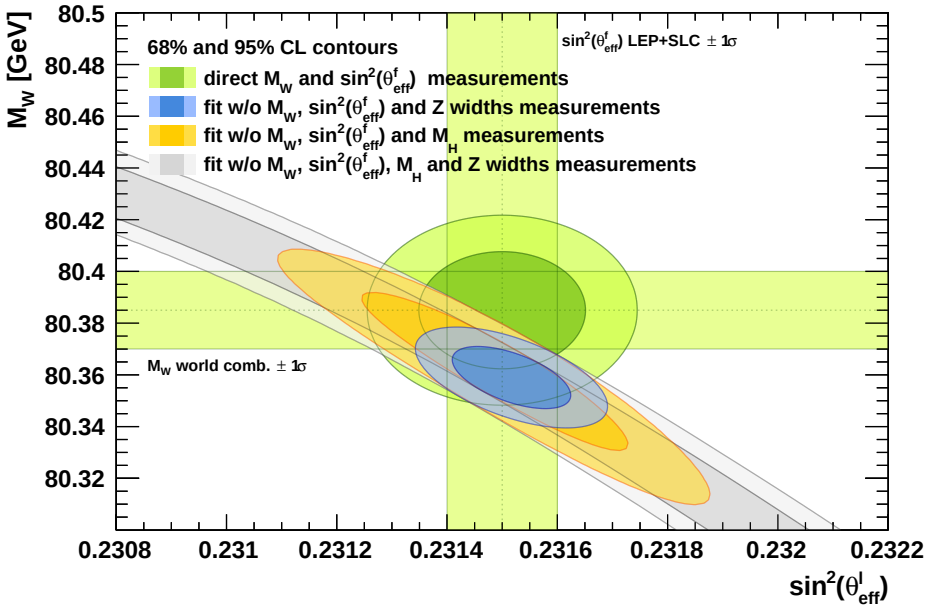

Figure A.1: Two-dimensional scans with contours at 68 % and 95 % CL of m_W versus $\sin^2\left(\theta^l_{\text{eff}}\right)$. Shown are indirect measurements of the two parameters including m_H (blue), Γ_Z (orange), and excluding both measurements (grey) as well as a direct measurement of m_W and $\sin^2\left(\theta^l_{\text{eff}}\right)$ (green bands and ellipses) (taken from [28]).

APPENDIX B

Additional information on the premise

Similar to Fig. 4.7 and Fig. 4.8, Fig. B.1 and Fig. B.2 show the not normalised variations of the W-boson mass and width concerning the nominal hypothesis for the kinematic observables p_{T}^{ℓ} and m_{T}^{W}. While the cross-section dependence is weak for the mass, it is more pronounced for the width.

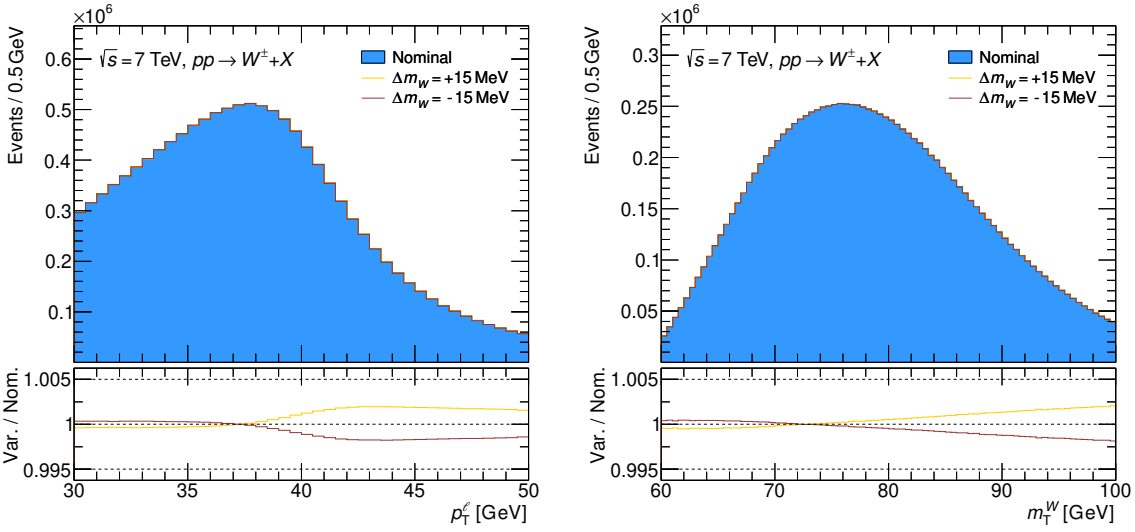

(a) p_{T}^{ℓ} (b) m_{T}^{W}

Figure B.1: Mass templates for the nominal hypothesis and two mass variations. Shown is the sum of all fitting categories of both processes initiated by a W-boson, $W \to \ell\nu$ and $W \to \tau\nu$, for the kinematic distributions p_{T}^{ℓ} (a) and m_{T}^{W} (b). The lower panel illustrates the ratio of the mass variations compared to the nominal mass template.

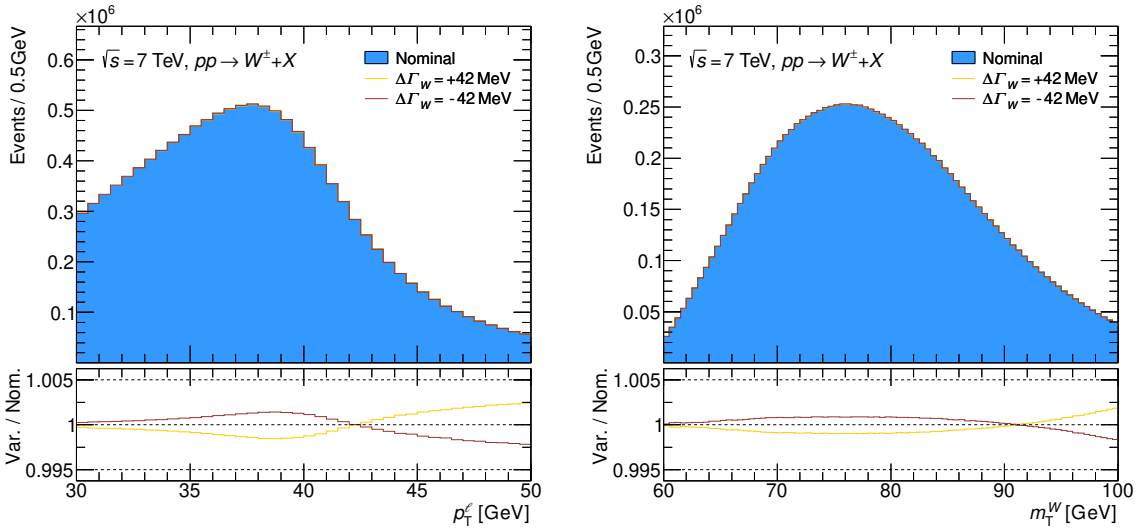

(a) p_{T}^{ℓ} (b) m_{T}^{W}

Figure B.2: Width templates for the nominal hypothesis and two width variations. Shown is the sum of all fitting categories of both processes initiated by a W-boson, $W \to \ell\nu$ and $W \to \tau\nu$, for the kinematic distributions p_{T}^{ℓ} (a) and m_{T}^{W} (b). The lower panel illustrates the ratio of the width variations compared to the nominal width template.

APPENDIX C

Additional information on the analysis design

C.1 Event selection

This section contains additional material on the validation of the reanalysis selection criteria and the validation of the distributions.

C.1.1 Validation of the reanalysis selection criteria

Similar to Table 5.5, Table C.1 shows the event yields of the $W^- \to e^- \overline{\nu}_e$ MC sample for the different productions of the electron channel.

$W^- \to e^- \overline{\nu}_e$							
Cut	A	B	C	D	E	F	2017 analysis
No cut	20092577	20092577	20092577	20092577	20092577	20092577	20092555
LAr noise bursts	20092577	20092577	20092577	20092577	20092577	20092577	20092555
Good PV	20014287	20014287	20014265	20014265	20014295	20014295	20014265
GRL	20014287	20014287	20014265	20014265	20014295	20014295	20014265
Trigger	8929889	8929889	8931525	8931525	8931067	8931067	8929879
$p_{\mathrm{T}}^{e} > 30\,\mathrm{GeV}$	5292160	5292160	5294271	5294271	5293677	5293677	5292189
Veto tight++	4295796	4295796	4297481	4297481	4296947	4296947	4295834
One tight++	4295712	4295712	4297396	4297396	4296862	4296862	4295749
Trigger matching	4295602	4295602	4297287	4297287	4296753	4296753	4295640
Jet cleaning	4294097	4294097	4295780	4295780	4295246	4295246	4294135
LAr simple veto	4289584	4289584	4291264	4291264	4290732	4290732	4289625
$E_{\mathrm{T}}^{\mathrm{cone20}}$	4237674	4237674	4239316	4239316	4238786	4238786	4237721
$p_{\mathrm{T}}^{\mathrm{cone40}}$	4145871	4145871	4147451	4147451	4146989	4146989	4145913
$p_{\mathrm{T}}^{W} < 30\,\mathrm{GeV}$	3090798	3090798	3091962	3091962	3091593	3091593	3090832
$m_{\mathrm{T}}^{W} > 60\,\mathrm{GeV}$	2637405	2637405	2638831	2638831	2638600	2638600	2637380
$E_{\mathrm{T}}^{\mathrm{miss}} > 30\,\mathrm{GeV}$	2335608	2335608	2336993	2336993	2336727	2336727	2335603

Table C.1: Cutflow comparison for the $W^- \to e^- \overline{\nu}_e$ sample of the electron channel. Compared are the number of events for the interesting production sets and the 2017 analysis for the given cut stages. The numbers are normalised to their cross-section and an integrated luminosity of $\mathcal{L}_{\mathrm{int}} = 4\,591.01\,\mathrm{pb}^{-1}$.

C.1.2 Validation of distributions

This section contains additional information on the validation of the distributions of the muon and the electron channel. Furthermore, it completes the comparison of the reprocessed distributions to the 2017 analysis of Figs. 5.2 and 5.3.

Muon channel For the η_ℓ plots in the muon channel of the 2017 analysis, the original binning was 24 equidistant bins between −2.4 and 2.4 of width 0.2. At some point, this was changed to a variable binning. The rebinning was performed in the plotting step. Each bin content was divided by the new bin width and multiplied by the "old" bin width of 0.2. This rebinning procedure was still applied in the plotting step even though the binning was changed before the production step in the definition of the histogram. So the η_ℓ plots of the muon channel are not correct in the publication of the 2017 analysis, the plots in the supporting document were not affected by this bug. By repeating this bug, the wrong paper plots were exactly reproduced.

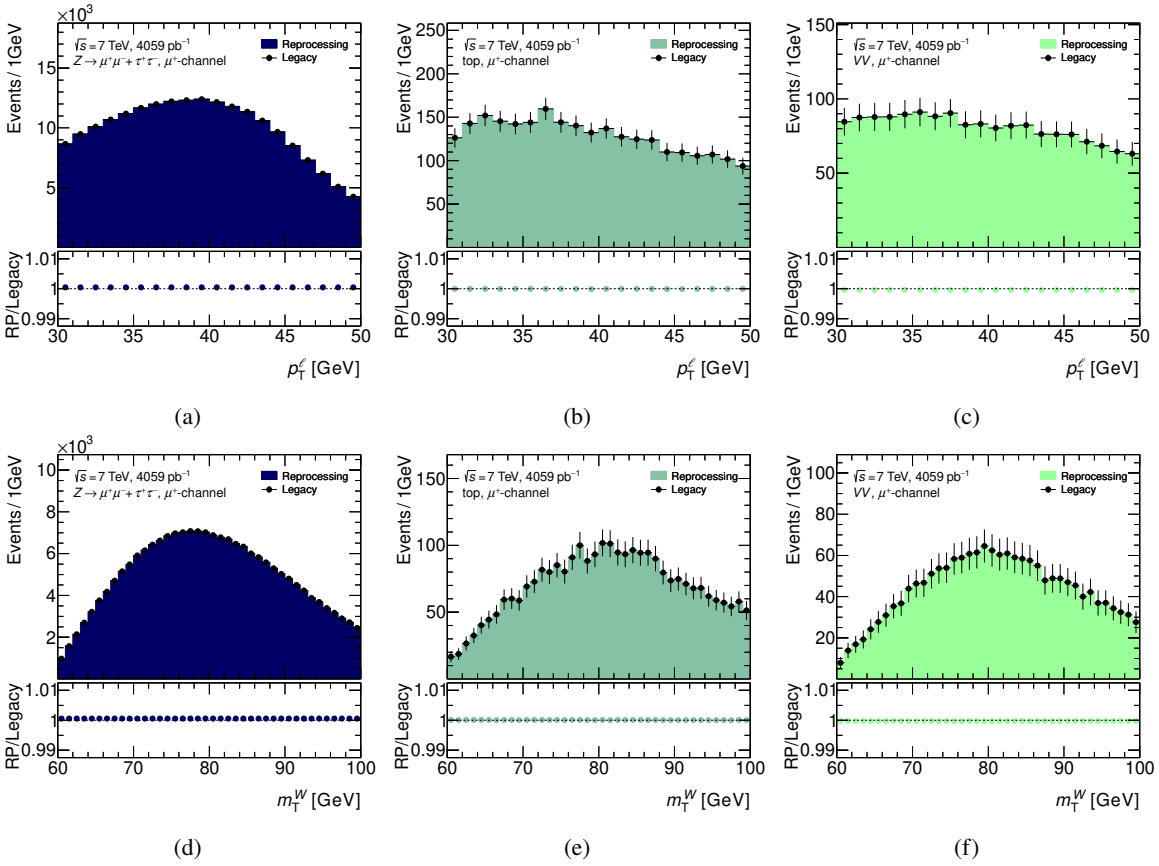

Figure C.1: Comparison between distributions published in the 2017 analysis (black dots) and the reprocessed samples (coloured filled areas) for negatively charged muons and the observables p_{T}^{ℓ} (first row) and m_{T}^{W} (second row). Shown are the distributions of three background processes.

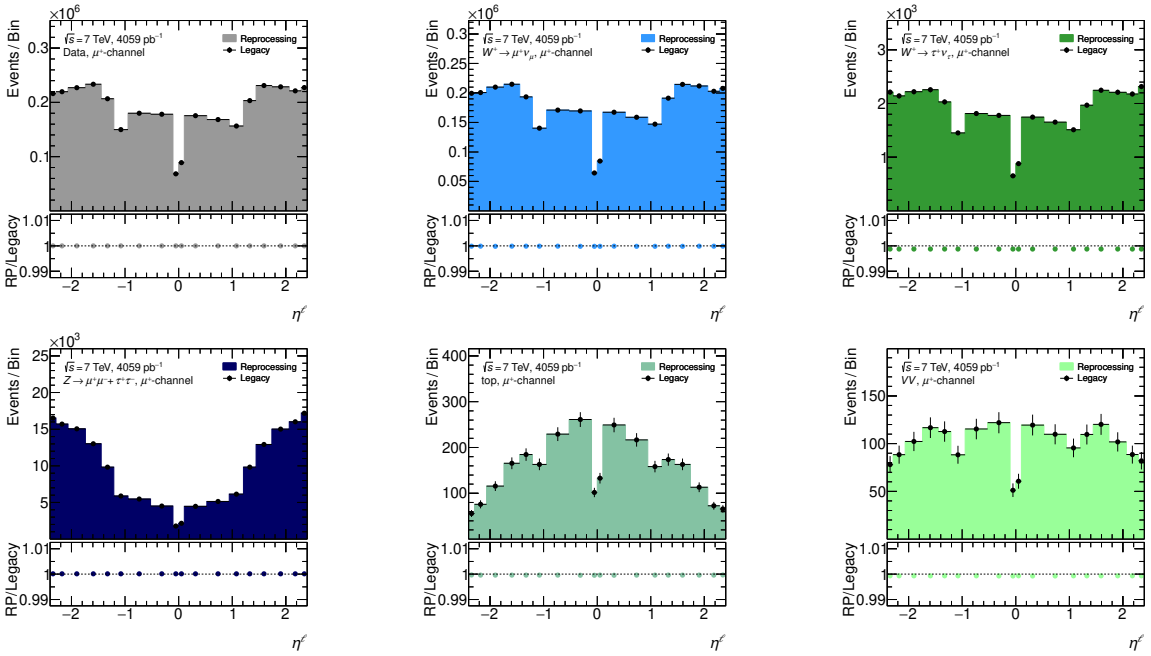

Figure C.2: Comparison between distributions published in the 2017 analysis (black dots) and the reprocessed samples (coloured filled areas) for muons with charge $q = +1$ and the observable η_ℓ. Shown are the distributions of the data sample and the five MC samples.

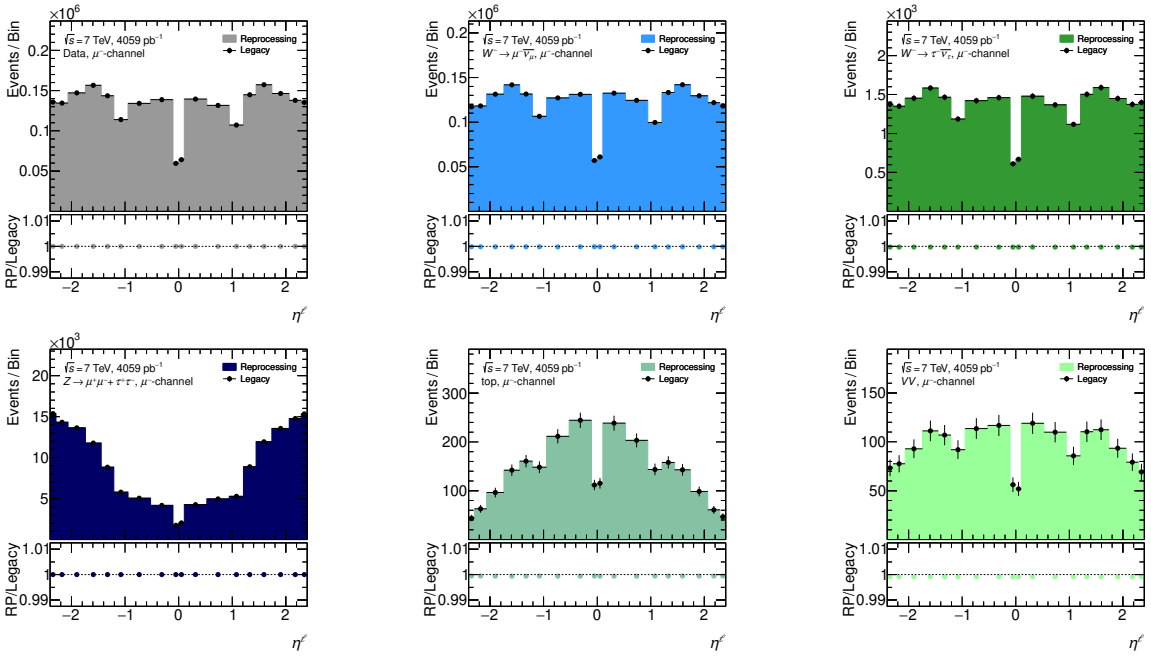

Figure C.3: Comparison between distributions published in the 2017 analysis (black dots) and the reprocessed samples (coloured filled areas) for muons with charge $q = -1$ and the observable η_ℓ. Shown are the distributions of the data sample and the five MC samples.

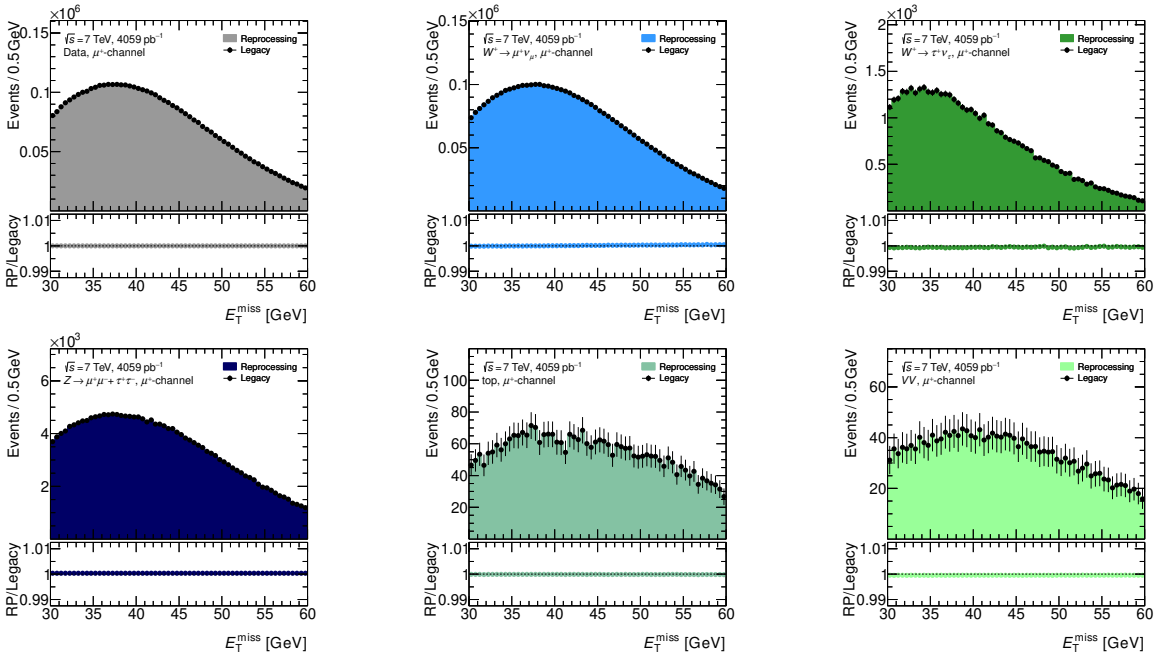

Figure C.4: Comparison between distributions published in the 2017 analysis (black dots) and the reprocessed samples (coloured filled areas) for muons with charge $q = +1$ and the observable $E_{\mathrm{T}}^{\mathrm{miss}}$. Shown are the distributions of the data sample and the five MC samples.

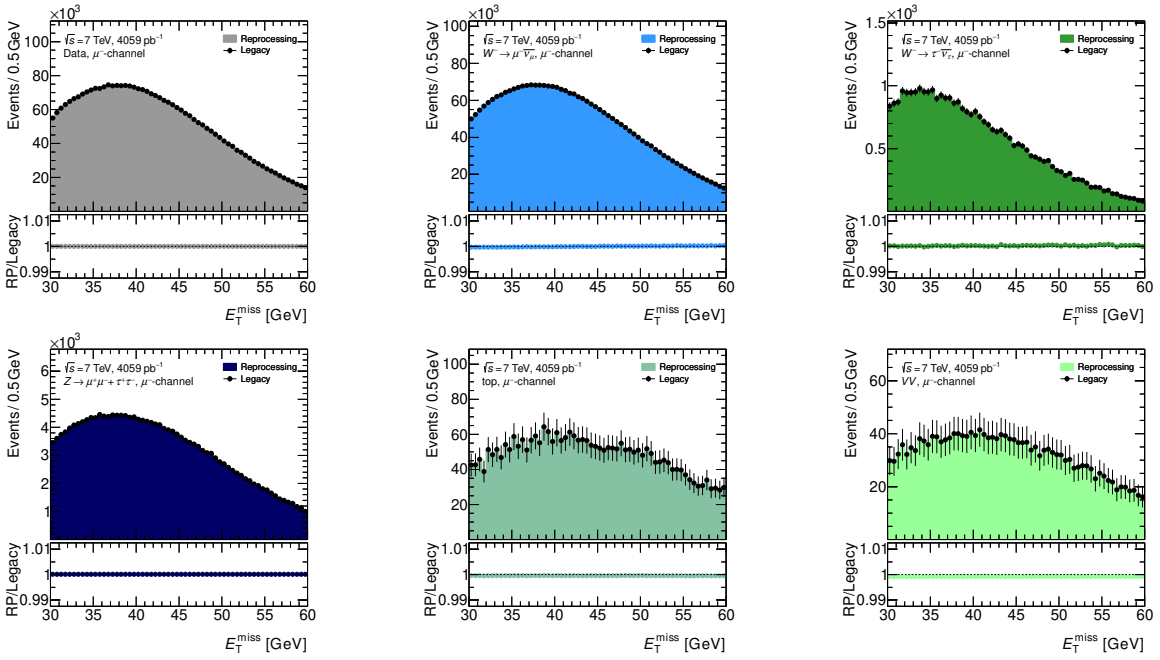

Figure C.5: Comparison between distributions published in the 2017 analysis (black dots) and the reprocessed samples (coloured filled areas) for muons with charge $q = -1$ and the observable $E_{\mathrm{T}}^{\mathrm{miss}}$. Shown are the distributions of the data sample and the five MC samples.

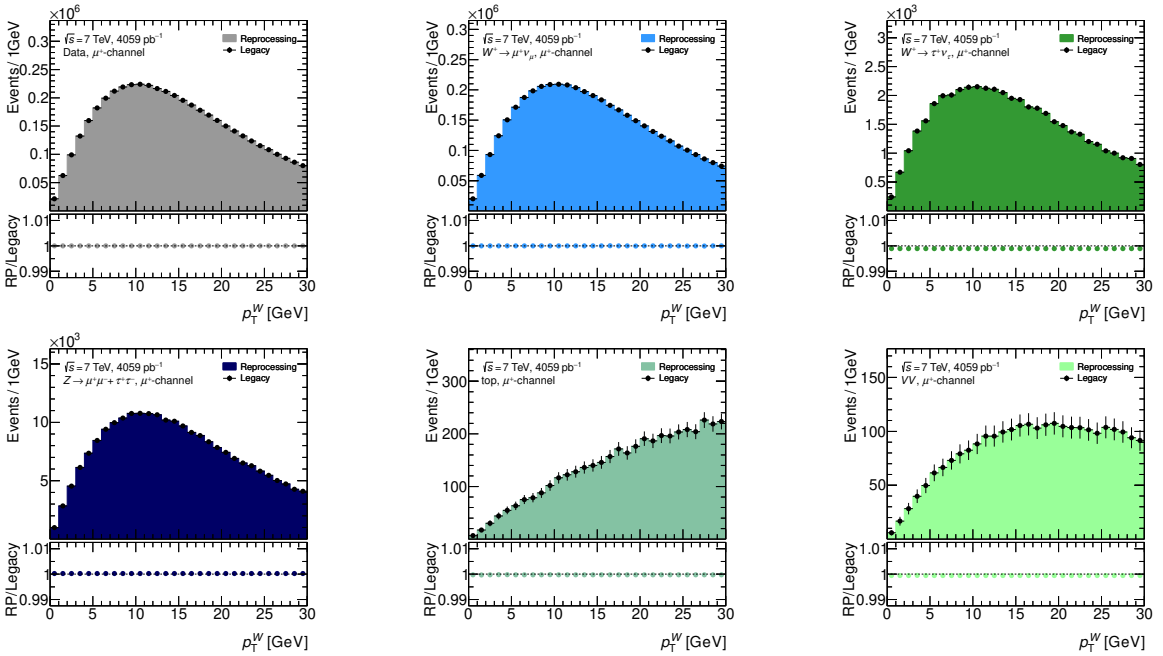

Figure C.6: Comparison between distributions published in the 2017 analysis (black dots) and the reprocessed samples (coloured filled areas) for muons with charge $q = +1$ and the observable u_{T}. Shown are the distributions of the data sample and the five MC samples.

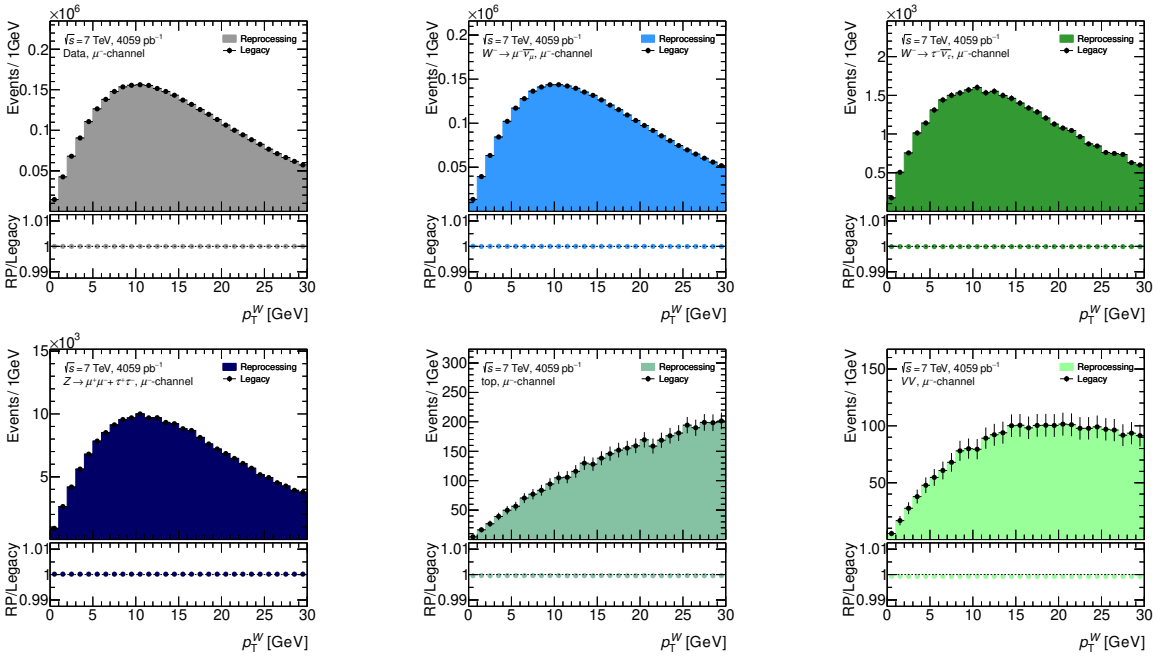

Figure C.7: Comparison between distributions published in the 2017 analysis (black dots) and the reprocessed samples (coloured filled areas) for muons with charge $q = -1$ and the observable u_{T}. Shown are the distributions of the data sample and the five MC samples.

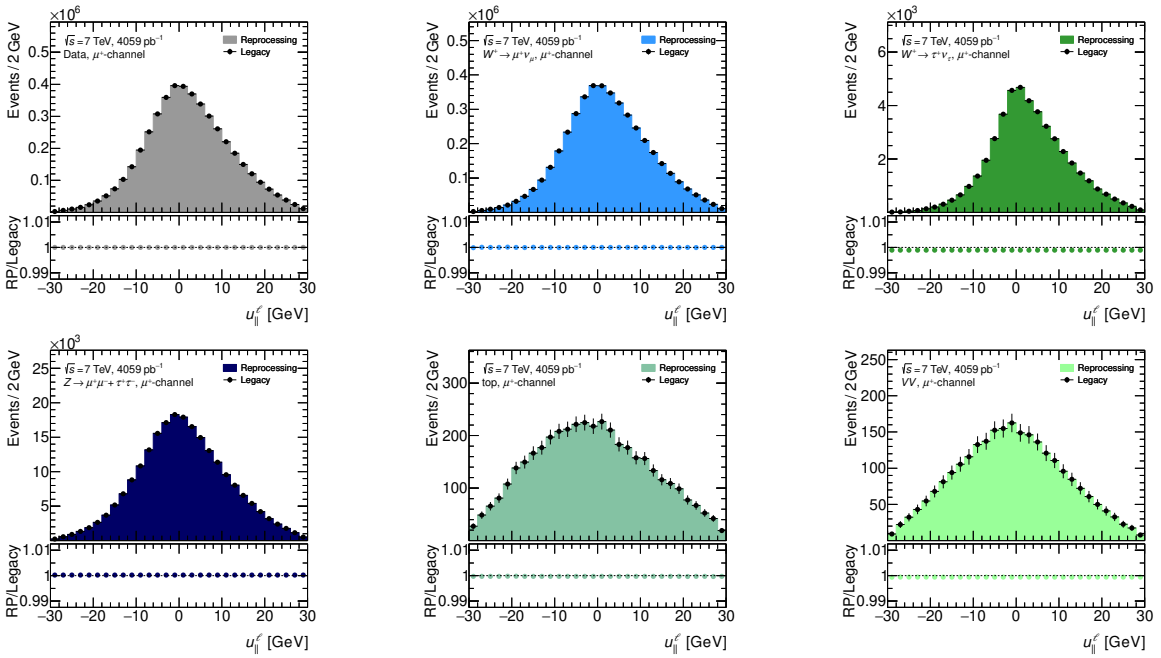

Figure C.8: Comparison between distributions published in the 2017 analysis (black dots) and the reprocessed samples (coloured filled areas) for muons with charge $q = +1$ and the observable $u_{\parallel}^{\ell}$. Shown are the distributions of the data sample and the five MC samples.

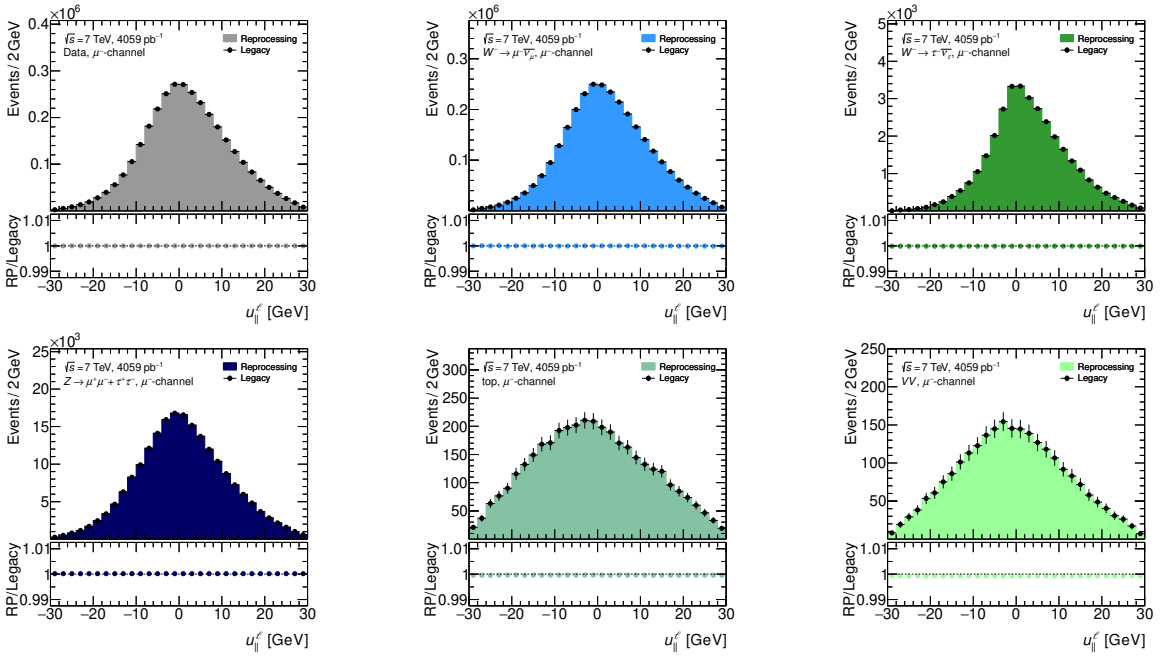

Figure C.9: Comparison between distributions published in the 2017 analysis (black dots) and the reprocessed samples (coloured filled areas) for muons with charge $q = -1$ and the observable $u_{\parallel}^{\ell}$. Shown are the distributions of the data sample and the five MC samples.

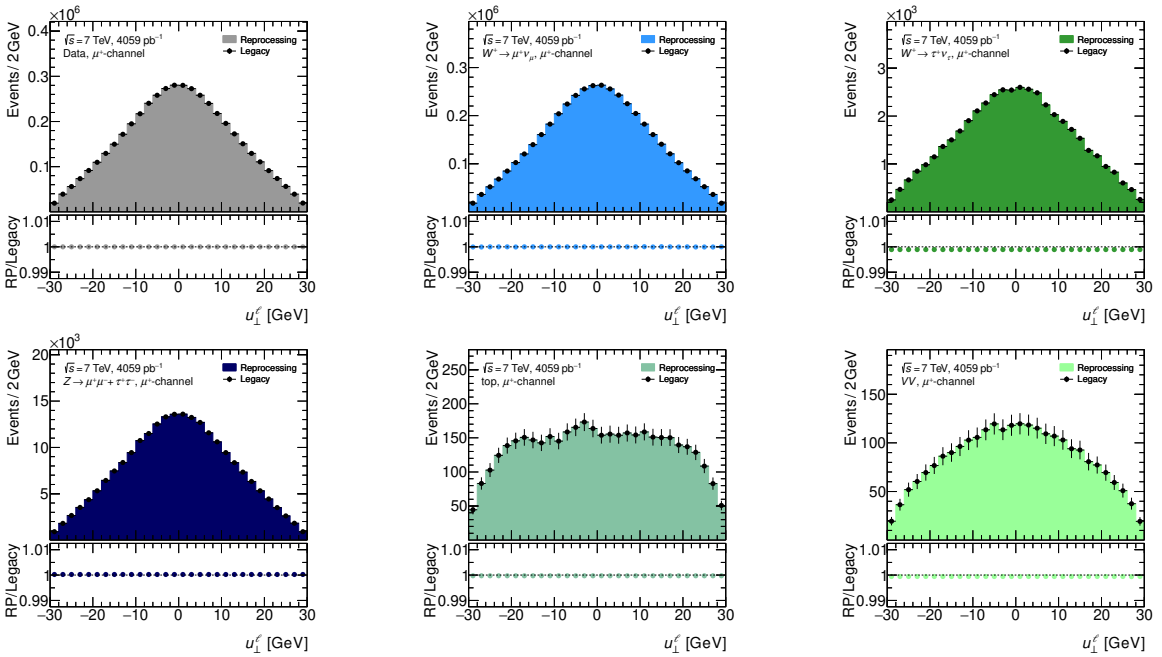

Figure C.10: Comparison between distributions published in the 2017 analysis (black dots) and the reprocessed samples (coloured filled areas) for muons with charge $q = +1$ and the observable $u_\perp^\ell$. Shown are the distributions of the data sample and the five MC samples.

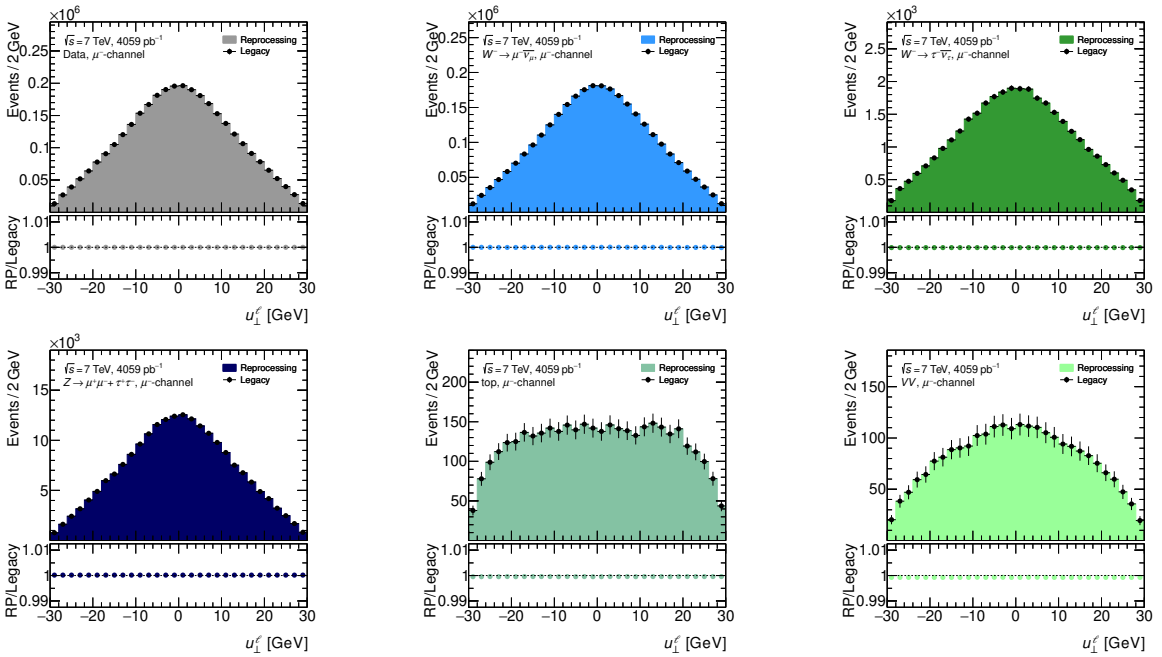

Figure C.11: Comparison between distributions published in the 2017 analysis (black dots) and the reprocessed samples (coloured filled areas) for muons with charge $q = -1$ and the observable $u_\perp^\ell$. Shown are the distributions of the data sample and the five MC samples.

Electron channel The η_ℓ plots in the electron channel were erroneously rebinned with the same procedure as for the muons. This did not have any effect on the bin contents as the bins had a width of 0.2 except for the bin between 1.82–2.0. This bin content was artificially multiplied by $0.2/0.18 = 1.1111$. This explains why exactly 90 % of the old bin content was reproduced. The plots in the supporting document were not affected by this bug.

The electron recoil plots of the 2017 analysis were produced including the data file containing 721 276 events.

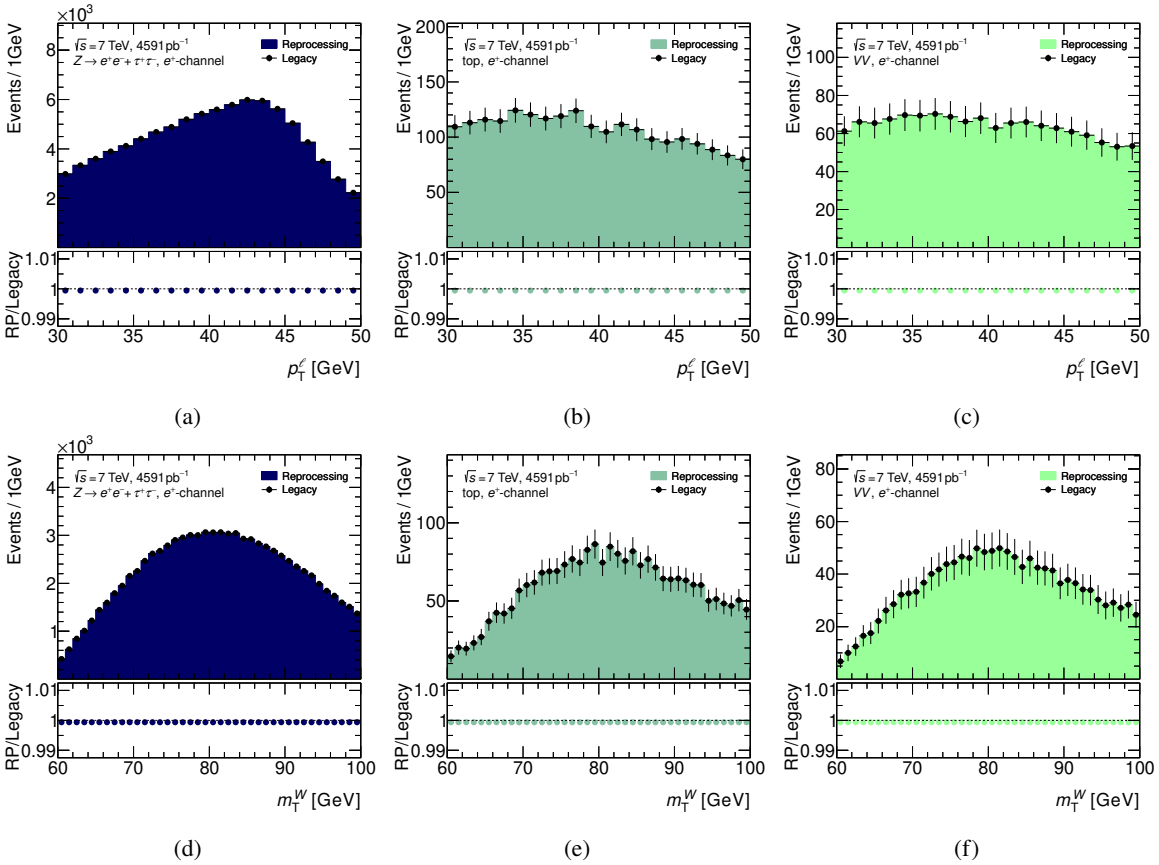

Figure C.12: Comparison between distributions published in the 2017 analysis (black dots) and the reprocessed samples (coloured filled areas) for negatively charged electrons and the observables p_T^ℓ (first row) and m_T^W (second row). Shown are the distributions of three background processes.

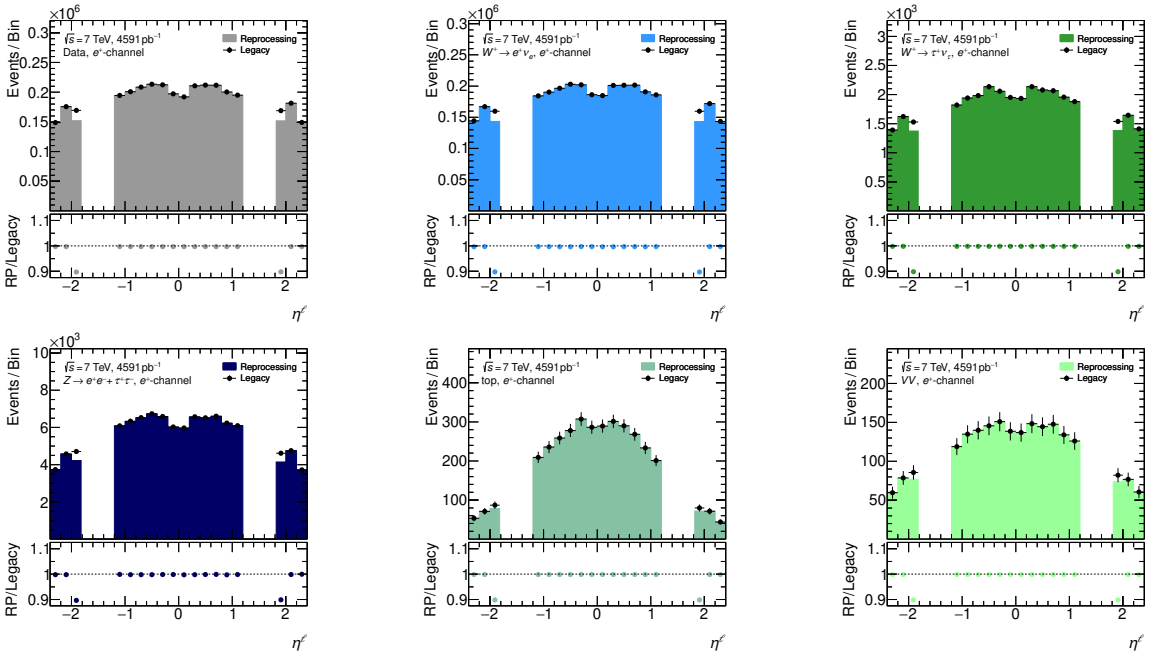

Figure C.13: Comparison between distributions published in the 2017 analysis (black dots) and the reprocessed samples (coloured filled areas) for electrons with charge $q = +1$ and the observable η_ℓ. Shown are the distributions of the data sample and the five MC samples.

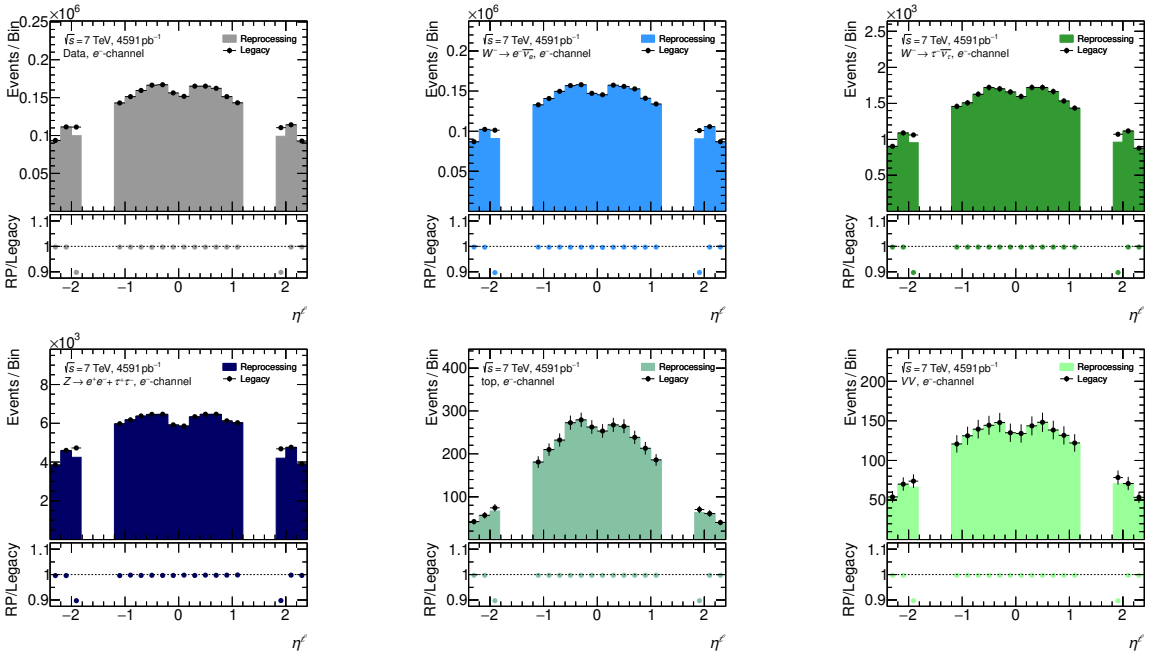

Figure C.14: Comparison between distributions published in the 2017 analysis (black dots) and the reprocessed samples (coloured filled areas) for electrons with charge $q = -1$ and the observable η_ℓ. Shown are the distributions of the data sample and the five MC samples.

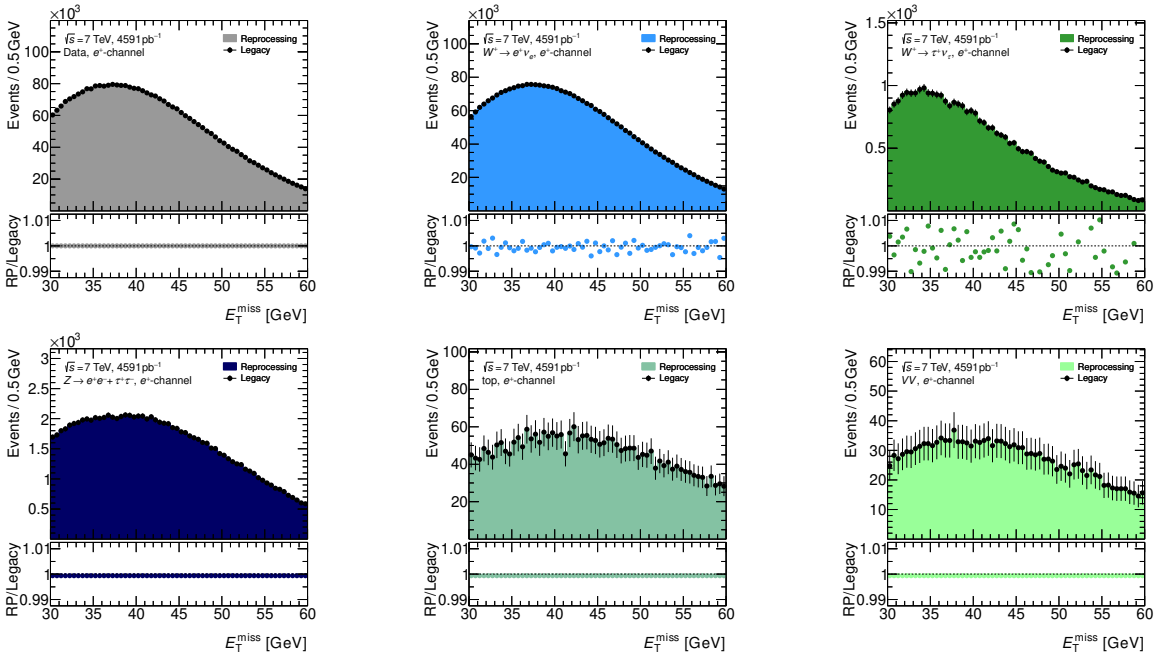

Figure C.15: Comparison between distributions published in the 2017 analysis (black dots) and the reprocessed samples (coloured filled areas) for electrons with charge $q = +1$ and the observable $E_{\mathrm{T}}^{\mathrm{miss}}$. Shown are the distributions of the data sample and the five MC samples.

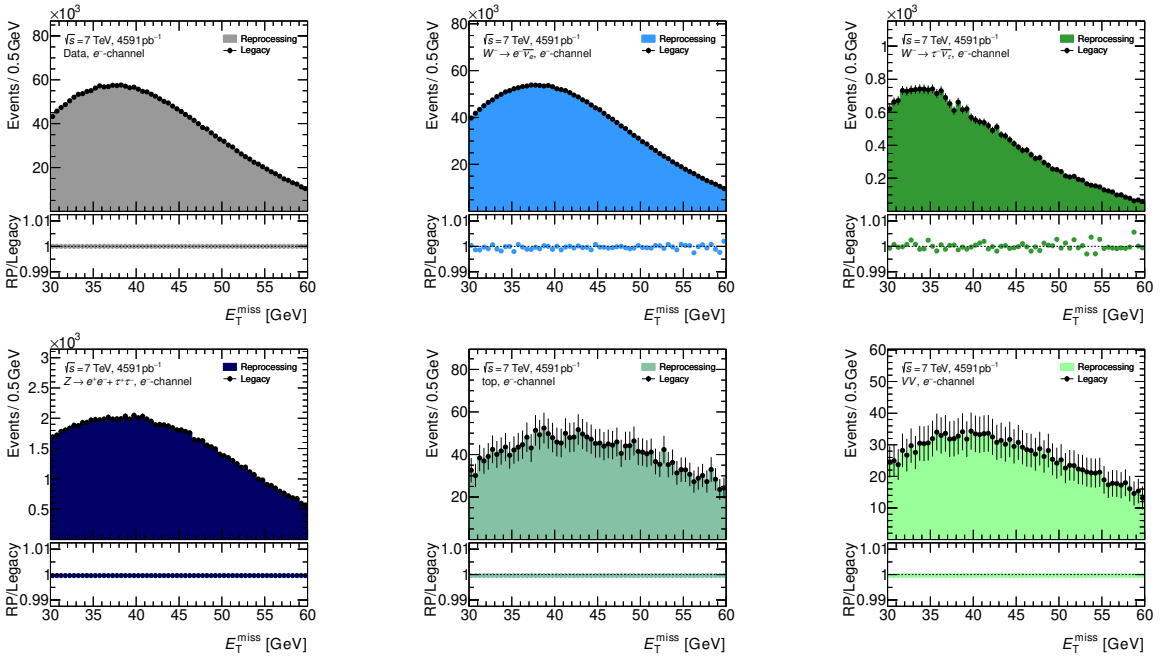

Figure C.16: Comparison between distributions published in the 2017 analysis (black dots) and the reprocessed samples (coloured filled areas) for electrons with charge $q = -1$ and the observable $E_{\mathrm{T}}^{\mathrm{miss}}$. Shown are the distributions of the data sample and the five MC samples.

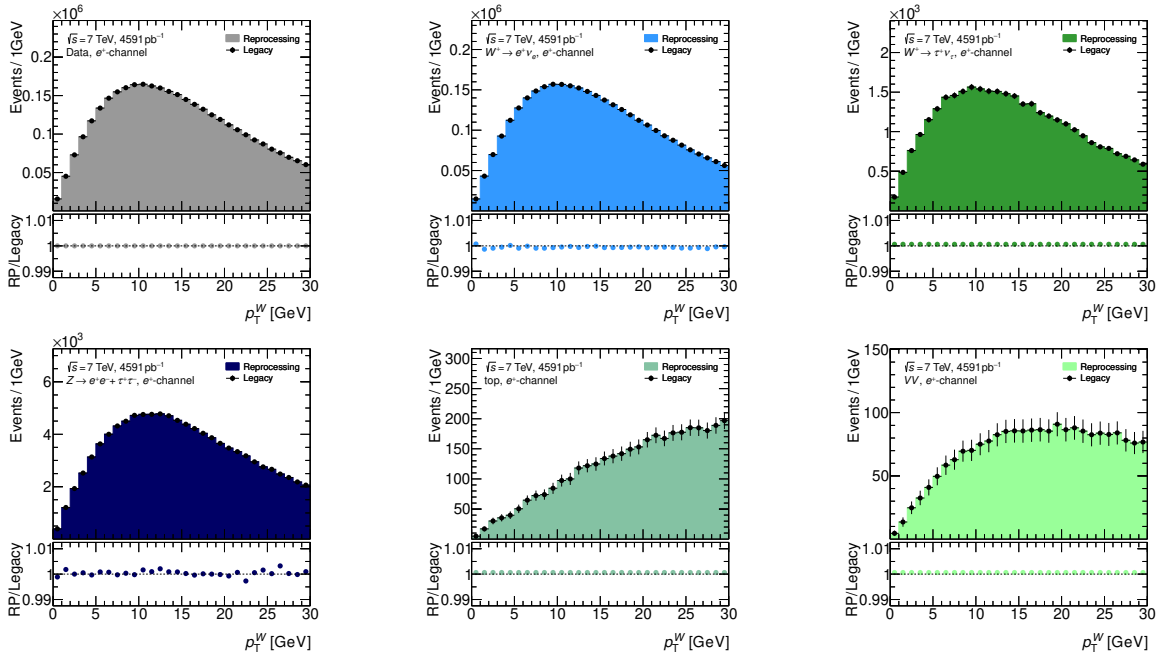

Figure C.17: Comparison between distributions published in the 2017 analysis (black dots) and the reprocessed samples (coloured filled areas) for electrons with charge $q = +1$ and the observable u_{T}. Shown are the distributions of the data sample and the five MC samples.

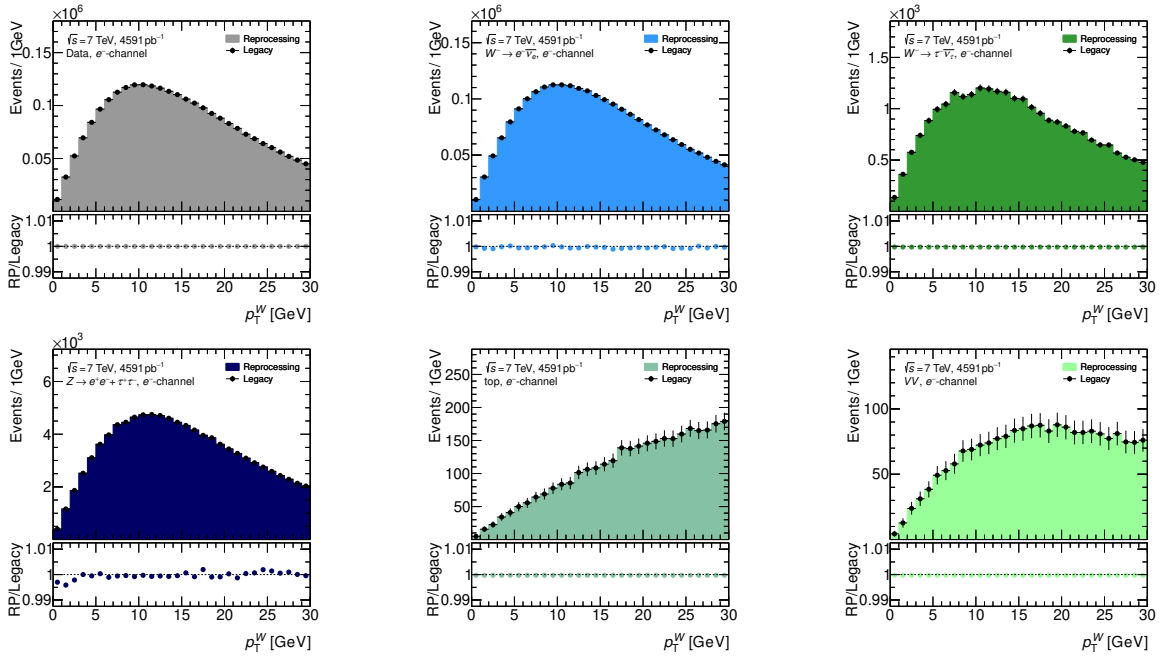

Figure C.18: Comparison between distributions published in the 2017 analysis (black dots) and the reprocessed samples (coloured filled areas) for electrons with charge $q = -1$ and the observable u_{T}. Shown are the distributions of the data sample and the five MC samples.

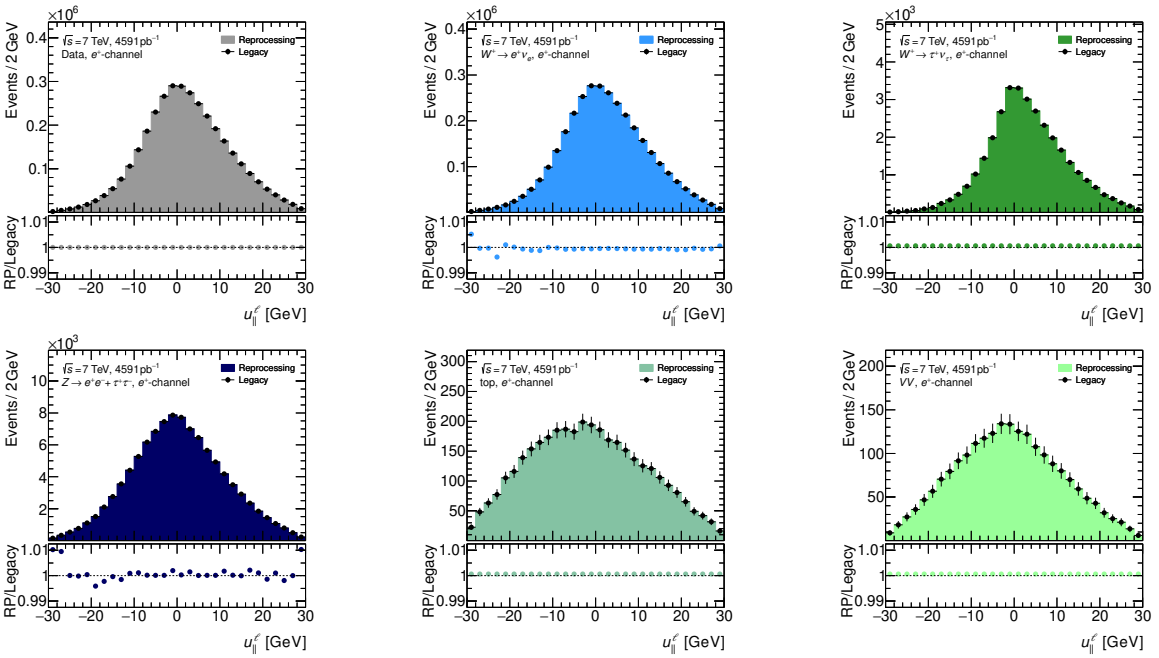

Figure C.19: Comparison between distributions published in the 2017 analysis (black dots) and the reprocessed samples (coloured filled areas) for electrons with charge $q = +1$ and the observable $u_{\parallel}^{\ell}$. Shown are the distributions of the data sample and the five MC samples.

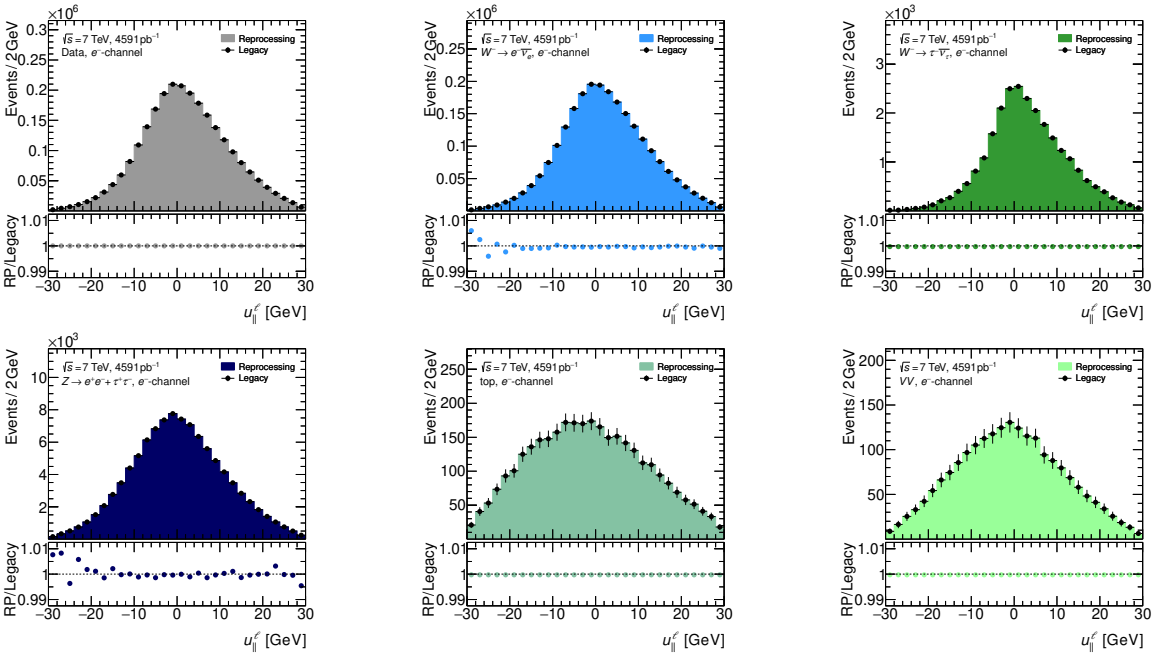

Figure C.20: Comparison between distributions published in the 2017 analysis (black dots) and the reprocessed samples (coloured filled areas) for electrons with charge $q = -1$ and the observable $u_{\parallel}^{\ell}$. Shown are the distributions of the data sample and the five MC samples.

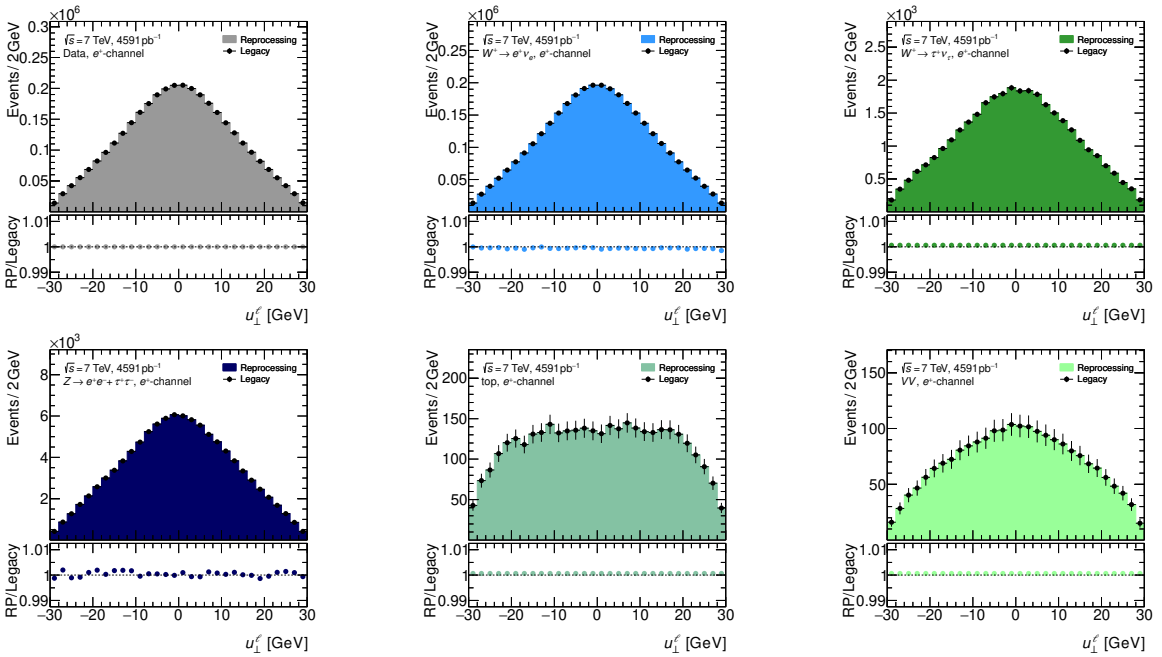

Figure C.21: Comparison between distributions published in the 2017 analysis (black dots) and the reprocessed samples (coloured filled areas) for electrons with charge $q = +1$ and the observable $u_{\perp}^{\ell}$. Shown are the distributions of the data sample and the five MC samples.

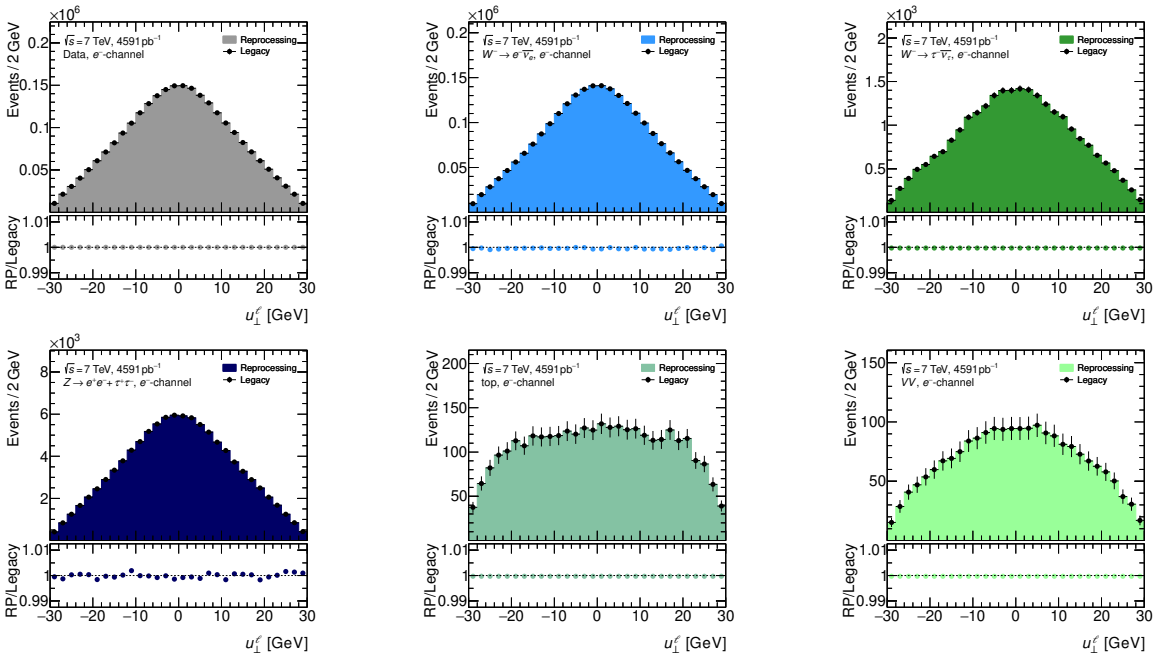

Figure C.22: Comparison between distributions published in the 2017 analysis (black dots) and the reprocessed samples (coloured filled areas) for electrons with charge $q = -1$ and the observable $u_{\perp}^{\ell}$. Shown are the distributions of the data sample and the five MC samples.

C.2 Multijet background fit

This section contains additional material about the multijet background fits.

C.2.1 Determination of the multijet contamination fraction

Muon channel Similar to Fig. 5.4, Fig. C.23 shows the data to simulation agreement of the $E_{\mathrm{T}}^{\mathrm{miss}}$ distribution in the μ^--channel for extrapolating the shape of the multijet background from different isolation regions. Figure C.24 completes the illustration of Fig. 5.5 by showing the template fit plots of the negatively charged muons.

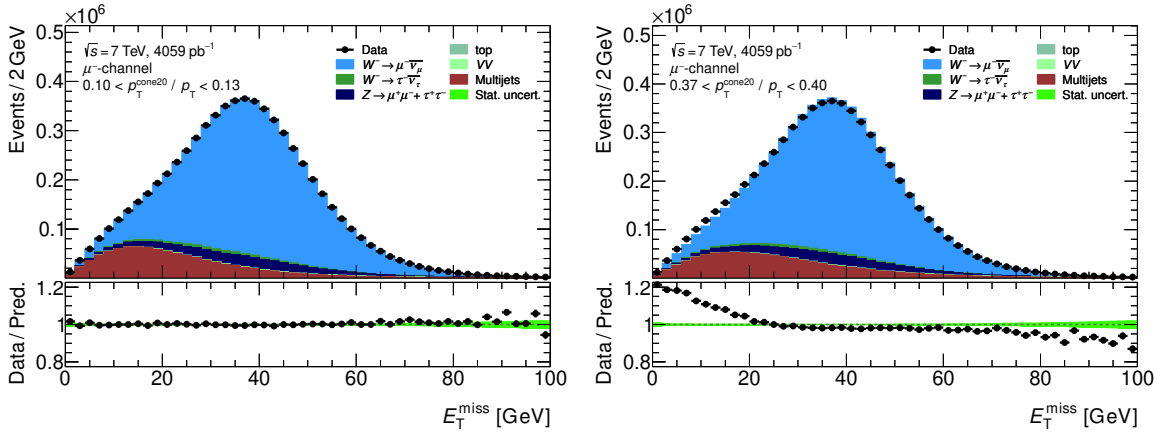

(a) (b)

Figure C.23: The $E_{\mathrm{T}}^{\mathrm{miss}}$ distribution in the μ^--channel for data and simulation where the shape of the multijet background is extracted from different isolation regions but the fraction is the same. Compared are the first CR $0.10 < p_{\mathrm{T}}^{\mathrm{cone20}}/p_{\mathrm{T}} < 0.13$ (a) and the last CR $0.37 < p_{\mathrm{T}}^{\mathrm{cone20}}/p_{\mathrm{T}} < 0.40$ (b). The cuts $E_{\mathrm{T}}^{\mathrm{miss}} > 30\,\mathrm{GeV}$, $m_{\mathrm{T}}^{W} > 60\,\mathrm{GeV}$ and $p_{\mathrm{T}}^{W} < 30\,\mathrm{GeV}$ are removed to increase the impact of the multijet background.

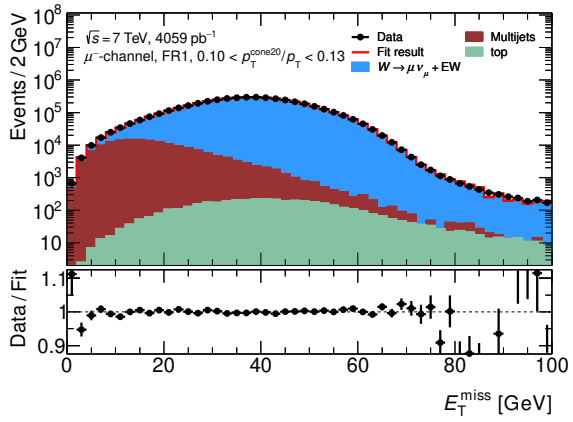

(a)

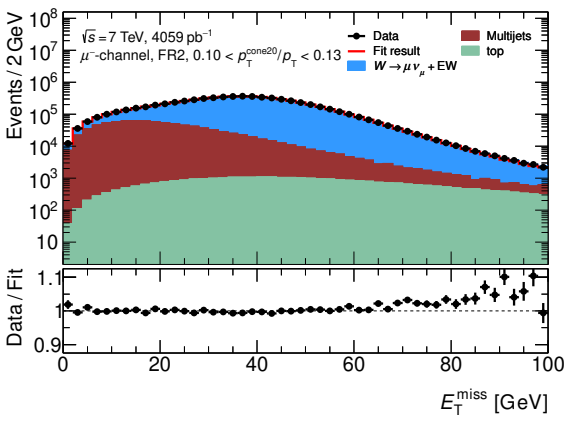

(b)

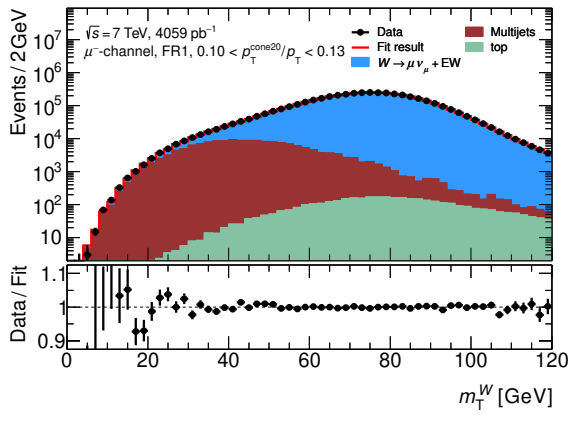

(c)

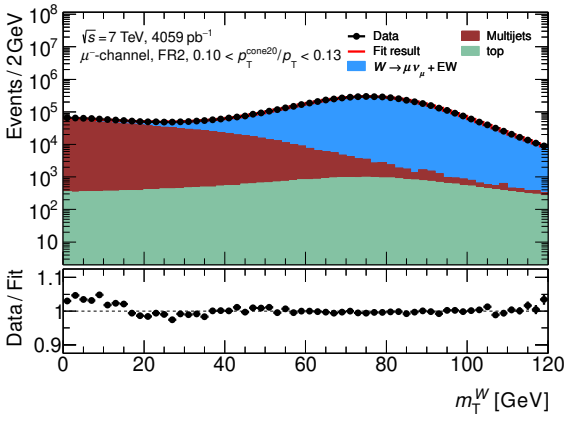

(d)

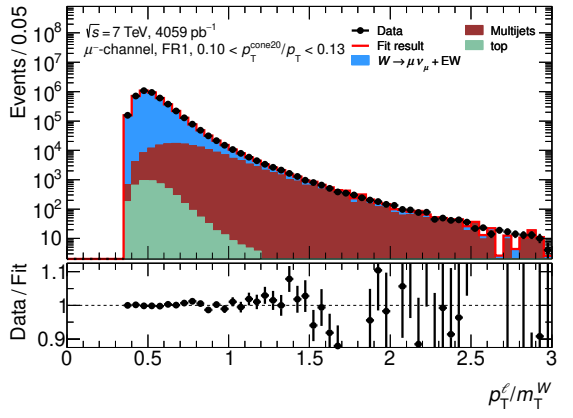

(e) FR1 without $E_{\mathrm{T}}^{\mathrm{miss}}$ and m_{T}^{W} cuts.

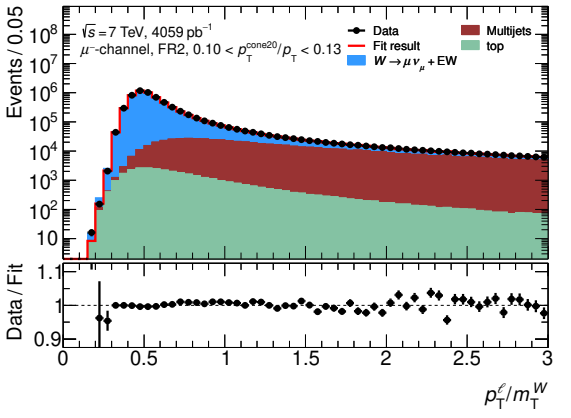

(f) FR2 without $E_{\mathrm{T}}^{\mathrm{miss}}$, m_{T}^{W}, and p_{T}^{W} cuts.

Figure C.24: Example of multijet template fits of the observables $E_{\mathrm{T}}^{\mathrm{miss}}$, m_{T}^{W}, and $p_{\mathrm{T}}^{\ell}/m_{\mathrm{T}}^{W}$ in FR1 (left) and FR2 (right) for the μ^{-}-channel. The multijet distribution is extracted from the first CR ($0.10 < p_{\mathrm{T}}^{\mathrm{cone20}}/p_{\mathrm{T}} < 0.13$). The ratio shows the agreement between data and the template fits.

Electron channel Figures C.25 and C.26 show the data to simulation agreement of the $E_{\mathrm{T}}^{\mathrm{miss}}$ distribution in the e^{+}-channel and the e^{-}-channel, respectively, for extrapolating the shape of the multijet background from different isolation regions. Figures C.27 and C.28 illustrate the template fits in the electron channel for three kinematic distributions and the two fitting regions.

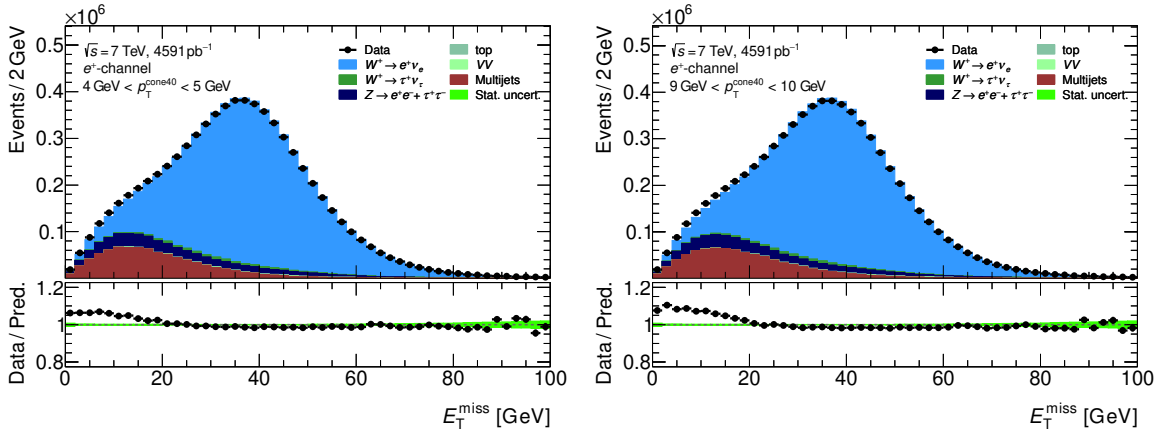

(a) (b)

Figure C.25: The $E_{\mathrm{T}}^{\mathrm{miss}}$ distribution in the e^{+}-channel for data and simulation where the shape of the multijet background is extracted from different isolation regions but the fraction is the same. Compared are the first CR $4\,\mathrm{GeV} < p_{\mathrm{T}}^{\mathrm{cone40}} < 5\,\mathrm{GeV}$ (a) and the last CR $9\,\mathrm{GeV} < p_{\mathrm{T}}^{\mathrm{cone40}} < 10\,\mathrm{GeV}$ (b). The cuts $E_{\mathrm{T}}^{\mathrm{miss}} > 30\,\mathrm{GeV}$, $m_{\mathrm{T}}^{W} > 60\,\mathrm{GeV}$ and $p_{\mathrm{T}}^{W} < 30\,\mathrm{GeV}$ are removed to increase the impact of the multijet background.

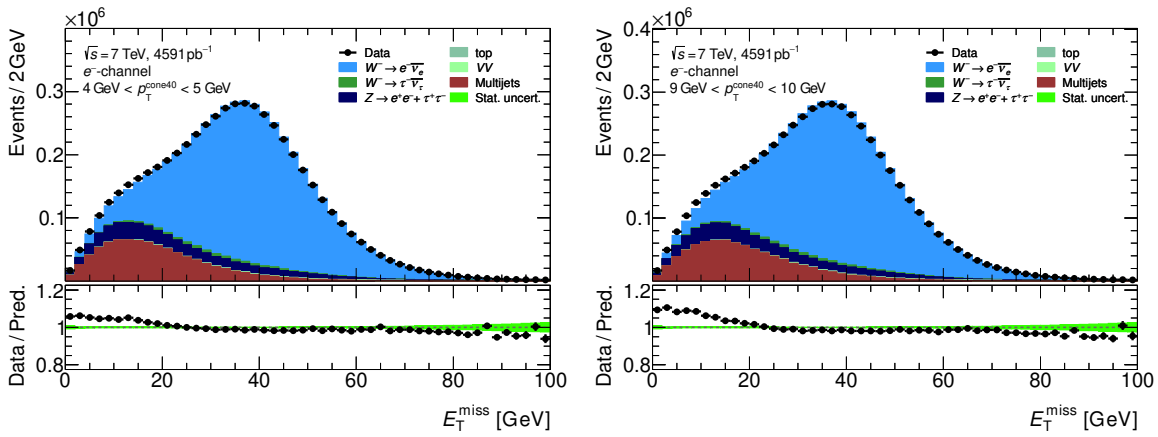

(a) (b)

Figure C.26: The $E_{\mathrm{T}}^{\mathrm{miss}}$ distribution in the e^{-}-channel for data and simulation where the shape of the multijet background is extracted from different isolation regions but the fraction is the same. Compared are the first CR $4\,\mathrm{GeV} < p_{\mathrm{T}}^{\mathrm{cone40}} < 5\,\mathrm{GeV}$ (a) and the last CR $9\,\mathrm{GeV} < p_{\mathrm{T}}^{\mathrm{cone40}} < 10\,\mathrm{GeV}$ (b). The cuts $E_{\mathrm{T}}^{\mathrm{miss}} > 30\,\mathrm{GeV}$, $m_{\mathrm{T}}^{W} > 60\,\mathrm{GeV}$ and $p_{\mathrm{T}}^{W} < 30\,\mathrm{GeV}$ are removed to increase the impact of the multijet background.

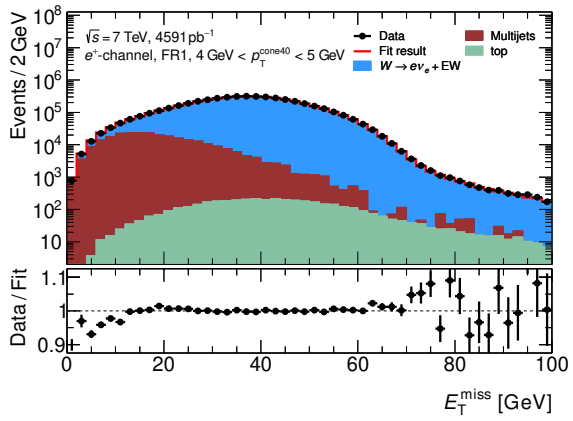

(a)

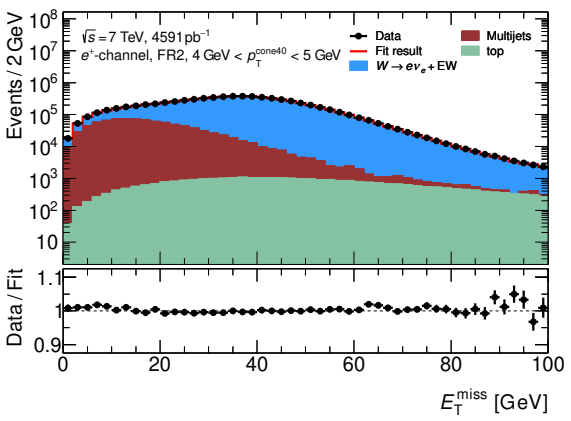

(b)

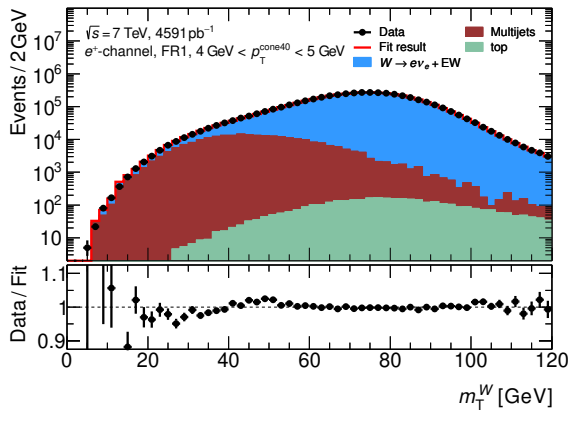

(c)

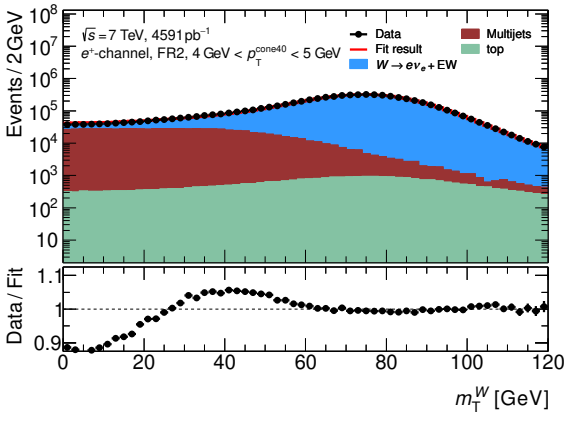

(d)

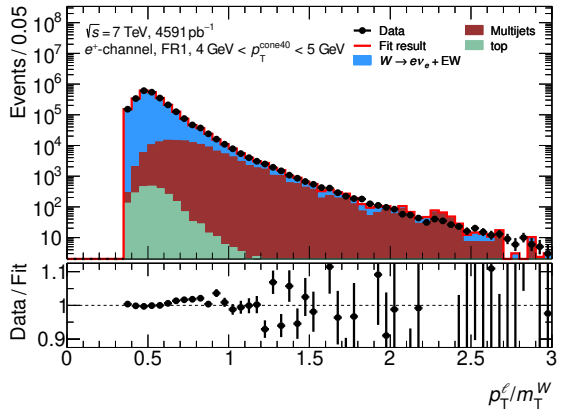

(e) FR1 without $E_{\mathrm{T}}^{\mathrm{miss}}$ and m_{T}^{W} cuts.

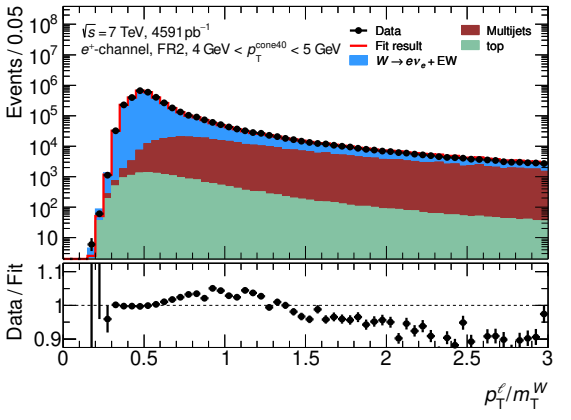

(f) FR2 without $E_{\mathrm{T}}^{\mathrm{miss}}$, m_{T}^{W}, and p_{T}^{W} cuts.

Figure C.27: Example of multijet template fits of the observables $E_{\mathrm{T}}^{\mathrm{miss}}$, m_{T}^{W}, and $p_{\mathrm{T}}^{\ell}/m_{\mathrm{T}}^{W}$ in FR1 (left) and FR2 (right) for the e^{+}-channel. The multijet distribution is extracted from the first CR ($4\,\mathrm{GeV} < p_{\mathrm{T}}^{\mathrm{cone40}} < 5\,\mathrm{GeV}$). The ratio shows the agreement between data and the template fits.

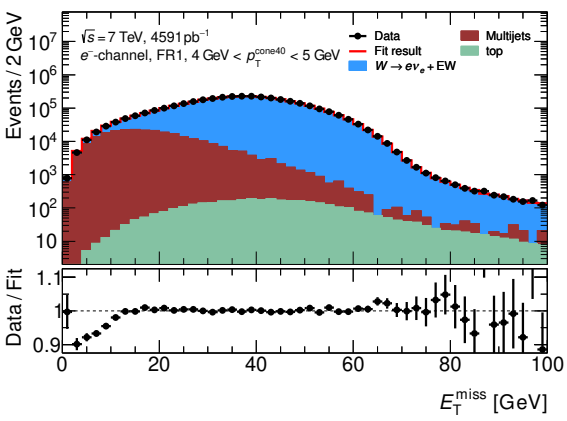

(a)

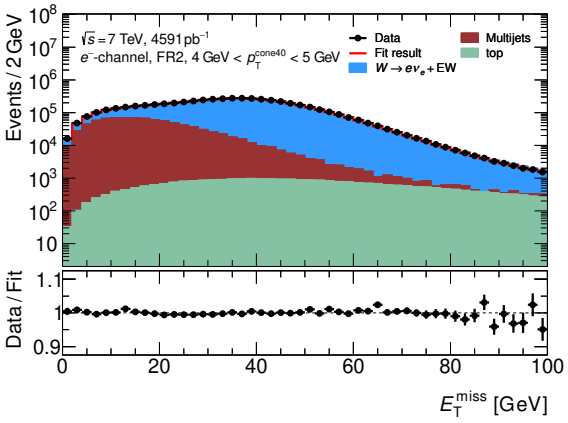

(b)

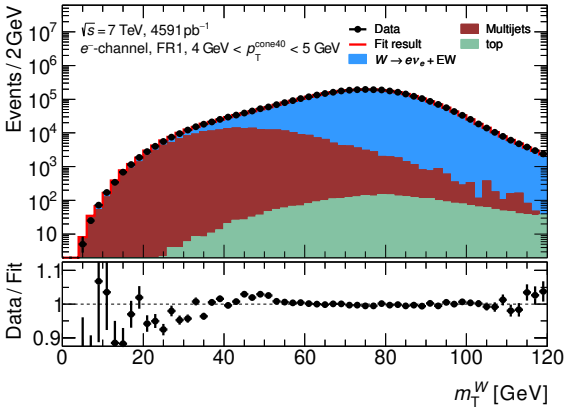

(c)

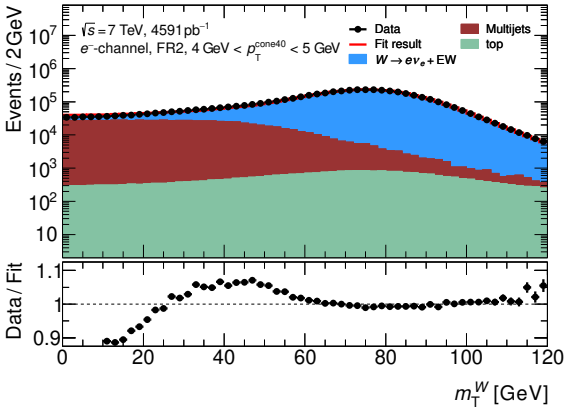

(d)

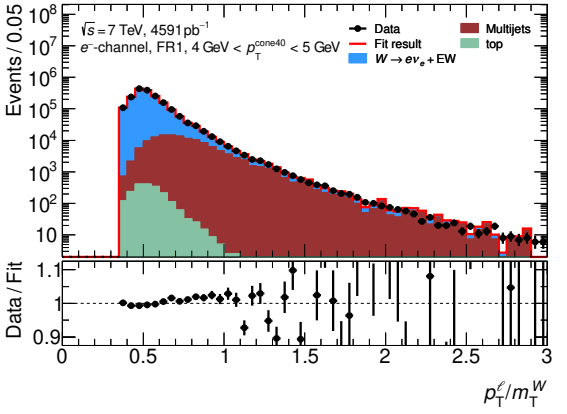

(e) FR1 without $E_{\mathrm{T}}^{\mathrm{miss}}$ and m_{T}^{W} cuts.

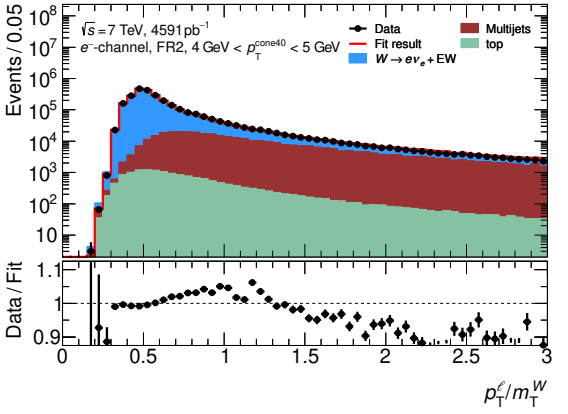

(f) FR2 without $E_{\mathrm{T}}^{\mathrm{miss}}$, m_{T}^{W}, and p_{T}^{W} cuts.

Figure C.28: Example of multijet template fits of the observables $E_{\mathrm{T}}^{\mathrm{miss}}$, m_{T}^{W}, and $p_{\mathrm{T}}^{\ell}/m_{\mathrm{T}}^{W}$ in FR1 (left) and FR2 (right) for the e^{-}-channel. The multijet distribution is extracted from the first CR ($4\,\mathrm{GeV} < p_{\mathrm{T}}^{\mathrm{cone40}} < 5\,\mathrm{GeV}$). The ratio shows the agreement between data and the template fits.

C.2.2 Extrapolation of the multijet background shapes

The ratio of the two control regions to extrapolate the shape of the multijet background into the SR is shown in Fig. C.29 for the observable m_{T}^{W}. As Fig. 5.9 shows the agreement of the p_{T}^{ℓ} multijet background shape, Figs. C.30, C.31 and C.32 illustrate the agreement for the observables m_{T}^{W}, $E_{\mathrm{T}}^{\mathrm{miss}}$, and p_{T}^{W}.

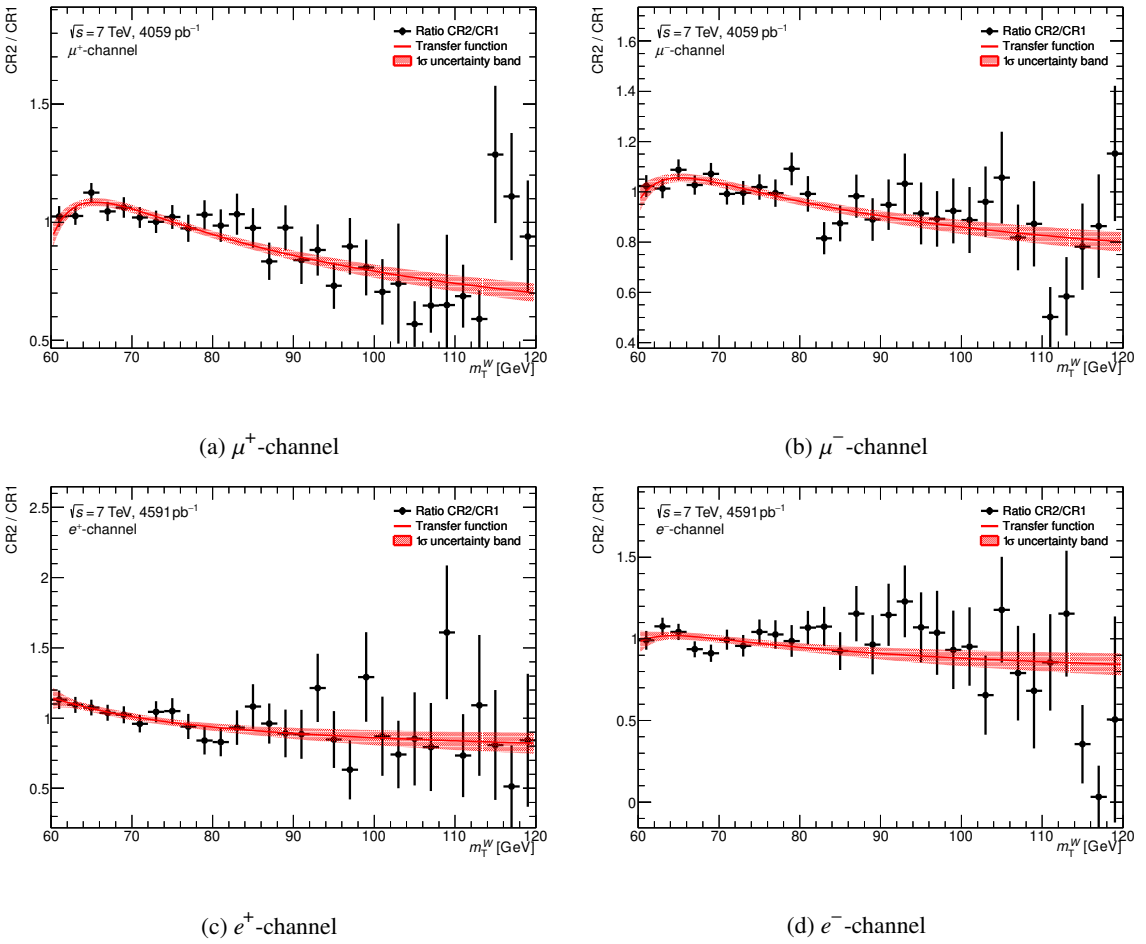

(a) μ^{+}-channel

(b) μ^{-}-channel

(c) e^{+}-channel

(d) e^{-}-channel

Figure C.29: Ratio of the multijet background distributions of the two control regions CR2/CR1 for the m_{T}^{W} distribution. The black points represent the ratio of the histograms of the two CRs, the red line refers to the fitted transfer function and the red band corresponds to the 1 σ confidence interval. The shape extrapolation is shown for W^{+} (left) and W^{-} (right) for the muon (upper row) and the electron channel (lower row).

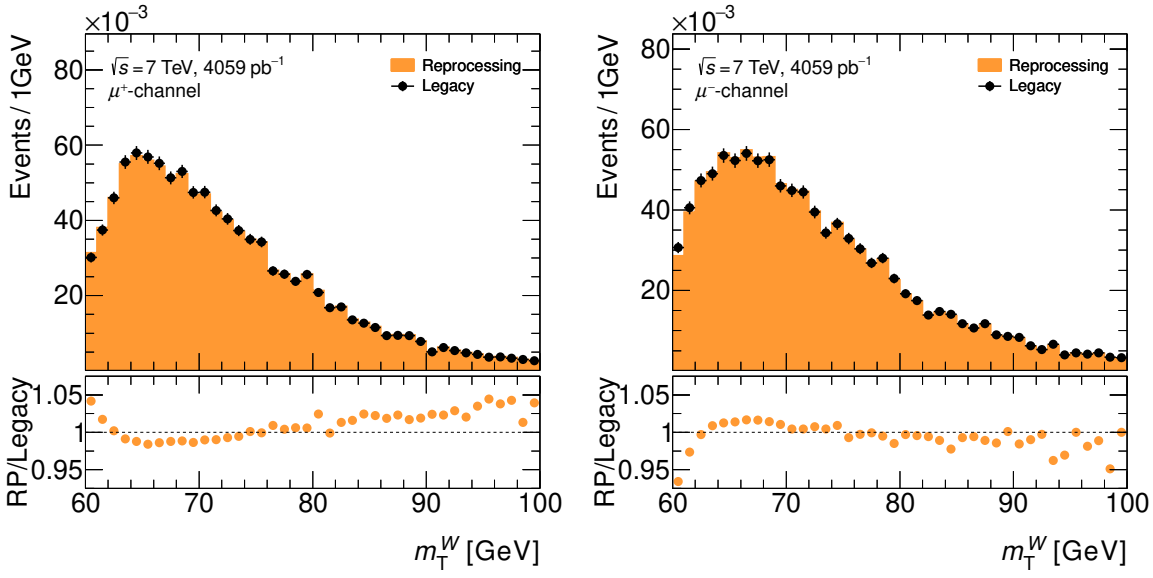

(a) μ^+-channel

(b) μ^--channel

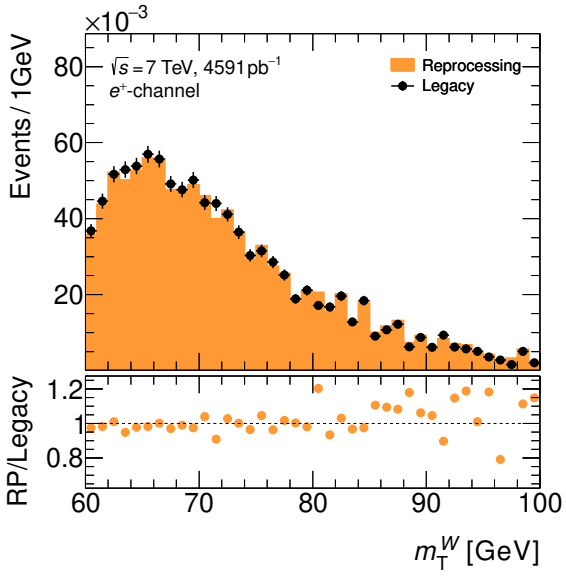

(c) e^+-channel

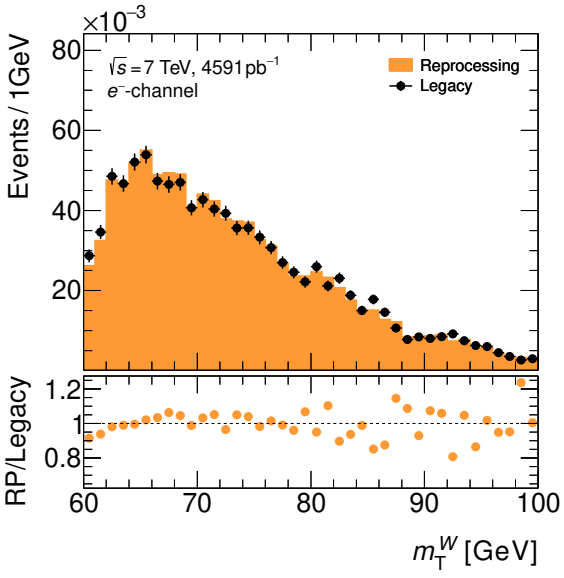

(d) e^--channel

Figure C.30: Comparison of the multijet background shape between the 2017 analysis and the reanalysis in the observable m_{T}^{W}. The agreement is shown for W^+ (left) and W^- (right) for the muon (upper row) and the electron channel (lower row).

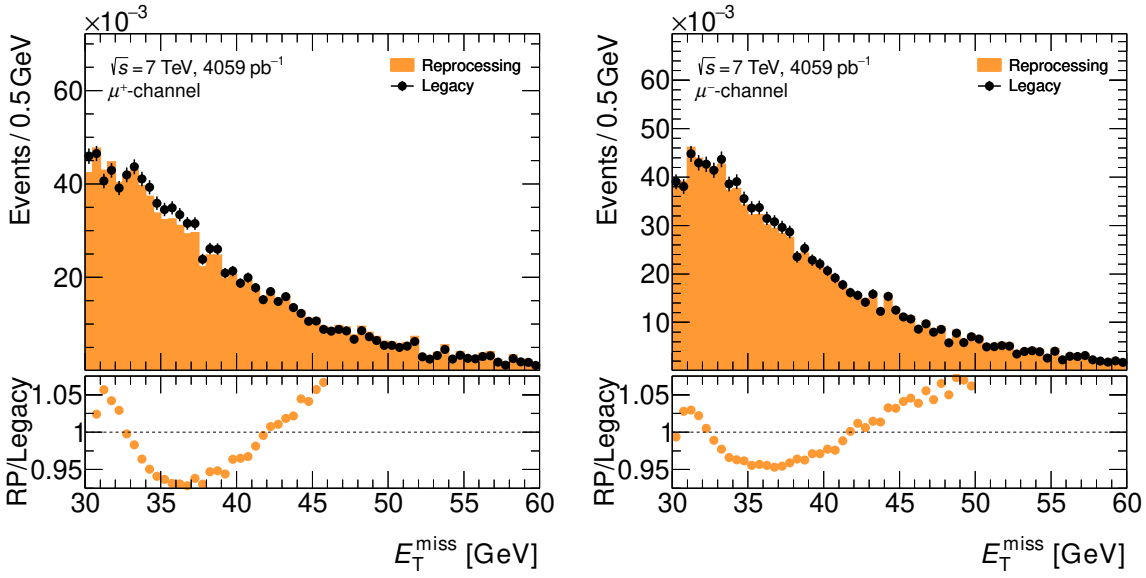

(a) μ^+-channel

(b) μ^--channel

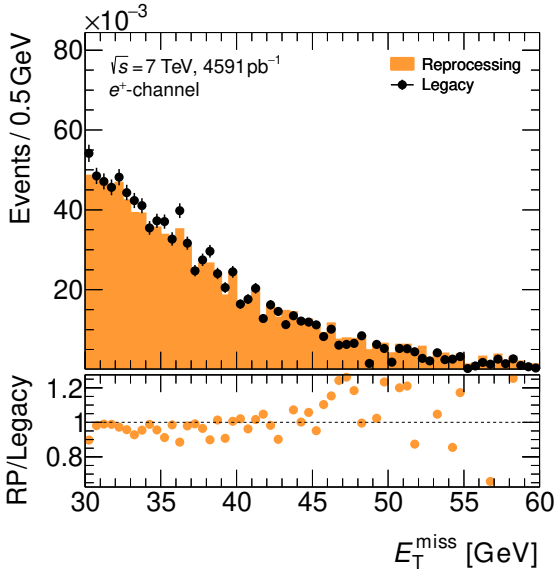

(c) e^+-channel

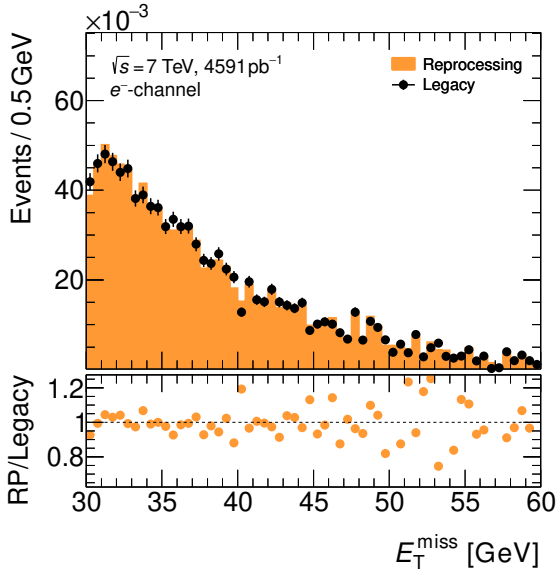

(d) e^--channel

Figure C.31: Comparison of the multijet background shape between the 2017 analysis and the reanalysis in the observable $E_{\mathrm{T}}^{\mathrm{miss}}$. The agreement is shown for W^+ (left) and W^- (right) for the muon (upper row) and the electron channel (lower row).

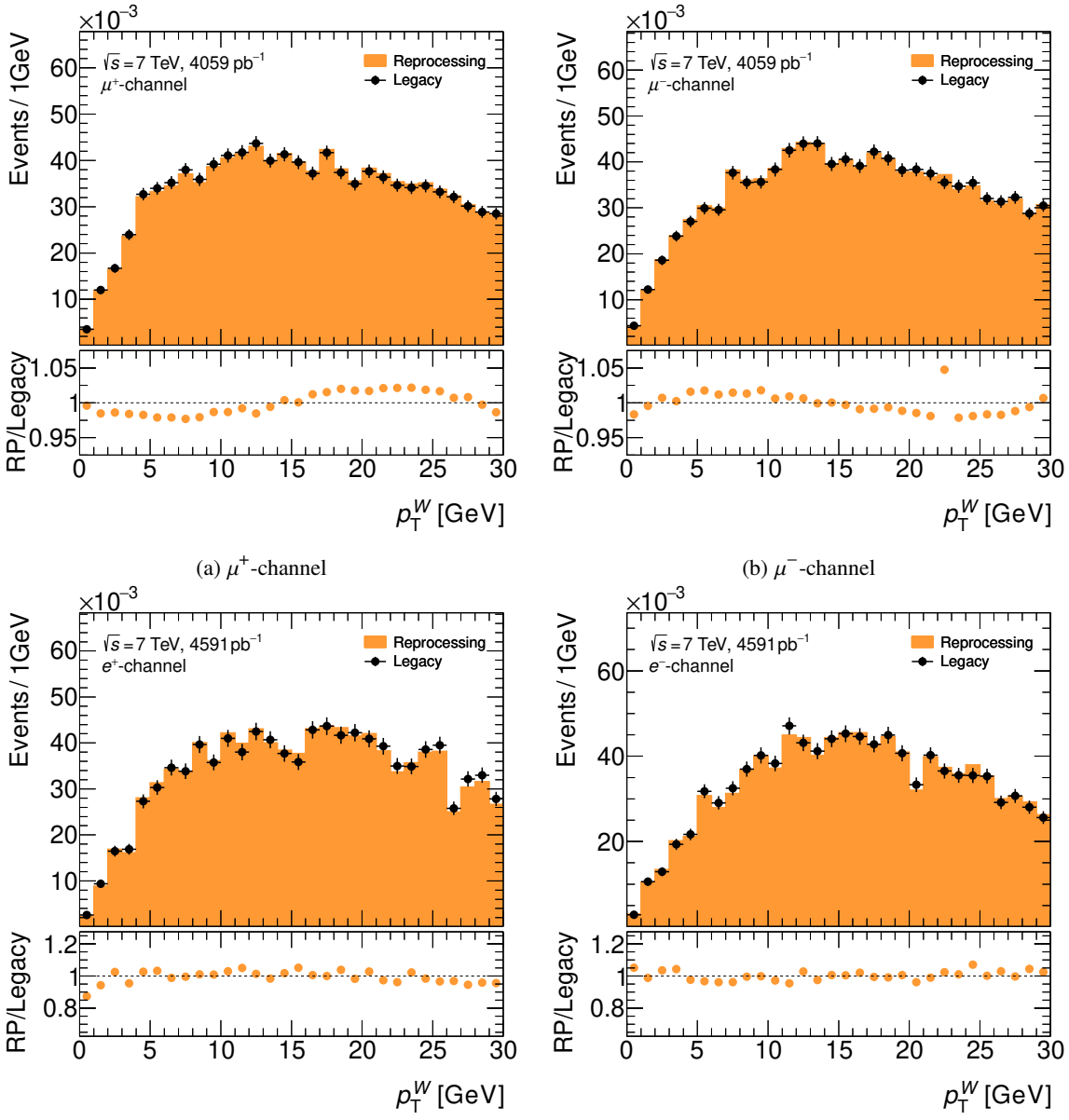

(a) μ^+-channel

(b) μ^--channel

(c) e^+-channel

(d) e^--channel

Figure C.32: Comparison of the multijet background shape between the 2017 analysis and the reanalysis in the observable p_{T}^{W}. The agreement is shown for W^+ (left) and W^- (right) for the muon (upper row) and the electron channel (lower row).

APPENDIX D

Additional information on the statistical methods

This chapter contains additional information about the interpolation methods used in the PLH fit.

D.1 One-dimensional interpolation

Linear interpolation Figure D.1 is the full version of Figure 6.4 without zoom.

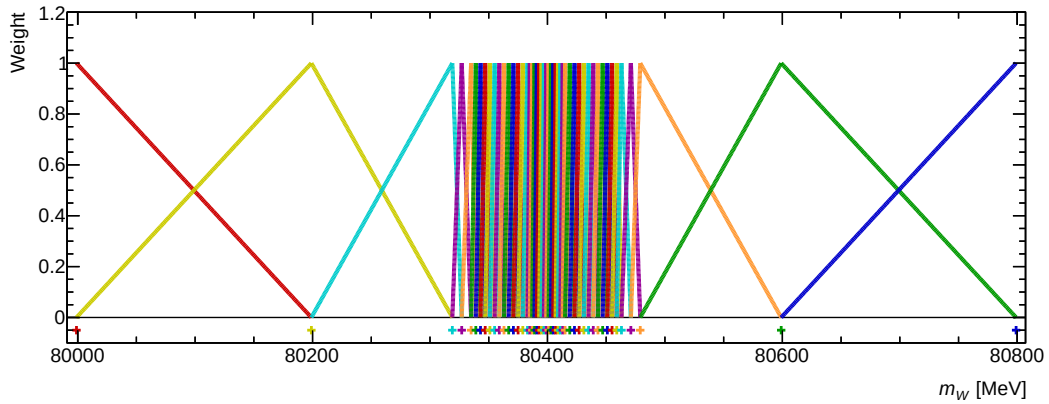

Figure D.1: Graphical illustration of the linear morphing for the W-boson mass over the whole template range. The different mass templates are indicated with a coloured cross below the x-axis, whereas the weight for each template of the interpolation function is inked with the same colour as the template itself.

Quadratic interpolation The linear template weighting introduced in Section 6.2.2 can be generalised with the help of Lagrange polynomials first mentioned in 1779 [189]. The description follows mainly [190]. Again, each template of any desired mass value m_W can be achieved with the relation

$$T\left(m_W\right) = \sum_{k=1}^{N} w_k\left(m_W\right) T_k, \tag{D.1}$$

Each template T can be approximated by a sum of quadratic functions of the form

$$T\left(\Delta m_W\right) = c_1 + c_2 \cdot \Delta m_W + c_3 \cdot \left(\Delta m_W\right)^2, \tag{D.2}$$

where Δm_W is the mass difference with respect to the lowest of the three mass values in a given interval. In every interval, three templates T_1, T_2, and T_3 are needed to derive the prefactors of the

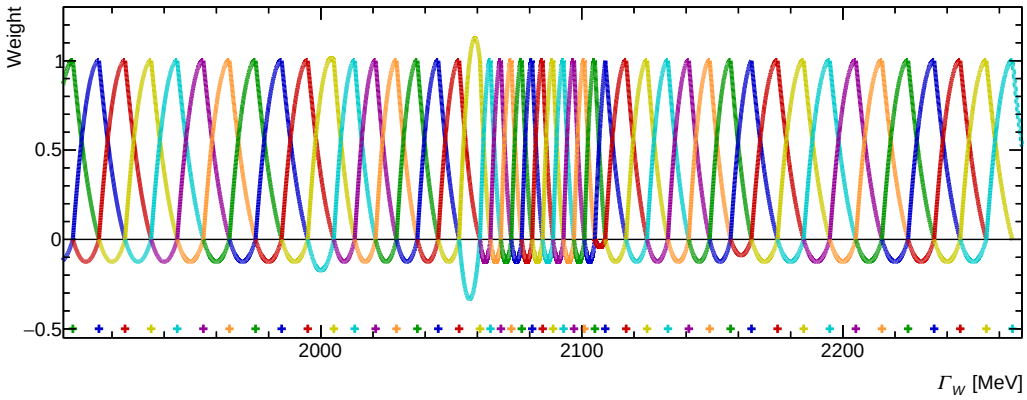

Figure D.2: Graphical illustration of the quadratic morphing for the W-boson width. The different mass templates are indicated with a coloured cross below the x-axis, whereas the weight for each template of the interpolation function is inked with the same colour as the template itself.

quadratic function with a set of three equations constituting like

$$\begin{aligned}
T_1 &= c_1 \\
T_2 &= c_1 + c_2 \cdot \left(m_{W,1} - m_{W,2}\right) + c_3 \cdot \left(m_{W,1} - m_{W,2}\right)^2 \\
T_3 &= c_1 + c_2 \cdot \left(m_{W,1} - m_{W,3}\right) + c_3 \cdot \left(m_{W,1} - m_{W,3}\right)^3
\end{aligned}$$

This can be formulated using the matrix notation

$$t = A \cdot c,$$

where the vectors t and c look like

$$t = \begin{pmatrix} T_1 \\ T_2 \\ T_3 \end{pmatrix}, \qquad c = \begin{pmatrix} c_1 \\ c_2 \\ c_3 \end{pmatrix}$$

and the matrix A is defined as

$$A = \begin{pmatrix} 1 & 0 & 0 \\ 1 & m_{W,1} - m_{W,2} & \left(m_{W,1} - m_{W,2}\right)^2 \\ 1 & m_{W,1} - m_{W,3} & \left(m_{W,1} - m_{W,3}\right)^2 \end{pmatrix}.$$

The second and third elements of the first row are zero as $m_{W,1} - m_{W,1} = 0$ which is the reason why the masses are taken as a difference to the lowest mass value of the three mass templates. This simplifies the inversion of the matrix A which is necessary to get the coefficients c_1, c_2, and c_3 via the relation

$$c = A^{-1} \cdot t,$$

such that Equation (D.2) expands to

$$\begin{aligned} T\left(\Delta m_W\right) &= c_1 + c_2 \cdot \Delta m_W + c_3 \cdot \left(\Delta m_W\right)^2 \\ &= T_1\left(a_{11} + a_{12} \cdot \Delta m_{W,1} + a_{13} \cdot \left(\Delta m_{W,1}\right)^2\right) + T_2\left(a_{22} \cdot \Delta m_{W,2} + a_{23} \cdot \left(\Delta m_{W,2}\right)^2\right) \\ &+ T_3\left(a_{32} \cdot \Delta m_{W,3} + a_{33} \cdot \left(\Delta m_{W,3}\right)^2\right) \\ &= \sum_{i=1}^{3} T_i N_i\left(\Delta m_W\right), \end{aligned}$$

where the a_{ij} is the element of the inverted matrix A^{-1} in row i and column j. The elements a_{21} and

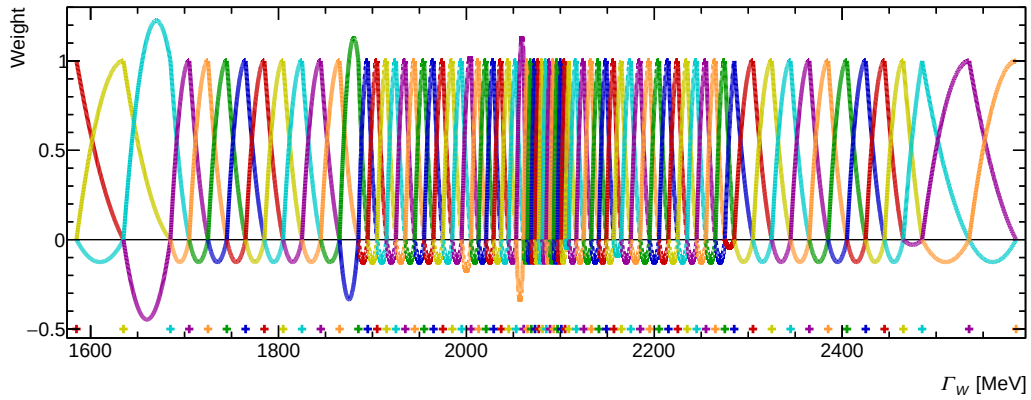

Figure D.3: Graphical illustration of the quadratic morphing for the W-boson width over the whole template range. The different mass templates are indicated with a coloured cross below the x-axis, whereas the weight for each template of the interpolation function is inked with the same colour as the template itself.

a_{31} are zero due to vanishing elements in the first row of the matrix A. The N_i are the weight factors for the three different templates T_1, T_2, and T_3 in the interval $m_{W,1} < T < m_{W,2}$, whereas the next three templates are used for deriving the functions in the next interval. This procedure continues until the last interval which uses the weight factors N_i in addition in the interval $m_{W,2} < T < m_{W,3}$. The weight functions of any template are shown in Figures D.2 and D.3. The entity of N_i belonging to a given template T_k defines the weights w_k of Equation (D.1) which are piecewise-defined weight functions.

D.2 Two-dimensional interpolation

The simultaneous fit of two morphing parameters acting as POIs is outlined and implemented in `TRExFitter`. The working principle is the same as for the morphing of one parameter, but the template $T\left(m_W, \Gamma_W\right)$ depends on the W-boson mass and width value. The individual weights are based again on a piecewise linear interpolation in both dimensions

$$w_k\left(m_W, \Gamma_W\right) = \begin{cases} \left(1 - \frac{m_W^k - m_W}{m_W^k - m_W^{k-1}}\right) * \left(1 - \frac{\Gamma_W^k - \Gamma_W}{\Gamma_W^k - \Gamma_W^{k-1}}\right), & \text{for } m_W^{k-1} \leq m_W \leq m_W^k,\ \Gamma_W^{k-1} \leq \Gamma_W \leq \Gamma_W^k \\ \left(1 - \frac{m_W^k - m_W}{m_W^k - m_W^{k-1}}\right) * \left(1 - \frac{\Gamma_W - \Gamma_W^k}{\Gamma_W^{k+1} - \Gamma_W^k}\right), & \text{for } m_W^{k-1} \leq m_W \leq m_W^k,\ \Gamma_W^k \leq \Gamma_W \leq \Gamma_W^{k+1} \\ \left(1 - \frac{m_W - m_W^k}{m_W^{k+1} - m_W^k}\right) * \left(1 - \frac{\Gamma_W^k - \Gamma_W}{\Gamma_W^k - \Gamma_W^{k-1}}\right), & \text{for } m_W^k \leq m_W \leq m_W^{k+1},\ \Gamma_W^{k-1} \leq \Gamma_W \leq \Gamma_W^k \\ \left(1 - \frac{m_W - m_W^k}{m_W^{k+1} - m_W^k}\right) * \left(1 - \frac{\Gamma_W - \Gamma_W^k}{\Gamma_W^{k+1} - \Gamma_W^k}\right), & \text{for } m_W^k \leq m_W \leq m_W^{k+1},\ \Gamma_W^k \leq \Gamma_W \leq \Gamma_W^{k+1} \\ 0, & \text{else.} \end{cases} \tag{D.3}$$

The weights of Equation (D.3) can be graphically understood by studying Figure D.4. It is shown how any combination of m_W and Γ_W can be achieved by interpolating in a rectangle. The corner points of this rectangle are given by all four possible combinations of the two mass values m_W^A and m_W^B and the two width values Γ_W^A and Γ_W^B. The black dot in the centre of the rectangle illustrates the desired template. Each template has to be weighted by the area of the sub-rectangle which is lying diagonal opposite to the corner point. The corner point and the sub-rectangle belonging together are inked with the same colour.

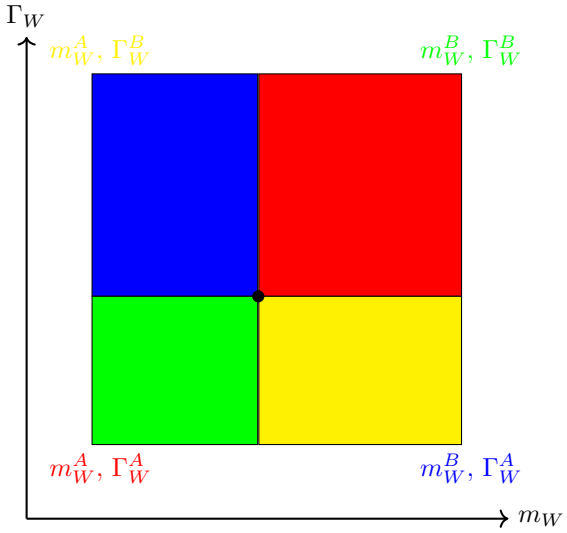

Figure D.4: Graphical interpretation of the morphing of two POIs. Shown is the interpolation to a given point represented by the black dot in the rectangular determined by four corner points with the two mass values m_W^A and m_W^B and the two width values Γ_W^A and Γ_W^B.

APPENDIX E

Additional information on the systematic uncertainties

This chapter presents additional material on the systematic uncertainties.

E.1 Calibration of light leptons

Figures E.1 and E.2 show the agreement between data and simulation of the leptonic pseudorapidity in the muon and the electron channel, respectively, for the 2017 analysis and the reanalysis.

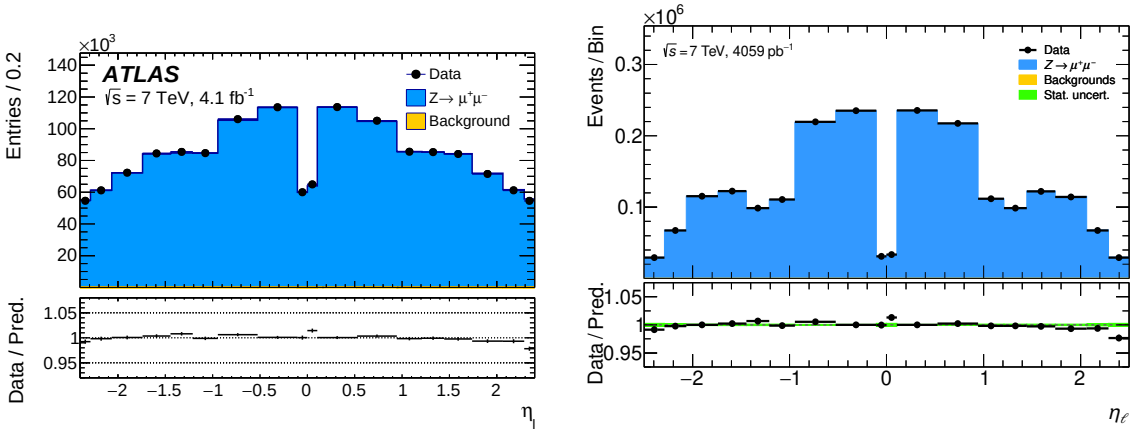

(a) (b)

Figure E.1: Comparison of the data to simulation agreement of the leptonic pseudorapidity in $Z \to \mu\mu$ events between the 2017 analysis and the reanalysis. Compared are the agreement between data and simulation consisting of Z signal and backgrounds for (a) the 2017 analysis (taken from [86]) and (b) the reanalysis. All corrections concerning the momentum calibration and the selection efficiency are applied to the simulation. The lower panel shows the ratio of data to simulation where the error bars indicate the statistical uncertainty.

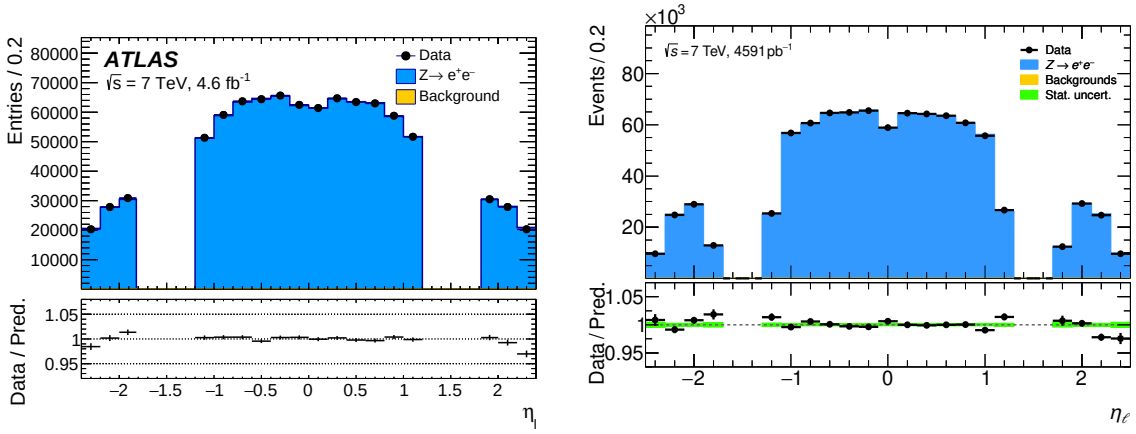

(a) (b)

Figure E.2: Comparison of the data to simulation agreement of the leptonic pseudorapidity in $Z \to ee$ events between the 2017 analysis and the reanalysis. Compared are the agreement between data and simulation consisting of Z signal and backgrounds for (a) the 2017 analysis (taken from [86]) and (b) the reanalysis. The corrections concerning the energy resolution and the selection efficiency are applied to the simulation whereas the energy scale corrections are applied to the data. The lower panel shows the ratio of data to simulation where the error bars indicate the statistical uncertainty.

E.2 Calibration of the recoil

Figure E.3 shows the data to simulation agreement for the kinematic distributions of $u_{\parallel}^{Z}$, $u_{\parallel}^{Z} + p_{\mathrm{T}}^{\ell\ell}$, and $u_{\perp}^{Z}$ in $Z \to \mu\mu$ events for the 2017 analysis and the reanalysis. Furthermore, Fig. E.4 illustrates the data to simulation agreement for the recoil distributions $u_{\parallel}^{Z}$, $u_{\parallel}^{Z} + p_{\mathrm{T}}^{\ell\ell}$, $u_{\perp}^{Z}$, and u_{T} in $Z \to ee$ events.

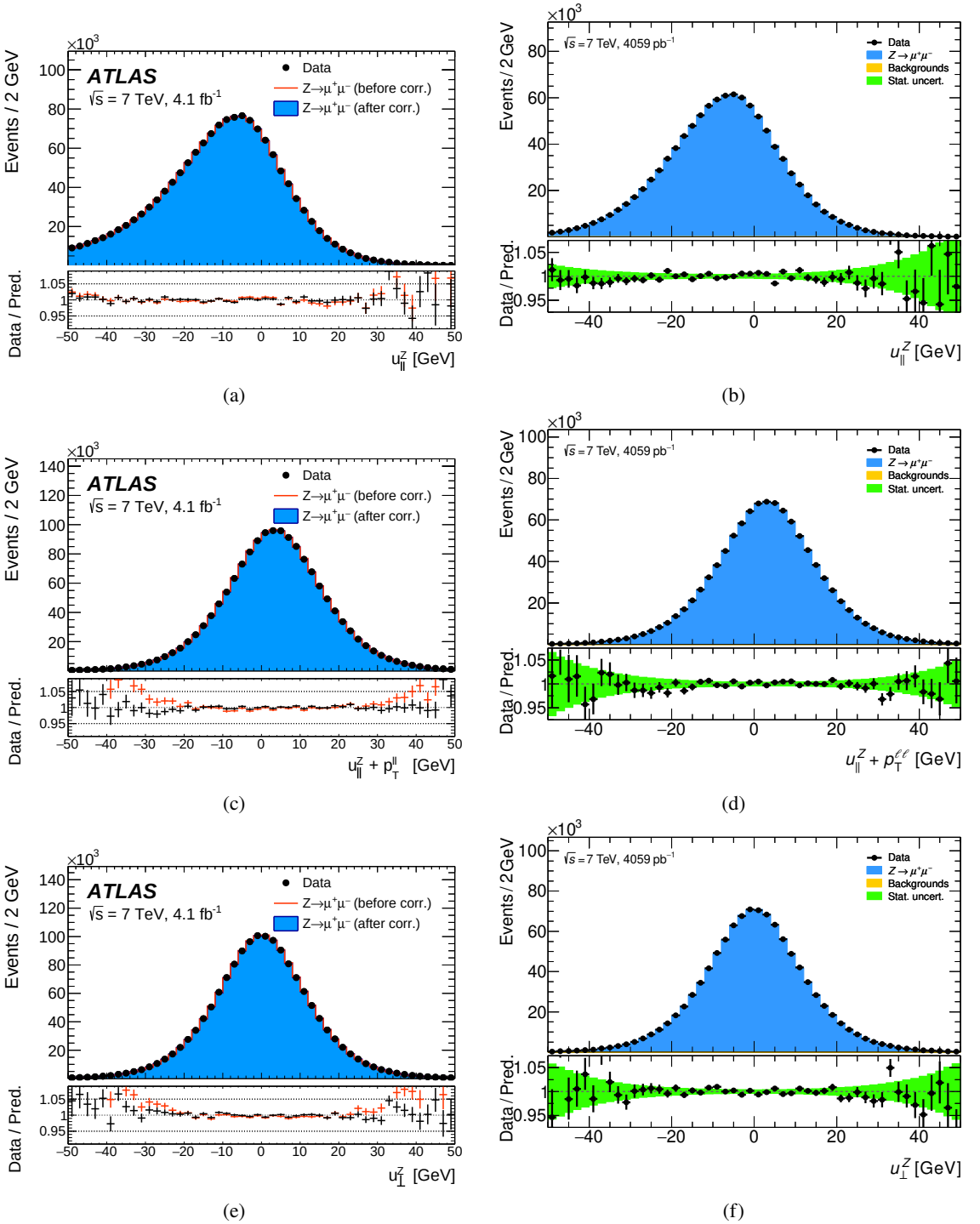

Figure E.3: Comparison of the data to simulation agreement of the recoil distributions $u_{\parallel}^{Z}$ (a,b), $u_{\parallel}^{Z} + p_{\mathrm{T}}^{\ell\ell}$ (c,d), and $u_{\perp}^{Z}$ (e,f) in $Z \to \mu\mu$ events between the 2017 analysis and the reanalysis. Compared are the agreement between data and simulation consisting of Z signal and backgrounds for (a), (c), (e) the 2017 analysis before and after applying all corrections (taken from [86]) and (b), (d), (f) the reanalysis including all recoil corrections. The lower panel shows the ratio of data to simulation where the error bars indicate the statistical uncertainty.

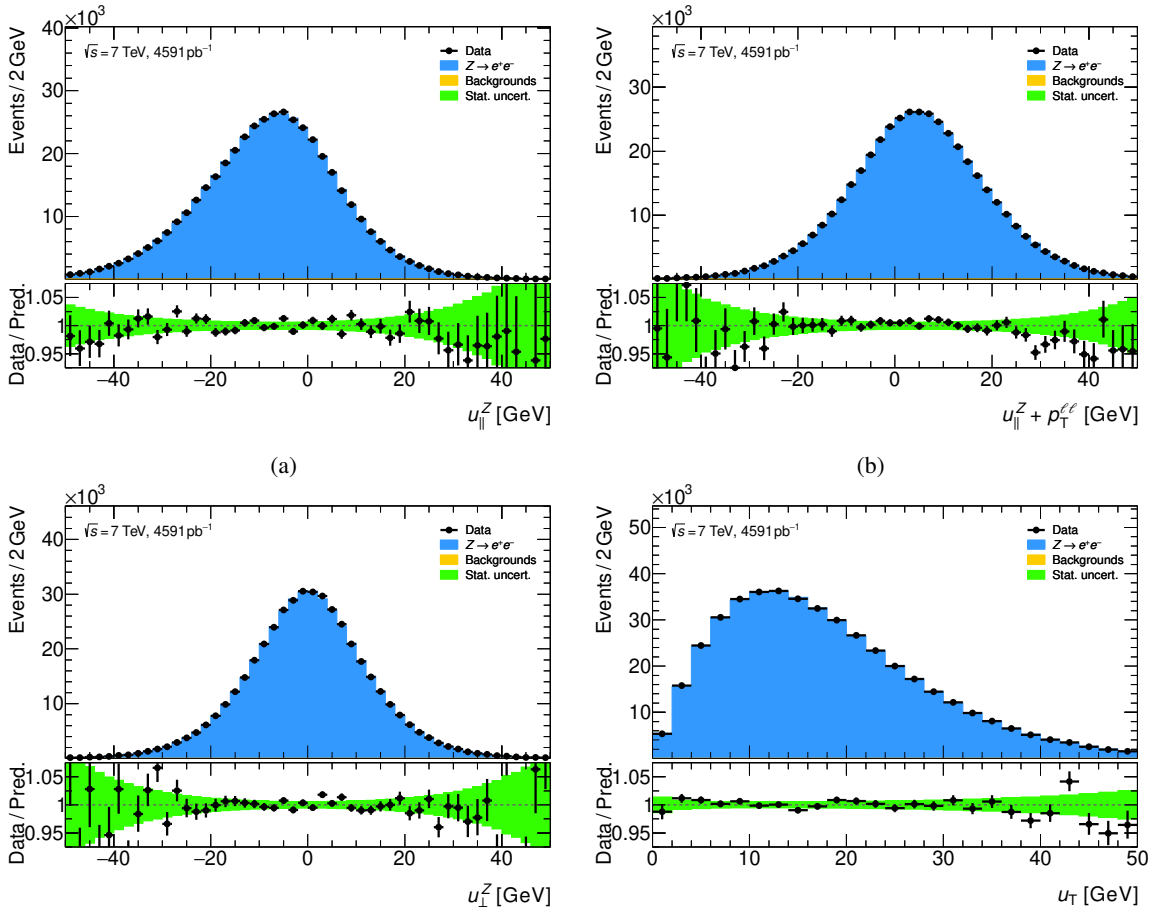

Figure E.4: Comparison of the data to simulation agreement of the recoil distributions $u_{\parallel}^{Z}$ (a), $u_{\parallel}^{Z} + p_{\mathrm{T}}^{\ell\ell}$ (b), $u_{\perp}^{Z}$ (c), and u_{T} (d) in $Z \rightarrow ee$ events for the reanalysis. Compared are the agreement between data and simulation consisting of Z signal and backgrounds after applying all recoil corrections. The lower panel shows the ratio of data to simulation where the error bars indicate the statistical uncertainty.

E.3 Cross check tests with Z-boson events

Complementary to Figs. 7.10 and 7.11, Figs. E.5, E.6 and E.7 show the data to simulation agreement of the recoil rapidity distributions, the $m_{\mathrm{T}}^{Z}\left(\ell^{+}\right)$, and the $m_{\mathrm{T}}^{Z}\left(\ell^{-}\right)$ distributions, respectively, for the 2017 analysis and the reanalysis in $Z \rightarrow \mu\mu$ and $Z \rightarrow ee$ events.

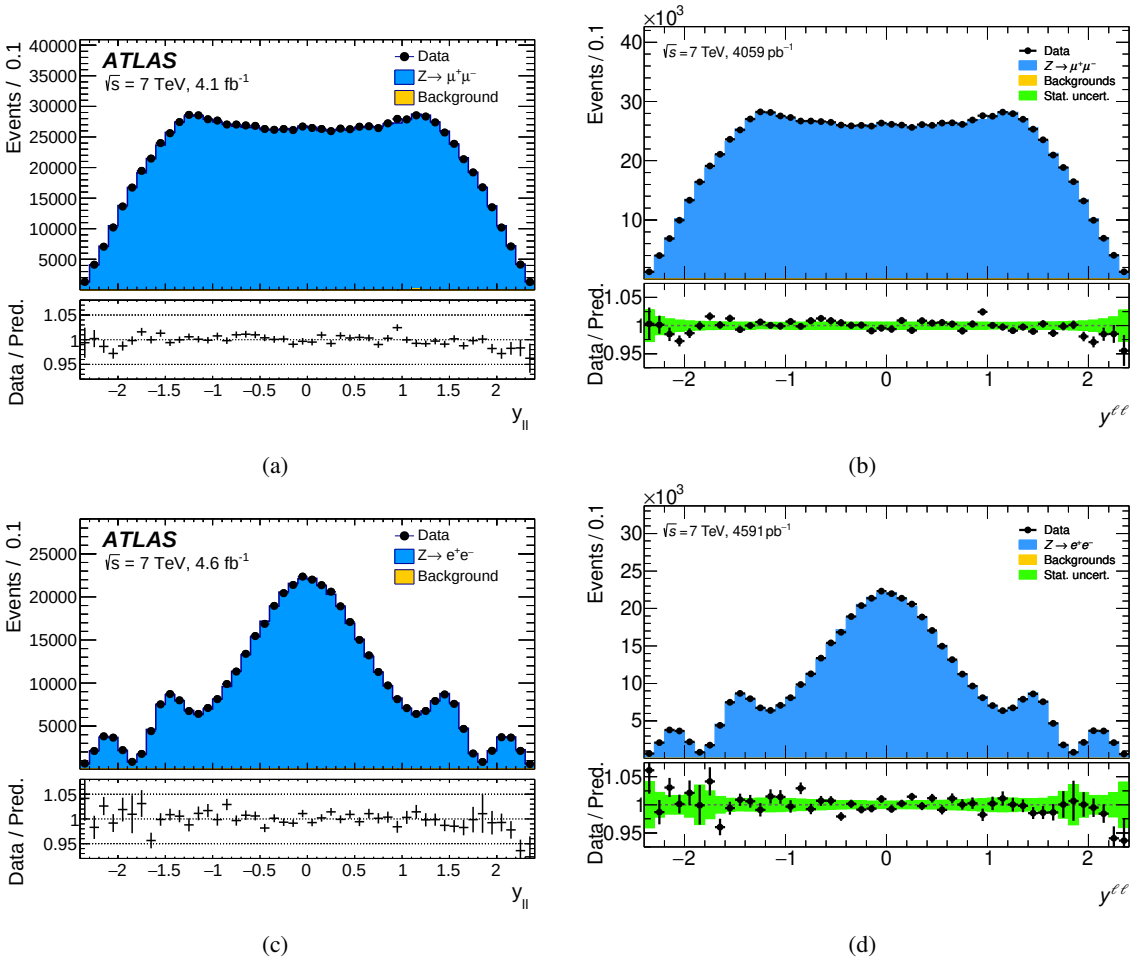

Figure E.5: Comparison of the data to simulation agreement of the recoil rapidity distributions from Z-boson events between the 2017 analysis (a,c) (taken from [86]) and the reanalysis (b,d). Shown are $Z \rightarrow \mu\mu$ events (a,b) and $Z \rightarrow ee$ events (c,d). The physics-modelling corrections and detector calibrations are applied to the simulation. The lower panel illustrates the data-to-prediction ratio with the error bars indicating the statistical uncertainties.

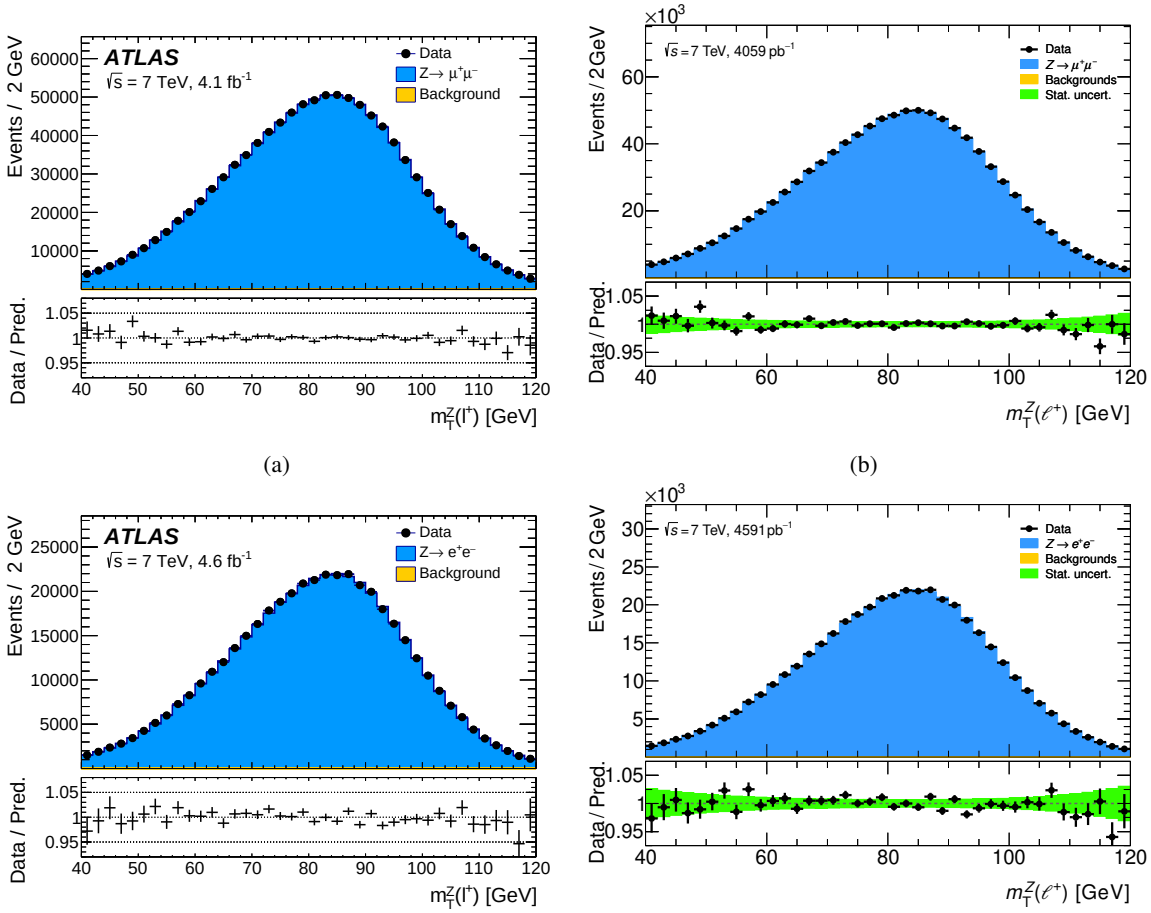

Figure E.6: Comparison of the data to simulation agreement of the $m_{\mathrm{T}}^{Z}\left(\ell^{+}\right)$ distributions from Z-boson events between the 2017 analysis (a,c) (taken from [86]) and the reanalysis (b,d). Shown are $Z \to \mu\mu$ events (a,b) and $Z \to ee$ events (c,d). The physics-modelling corrections and detector calibrations are applied to the simulation. The lower panel illustrates the data-to-prediction ratio with the error bars indicating the statistical uncertainties.

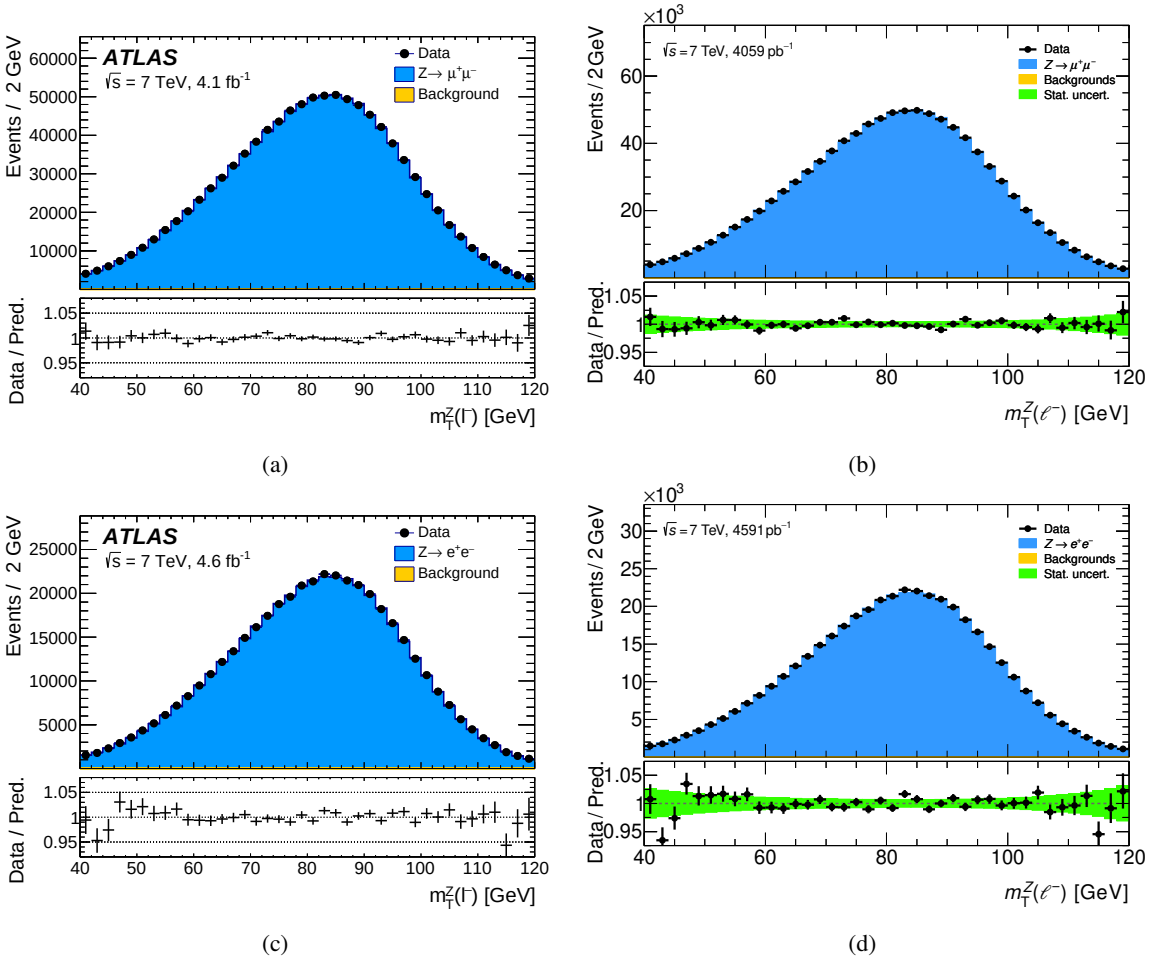

Figure E.7: Comparison of the data to simulation agreement of the $m_{\mathrm{T}}^{Z}\left(\ell^{-}\right)$ distributions from Z-boson events between the 2017 analysis (a,c) (taken from [86]) and the reanalysis (b,d). Shown are $Z \to \mu\mu$ events (a,b) and $Z \to ee$ events (c,d). The physics-modelling corrections and detector calibrations are applied to the simulation. The lower panel illustrates the data-to-prediction ratio with the error bars indicating the statistical uncertainties.

E.4 Principal component analysis

E.4.1 Toy study

This section describes the toy study to prove the working principle and find the correct normalisation of the eigenvectors. A Gaussian distribution generated by throwing 10^5 toys serves as a starting point for this toy example as shown in Fig. E.8(a). The histogram of the Gaussian distribution is smeared by a constant factor and a linear or quadratic function. The constant factor c is a random number from a gauss with mean $\mu = 0$ and width $\sigma = 0.1$. The linear and quadratic functions have the form

$$f_{\text{linear}}(x) = m \cdot x, \qquad f_{\text{quadratic}}(x) = m \cdot x^2, \tag{E.1}$$

where m is a random number drawn from a uniform distribution between -0.1 and 0.1. Both c and m are diced 10^4 times to generate the same number of correlated toys. The relative deviation of those toys with respect to the original Gaussian distribution served as an input for the PCA. The degree of freedom of the five components gives the PCA the flexibility to fully cover the two effects inserted. Only those eigenvectors are considered where the sum of the eigenvalues is greater than 99 % of the sum of all eigenvalues. If the dimensionality of the original pattern space is unknown, e.g. if processing systematic uncertainties, the number of components should be higher than the number of bins of the analysed histogram to allow the PCA to close.

In the case of the smearing with the linear function, the PCA finds back two eigenvectors shown in Figs. E.8(c) and E.8(d). They exactly describe the original pattern space as expected because one eigenvector describes the smearing with the linear function and the other one the smearing with a constant factor. A figure of merit is defined in a way to prove the integrity of the PCA. Therefore, the RMS of the correlated toys and the uncorrelated PCA eigenvectors is compared

$$x_{\text{RMS}}^{\text{correlated}} = \sqrt{\frac{1}{N}\sum_i^N \left(\frac{x_i - x_{\text{nom}}}{x_{\text{nom}}}\right)}, \qquad x_{\text{RMS}}^{\text{uncorrelated}} = \sqrt{\sum_i^N \left(\frac{x_i - x_{\text{nom}}}{x_{\text{nom}}}\right)}. \tag{E.2}$$

In the case of the toys, the correlated definition of the RMS of Eq. (7.4) is taken by summing over all toys while the uncorrelated definition of the RMS is used for all eigenvectors of the PCA included by the termination criterion. Depending on the choice of the smearing function as defined in Eq. (E.1), both figures of merit Figs. E.8(e) and E.8(f) demonstrate perfectly the working principle of the PCA with the ratio of the RMS of the toys and of the eigenvectors of the PCA being at 1.

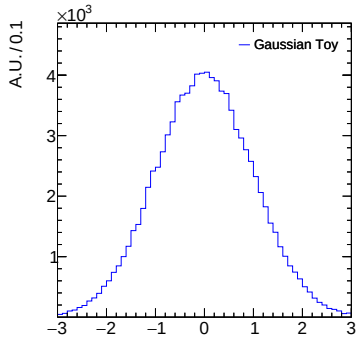

(a) Gaussian toy distribution.

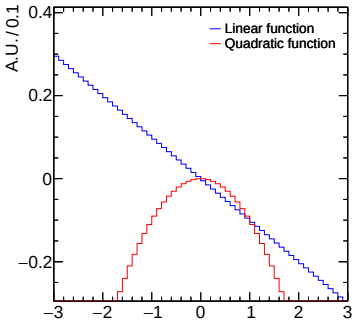

(b) Linear and quadratic functions.

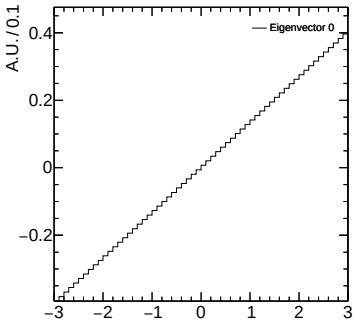

(c) 0^{th} eigenvector for smearing with linear function.

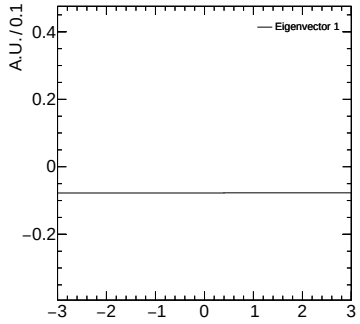

(d) 1^{st} eigenvector for smearing with linear function.

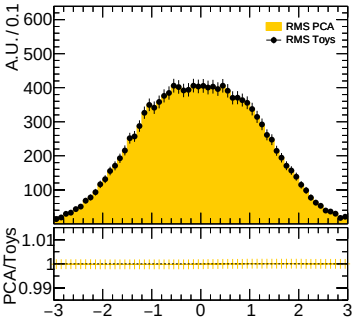

(e) Figure of merit for smearing with linear function.

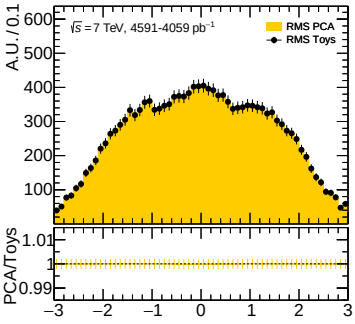

(f) Figure of merit for smearing with quadratic function.

Figure E.8: Graphical illustration of the toy example for the PCA. (a) shows the gaussian toy distribution being the base and (b) the linear (blue) and the quadratic (red) function the base distribution is smeared with. The two eigenvectors originating from the smearing with the linear function are shown in (c) (0^{th} eigenvector) and (d) (1^{st} eigenvector). The figures of merit in (e) and (f) for the two different smearings compare the RMS of the toys (black points) to the RMS of the PCA eigenvectors (solid orange histogram) and their ratio indicates the closure between both quantities.

E.4.2 Additional figures of merit

The additional figures of merit demonstrating the closure of the applied PCAs are shown in Figs. E.9, E.10, E.11, E.12, E.13, E.14, E.15 and E.16.

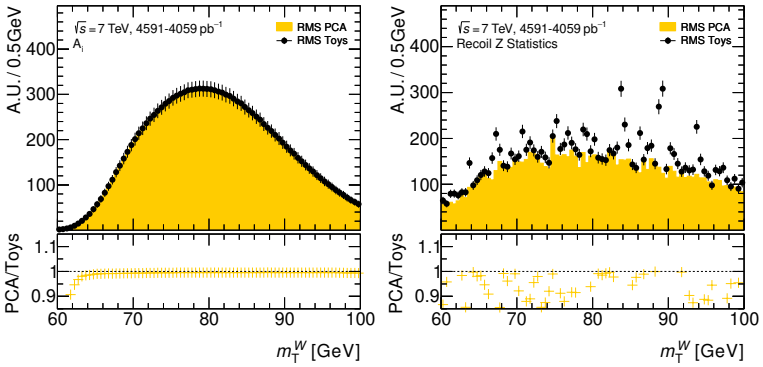

(a) A_i systematic. (b) Recoil Z statistics systematic.

Figure E.9: Figure of merits demonstrating the closure of the PCA for (a) the A_i systematic and (b) the Recoil Z statistics systematic for the m_{T}^{W} distribution. Shown is the RMS for toys (black points) compared to the RMS of the PCA eigenvectors (orange).

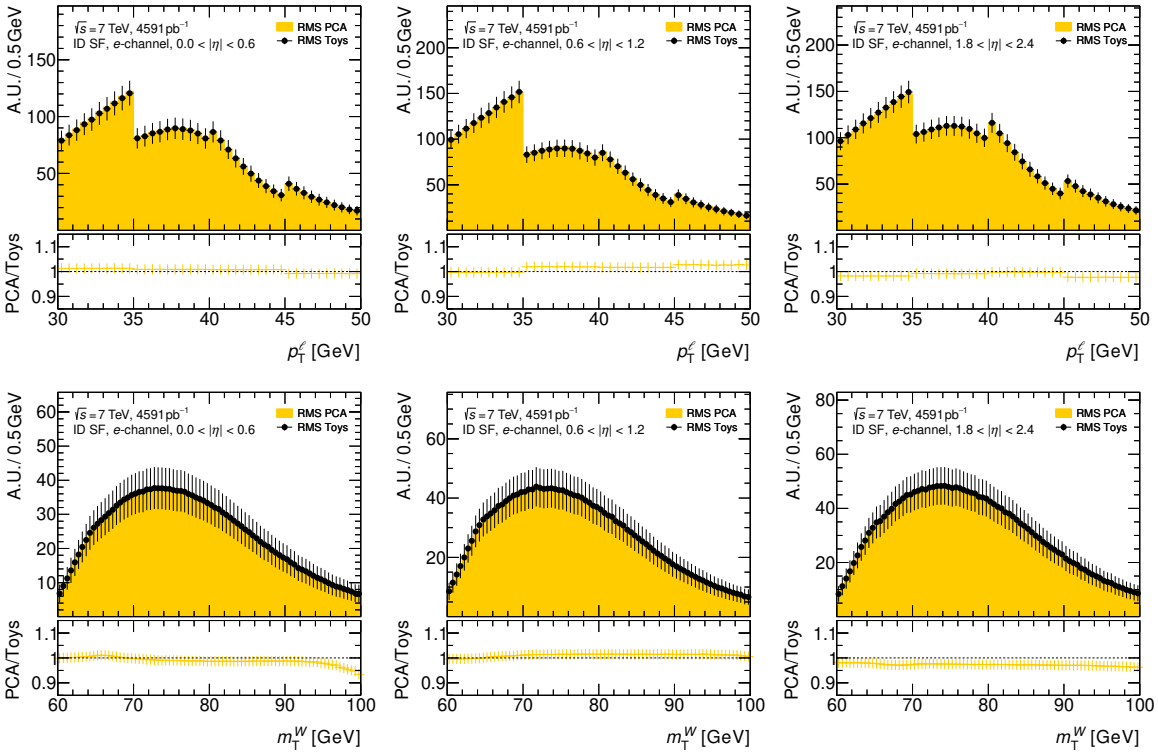

Figure E.10: Figure of merits demonstrating the closure of the PCA for the electron identification SF systematic. Shown is the RMS for toys (black points) compared to the RMS of the PCA eigenvectors (orange) for the two kinematic distributions p_{T}^{ℓ} and m_{T}^{W} and all η_{ℓ} categories.

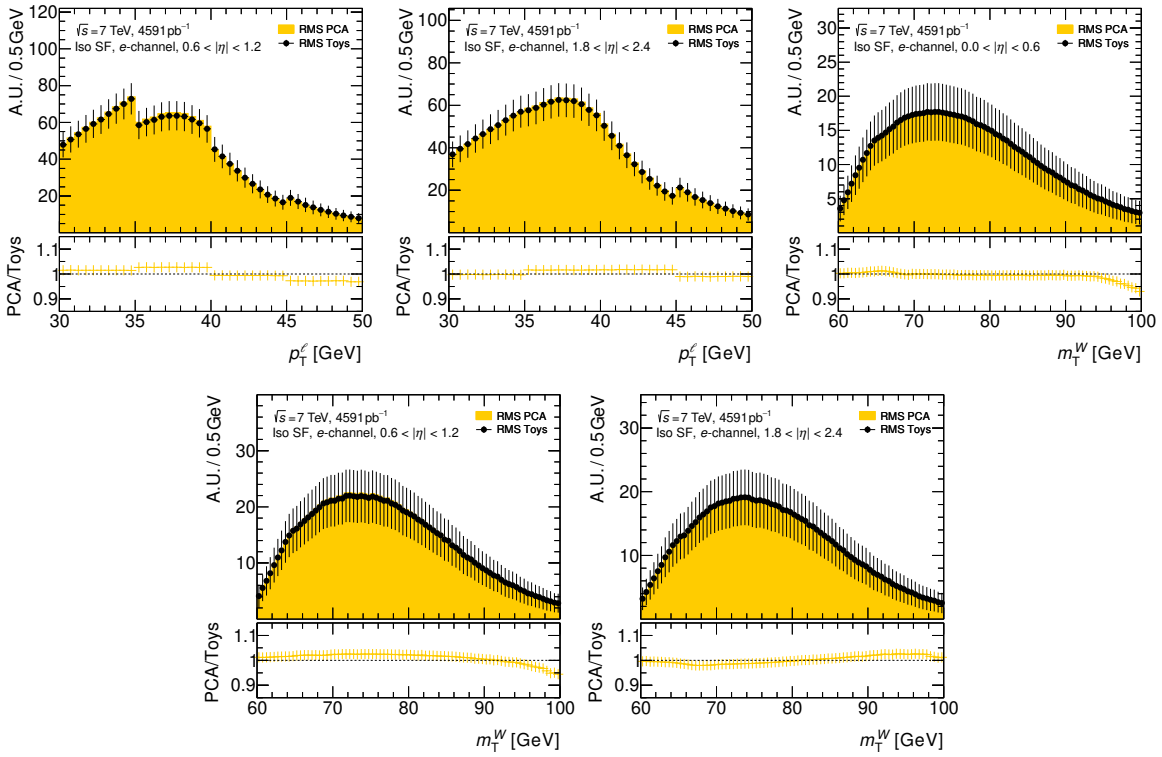

Figure E.11: Figure of merits demonstrating the closure of the PCA for the electron isolation SF systematic. Shown is the RMS for toys (black points) compared to the RMS of the PCA eigenvectors (orange) for the two kinematic distributions p_{T}^{ℓ} and m_{T}^{W} and all η_{ℓ} categories.

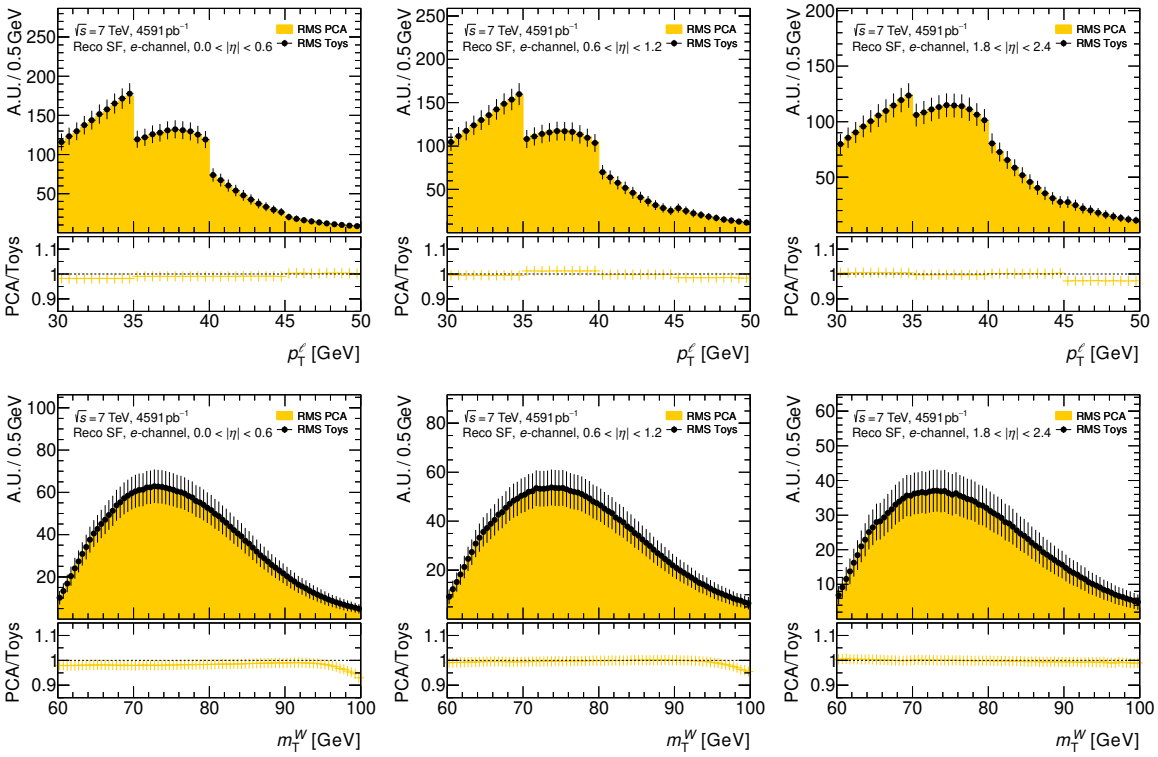

Figure E.12: Figure of merits demonstrating the closure of the PCA for the electron reconstruction SF systematic. Shown is the RMS for toys (black points) compared to the RMS of the PCA eigenvectors (orange) for the two kinematic distributions p_{T}^{ℓ} and m_{T}^{W} and all η_{ℓ} categories.

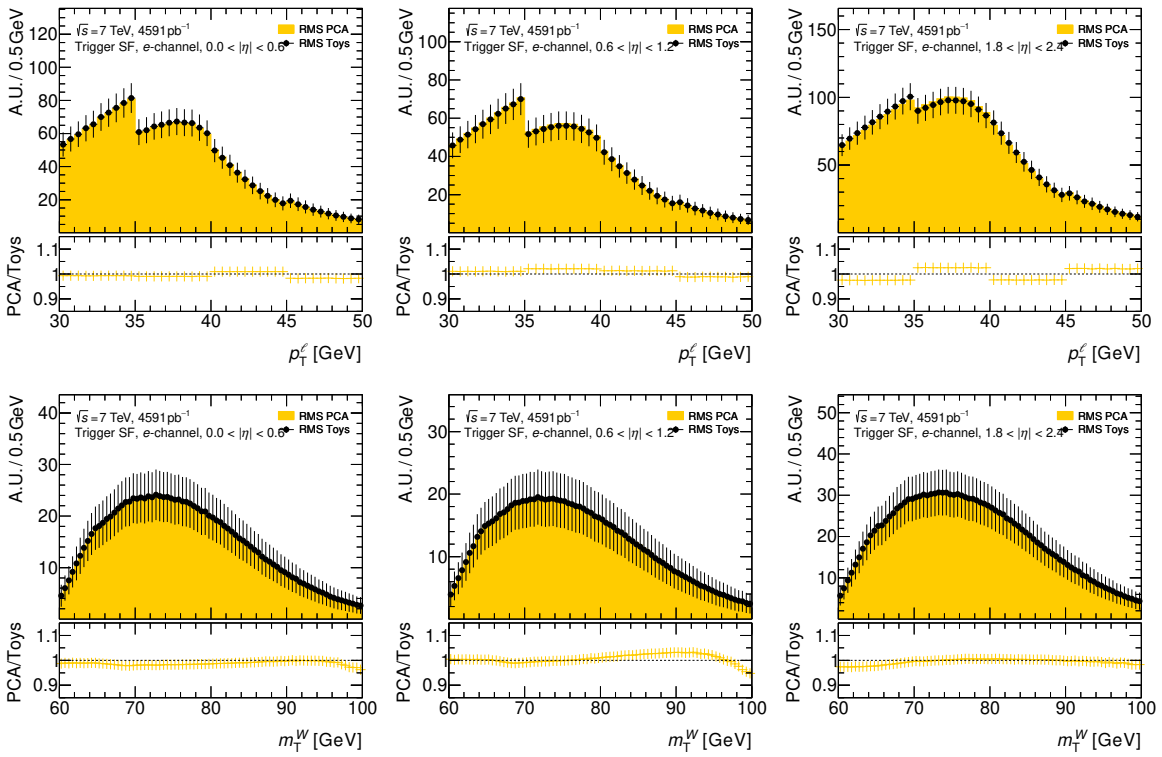

Figure E.13: Figure of merits demonstrating the closure of the PCA for the electron trigger SF systematic. Shown is the RMS for toys (black points) compared to the RMS of the PCA eigenvectors (orange) for the two kinematic distributions p_{T}^{ℓ} and m_{T}^{W} and all η_{ℓ} categories.

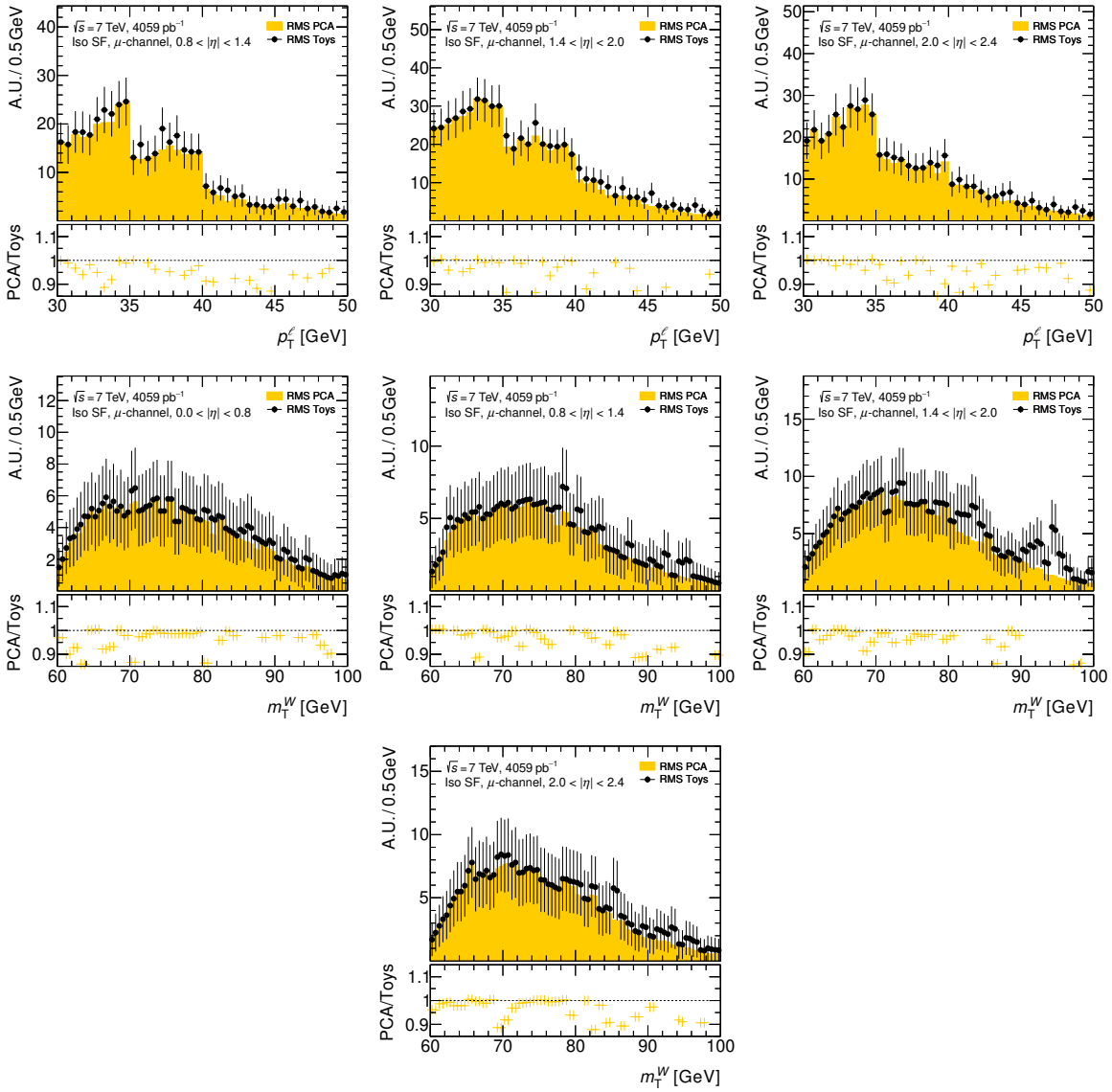

Figure E.14: Figure of merits demonstrating the closure of the PCA for the muon isolation SF systematic. Shown is the RMS for toys (black points) compared to the RMS of the PCA eigenvectors (orange) for the two kinematic distributions p_{T}^{ℓ} and m_{T}^{W} and all η_{ℓ} categories.

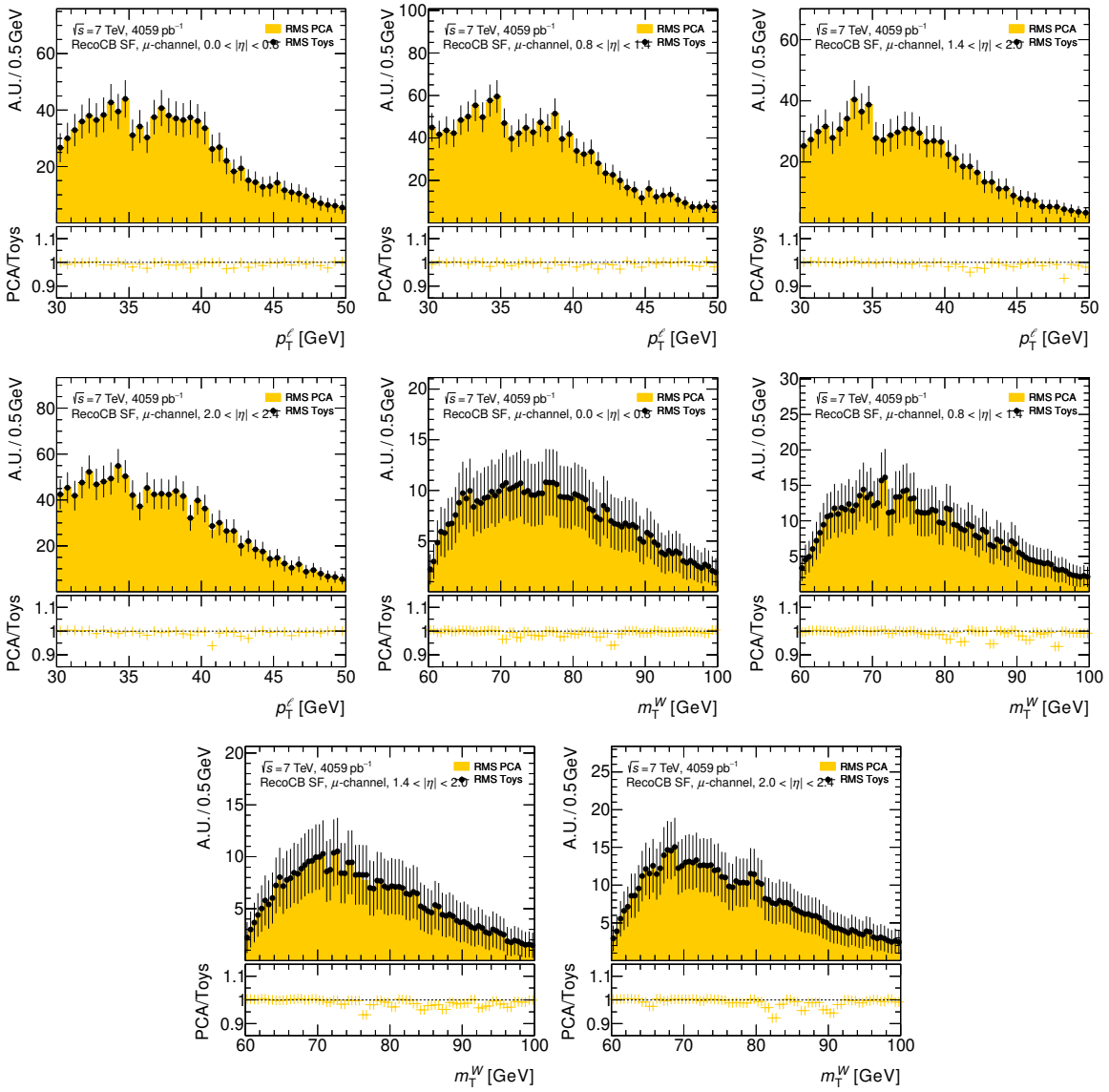

Figure E.15: Figure of merits demonstrating the closure of the PCA for the muon reconstruction SF systematic. Shown is the RMS for toys (black points) compared to the RMS of the PCA eigenvectors (orange) for the two kinematic distributions p_T^ℓ and m_T^W and all η_ℓ categories.

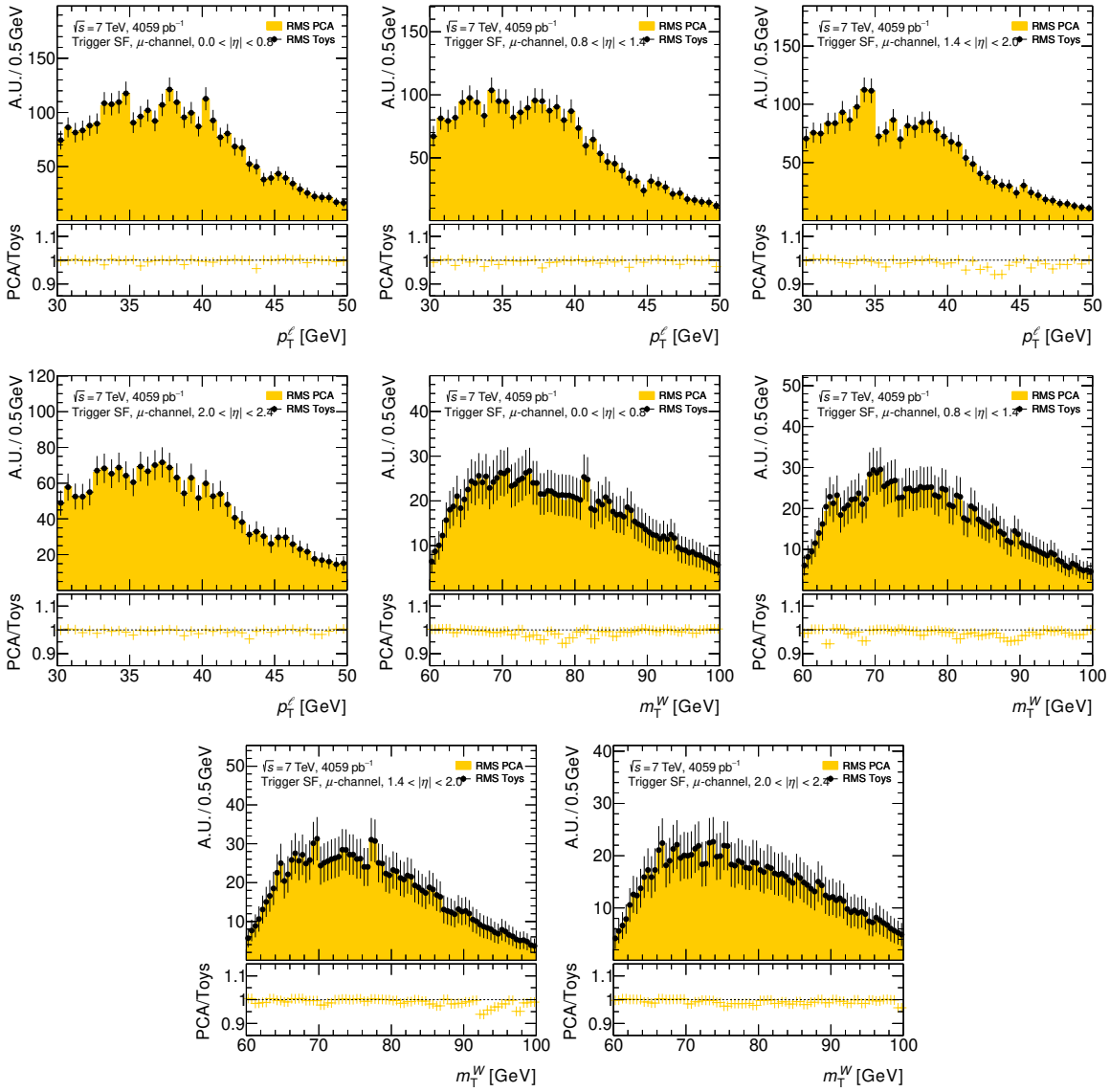

Figure E.16: Figure of merits demonstrating the closure of the PCA for the muon trigger SF systematic. Shown is the RMS for toys (black points) compared to the RMS of the PCA eigenvectors (orange) for the two kinematic distributions p_T^ℓ and m_T^W and all η_ℓ categories.

APPENDIX F

Additional information on the fit results

This chapter contains additional information on the fit results.

F.1 The optimisation of the fit setup

This section complements Section 8.1 by showing further plots and tables.

F.1.1 Normalisation

Table F.1 compares the predicted cross-sections at NLO for different W-boson mass and width values. Whereas the dependence of the W production cross-section on m_W is weak, it is more pronounced for Γ_W.

m_W [MeV]	Γ_W [MeV]	$\sigma(pp \to W^+)$ [nb]
80085	2.085	6.1338 ± 0.0092
80285	2.085	6.1653 ± 0.0092
80385	2.085	6.1811 ± 0.0092
80485	2.085	6.1969 ± 0.0092
80685	2.085	6.2285 ± 0.0092
80385	1.785	7.2270 ± 0.0110
80385	1.985	6.4947 ± 0.0097
80385	2.085	6.1811 ± 0.0092
80385	2.185	5.8961 ± 0.0088
80385	2.385	5.3980 ± 0.00819

Table F.1: Predicted cross-sections using DYTURBO at NLO for $pp \to W^+$ for different values of m_W and Γ_W.

F.1.2 Smoothing and symmetrisation

The given illustrations complete Fig. 8.1 and illustrate all systematic uncertainties which are smoothed and symmetrised. Shown are the distributions of the first η_ℓ slice for positively charged leptons in both leptonic decay channels.

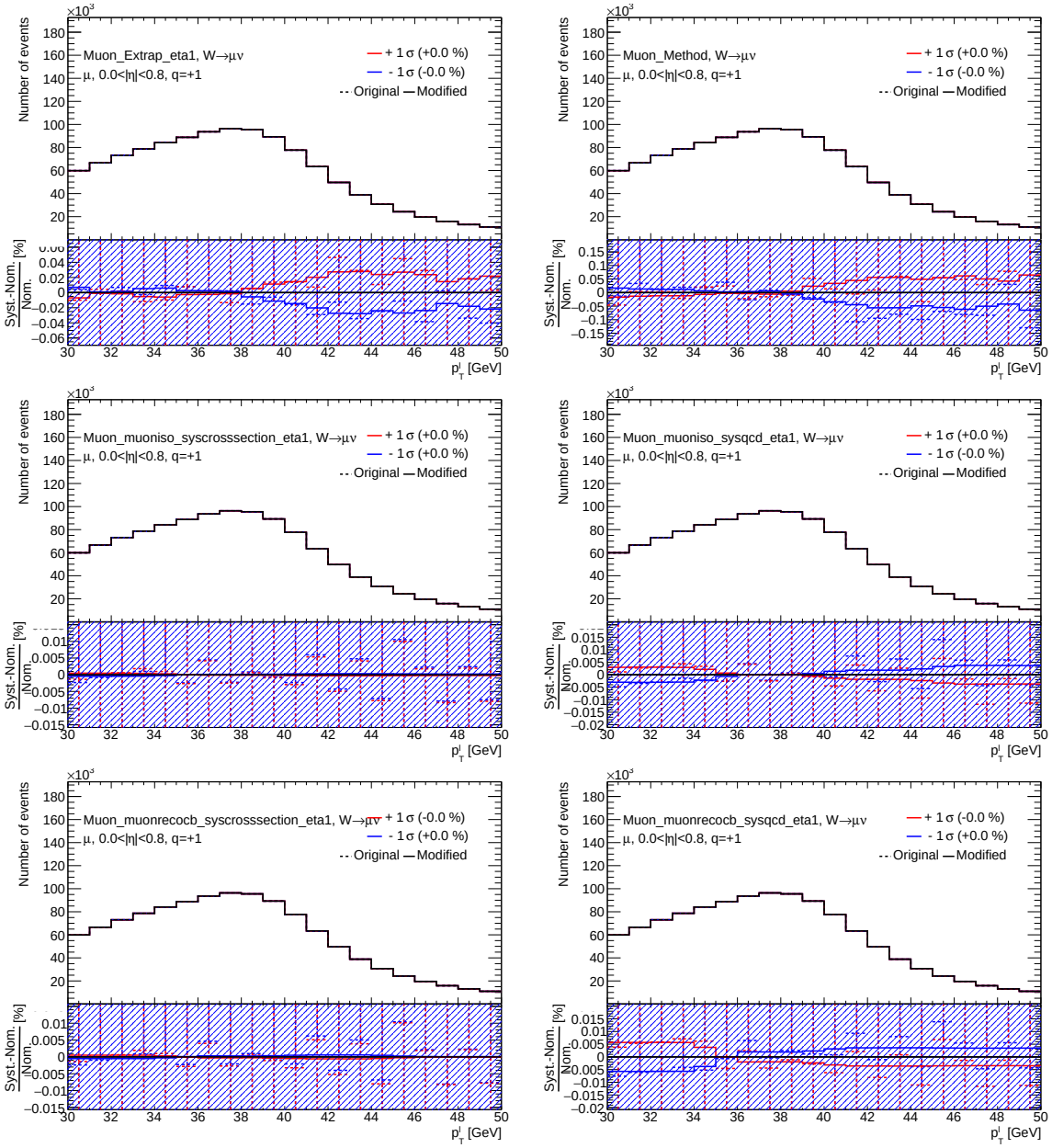

Figure F.1: Distributions of different systematic uncertainties of the muon channel comparing the original (dashed lines) and the modified (solid lines) envelopes. The lower panel illustrates the relative uncertainty compared to the nominal distribution given in per cent where the hatched area represents the statistical uncertainty of the nominal distribution.

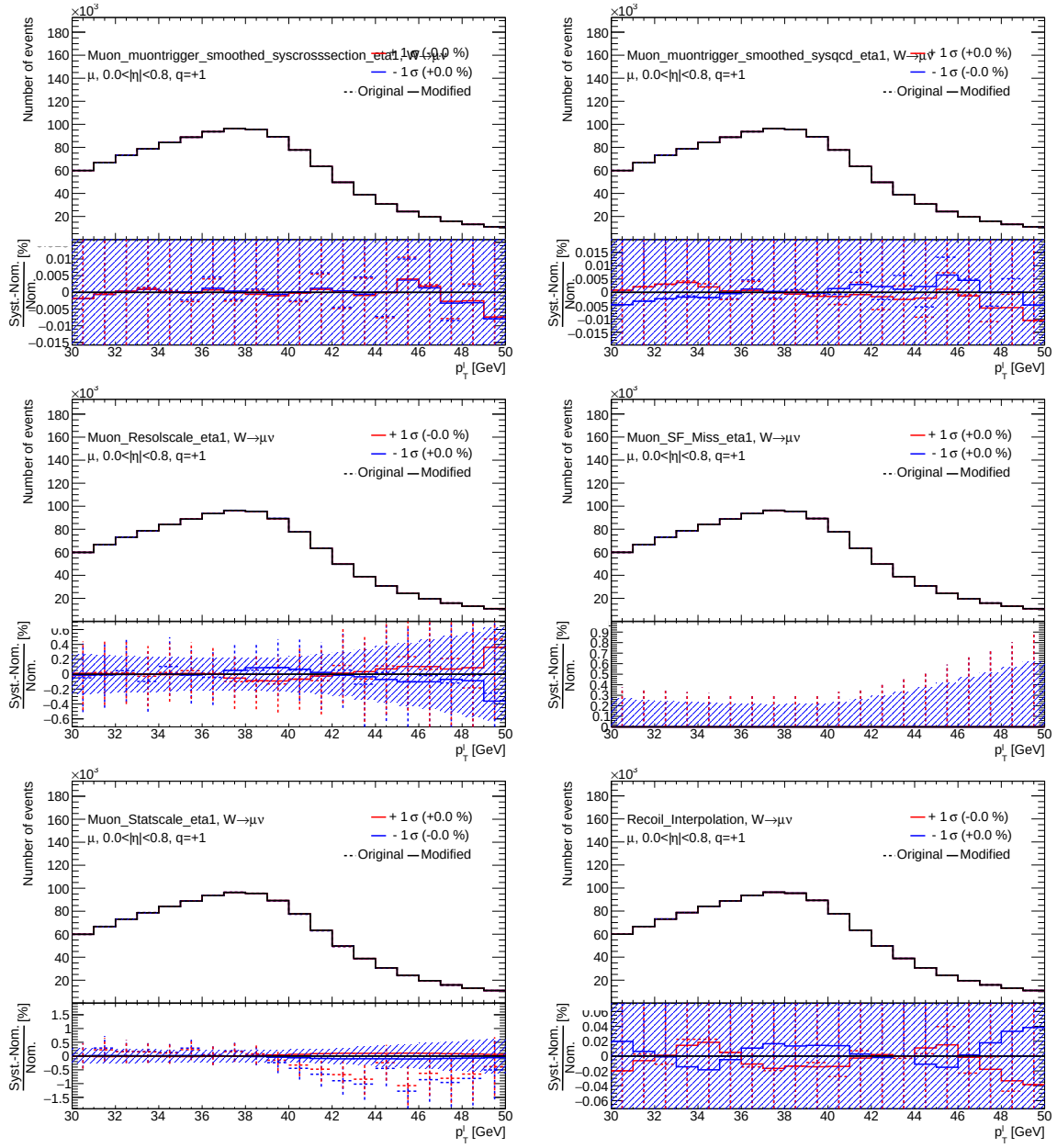

Figure F.2: Distributions of different systematic uncertainties of the muon channel comparing the original (dashed lines) and the modified (solid lines) envelopes. The lower panel illustrates the relative uncertainty compared to the nominal distribution given in per cent where the hatched area represents the statistical uncertainty of the nominal distribution.

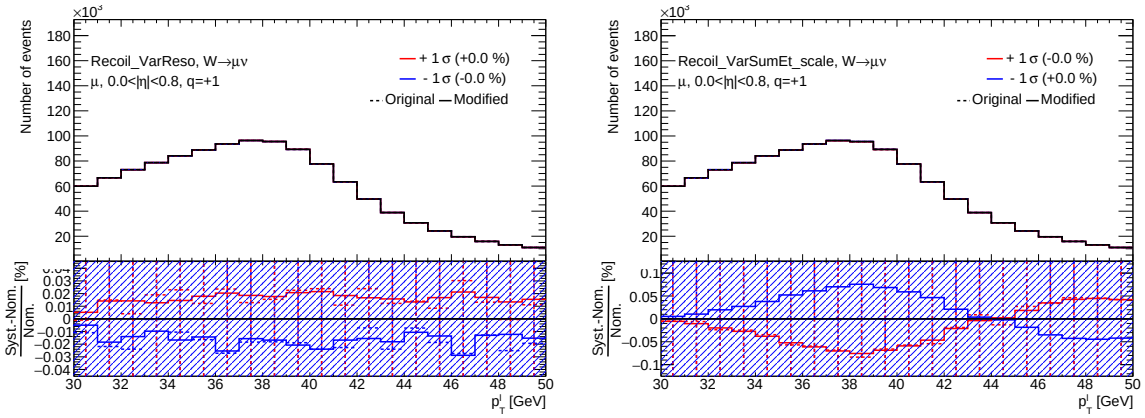

Figure F.3: Distributions of different systematic uncertainties of the muon channel comparing the original (dashed lines) and the modified (solid lines) envelopes. The lower panel illustrates the relative uncertainty compared to the nominal distribution given in per cent where the hatched area represents the statistical uncertainty of the nominal distribution.

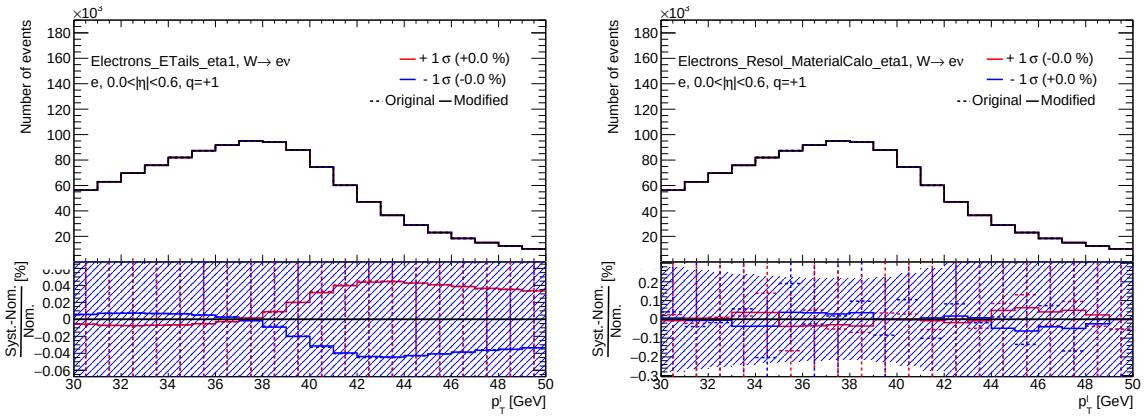

Figure F.4: Distributions of different systematic uncertainties of the electron channel comparing the original (dashed lines) and the modified (solid lines) envelopes. The lower panel illustrates the relative uncertainty compared to the nominal distribution given in per cent where the hatched area represents the statistical uncertainty of the nominal distribution.

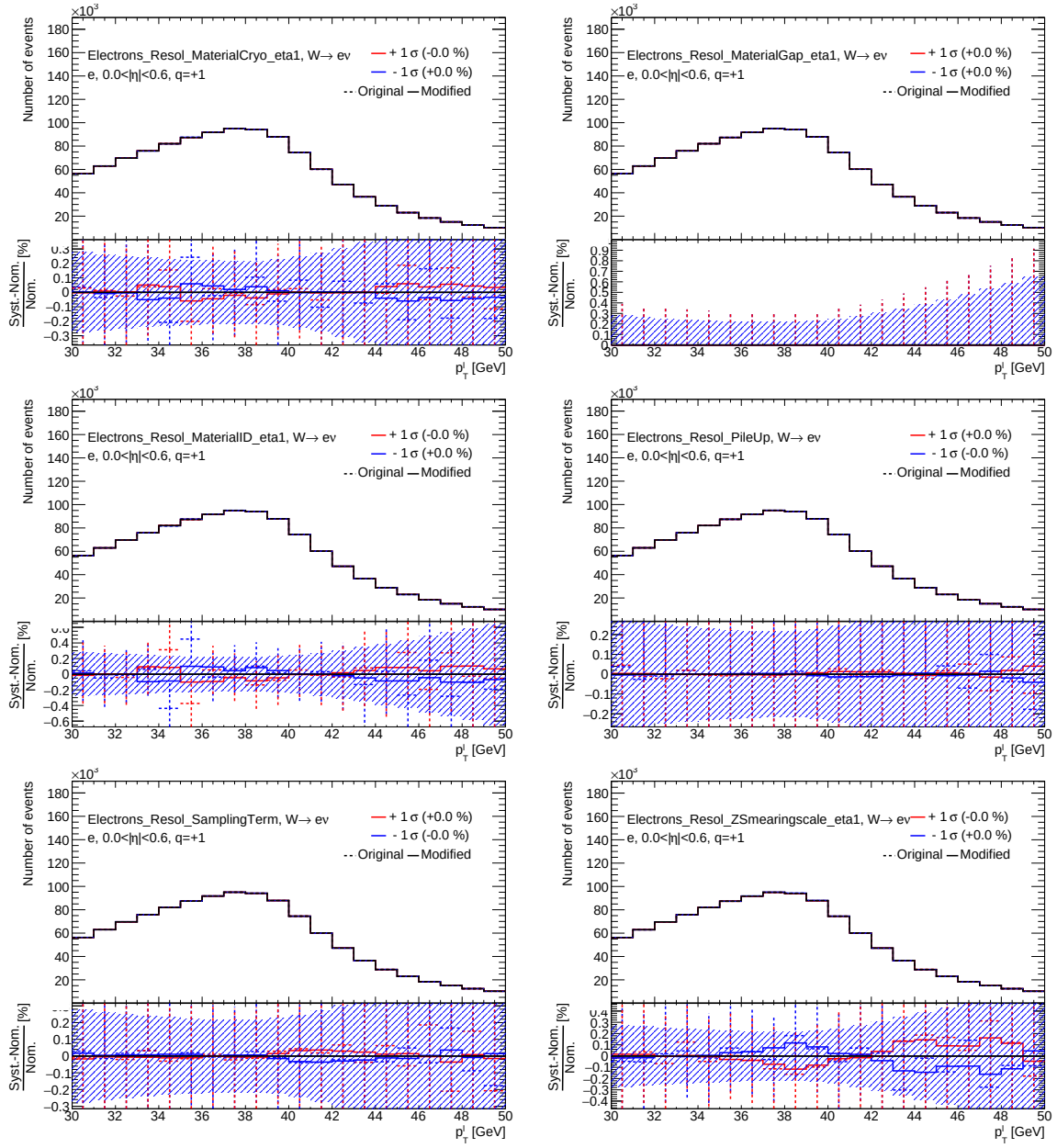

Figure F.5: Distributions of different systematic uncertainties of the electron channel comparing the original (dashed lines) and the modified (solid lines) envelopes. The lower panel illustrates the relative uncertainty compared to the nominal distribution given in per cent where the hatched area represents the statistical uncertainty of the nominal distribution.

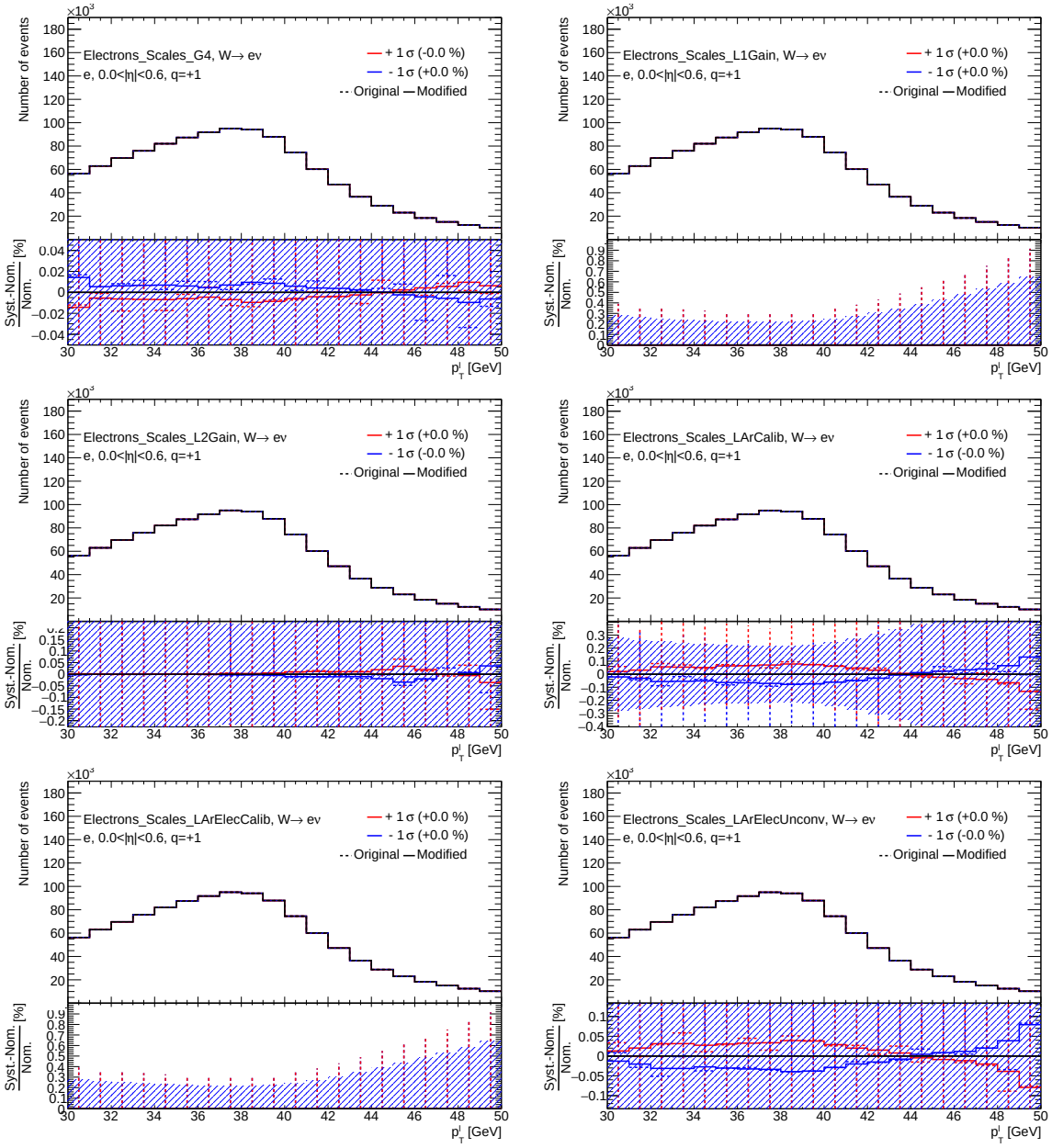

Figure F.6: Distributions of different systematic uncertainties of the electron channel comparing the original (dashed lines) and the modified (solid lines) envelopes. The lower panel illustrates the relative uncertainty compared to the nominal distribution given in per cent where the hatched area represents the statistical uncertainty of the nominal distribution.

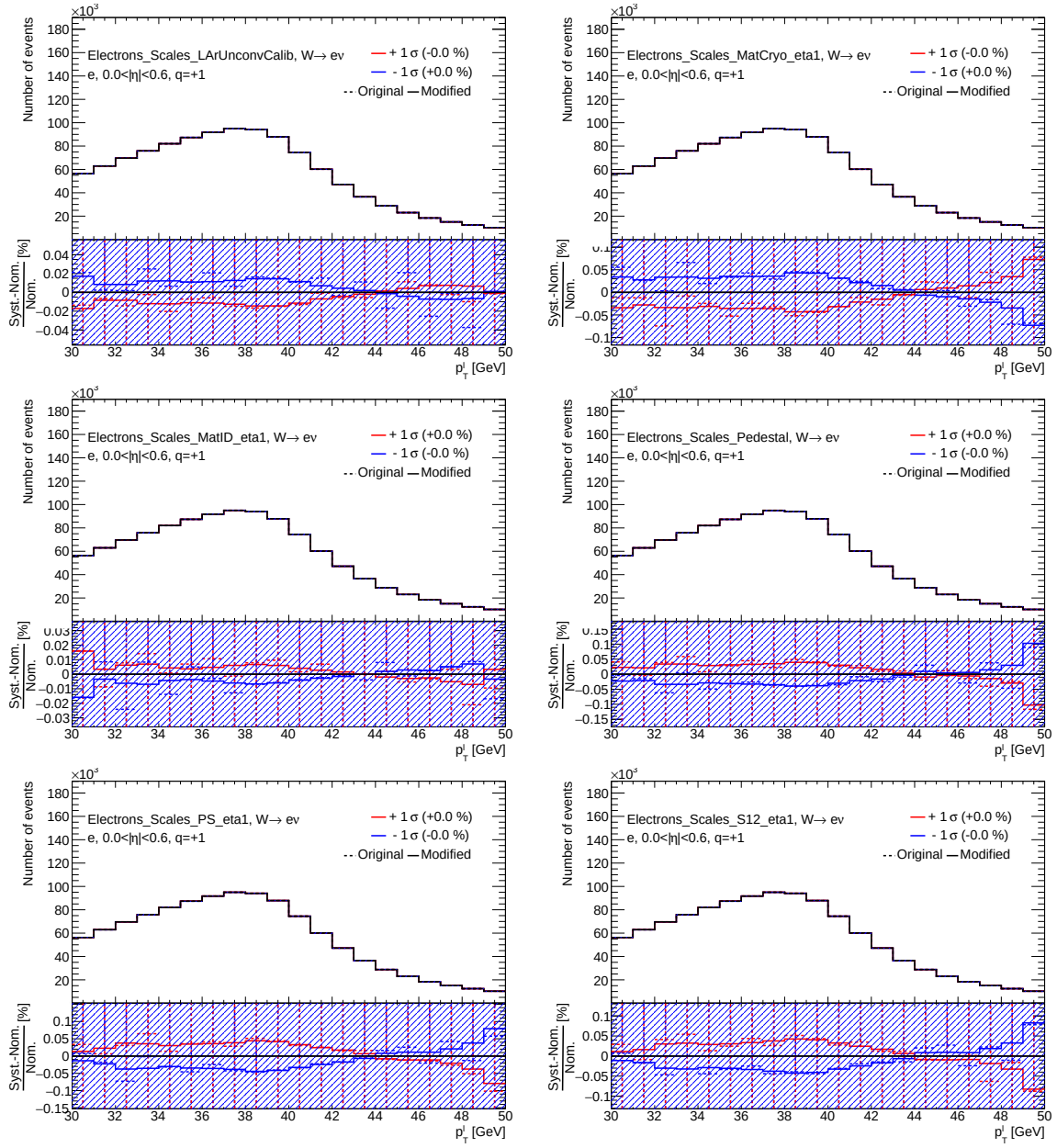

Figure F.7: Distributions of different systematic uncertainties of the electron channel comparing the original (dashed lines) and the modified (solid lines) envelopes. The lower panel illustrates the relative uncertainty compared to the nominal distribution given in per cent where the hatched area represents the statistical uncertainty of the nominal distribution.

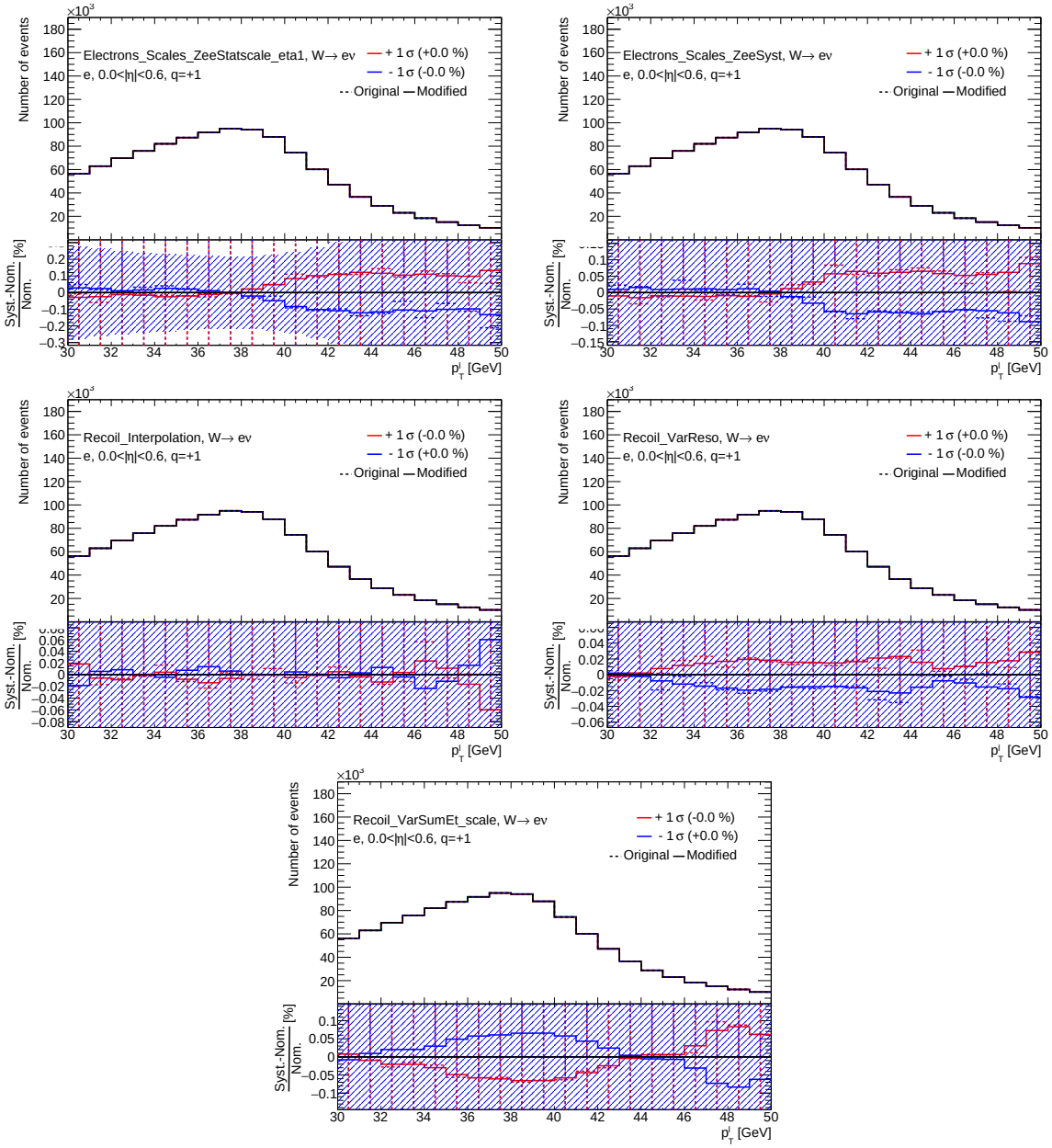

Figure F.8: Distributions of different systematic uncertainties of the electron channel comparing the original (dashed lines) and the modified (solid lines) envelopes. The lower panel illustrates the relative uncertainty compared to the nominal distribution given in per cent where the hatched area represents the statistical uncertainty of the nominal distribution.

F.1.3 Pruning

The following condition has to be fulfilled for every given bin i of a distribution to drop the shape part of a systematic uncertainty

$$\frac{b_{i,\text{variation}} - b_{i,\text{nominal}}}{b_{i,\text{nominal}}} < t_{\text{shape}},$$

where $b_{i,\text{variation}}$ and $b_{i,\text{nominal}}$ are the bin entries of bin i for the up or down variation and the nominal distribution. The value t_{shape} is the threshold value determining the requirement on the relative shape fluctuation of the variation. The variations and the nominal distribution are normalised to the same area before checking the pruning requirement. The optimal threshold value for the shape combines trimming most of the NPs without reducing the total uncertainty too much. The total uncertainties for different threshold values are shown in Tables F.2 and F.3. The total number of NPs is determined by counting every systematic uncertainty in every measurement category regardless of whether it is correlated across several measurement categories or not. For the two morphing measurements on m_W and Γ_W, the model-independent normalisation scheme is used as the normalisation does not play any role. Hence, no pruning on the normalisation is considered for this study. The optimal pruning values for the shape are determined to be 0.2 ‰ for p_{T}^{ℓ} and 0.1 ‰ for m_{T}^{W} as for both kinematic observables about half of the shape systematics are pruned away but the total uncertainty changes by less than 1 % for the considered measurements.

Pruning threshold shape	m_W	Γ_W	$R_{\tau\ell}$	No. of NPs dropped
No pruning	14.6 MeV	68.1 MeV	10.4 %	0/2266
0.1 ‰	14.5 MeV	68.0 MeV	10.4 %	716/2266
0.2 ‰	14.5 MeV	68.0 MeV	10.3 %	1046/2266
0.3 ‰	14.2 MeV	67.9 MeV	10.2 %	1272/2266
0.4 ‰	14.0 MeV	67.7 MeV	10.1 %	1455/2266
0.5 ‰	13.5 MeV	67.1 MeV	9.6 %	1586/2266

Table F.2: Impact of the different shape pruning thresholds on the different measurements of W-boson properties for the kinematic observable p_{T}^{ℓ}. For each of the three POIs m_W, Γ_W, and $R_{\tau\ell}$, the total uncertainty for different threshold values is compared. The PLH fit on Asimov data is performed in the kinematic observable p_{T}^{ℓ} in the fitting range 30–50 GeV. The model-dependent normalisation scheme is used for the fits including morphing. The MC gammas are not considered for this study. In addition, the number of NPs of morphing fits for which the shape is dropped for a certain threshold value is shown for the two considered kinematic observables.

The condition a systematic uncertainty has to pass to drop the normalisation part of a systematic uncertainty is

$$\frac{\int_{\text{variation}} - \int_{\text{nominal}}}{\int_{\text{nominal}}} < t_{\text{normalisation}},$$

where $\int_{\text{variation}}$ and $\int_{\text{nominal}}$ are the integrals of the up or down variations and the nominal distribution. Similar to the shape requirement, $t_{\text{normalisation}}$ is the threshold value for the normalisation condition. Again, a study is carried out to find out the optimal pruning threshold value for the normalisation as outlined in Tables F.4 and F.5. The numbers for the three measurements and the two kinematic observables p_{T}^{ℓ} and m_{T}^{W} are stated. Again, the model-independent normalisation scheme is used for the

Pruning threshold shape	m_W	Γ_W	$R_{\tau\ell}$	No. of NPs dropped
No pruning	21.8 MeV	42.9 MeV	14.5 %	0/2694
0.1 ‰	21.7 MeV	42.7 MeV	14.5 %	1159/2694
0.2 ‰	21.7 MeV	42.1 MeV	14.5 %	1702/2694
0.3 ‰	21.2 MeV	41.7 MeV	14.3 %	1919/2694
0.4 ‰	21.0 MeV	41.5 MeV	14.3 %	2041/2694
0.5 ‰	20.3 MeV	41.3 MeV	14.0 %	2147/2694

Table F.3: Impact of the different shape pruning thresholds on the different measurements of W-boson properties for the kinematic observable m_{T}^{W}. For each of the three POIs m_W, Γ_W, and $R_{\tau\ell}$, the total uncertainty for different threshold values is compared. The PLH fit on Asimov data is performed in the kinematic observable m_{T}^{W} in the fitting range 60–100 GeV. The model-dependent normalisation scheme is used for the fits including morphing. The MC gammas are not considered for this study. In addition, the number of NPs of morphing fits for which the shape is dropped for a certain threshold value is shown for the two considered kinematic observables.

morphing fits. The total uncertainties increase sometimes with increasing pruning threshold as shown in Tables F.4 and F.5. This counter-intuitive behaviour can be explained by numerical instabilities in the fit. The pruning of the shape is fixed to the optimal values for the kinematic observables. Most of the normalisation NPs can be pruned away without changing significantly the total uncertainty. The optimal pruning thresholds on the normalisation are found to be 2 ‰ for both kinematic observables as the impact on the total uncertainty is again less than 1 %. In contrast, the pruning normalisation threshold of the lepton universality measurement for m_{T}^{W} is fixed to 0.25 ‰.

Pruning threshold normalisation	m_W	Γ_W	$R_{\tau\ell}$	No. of NPs dropped
No pruning	14.5 MeV	68.0 MeV	10.3 %	0/2280
0.25 ‰	14.4 MeV	68.0 MeV	10.3 %	1588/2280
0.5 ‰	14.5 MeV	67.9 MeV	10.2 %	1730/2280
1.0 ‰	14.4 MeV	68.0 MeV	10.2 %	1849/2280
2.0 ‰	14.5 MeV	67.7 MeV	10.3 %	1989/2280
3.0 ‰	14.4 MeV	66.9 MeV	10.2 %	2063/2280

Table F.4: Impact of the different normalisation pruning thresholds on the different measurements of W-boson properties for the kinematic observable p_{T}^{ℓ}. For each of the three POIs m_W, Γ_W, and $R_{\tau\ell}$, the total uncertainty for different threshold values is compared. The PLH fit on Asimov data is performed in the kinematic observable p_{T}^{ℓ} in the fitting range 30–50 GeV. The model-independent normalisation scheme is used for the fits including morphing. The MC gammas are not considered for this study. The shape pruning value is fixed to 0.2 ‰. In addition, the number of NPs of morphing fits for which the normalisation is dropped for a certain threshold value is shown for the two considered kinematic observables.

Pruning threshold normalisation	m_W	Γ_W	$R_{\tau\ell}$	No. of NPs dropped
No pruning	21.7 MeV	42.7 MeV	14.5 ‰	0/2708
0.25 ‰	21.7 MeV	42.5 MeV	14.4 ‰	2036/2708
0.5 ‰	21.6 MeV	42.7 MeV	14.1 ‰	2163/2708
1.0 ‰	21.6 MeV	42.7 MeV	14.0 ‰	2278/2708
2.0 ‰	21.8 MeV	42.7 MeV	14.0 ‰	2418/2708
3.0 ‰	21.7 MeV	42.8 MeV	13.5 ‰	2489/2708

Table F.5: Impact of the different normalisation pruning thresholds on the different measurements of W-boson properties for the kinematic observable m_{T}^{W}. For each of the three POIs m_W, Γ_W, and $R_{\tau\ell}$, the total uncertainty for different threshold values is compared. The PLH fit on Asimov data is performed in the kinematic observable m_{T}^{W} in the fitting range 60–100 GeV. The model-independent normalisation scheme is used for the fits including morphing. The MC gammas are not considered for this study. The shape pruning value is fixed to 0.1 ‰. In addition, the number of NPs of morphing fits for which the normalisation is dropped for a certain threshold value is shown for the two considered kinematic observables.

F.1.4 Fitting ranges

Table F.6 complements Table 8.3 by showing the expected sensitivity of the model-dependent normalisation scheme for different fitting ranges, the two morphing POIs m_W and Γ_W, and the two kinematic observables p_{T}^{ℓ} and m_{T}^{W}.

p_{T}^{ℓ}			m_{T}^{W}		
Range	m_W	Γ_W	Range	m_W	Γ_W
30–45 GeV	15.9 MeV	26.1 MeV	60–90 GeV	24.0 MeV	27.1 MeV
32–45 GeV	16.1 MeV	26.5 MeV	66–99 GeV	23.3 MeV	23.8 MeV
35–50 GeV	15.9 MeV	26.4 MeV	70–100 GeV	24.8 MeV	24.4 MeV
35–45 GeV	16.1 MeV	27.2 MeV	70–90 GeV	26.2 MeV	28.6 MeV
30–50 GeV	15.6 MeV	25.8 MeV	60–100 GeV	22.9 MeV	23.0 MeV

Table F.6: Expected total uncertainty for different fitting ranges on the two morphing measurements of the W-boson with the model-dependent normalisation. The sensitivity is evaluated with fits on Asimov data in both kinematic observables p_{T}^{ℓ} and m_{T}^{W} for the indicated ranges and both morphing POIs m_W and Γ_W. All kinds of uncertainties are considered in this study.

F.2 Measurement of the W-boson mass

In this section, the post-fit distributions of p_{T}^{W}, $u_{\parallel}^{\ell}$, and $u_{\perp}^{\ell}$ of W-boson mass fits performed in the p_{T}^{ℓ} distribution are shown in Figs. F.9 and F.10. The normalisation discrepancy in the recoil post-fit plots of the e^{-}-channel which is, in addition, visible for the W-boson width and the lepton universality measurement could be explained by potential mismodelling of systematic uncertainties beyond the used fitting range in p_{T}^{ℓ}. 5 % of the events passing the event selection have $p_{\mathrm{T}}^{\ell} > 50\,\mathrm{GeV}$ but those events are included in the recoil post-fit plots. The next step is to exclude those events for all kind of post-fit distributions and repeat the comparison between data and simulation afterwards. The results of PLH fits performed in the p_{T}^{ℓ} or the m_{T}^{W} distributions are compared in Fig. F.11.

Furthermore, a comparison of the fit results of the individual measurement categories and the combination and the comparison of the impact of different sources of uncertainty on the W-boson mass measurement between the χ^2 fit and the PLH fit are given in Fig. F.12 and Table F.7, respectively. The illustrations of the m_{T}^{W} fits are completed by the ranking plot in Fig. F.13, the consistency checks in Fig. F.14, and the comparison of the post-fit m_{T}^{W} distributions between the χ^2 fit and the PLH fit in Figs. F.15 and F.16.

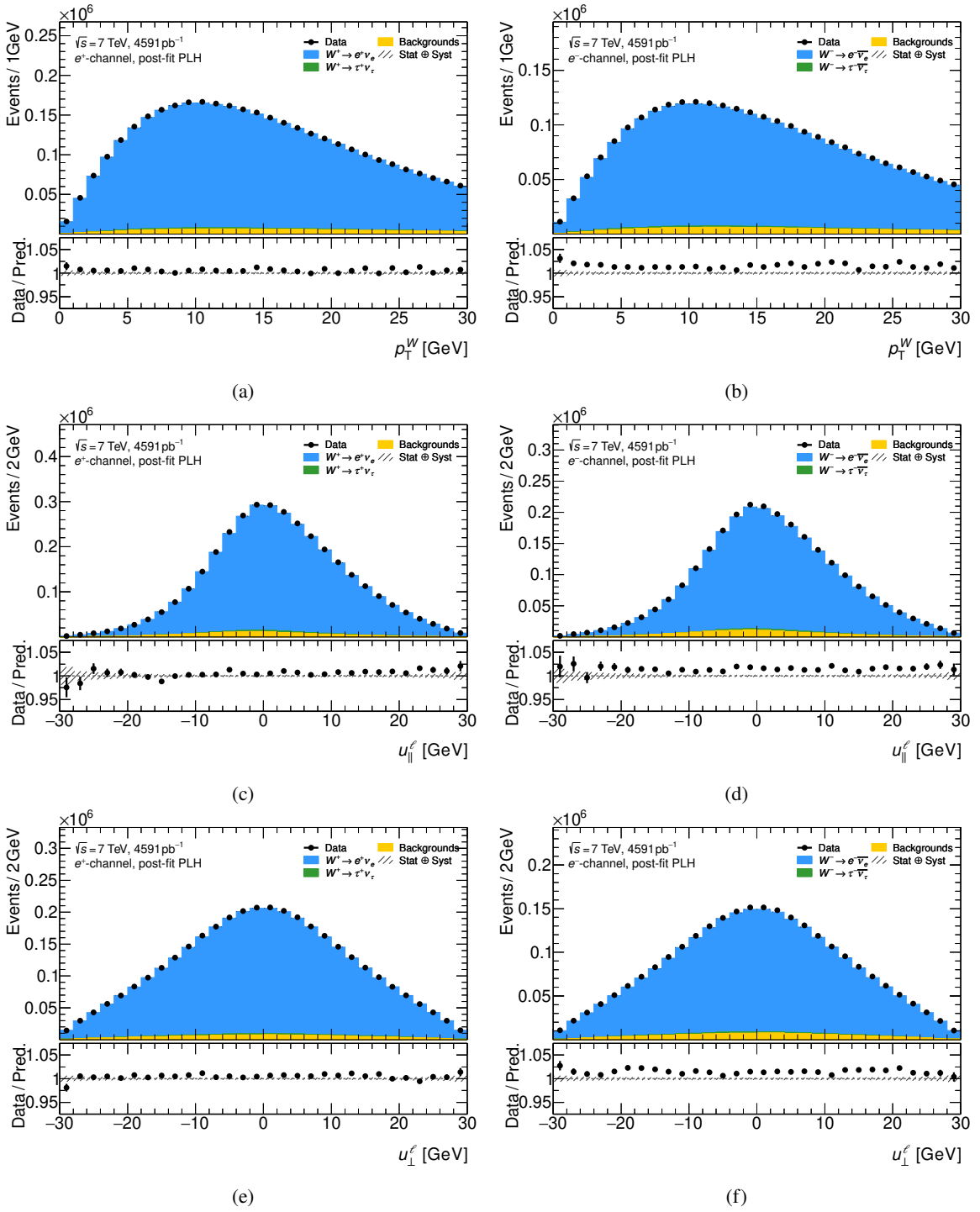

Figure F.9: Illustration of the post-fit recoil distribution in the electron channel for p_T^ℓ fits of the W-boson mass. Shown are the distributions of p_T^W (a,b), $u_\parallel^\ell$ (c,d), and $u_\perp^\ell$ (e,f) for positively (a,c,e) and negatively (b,d,f) charged electrons.

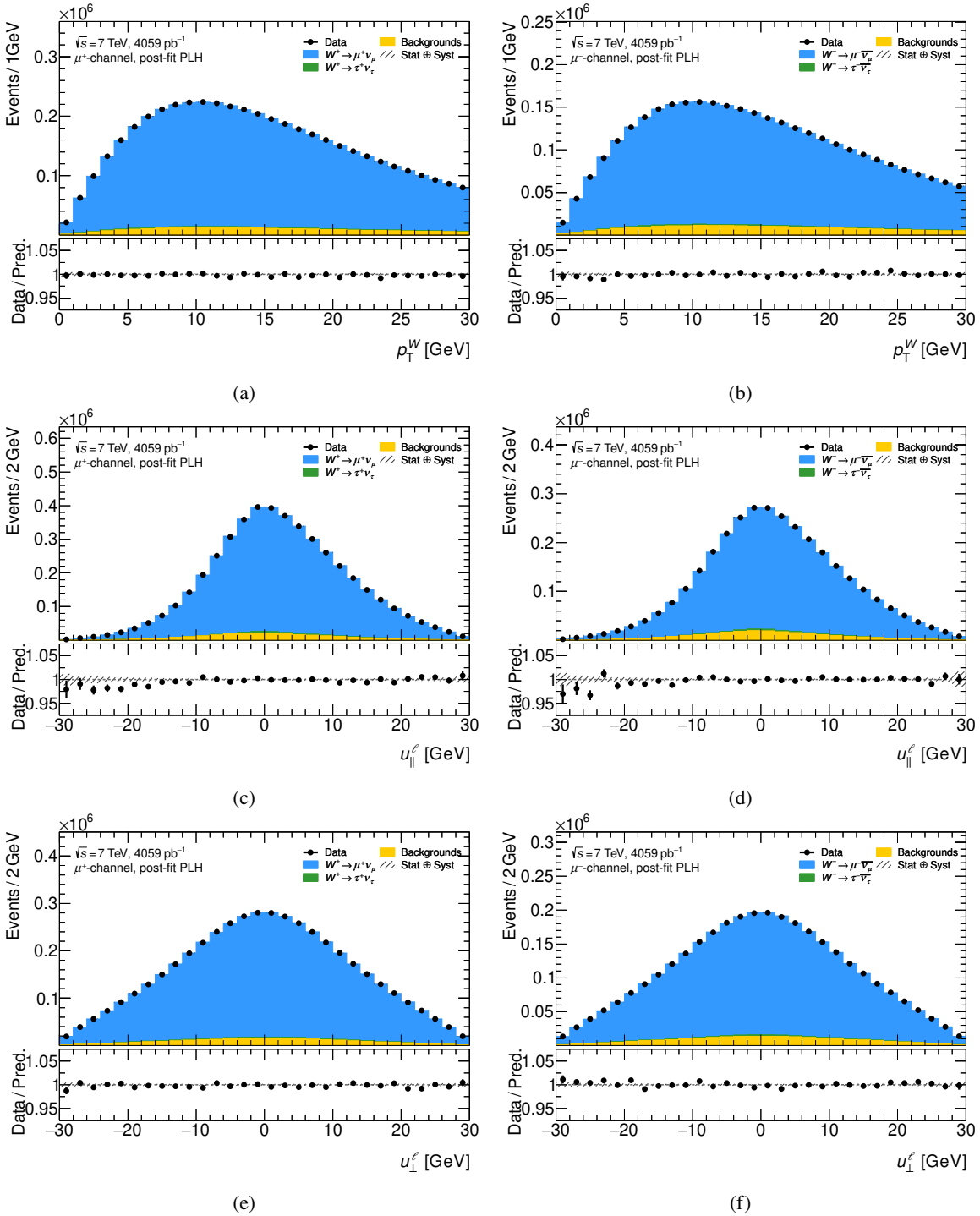

Figure F.10: Illustration of the post-fit recoil distribution in the muon channel for p_{T}^{ℓ} fits of the W-boson mass. Shown are the distributions of p_{T}^{W} (a,b), $u_{\parallel}^{\ell}$ (c,d), and $u_{\perp}^{\ell}$ (e,f) for positively (a,c,e) and negatively (b,d,f) charged muons.

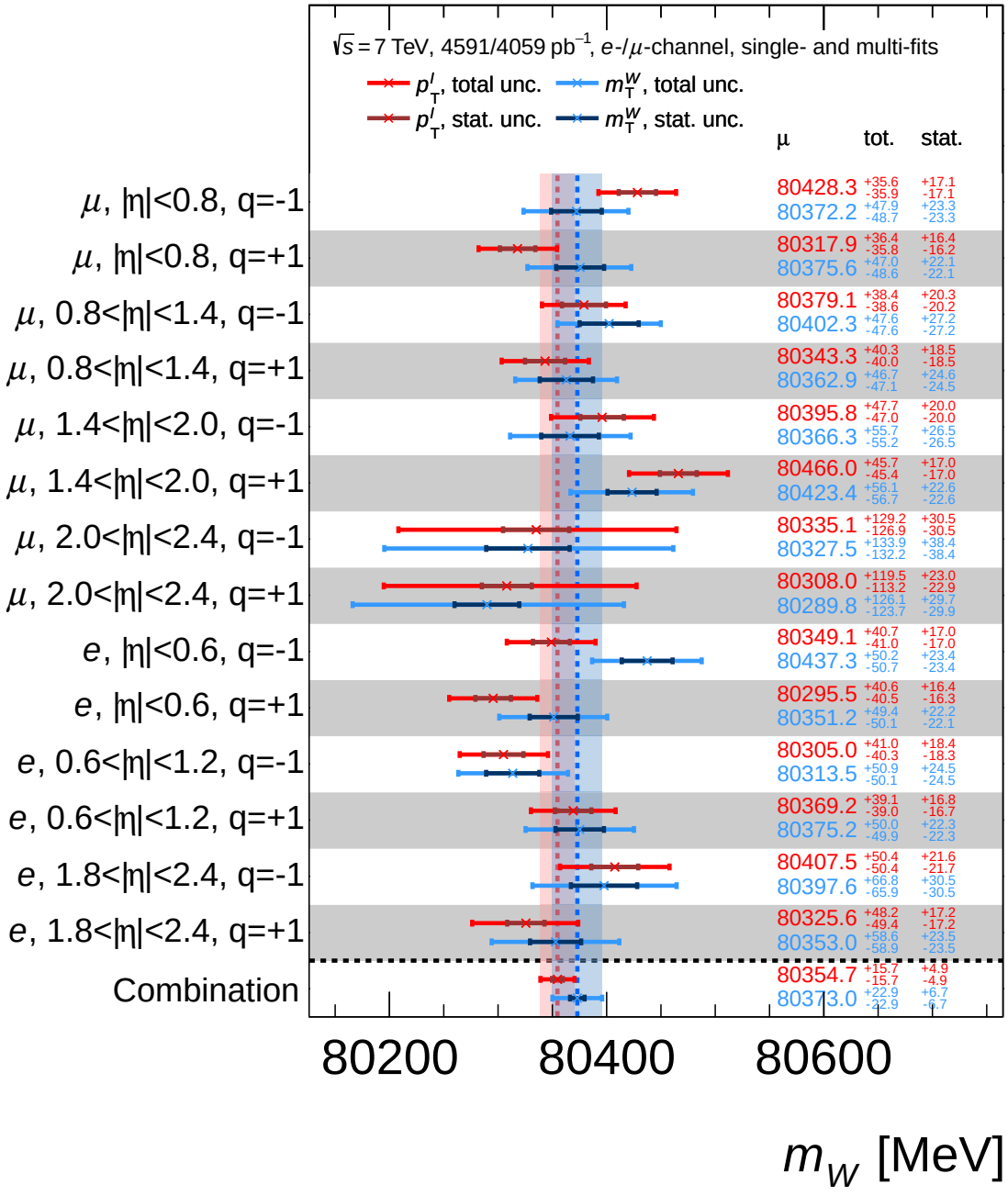

Figure F.11: Results of the PLH fit for the measurement of the W-boson mass for the individual measurement categories and their combined fit using the kinematic observables p_{T}^{ℓ} (red) and m_{T}^{W} (blue). Indicated are the central values, the total uncertainties, and the statistical uncertainties.

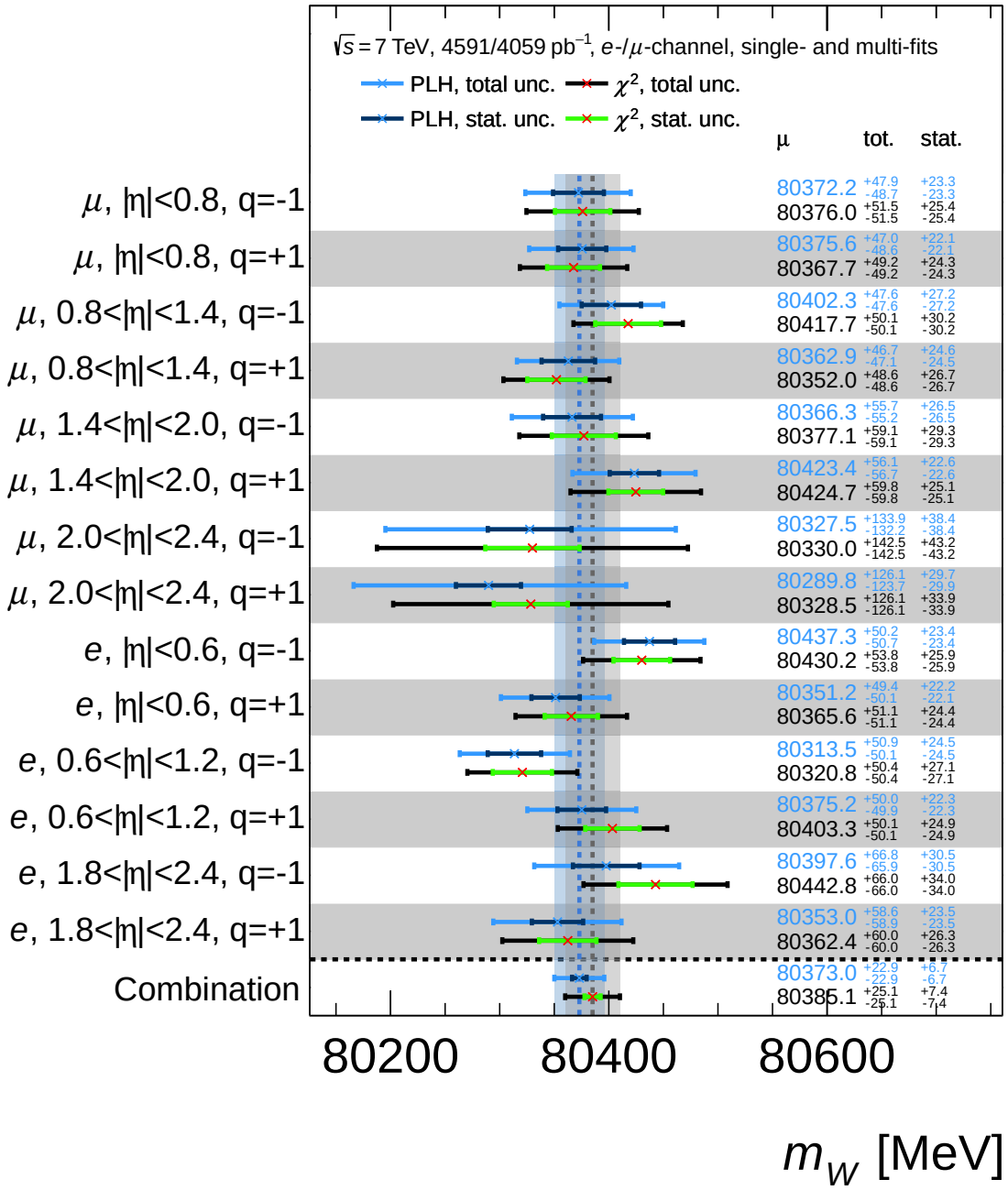

Figure F.12: Comparison of the results of the PLH fit and the χ^2 fit for the W-boson mass measurement performed in the m_{T}^{W} distribution for the individual measurement categories and their combined fit. Indicated are the central values, the total uncertainties, and the statistical uncertainties. The red and the black line mark the central values of the combination.

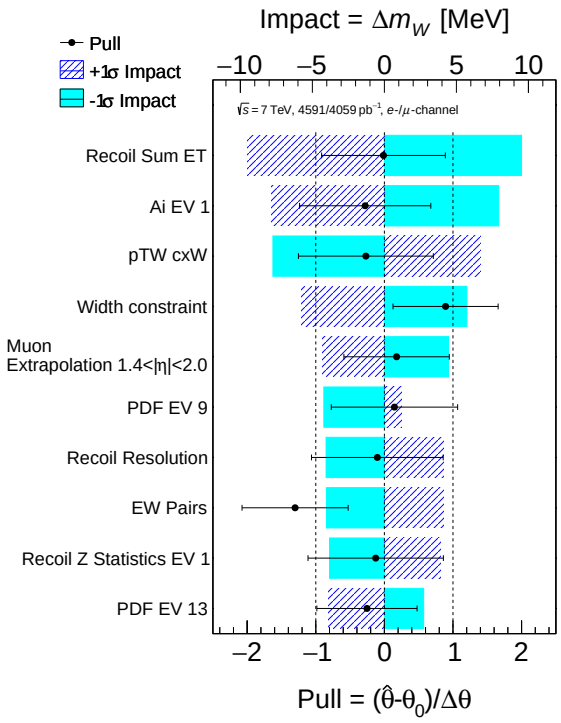

Figure F.13: The ten NPs with the highest impact on the W-boson mass measurement performed in the m_{T}^{W} distribution. Indicated are the $+1\,\sigma$ and $-1\,\sigma$ impacts, as well as the pull with its uncertainty.

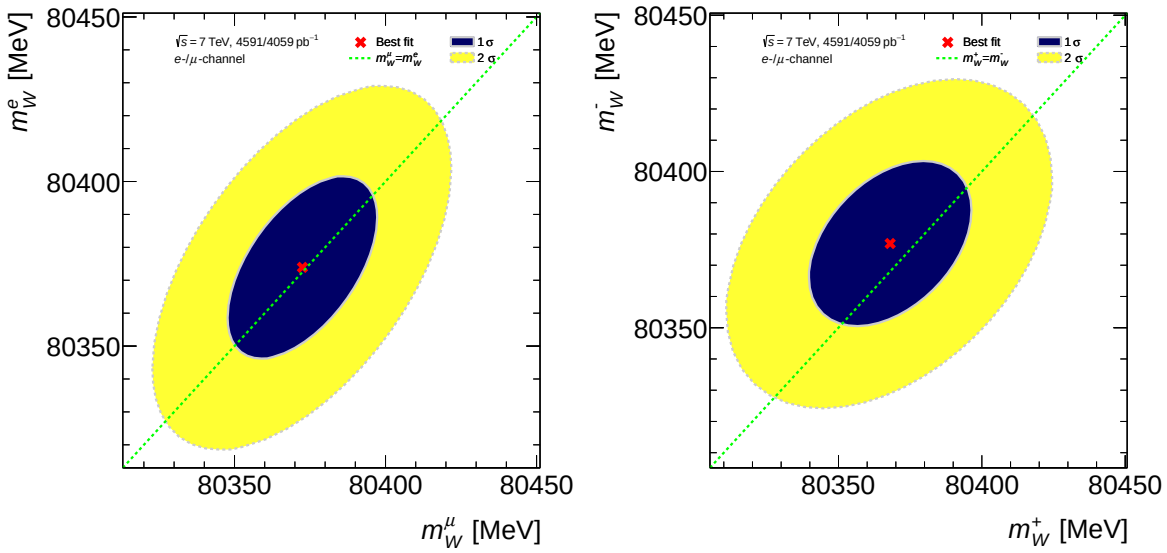

Figure F.14: Consistency plots for different sub-fits of the W-boson mass measurement performed in the m_{T}^{W} distribution. Shown are the central value and the $1\,\sigma$ and $2\,\sigma$ uncertainty contours for two POIs acting (a) on the different leptonic decay channels and (b) on the different charges of the final state lepton.

Source of uncertainty	Impact on m_W [MeV]		Ratio
	PLH fit	χ^2 fit	$\frac{\chi^2 \text{ fit}}{\text{PLH fit}}$
Recoil calibrations	11.6	15.0	1.29
Parton shower predictions and angular coefficients	10.7	9.6	0.90
PDFs	9.3	9.4	1.02
Muon calibrations	8.3	6.8	0.82
Electron calibrations	7.9	6.1	0.77
EW corrections	5.9	4.6	0.78
External measurement constraint	5.7	not included	-
Cross-section and multijet background uncertainties	5.0	5.0	1.00
Simulation sample size	2.0	6.3	3.11
Luminosity	1.7	not included	-
Total systematic uncertainty	15.1	24.0	1.59
Data sample size	5.0	7.4	1.49
Total	15.9	25.1	1.58

Table F.7: Comparison of the impact of the different uncertainty categories on the total uncertainty of the W-boson mass measurement performed in the m_{T}^{W} distribution between the χ^2 fit and the PLH fit. Shown are the $1\,\sigma$ standard deviations which are in the PLH fit calculated by leaving out a group of systematic uncertainties and determining the impact via quadratic error propagation compared to the original fit. In addition, the ratio of the impacts between the two fitting methods is given.

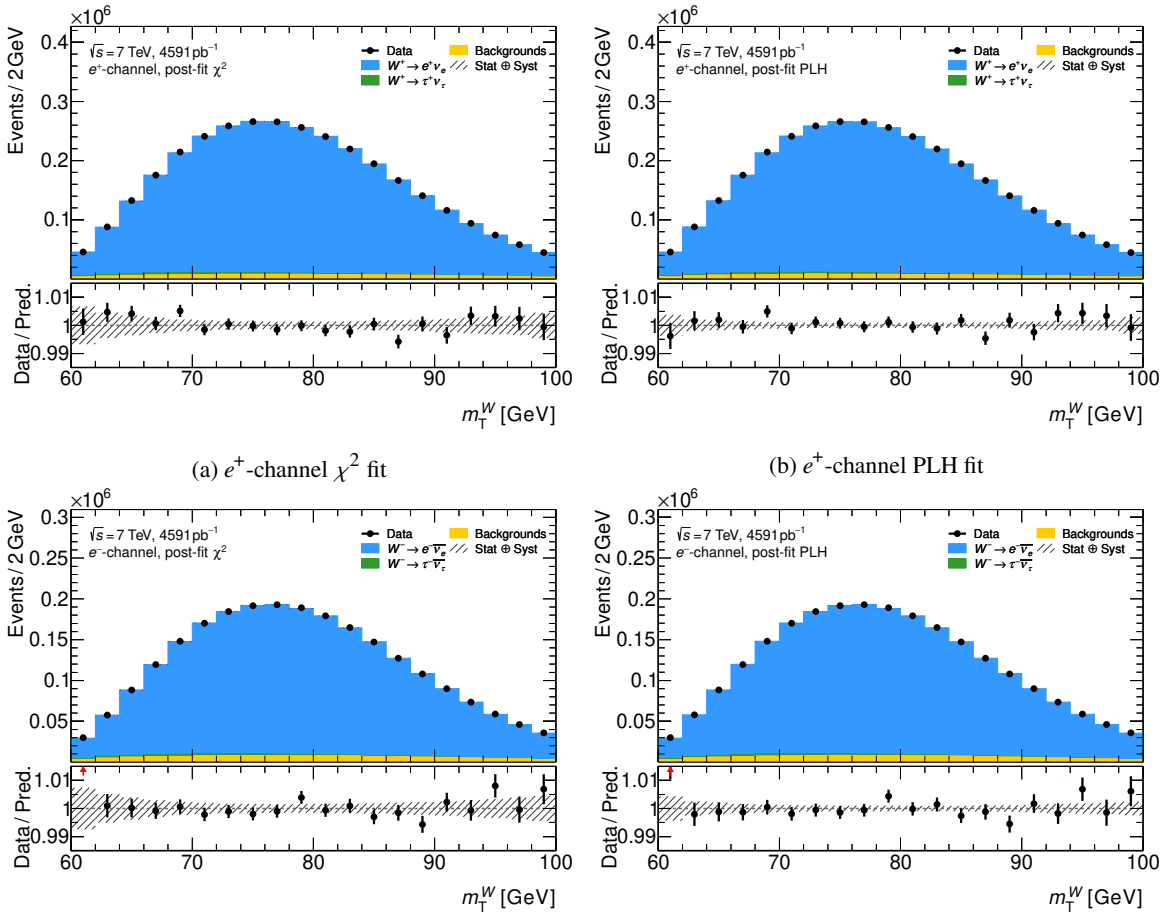

(a) e^+-channel χ^2 fit

(b) e^+-channel PLH fit

(c) e^--channel χ^2 fit

(d) e^--channel PLH fit

Figure F.15: Comparison of the post-fit m_{T}^{W} distributions in the electron channel between χ^2 fit (a,c) and PLH fit (b,d) for the W-boson mass measurement. The distributions are inclusive in pseudorapidity but given explicitly for positively (a,b) and negatively charged electrons (c,d). The lower panel shows the ratio of data to simulation where the error bars indicate the statistical uncertainty and the shaded band represents the total uncertainty.

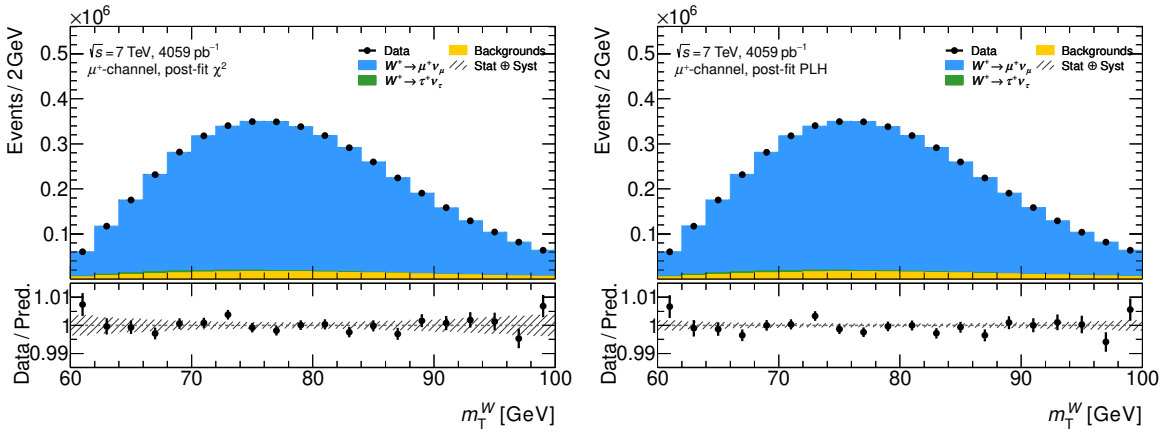

(a) μ^+-channel χ^2 fit

(b) μ^+-channel PLH fit

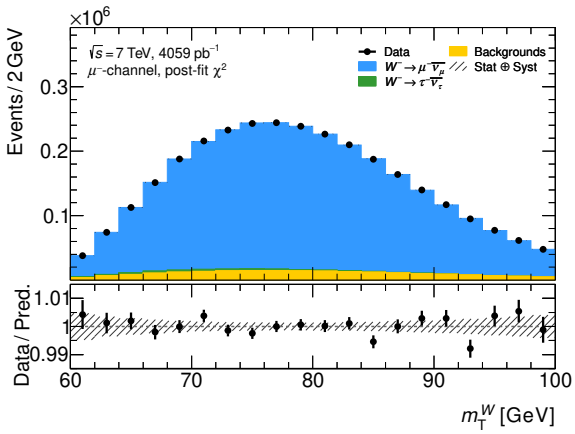

(c) μ^--channel χ^2 fit

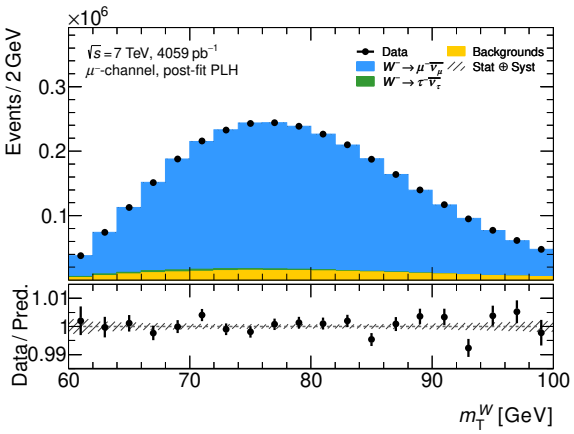

(d) μ^+-channel PLH fit

Figure F.16: Comparison of the post-fit m_{T}^{W} distributions in the muon channel between χ^2 fit (a,c) and PLH fit (b,d) for the W-boson mass measurement. The distributions are inclusive in pseudorapidity but given explicitly for positively (a,b) and negatively charged muons (c,d). The lower panel shows the ratio of data to simulation where the error bars indicate the statistical uncertainty and the shaded band represents the total uncertainty.

F.3 Measurement of the W-boson width

Shown are the recoil post-fit distributions of the observables p_{T}^{W}, $u_{\parallel}^{\ell}$, and $u_{\perp}^{\ell}$ in Figs. F.17 and F.18 for the W-boson width measurement performed in the m_{T}^{W} distribution. Beyond that, several illustrations of the p_{T}^{ℓ} fits are shown: the impact table in Table F.8, the ranking plot in Fig. F.19, the consistency checks in Fig. F.20, and the post-fit p_{T}^{ℓ} distributions in Fig. F.21.

Source of uncertainty	Impact on Γ_W [MeV]
Parton shower predictions and angular coefficients	69.2
PDFs	24.2
Electron calibrations	20.0
Muon calibrations	15.4
External measurement constraint	14.2
Cross-section and multijet background uncertainties	13.4
Recoil calibrations	13.2
Luminosity	11.0
EW corrections	8.0
Simulation sample size	5.5
Total systematic uncertainty	77.4
Data sample size	13.6
Total	78.6

Table F.8: Impact of the different uncertainty categories on the total uncertainty of the W-boson width measurement performed in the p_{T}^{ℓ} distribution. Shown are the 1 σ standard deviations which are calculated by leaving out a group of systematic uncertainties and determining the impact via quadratic error propagation compared to the original fit.

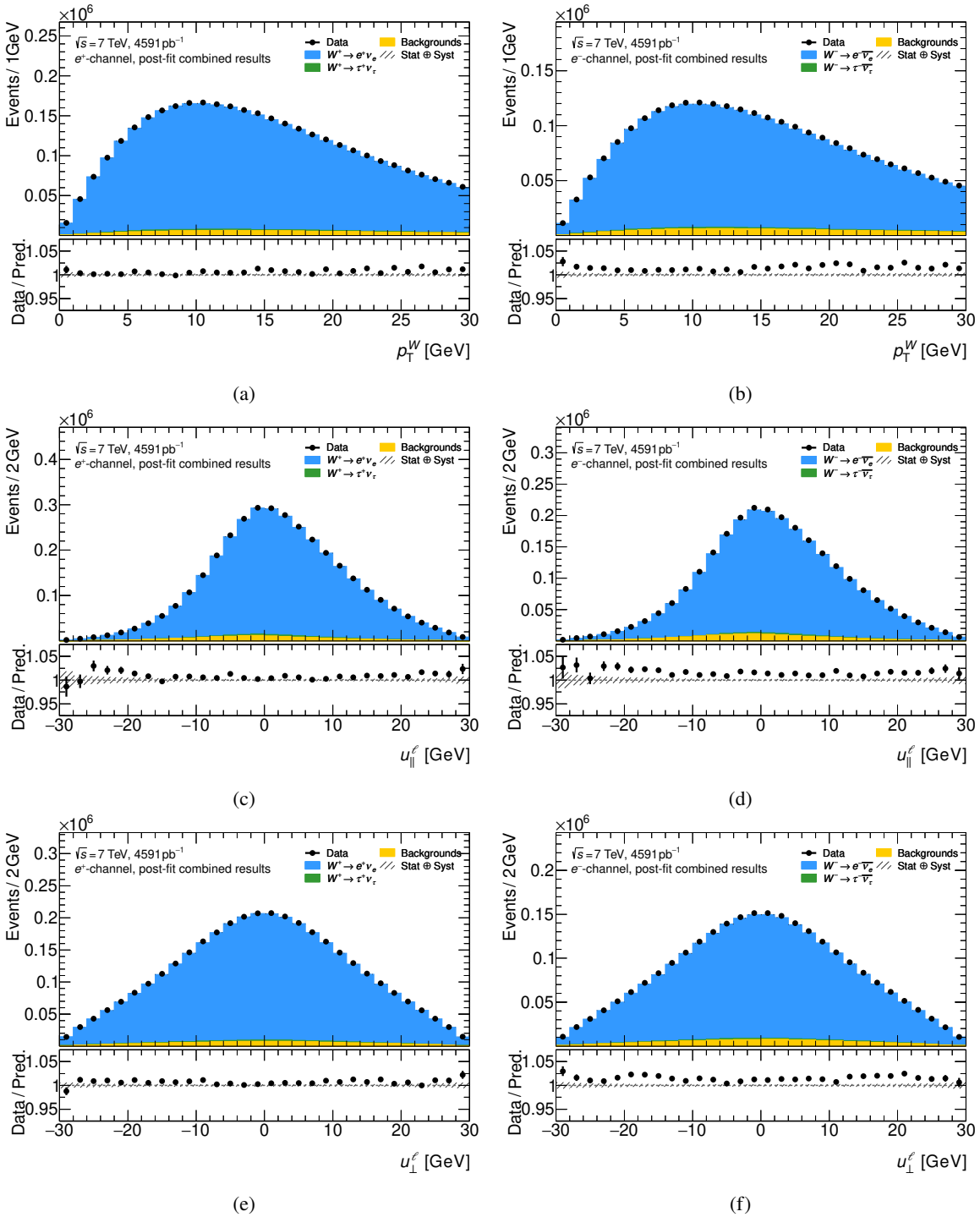

Figure F.17: Illustration of the post-fit recoil distribution in the electron channel for p_{T}^{ℓ} fits of the W-boson width. Shown are the distributions of p_{T}^{W} (a,b), $u_{\parallel}^{\ell}$ (c,d), and $u_{\perp}^{\ell}$ (e,f) for positively (a,c,e) and negatively (b,d,f) charged electrons.

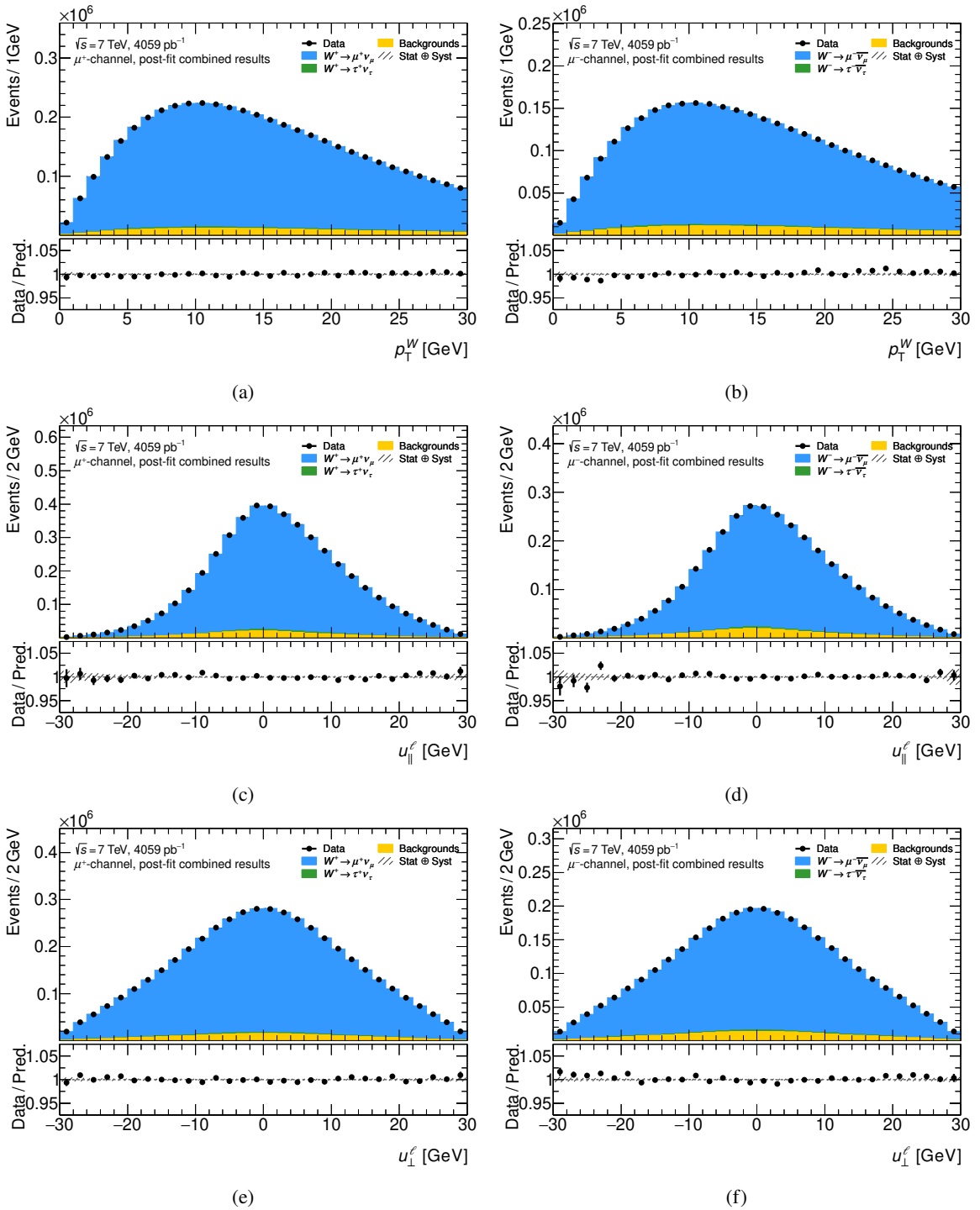

Figure F.18: Illustration of the post-fit recoil distribution in the muon channel for p_{T}^{ℓ} fits of the W-boson width. Shown are the distributions of p_{T}^{W} (a,b), $u_{\parallel}^{\ell}$ (c,d), and $u_{\perp}^{\ell}$ (e,f) for positively (a,c,e) and negatively (b,d,f) charged muons.

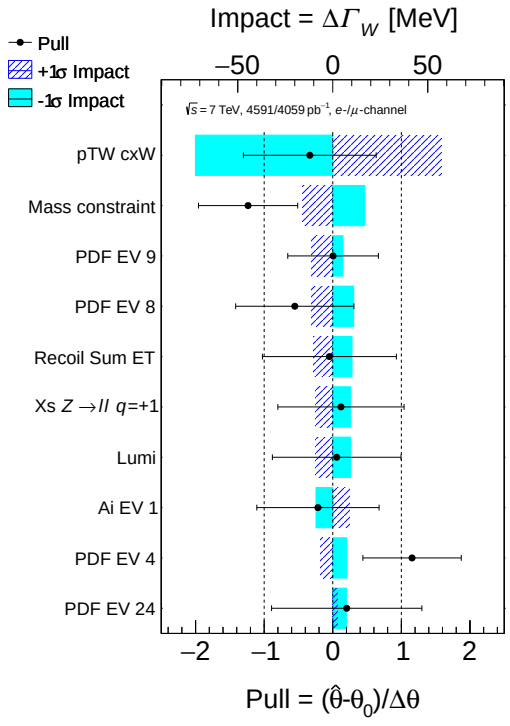

Figure F.19: The ten NPs with the highest impact on the W-boson width measurement performed in the p_{T}^{ℓ} distribution. Indicated are the $+1\,\sigma$ and $-1\,\sigma$ impacts, as well as the pull with its uncertainty.

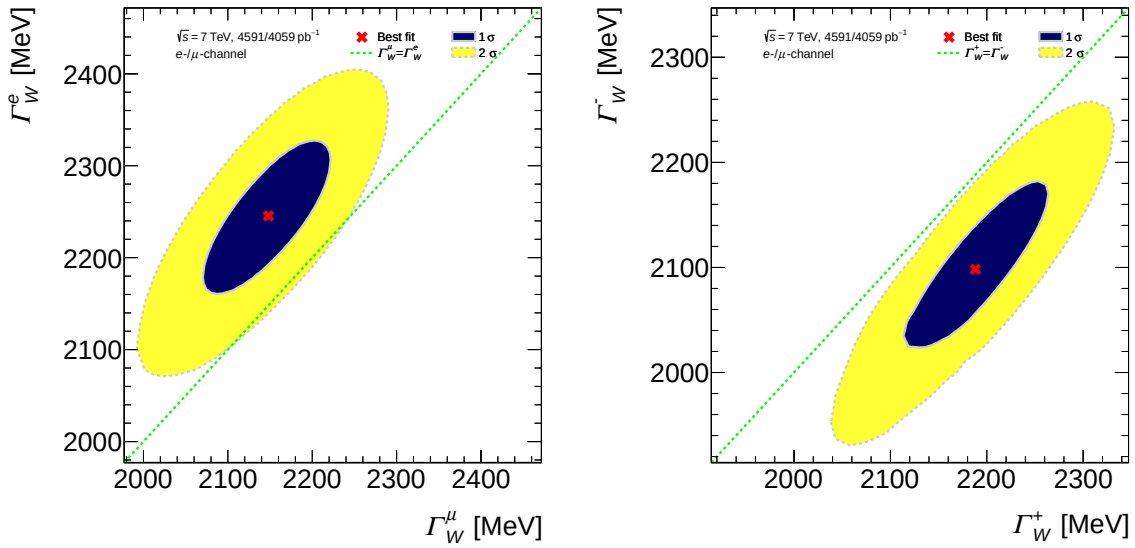

(a) (b)

Figure F.20: Consistency plots for different sub-fits of the W-boson width measurement performed in the p_{T}^{ℓ} distribution. Shown are the central value and the $1\,\sigma$ and $2\,\sigma$ uncertainty contours for two POIs acting (a) on the different leptonic decay channels and (b) on the different charges of the final state lepton.

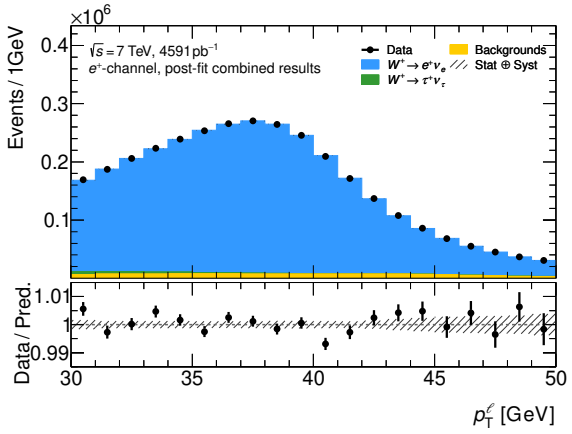

(a) e^+-channel.

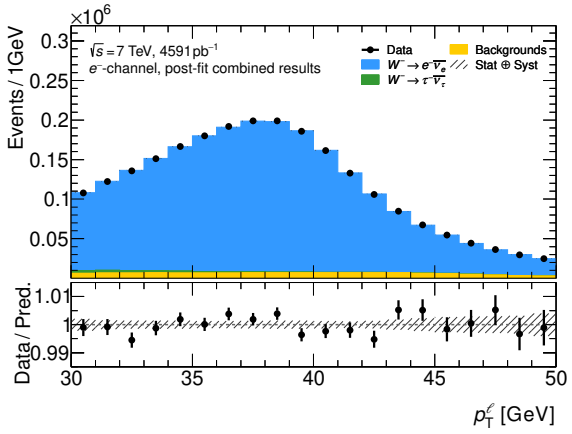

(b) e^--channel.

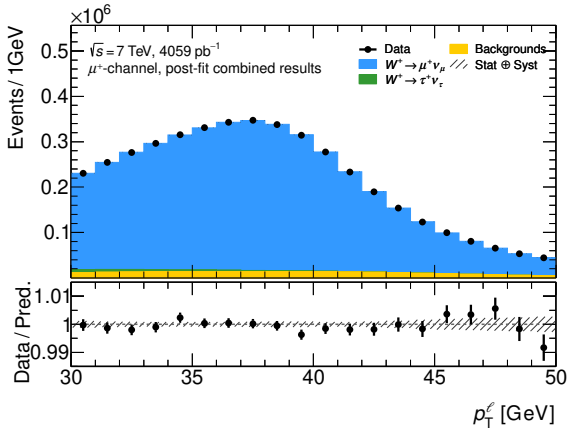

(c) μ^+-channel.

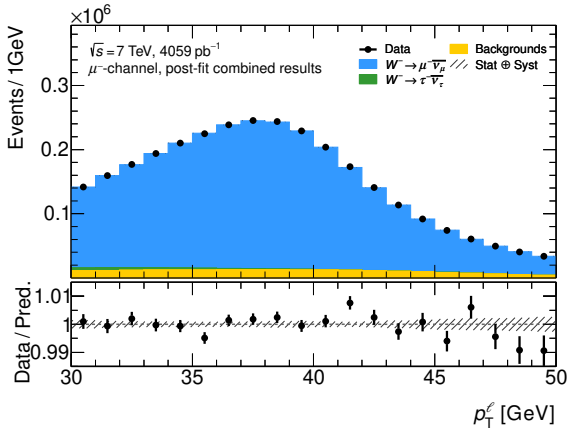

(d) μ^--channel.

Figure F.21: Post-fit distributions of p_{T}^{ℓ} for the W-boson width measurement. The distributions are inclusive in pseudorapidity but given explicitly for positively (a) and negatively charged electrons (b), and positively (c) and negatively charged muons (d). The lower panel shows the ratio of data to simulation where the error bars indicate the statistical uncertainty and the shaded band represents the total uncertainty.

F.4 Measurement of the lepton universality

Figures F.22 and F.23 show the post-fit distributions of p_{T}^{W}, $u_{\parallel}^{\ell}$, and $u_{\perp}^{\ell}$ of the lepton universality measurement performed in the p_{T}^{ℓ} distribution. Furthermore, the impact table in Table F.9, the ranking plot in Fig. F.24, the consistency checks in Fig. F.25, and the post-fit m_{T}^{W} distributions in Fig. F.26 are given for the lepton universality measurement performed in the m_{T}^{W} distribution. Tables F.10 and F.11 indicate the multijet background fractions in the SR for the electron and muon channel in the case of relaxed kinematic cuts.

Source of uncertainty	Impact on $R_{\tau\ell}$ [%]
Muon calibrations	8.0
PDFs	7.9
External measurement constraints	6.6
Parton shower predictions and angular coefficients	5.5
Cross-section and multijet background uncertainties	5.5
Simulation sample size	4.8
Electron calibrations	4.3
Recoil calibrations	3.7
EW corrections	3.3
Total systematic uncertainty	15.0
Data sample size	4.4
Total	15.2

Table F.9: Impact of the different uncertainty categories on the total uncertainty of the lepton universality measurement performed in the m_{T}^{W} distribution. Shown are the $1\,\sigma$ standard deviations which are calculated by leaving out a group of systematic uncertainties and determining the impact via quadratic error propagation compared to the original fit.

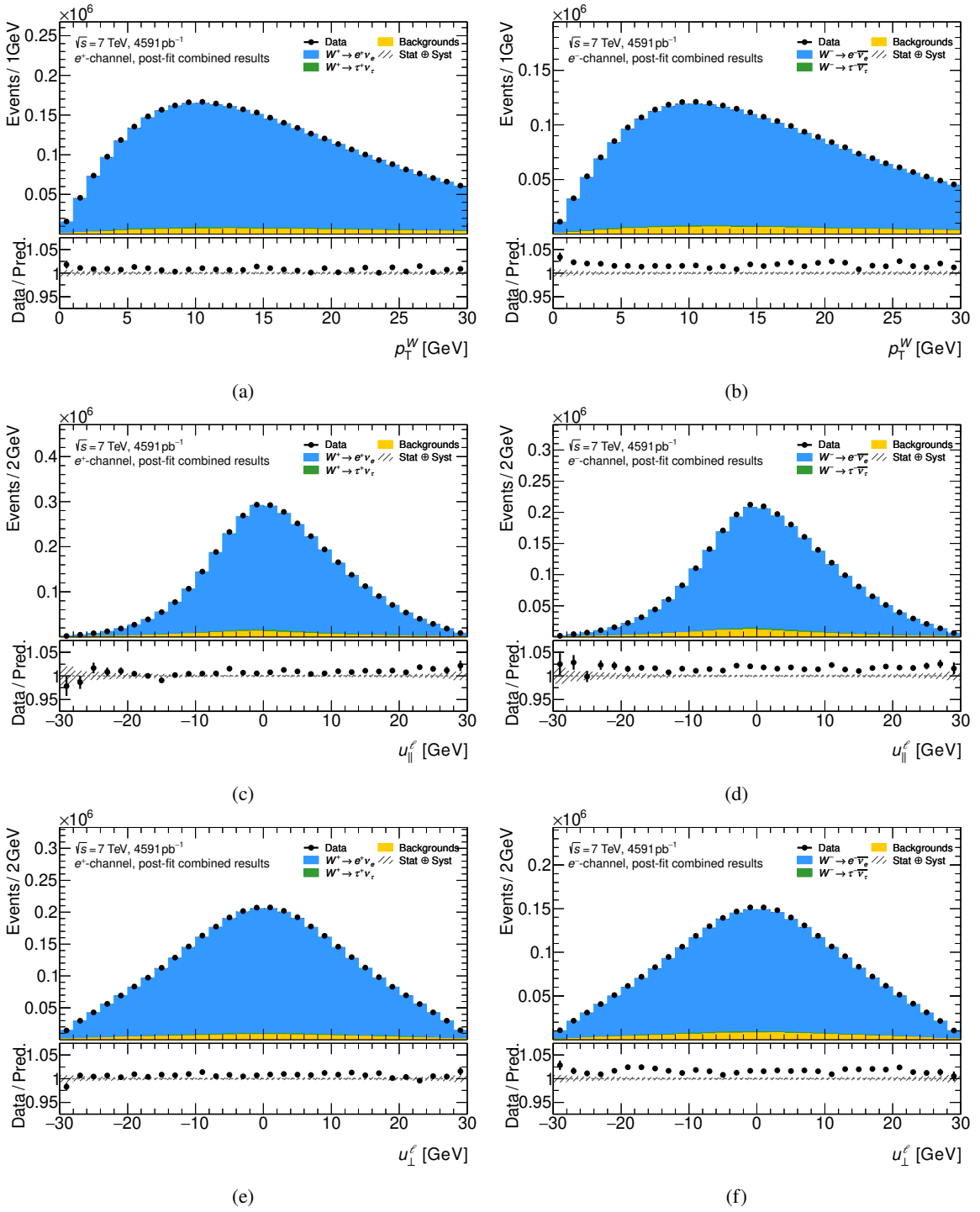

Figure F.22: Illustration of the post-fit recoil distribution in the electron channel for p_{T}^{ℓ} fits of the lepton universality. Shown are the distributions of p_{T}^{W} (a,b), $u_{\parallel}^{\ell}$ (c,d), and $u_{\perp}^{\ell}$ (e,f) for positively (a,c,e) and negatively (b,d,f) charged electrons.

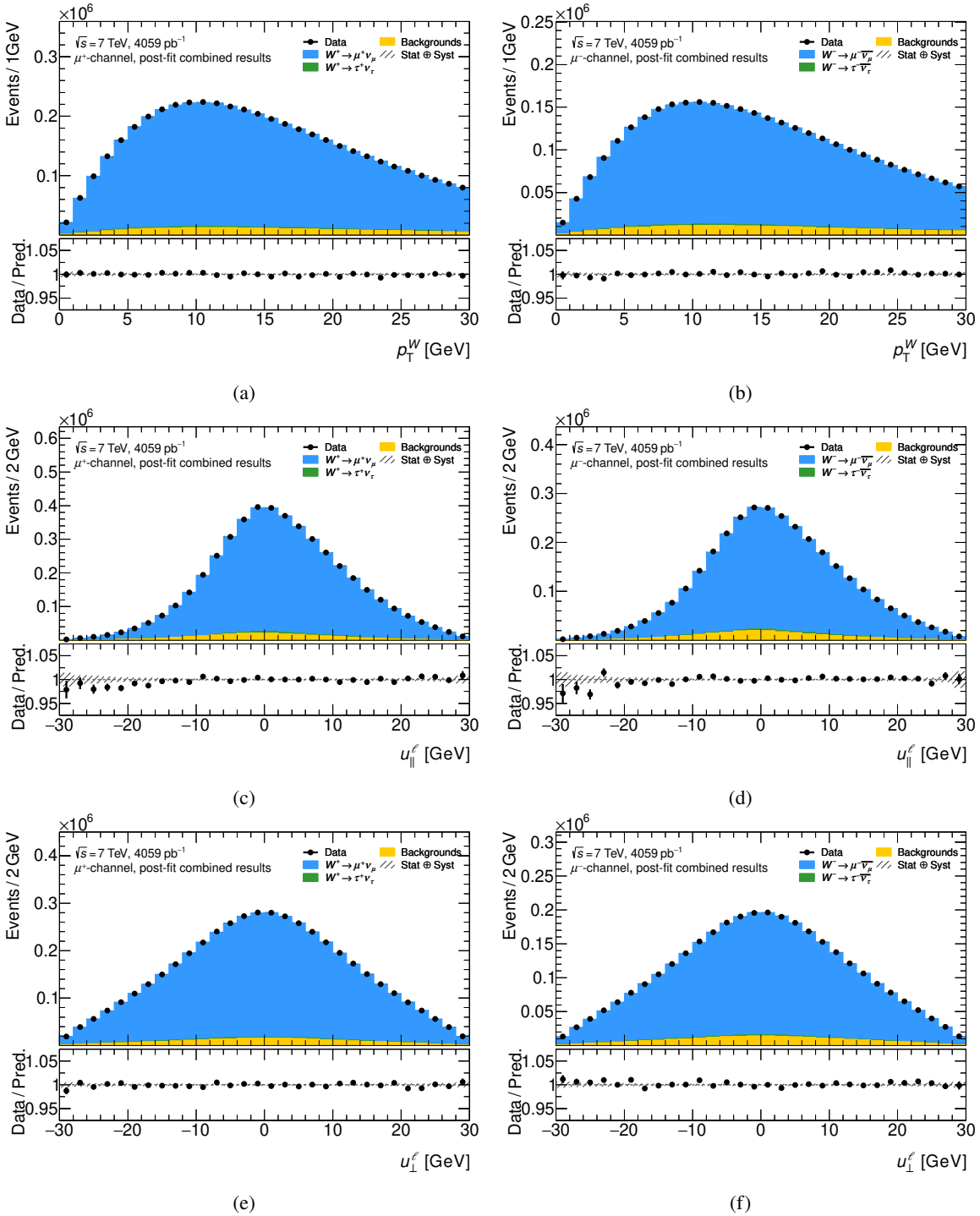

Figure F.23: Illustration of the post-fit recoil distribution in the muon channel for p_{T}^{ℓ} fits of the lepton universality. Shown are the distributions of p_{T}^{W} (a,b), $u_{\parallel}^{\ell}$ (c,d), and $u_{\perp}^{\ell}$ (e,f) for positively (a,c,e) and negatively (b,d,f) charged muons.

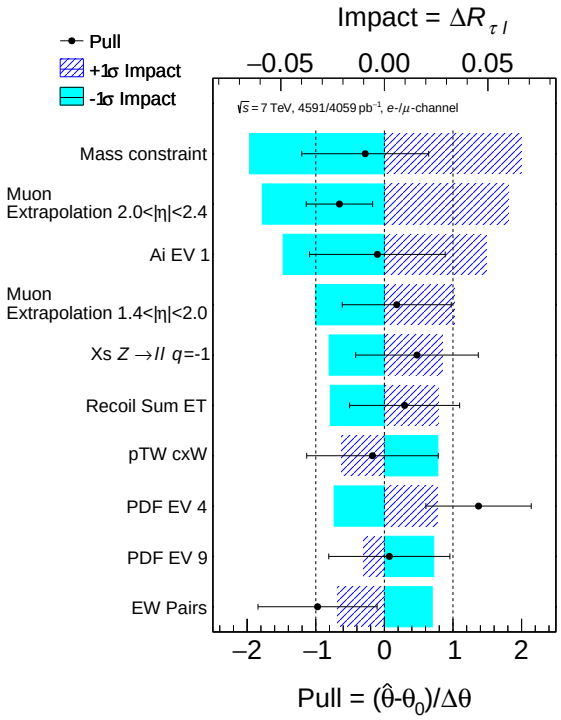

Figure F.24: The ten NPs with the highest impact on the lepton universality measurement performed in the m_{T}^{W} distribution. Indicated are the $+1\,\sigma$ and $-1\,\sigma$ impacts, as well as the pull with its uncertainty.

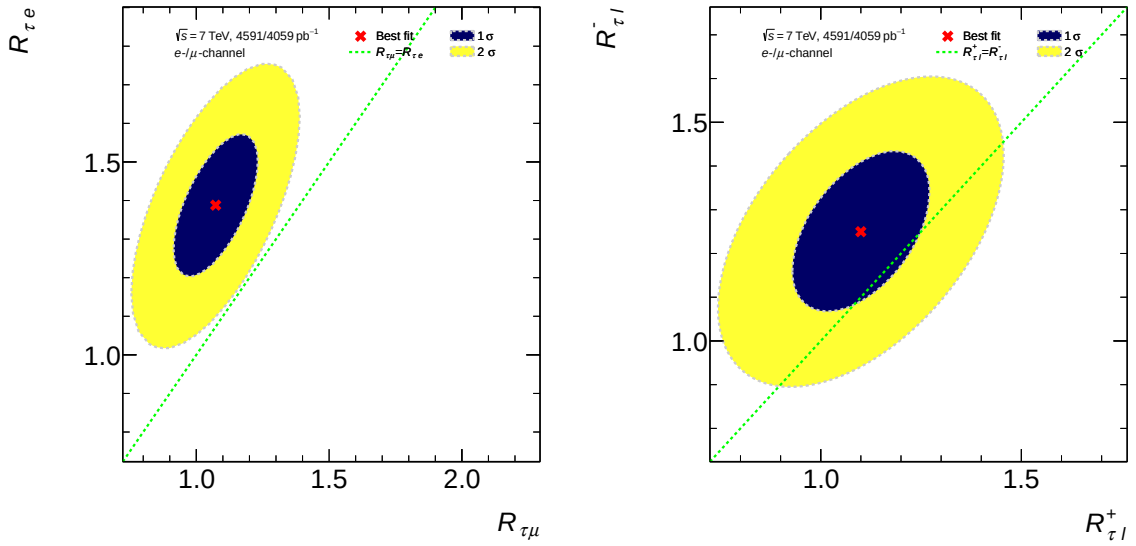

(a) (b)

Figure F.25: Consistency plots for different sub-fits of the lepton universality measurement performed in the m_{T}^{W} distribution. Shown are the central value and the $1\,\sigma$ and $2\,\sigma$ uncertainty contours for two POIs acting (a) on the different leptonic decay channels and (b) on the different charges of the final state lepton.

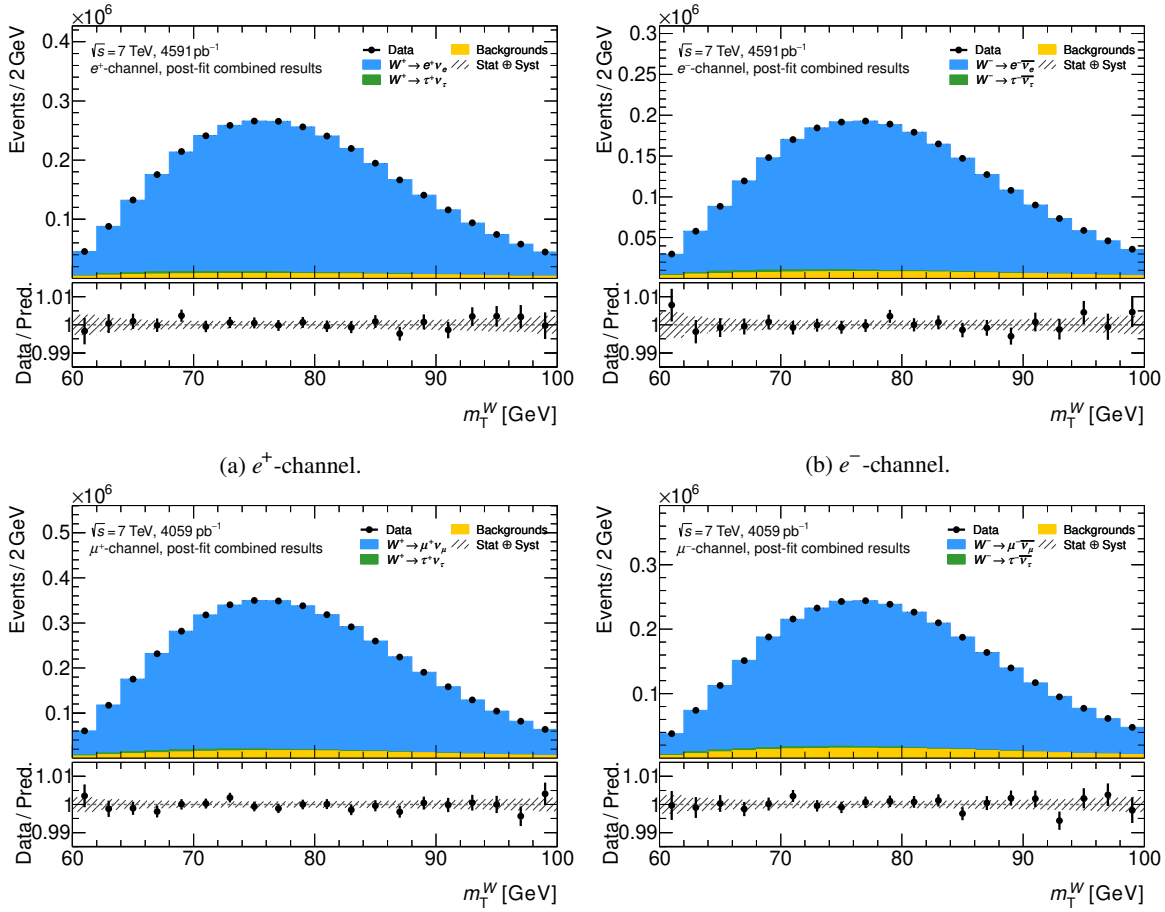

(a) e^+-channel.

(b) e^--channel.

(c) μ^+-channel.

(d) μ^--channel.

Figure F.26: Post-fit distributions of m_{T}^{W} for the lepton universality measurement. The distributions are inclusive in pseudorapidity but given explicitly for positively (a) and negatively charged electrons (b), and positively (c) and negatively charged muons (d). The lower panel shows the ratio of data to simulation where the error bars indicate the statistical uncertainty and the shaded band represents the total uncertainty.

	Fractions [%]	Number of Events	
W^+	1.20 ± 0.04	65 195	±2 483
W^+, $\|\eta\| < 0.8$	1.50 ± 0.08	23 148	±1 253
W^+, $0.8 < \|\eta\| < 1.4$	1.20 ± 0.05	15 087	± 583
W^+, $1.4 < \|\eta\| < 2.0$	1.00 ± 0.04	17 373	± 619
W^+, $2.0 < \|\eta\| < 2.4$	0.87 ± 0.04	9 260	± 396
W^-	1.60 ± 0.06	62 029	±2 352
W^-, $\|\eta\| < 0.8$	1.90 ± 0.09	22 834	±1 050
W^-, $0.8 < \|\eta\| < 1.4$	1.60 ± 0.06	14 673	± 517
W^-, $1.4 < \|\eta\| < 2.0$	1.50 ± 0.04	16 016	± 468
W^-, $2.0 < \|\eta\| < 2.4$	1.30 ± 0.06	14 673	± 517

Table F.10: Multijet background fractions f_{MJ} in the muon channel for relaxed kinematic cuts. Shown are the results and uncertainties for both charges of the W-boson and the different regions in pseudorapidity as well as the η inclusive result.

	Fractions [%]	Number of Events	
W^+	1.80 ± 0.16	75 646	±6 474
W^+, $\|\eta\| < 0.6$	1.20 ± 0.13	17 698	±1 914
W^+, $0.6 < \|\eta\| < 1.2$	1.70 ± 0.17	24 585	±2 495
W^+, $1.8 < \|\eta\| < 2.4$	2.60 ± 0.24	29 597	±2 767
W^-	2.80 ± 0.19	82 568	±5 500
W^-, $\|\eta\| < 0.6$	1.80 ± 0.15	20 588	±1 709
W^-, $0.6 < \|\eta\| < 1.2$	2.50 ± 0.26	26 539	±2 713
W^-, $1.8 < \|\eta\| < 2.4$	4.40 ± 0.23	31 594	±1 621

Table F.11: Multijet background fractions f_{MJ} in the electron channel for relaxed kinematic cuts. Shown are the results and uncertainties for both charges of the W-boson and the different regions in pseudorapidity as well as the η inclusive result.

Bibliography

[1] t. b. W. L. Plato, *Plato in Twelve Volumes, Vol. 9*, William Heinemann, 1925 (cit. on p. 1).

[2] S. Glashow, *Partial Symmetries of Weak Interactions*, Nucl. Phys. **22** (1961) 579 (cit. on p. 3).

[3] A. Salam, "Weak and Electromagnetic Interactions", *Elementary particle theory. Relativistic groups and analyticity. Proceedings of the Eighth Nobel Symposium*, ed. by N. Svartholm, Stockholm: Almquist & Wiksell, 1968 367 (cit. on p. 3).

[4] S. Weinberg, *A Model of Leptons*, Phys. Rev. Lett. **19** (1967) 1264 (cit. on p. 3).

[5] F. Halzen and A. D. Martin,
Quarks and Leptons: An Introductory Course in Modern Particle Physics, Wiley, 1984,
ISBN: 9780471887416 (cit. on pp. 3, 5, 7, 8, 10, 14, 17).

[6] M. Thomson, *Modern particle physics*, New York: Cambridge University Press, 2013,
ISBN: 978-1-107-03426-6 (cit. on pp. 3, 5, 7, 10, 14, 17, 20, 21, 27).

[7] M. J. Herrero, *The Standard Model*, (1998), arXiv: hep-ph/9812242 [hep-ph]
(cit. on pp. 3, 7, 8, 17).

[8] A. Purcell, *The Standard Model, infographic*, 2012,
URL: https://cds.cern.ch/record/1473657/files/SMinfographic_image.png
(visited on 16/07/2020) (cit. on p. 4).

[9] ATLAS Collaboration, *Observation of a new particle in the search for the Standard Model Higgs boson with the ATLAS detector at the LHC*, Phys. Lett. B **716** (2012) 1,
arXiv: 1207.7214 [hep-ex] (cit. on pp. 5, 26).

[10] CMS Collaboration,
Observation of a new boson at a mass of 125 GeV with the CMS experiment at the LHC,
Phys. Lett. B **716** (2012) 30, arXiv: 1207.7235 [hep-ex] (cit. on pp. 5, 26).

[11] C. S. Wu, E. Ambler, R. W. Hayward, D. D. Hoppes and R. P. Hudson,
Experimental Test of Parity Conservation in Beta Decay, Phys. Rev. **105** (4 1957) 1413,
URL: https://link.aps.org/doi/10.1103/PhysRev.105.1413 (cit. on p. 8).

[12] M. Goldhaber, L. Grodzins and A. W. Sunyar, *Helicity of Neutrinos*,
Phys. Rev. **109** (3 1958) 1015,
URL: https://link.aps.org/doi/10.1103/PhysRev.109.1015 (cit. on p. 8).

[13] S. Raby, *Family mixing and the origin of mass: The difference between weak eigenstates and mass eigenstates*, Los Alamos Sci. **25** (1997) 72 (cit. on p. 10).

[14] N. Cabibbo, *Unitary Symmetry and Leptonic Decays*, Phys. Rev. Lett. **10** (12 1963) 531,
URL: https://link.aps.org/doi/10.1103/PhysRevLett.10.531 (cit. on p. 10).

[15] M. Kobayashi and T. Maskawa,
CP-Violation in the Renormalizable Theory of Weak Interaction,
Progress of Theoretical Physics **49** (1973) 652, ISSN: 0033-068X, eprint: https://academic.oup.com/ptp/article-pdf/49/2/652/5257692/49-2-652.pdf,
URL: https://doi.org/10.1143/PTP.49.652 (cit. on p. 10).

[16] P. Higgs, *Broken symmetries, massless particles and gauge fields*,
Physics Letters **12** (1964) 132, ISSN: 0031-9163,
URL: http://www.sciencedirect.com/science/article/pii/0031916364911369
(cit. on p. 12).

[17] P. W. Higgs, *Broken Symmetries and the Masses of Gauge Bosons*,
Phys. Rev. Lett. **13** (16 1964) 508,
URL: https://link.aps.org/doi/10.1103/PhysRevLett.13.508 (cit. on p. 12).

[18] P. W. Higgs, *Spontaneous Symmetry Breakdown without Massless Bosons*,
Phys. Rev. **145** (4 1966) 1156,
URL: https://link.aps.org/doi/10.1103/PhysRev.145.1156 (cit. on p. 12).

[19] F. Englert and R. Brout, *Broken Symmetry and the Mass of Gauge Vector Mesons*,
Phys. Rev. Lett. **13** (9 1964) 321,
URL: https://link.aps.org/doi/10.1103/PhysRevLett.13.321 (cit. on p. 12).

[20] J. Goldstone, A. Salam and S. Weinberg, *Broken Symmetries*, Phys. Rev. **127** (3 1962) 965,
URL: https://link.aps.org/doi/10.1103/PhysRev.127.965 (cit. on p. 14).

[21] Y. Fukuda et al., *Evidence for oscillation of atmospheric neutrinos*,
Phys. Rev. Lett. **81** (1998) 1562, arXiv: hep-ex/9807003 (cit. on p. 17).

[22] Q. R. Ahmad et al., *Measurement of the Rate of $\nu_e + d \rightarrow p + p + e^-$ Interactions Produced by ^8B Solar Neutrinos at the Sudbury Neutrino Observatory*,
Phys. Rev. Lett. **87** (7 2001) 071301,
URL: https://link.aps.org/doi/10.1103/PhysRevLett.87.071301 (cit. on p. 17).

[23] G. Arnison et al., *Experimental observation of isolated large transverse energy electrons with associated missing energy at s=540 GeV*, Physics Letters B **122** (1983) 103, ISSN: 0370-2693,
URL: http://www.sciencedirect.com/science/article/pii/0370269383911772
(cit. on pp. 17, 53).

[24] M. Banner et al., *Observation of single isolated electrons of high transverse momentum in events with missing transverse energy at the CERN pp collider*,
Physics Letters B **122** (1983) 476, ISSN: 0370-2693,
URL: http://www.sciencedirect.com/science/article/pii/0370269383916052
(cit. on pp. 17, 53).

[25] P. Zyla et al., *Review of Particle Physics*, PTEP **2020** (2020) 083C01
(cit. on pp. 17, 25, 54, 56, 61, 65, 133).

[26] M. Awramik, M. Czakon, A. Freitas and G. Weiglein,
Precise prediction for the W-boson mass in the standard model, Physical Review D **69** (2004),
ISSN: 1550-2368, URL: http://dx.doi.org/10.1103/PhysRevD.69.053006
(cit. on p. 18).

[27] A. Sirlin,
Radiative corrections in the $\mathrm{SU}(2)_L \times \mathrm{U}(1)$ *theory: A simple renormalization framework*,
Phys. Rev. D **22** (4 1980) 971,
URL: https://link.aps.org/doi/10.1103/PhysRevD.22.971 (cit. on pp. 18, 52).

[28] M. Baak et al., *The global electroweak fit at NNLO and prospects for the LHC and ILC*,
The European Physical Journal C **74** (2014), ISSN: 1434-6052,
URL: http://dx.doi.org/10.1140/epjc/s10052-014-3046-5
(cit. on pp. 18, 19, 144, 158).

[29] J. M. Campbell, J. W. Huston and W. J. Stirling,
Hard interactions of quarks and gluons: a primer for LHC physics,
Reports on Progress in Physics **70** (2006) 89, ISSN: 1361-6633,
URL: http://dx.doi.org/10.1088/0034-4885/70/1/R02 (cit. on pp. 23, 25, 45).

[30] T.-J. Hou et al., *New CTEQ global analysis of quantum chromodynamics with high-precision data from the LHC*, Physical Review D **103** (2021), ISSN: 2470-0029,
URL: http://dx.doi.org/10.1103/PhysRevD.103.014013 (cit. on p. 24).

[31] M. L. Perl et al., *Evidence for Anomalous Lepton Production in* $e^+ - e^-$ *Annihilation*,
Phys. Rev. Lett. **35** (22 1975) 1489,
URL: https://link.aps.org/doi/10.1103/PhysRevLett.35.1489 (cit. on p. 25).

[32] S. Weinberg, *Implications of dynamical symmetry breaking*, Phys. Rev. D **13** (4 1976) 974,
URL: https://link.aps.org/doi/10.1103/PhysRevD.13.974 (cit. on p. 26).

[33] E. Gildener, *Gauge-symmetry hierarchies*, Phys. Rev. D **14** (6 1976) 1667,
URL: https://link.aps.org/doi/10.1103/PhysRevD.14.1667 (cit. on p. 26).

[34] L. Susskind, *Dynamics of spontaneous symmetry breaking in the Weinberg-Salam theory*,
Phys. Rev. D **20** (10 1979) 2619,
URL: https://link.aps.org/doi/10.1103/PhysRevD.20.2619 (cit. on p. 26).

[35] G. 't Hooft et al., eds., *Recent Developments in Gauge Theories. Proceedings, Nato Advanced Study Institute, Cargese, France, August 26 - September 8, 1979*, vol. 59, 1980 pp.1
(cit. on p. 26).

[36] S. P. MARTIN, *A SUPERSYMMETRY PRIMER*,
Advanced Series on Directions in High Energy Physics (1998) 1, ISSN: 1793-1339,
URL: http://dx.doi.org/10.1142/9789812839657_0001 (cit. on pp. 26, 27).

[37] N. Aghanim et al., *Planck 2018 results. VI. Cosmological parameters*,
Astron. Astrophys. **641** (2020) A6, arXiv: 1807.06209 [astro-ph.CO] (cit. on p. 27).

[38] Y. A. Gelfand and E. P. Likhtman,
Extension of the algebra of Poincare group generators and violation of P invariance,
JETP Lett. **13** (1971) 323, URL: http://cds.cern.ch/record/433516 (cit. on p. 27).

[39] D. Volkov and V. Akulov, *Is the neutrino a goldstone particle?*,
Physics Letters B **46** (1973) 109, ISSN: 0370-2693,
URL: https://www.sciencedirect.com/science/article/pii/0370269373904905
(cit. on p. 27).

[40] J. Wess and B. Zumino, *Supergauge transformations in four dimensions*, Nuclear Physics B **70** (1974) 39, ISSN: 0550-3213, URL: https://www.sciencedirect.com/science/article/pii/0550321374903551 (cit. on p. 27).

[41] J. Wess and B. Zumino, *Supergauge invariant extension of quantum electrodynamics*, Nuclear Physics B **78** (1974) 1, ISSN: 0550-3213, URL: https://www.sciencedirect.com/science/article/pii/0550321374901126 (cit. on p. 27).

[42] S. Ferrara and B. Zumino, *Supergauge invariant Yang-Mills theories*, Nuclear Physics B **79** (1974) 413, ISSN: 0550-3213, URL: https://www.sciencedirect.com/science/article/pii/0550321374905598 (cit. on p. 27).

[43] A. Salam and J. Strathdee, *Super-symmetry and non-Abelian gauges*, Physics Letters B **51** (1974) 353, ISSN: 0370-2693, URL: https://www.sciencedirect.com/science/article/pii/0370269374902263 (cit. on p. 27).

[44] P. Fayet, *Supersymmetry and weak, electromagnetic and strong interactions*, Physics Letters B **64** (1976) 159, ISSN: 0370-2693, URL: https://www.sciencedirect.com/science/article/pii/0370269376903191 (cit. on p. 27).

[45] P. Fayet, *Spontaneously broken supersymmetric theories of weak, electromagnetic and strong interactions*, Physics Letters B **69** (1977) 489, ISSN: 0370-2693, URL: https://www.sciencedirect.com/science/article/pii/0370269377908528 (cit. on p. 27).

[46] H. Nilles, *Supersymmetry, supergravity and particle physics*, Physics Reports **110** (1984) 1, ISSN: 0370-1573, URL: https://www.sciencedirect.com/science/article/pii/0370157384900085 (cit. on p. 27).

[47] S. Heinemeyer, W. Hollik, D. Stöckinger, A. M. Weber and G. Weiglein, *Precise prediction for M_W in the MSSM*, Journal of High Energy Physics **2006** (2006) 052, ISSN: 1029-8479, URL: http://dx.doi.org/10.1088/1126-6708/2006/08/052 (cit. on p. 28).

[48] S. Heinemeyer, W. Hollik, G. Weiglein and L. Zeune, *Implications of LHC search results on the W boson mass prediction in the MSSM*, Journal of High Energy Physics **2013** (2013), ISSN: 1029-8479, URL: http://dx.doi.org/10.1007/JHEP12(2013)084 (cit. on p. 28).

[49] G. Weiglein, "Electroweak Theory", LHC days in Split, 2018, URL: https://indico.cern.ch/event/704801/contributions/2998208/attachments/1719875/2776028/lhc-split_ewtheory_18.pdf (cit. on p. 28).

[50] T. D. Lee, *A Theory of Spontaneous T Violation*, Phys. Rev. D **8** (4 1973) 1226, URL: https://link.aps.org/doi/10.1103/PhysRevD.8.1226 (cit. on p. 28).

[51] G. Branco et al., *Theory and phenomenology of two-Higgs-doublet models*, Physics Reports **516** (2012) 1, ISSN: 0370-1573, URL: http://dx.doi.org/10.1016/j.physrep.2012.02.002 (cit. on p. 28).

[52] O. S. Brüning et al., *LHC Design Report*, CERN Yellow Reports: Monographs, Geneva: CERN, 2004, URL: https://cds.cern.ch/record/782076 (cit. on p. 29).

[53] J. Wenninger, *LHC status and performance*, PoS **CHARGED2018** (2019) 001 (cit. on pp. 29, 38).

[54] E. Mobs, *The CERN accelerator complex - August 2018. Complexe des accélérateurs du CERN - Août 2018*, (2018), General Photo, URL: https://cds.cern.ch/record/2636343 (cit. on p. 30).

[55] D. J. Warner, *Project study for a new 50 MeV linear accelerator for the C. P. S*, (1973), URL: http://cds.cern.ch/record/414071 (cit. on p. 29).

[56] K. Schindl, *The PS Booster as Pre-Injector for LHC*, (1997), URL: http://cds.cern.ch/record/323757 (cit. on p. 29).

[57] R. Cappi, *The PS in the LHC injector chain*, Part. Accel. **58** (1997) 79, URL: https://cds.cern.ch/record/323933 (cit. on p. 29).

[58] P. Collier et al., *The SPS as Injector for LHC: Conceptual Design*, (1997), URL: https://cds.cern.ch/record/322782 (cit. on p. 29).

[59] ATLAS Collaboration, *The ATLAS Experiment at the CERN Large Hadron Collider*, JINST **3** (2008) S08003 (cit. on p. 30).

[60] CMS Collaboration, *The CMS experiment at the CERN LHC*, JINST **3** (2008) S08004 (cit. on p. 31).

[61] LHCb Collaboration, *The LHCb Detector at the LHC*, JINST **3** (2008) S08005, Also published by CERN Geneva in 2010, URL: http://cds.cern.ch/record/1129809 (cit. on p. 31).

[62] ALICE Collaboration, *The ALICE experiment at the CERN LHC. A Large Ion Collider Experiment*, JINST **3** (2008) S08002. 259 p, Also published by CERN Geneva in 2010, URL: http://cds.cern.ch/record/1129812 (cit. on p. 31).

[63] ATLAS Collaboration, *Improved luminosity determination in pp collisions at $\sqrt{s}$ = 7 TeV using the ATLAS detector at the LHC*, Eur. Phys. J. C **73** (2013) 2518, arXiv: 1302.4393 [hep-ex] (cit. on pp. 31, 39).

[64] K. Wille, *Physik der Teilchenbeschleuniger und Synchrotronstrahlungsquellen*, B. G. Teubner Stuttgart, 1996 (cit. on p. 31).

[65] E. Wilson, *An introduction to particle accelerators*, Oxford University Press, 2001, ISBN: 0-19-850829-8 (cit. on p. 31).

[66] J. Pequenao, "Computer generated image of the whole ATLAS detector", 2008, URL: https://cds.cern.ch/record/1095924 (cit. on p. 32).

[67] ATLAS Collaboration, *ATLAS Inner Detector: Technical Design Report, 2*, ATLAS-TDR-5, CERN, 1997, URL: https://cds.cern.ch/record/331064 (cit. on p. 33).

[68] J. Pequenao, "Computer generated image of the ATLAS inner detector", 2008, URL: https://cds.cern.ch/record/1095926 (cit. on p. 34).

[69] J. Pequenao, "Computer Generated image of the ATLAS calorimeter", 2008, URL: https://cds.cern.ch/record/1095927 (cit. on p. 35).

[70] ATLAS Collaboration, *ATLAS Liquid-Argon Calorimeter: Technical Design Report*, ATLAS-TDR-2, CERN, 1996, URL: https://cds.cern.ch/record/331061 (cit. on p. 35).

[71] ATLAS Collaboration, *ATLAS Tile Calorimeter: Technical Design Report*, ATLAS-TDR-3, CERN, 1996, URL: https://cds.cern.ch/record/331062 (cit. on p. 36).

[72] A. Henriques, "The ATLAS tile calorimeter", *2015 4th International Conference on Advancements in Nuclear Instrumentation Measurement Methods and their Applications (ANIMMA)*, 2015 1 (cit. on p. 36).

[73] ATLAS Collaboration, *ATLAS Muon Spectrometer: Technical Design Report*, ATLAS-TDR-10, CERN, 1997, URL: https://cds.cern.ch/record/331068 (cit. on p. 37).

[74] J. Pequenao, "Computer generated image of the ATLAS Muons subsystem", 2008, URL: https://cds.cern.ch/record/1095929 (cit. on p. 37).

[75] ATLAS Collaboration, *ATLAS Magnet System: Technical Design Report, 1*, ATLAS-TDR-6, CERN, 1997, URL: https://cds.cern.ch/record/338080 (cit. on p. 38).

[76] ATLAS Collaboration, *ATLAS Central Solenoid: Technical Design Report*, ATLAS-TDR-9, CERN, 1997, URL: https://cds.cern.ch/record/331067 (cit. on p. 38).

[77] ATLAS Collaboration, *ATLAS Barrel Toroid: Technical Design Report*, ATLAS-TDR-7, CERN, 1997, URL: https://cds.cern.ch/record/331065 (cit. on p. 38).

[78] ATLAS Collaboration, *ATLAS End-Cap Toroids: Technical Design Report*, ATLAS-TDR-8, CERN, 1997, URL: https://cds.cern.ch/record/331066 (cit. on p. 38).

[79] ATLAS Collaboration, *Performance of the ATLAS Trigger System in 2010*, Eur. Phys. J. C **72** (2012) 1849, arXiv: 1110.1530 [hep-ex] (cit. on p. 39).

[80] R. S., *The Performance of the ATLAS Trigger System in the LHC proton-proton Collisions*, Physics Procedia **37** (2012) (cit. on p. 39).

[81] A. Collaboration, *ATLAS Experiment - Luminosity Public Results*, 2011, URL: https://twiki.cern.ch/twiki/bin/view/AtlasPublic/LuminosityPublicResults (visited on 21/10/2020) (cit. on p. 39).

[82] J. Pequenao and P. Schaffner, "How ATLAS detects particles: diagram of particle paths in the detector", 2013, URL: https://cds.cern.ch/record/1505342 (cit. on p. 40).

[83] ATLAS Collaboration, *Electron reconstruction and identification efficiency measurements with the ATLAS detector using the 2011 LHC proton–proton collision data*, Eur. Phys. J. C **74** (2014) 2941, arXiv: 1404.2240 [hep-ex] (cit. on pp. 41, 42, 59, 60, 110, 114).

[84] ATLAS Collaboration,
Electron and photon energy calibration with the ATLAS detector using LHC Run 1 data,
Eur. Phys. J. C **74** (2014) 3071, arXiv: 1407.5063 [hep-ex] (cit. on pp. 41, 59, 113).

[85] *Performance of the ATLAS Electron and Photon Trigger in p-p Collisions at sqrts = 7 TeV in 2011*, tech. rep., All figures including auxiliary figures are available at https://atlas.web.cern.ch/Atlas/GROUPS/PHYSICS/CONFNOTES/ATLAS-CONF-2012-048: CERN, 2012, URL: https://cds.cern.ch/record/1450089 (cit. on p. 41).

[86] ATLAS Collaboration,
Measurement of the W-boson mass in pp collisions at $\sqrt{s} = 7$ TeV with the ATLAS detector,
Eur. Phys. J. C **78** (2018) 110, arXiv: 1701.07240 [hep-ex] (cit. on pp. 41, 43, 54, 58, 60, 68, 87, 101–106, 108–121, 123, 135, 136, 153, 187–189, 191–193),
Erratum: Eur. Phys. J. C **78** (2018) 898.

[87] ATLAS Collaboration, *Measurement of the muon reconstruction performance of the ATLAS detector using 2011 and 2012 LHC proton–proton collision data*,
Eur. Phys. J. C **74** (2014) 3130, arXiv: 1407.3935 [hep-ex]
(cit. on pp. 42, 59, 60, 109, 111).

[88] T. Matsushita, *Performance of the ATLAS muon trigger in 2011*, tech. rep., CERN, 2012,
URL: https://cds.cern.ch/record/1455099 (cit. on p. 42).

[89] M. Cacciari, G. P. Salam and G. Soyez, *The anti-ktjet clustering algorithm*,
Journal of High Energy Physics **2008** (2008) 063,
URL: https://doi.org/10.1088%2F1126-6708%2F2008%2F04%2F063 (cit. on p. 43).

[90] ATLAS Collaboration, *Identification and energy calibration of hadronically decaying tau leptons with the ATLAS experiment in pp collisions at $\sqrt{s} = 8$ TeV*,
Eur. Phys. J. C **75** (2015) 303, arXiv: 1412.7086 [hep-ex] (cit. on p. 43).

[91] ATLAS Collaboration, *Performance of missing transverse momentum reconstruction in proton–proton collisions at $\sqrt{s} = 7$ TeV with ATLAS*, Eur. Phys. J. C **72** (2012) 1844,
arXiv: 1108.5602 [hep-ex] (cit. on p. 44).

[92] ATLAS Collaboration,
Topological cell clustering in the ATLAS calorimeters and its performance in LHC Run 1,
Eur. Phys. J. C **77** (2017) 490, arXiv: 1603.02934 [hep-ex] (cit. on p. 44).

[93] S. Höche, "Introduction to parton-shower event generators",
Theoretical Advanced Study Institute in Elementary Particle Physics: Journeys Through the Precision Frontier: Amplitudes for Colliders, 2015 235, arXiv: 1411.4085 [hep-ph]
(cit. on pp. 45, 46).

[94] A. Buckley et al., *General-purpose event generators for LHC physics*,
Physics Reports **504** (2011) 145, ISSN: 0370-1573,
URL: http://www.sciencedirect.com/science/article/pii/S0370157311000846
(cit. on p. 45).

[95] ATLAS Collaboration, *The ATLAS Simulation Infrastructure*, Eur. Phys. J. C **70** (2010) 823,
arXiv: 1005.4568 [physics.ins-det] (cit. on p. 45).

[96] S. Agostinelli et al., *Geant4—a simulation toolkit*,
Nuclear Instruments and Methods in Physics Research Section A: Accelerators, Spectrometers, Detectors and Associated Equipment **506** (2003) 250, ISSN: 0168-9002,
URL: http://www.sciencedirect.com/science/article/pii/S0168900203013688 (cit. on p. 45).

[97] P. Nason, *A New Method for Combining NLO QCD with Shower Monte Carlo Algorithms*,
Journal of High Energy Physics **2004** (2004) 040,
URL: https://doi.org/10.1088%2F1126-6708%2F2004%2F11%2F040 (cit. on p. 45).

[98] S. Frixione, P. Nason and C. Oleari,
Matching NLO QCD computations with parton shower simulations: the POWHEG method,
Journal of High Energy Physics **2007** (2007) 070,
URL: https://doi.org/10.1088%2F1126-6708%2F2007%2F11%2F070 (cit. on p. 45).

[99] S. Alioli, P. Nason, C. Oleari and E. Re, *A general framework for implementing NLO calculations in shower Monte Carlo programs: the POWHEG BOX*,
Journal of High Energy Physics **2010** (2010), ISSN: 1029-8479,
URL: http://dx.doi.org/10.1007/JHEP06(2010)043 (cit. on p. 45).

[100] H.-L. Lai et al., *New parton distributions for collider physics*, Physical Review D **82** (2010), ISSN: 1550-2368, URL: http://dx.doi.org/10.1103/PhysRevD.82.074024 (cit. on p. 45).

[101] T. Sjöstrand, S. Mrenna and P. Skands, *PYTHIA 6.4 physics and manual*,
Journal of High Energy Physics **2006** (2006) 026, ISSN: 1029-8479,
URL: http://dx.doi.org/10.1088/1126-6708/2006/05/026 (cit. on p. 45).

[102] T. Sjöstrand, S. Mrenna and P. Skands, *A brief introduction to PYTHIA 8.1*,
Computer Physics Communications **178** (2008) 852, ISSN: 0010-4655,
URL: http://dx.doi.org/10.1016/j.cpc.2008.01.036 (cit. on p. 45).

[103] J. Pumplin et al.,
New Generation of Parton Distributions with Uncertainties from Global QCD Analysis,
Journal of High Energy Physics **2002** (2002) 012, ISSN: 1029-8479,
URL: http://dx.doi.org/10.1088/1126-6708/2002/07/012 (cit. on p. 46).

[104] ATLAS Collaboration, *Measurement of the Z/γ^* boson transverse momentum distribution in pp collisions at $\sqrt{s} = 7$ TeV with the ATLAS detector*, JHEP **09** (2014) 145,
arXiv: 1406.3660 [hep-ex] (cit. on pp. 46, 104).

[105] P. Golonka and Z. Was,
PHOTOS Monte Carlo: a precision tool for QED correctionsin Z and W decays,
The European Physical Journal C **45** (2006) 97, ISSN: 1434-6052,
URL: http://dx.doi.org/10.1140/epjc/s2005-02396-4 (cit. on p. 46).

[106] S. Frixione and B. R. Webber,
Matching NLO QCD computations and parton shower simulations,
Journal of High Energy Physics **2002** (2002) 029, ISSN: 1029-8479,
URL: http://dx.doi.org/10.1088/1126-6708/2002/06/029 (cit. on p. 46).

[107] S. Frixione, P. Nason and B. R. Webber,
Matching NLO QCD and parton showers in heavy flavour production,
Journal of High Energy Physics **2003** (2003) 007, ISSN: 1029-8479,
URL: http://dx.doi.org/10.1088/1126-6708/2003/08/007 (cit. on p. 46).

[108] S. Frixione, E. Laenen, P. Motylinski and B. R. Webber, *Single-top production in MC@NLO*,
Journal of High Energy Physics **2006** (2006) 092, ISSN: 1029-8479,
URL: http://dx.doi.org/10.1088/1126-6708/2006/03/092 (cit. on p. 46).

[109] G. Corcella et al., *HERWIG 6: an event generator for hadron emission reactions with interfering gluons (including supersymmetric processes)*,
Journal of High Energy Physics **2001** (2001) 010, ISSN: 1029-8479,
URL: http://dx.doi.org/10.1088/1126-6708/2001/01/010 (cit. on p. 46).

[110] J. M. Butterworth, J. R. Forshaw and M. H. Seymour,
Multiparton interactions in photoproduction at HERA,
Zeitschrift für Physik C: Particles and Fields **72** (1996) 637, ISSN: 1431-5858,
URL: http://dx.doi.org/10.1007/s002880050286 (cit. on p. 46).

[111] J. Smith, W. L. van Neerven and J. A. M. Vermaseren,
Transverse Mass and Width of the W Boson, Phys. Rev. Lett. **50** (22 1983) 1738,
URL: https://link.aps.org/doi/10.1103/PhysRevLett.50.1738 (cit. on p. 50).

[112] M. Boonekamp, *Private communication*, 2022 (cit. on pp. 51, 52).

[113] E. R. Cohen, *1973 table of the fundamental physical constants*,
At. Data Nucl. Data Tables; (United States) **18:6** (1976),
URL: https://www.osti.gov/biblio/7106645 (cit. on p. 52).

[114] W. J. Marciano and A. Sirlin, *Radiative corrections to neutrino-induced neutral-current phenomena in the* $\mathrm{SU}(2)_L \times \mathrm{U}(1)$ *theory*, Phys. Rev. D **22** (11 1980) 2695,
URL: https://link.aps.org/doi/10.1103/PhysRevD.22.2695 (cit. on p. 52).

[115] C. Llewellyn Smith and J. Wheater,
Electroweak radiative corrections and the value of $\sin^2\theta_w$, Physics Letters B **105** (1981) 486,
ISSN: 0370-2693,
URL: https://www.sciencedirect.com/science/article/pii/0370269381912107
(cit. on p. 53).

[116] J. Abdallah et al.,
Measurement of the mass and width of the W boson in e+e- collisions at $\sqrt{s}$*= 161–209 GeV*,
The European Physical Journal C **55** (2008), ISSN: 1434-6052,
URL: http://dx.doi.org/10.1140/epjc/s10052-008-0585-7 (cit. on pp. 53, 56).

[117] G. Abbiendi, *Measurement of the mass and width of the W boson*,
The European Physical Journal C **45** (2005) 307, ISSN: 1434-6052,
URL: http://dx.doi.org/10.1140/epjc/s2005-02440-5 (cit. on pp. 53, 56).

[118] *Measurement of the mass and the width of the W boson at LEP*,
The European Physical Journal C **45** (2006) 569, ISSN: 1434-6052,
URL: http://dx.doi.org/10.1140/epjc/s2005-02459-6 (cit. on pp. 53, 56).

[119] S. Schael et al., *Measurement of the W boson mass and width in e+e- collisions at LEP*, The European Physical Journal C **47** (2006) 309, ISSN: 1434-6052, URL: http://dx.doi.org/10.1140/epjc/s2006-02576-8 (cit. on pp. 53, 56).

[120] *Electroweak measurements in electron–positron collisions at W-boson-pair energies at LEP*, Physics Reports **532** (2013) 119, Electroweak Measurements in Electron-Positron Collisions at W-Boson-Pair Energies at LEP, ISSN: 0370-1573, URL: http://www.sciencedirect.com/science/article/pii/S0370157313002706 (cit. on pp. 53, 56, 57).

[121] J. Erler and M. Schott, *Electroweak precision tests of the Standard Model after the discovery of the Higgs boson*, Progress in Particle and Nuclear Physics **106** (2019) 68, ISSN: 0146-6410, URL: http://dx.doi.org/10.1016/j.ppnp.2019.02.007 (cit. on pp. 54, 56).

[122] V. M. Abazov et al., *Measurement of the W-Boson Mass with the D0 Detector*, Physical Review Letters **108** (2012), ISSN: 1079-7114, URL: http://dx.doi.org/10.1103/PhysRevLett.108.151804 (cit. on p. 53).

[123] T. Aaltonen et al., *Precise Measurement of the W-Boson Mass with the CDF II Detector*, Physical Review Letters **108** (2012), ISSN: 1079-7114, URL: http://dx.doi.org/10.1103/PhysRevLett.108.151803 (cit. on pp. 53, 55).

[124] T. Aaltonen et al., *Combination of CDF and D0 W-Boson mass measurements*, Physical Review D **88** (2013), ISSN: 1550-2368, URL: http://dx.doi.org/10.1103/PhysRevD.88.052018 (cit. on p. 53).

[125] L. collaboration, *Measurement of the W boson mass*, 2021, arXiv: 2109.01113 [hep-ex] (cit. on p. 54).

[126] T. Aaltonen et al., *High-precision measurement of the W boson mass with the CDF II detector*, Science **376** (2022) 170 (cit. on pp. 55, 136, 154).

[127] V. M. Abazov et al., *Direct Measurement of the W-Boson Width*, Physical Review Letters **103** (2009), ISSN: 1079-7114, URL: http://dx.doi.org/10.1103/PhysRevLett.103.231802 (cit. on p. 56).

[128] T. Aaltonen et al., *Direct Measurement of the W Boson Width in $p\overline{p}$ Collisions at $\sqrt{s} = 1.96$ TeV*, Physical Review Letters **100** (2008), ISSN: 1079-7114, URL: http://dx.doi.org/10.1103/PhysRevLett.100.071801 (cit. on p. 56).

[129] L. Collaboration, *Measurement of the Ratio of Branching Fractions $\mathcal{B}(\overline{B}^0 \to D^{*+}\tau^-\overline{\nu}_\tau)/\mathcal{B}(\overline{B}^0 \to D^{*+}\mu^-\overline{\nu}_\mu)$*, Phys. Rev. Lett. **115** (11 2015) 111803, URL: https://link.aps.org/doi/10.1103/PhysRevLett.115.111803 (cit. on p. 58).

[130] A. Collaboration, *Test of the universality of τ and μ lepton couplings in W-boson decays with the ATLAS detector*, Nature Physics **17** (2021) 813 (cit. on p. 58).

[131] N. Andari et al., *Measurement of m_W with 7 TeV data: W boson mass measurement*, tech. rep., CERN, 2014, URL: https://cds.cern.ch/record/1976186 (cit. on pp. 58, 68, 88).

[132] D. Bardin, A. Leike, T. Riemann and M. Sachwitz,
Energy-dependent width effects in e^+e^--annihilation near the Z-boson pole,
Physics Letters B **206** (1988) 539, ISSN: 0370-2693,
URL: https://www.sciencedirect.com/science/article/pii/0370269388916279
(cit. on p. 59).

[133] C. Patrignani et al., *Review of Particle Physics*, Chin. Phys. C **40** (2016) 100001
(cit. on pp. 59, 61).

[134] ATLAS collaboration, *Studies of theoretical uncertainties on the measurement of the mass of the W boson at the LHC*, tech. rep., All figures including auxiliary figures are available at https://atlas.web.cern.ch/Atlas/GROUPS/PHYSICS/PUBNOTES/ATL-PHYS-PUB-2014-015: CERN, 2014, URL: https://cds.cern.ch/record/1956455 (cit. on pp. 59, 107).

[135] *Precision electroweak measurements on the Z resonance*, Physics Reports **427** (2006) 257,
ISSN: 0370-1573, URL:
https://www.sciencedirect.com/science/article/pii/S0370157305005119
(cit. on pp. 59, 103).

[136] ATLAS Collaboration, *Precision measurement and interpretation of inclusive W^+, W^- and Z/γ^* production cross sections with the ATLAS detector*, Eur. Phys. J. C **77** (2017) 367,
arXiv: 1612.03016 [hep-ex] (cit. on pp. 65, 78, 105).

[137] ATLAS Collaboration, *Measurement of the $t\bar{t}$ production cross-section using $e\mu$ events with b-tagged jets in pp collisions at $\sqrt{s} = 7$ and 8 TeV with the ATLAS detector*,
Eur. Phys. J. C **74** (2014) 3109, arXiv: 1406.5375 [hep-ex] (cit. on p. 65),
Addendum: Eur. Phys. J. C **76** (2016) 642.

[138] N. Kidonakis, *Next-to-next-to-leading-order collinear and soft gluon corrections for t-channel single top quark production*, Phys. Rev. D **83** (9 2011) 091503,
URL: https://link.aps.org/doi/10.1103/PhysRevD.83.091503 (cit. on p. 65).

[139] N. Kidonakis,
Next-to-next-to-leading logarithm resummation for s-channel single top quark production,
Phys. Rev. D **81** (5 2010) 054028,
URL: https://link.aps.org/doi/10.1103/PhysRevD.81.054028 (cit. on p. 65).

[140] N. Kidonakis, *Two-loop soft anomalous dimensions for single top quark associated production with a W^- or H^-*, Phys. Rev. D **82** (5 2010) 054018,
URL: https://link.aps.org/doi/10.1103/PhysRevD.82.054018 (cit. on p. 65).

[141] J. M. Campbell and R. K. Ellis, *Update on vector boson pair production at hadron colliders*,
Phys. Rev. D **60** (11 1999) 113006,
URL: https://link.aps.org/doi/10.1103/PhysRevD.60.113006 (cit. on p. 65).

[142] T. Gehrmann et al.,
W^+W^- Production at Hadron Colliders in Next to Next to Leading Order QCD,
Phys. Rev. Lett. **113** (21 2014) 212001,
URL: https://link.aps.org/doi/10.1103/PhysRevLett.113.212001 (cit. on p. 65).

[143] R. Nisius, *BLUE: combining correlated estimates of physics observables within ROOT using the Best Linear Unbiased Estimate method*, SoftwareX **11** (2020) 100468,
arXiv: 2001.10310 [physics.data-an] (cit. on pp. 90, 133).

[144] K. Cranmer, G. Lewis, L. Moneta, A. Shibata and W. Verkerke, *HistFactory: A tool for creating statistical models for use with RooFit and RooStats*, tech. rep., New York U., 2012, URL: https://cds.cern.ch/record/1456844 (cit. on p. 91).

[145] W. Verkerke and D. Kirkby, *The RooFit toolkit for data modeling*, (2003) (cit. on p. 91).

[146] L. Moneta et al., *The RooStats Project*, 2011, arXiv: 1009.1003 [physics.data-an] (cit. on p. 91).

[147] G. Cowan, K. Cranmer, E. Gross and O. Vitells, *Asymptotic formulae for likelihood-based tests of new physics*, The European Physical Journal C **71** (2011), ISSN: 1434-6052, URL: http://dx.doi.org/10.1140/epjc/s10052-011-1554-0 (cit. on p. 92).

[148] K. Cranmer, *Practical Statistics for the LHC*, 2015, arXiv: 1503.07622 [physics.data-an] (cit. on pp. 93, 97).

[149] L. Lista, *Statistical Methods for Data Analysis in Particle Physics*, Springer, 2016, ISBN: 978-3-319-20175-7 (cit. on p. 93).

[150] A. L. Read, *Linear interpolation of histograms*, Nucl. Instrum. Meth. A **425** (1999) 357 (cit. on p. 96).

[151] M. Baak, S. Gadatsch, R. Harrington and W. Verkerke, *Interpolation between multi-dimensional histograms using a new non-linear moment morphing method*, Nucl. Instrum. Meth. A **771** (2015) 39, arXiv: 1410.7388 [physics.data-an] (cit. on p. 96).

[152] R. Barlow and C. Beeston, *Fitting using finite Monte Carlo samples*, Computer Physics Communications **77** (1993) 219, ISSN: 0010-4655, URL: https://www.sciencedirect.com/science/article/pii/001046559390005W (cit. on p. 97).

[153] S. D. Drell and T.-M. Yan, *Massive Lepton-Pair Production in Hadron-Hadron Collisions at High Energies*, Phys. Rev. Lett. **25** (5 1970) 316, URL: https://link.aps.org/doi/10.1103/PhysRevLett.25.316 (cit. on p. 102).

[154] E. Mirkes, *Angular decay distribution of leptons from W-bosons at NLO in hadronic collisions*, Nuclear Physics B **387** (1992) 3, ISSN: 0550-3213, URL: https://www.sciencedirect.com/science/article/pii/055032139290046E (cit. on p. 103).

[155] J. Gao et al., *CT10 next-to-next-to-leading order global analysis of QCD*, Physical Review D **89** (2014), ISSN: 1550-2368, URL: http://dx.doi.org/10.1103/PhysRevD.89.033009 (cit. on p. 103).

[156] S. Catani, L. Cieri, G. Ferrera, D. de Florian and M. Grazzini, *Vector Boson Production at Hadron Colliders: A Fully Exclusive QCD Calculation at Next-to-Next-to-Leading Order*, Physical Review Letters **103** (2009), ISSN: 1079-7114, URL: http://dx.doi.org/10.1103/PhysRevLett.103.082001 (cit. on p. 103).

[157] T. Hahn, *Cuba—a library for multidimensional numerical integration*, Computer Physics Communications **168** (2005) 78, ISSN: 0010-4655, URL: http://dx.doi.org/10.1016/j.cpc.2005.01.010 (cit. on p. 103).

[158] J. Collins, D. E. Soper and G. Sterman, *Transverse momentum distribution in Drell-Yan pair and W and Z boson production*, Nuclear Physics B **250** (1985) 199, ISSN: 0550-3213, URL: https://www.sciencedirect.com/science/article/pii/0550321385904791 (cit. on p. 104).

[159] G. A. Ladinsky and C.-P. Yuan, *Nonperturbative regime in QCD resummation for gauge boson production at hadron colliders*, Physical Review D **50** (1994) R4239, ISSN: 0556-2821, URL: http://dx.doi.org/10.1103/PhysRevD.50.R4239 (cit. on p. 104).

[160] C. Balázs and C.-P. Yuan, *Soft gluon effects on lepton pairs at hadron colliders*, Physical Review D **56** (1997) 5558, ISSN: 1089-4918, URL: http://dx.doi.org/10.1103/PhysRevD.56.5558 (cit. on p. 104).

[161] S. Catani, D. de Florian, G. Ferrera and M. Grazzini, *Vector boson production at hadron colliders: transverse-momentum resummation and leptonic decay*, Journal of High Energy Physics **2015** (2015) 1, ISSN: 1029-8479, URL: http://dx.doi.org/10.1007/JHEP12(2015)047 (cit. on p. 104).

[162] T. Becher, M. Neubert and D. Wilhelm, *Electroweak gauge-boson production at small q_T: Infrared safety from the collinear anomaly*, Journal of High Energy Physics **2012** (2012), ISSN: 1029-8479, URL: http://dx.doi.org/10.1007/JHEP02(2012)124 (cit. on p. 104).

[163] R. Corke and T. Sjöstrand, *Interleaved parton showers and tuning prospects*, Journal of High Energy Physics **2011** (2011), ISSN: 1029-8479, URL: http://dx.doi.org/10.1007/JHEP03(2011)032 (cit. on p. 104).

[164] ATLAS Collaboration, *Measurement of the transverse momentum distribution of W bosons in pp collisions at $\sqrt{s} = 7$ TeV with the ATLAS detector*, Phys. Rev. D **85** (2012) 012005, arXiv: 1108.6308 [hep-ex] (cit. on p. 104).

[165] S. Dulat et al., *New parton distribution functions from a global analysis of quantum chromodynamics*, Physical Review D **93** (2016), ISSN: 2470-0029, URL: http://dx.doi.org/10.1103/PhysRevD.93.033006 (cit. on p. 105).

[166] L. A. Harland-Lang, A. D. Martin, P. Motylinski and R. S. Thorne, *Parton distributions in the LHC era: MMHT 2014 PDFs*, The European Physical Journal C **75** (2015), ISSN: 1434-6052, URL: http://dx.doi.org/10.1140/epjc/s10052-015-3397-6 (cit. on p. 105).

[167] ATLAS Collaboration, *Measurement of the angular coefficients in Z-boson events using electron and muon pairs from data taken at $\sqrt{s} = 8$ TeV with the ATLAS detector*, JHEP **08** (2016) 159, arXiv: 1606.00689 [hep-ex] (cit. on pp. 105, 107).

[168] M. W. Krasny, F. Dydak, F. Fayette, W. Płaczek and A. Siódmok, *$\Delta M_W \leq 10$ MeV/c^2 at the LHC: a forlorn hope?*, The European Physical Journal C **69** (2010) 379, ISSN: 1434-6052, URL: http://dx.doi.org/10.1140/epjc/s10052-010-1417-0 (cit. on p. 106).

[169] M. Krasny, F. Fayette, W. Płaczek and A. Siódmok, *Z boson as "the standard candle" for high-precision W boson physics at LHC*, The European Physical Journal C **51** (2007) 607, ISSN: 1434-6052, URL: http://dx.doi.org/10.1140/epjc/s10052-007-0321-8 (cit. on p. 106).

[170] F. Fayette, M. W. Krasny, W. Płaczek and A. Siódmok, *Measurement of $M_{W^+} - M_{W^-}$ at LHC*, The European Physical Journal C **63** (2009) 33, ISSN: 1434-6052, URL: http://dx.doi.org/10.1140/epjc/s10052-009-1084-1 (cit. on p. 106).

[171] G. Bozzi, L. Citelli and A. Vicini, *Parton density function uncertainties on theWboson mass measurement from the lepton transverse momentum distribution*, Physical Review D **91** (2015), ISSN: 1550-2368, URL: http://dx.doi.org/10.1103/PhysRevD.91.113005 (cit. on p. 106).

[172] J. Pumplin et al., *Uncertainties of predictions from parton distribution functions. II. The Hessian method*, Phys. Rev. D **65** (1 2001) 014013, URL: https://link.aps.org/doi/10.1103/PhysRevD.65.014013 (cit. on p. 106).

[173] H1 and Z. Collaborations, *Combination of Measurements of Inclusive Deep Inelastic $e^{\pm}p$ Scattering Cross Sections and QCD Analysis of HERA Data*, 2015, arXiv: 1506.06042 [hep-ex] (cit. on p. 107).

[174] M. Bonvini, A. S. Papanastasiou and F. J. Tackmann, *Matched predictions for the $b\bar{b}H$ cross section at the 13 TeV LHC*, Journal of High Energy Physics **2016** (2016), ISSN: 1029-8479, URL: http://dx.doi.org/10.1007/JHEP10(2016)053 (cit. on p. 107).

[175] *Study of alignment-related systematic effects on the ATLAS Inner Detector tracking*, tech. rep., All figures including auxiliary figures are available at https://atlas.web.cern.ch/Atlas/GROUPS/PHYSICS/CONFNOTES/ATLAS-CONF-2012-141: CERN, 2012, URL: https://cds.cern.ch/record/1483518 (cit. on p. 108).

[176] L. Devroye, *Non-Uniform Random Variate Generation*, Springer, 1986, URL: http://www.eirene.de/Devroye.pdf (cit. on p. 116).

[177] A. Dimitrievska, N. Vranjes, M. Schott and M. Boonekamp, *Measurement of m_W at 7 TeV: Hadronic recoil corrections*, tech. rep., CERN, 2015, URL: https://cds.cern.ch/record/2013274 (cit. on p. 118).

[178] I. T. Jolliffe, *Principal Component Analysis*, vol. 2, New York: Springer, 2002, ISBN: 978-0-387-95442-4 (cit. on p. 124).

[179] I. T. Jolliffe and J. Cadima, *Principal component analysis: a review and recent developments*, Philosophical Transactions of the Royal Society A: Mathematical, Physical and Engineering Sciences **374** (2016) 20150202, eprint: https://royalsocietypublishing.org/doi/pdf/10.1098/rsta.2015.0202, URL: https://royalsocietypublishing.org/doi/abs/10.1098/rsta.2015.0202 (cit. on p. 124).

[180] K. P. F.R.S., *LIII. On lines and planes of closest fit to systems of points in space*, The London, Edinburgh, and Dublin Philosophical Magazine and Journal of Science **2** (1901) 559, URL: https://doi.org/10.1080/14786440109462720 (cit. on p. 124).

[181] H. Hotelling, *Analysis of a complex of statistical variables into principal components*, Journal of Educational Psychology (1933) 417, URL: https://doi.org/10.1037/h0071325 (cit. on p. 124).

[182] F. Pedregosa et al., *Scikit-learn: Machine Learning in Python*, Journal of Machine Learning Research **12** (2011) 2825 (cit. on p. 124).

[183] M. Boonekamp, *Private communication*, 2022 (cit. on p. 138).

[184] H. Schmitz, *Messung des Verhältnisses der Verzweigungsverhältnisse der Zerfälle $W \to \tau\nu \to l\nu\nu\nu$ und $W \to l\nu$*, 2019, URL: https://www.lhc-ilc.physik.uni-bonn.de/ergebnisse/dateien/t00000103.pdf?c=t&id=103 (cit. on pp. 151, 152).

[185] N. Ainouz, *Using impact parameter information for leptonic τ decays in the measurement of the $W \to \mu\nu$ decay*, 2021, URL: https://www.lhc-ilc.physik.uni-bonn.de/ergebnisse/dateien/t00000125.pdf?c=t&id=125 (cit. on p. 151).

[186] ATLAS Collaboration, *Prospects for the measurement of the W-boson mass at the HL- and HE-LHC*, tech. rep., All figures including auxiliary figures are available at https://atlas.web.cern.ch/Atlas/GROUPS/PHYSICS/PUBNOTES/ATL-PHYS-PUB-2018-026: CERN, 2018, URL: https://cds.cern.ch/record/2645431 (cit. on p. 155).

[187] HiLumi LHC Collaboration, *HL-LHC Preliminary Design Report: Deliverable: D1.5*, (2014), URL: http://cds.cern.ch/record/1972604 (cit. on p. 155).

[188] FCC Collaboration, *HE-LHC: The High-Energy Large Hadron Collider*, The European Physical Journal Special Topics **228** (2019) 1109 (cit. on p. 155).

[189] E. Waring, *VII. Problems concerning interpolations*, Philosophical Transactions of the Royal Society of London **69** (1779) 59, eprint: https://royalsocietypublishing.org/doi/pdf/10.1098/rstl.1779.0008, URL: https://royalsocietypublishing.org/doi/abs/10.1098/rstl.1779.0008 (cit. on p. 183).

[190] H. Igel, *Lecture on Numerical Geophysics 2*, URL: https://www.geophysik.uni-muenchen.de/~igel/downloads/nmgiifemelements.pdf (cit. on p. 183).

List of Figures

List of Tables

Glossary

2HDM two Higgs-doublet model. 28

BDT Boosted Decision Tree. 43

BSM beyond Standard Model. 18, 23, 26–28, 44, 63, 251

CaloTag muons Calorimeter-tagged muons. 42

CB muons Combined muons. 42–44

CKM matrix Cabibbo-Kobayashi-Maskawa matrix. 10, 17, 21, 50

CL confidence level. 19, 28, 55, 106, 140, 158, 251, 254

CR control region. 75–77, 79, 81, 82, 92, 142, 174–179

CR1 control region 1. 81, 82, 121, 122, 179, 252, 255

CR2 control region 2. 81, 82, 121, 122, 179, 252, 255

CSCs Cathode Strip Chambers. 37, 42

d.o.f. degree of freedom. 14, 28

e.o.m. equation of motion. 5

ECAL Electromagnetic Calorimeter. 35–37, 40, 41, 110, 113

EF Event Filter. 38, 39, 43

EW electroweak. 6, 8–10, 14–18, 21, 27, 54, 55, 74–76, 78, 85, 102, 103, 120, 134, 136, 138, 140, 144, 149, 220, 223, 228, 251, 259

FCAL Forward Calorimeter. 36, 41

FR1 fitting region 1. 76–78, 80, 175, 177, 178, 252, 255

FR2 fitting region 2. 76–78, 80, 175, 177, 178, 252, 255

FSR final state radiation. 51, 102, 120

GRL Good Run List. 39, 65, 67, 69, 71, 72, 161

HCAL Hadronic Calorimeter. 36

HEC Hadronic End-Cap Calorimeter. 36

HLT High-Level Trigger. 38, 39, 41, 43

ID Inner Detector. 33–36, 38, 40–43, 66, 108–110, 112, 113, 151, 251

IP interaction point. 30–32, 37, 41, 116

ISR initial state radiation. 51, 102–104, 107, 120

L1 first level. 38, 39, 41–43

L2 second level. 38, 39, 43

LAr Liquid-Argon Calorimeter. 35, 38, 67, 69, 71, 72, 161

LEP Large Electron-Positron Collider. 53–58, 60, 61, 133, 147

LHC Large Hadron Collider. 29–32, 37–40, 50, 53, 54, 57, 107, 138, 251

LINAC 2 LINear ACcelerator 2. 29

LINAC 4 LINear ACcelerator 4. 29

LO leading-order. 7, 18, 21, 45, 46, 50–53, 120, 136

MC Monte Carlo. 45–47, 56, 67–72, 74–76, 78, 85–88, 90, 91, 97, 98, 102, 104–106, 108, 109, 117, 120–122, 127, 149, 151, 152, 161, 163–167, 169–173, 211–213, 259

MDTs Muon Drift Tubes. 37, 38, 42, 43

MS Muon Spectrometer. 37, 38, 41–44, 67, 112, 251

MSSM Minimal Supersymmetric Standard Model. 27, 28, 55

NLO next-to-leading-order. 7, 21, 45, 46, 65, 203, 260

NNLO next-to-next-to-leading-order. 65, 85, 103, 105, 107

NP nuisance parameter. 91–93, 96–98, 101, 128, 131, 132, 136, 138–140, 142, 144–146, 149, 150, 211–213, 219, 226, 231, 253, 257

p.d.f. probability density function. 91, 97

PBS Proton Synchrotron Booster. 29

PCA Principal Component Analysis. 124–126, 131, 194–202, 253, 256

PDF parton distribution function. 24, 25, 45, 46, 59, 105–107, 127, 134, 135, 138–140, 144, 145, 149, 220, 223, 228, 251, 259

Pixel Pixel Detector. 33, 35, 39, 41, 151

PLH fit profile likelihood fit. 58, 60, 85, 91–94, 97–99, 122, 124, 125, 127–133, 136–139, 141–144, 148, 151, 183, 211–214, 217, 218, 220–222, 252, 253, 257, 260

POI parameter of interest. 65, 91, 93, 96, 128, 129, 131, 132, 140, 146, 150, 186, 211–214, 219, 226, 231, 255, 259

PS Proton Synchrotron. 29

PV primary vertex. 66, 69, 71, 72, 161

QCD Quantum Chromodynamics. 10–12, 21, 23–25, 51, 75, 102–108, 138, 157, 259

QED Quantum Electrodynamics. 6–8, 12, 51, 102, 251

RF radio frequency. 30

RMS root-mean-square. 124–126, 194–202

ROBs Readout Buffers. 39

RoIs Regions of Interest. 38, 39, 41, 43

RPCs Resistive Plate Chambers. 37, 67

SA muons Stand-Alone muons. 41–43

SCT Silicon Tracker. 33–35, 41

SF scale factor. 41, 47, 67, 88, 111, 114, 117, 125, 126, 196–202, 252, 256

SM Standard Model. 3–5, 8, 10, 12, 14, 15, 17–19, 23, 26–29, 45, 55, 57–59, 63, 251

Sp$\bar{\text{p}}$S Super Proton-Antiproton Synchrotron. 53, 153

SPS Super Proton Synchrotron. 29

SR signal region. 75, 76, 78–81, 90, 92, 98, 121, 179, 228

SSB spontaneous symmetry breaking. 12

ST muons Segment-tagged muons. 42

SUSY Supersymmetry. 27, 28, 44, 55

TGCs Thin Gap Chambers. 38

Tile Tile Calorimeter. 36

TRT Transition Radiation Tracker. 34, 41, 43

VEV vacuum expectation value. 13, 14

Acknowledgements

First of all, I am very grateful to Klaus Desch for allowing me to do my PhD in his research group. From my first appearance as a Bachelor student, he gave me personal and scientific freedom but provided me with helpful suggestions whenever needed. I appreciate your support whenever there has been trouble, your help, and your inspiration. It was and still is valuable to have a confidential relationship with your boss. In addition, I would like to thank Philip Bechtle, my supervisor and mentor, for answering me an uncountable number of questions always with a precise answer if asked for - regardless of scientific background or not. Thank you for your motivation, your enthusiasm, your trust, and all the non-work-related conversations. Christian Grefe always helped me out when I had a programming-related question and gave me continuously helpful suggestions. I thank Ian Brock, the co-head of our group, for all his tips, the discussions, the months we spent together at CERN in 2017, and last but not least serving as my second referee.

I am extremely thankful to Steffen Schaepe and Oliver Ricken who taught me a lot during the beginning of my scientific career. I still admire your balance between serious (scientific) work and fun conversations. I enjoyed all the discussions and the mutual support with Michael Hübner who became a true friend over time. Thank you for listening and often sharing the same opinion on hot topics. My eight months at CERN were real fun, also thanks to Anjishnu Bandhyophadyay who introduced me to the world of literature, series, and Indian cuisine. Thank you for always drinking a glass of wine or beer with me in the cave! The lively atmosphere in the Desch-Brock research group, which came alive in the numerous jamborees, facilitated the work quite a lot. Hence, I would further like to thank Björn Sarrazin, Martin Schultens, Maike Hansen, Ozan Arslan, Irina Cioară, Rui Zhang, Regina Moles-Valls, Matthias Hamer, Tobias Klingl, Lara Schildgen, Patrick Bauer, Jan Heinrichs, Lena Herrmann, Michael Lupberger, Christoph Krieger, Tobias Schiffer, Markus Gruber, Laura Rodríguez Gómez, Florian Hinterkeuser, Tanja Holm, Christian Kirfel, Federico Caprilles Diaz, Florian Kirfel, any many more.

A software thesis would be impossible without the needed computing infrastructure. Therefore, I would like to thank the whole IT team of the institute for always providing a reliable cluster. In particular, my thank goes to Peter Wienemann and Oliver Freyermuth for their explanations, their patience when my jobs were slowing down the cluster, and their help also regarding my webmaster related tasks. I thank Barbara Valeriani-Kaminski for the opportunity to collaborate in many outreach projects and the nice conversations. I am grateful for the support I received from the administration section of the institute, namely Andrea Fürstenberg, Jacqueline Weigelt, and Nicole Felde, who backed me in all these nasty bureaucratic belongings.

Outside of the Bonn analysis group and the institute, I met many people who helped me finish this thesis. The analysis group of the W mass reanalysis effort directly contributed to the results of the thesis. I want to thank Maarten Boonekamp and Matthias Schott for intense discussions, good suggestions, and the supervision of my work. Furthermore, I want to mention Oleh Kivernyk,

Aleksandra Dimitrievska, Jakub Kremer, Nenad Vranješ, Philip Kennedy, and Lennart Adam as part of the analysis group. It was also fun to start with the lepton universality measurement together with Andreas Düdder. I had the opportunity to participate in two summer schools where I had an educational and fun time in Maria Laach together with Dominik, Mario, Yannick, Julia, Frank, and Manuel, and expanded my horizon at the Baikal Summer School in Bolshie Koty.

Besides Klaus Desch and Ian Brock, my thanks go to Claude Duhr and Ulrike Endesfelder for accepting my inquiry to be a member of my PhD committee. I would like to thank my proof-reading team consisting of Dominik Köhler, Christian Grefe, Jan Heinrichs, Lena Herrmann, Anjishnu Bandhyophadyay, Michael Hübner, Philip Bechtle, Philip Kennedy, and Stefan Kriesmer.

A PhD thesis is not possible with the previous bachelor's and master's studies. Without my classmates' group, also known as the "physics skittles club" or the "Kemal fan club", I would not have finished my degree and did not have had such an amazing time in Bonn. I would like to thank Till, Hendrik, Peter, Sahand, Christian, Erik, Jannes, David, and Roberto. I am grateful for all the opportunities to play some music in different groups that distracted me from work and introduced me to many great people and friends.

Last but not least, my sincere thanks go to my whole family. I want to explicitly mention my parents who supported and promoted me in many ways always making sure I also develop my social intelligence. Words cannot express how thankful I am but I would not have been in the position to start and complete my PhD without you. I am very grateful to my two brothers for their backing even though they think I am the biggest wiseacre of the family. I would also like to thank my grandparents and great-grandparents who offered me a happy childhood. In addition, I would like to mention my godparents Uti and Thomas ("Louis") for their enduring support. Last but not least, I want to thank Anna for her love, her patience, her care, and many more things that would go beyond the scope of this thesis. Our son Marlon is the greatest gift that ever came into my life. I love you both and I am looking forward to the many years to come!